Atmospheric Pressure Plasma Sources for Plasma Medicine

by

Amanda M. Lietz

A dissertation submitted in partial fulfillment
of the requirements for the degree of
Doctor of Philosophy
(Nuclear Engineering and Radiological Sciences)
in the University of Michigan
2019

Doctoral Committee:

Professor Mark J. Kushner, Chair
Professor John E. Foster
Professor Eric Johnsen
Professor Ryan D. McBride
Professor Krista Wigginton

ORCiD: 0000-0001-6423-5042

lietz@umich.edu

For Matt and our growing family.

ACKNOWLEDGEMENTS

During my PhD at the University of Michigan, I have had the good fortune to work with many amazing people, and I can only begin to thank them here. First, I would like to thank my advisor, Mark J. Kushner. He has always taken the time to give me advice when I needed it, and has been incredibly supportive of all of my goals. He is an inspiration through his hard work and his dedication to all of his students as well as the broader research community.

I would also like to extend my gratitude to all my labmates, past and present, for many insightful conversations, collaborations, and chalk talks. I've learned so much from each of you and am grateful for all the time we have spent together. Beyond that, this group has made the time much more enjoyable, during conference travel, meetings, and long days at the office. Thanks to Shuo Huang, Chad Huard, Juliusz Kruszelnicki, Steven Lanham, Michael Logue, Seth Norberg, Runchu Ma, Aram Markosyan, Soheila Mohades, Guy Parsey, Jordyn Polito, Chenhui Qu, Wei Tian, Peng Tian, Xifeng Wang, and Yiting Zhang.

During my PhD studies, I had the opportunity to spend a semester at Sandia National Laboratories working with Dr. Edward V. Barnat. I am extremely grateful not only for the opportunity to work there, but to Ed for welcoming a modeler into his experimental laboratory, being extremely generous with his time, and supporting the project at every step along the way.

I would also like to thank several other collaborators who have made this work possible. Xavier Damany, Dr. Eric Robert, and Dr. Jean-Michel Pouvesle were a pleasure to work with and I am appreciative of all of their efforts. Dr. John Foster and several students in his group

including Kenneth Engeling, Selman Mujovic, and Joseph Groele were also very helpful to me on the experimental design in this work.

I am also grateful for the colleagues in the low temperature plasma research community globally. There is a welcoming, supportive, and collaborative attitude in this research field that has made my graduate school experience much more gratifying and positive. I have made many friends and received great advice and feedback on all the work in this dissertation countless times. I am honored to be a part of this research community, and hope to continue that involvement into the future. I would also like to acknowledge the financial support I have received from the National Science Foundation and the Department of Energy in these areas which has made this work possible.

To my committee members Dr. John E. Foster, Dr. Eric Johnsen, Dr. Ryan D. McBride, and Dr. Krista Wigginton, I am grateful for their feedback over the course of my PhD, both on the technical aspects and on my career and research direction. I am also grateful to each of them for reviewing this dissertation and providing their valuable insights.

I would like to thank my parents for supporting my academic endeavors from the start. They have encouraged my interest in math and science, reassured me in difficult moments, and financially supported much of my education.

Lastly, and most importantly, I would like to thank my husband, Matthew Lietz, without whom this would not have been possible. He has done countless things that have made all of this work possible. He moved to Ann Arbor with me, he changed his name when we got married so I could have continuity in my publication record, and he supported me being gone for several months for an internship. His patience and emotional support through all the trying moments of

graduate school, especially in the past few months, has been invaluable. I look forward to our future adventures together.

TABLE OF CONTENTS

LIST OF FIGURES

LIST OF TABLES

LIST OF APPENDICES

ABSTRACT

Several low temperature, atmospheric pressure plasma sources have been developed in recent years, opening new possible applications for plasmas in environmental and biomedical fields. Low temperature atmospheric pressure plasma treatment has recently been shown to kill bacteria, heal chronic diabetic wounds, and selectively kill cancer cells. The biomedical outcomes are primarily attributed to the production of reactive oxygen and nitrogen species, which include OH, $O_2(^1\Delta)$, HO_2, and NO. Tailoring the composition of reactive species produced by the plasma that solvate in the liquid is critical to providing a consistent outcome in a given application.

Two models are used to investigate this problem. *GlobalKin* is a 0-D plasma kinetics model which considers the plasma chemistry to be a well stirred reactor. *GlobalKin* has been upgraded to include a liquid module, which considers well-stirred liquid chemistry coupled with the plasma chemistry. This model runs quickly, so large parameter spaces and complex chemistries can be explored. *nonPDPSIM* is a 2-dimensional plasma hydrodynamics model which solves Poisson's equation, charged species transport, and the chemistry of charged and neutral species. Photoionization, fluid dynamics effects, and solvation into liquid are all included. Updates to *nonPDPSIM* include improvements in the liquid solvation calculation, performance improvements based on switching from numerical to analytical derivatives, and the

ability to more tightly couple the fluid dynamics calculation and the plasma chemistry calculation.

A GlobalKin study of air dielectric barrier discharge treatment of liquid covered tissue has highlighted the role of HO_2NO_2 in decaying to deliver HO_2 and NO_2 at long timescales. Gas flow can be used to tailor the ratio of various reactive species delivered to the liquid, particularly decreasing HNO_x at higher gas flow rates. A study of water droplets and aerosols treated in an air plasma has also shown the importance of droplet size and density in controlling the densities of species in the liquid based on their Henry's law constants (their proclivity to solvate in water).

nonPDPSIM has been used to model helium atmospheric pressure plasma jets (APPJs) operating in humid air. The plasma in these devices propagate as an ionization wave, which lasts for 10s to 100s of ns and is repetitively pulsed. The effects of nearby grounds and impurities in the helium, which are often not controlled, were revealed in this study. Other parameters such as gas composition and electrode configuration were also examined for their effect on ionization wave propagation and the resulting reactive species production. The behavior of a unique APPJ source, referred to as a multi-jet, is also explored. This relies on the propagation of an ionization wave through holes in a dielectric tube to form an array of jets. Qualitative agreement has been shown with fast camera imaging of the ionization wave.

Another study has shown the cause of plasma-induced flow instabilities to be the expansion of gas after localized gas heating during the discharge pulse (10s of ns). An acoustic wave propagates out of the plasma jet and disturbs the shear layer between the high velocity helium and the slow ambient air, causing a shear instability.

Experimental measurements of spatially and time resolved electron densities in a He APPJ contacting a dielectric surface were performed in a well-controlled environment. The

observed electron densities and ionization wave behavior were compared to modeling, and highlight the capabilities and limitations of this model.

Chapter 1 Introduction

Plasma is the fourth state of matter, containing charged species including positive ions, electrons, and/or negative ions. Low temperature plasmas (LTPs) are currently being investigated for therapeutic uses including treatment selectively killing cancer, chronic ulcers and psoriasis.[1–4] In order to bring these therapeutic applications to fruition, a more complete understanding of the behavior of certain low temperature, atmospheric pressure plasma sources is required. The focus of this dissertation is on the use of computational modeling to better understand the physics and chemistry of these LTP sources.

In this chapter, a general background on LTPs is discussed (Sec. 1.1). Several examples of atmospheric pressure plasma sources and their basic dynamics are described (Sec. 1.2), followed by the key findings of studies on plasma medicine and similar applications (Sec. 1.3). Approaches to plasma modeling and key modeling studies in this field are also discussed (Sec. 1.4). The scope and organization of the remaining chapters of this dissertation are then described (Secs. 1.5-1.6).

1.1 Low Temperature Plasma (LTP)

Plasma contains charged species having a large enough density that they respond to electric and magnetic fields. Low temperature plasmas, which are the focus of this work, have been used in manufacturing to etch and deposit materials in microelectronics and to activate hydrophobic plastics for the application of inks.[5–7] More recently, plasmas have been investigated for their therapeutic potential in the field of plasma medicine.[8,9]

Though plasma may seem like an uncommon state here on Earth, it is believed to be the most abundant type of ordinary matter in the universe.[10] Plasmas span a parameter space that is extremely large, and can therefore have a diverse set of behaviors. As shown in Fig. 1.1, plasmas exist in a range of 30 orders of magnitude in density and 6 orders of magnitude in temperature. Many space plasmas have lower temperature and density, while higher density and temperature plasmas include astrophysical plasmas and those used in nuclear fusion devices. The ionization fraction of these plasmas also spans a large parameter space, with higher energy density plasmas often being fully ionized or multiply ionized, and low energy density laboratory plasmas with ionization fractions on the order of parts per million or less.

Quasineutrality is an important property of plasmas. Though they contain charged species, a plasma is charge neutral if averaged in space and time.[10] Plasmas often deviate from neutrality on short timescales or small length scales, as the charged species undergo stochastic fluctuations and respond to electric fields that are changing in space and time. The characteristic timescale below which non-neutrality can occur is governed by the plasma frequency. The plasma frequency is, conceptually, the frequency of oscillation about charge neutrality if the charged species are spatially offset.[11] In the case of low temperature, electron-ion plasmas, the plasma frequency is the same as the electron plasma frequency, and is

$$\omega_{pe} = \sqrt{\frac{e^2 n_0}{\varepsilon_0 m_e}} \tag{1.1}$$

where n_0 is the plasma density, e is the electron charge, m_e is the electron mass, and ε_0 is the permittivity of free space. If the positive and negative charges are spatially offset in a perturbation, the electric fields which are generated by the space charge accelerate the charged particles back toward neutrality on this timescale. In the plasmas discussed in this dissertation

the typical plasma frequency is 10^9 to 10^{12} Hz, corresponding to timescales on the order of picoseconds to nanoseconds. Because of the rapid evolution that occurs in plasma sources used for plasma medicine, non-neutrality often occurs, as will be seen throughout the results in this dissertation. The Debye length is the length scale over which a plasma can be non-uniform. The electron Debye length, which is the dominant Debye length in low temperature electron-ion plasmas, is

$$\lambda_D = \sqrt{\frac{\varepsilon_0 k_B T_e}{e^2 n_0}} \tag{1.2}$$

where ε_0 is the permittivity of free space, k_B is Boltzmann's constant, T_e is the electron temperature, e is the electron charge, and n_e is the electron density.[10] The Debye length, which in the LTPs discussed in this dissertation are typically 1 μm – 1 mm, becomes important when the plasma is interacting with materials. If a charged object is immersed in a plasma, the plasma will respond to the electric field with net charge surrounding that body. The characteristic length scale of this non-neutrality is λ_D, and this region is called the sheath. Sheaths develop whenever a plasma is in contact with a surface, and are therefore important to consider when treating a surface is the primary use of a plasma.

The plasmas studied in this dissertation are LTPs, which occur commonly in nature as well as in laboratory discharges. These plasmas differ from thermal plasmas by their non-equilibrium thermodynamic nature. Thermal plasmas occur when a gas becomes hot enough to exceed the ionization energy of the atoms it contains (for full ionization this requires ~10 eV per atom or molecule). In contrast, LTPs have neutral gas temperatures which can be near 300 K (equivalent to 0.025 eV), but still contain charged species. The ionization fraction of LTPs is often low, typically with only one charged particle for every 10^5 to 10^{10} neutral gas particles.

Ionization sustains the plasma, most often electron impact ionization, as charged species are continually lost due to electron-ion recombination. To cause ionization, some of the electrons have energies greater than the ionization energy of the background gas (~10 eV). The electron temperature (T_e), which refers to the average electron energy, is often much greater than the temperature of the surrounding gas, with typical values in the range of 2-20 eV.

Electron energy distribution functions (EEDFs) in LTPs often diverge significantly from the Maxwell-Boltzmann distribution that would occur at thermodynamic equilibrium.[12] When energetic electrons collide with neutral gas molecules, they can undergo elastic or inelastic collisions. During elastic collisions, the total kinetic energy is conserved, and in most cases, the velocity of the neutral particle increases, and the electron loses energy to gas heating. With the large mass difference between electrons and atoms or molecules, only a small fraction of the electron's energy can be transferred in each collision. Many types of inelastic collisions can also occur, and have a much greater effect on the EEDF. The inelastic collision, electron impact ionization

$$e(\varepsilon > \varepsilon_{iz}) + M \rightarrow M^+ + e + e, \qquad (1.3)$$

only occurs when the colliding electron energy (ε) is greater than the ionization energy of the neutral atom or molecule, referred to as M. This selective reactivity depletes electrons with $\varepsilon > \varepsilon_{iz}$ from the EEDF, sometimes resulting in a distribution which is cutoff above the threshold energy. Other important inelastic collisions include electronic excitation, dissociation of molecules, and vibrational or rotational excitation of molecules. As a result, the EEDF in a LTP is a function of the number density of the background gas, the chemical composition of this gas, and the electric field which is accelerating the electrons.

1.2 Atmospheric pressure plasma sources

Many LTPs, such as those used in microelectronics fabrication, are operated at a reduced pressure on the order of mTorr or Torr (100s of mPa to 100s of Pa). However, more recently, the number of low temperature, atmospheric pressure plasma sources have expanded and extended the potential applications for plasma processing. Substrates which are not compatible with a vacuum environment (for example, biological tissue) can now be more easily treated by plasmas. Because atmospheric pressure plasmas do not require expensive vacuum equipment, this also broadens the applicability of these systems to less valuable products than microelectronics.

In medical and agricultural applications of atmospheric pressure LTPs, the gas temperatures must be kept close to room temperature to avoid damage. Atmospheric pressure LTPs are often pulsed to limit the total energy deposition, and therefore the gas heating. The plasma can be pulsed by applying short voltage pulses, or by intrinsically limiting the current. The most common method is some type of dielectric barrier discharge (DBD), which contains a dielectric covering one or both of the electrodes. The dynamics of a DBD are depicted in Fig. 1.2. When the voltage (AC or pulsed DC) is applied, a discharge forms, charging the surface of this dielectric until its capacitance fills, and there is no longer an electric field across the gap to sustain the discharge. This charging often occurs in 10s to 100s of ns.

Another popular plasma source is an atmospheric pressure plasma jet (APPJ). There are a large variety of APPJ designs, with the main unifying feature being a gas flow through a tube or channel from which a plasma propagates.[13] The applied power can range from a few Hz to GHz, with kHz or radiofrequency (MHz) frequencies being the most common. These frequencies do not apply so much energy as to result in large gas heating, but apply enough energy that significant densities of plasma-produced species result. In many of these APPJ

designs, such as the one shown in Fig. 1.3, the charging of a dielectric limits the current per cycle, as would be done in a DBD.

Although APPJs appear continuous, fast camera imaging (such as that of Fig. 1.4) has shown that they are made up of distinct ionization waves (IWs). These IWs are also referred to as "plasma bullets". The light detected in the imaging comes from the photon emission by electronically excited states. The IWs propagate at speeds of $10^4 - 10^5$ m/s, fast enough to allow for a divergence from neutrality, and space charge occurs at the wave front.[14]

In both cathode- and anode-directed IWs, electron impact ionization is typically the dominant source of electrons. When an IW originates from a negatively biased electrode, electrons which are at the leading edge of the IW are accelerated ahead of the IW by the electric field. This electron drift supplies a small number of electrons ahead of the IW which can cause an avalanche and sustain the propagation. For positive polarity, any electrons generated near the front of the IW are accelerated back toward the bulk plasma, as shown in Fig. 1.5. In this case the propagation of the plasma depends on other sources to provide a small number of electrons ahead of the IW and sustain the propagation. Depending on the system, these include photoionization of impurities, the small number of charged species which are present thermodynamically, or remaining charged species from previous plasma pulses.

1.3 Medicine, sterilization, and water treatment

In recent years, plasma treatment has been shown to influence biological systems in unique ways. Plasma treatment of cells can selectively kill bacteria and leave eukaryotic cells unharmed, and therefore can be used to sterilize chronic wounds and surfaces [15,16] or treat produce to increase shelf life [17]. Plasma-treated (i.e. "plasma-activated") liquids including water, saline and cell culture, have also been shown to have similar effects on biological

systems.[18,19] It was therefore concluded that the plasma-produced chemistry, which can be stored for short periods in a liquid, is a major mechanism of interaction between the plasma and biology.

The unique non-equilibrium chemistry which influences biological systems is produced when LTPs contain molecular gases. The energetic electrons in the plasma collide inelastically with molecules, for example, nitrogen, resulting in the following processes

$$e + N_2 \rightarrow N + N + e, \tag{1.4}$$

$$e + N_2 \rightarrow N_2^* + e, \tag{1.5}$$

$$e + N_2 \rightarrow N_2^+ + e + e, \tag{1.6}$$

where N_2* refers to an electronically excited state of N_2. When air is present in the plasma system, these types of collision produce ions, as well as reactive oxygen and nitrogen species (RONS) including oxygen atoms (O), ozone (O_3), hydroxyl radicals (OH), and nitrogen oxides (NO_x). It is these RONS which have powerful effects on many biological systems. Since the discovery of this property, experiments have been done to assess the efficacy of LTPs in biomedical applications. This section provides an overview of the important findings relevant to plasma medicine, as well as to other similar applications including sterilization and water treatment.

One of the first and simplest indications that LTPs would be interesting in biomedical applications came from the observation that atmospheric pressure plasma treatment resulted in the inactivation of bacteria. Applying plasma directly to bacteria was a natural extension of the use of LTPs to generate ozone in water treatment, which began in the 1850s.[20] In 2000, Laroussi *et al*. observed successful inactivation by nonthermal plasma of bacteria both on surfaces and suspended in broth.[21] Since then, more research has been done to optimize the

efficacy of bacterial inactivation using different plasma sources and operating conditions, as well as to identify the mechanisms for this inactivation. For example, Ke *et al*. showed that in a pin-to-plane discharge, air was more effective than O_2 or N_2 alone, resulting in more than 99% inactivation of *E. coli* after 20 s of plasma treatment.[3] Correlations with measurements of RONS indicate a synergistic effect of NO_2^- and H_2O_2. Treatment of cultures by an argon atmospheric pressure plasma jet has been used to kill endospores, which can be useful in the healing of chronic wounds.[22]

V. S. S. K. Kondeti *et al*. concluded that the chlorine present in saline solutions can react with the plasma produced species, producing ClO^-_{aq} which contributes to the bactericidal effect, but if chlorine ions are not present in the solution, O_{aq}, $O_2^-{}_{aq}$, and OH_{aq} play more significant role in deactivation of bacteria.[23] Privat-Maldonado *et al*. showed that organic molecules present in the liquid containing the bacteria can reduce the bactericidal effect of plasma.[24] Bacteria suspended in phosphate buffered saline were inactivated at a much higher rate than those in media containing organics (a 90-99% reduction rather than a 99.9-99.99% reduction in bacteria). This indicates that the reactive species produced by the plasma which have the strongest bactericidal effects also react with other organic molecules.

Many chronic wounds are exacerbated by a significant bacterial load, and therefore the antibacterial properties of plasma can also be utilized in wound healing. In 2006, Fridman *et al*. directly treated living tissue with an air DBD, resulting in deactivation of bacteria without harming the tissue, indicating that LTPs could be beneficial to wound healing.[25] Xu, *et al*. later showed that wounds in mice heal twice as fast when treated daily by an APPJ for 30 seconds.[26] Bacterial loads in chronic wounds were measured in a clinical trial, and plasma reduced these loads in chronic wounds 34% more than standard treatment.[27]

The reduction of bacterial load may not be the only mechanism through which plasma treatment improves wound healing, because there is also a more systemic effect on the immune and healing response. The complex influence of plasma on a wound has been investigated by both animal models and human clinical trials. In the mouse study by Xu, *et al*., the right dose of plasma treatment inactivated bacteria and stimulated fibroblast proliferation (promoting collagen formation) without causing cell death. In clinical trials, treatment of chronic wounds with an Ar LTP caused reduction in wound sizes without any reported side effects.[2]

Plasma treatment has also been shown to selectively kill cancer cells over normal cells. In 2006, Stoffels *et al*. first observed apoptosis, or programmed cell death, in cancer cells after treatment with a He APPJ, though its occurrence was relatively rare (3% of cells).[28] Soon after, Fridman *et al*. observed more prevalent apoptosis in 73% of treated cancer cells.[29] In 2010, Georgescu and Lupu showed that this plasma-induced apoptosis is selective to cancer cells, with 74% of cancer cells undergoing apoptosis, and none observed in normal cells.[30] This selective behavior was soon verified by other studies using a variety of cell types and plasma sources.[9] A review by Schlegel *et al.* on plasma for cancer treatment concluded that shorter treatment times stop tumor growth, while longer treatment times cause cell death.[9]

The mechanism for the effect of plasma treatment on cancer cells, is a subject of active investigation in the field. The simplest and one of the earliest proposed explanations is that cancer cells are more metabolically active, and therefore have a higher baseline level of oxidative stress. By introducing externally RONS at the correct dose, it is possible to exceed the threshold oxidative stress for apoptosis in cancer cells, while remaining below this threshold in normal cells.[31,32] Since this early explanation, researchers have proposed more specific mechanisms, emphasizing the importance of different species.

In 2016, Bauer and Graves presented analyzed cell signaling pathways in cancer cells and normal cells.[33] Based on the signaling pathways, they developed a theory that $O_2(^1\Delta_g)$, a metastable electronically excited state, can disable a tumor cell's defenses against extracellular RONS. $O_2(^1\Delta_g)$ can disable a cell membrane protein responsible for breaking down other RONS, resulting in a wave of apoptosis that spreads from cell to cell. Yan *et al*. concluded that aquaporins, membrane proteins that channel water and other small molecules across the cell membrane, are critical for facilitating the effects of plasma treatment in cancer cells.[34] The effect of plasma treatment in their experiments could be mitigated by blocking these channels on the cell membrane. Aquaporins are known to be the main mechanism by which H_2O_{2aq} enters the cell, but could also transmit other RONS.

In treatment of mammalian cells by an Ar APPJ, scavengers were used to determine the most significant species for impact on cell viability by Wende *et al*.[18] In the case of Ar and Ar/H_2O plasmas, H_2O_{2aq} was identified as the dominant species reducing viability, but with air or O_2 admixtures, no H_2O_{2aq} could be detected. The potential active species in these cases is likely RNS or chlorine molecules generated from Cl^-_{aq} in the buffer solution. By using scavengers of H_2O_{2aq} and OH_{aq}, Kaushik *et al.* showed that both species play a role in the effects of plasma on cancer cells.[1]

Leveraging the immune system in plasma cancer treatment has recently been proposed by Miller *et al*.[35] Tumor growth can only occur when the immune system fails to recognize and eliminate the mutated cells. LTP treatment shows promising results for cancer immunotherapy, a type of treatment which utilizes the patient's immune system to treat cancer, summarized in Fig. 1.6. Plasmas have been shown to stimulate macrophages, a type of immune cell, and may be able to cause cancer cells to secrete molecules which signal "eat me" to the immune system.

This could allow the immune system to recognize not only those cells stimulated by plasma, but also to generate memory T-cells which would attack later occurrences of that cancer in the patient.

Though the most researched applications of plasma in medicine are wound healing and cancer treatment, many other applications are also being explored. In dermatology, LTP treatment has shown positive results in treatment of psoriasis and atopic dermatitis.[4] In dentistry, LTPs have been used to activate or coat the surfaces of implants, for decontamination of intraoral surfaces covered in bacteria or biofilms, and even for tooth bleaching.[36] Plasma treatment can also be used to enable transdermal drug delivery.[37]

Although plasma medicine is the primary motivation of this work, an understanding of these plasma sources is also essential for applications in agriculture, material activation, and water treatment. LTPs can be used to reduce pathogens and spoilage organisms on produce.[17] Air LTP treatments of seeds can be used to increase growth rates of crops.[38] Improved modeling capabilities and a better understanding of the chemistry and discharge dynamics of pulsed LTPs may also benefit the industry of surface activation of polymers.[6] Plasma may also be an effective way to eliminate contaminants of emerging concern in water treatment.[39] Each of these applications relies on the chemistry generated by atmospheric pressure LTP sources, which is discussed throughout this dissertation.

1.4 Modeling of LTPs

For atmospheric pressure LTPs, which are often pulsed, can be extremely challenging to experimentally measure the chemical content of these plasmas. They can contain thousands of different ions, excited states, and ground state neutrals, most of which do not survive long enough to be measured with traditional chemical analysis techniques. These challenges in

experimental measurements make modeling particularly useful to understand these systems. This section includes a description of the general types of LTP models and summarizes the contributions of modeling to the field of plasma medicine.

There are many approaches that have been used to model low temperature plasmas.[40–43] Global models are the simplest, treating the plasma as a well stirred reactor and calculating the density of each species as a function of time. Fluid models treat each species like a fluid, with spatially resolved densities and velocities in 1 to 3 dimensions. Kinetic methods calculate the energy distribution function of each species, at each point in space, either as a continuum (direct kinetic methods) or via particle simulations (particle in cell methods).

Because global models neglect any spatially dependent phenomena, they do not address complex structure, but are useful in investigating plasma chemistry. Some spatial information can be accounted for in a volume-averaged way, including losses to surface reactions. Gas flow can be considered by including a source of the incoming gas and an outflow of all current species. Plug flow methods can be used to convert a time-dependent global model calculation to the evolution of a flowing gas as it moves through space.[44] These models are straightforward to develop and some open source models are available.[45] Global models have been used extensively for the testing and development of reactions mechanisms, and for studying the general scaling of plasma chemistry with variables like applied power and flow rates.[18,46–48]

Fluid models assume that the energy distribution function of each species is Maxwellian, and the treats these species as a continuum, defining a density at each point in space. Poisson's equation is solved for the electric field, which then defines the force on the electron and ion fluids. 2-D fluid simulations are the most common as they can address many plasma sources

without the computational cost of 3-D. Fluid models have been used to model the propagation of streamers, using adaptive mesh refinement to resolve the large gradients at the streamer head.[41]

In both global models and fluid models, the electrons must be treated uniquely to account for the non-Maxwellian electron energy distribution function that is common in LTPs. This is most commonly addressed by solving Boltzmann's equation for electrons

$$\frac{\partial f}{\partial t} + \vec{v} \cdot \nabla_{\vec{r}} f + \frac{\vec{F}}{m} \cdot \nabla_{\vec{v}} f = \left(\frac{\partial f}{\partial t} \right)_{coll} \tag{1.8}$$

where f is the electron velocity distribution function as a function of time and space. $\vec{v}$ is the velocity, $\nabla_{\vec{r}}$ is the gradient in physical space, and $\nabla_{\vec{v}}$ is the velocity space. $\vec{F}$ is the total force on the particle, which in this case is driven by Coulomb forces due to the local electric field. The right-hand side represents the effect of collisions, which results in gains or losses of electrons or electron energy. For global and fluid models, Boltzmann's equation is typically solved for electrons in 0-D, and used to provide the transport coefficients (mobility and diffusivity) as a function of electric field and gas composition.

Direct kinetic methods still solve for the density and velocity as a continuum, but no longer assume a Maxwellian distribution function for any species; instead Boltzmann equation (Eq. 1.8) is solved for each species.[42] Particle in cell models use particles to represent charged species, and therefore also do not assume a Maxwellian distribution function. Particle methods can result in some numerical noise, because in most cases one computational particle is used to represent many physical particles. Kinetic methods are much less commonly used because they have a significantly higher computational cost. However they have the advantage of fewer assumptions and validity in a wider range of conditions.

1.4.1 Modeling of Plasma Medicine Sources

Each of the computational approaches described above can provide complementary information to the field of plasma medicine. Global models, with their low computational cost, provide a means to include large reaction mechanisms, and model the how the chemistry evolves over thousands of pulses and many minutes. Fluid simulations provide an intermediate balance where spatial behavior like IW behavior can be observed, and some technologically relevant timescales are achievable. Kinetic methods highlight cases in which the fluid approximation is valid or will over or underestimate different processes. Several examples of contributions to the field of plasma medicine by modeling studies are summarized in this section.

An analysis of the COST reference jet, an RF APPJ, was conducted with experiments and modeling to determine the origin of reactive species from the gas flow, surrounding environment, or in the liquid being treated.[49] Global modeling of COST reference jet in combination with isotopic labeling were used to conclude H_2O_{2aq}, OH_{aq}, and H_{aq} were primarily produced inside the APPJ, and at low feedgas humidity, the production of these species was primarily a result of impurities in the feedgas.

Schmidt-Bleker *et al*. modeled a plasma jet using a global model coupled with a computational fluid dynamics model.[50] The global model addressed the plasma dynamics and the chemistry generated by an radiofrequency (RF) APPJ in a plug flow approach. The results were used to determine the main sources of NO, NO_2, O, and O_3 and highlight the sensitivity of the production of NO_2 and O_3 to the composition of the shielding gas surrounding the jet. A good agreement was achieved with the experiment in both the trends and the absolute values of densities.

Naidis used a 2-D fluid model to examine the effect of an air admixture and humidity on the species produced by a He APPJ.[51] Increasing humidity increased OH, decreased O and O_3, and left NO unaffected. The results were used to determine the dominant production pathways of formation of O, O_3, OH, and NO.

Zheng *et al*. used a fluid simulation to model a He APPJ with oxygen admixtures.[43] They found that the oxygen admixture changed the shape of the IW from a ring to a disk, a behavior which has also been observed in experiments.

Norberg *et al*. used a 2-D fluid model to investigate helium APPJs, illustrating the importance of pulse repetition frequency (PRF) on the production of RONS.[52] When the PRF is high or the gas flow rate is low, the reactive species accumulate from pulse to pulse and react with RONS from previous pulses. Oxygen admixtures were also investigated, with low admixture concentrations leading to a more intense IW and therefore a greater production of most RONS.

Using the same model, Tian *et al*. investigated the chemistry in a liquid layer treated by an air DBD, as would be the case in direct treatment of tissue.[53] The effect of UV photons, dissolved O_{2aq}, and organics in the liquid all significantly affected the fluxes of reactive species which reach the tissue underlying the liquid layer.

Levko *et al*. used a particle in cell approach to model streamer propagation into liquid water.[54] Based on these results, the energetic electrons which reach the liquid and are not typically captured in fluid models result in significant ionization within the liquid phase.

1.5 Motivation

Because the chemistry produced in these LTPs is transient, measurements of plasma-produced species in these systems can be quite challenging. High quality measurements of

certain species can be made by advanced laser diagnostics, such as laser induced fluorescence and two-photon absorption laser induced fluorescence, but these diagnostics are costly and require expertise to operate.[55–60] A few research groups have developed mass-spectrometers that can sample gas *in situ* during plasma treatment, but most standard chemical analysis methods cannot be used due to the short lifetime (ns-ms) of many species.[61–63]

Measuring the reactive chemistry in plasma activated liquids can be even more challenging. In many studies, scavengers of particular RONS have been added to liquids to determine the role of that species in a biological outcome.[1,18] However, the scavengers are often not sufficiently specific to particular plasma-produced species.[64] Spin traps are a type of chemical marker which preserves unpaired electrons in a solution from radicals which often have short lifetimes, so that they can be quantified by electron paramagnetic resonance spectroscopy.[64,65] The same selectivity challenges exist in spin traps reacting with various reactive species.

Computational modeling can provide insight in time and spatially resolved reactive species at levels of completeness which current diagnostics cannot provide. Modeling also allows detailed analysis of the underlying physics of IW propagation, including the role of photoionization and surface processes, which can enable more informed design and operation of atmospheric pressure plasma sources for biomedical applications. The work presented in this dissertation focuses on providing key insights on the chemistry and physics of atmospheric pressure plasma sources using global and fluid models.

1.6 Scope of this dissertation

In Chapter 2, the two models used in this dissertation are described. *GlobalKin* is a 0-dimensional model that treats the plasma as a well stirred reactor. As part of this work,

GlobalKin has been extended to include liquid interactions – liquid chemistry that is directly coupled to the plasma chemistry. A 2-dimensional plasma hydrodynamics model, *nonPDPSIM*, will also be described, including the updates made to model during this dissertation work.

In Chapter 3, results of modeling a dielectric barrier discharge treatment of liquid covered tissue with *GlobalKin* are discussed. This global model has a low computational cost, and therefore allows examination of general scaling trends, and the behavior of thousands of discharge pulses with a complex reaction mechanism. This study showed the importance of solvated reactive nitrogen species such as ONOOH and HO_2NO_2 as a method of delivering more reactive species such as OH and HO_2 many seconds after the plasma treatment.

In Chapter 4, results of a study of plasma activation of droplets in air using *GlobalKin* will be discussed. The general scaling laws, the role of the Henry's Law equilibrium in determining the behavior as a function of droplet radius or droplet density will be discussed.

In Chapter 5, the plasma dynamics of an APPJ will be explained based on *nonPDPSIM* simulations. In particular the effect of electrode configuration, which is often not explored in experimental studies, on IW propagation, energy deposition, and RONS production will be discussed.

In Chapter 6, the result of 2-dimensional modeling on the effect of gas composition on the RONS production in a He APPJ are presented. When no intentional admixture is added to the helium flow, the impurities at concentrations less than 10 ppm are responsible for 79-98% of the RONS production. Admixtures are commonly used as a method of tailoring the type of reactive species produced by an APPJ, but because the admixtures effect the IW propagation and electron density, the dependence on admixture is often non-linear. The effect of O_2 and H_2O admixtures are the focus of this chapter.

In Chapter 7, the source of flow instabilities in an APPJ is examined using *nonPDPSIM*. In many experimental studies, a previously laminar flow jet was seen to become unstable when the plasma was initiated. Localized gas heating was observed in the modeling results, causing an acoustic wave. The acoustic wave perturbs the shear flow which results in a growing shear instability.

In Chapter 8, an atmospheric pressure plasma multi-jet is discussed. For applications using atmospheric pressure plasma jets for materials processing or larger wounds, it is often desirable to use an array of APPJs, but electrostatic interactions and some stochastic breakdown processes make it challenging to get an IW at every jet. One proposed solution to this is a multi-jet, which consists of a dielectric tube, with a series of holes along one side. The IW propagation dynamics are investigated and the effect of several design and operation parameters.

Experimental validation of *nonPDPSIM* for a plasma jet in a helium environment interacting with a dielectric substrate is discussed in Chapter 9. Fast camera imaging of plasma emission as the IW propagates were collected in addition to time and spatially resolved electron density measurements. In order to simplify the study for both the model and the diagnostic, this was done for a jet in a controlled environment, of either helium or humidified helium, rather than surrounding air.

The summary and conclusions are presented in Chapter 10. Perspectives on future work are also discussed in this chapter.

1.7 Figures

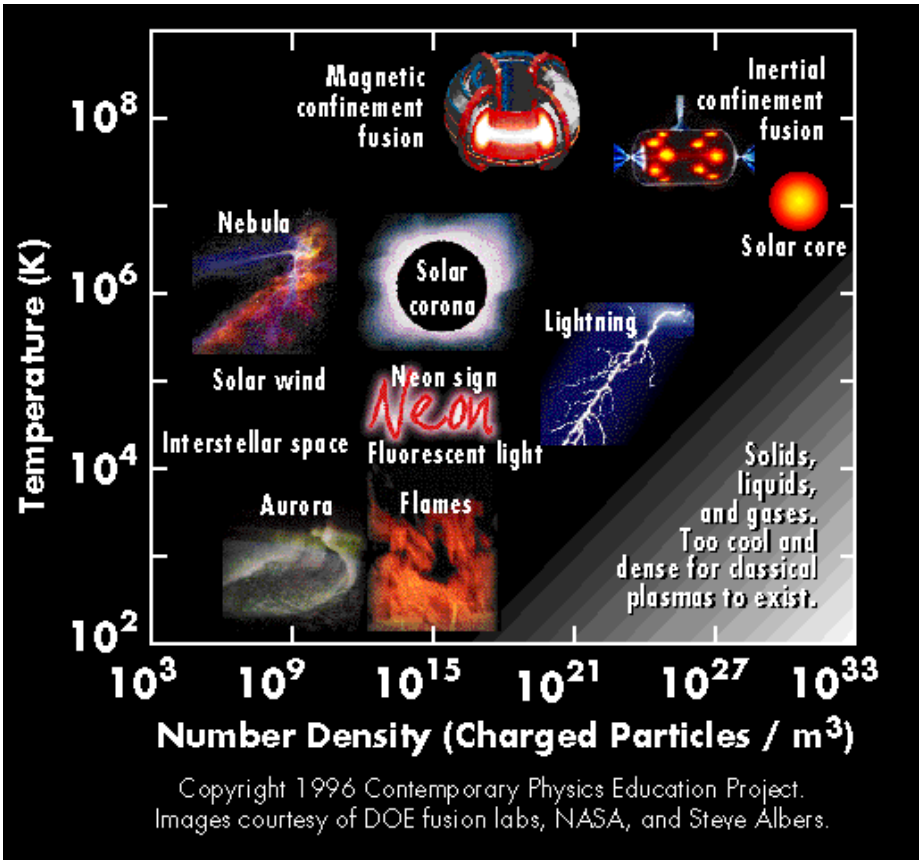

Fig. 1.1 Examples of several common plasmas as a function of temperature and plasma number density.[66]

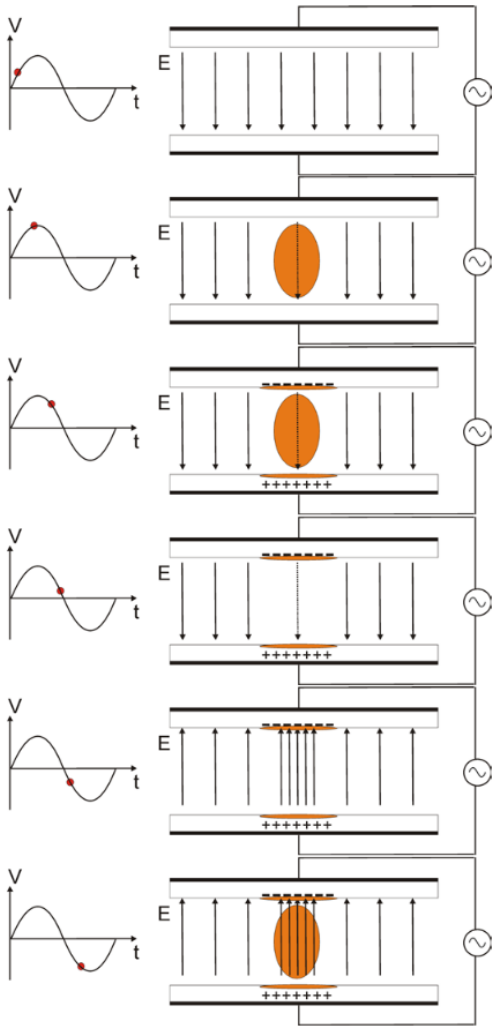

Fig. 1.2 Dynamics of a dielectric barrier discharge driven by an AC voltage. [67]

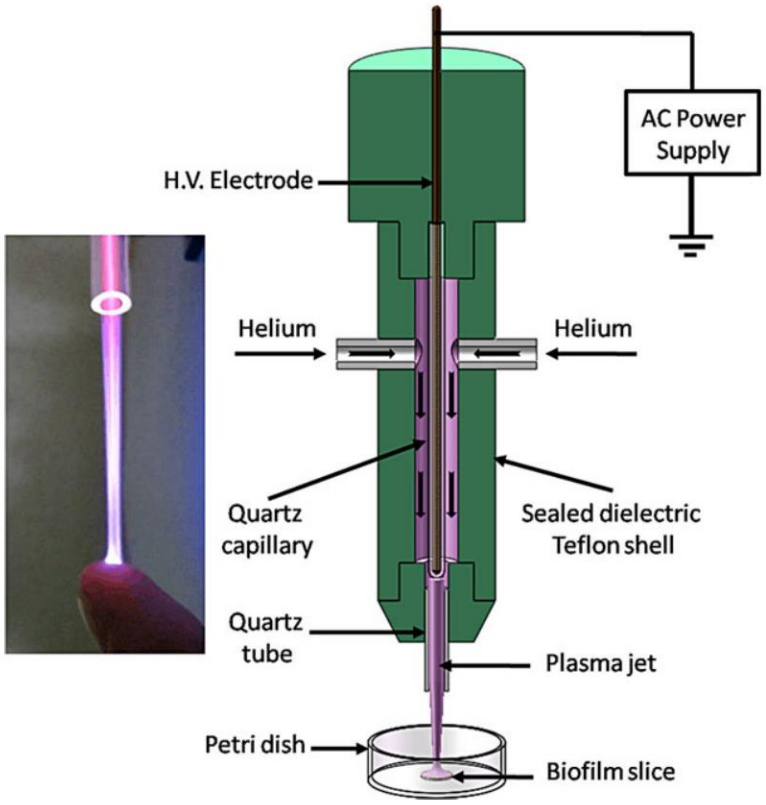

Fig. 1.3 A He atmospheric pressure plasma jet used in a study of plasma inactivation of biofilms.[68]

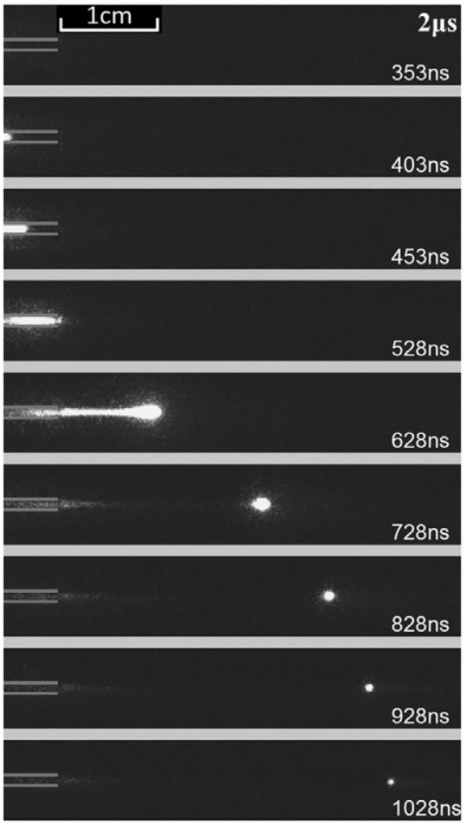

Fig. 1.4 High speed imaging of an ionization wave propagating from a He APPJ, with a camera gate of 5 ns.[69]

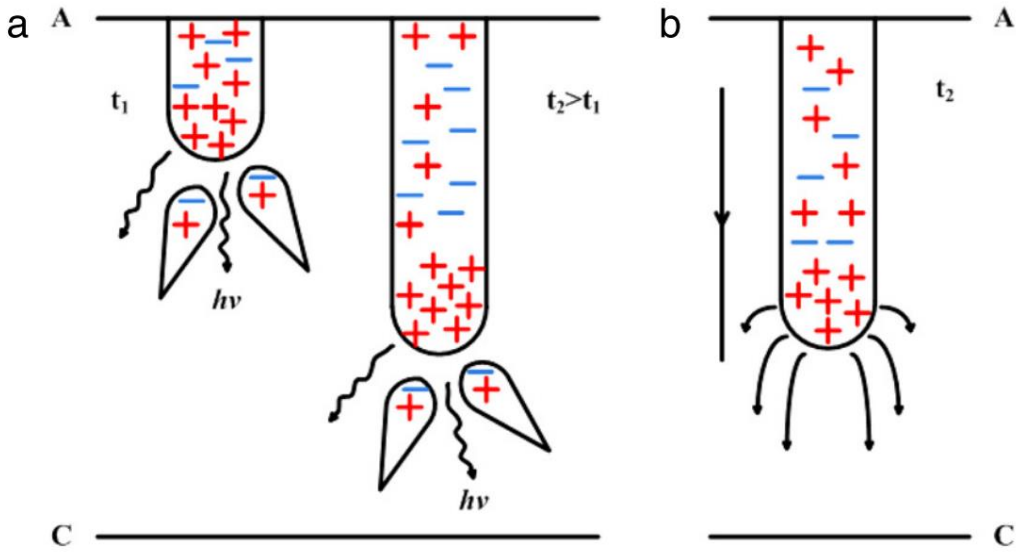

Fig. 1.5 A schematic of streamer propagation for a cathod-directed, or positive streamer. [70]

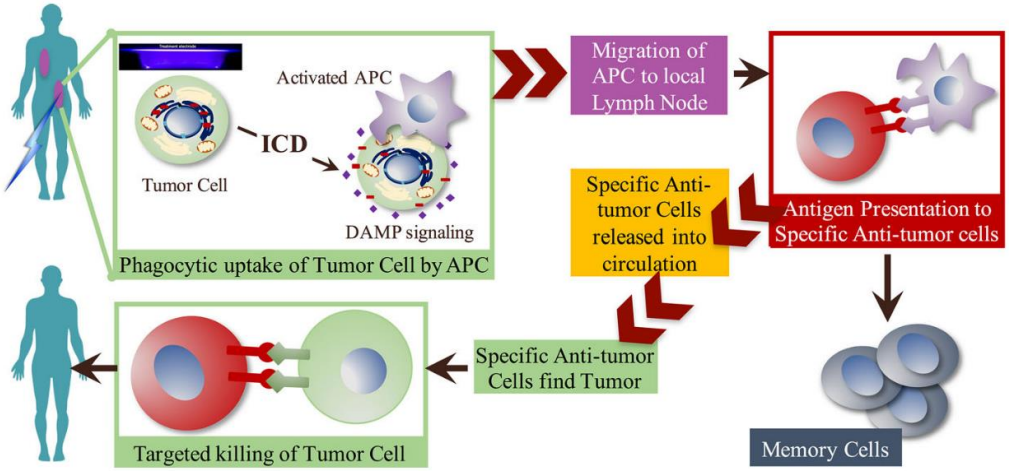

Fig. 1.6 A schematic of the use of plasma in cancer immunotherapy. Tumor cells would be treated with plasma, triggering antigen presenting cells (APCs) of the immune system ingest the tumor cells. The APCs initiate the production of T-cells which are specifically programmed to fight that type of cancerous cell throughout the body.[35]

1.8 References

[1] N. Kaushik, N. Uddin, G. B. Sim, Y. J. Hong, K. Y. Baik, C. H. Kim, S. J. Lee, N. K. Kaushik and E. H. Choi, Nat. Sci. Reports **5,** 8587 (2015).

[2] G. Isbary et al., Clin. Plasma Med. **1,** 25 (2013).

[3] Z. Ke, P. Thopan, G. Fridman, V. Miller, L. Yu, A. Fridman and Q. Huang, Clin. Plasma Med. **7–8,** 1 (2017).

[4] L. Gan, S. Zhang, D. Poorun, D. Liu, X. Lu, M. He, X. Duan and H. Chen, J. Ger. Soc. Dermatology **16,** 7 (2017).

[5] C.-M. Chan, T.-M. Ko and H. Hiraoka, Surf. Sci. Rep. **24,** 1 (1996).

[6] M. Strobel and C. S. Lyons, J. Adhes. Sci. Technol. **17,** 15 (2003).

[7] C. G. N. Lee, K. J. Kanarik and R. A. Gottscho, J. Phys. D: Appl. Phys. **47,** 273001 (2014).

[8] M. G. Kong, G. Kroesen, G. Morfill, T. Nosenko, T. Shimizu, J. Van Dijk and J. L. Zimmermann, New J. Phys. **11,** 115012 (2009).

[9] J. Schlegel, J. Köritzer and V. Boxhammer, Clin. Plasma Med. **1,** 2 (2013).

[10] Francis F. Chen, "*Introduction to Plasma Physics and Controlled Fusion, Volume 1: Plasma Physics*", (Plenum Press, New York, 1984).

[11] M. A. Lieberman and A. J. Lichtenberg, "*Principles of Plasma Discharges and Materials Processing*", (John Wiley & Sons, Inc., 2005).

[12] G. J. M. Hagelaar and L. C. Pitchford, Plasma Sources Sci. Technol. **14,** 722 (2005).

[13] J. Winter, R. Brandenburg and K.-D. Weltmann, Plasma Sources Sci. Technol. **24,** 064001 (2015).

[14] X. Lu, M. Laroussi and V. Puech, Plasma Sources Sci. Technol. **21,** 034005 (2012).

[15] Z. Kovalova, M. Leroy, C. Jacobs, M. J. Kirkpatrick, Z. Machala, F. Lopes, C. O. Laux, M. S. DuBow and E. Odic, J. Phys. D: Appl. Phys. **48,** 464003 (2015).

[16] G. Daeschlein et al., Plasma Process. Polym. **11,** 175 (2014).

[17] M. Ito, T. Ohta and M. Hori, J. Korean Phys. Soc. **60,** 937 (2012).

[18] K. Wende et al., Biointerphases **10,** 029518 (2015).

[19] W. Van Boxem, J. Van der Paal, Y. Gorbanev, S. Vanuytsel, E. Smits, S. Dewilde and A. Bogaerts, Nat. Sci. Reports **7,** 16478 (2017).

[20] M. Laroussi, IEEE Trans. Plasma Sci. **36,** 1612 (2008).

[21] M. Laroussi, I. Alexeff and W. L. Kang, IEEE Trans. Plasma Sci. **28,** 184 (2000).

[22] Z.-H. Lin, C.-Y. Tobias Tschang, K.-C. Liao, C.-F. Su, J.-S. Wu and M.-T. Ho, IEEE Trans. Plasma Sci. **44,** 3140 (2016).

[23] V. S. S. K. Kondeti, C. Q. Phan, K. Wende, H. Jablonowski, U. Gangal, J. L. Granick, R. C. Hunter and P. J. Bruggeman, Free Radic. Biol. Med. **124,** 275 (2018).

[24] A. Privat-Maldonado, Y. Gorbanev, D. O'Connell, R. Vann, V. Chechik and M. W. van der Woude, IEEE Trans. Radiat. Plasma Med. Sci. **2,** 121 (2018).

[25] G. Fridman, M. Peddinghaus, H. Ayan, A. Fridman, M. Balasubramanian, A. Gutsol, A. Brooks and G. Friedman, Plasma Chem. Plasma Process. **26,** 425 (2006).

[26] G.-M. Xu, X.-M. Shi, J.-F. Cai, S.-L. Chen, P. Li, C.-W. Yao, Z.-S. Chang and G.-J. Zhang, Wound Repair Regen. **23,** 878 (2015).

[27] G. Isbary et al., Br. J. Dermatol. **163,** 78 (2010).

[28] E. Stoffels, I. E. Kieft, R. E. J. Sladek, L. J. M. van den Bedem, E. P. van der Laan and M. Steinbuch, Plasma Sources Sci. Technol. **15,** S169 (2006).

[29] G. Fridman, A. Shereshevsky, M. M. Jost, A. D. Brooks, A. Fridman, A. Gutsol, V. Vasilets and G. Friedman, Plasma Chem. Plasma Process. **27,** 163 (2007).

[30] N. Georgescu and A. R. Lupu, IEEE Trans. Plasma Sci. **38,** 1949 (2010).

[31] D. B. Graves, J. Phys. D: Appl. Phys. **45,** 263001 (2012).

[32] D. B. Graves, Plasma Process. Polym. **11,** 1120 (2014).

[33] G. Bauer and D. B. Graves, Plasma Process. Polym. **13,** 1157 (2016).

[34] D. Yan, H. Xiao, W. Zhu, N. Nourmohammadi, L. G. Zhang, K. Bian and M. Keidar, J. Phys. D: Appl. Phys. **50,** 055401 (2017).

[35] V. Miller, A. Lin and A. Fridman, Plasma Chem. Plasma Process. **36,** 259 (2016).

[36] S. Cha and Y. S. Park, Clin. Plasma Med. **2,** 4 (2014).

[37] O. Lademann, H. Richter, M. C. Meinke, A. Patzelt, A. Kramer, P. Hinz, K.-D. Weltmann, B. Hartmann and S. Koch, Exp. Dermatol. **20,** 488 (2011).

[38] D. Dobrin, M. Magureanu, N. B. Mandache and M.-D. Ionita, Innov. Food Sci. Emerg. Technol. **29,** 255 (2015).

[39] J. E. Foster, Phys. Plasmas **24,** 055501 (2017).

[40] N. Y. Babaeva and G. V. Naidis, Trends Biotechnol. **36,** 603 (2018).

[41] A. Luque, V. Ratushnaya and U. Ebert, J. Phys. D: Appl. Phys. **41,** 234005 (2008).

[42] K. Hara and K. Hanquist, Plasma Sources Sci. Technol. **27,** 065004 (2018).

[43] Y. Zheng, L. Wang and D. Wang, J. Appl. Phys. **124,** 123301 (2018).

[44] W. Van Gaens and A. Bogaerts, J. Phys. D: Appl. Phys. **47,** 079502 (2014).

[45] S. Pancheshnyi, B. Eismann, G. J. M. Hagelaar and L. C. Pitchford, "Computer code ZDPlasKin", University of Toulouse, LAPLACE, CNRS-UPS-INP, Toulouse, France (2008) http://www.zdplaskin.laplace.univ-tlse.fr.

[46] G. Park, H. Lee, G. Kim and J. K. Lee, Plasma Process. Polym. **5,** 569 (2008).

[47] S. Schröter, A. R. Gibson, M. J. Kushner, T. Gans and D. O'Connell, Plasma Phys. Control. Fusion **60,** 014035 (2018).

[48] D. X. Liu, P. Bruggeman, F. Iza, M. Z. Rong and M. G. Kong, Plasma Sources Sci. Technol. **19,** 025018 (2010).

[49] Y. Gorbanev, C. C. W. Verlackt, S. Tinck, E. Tuenter, K. Foubert, P. Cos and A. Bogaerts, Phys. Chem. Chem. Phys. **20,** 2797 (2018).

[50] A. Schmidt-Bleker, J. Winter, S. Iseni, M. Dünnbier, K.-D. Weltmann and S. Reuter, J. Phys. D: Appl. Phys. **47,** 145201 (2014).

[51] G. V. Naidis, Plasma Sources Sci. Technol. **23,** 065014 (2014).

[52] S. A. Norberg, E. Johnsen and M. J. Kushner, Plasma Sources Sci. Technol. **24,** 035026 (2015).

[53] W. Tian and M. J. Kushner, J. Phys. D: Appl. Phys. **47,** 165201 (2014).

[54] D. Levko, A. Sharma and L. L. Raja, Phys. Plasmas **25,** 033515 (2018).

[55] S. Yatom, Y. Luo, Q. Xiong and P. J. Bruggeman, J. Phys. D: Appl. Phys. **50,** 415204 (2017).

[56] C. Winters, V. Petrishchev, Z. Yin, W. R. Lempert and I. V Adamovich, J. Phys. D: Appl. Phys. **48,** 424002 (2015).

[57] E. Barnat and A. Fierro, J. Phys. D: Appl. Phys. **50,** 14LT01 (2017).

[58] A. F. H. van Gessel, K. M. J. Alards and P. J. Bruggeman, J. Phys. D: Appl. Phys. **46,** 265202 (2013).

[59] S. Baldus, D. Schröder, N. Bibinov, V. Schulz-von der Gathen and P. Awakowicz, J. Phys.

D: Appl. Phys. **48,** 275203 (2015).

[60] Y. Yue, X. Pei and X. Lu, J. Appl. Phys. **119,** 033301 (2016).

[61] S. Große-Kreul, S. Hübner, S. Schneider, A. von Keudell and J. Benedikt, EPJ Tech. Instrum. **3,** 6 (2016).

[62] B. T. J. van Ham, S. Hofmann, R. Brandenburg and P. J. Bruggeman, J. Phys. D: Appl. Phys. **47,** 224013 (2014).

[63] P. Bruggeman, F. Iza, D. Lauwers and Y. A. Gonzalvo, J. Phys. D: Appl. Phys. **43,** 12003 (2010).

[64] P. J. Bruggeman et al., Plasma Sources Sci. Technol. **25,** 053002 (2016).

[65] Y. Gorbanev, D. O'Connell and V. Chechik, Chem. Eur. J. **22,** 3496 (2016).

[66] "Fusion: Physics of a Fundamental Energy Source", Project, Contemporary Physics Eductation (1996) http://www.cpepphysics.org/fusion_chart.html.

[67] J.-C. Wang, PhD Thesis, "Modeling Studies of Atmospheric Pressure Microplasmas: Plasma Dynamics, Surface Interaction and Applications", (University of Michigan, 2014).

[68] Z. Xu et al., Plasma Process. Polym. **12,** 827 (2015).

[69] Y. Xian, P. Zhang, X. Lu, X. Pei, S. Wu, Q. Xiong and K. Ostrikov, Sci. Rep. **3,** 1599 (2013).

[70] X. Lu, G. V. Naidis, M. Laroussi and K. Ostrikov, Phys. Rep. **540,** 123 (2014).

Chapter 2 Description of the Models

2.1 Description of *GlobalKin*

The first model used in this dissertation, *GlobalKin*, is a general purpose 0-dimensional plasma kinetics model, summarized by Fig. 2.1. It includes a circuit module, options to address gas flow using plug-flow or residence time approximations, diffusion to surfaces, surface kinetics using a surface site balance model, and most recently, a liquid interactions module.[1] The circuit module can provide the current through and voltage across the plasma which results in power deposition. Alternatively, the power deposition in the plasma can be directly specified as a function of time.

An electron energy equation is used for the average electron energy or temperature. Electron energy distributions (EEDs) are obtained from solutions of Boltzmann's equation and are the basis of lookup tables that provides the reaction rate coefficients and transport coefficients of electron impact processes as a function of average energy. These tables are updated at a frequency specified by the user to reflect the change in these coefficients as the gas mixture evolves. The electron temperature (T_e) is calculated from,

$$\frac{\partial\left(\frac{3}{2}n_e k_b T_e\right)}{\partial t} = \vec{j}\cdot\vec{E} + n_e\sum_i \Delta\varepsilon_i k_i n_i + \sum_i \Delta\varepsilon_i k_i n_i m_i - \sum_i \frac{3}{2} n_e \nu_{mi}\left(\frac{2m_e}{M_i}\right)k_b(T_e - T_i) \qquad (2.1)$$

where n_e is the electron density and k_b is Boltzmann's constant. The first term on the right-hand-side is the power deposition. All power is assumed to initially be deposited in electrons due to the low mobility of the ions. This assumption is reasonable for the cases considered in this work at atmospheric pressure, but becomes less accurate in low pressure plasmas where significant

power is deposited in the sheath by ions. The current density j and the electric field E were obtained from the circuit module or from the specified power deposition. The second term represents changes in electron energy (positive or negative) due to inelastic collisions where $\Delta\varepsilon$ is the change energy during the collision with the species of density n_i for the process having reaction rate coefficient k_i. The third term represents sources of electron energy density due to collisions between gas phase species n_i and m_i (such as Penning ionizations). The last term represents the electrons transferring momentum to the neutral atoms and molecules through elastic collisions where υ_{mi} is the momentum transfer collision frequency, m_e and M_i are the mass of the electrons and the other species, and T_i is the temperature of the neutral gas.

The density of all gas species was given by

$$\frac{dn_i}{dt} = \sum_j \left\{ \left(a_{ij}^{(R)} - a_{ij}^{(L)}\right) k_j \prod_l n_l^{a_{lj}^{(L)}} \right\} + \frac{1}{\tau_{flow}} \left(n_{io} - n_i \left(1 + \frac{\left(P - P_0\right)}{P_0} \right) \right) + \sum_m \left\{ -\frac{D_i n_i}{\Lambda^2} f_m S_{im} + \sum_k \frac{D_k n_k}{\Lambda^2} f_m S_{km} g_{ikm} \right\} . \quad (2.2)$$

The first term represents the gas phase reactions j which are sources or losses of species i. $a_{ij}^{(R)}$ and $a_{ij}^{(L)}$ are the number of molecules of species i which is on the right hand side and the left hand side of reaction j. The second term represents the sources and losses from flow, where τ_{flow} is the average residence time of the gas in the plasma, n_{io} is the number density of the species flowing into the reactor, P is the instantaneous pressure and P_0 is the desired operating pressure. The pressure dependent term accounts for changes in flow speed that may occur due to increases in pressure resulting from dissociation or gas heating. Diffusion losses including recombination or reactions at the wall are addressed by the third term. The third term includes diffusion losses of species i at the surface of material m and the source due to the return flux after surface reactions occur with other species. f_m is the fractional area of wall material m and D_i is the

diffusion coefficient of species *i*. Λ is the diffusion length of the plasma, defined by the geometry of the reactor. The sticking coefficient, S_{km}, is the fraction of the diffusion flux which disappears at the wall, and the give fraction, g_{ikm}, is the fraction of the consumed flux of species *k* which returns as species *i*.

The diffusion coefficient, D_i, of neutral species *i* in the gas mixture is

$$D_i = \frac{k_B T_g}{\sum_j \frac{1}{\mu_{ij}} \frac{n_j}{N_{STP}}} \tag{2.3}$$

where n_j is the number density of species *j*, T_g is the gas temperature, N_{STP} is the number density at standard temperature and pressure (2.5×10^{19} cm^{-3}) and μ_{ij} is the neutral mobility of species *i* in gas *j*. This mobility is calculated based on Lennard-Jones potentials and assuming hard-sphere collisions,

$$\mu_{ij} = \sqrt{\frac{m_i m_j}{m_i + m_j}} \sqrt{\frac{\pi}{8 k_B T_g}} \frac{1}{m_i N_{STP} \sigma_{ij}} \tag{2.4}$$

$$\sigma_{ij} = \pi \left(\frac{\sigma_{LJi} + \sigma_{LJi}}{2} \right)^2 \tag{2.5}$$

where m_i and m_j are the molecular weight of species *i* and *j*. σ_{ij} is the collision cross section and σ_{LJi} and σ_{LJj} are the Lennard-Jones radii of species *i* and *j*.

For charged species the diffusion coefficient is their ambipolar diffusion coefficient. The ion mobilities are based on experimental data where available, and the mixture is calculated in the same way as Eq. 2.3, but multiplied by a scaling factor to account for the ambipolar field. For positive ions, this scaling factor is

$$D_{+a} = D_+ \left(1 + \frac{q T_e}{T_g} \right) \tag{2.6}$$

where q is the ion charge. For negative ions, their diffusion coefficients are reduced by a Boltzmann factor,

$$D_{-a} = D_{-} \exp\left(-\frac{V_{float}}{k_B T_g} \frac{n_e}{n_+} \right) \tag{2.7}$$

$$V_{float} = \frac{T_e(\text{eV})}{2 \ln\left(\frac{T_e}{T_g} \frac{m_e}{M} \right)} \tag{2.8}$$

where V_{float} is the plasma floating potential, and n_+ is the total density of positive ions. M is the average mass of heavy species. The diffusion fluxes for electrons are set as the total flux of positive ions to that of negative ions, to maintain a charge neutral flux. The diffusion losses for electrons are set to insure the total flux to the surface is charge neutral.

The gas temperature was calculated by

$$\begin{aligned} \frac{d\left(\frac{3}{2} N_g c_p T_g\right)}{dt} = P_{ion} + \sum_i \frac{3}{2} n_e \nu_{mi} \left(\frac{2m_e}{M_i} \right) k_b (T_e - T_i) + \sum_i \Delta \varepsilon_i^{fc} R_i - \sum_i \Delta H_i R_i \\ + \frac{1}{\tau_{flow}} \left(N_{g0} c_{p0} T_{g0} - N_g c_p T_g \left(\frac{P}{P_0} \right) \right) - \frac{\kappa}{\Lambda^2} (T_g - T_w) \end{aligned} \tag{2.9}$$

where N_g is the total gas density, c_p is the specific heat of the gas, and T_g is the gas temperature. P_{ion} is the power deposited into the ions by the ambipolar electric field. The second term is the gas heating due to elastic collisions between the electrons and all other species. Franck-Condon heating is captured by the third term, where $\Delta\varepsilon_i^{fc}$ is the energy released as gas heating in dissociation reactions and R_i is the rate of reaction i. The fourth term includes the change in enthalpy from all reactions, including charge exchange, where ΔH_i is the change in enthalpy of reaction i, and R_i is the reaction rate. The fifth term is advective cooling due to gas flow, where N_{g0}, c_{p0}, and T_{g0}, are the density, specific heat, and temperature of the gas flowing into the reactor. P_0 is the set-point pressure, and P is the current pressure. The last term addresses thermal

conduction to surfaces, where κ is the thermal conductivity, and T_w is the surface or wall temperature. The term P_{ion} in Eq. 2.9 is calculated by

$$P_{ion} = E_a^{\,2} \sum_i^{positive} \mu_i q_i n_i \tag{2.10}$$

$$E_a = \frac{T_e}{\Lambda} \frac{n_e}{n_+} \tag{2.11}$$

where the sum in Eq. 2.10 is over all positive ions, n_+ is the total density of all positive ions, and the E_a is the ambipolar electric field.

During each voltage cycle, the timestep is determined by user input. For atmospheric pressure plasmas, typically the densities vary rapidly during the plasma pulse (which often lasts 10s of ns). For these cases, the initial timestep for each cycle is typically 10^{-13} - 10^{-12} s. This is multiplied by a constant value with each timestep to achieve the total number of timesteps requested by the user. This method produces a timestep which increases geometrically during each cycle. If an afterglow period is included in the simulation, a fixed timestep is used during this time.

The set of ordinary differential equations that are generated by Eq. 2.1, 2.2, and 2.9 are solved using a general purpose ODE solver called DVODE.[2] It uses Adams-Moulton methods and backward differentiation formula and provides solutions in double precision. This package generates the full Jacobian matrix internally. A relative tolerance of 10^{-8} – 10^{-6} is typically used for convergence. This criterion is not enforced for species with a density below a physically insignificant value (typically 10^6 cm^{-3}).

2.1.1 Liquid Module

To address the activation of a liquid layer in contact with the plasma, a second set of species and a separate reaction mechanism were included in the global model. First, a duplicate

solvated species was added for each gas phase species (i.e., H_2O_{2aq} was added for H_2O_2). The liquid-resident species and reaction mechanism are restricted to a second zone in the model. The species in these two zones (gas and liquid) only interact through the interface between the zones by means of diffusion into or out of the liquid. Conceptually, the gas-liquid interface is treated as one of the materials to which species diffuse and so is mechanically included in the sum of materials in Eq. 2.2. For the material that represents the gas-liquid interface, the sticking coefficient for the diffusion losses of neutral species from the gas to the liquid is determined by the Henry's law equilibrium constant, h_i. For species i and liquid material m,

$$S_{im} = \frac{h_i n_{i,g} - n_{i,l}}{h_i n_{i,g}} \tag{2.12}$$

where $n_{i,g}$ is the gas phase density of species i and $n_{i,l}$ is its liquid phase density. This sticking coefficient is used for $n_{i,l}/n_{i,g} < h_i$ and accounts for a diminishing rate of loss of the gas phase species into the liquid as the liquid density approaches its Henry's law equilibrium values. If $n_{i,l}/n_{i,g} > h_i$ at any time, then the liquid is oversaturated and transport of the species is from the liquid into the gas. The flux from the oversaturated liquid to the gas is given by:

$$\Gamma_i = \frac{D_i\left(n_{i,l} - h_i n_{i,g}\right)}{\Lambda^2}\frac{V_p}{A_l} \tag{2.13}$$

where V_p is the volume of the plasma region and A_l is the surface area of the face representing the gas-liquid interface. Once a species enters the liquid, transport in the liquid phase is assumed to be well stirred.[3,4] In making this assumption, the global model does not capture formation of a boundary layer in the liquid at each pulse which may saturate. The well stirred approximation captures the solvation behavior most accurately for species with a higher Henry's law constant and at longer timescales where convection can occur.

The liquid species densities are given by

$$\frac{dn_i}{dt} = \sum_j \left\{ \left(a_{ij}^{(R)} - a_{ij}^{(L)}\right) k_j \prod_l n_l^{a_{ij}^{(L)}} \right\} + \frac{D_i n_{i,g}}{\Lambda^2} f_l S_{i,liquid} \frac{V_p}{V_l} - \max\left\{0, \frac{D_i\left(n_{i,l} - h_i n_{i,g}\right)}{\Lambda^2} \frac{V_p}{V_l}\right\} \quad (2.14)$$

where n_i is the density of the liquid species i. The first term represents the liquid phase reactions j which are sources or losses of species i. $a_{ij}^{(R)}$ and $a_{ij}^{(L)}$ are the number of molecules of species i which is on the right hand side and the left hand side of reaction j. k_j is the reaction rate coefficient of reaction j. The second term represents diffusion of species from the gas into the liquid, where D_i is the diffusion coefficient of gas phase species i, $n_{i,g}$ is the density of species i in the gas, Λ is the diffusion length of the plasma, defined by the geometry. $S_{i,liquid}$, is the sticking coefficient of species i on the liquid and f_l is the fraction of the area of the plasma which is in contact with the liquid V_p and V_l are the volumes of the plasma and liquid region. The third term represents transport out of the liquid when the liquid is oversaturated. This term is only nonzero when the liquid is oversaturated, and it represents the flux in Eq. 2.13.

With liquid in contact with the gas, evaporation of the liquid into the gas phase is included in Eq. 2.2 to account for, for example, humidifying the gas. The flux into the gas phase due to evaporation increases the density of the vapor phase but the evaporation losses of mass from the liquid are ignored, as they are assumed to be much smaller than the total liquid volume. The evaporating flux is

$$\Gamma_{i,e} = \frac{D_i\left(n_{i,s} - n_{i,g}\right)}{\Lambda^2} \frac{V_p}{A_l} \quad (2.15)$$

where $n_{i,s}$ is the gas number density corresponding to the saturated vapor pressure of the liquid.

2.1.2 Boltzmann's Equation

In order to account for the non-Maxwellian electron energy distribution functions which occur in low temperautre plasmas, Boltzmann's equation is solved for a series of E/N with the current gas composition. This solver generates a lookup table of T_e and the rate of each electron

impact reaction for each E/N, which is necessary for the electron energy equation. Boltzmann's equation is

$$\frac{\partial f}{\partial t} + \vec{v} \cdot \nabla_{\vec{r}} f + \frac{\vec{F}}{m} \cdot \nabla_{\vec{v}} f = \left(\frac{\partial f}{\partial t} \right)_{coll} , \tag{2.16}$$

where f is the electron energy distribution, $\vec{v}$ is the velocity, $\nabla_{\vec{r}}$ is the spatial gradient, $\vec{F}$ is the total force on electrons, m is the electron rest mass, and $\nabla_{\vec{v}}$ is the gradient in velocity space. The right hand side addresses the changes in electron energy due to collisions. In *GlobalKin*, Boltzmann's equation is solved to the steady state in zero dimensions for a discrete set of reduced electric fields. This simplifies the equation by $\nabla_{\vec{r}} f = 0$ and $\partial f / \partial t = 0$, to

$$\frac{\vec{F}}{m} \cdot \nabla_{\vec{v}} f = \left(\frac{\partial f}{\partial t} \right)_{coll} . \tag{2.17}$$

In the model, a two-term spherical harmonic expansion is applied by assuming f in the form

$$f(\vec{v}) = f_0(|\vec{v}|) + f_1(v_z)\cos\theta , \tag{2.18}$$

where f_0 is the isotropic component and f_1 is the anisotropic component. z is the direction of the applied electric field, and θ is the polar angle from the z-axis. This approximation and its limitations are described in more detail by Hagelaar and Pitchford.[5] Initially a Maxwellian electron energy distribution function is imposed, and the distribution is integrated in time based on the cross section database until it reaches a steady state value.

Boltzmann's equation is typically solved for several tens of values of E/N in the range of 10^{-18} – 10^{-13} V·cm^2 (10^{-1} – 10^4 Td). The resulting electron energy distribution is used to calculate the rate coefficients for each reaction by integrating the product of the cross section and the f.

2.1.3 Circuit Model

The circuit model in *GlobalKin* includes a default circuit, shown in Fig. 2.2, or a custom circuit can be implemented. If the default circuit is used, the storage capacitor ($C_{storage}$) begins at the applied voltage at the start of each cycle. At the beginning of each cycle, the switch is closed and current begins to flow from the storage capacitor. The presence of a diode shuts off as any current begins to flow in the opposite direction, and the circuit module is turned off for the remainder of that cycle and the power coupled to the plasma is fixed to zero. The plasma is treated as a purely resistive circuit element in this default model. The resistance of the plasma is updated at every timestep based on the current electron density and gas composition.

$$R_{discharge} = \frac{m_e \upsilon_m}{e^2 n_e} \frac{d}{A} \tag{2.19}$$

where the momentum transfer collision frequency, υ_m, is determined by the Boltzmann solver. d is the gap between the electrodes and A is the area of the electrodes.

The power deposition in the plasma is calculated based on the circuit model and is used as input in the electron energy equation ($\vec{j} \cdot \vec{E} = I_{discharge} V_{discharge} / V_p$, where $I_{discharge}$ and $V_{discharge}$ are the discharge current and voltage, and V_p is the plasma volume).

The circuit parameters, including the voltage across each capacitor and the current through the inductor, are each represented by ordinary differential equations. These are solved in the same matrix as the densities and temperatures by the ODE solver, as described above.

2.2 Description of *nonPDPSIM*

The second model used in this dissertation, *nonPDPSIM*, is a 2-dimensional plasma hydrodynamics model which is also described in detail in Ref. [6]. The model uses time slicing algorithms to address the multiple timescales of the discharge and flow dynamics. The model

includes a solution of Boltzmann's equation for the electron energy distribution to provide transport coefficients as a function of average electron energy, a solution of the compressible Navier-Stokes equations for fluid flow, and a radiation transport module. Poisson's equation is solved for the electrical potential, including applied voltages, charged species in the gas phase, surface charging, and different electrical solid material properties as expressed through dielectric constant and conductivity. The model utilizes an unstructured numerical mesh to enable greater spatial refinement in regions where an ionization wave propagates and gradients in densities and electrical properties are large. The charged species densities and potentials are solved using a fully implicit algorithm with timesteps that are dynamically chosen, usually 1-30 ps during the active plasma portion of the simulation. The electron energy transport and conservation equation that provides the average electron energy is also implicitly solved following the update of densities and potential.

A block diagram of the use of *nonPDPSIM* with the modules used in this dissertation is shown in Fig. 2.3. The required input includes a mesh, which defines the system geometry and the spatial discretization. A namelist file specifies the material properties, all physics modules, and the options which control the timestep of each module. The chemistry file provides the species properties including the charge, molecular weight, enthalpy of formation, and wall recombination properties, as well as all reactions and their rates. For those electron impact reactions which are calculated from cross sections, an identifying number in the chemistry file refers the reaction to a cross section in a database internal to *nonPDPSIM*. The parsing of input files is followed by many initial setup calculations, which do not need to be repeated at each timestep. For example, the volume associated with each node, lists of node numbers of each nodes neighbors, and the Green's functions which will be used in radiation transport are all

defined at this time.

In simulations with an imposed gas flow, including all of the simulations in this dissertation, the initial flow profile is established before the voltage is applied. This is referred to as the "Fluid Period" in Fig. 2.3. During this time, the fluid module is solved, as well as the transport of neutral species, to address the mixing of different gases, typically with timesteps of $10^{-7} – 10^{-5}$ s.

After solving the steady state flow field, the plasma pulse period is initialized with a user specified density of charged species (typically a cloud of electrons and ions near the powered electrode). The full plasma calculation period is when the discharge dynamics are solved, including Poisson's equation coupled with charged species transport and the electron temperature. This is done with an automatic timestep, and during this time, time slicing algorithms address processes that occur much more slowly than the plasma timestep. The bulk fluid velocity is updated at a user specified frequency, usually on the order of 10^{-9} s, to include any small changes in the overall fluid density and velocity caused by gas heating and dissociation during the pulse. This time slicing also addresses updates to the surface kinetics, if used, and saving the data to output files. The plasma pulse period typically ends after the applied voltage returns to zero and enough time has passed that most of the space charge and surface charge has been neutralized.

If desired, an afterglow calculation is included to calculate the chemistry after the pulse and address longer timescales than would be feasible while solving Poisson's equation. During this period, the plasma is assumed to be charge neutral. An averaged diffusion coefficient is applied to all charged species to approximate the ambipolar diffusion that would occur and charge neutrality is enforced at every timestep.

2.2.1 Geometry and Mesh

The equations in *nonPDPSIM* are solved on an unstructured mesh generated by Skymesh2 by SkyBlue systems. An example geometry and mesh is shown in Fig. 2.4, which will be used in the simulations in Ch. 7. In this geometry, materials are assigned to each region, and then the properties of each material (e.g. conductivity, dielectric constant) can be specified by the namelist file. The nodes on the boundary between two regions are assigned a material number based on a hierarchy. A node on the boundary of a metal takes on the properties of the metal. A node on the boundary of the plasma and a dielectric takes on the properties of the dielectric. For the plasma nodes, a zone can also be specified, which allows different regions of the computational mesh to be initialized with different gas compositions, expediting the steady state fluid calculation and making it possible to include liquids.

The mesh cells are triangular, and each node is connected to its nearest neighbors by chords. The vertex centered finite volume method (FVM) is used when solving the differential equations discussed throughout this chapter. The volume associated with each node is illustrated in Fig. 2.5. To calculate this volume, a conceptual polygon is drawn from the perpendicular bisector of each chord. The area of this polygon (often a hexagon) is then calculated. To determine the volume, this is multiplied by the depth of the simulation or in the case of the cylindrically symmetric geometry, calculated based on the radius of the node. The area of each face of this control volume is necessary for addressing transport of species from a node to its neighbor. This area is determined by calculating the length of each perpendicular bisector, multiplied by the depth of the simulation (Cartesian) or integrated about the axis (cylindrical). In a Cartesian geometry, the depth generally does not affect the discharge dynamics, but does determine the interpretation of some volumetric quantities like the mass flow rate of gases or the

volume-integrated energy deposition. Because the mesh is unchanging during the simulation, the calculation of these volumes and areas occurs only once during the initialization of the model.

2.2.2 Poisson's Equation and Charged Species Transport

Poisson's equation for electric field and charged species transport are solved together by fully implicit algorithms in *nonPDPSIM*. This is represented by the equation

$$\nabla \cdot (\varepsilon \nabla \Phi) = -\left(\sum_i n_i q_i + \rho_m \right), \tag{2.20}$$

where Φ is the electric potential and ε is the permittivity. The right-hand side includes all space charge, where q_i is the charge of species i with a density of n_i, and ρ_m is the electric charge on the surface of materials. Charged species transport is addressed by the equation

$$\frac{\partial n_i}{\partial t} = -\nabla \cdot \vec{\Gamma}_i + S_i + \left[\sum_j -\nabla \cdot \vec{\Gamma}_j \gamma_j + \sum_k -\nabla \cdot \vec{\phi}_k \gamma_k \right]_b , \tag{2.21}$$

where $\vec{\Gamma}_i$ is the flux of species i, S_i is the source of species i due to reactions. The terms in brackets apply only to electrons on plasma nodes which neighbor material surfaces. The first sum is ion-induced secondary electron emission, where $\vec{\Gamma}_j$ is the flux of ion j with secondary electron emission coefficient γ_j. The second sum is photoelectron emission, where $\vec{\phi}_k$ is the flux of photon k, with electron emission coefficient γ_k. The charge on materials is solved by

$$\frac{\partial \rho_m}{\partial t} = \left[\sum_i q_i \left(-\nabla \cdot \vec{\Gamma}_i (1 + \gamma_i) \right) + \sum_k e \phi_k \gamma_k \right]_s + \nabla \cdot (\sigma \nabla \Phi), \tag{2.22}$$

where the sums in brackets apply only to nodes on the surface which are in contact with the plasma. The first sum accounts for all charged species incident upon the surface, and the effect of ion induced secondary electron emission. The second sum accounts for charge lost by photoelectron emission from the surface. The final term applies Ohm's law within the material,

where σ is the conductivity.

2.2.2.1 Analytical Jacobian Elements

Since the description of the model found in Ref. [6], several updates to the algorithms for implicit charged particle transport have been made to improve the performance and stability of the model. The numerically most time-consuming portion of the simulation requiring the shortest timestep is solving for the charged species densities and electric potential at each node (Eq. 2.20 and 2.21).

To obtain implicitness in the solution for charged species densities and potentials, Jacobian elements are included in the resulting matrix. These Jacobian elements are, for example, $\partial n_{ki}/\partial n_{mj}$ – the incremental change in the density of a species *k* at node *i* due to a change in density of species *m* at neighboring node *j*. In the previous formulation, a perturbation technique was used to compute the values of Jacobian elements. In this technique, for timestep Δt,

$$\frac{\partial n_i}{\partial n_j} = \Delta t \frac{\left[dn_i\left(n_j\right)/dt - dn_i\left(n_j + \Delta n_j\right)/dt \right]}{\Delta n_j}, \tag{2.23}$$

where Δn_j is a small perturbation in the value of n_j. (To simplify notation, we consider Jacobian elements of a single species with its own density at a neighboring node.)

The resulting system of equations is iteratively solved using different sparse matrix operators depending on the properties of the resulting matrix. The system we solve is

$$\overleftrightarrow{F}\,\vec{x} = \vec{b} \tag{2.24}$$

where $\vec{x}$ is an array of the potentials, charged species densities and surface charge densities at every node in the mesh. $\overleftrightarrow{F}$ is a matrix containing the finite-volume form of the partial derivatives representing the transport equations including the Jacobian elements. Since a Newton-iterations

method is being used to refine the solution, $\vec{b}$ is the residual of the potential or charged species density, which reduces to 0 as the solution converges. This problem is solved iteratively, until the residual is below the maximum allowed error, generally requiring 5-10 iterations for each timestep. The system of equations minimizes a residual, rather than directly solving for the species densities and potentials.

In the results presented in this dissertation, Eq. 2.24 was solved using a sparse matrix solver, SPARSKIT, by Y. Saad.[7] This package uses the generalized minimum residual method and an incomplete LU factorization (ILUT) for preconditioning. At each timestep, Eq. 2.24 is solved for each Newton's iteration until the relative error is below a user specified criterion, typically 5×10^{-7} - 2×10^{-6}. The timestep is selected automatically based on the number of Newton iterations required to solve the last two timesteps. If the average number of Newton iterations required is less than the ideal value, the timestep increases. If the average number of iterations is greater than the ideal value, the timestep decreases. The best balance of stability and runtime is typically achieved with 5-10 Newton iterations. If the error criterion is not achieved in a maximum number of Newton iterations (usually 30), then the timestep is reduced by a factor of two and the calculation is attempted again. The maximum timestep is typically limited to 50-100 ps to prevent numerical instabilities which can occur if the timestep is too large.

The elements of $\overleftrightarrow{F}$ can be described in terms of the physical Jacobian elements in Eq. 2.23 by

$$F_{ij} = \frac{1}{\Delta t}\left(\delta_{ij} - \frac{\partial n_i}{\partial n_j} \right) \tag{2.25}$$

where n_i and n_j are a density of a charged species or a potential at any node and $\delta_{ij} = 1$ if $i = j$ and 0 otherwise. For clarity, the discussion that follows will be in terms of the more physically

intuitive partial derivatives rather than the matrix elements. These include the partial derivative of potentials with respect to charged species densities ($\partial\Phi_i/\partial n_i$, $\partial\Phi_i/\partial n_j$), as well as the derivatives of densities with respect to densities at other nodes and the potentials ($\partial n_i/\partial n_j$, $\partial n_i/\partial\Phi_i$, $\partial n_i/\partial\Phi_j$). The Jacobian elements between node-pairs for potentials ($\partial\Phi_i/\partial\Phi_j$) depend only on geometry and permittivity of materials. Those Jacobian elements can be computed once and stored. The matrix elements containing partial derivatives of densities or surface charges change with each Newton-iteration and their calculation should be as efficient as possible. In this regard, the previous numerical method to compute Jacobian elements was replaced with closed form expressions.

One of the equations being solved by this matrix formulation is the density of charged species *s* at node *i* given by

$$n_{si}(t_1) = n_{si}(t_0) + \Delta t\left(S_{1si} n_e(t_1) + S_{2si} + \sum_j \Gamma_{sij}(t_1)\frac{A_{ij}}{V_i} \right) \tag{2.26}$$

where t_0 refers to the previous time at which the solution was obtained, t_1 is the time at which the solution is desired and $\Delta t = t_1 - t_0$. $n_{si}(t_1)$ is the working density at the current time that becomes increasingly accurate with each Newton iteration. $\Gamma_{sij}(t_1)$ is the flux of species *s* from node *i* to neighbor *j* based on the current solution, A_{ij} is the area of interface between a cell and its neighbor *j*, and V_i is the volume associated with the current node. S_{1sj} is the source of species *s* at node *j* due to electron impact processes, which is updated at every iteration. S_{2sj} is the source of species *s* at node *j* that is independent of electron density, for example due to photoionization or Penning ionization. In order to tune the implicitness of the scheme to the particular problem, the parameter β is used, where $\beta = 0$ is fully explicit and $\beta = 1$ is fully implicit. The more general equation becomes

$$n_{si}(t_1) = n_{si}(t_0) + \Delta t\left(\left[\beta n_e(t_1) + (1-\beta) n_e(t_0) \right] S_{1si} + S_{2si} + \sum_j \left(\beta \Gamma_{sij}(t_1) + (1-\beta)\Gamma_{sij}(t_0) \right) \frac{A_{ij}}{V_i} \right) \quad (2.27)$$

The fluxes for charged particles are provided by a modified version of the formulation developed by Scharfetter and Gummel [8],

$$\Gamma_{sij} = \alpha \left(\frac{D_{si} + D_{sj}}{2} \right) \frac{n_{si} - n_{sj} \exp(\alpha \Delta x_{ij})}{1 - \exp(\alpha \Delta x_{ij})} \quad (2.28)$$

$$\alpha = \frac{-q_s \left(\mu_{si} + \mu_{sj} \right) \left(\Phi_i - \Phi_j \right) - 2v_{ij}}{\left(D_i + D_j \right) \Delta x_{ij}} = \frac{-q_s \left(\mu_{si} + \mu_{sj} \right) E_{ij} - 2v_{ij}}{\left(D_i + D_j \right)} \quad (2.29)$$

where D_{si} is the diffusion coefficient of species *s* at node *i*, and μ_{si} is the mobility of species *s* at node *i*. Φ_i is the electric potential at node *i*. v_{ij} is the fluid velocity assuming that charged species are entrained in the bulk fluid flow, and E_{ij} is the electric field along the chord from node *j* to node *i*. Δx_{ij} is the chord length between the node and its neighbor.

The real values of the species densities, potentials, charge densities, and matrix elements could vary by many orders of magnitude, which makes for difficulty in the linear algebra. In order for these values to be closer to the same order of magnitude, all densities and potentials are globally normalized by an expected value.

The previous perturbative technique uses a function which returns a normalized value of the residual *b* to compute the normalized matrix element, F_{ij}. If the perturbation is too small, the change in *b* may be below precision limits. If the perturbation is too large, the derivative will not be accurate. The perturbative calculation results in unnecessary effort. For example, only one term in the summation of fluxes over faces in Eq. 2.26 will contribute to the matrix element for any pair of mesh points.

As an improvement to the perturbation technique, analytical derivatives are calculated directly for potentials and densities. These analytical derivatives are shown below where all time

dependent variables refer to the value at t_1. The Jacobian element for density at the central node is

$$\frac{\partial n_{si}}{\partial n_{si}} = \beta \sum_j \left[\frac{\alpha \left(D_{si} + D_{sj} \right)}{1 - \exp(\alpha \Delta x_{ij})} \right] \frac{A_{ij}}{V_i} \Delta t \tag{2.30}$$

This calculation becomes less accurate at small values of α, where the denominator goes to zero. If $\alpha \Delta x_{ij} < 10^{-4}$, the analytical limit is used.

$$\lim_{x \to 0} \frac{x}{1 - e^x} = -1 \tag{2.31}$$

$$\frac{\partial n_{si}}{\partial n_{si}} = \sum_j^{neighbors} \frac{\beta A_{ij} \Delta t \left(D_{si} + D_{sj} \right)}{2 V_i} \begin{cases} \dfrac{\alpha}{1 - \exp(\alpha \Delta x_{ij})} & \alpha \Delta x_{ij} \geq 10^{-4} \\ -\dfrac{1}{\Delta x_{ij}} & \alpha \Delta x_{ij} < 10^{-4} \end{cases} \tag{2.32}$$

A small α indicates a small electric field for which transport converges to diffusion as α approaches zero. The application of the limit produces errors that are less than 0.01%. The maximum allowed value of $\alpha \Delta x_{ij}$ is 500, a value for which the magnitude of the denominator is sufficiently large to properly represent the transport. A similar limit is applied to the derivative with respect to the density at the neighboring node.

$$\frac{\partial n_{si}}{\partial n_{sj}} = -\frac{\Delta t \beta A_{ij} \left(D_{si} + D_{sj} \right)}{2 V_i} \begin{cases} \dfrac{\alpha \exp(\alpha \Delta x_{ij})}{1 - \exp(\alpha \Delta x_{ij})} & \alpha \Delta x_{ij} \geq 10^{-4} \\ -\dfrac{1}{\Delta x_{ij}} & \alpha \Delta x_{ij} < 10^{-4} \end{cases} \tag{2.33}$$

Due to the second term in Eq. 2.26, which represents electron impact reactions, the derivative with respect to the electron density must also be included in the matrix.

$$\frac{\partial n_{si}}{\partial n_e(t_1)} = -\Delta t \beta S_{1si} \tag{2.34}$$

In the case of electrons, this is added to the matrix element in Eq. 2.30, but for all other species, this is an additional matrix element.

The derivatives with respect to potentials are slightly more complicated because α is a function of potential.

$$\frac{\partial n_{si}}{\partial \Phi_i} = -\sum_j \frac{\Delta t \beta A_{ij}}{V_i} \frac{q_s\left(\mu_{si}+\mu_{sj}\right)}{2\Delta x_{ij}} \begin{cases} \dfrac{n_{si}-n_{sj}\exp(\alpha\Delta x_{ij})}{1-\exp(\alpha\Delta x_{ij})} + \dfrac{\left(n_{si}-n_{sj}\right)\alpha\Delta x_{ij}\exp(\alpha\Delta x_{ij})}{\left(1-\exp(\alpha\Delta x_{ij})\right)^2} & \alpha\Delta x_{ij} \geq 10^{-3} \\ \dfrac{n_{si}+n_{sj}}{2} & \alpha\Delta x_{ij} < 10^{-3} \end{cases} \quad (2.35)$$

The derivative of the density with respect to the potential at a neighboring node is simply the negative of the function above, without summing over the neighbors.

$$\frac{\partial n_{si}}{\partial \Phi_j} = \frac{\Delta t \beta A_{ij}}{V_i} \frac{q_s\left(\mu_{si}+\mu_{sj}\right)}{2\Delta x_{ij}} \begin{cases} \dfrac{n_{si}-n_{sj}\exp(\alpha\Delta x_{ij})}{1-\exp(\alpha\Delta x_{ij})} + \dfrac{\left(n_{si}-n_{sj}\right)\alpha\Delta x_{ij}\exp(\alpha\Delta x_{ij})}{\left(1-\exp(\alpha\Delta x_{ij})\right)^2} & \alpha\Delta x_{ij} \geq 10^{-3} \\ \dfrac{n_{si}+n_{sj}}{2} & \alpha\Delta x_{ij} < 10^{-3} \end{cases} \quad (2.36)$$

Applying the analytical limit at $\alpha\Delta x_{ij} = 10^{-3}$ results in errors < 0.1% compared to the exact solution.

When implementing these expressions, the more accurate analytic Jacobian elements resulted in computational speedups as much as a factor of 4. With more accurate Jacobian matrix elements, the solution converged in fewer iterations, leading to the ability to take larger timesteps without increasing the error or decreasing the stability.

2.2.3 Boltzmann's Equation

The solution to Boltzmann's equation in *nonPDPSIM* uses the same method as that of *GlobalKin* described in Sec. 2.12 This generates a lookup table that relates many values of the

reduced electric field (E/N) to the electron temperature (T_e), the reaction rate coefficient (k) for each reaction, and the transport coefficients. Then the electron energy equation is solved at each mesh point to calculate T_e. Using this value of T_e, rate and transport coefficients at that mesh point are then interpolated from the table.

In order to better represent the variation in electron energy distributions that occur in the mixing zone of two gases (such as that of He and humid air which occurs in plasma jets), the method of defining zones for solutions to Boltzmann's equation was improved. Zones are regions of the mesh that share properties such as total gas density and mole fractions. Boltzmann's equation is solved using the two-term spherical harmonic expansion for the average gas composition in a given zone. The resulting lookup tables will provide significantly different rate coefficients in that portion of the mesh that is composed of pure helium compared to humid air. Previously the grouping of nodes into zones was defined explicitly in the model geometry. If there were not enough zones to capture gradations in mole fractions, discontinuities occurred in the IW propagation due to discontinuities in rate coefficients for inelastic processes across zone boundaries.

To better address the continuous gradation of mole fraction from, for example, the core of the He plume into ambient air, the spatially based zones for which Boltzmann's equation was solved were replaced with zones based on the mole fraction of air in He. After the initial fluid simulation has reached its steady state, but before the voltage pulse, the computational nodes are binned into zones by the mole fraction of a specified species. With prior knowledge of the dependence of the electron energy distribution (EED) on the specified mole fractions, the binning of zones could be, for example, a linear or log-scale list of cut-off mole fractions. In the case of a molecular gas (air) mixing with an atomic gas (He), the EED is highly sensitive to

small amounts of molecular gas, due to the low threshold energy of electron impact excitation to rotational and vibrational modes. For this type of mixing the Boltzmann zones are best defined based on a log-scale in molecular gas concentration.

Using this method means that updates to the Boltzmann lookup tables during the simulation are typically not required. In the geometrically defined zones previously used, electron-density weighted mole fractions of gases were used to define mole fractions in zones and updates were required as the IW propagates and the spatial distribution of electron density changed. This method required updates to the Boltzmann tables as frequently as every 0.1 ns, which becomes a computational burden and motivates having a small number zones. When using mole-fraction based zones, and the changes in gas composition are not significant (i.e. dissociation and ionization fractions are low), updates to the lookup tables are not required. This reduces the computational cost of the additional zones, thereby enabling a large number of zones.

2.2.4 Electron Energy Equation

The electron temperature is calculated by solving the electron energy equation

$$\frac{\partial}{\partial t}\left(\frac{3}{2}n_e k_B T_e\right) = \vec{j}_e \cdot \vec{E} - \nabla \cdot \left(\frac{5}{2}\vec{\Gamma}_e k_B T_e - \kappa\left(T_e\right)\nabla T_e\right) - \sum_i \Delta\varepsilon_i R_i \tag{2.37}$$

$$\vec{j}_e = e\vec{\Gamma}_e \tag{2.38}$$

$$R_i = k_i(T_e)\prod_j n_j^{a_{ij}^{(L)}} \tag{2.39}$$

where n_e is the electron density, k_B is Boltzmann's constant, and T_e is the electron temperature. The first term of Eq. 2.37 is energy transferred to electrons by the local electric field, the terms in parentheses address the convection and conduction of electron energy. The last term addresses losses (and gains) of electron energy due to elastic and inelastic collisions. $\vec{j}_e$ is the electron

current density, $\vec{\Gamma}_e$ is the electron flux, κ is the electron thermal conductivity, $\Delta\varepsilon_i$ is the change in electron energy in reaction i. The reaction rate, R_i, is defined in Eq. 2.39 where $k_i(T_e)$ is the rate as a function of electron temperature by interpolating the lookup table generated by solving Boltzmann's equation, or by the Arrhenius form in some cases. n_j is the density of reactant species j which appears on the left hand side of the reaction i $a_{ij}^{(L)}$ times.

The electron energy equation (Eq. 2.37) is solved at every plasma timestep using successive over-relaxation (SOR) with a relaxation factor of 1.7 to 1.8. In Eq. 2.37, the T_e has units of temperature, but in the results reported throughout this dissertation, T_e refers to the product of $\frac{3}{2}k_B T_e$ in units of eV, as is the convention in the field. In the case of non-Maxwellian electron energy distributions, the T_e is defined by the average electron energy, $\frac{3}{2}\int_0^\infty f(\varepsilon')\varepsilon' d\varepsilon'$.

2.2.5 Neutral Transport

The density of neutral species is calculated by

$$\frac{\partial n_i}{\partial t} = -\nabla\cdot\left(\vec{v}n_i\right) + -\nabla\cdot\left(-D_i\nabla n_i\right) + S_{vi} + \left[S_{si}\right]_b \tag{2.40}$$

where n_i is the density of neutral species i, $\vec{v}$ is the fluid velocity, D_i is the diffusion coefficient of species i, and S_{vi} is the volumetric source of species i due to all gas phase reactions. S_{si} is the source or loss of species i as a result of wall reactions and applies only to plasma nodes which neighbor nodes on the surface of materials. The neutral densities are solved using a Runge-Kutta method or implicitly using an SOR method.

The diffusion coefficients of neutral species are estimated using the Lennard-Jones potentials.[9] The diffusion coefficient of species i in gas j is

$$D_{ij} = 0.001858\sqrt{\frac{m_i + m_j}{m_i m_j}}\frac{T_g}{p_j \sigma_{ij} \Omega\left(\frac{T_g}{\varepsilon_i \varepsilon_j}\right)}, \tag{2.41}$$

where p_j is the partial pressure of species j in atmospheres, σ_{ij} is given by Eq. 2.5, and Ω is a collision integral, a function of gas temperature and the Lennard-Jones potentials.[9]

D_i is a density-weighted average of the diffusion coefficients of species i in all the species included in the model. Because these diffusion coefficients are defined by the local gas composition and updated at every timestep, their calculation can be a significant computational cost. To reduce this, the density-weighted average is limited to species whose mole fraction is above a certain threshold, in these cases 0.01%, on at least one node. This simplification of the transport coefficients results in a 25-40% decrease in overall computational time.

During the afterglow calculation, the ions densities are also calculated using Eq. 2.40 because Poisson's equation is no longer solved. The primary difference is that during this afterglow, the diffusion coefficients of the ions are averaged to reduce unphysical charge separation.

$$D_{ave,i} = \frac{\sum_i D_i n_i}{\sum_i n_i} \tag{2.42}$$

where D_i is the diffusion coefficient of ion i, having a density n_i. After this average is applied, charge neutrality is also enforced by setting the electron density equal to the difference in positive and negative charges at each timestep.

2.2.6 Fluid Dynamics

Because atmospheric pressure plasmas are highly collisional, the flow can be represented by a single advective velocity, allowing the fluid dynamics to be solved as a single fluid system.

However, because the density is non-uniform as different gases mix together (e.g. He flowing into air), the Navier-Stokes Equations must be modified to address a non-uniform mass density. The modified continuity equations used in the model are

$$\frac{\partial N}{\partial t} = -\nabla \cdot \left(N\vec{v} + \sum_{i,k} \frac{f_{ik}}{A_k} \hat{n}_k \right) \tag{2.43}$$

$$\frac{\partial NM}{\partial t} = -\nabla \cdot \left(\sum_i m_i \Gamma_i + \sum_{i,k} \frac{m_i f_{ik}}{A_k} \hat{n}_k \right) \tag{2.44}$$

where N is the total gas number density of charged and neutral species, M is the average molecular weight and $\vec{v}$ is the single fluid velocity. The sum in Eq. 2.43 is the contribution of the inlet flowing f_{ik} molecules per second of species i into an area of A_k. $\hat{n}_k$ is the normal vector of inlet surface k. m_i is the molecular weight of and $\vec{\Gamma}_i$ is the flux of species i.

The momentum equation is

$$\frac{\partial \left(NM\vec{v} \right)}{\partial t} = -\nabla P - \nabla \cdot \left(MN\vec{v}\vec{v} \right) - \nabla \cdot \bar{\tau} + \sum_i q_i n_i \vec{E} + NM\vec{g} \tag{2.45}$$

P is the pressure, q_i is the charge of species i, n_i is the density of species i, and E is the electric field. $\bar{\tau}$ is the stress tensor due to viscosity, and $\vec{g}$ is the acceleration due to gravity. The fourth term addresses the momentum transfer from charged species to the bulk fluid.

The fluid energy equation is used to calculate the gas temperature

$$\frac{\partial \left(Nc_v T_g \right)}{\partial t} = -\nabla \left(-\kappa \nabla T_g + \rho \vec{v} c_v T_g \right) + P\nabla \cdot \vec{v} - \sum_m R_m \Delta H_m + \sum_i \vec{j}_i \cdot \vec{E} + \Phi \tag{2.46}$$

where c_v is the constant volume specific heat, T_g is the gas temperature and κ is the thermal conductivity. ρ is the fluid mass density. R_m is the rate of chemical or electron impact reaction m, including elastic electron heating, ΔH_m is the change in enthalpy of reaction m, $\vec{j}_i$ is the

current density of ion *i*, and Φ is the viscous dissipation. At atmospheric pressure, the collision frequency is high enough that all neutral species have the same advective velocity, but individual species diffuse within this bulk flow. These equations are solved on the gaseous plasma nodes implicitly, using an approach described by Norberg, *et al*.[6] The resulting system of equations is solved using DSLUCS, a sparse matrix solver from the SLATEC Common Mathematical Library.[10] This solver uses a biconjugate gradient squared method with incomplete LU decomposition preconditioning. A relative error of 10^{-6} is used for convergence at each call to the solver. During the plasma calculation, the fluid velocities are updated approximately every 10^{-9} s.

Solving the Navier-Stokes equations in the fluid module means solving for the total number density of all species, *N*. However, this quantity is also calculated in the plasma chemistry modules which produce the density of each species. To reconcile these two calculations, a renormalization of the plasma species occurs. This coupling has been improved to make the fluid calculation more self-consistent. If the advective flow field is updated every 01 ns, the densities produced in the plasma chemistry module, including solution for charged species and Poisson's equation, are updated much more frequently. Before an update to the fluid values,

$$N_0 = \sum_{i}^{species} n_{0i} \,, \tag{2.47}$$

is set to the sum of all of the species densities. N_0 and n_{0i} refer to the total density and the density of individual species before the fluid update. This will reflect any change in number density due to dissociation that has occurred over the last 1 ns. After the fluid update is complete, a new value of *N* is obtained. This value may have changed as the result of expansion from

highly dissociated regions. The gas phase species are scaled so they add up to the total density *N* before continuing with the plasma chemistry calculation by setting

$$n_i = n_{0i} \frac{N}{N_0}. \tag{2.48}$$

This improved coupling of the two number density calculations enables gas expansion to be accurately captured by *nonPDPSIM*.

2.2.7 Radiation Transport

The rate of photoionization (or photodissociation), $S_{p,ik}$, for photon *k* interacting with species *i*, at position $\vec{r}$ in the plasma is given by

$$S_{p,ik}(\vec{r}) = n_i(\vec{r}) \cdot \sigma_{ik} \int A_k n_k(\vec{r}') G_k(\vec{r}', \vec{r}) d^3\vec{r}', \tag{2.49}$$

where $n_i(\vec{r})$ is the density of absorber species *i*, and σ_{ik} is the cross section for the photoionization (or photodissociation) reaction of photon *k* with species *i*. The integral represents the flux of photons at the computational node at position $\vec{r}$. This is the integral of photoemission at all other nodes ($\vec{r}'$), multiplied by a transfer function. A_k is the Einstein emission coefficient of photon *k* emitted form species *k*, which has a density of n_k. The Green's function operator, $G_k(\vec{r}', \vec{r})$, is the fraction of the photons emitted from the node at $\vec{r}'$ which reach the node at $\vec{r}$. Because the computational cost of including photoionization between every pair of nodes scales with the number of nodes squared, the integral is typically limited to a subset of the computational domain. First, a user specified maximum distance between pairs of nodes is applied. Second, materials are assumed to be opaque, therefore only pairs of nodes which have a line of site through the plasma are considered. The Green's function operator in Eq. 2.49 is

$$G_k\left(\vec{r}',\vec{r}\right) = \frac{\exp\left(-\int_{\vec{r}}^{\vec{r}'} \sum_m \sigma_{mk} n_m\left(\vec{r}''\right) d\vec{r}''\right)}{4\pi\left|\vec{r}'-\vec{r}\right|^2}, \qquad (2.50)$$

where σ_{mk} is the absorption cross section of the photon *k* by species *m*. n_m is the density of absorbing species *m*, and $\vec{r}''$ is the line of sight vector from $\vec{r}'$ to $\vec{r}$. The integral along $\vec{r}''$ describes the rate at which photons are absorbed between $\vec{r}'$ and $\vec{r}$, and the denominator accounts for the reduction of the flux as the photons spread isotopically in 3-dimensional space.

The integral inside the exponential in Eq. 2.50 is the most challenging portion of the calculation. In order to compute this integral, the line of sight vector, $\vec{r}''$, is drawn from the emitting node (at $\vec{r}'$) to the absorbing node (at $\vec{r}$). The emitting node is considered the initial *base node*. The two neighbors of the base node, which are closest to $\vec{r}''$ are selected, and the chord connecting these neighbors intersects $\vec{r}''$. If this intersection is within a material, $G_k\left(\vec{r}',\vec{r}\right)$ = 0, otherwise, the density of n_m is interpolated onto $\vec{r}''$ and added to the integral. Of the two selected neighbors, the node which is closest to $\vec{r}''$ is selected as the next base node. The process is then repeated until reaching the absorbing node at $\vec{r}$. The value of $G_k\left(\vec{r}',\vec{r}\right)$ for each pair of nodes is calculated once, just before the start of the plasma pulse and after establishing the steady state flow dynamics.

2.2.8 Liquid Module

Liquids are addressed in essentially the same ways as the plasma in the model, with a density that is much higher. Charged and neutral species transport and potential are solved in the same way as in the gas phase. The liquid is assumed to be stagnant, Navier-Stokes equations are not solved in this region, and the electron temperature is fixed at the thermal value because

electrons will rapidly lose energy to collisions at these large densities. Though the model can address liquids in general, it has primarily been used with liquid water.

The chemistry is also modified to address the fact that the reaction rates and stable species in the liquid are in many cases distinct from that of the gas phase. In the case of species which have these distinct reaction mechanisms, a liquid version of the same gas phase species is included. For example $H_3O^+_{aq}$ is the liquid version of H_3O^+. As soon as a molecule of H_3O^+ enters the liquid region, it is automatically converted to $H_3O^+_{aq}$.

Some species have a very short lifetime in liquid water, and rapidly react with H_2O_l. For these species, it is not necessary to have a separate reaction mechanism for the liquid. For example, electronically excited states of He, such as $He(2^3S)$ react rapidly in the liquid $He(2^3S) + H_2O_l \rightarrow He_{aq} + H_2O^+_{aq} + e_{aq}$. Therefore no $He(2^3S)_{aq}$ is required in the mechanism, limiting the total number of species and the computational time. This logic applies to most rotationally, vibrationally, and electronically excited states, as well as many ions which rapidly charge exchange with H_2O_l.

Transport of charged and neutral species across the gas-liquid interface also requires some special considerations. Charged species are assumed to solvate upon contact with the liquid surface. They are not allowed to exit the liquid and return to the gas phase. Henry's law is applied for each neutral species by defining the flux from the gas to a neighboring liquid node as

$$\begin{aligned} \Gamma_{gl} &= \frac{D_g}{\Delta x}\left(1 - \frac{n_l}{n_g h}\right)\left(n_g - n_l\right), \quad n_l \le n_g h \\ &= 0, \quad n_l > n_g h \end{aligned} \tag{2.51}$$

where D_g is the diffusion coeffecient at the gas phase node, Δx is the distance between the gas and liquid neighbors, n_g is the number density of the species at the gas node, and n_l is the number

density at the liquid node. h is the Henry's law constant. If the liquid density is greater than the Henry's law equilibrium value, the flux from the gas to liquid node is is in the reverse direction. The flux of neutral species from the liquid node to its neighboring gas node is

$$\begin{aligned}\Gamma_{lg} &= \frac{D_l}{\Delta x}\left(1-\frac{n_g h}{n_l}\right)\left(n_l - n_g\right), \quad n_g \le \left(n_l \middle/ h\right) \\ &= 0, \quad n_g > \left(n_l \middle/ h\right)\end{aligned} \tag{2.52}$$

where D_l, the diffusion coefficient at the liquid node is used instead of that of the gas node. By using the de-solvation rate is lower than that of the solvation rate.

2.2.9 Electron Monte Carlo Simulation

In some circumstances, treating electrons as a fluid introduces some errors. For example, in a sheath along a surface, often E/N is large enough that electron transport can be more beam-like, and a kinetic approach is more appropriate. In this case, electrons can be treated as particles using a Monte Carlo approach. In *nonPDPSIM*, the electrons emitted from surfaces (from photoemission, ion-induced secondary electron emission, or field emission) can be treated using the electron Monte Carlo simulation (eMCS).

In this case, at each call to the eMCS a number of pseudoparticles (typically a few hundred) is released from each surface node. The weight of these pseudoparticles (number of electrons per computational particle) depends on the electron emission rate from the material. These electrons are assumed to have an initial energy of 4 eV and a trajectory which is selected randomly. The position and velocity of each electron is updated according to the local electric field. As the electron loses energy to collisions, if its energy drops below 3.6 eV (90% of its

initial energy), it is added to the bulk electron fluid. This serves as a source of net charge, electron density, and electron density in the fluid equations.

Electron energy distributions (EEDs) are computed separately for Monte Carlo electrons, and these provide additional sources of ionization and excitation rates that are added to those contributions from the continuum.

The particles are tracked until they are transferred to the bulk fluid, are lost to recombination or attachment, are lost to surfaces, or exit the region in which the eMCS is applied. Electrons produced by electron-impact ionization by eMCS particles are tracked as additional eMCS particles.

Because tracking Monte Carlo particles on an unstructured mesh is challenging, the eMCS module uses a structured cartesian mesh which overlays the existing unstructured mesh. The electric field on the unstructured mesh is interpolated onto the structured mesh at the beginning of each call to the eMCS. Sources of electrons and electron impact ionization are interpolated onto the unstructured mesh. This is typically applied only over the region of the geometry where the eMCS particles would be present. The eMCS can be used for only electrons emitted from particular materials relevant to this process.

The eMCS module is updated at a user specified frequency, typically every 10^{-9} s. During each update, the electric field and gas composition is held constant. Between each update, the secondary electron emission source and the electron impact ionization source due to secondary electrons and their progeny are held constant.

2.3 Author's Contributions

Though both of the models discussed in this chapter were created by others, the author has made significant contributions to the model described above. In *GlobalKin*, the module for

addressing liquids, including solvation of charged and neutrals species and evaporation, was created. In *nonPDPSIM*, the analytical method of calculating matrix elements for the charged species described in Sec. 2.2.2 was derived and implemented. This has led to increased stability of the simulations and improved efficiency. The close coupling of the fluid dynamics and the neutral species densities calculations described in Sec. 2.2.6 was implemented. This coupling enabled the more accurate tracking of the expansion of the gas after localized heating and dissociation. Henry's law was implemented in a way that is more consistent with the liquid reaction mechanism. The transport of charged species during the afterglow calculation, described in Sec. 2.2.5, was improved to provide limit the artificial production of electrons that can occur by assuming charge neutrality. The improvements in the afterglow calculation were done in collaboration with other users.

2.4 Figures

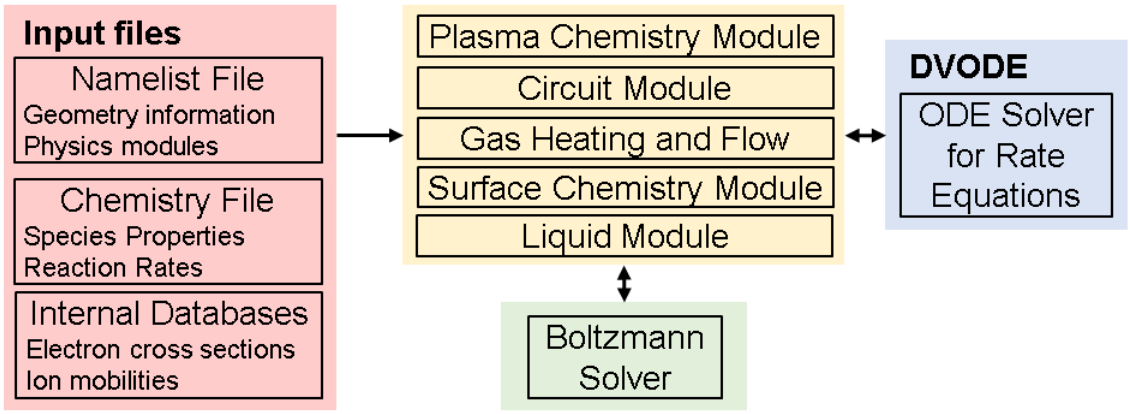

Fig. 2.1 Flow chart of *GlobalKin*, the 0-dimensional plasma model used in this dissertation.

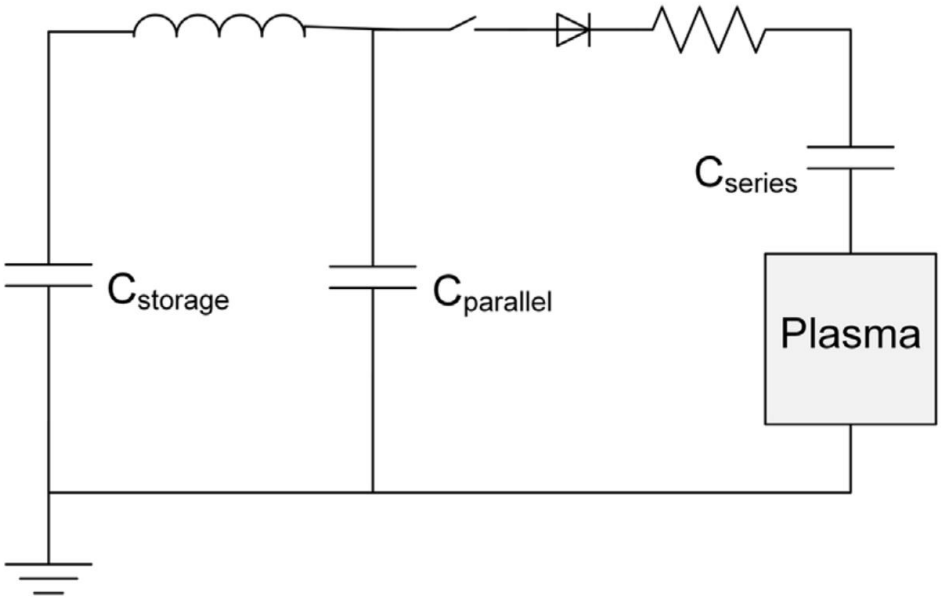

Fig. 2.2 Default circuit in *GlobalKin*.[11]

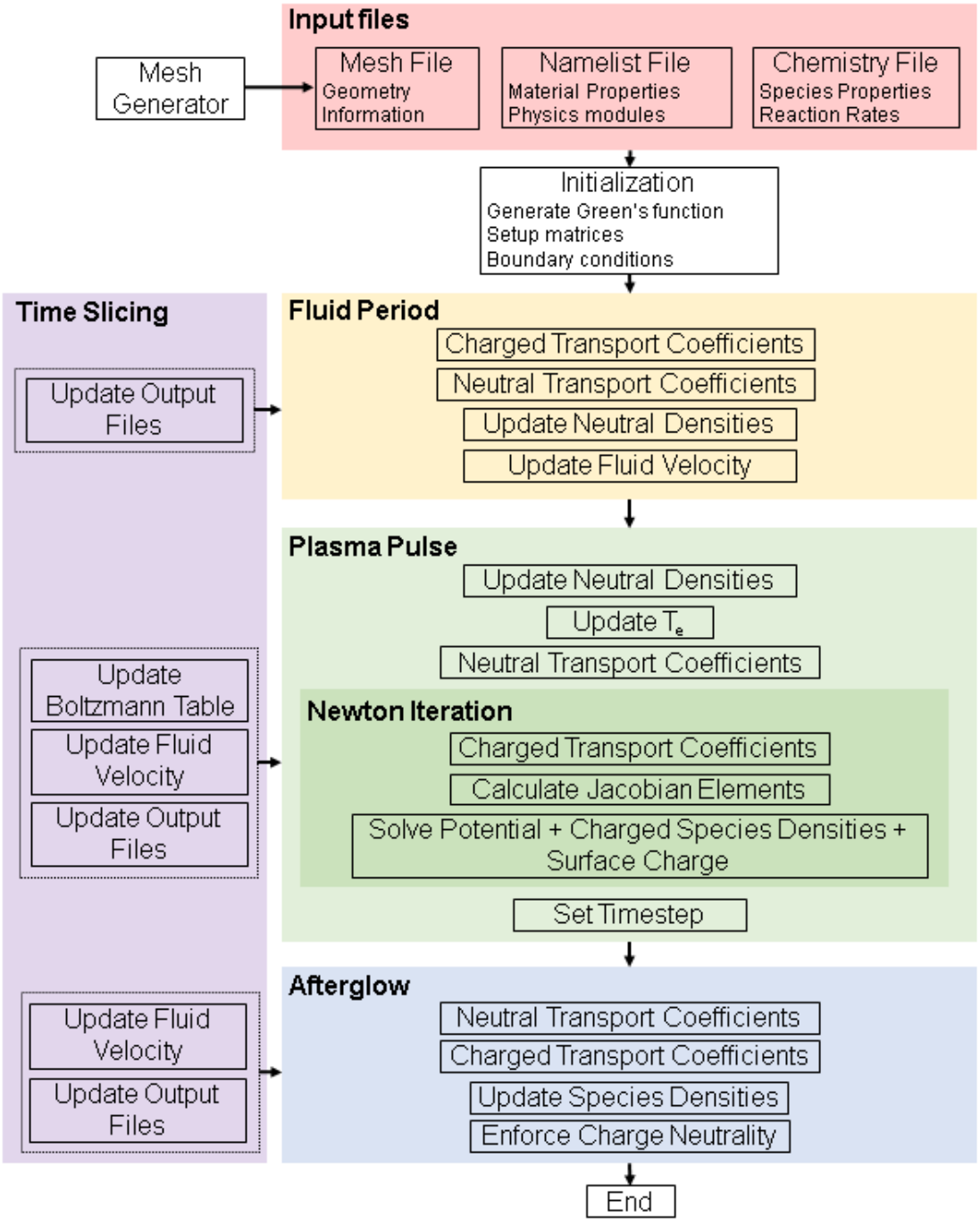

Fig. 2.3 Flow chart of *nonPDPSIM*, the 2-dimensional plasma hydrodynamics model used in this work.

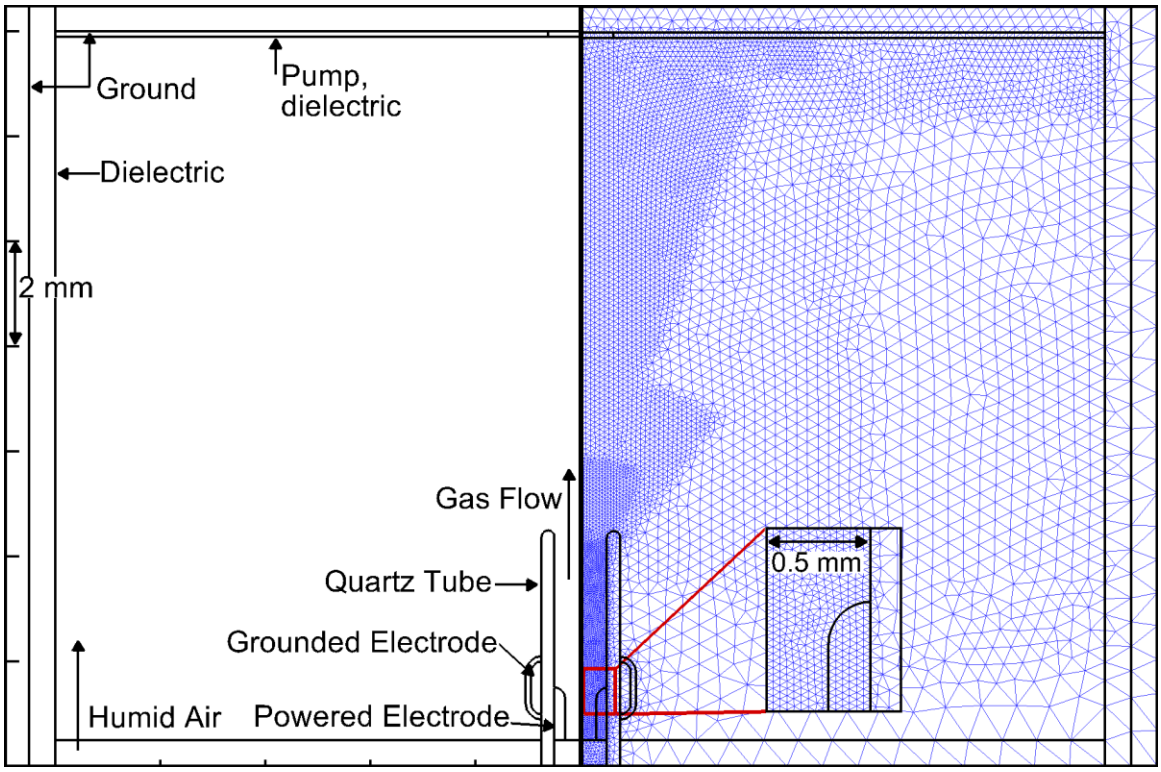

Fig. 2.4 An example of a cylindrically symmetric geometry of an APPJ for use in *nonPDPSIM*. (left) The material properties and (right) the computational mesh.

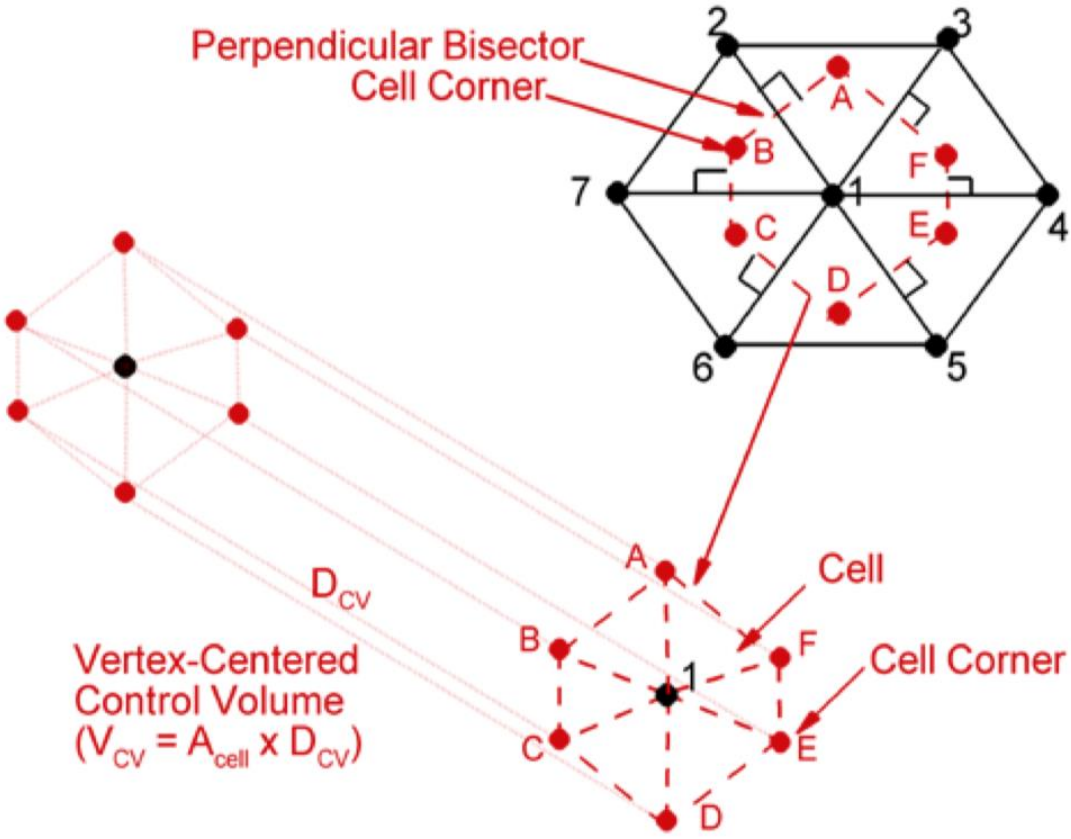

Fig. 2.5 The control volume interpretation of the computational mesh. The control volume surrounding a node defined by the perpendicular bisectors of each chord.[12]

2.5 References

[1] R. Dorai and M. J. Kushner, J. Phys. D: Appl. Phys. **35,** 2954 (2002).

[2] P. N. Brown, G. D. Byrne and A. C. Hindmarsh, SIAM J. Sci. Stat. Comput. **10,** 1038 (1989).

[3] J. F. M. van Rens, J. T. Schoof, F. C. Ummelen, D. C. van Vugt, P. J. Bruggeman and E. M. van Veldhuizen, IEEE Trans. Plasma Sci. **42,** 2622 (2014).

[4] P. Rumbach, N. Griggs, R. M. Sankaran and D. B. Go, IEEE Trans. Plasma Sci. **42,** 2610 (2014).

[5] G. J. M. Hagelaar and L. C. Pitchford, Plasma Sources Sci. Technol. **14,** 722 (2005).

[6] S. A. Norberg, E. Johnsen and M. J. Kushner, Plasma Sources Sci. Technol. **24,** 035026 (2015).

[7] Yousef Saad, "SPARSKIT: A basic tool-kit for sparse matrix computations", (2005).

[8] D.L. Scharfetter and H. K. Gummel, IEEE Trans. Electron Devices **16,** 64 (1969).

[9] J. O. Hirschfelder, C. F. Curtiss and R. B. Bird, "*Molecular Theory of Gases and Liquids*", (Wiley, 1954).

[10] "SLATEC Common Mathematical library", (1993).

[11] A. M. Lietz and M. J. Kushner, J. Phys. D: Appl. Phys. **49,** 425204 (2016).

[12] J.-C. Wang, PhD Thesis, "Modeling Studies of Atmospheric Pressure Microplasmas: Plasma Dynamics, Surface Interaction and Applications", (University of Michigan, 2014).

Chapter 3 Air Plasma Treatment of Liquid Covered Tissue: Long Timescale Chemistry[1]

Atmospheric pressure plasmas have shown great promise for the treatment of wounds and cancerous tumors. In these applications, the sample is usually covered by a thin layer of a biological liquid. The reactive oxygen and nitrogen species (RONS) generated by the plasma activate and are processed by the liquid before the plasma produced activation reaches the tissue. The synergy between the plasma and the liquid, including evaporation and the solvation of ions and neutrals, is critical to understanding the outcome of plasma treatment. The atmospheric pressure plasma sources used in these procedures are typically repetitively pulsed. The processes activated by the plasma sources have multiple timescales – from a few ns during the discharge pulse to many minutes for reactions in the liquid. In this chapter we discuss results from a computational investigation of plasma-liquid interactions and liquid phase chemistry using a global model with the goal of addressing this large dynamic range in timescales. In modeling air plasmas produced by a dielectric barrier discharge over liquid covered tissue, 5,000 voltage pulses were simulated. The chemistry was then simulated for 5 minutes after plasma treatment. Due to the accumulation of long-lived species such as ozone and N_xO_y, the gas phase dynamics of the 5,000th discharge pulse are different from those of the first pulse, particularly with regards to the negative ions. The consequences of applied voltage, gas flow, pulse repetition frequency,

[1] The results discussed and portion of the text in this chapter have been previously published in A. M. Lietz and M. J. Kushner, "Air plasma treatment of liquid covered tissue: long timescale chemistry", J. Phys. D.: Appl. Phys. **49,** 425204 (2016).

and the presence of organic molecules in the liquid on the gas and liquid reactive species are discussed.

3.1 Introduction

Atmospheric pressure plasmas (APPs) sustained in air are being investigated in the context of plasma medicine for treating human tissue to promote the healing of wounds [1], especially chronic wounds such as those associated with diabetes. APPs have also been shown to induce apoptosis in cancer cells [2] and to kill bacteria [3]. Reactive oxygen and nitrogen species (RONS) represent an important component of the influence of the plasma on biological systems – these species can trigger response pathways in individual cells, as well as produce systemic responses [4]. These RONS consist of radicals such as hydroxyl (OH), hydroperoxyl (HO_2), oxygen atoms (O), nitrogen dioxide (NO_2) and nitric oxide (NO), and other reactive neutrals such as ozone (O_3), singlet delta oxygen ($O_2(^1\Delta_g)$) and peroxynitrous acid (ONOOH). Although several of these reactive species are known to be important in normal biological processes, such as metabolism and response to bacterial invasion [5,6], the precise mechanisms and roles of these species are not well known.

During plasma treatment, the tissue is often covered by a thin layer of a blood serum-like liquid or a saline-like solution. Plasma produced species are processed by the liquid layer, reacting with each other, the liquid, and organic molecules in the liquid before reaching the underlying tissue. In the case of water dominated liquids, the reaction chemistry of the gas phase plasma-liquid system has multiple timescales. At one extreme are the ns duration processes during the gas phase plasma pulse which produces primary radicals such as O and OH by electron impact dissociation. These species are renewed on a pulse-by-pulse basis. At the other extreme, reactive nitrogen species (RNS) such as HNO_3 accumulate over many tens to thousands

of discharge pulses. There are similarly large dynamic ranges of timescales for plasma activated processes in the liquid. For example, solvated OH_{aq} (the aq subscript denotes an aqueous species) reacts on timescales as short as microseconds to form H_2O_{2aq}.[7] In contrast, the density of $ONOOH_{aq}$ may evolve over many hours in plasma activated water.[8–10]

The diagnostics available for measuring concentrations of reactive species in liquids are typically limited to long timescales, often minutes and sometimes hours after plasma treatment.[11] Although real-time measurements of selected species are possible, such as for solvated electrons and OH_{aq}, these are not widely applied techniques.[12,13] Investigations of the plasma activation of liquids may then need to address a large dynamic range in time approaching or exceeding minutes, not only to address the long term chemistry but also to enable comparisons with the available diagnostics.

Several computer models have been developed to address plasma-liquid interactions for biological and environmental investigations. Experiments on the removal of pollutants from a flowing water film by dielectric barrier discharges (DBDs) have been modeled using computational fluid dynamic (CFD) techniques.[14] O_3 and the pollutant were included in this multi-fluid model, while explicitly calculating liquid reactions and pollutant interactions. There was indication that the plasma increased the transport of pollutants from the liquid into the gas, most likely from induced mixing of the liquid. Y. Matsui *et al*. developed a model for discharges within O_2 bubbles moving through water.[15] The liquid and gas phase kinetics in this model were weakly coupled. The gas dynamics were solved on different timescales than the liquid and used to update the liquid species. The calculations closely matched experimental measurements of the breakdown of acetic acid by OH. Agreement with the experiments was achieved by including the reaction $O_{aq} + H_2O_{aq} \rightarrow OH_{aq} + OH_{aq}$, indicating that this process contributes

significantly to OH_{aq} levels in the liquid. A further study separated this system into 3 phases, gas, liquid, and plasma, with each phase represented by global kinetics models.[16] Increasing the water vapor density in the bubble resulted in more H_2O_{2aq} and less O_{3aq}. The water vapor density, and the resulting H_2O_{2aq}, increased as a function of discharge current.

Kelly and Turner developed a model of a radio frequency (RF) plasma jet sustained in He/O_2 while treating the liquid as a reactive surface.[17] The plasma and neutral chemistry were decoupled. Plasma dynamics were resolved as a 1-dimensional jet and solved to the steady state. The sources of neutrals based on the plasma dynamics calculations were extrapolated in time for use by a 2-dimensional fluid and neutral chemistry model. The treatment of a liquid substrate was considered by assuming a thin layer of gas saturated with water vapor. They showed that H_2O_2, O_3, and $O_2(^1\Delta_g)$ were the dominant RONS in the vapor layer above the liquid, and H_2O_2 would likely be the most abundant RONS in the liquid.

A comprehensive modelling study by Liu et al. addressed a surface microdischarge sustained remotely from the liquid being treated.[18] The physical domain was divided into 3-zones: plasma, gas consisting of long-lived neutral species, and liquid. The three zones were computationally tightly coupled, and the equations representing the zones were simultaneously integrated. The plasma zone was treated using global kinetics, while the neutral gas and liquid were treated using 1-dimensional transport. The most reactive neutral species NO, OH, O, and $O_2(^1\Delta_g)$ did not survive transport from the remote plasma source to the liquid. The most significant gas phase species influencing the liquid chemistry were H_2O_2, O_3, HNO_3, and HNO_2. These species are capable of producing more reactive species in the liquid, such as OH_{aq}, providing a source of reactivity at depths in the liquid that cannot be reached by the more reactive species produced in the remote plasma source.

The goal of the present investigation is to improve our understanding of the influence of operational parameters of atmospheric pressure discharges sustained in air on the chemical activation of liquids, in this case water, on timescales of ns to several minutes. Understanding the coupling of gas phase and liquid chemistry and their dependence on voltage, gas flow, pulse frequency, and the presence of organics in the water is required to optimize the application of these sources for desired biological outcomes. With this goal in mind, in this chapter, we discuss results from a computational investigation using a global model of DBD processing of thin water layers for long periods (thousands of discharge pulses) and sufficient post-pulse reaction time that the products in the gas phase and liquid essentially reach their final state.

The importance of multidimensional effects in plasma-liquid interactions is well known. It is true that 2- and 3-dimensional models can provide a more complete description of the gas phase breakdown processes, the spatial dependence of the discharge and transport into the liquid. However, the computational burden and complexity of these models make it difficult to address the hundreds to thousands of discharge pulses and many minutes of post-discharge reactions relevant to plasma treated liquids. With the large variety of plasma sources currently being experimentally investigated (e.g., DBDs, surface microdischarges, plasma jets), the parameter space is large. A global model which is capable of addressing both short and long time scales and which is generically applicable to all discharges may provide a viable method to investigate these multiscale processes.

The model employed in this investigation is a global simulation modified to have two zero dimensional zones – one gas phase and one liquid – which exchange species only through the interface between the gas and liquid. Separate reaction mechanisms were employed in each zone. Although this study focuses on the plasma activated liquid chemistry, the chemistry is not

the only means through which plasma affects the tissue. High electric fields can initiate electroporation of cell membranes [19], and the role of photons may also be significant, especially as a source of radicals in the liquid by photolysis of water.

We found that for a DBD sustained in humid air, the positive ion dynamics change little over thousands of discharge pulses. However, the negative ion and neutral dynamics evolve as long-lived species such as O_3 and NO_2 accumulate in the gas. In the liquid, many RONS accumulate over thousands of pulses and then decay in the post-plasma period. The pH of the liquid decreases due to the acids (e.g., HNO_x) that are produced in the gas and solvate into the liquid, or are produced directly in the liquid. Increasing voltage increases most of the reactive species densities due to the increase in power deposition. Due to the disparities in timescales for formation of reactive oxygen species (ROS) and RNS, gas flow can be used as a means to regulate the relative rates of solvation of ROS and RNS into the liquid. An increased gas flow rate decreases RNS, which are slower to form, in the liquid while increasing some ROS. Similarly, pulse repetition frequency (PRF) may be a control mechanism. An increase in PRF increases the ratio of O_{3aq} to HNO_{3aq} produced by the plasma. The presence of organic molecules in the liquid can largely consume the ROS, allowing a larger fluence of RONS to solvate in the liquid for species that normally saturate in the liquid.

The model used in this investigation is described in Sec. 3.2. Results from this investigation are discussed in Sec. 3.3. In addition to a detailed analysis of the base case, consequences of varying applied voltage, flow rate, pulse-repetition frequency and organic content of the water are discussed. Concluding remarks are in Sec. 3.4.

3.2 Description of the Model

The model used in this study, *GlobalKin*, is a 0-dimensional plasma model which treats the plasma as a well-stirred reactor. This model includes databases for electron impact cross sections, and ion mobilities, and modules addressing gas flow, diffusion, and liquid chemistry. *GlobalKin* is described in detail in Chapter 2.

3.2.1 Reaction Mechanism

The full reaction mechanism contains 79 gas phase species, 83 liquid phase species, 1680 gas phase reactions, and 448 liquid reactions. The mechanism includes the species associated with a humid air plasma interacting with water. Henry's law constants used in the model are listed in Table 3.1. In large part, the gas phase reaction mechanism developed by Van Gaens *et al*. [20] for argon atmospheric pressure plasma jets interacting with humid air was used for the gas phase portion of the mechanism with the addition of carbon dioxide (CO_2).

The liquid mechanism, shown in Table 3.2, is based on that of Tian *et al*. [21] with modifications to address all species in the gas phase mechanism and some improvements based on recent publications. Water cluster ions were added to the gas phase mechanism and assumed to charge exchange with water on timescales of several ns. In particular, the peroxynitrite chemistry has been improved based on recent experiments.[8] For each weak acid hydrolysis reaction, the reverse process was also added with an appropriate rate coefficient to fit with the dissociation constant for each acid. These updates enable a better estimate of the pH in the liquid. Long timescale decay reactions were added to address the many minutes studied here, including the thermal decay of peroxynitrite, ozone, $O_2(^1\Delta_g)$, and the ozone anion. Several excited states from the gas phase mechanism were added to the liquid mechanism. The liquid reactivity in this reaction mechanism may be overestimated, as excited states from the gas phase entering the

liquid with enough energy to dissociate H_2O were assumed to perform that dissociation. In reality there is some branching ratio between dissociative and non-dissociative deexcitation.

3.2.2 Geometry and Operation Parameters

The discussion of results from this investigation is organized into several sections – base case, varying voltage, flow rate of gases, pulse repetition frequency, and presence of biomolecules in the liquid. In all cases the geometry is as shown in Fig. 3.1, and represents treatment of tissue having an area of 1 cm^2 covered by 1 mm of water, with an air gap of 2 mm. The simulation is initialized with humid air at 100% relative humidity ($N_2/O_2/H_2O/CO_2$ = 76.6/20.3/3.5/0.03) as would occur over several minutes of exposure of the narrow gas gap to the liquid surface. The exception is when varying gas flow, where the initial humidity is 50% to reflect the incoming gas from the ambient. The liquid in the base case is pure water with 8.9 ppm dissolved N_2, 4.8 ppm dissolved O_2, and 140 ppb CO_2, which are their equilibrium values with air. The diffusion length in the gas phase is d/π = 637 μm, where d is the width of the air gap. In the base case, the applied voltage is 10 kV, at a PRF of 500 Hz. The simulation is run for 5,000 pulses (10 s) followed by a 290 s post-pulse period (5 minutes total). There is no significant gas heating in the base case because the top surface and the tissue is assumed to remain at 300 K. In reality some heating of these surfaces is expected. In the 5 minutes of post-pulse period in the base case, flow of gas phase species out of the plasma volume is fixed to zero, i.e. the gas volume is approximated as a closed container.

The circuit addressed in the model is shown in Fig. 3.1b. The capacitance of the water in the circuit model is 71 pF, and the total series capacitance, the due to the liquid and the tissue, is 1 pF. The circuit then consists of a capacitor (1 pF) and resistance (1 Ω) in series with the plasma, a capacitor in parallel with the plasma (1 pF), and a switch having an inductance of (100

nH). A constant voltage is applied by assuming that the storage capacitor ($C_{storage}$) is initially at the applied voltage. The storage capacitance is much greater than the parallel and series capacitance, so its charge is not depleted during the discharge pulse. The switch is closed at the beginning of each pulse. The circuit module turns off when the voltage across the plasma changes polarities, and is kept off until the beginning of the next pulse. All of the circuit parameters are reset with each pulse. The initial charge on the series capacitor is set to zero, the initial current is assumed to be zero, and the discharge voltage is set to 10 kV. At the beginning of each pulse the electron density is renormalized to be at least $n_e = 10^8$ cm^{-3} and electron temperature is set to $T_e = 0.025$ eV. Charged neutrality is maintained by the addition of the appropriate amount of N_2^+.

3.3 Plasma activation of water

3.3.1 Base Case: Multiple-pulse plasma activation of water

Upon application of the 10 kV at the start of each voltage pulse, the small initial electron density, 10^8 cm^{-3}, begins to avalanche. Since the impedance of the plasma is large at this time, the voltage across the discharge is essentially the applied voltage, which produces a slowly varying E/N (electric field/gas number density) of 2.0×10^{-15} V-cm^2 or 200 Td (1 Td = 10^{-17} V-cm^2). The electron temperature, T_e, remains at its pre-breakdown value of 4.3 eV until the electron avalanche produces a sufficiently large electron density to lower the impedance and the E/N of the discharge. This occurs when $n_e \approx 6 \times 10^{11}$ cm^{-3}, as shown in Fig. 3.2b. With the decrease in impedance and E/N of the plasma, T_e decreases. The avalanche proceeds, increasing the electron density to a maximum of 2.8×10^{12} cm^{-3} as long as T_e remains above 2.8 eV. Below this value, the net ionization coefficient is negative, attachment to O_2 begins to dominate electron losses, and the electron density decreases. As the discharge current increases, the voltage drop

across the series resistance becomes significant, and the discharge voltage further decreases. For this particular circuit, the capacitance in parallel with the discharge and the inductance produce a slight ringing in the discharge voltage. T_e follows the discharge voltage closely, and this ringing in discharge voltage is reflected in T_e. Note that at t = 2.4 ns and $T_e \approx 2.1$ eV, the rate of electron loss decreases. The attachment to O_2 in atmospheric pressure plasmas has two components – 3-body attachment which consumes thermal electrons and 2-body dissociative attachment which has a threshold energy. Over this range of electron temperature, the rate of 2-body attachment decreases as T_e decreases, thereby decreasing the total rate of electron loss. For these conditions, the duration of the current pulse is determined by the charging of the dielectric which is represented by the series capacitance.

As discussed below, with each successive discharge pulse, the composition of the ambient gas changes with the accumulation of products initiated by dissociation of the feedstock gases. The changes in composition of the gas on the basis of mole-fraction are relatively small. After 5,000 pulses, species other than the feedstock species (N_2, O_2, H_2O, CO_2) have a mole fraction of only 7.3×10^{-3}. However, even these small changes in composition in the gas at the beginning of a discharge pulse affect the characteristics of the discharge. For example, the electron temperature and electron density are shown in Fig. 3.2b for the 1st, 100th and 5,000th pulse. T_e is not particularly affected by these long timescale changes in composition. The value of T_e is in large part determined by the rate of electron energy loss as a function of T_e and the rate of avalanche which determines the impedance and so the E/N of the discharge. Both of these parameters are dominated by the major constituents of the gas. It is also for this reason that the maximum electron density does not appreciably change with successive pulses.

Electron losses can, however, be significantly affected by species having small mole fractions, particularly for processes that attach low energy or thermal electrons. For our conditions, the accumulation of ozone (O_3) and nitrous oxide (N_2O) on a pulse-to-pulse basis results in more attachment during the afterglow of the discharge pulse which produces a more rapid decrease in electron density. The dissociative attachment processes to O_3 are

$$e + O_3 \rightarrow O_2 + O^-, \quad (3.1a)$$

$$e + O_3 \rightarrow O_2^- + O, \quad (3.1b)$$

which have a total rate coefficient of 8×10^{-10} cm^3s^{-1} when T_e = 2.9 eV (corresponding to the maximum power deposition). N_2O, undergoes dissociative attachment,

$$e + N_2O \rightarrow O^- + N_2, \quad (3.2)$$

with rate coefficient 2×10^{-10} cm^3s^{-1} when T_e = 2.9 eV.

Since the air above the water is humid, the polar gas-phase water molecules often surround the ions in the afterglow forming water-cluster ions, denoted by $M^+(H_2O)_n$ or $M^-(H_2O)_n$.[22,23] The initial ions form cluster-ions in tens of ns. The ion-ion plasma containing mostly cluster ions decays several orders of magnitude between pulses, but does not fully recombine before the next pulse. Although the addition of water molecules to water cluster ions is exothermic up to 5-10 water molecules in humid atmospheric pressure environments [24], the reaction mechanism in this study was simplified to having clusters with no more than two water molecules.

Densities of ions which trace their origins to O_2, N_2 and H_2O are shown in Fig. 3.3 during the discharge pulse and afterglow for the 1st, 100th and 5000th pulses. For ions which trace their origins to O_2, the dominant positive ion during the avalanche phase of the discharge pulse is O_2^+. Formation of O_4^+ follows by 3-body associative charge exchange, though its density is two

orders of magnitude lower during the discharge pulse. The O_2^+ and O_4^+ then charge exchange with the ambient H_2O forming H_2O^+. O_2^- forms on two different timescales, producing the bimodal curve shown in Fig. 3.3. The first peak is due to charge exchange from O^- to O_2 and occurs while the T_e is still elevated. The formation of O^- is significant only during the discharge pulse since dissociative electron attachment to O_2 has a threshold energy of 3.6 eV. The second peak in O_2^- is due to three body attachment to O_2, which has a maximum at T_e = 0.06 eV, so the rate of reaction is largest as T_e is falling. Over several thousand pulses, the first peak in O_2^- density increases because of accumulation of O_3, and the dissociative attachment reactions shown in Eq. 3.1. The second peak decreases with increasing pulses since the electron density more rapidly decreases, and there are fewer electrons available when T_e = 0.06 eV.

The production of O_3^- has three dominant sources:

$$O^- + O_2 + M \rightarrow O_3^- + M, \tag{3.3a}$$

$$O^- + O_3 \rightarrow O + O_3^-, \tag{3.3b}$$

$$O_2^- + O_3 \rightarrow O_2 + O_3^-. \tag{3.3c}$$

As O_3 accumulates over many pulses, O_2^- and O^- densities increase during the first 10 ns, and as a result the O_3^- production increases as well. The surviving O^- and O_2^- are eventually converted to water cluster ions. At times exceeding hundreds of microseconds, $O^-(H_2O)$ and $O_2^-(H_2O)_n$ are the surviving negative ions.

For ions tracing their origin to nitrogen, N_2^+ is first formed by electron impact ionization of N_2 but quickly undergoes associative charge exchange to form the cluster ion N_4^+, which has the highest density of any nitrogen-containing ion during all discharge pulses. The larger RNS, such as NO_2, NO_3, N_2O_4, HNO_3, take several reactions to form, are not particularly reactive in the gas phase, and therefore accumulate over many pulses. Nitrite (NO_2^-) has a negligible

density on the first pulse and increases to be one of the dominant negative ions with a density of 2×10^{11} cm^{-3} during later pulses. As HNO_3 accumulates from the 1st to 100th pulse, dissociative attachment produces NO_2^-,

$$e + HNO_3 \rightarrow NO_2^- + OH. \quad (3.4)$$

As O_3 accumulates from the 100th pulse to the 5000th pulse, the charge exchange reaction

$$O_3 + NO_2^- \rightarrow NO_3^- + HNO_2, \quad (3.5)$$

rapidly converts NO_2^- to nitrate (NO_3^-) and is the primary source of NO_3^-.

The densities of N^+, NO^+, NO_2^+ and $NO^+(H_2O)_n$ are little affected by the accumulation of species over the succession of pulses. These ions indirectly come from electron impact ionization of the N_2 and O_2 followed by

$$O^+ + N_2 + M \rightarrow NO^+ + N + M, \quad (3.6a)$$

$$N_3^+ + O_2 \rightarrow NO_2^+ + N_2. \quad (3.6b)$$

where O^+ is produced dominantly by dissociative ionization of O_2 and secondarily by direct ionization of O, though this is a small source. N_3^+ is the result of dissociative ionization of N_2 (or direct ionization of N, though this is also a small source) followed by the reaction $N^+ + N_2 + M \rightarrow N_3^+ + M$. Although direct electron impact of NO, NO_2, and N_2O can produce NO^+ and NO_2^+, their contributions are not significant even after 5,000 pulses of accumulation.

H_2O^+ is formed by direct electron impact ionization of H_2O in the gas phase and from charge exchange from N_2^+, N_4^+, and O_2^+ to H_2O. H_2O^+ reaches a density of 6×10^{11} cm^{-3}, but is quickly depleted in formation of hydronium, H_3O^+, by,

$$H_2O + H_2O^+ \rightarrow H_3O^+ + OH, \quad (3.7a)$$

$$OH + H_2O^+ \rightarrow H_3O^+ + O. \quad (3.7b)$$

H_3O^+ forms cluster ions, $H_3O^+(H_2O)_n$ which is the cluster ion having the maximum density with each pulse. OH^- and its cluster ion are the most abundant anions originating from H_2O with a maximum density of 7×10^{11} cm^{-3}. The OH^- forms by dissociative attachment ($e + H_2O \rightarrow OH^- + H$) to H_2O. There is some H^- formation by an analogous dissociative attachment process, but its production is limited to the first 2 ns when T_e is high, and so its density is an order of magnitude smaller than OH^-. The lifetime of OH^- decreases with successive discharge pulses as it charge exchanges with the increasing density of O_3 to form with O_3^-, which helps buoy the density of O_3^-. During early pulses when the density of O_3 is low, OH^- is slowly consumed, and so the O_3^- density remains fairly low at 2×10^{10} cm^{-3} until 100 ns at which point the density of OH^- begins to decrease. By the $5{,}000^{th}$ pulse, OH^- is rapidly consumed by charge exchange to O_3, producing a density of O_3^- in excess of 10^{11} cm^{-3}. Depletion of OH^- also occurs through formation of $OH^-(H_2O)_n$, however the density of this cluster ion also increases with the accumulation of O_3. The density of $O^-(H_2O)_n$ increases with O_3, which in turn generates $OH^-(H_2O)_n$ in the reaction $O^-(H_2O)_n + H_2O \rightarrow OH^-(H_2O)_n + OH$. In this way the buildup of O_3 depletes OH^-, but increases the density of $OH^-(H_2O)_n$.

From this analysis, we find that stable neutral products accumulate over thousands of pulses in humid air plasmas, which in turn affect the density and identity of anions. For these particular conditions, much of this multi-pulse anion chemistry can be traced to the accumulation of O_3. Therefore increases in gas temperature, which typically reduce the accumulation of O_3, would have a second order effect on the anion densities. The gas phase cations produced at each pulse are less affected by the accumulation of neutrals due, in large part, to the high humidity. The formation of H_3O^+ and its clustering with water represents the terminal cation, a process that is little affected by the accumulation of reactant products.

The densities of ROS and RNS are shown in Fig. 3.4 during the 1st, 100th and 5000th pulses. These species can be divided into three categories based on the timescales of their evolution. During each discharge pulse, short-lived species are formed by electron impact and are generally quenched or consumed by reactions prior to the next pulse. $N_2(v)$, $O_2(v)$, $N_2(A^3\Sigma_u)$, and $O_2(^1\Sigma_u)$ are in this group. A second set of species achieve a quasi-steady state density which modulates on a pulse-to-pulse basis as the species is produced and consumed. These species include O, OH, HO_2, $O_2(^1\Delta_g)$, N, NO, and NO_3. Finally, the third set of species have long lifetimes with densities that accumulate from pulse-to-pulse. These species either continue to accumulate through the last pulse or reach a steady state density. In either case, the timescales of the dynamics are much longer than the interpulse period of 2 ms. O_3, H_2O_2, CO, N_2O, HNO_2, NO_2, and HNO_3 are in this category.

A large fraction of the power deposition is expended in forming the vibrational and electronic excited states of N_2 and O_2. The vibrationally excited states $O_2(v)$ and $N_2(v)$ are generated with densities up to 6×10^{14} cm^{-3} and 2×10^{13} cm^{-3}. This stored energy contributes to gas heating by vibrational-translational (V-T) collisions on microsecond timescales. The first metastable electronically excited state of N_2, $N_2(A^3\Sigma_u)$, is rapidly quenched by O_2 through dissociative excitation and excitation transfer.[25] $O_2(^1\Sigma_u)$, the second excited state of O_2, is rapidly quenched by collisions with water vapor to form $O_2(^1\Delta_g)$. The production of electronically excited states also affects the discharge by two-step electron impact ionization and dissociation processes, which can enable more ionization at a lower T_e. Electron impact dissociation of H_2O produces H, which reacts to form H_2 ($H + H + M \rightarrow H_2 + M$) in a few microseconds, so H does not accumulate.

In the second set of species, the only electronic excited state that lasts beyond a few microseconds is $O_2(^1\Delta_g)$, with a collisional lifetime on the order of the interpulse period (2 ms). As a result, there is some accumulation of $O_2(^1\Delta_g)$ on a pulse-to-pulse basis. Most of the O atoms, produced by electron impact dissociation of O_2 and dissociative quenching of $N_2(A^3\Sigma_u)$ by O_2, are consumed in making ozone, $O + O_2 + M \rightarrow O_3 + M$, and this is the primary source of O_3. This reaction occurs within 100 μs and so O is mostly depleted with each pulse.

Electron impact dissociation of H_2O produces OH which combines to form H_2O_2 ($OH + OH + M \rightarrow H_2O_2 + M$), and the H_2O_2 accumulates to a density of 3×10^{13} cm^{-3}. This conversion takes slightly longer than the interpulse period of 2 ms, so there is some accumulation of OH from pulse to pulse. HO_2 is mainly produced by $H + O_2 + M \rightarrow HO_2 + M$, but there are other reactions which contribute to its production. HO_2 is produced hundreds of nanoseconds to several microseconds after the pulse, rather than during the discharge pulse as do species which result directly from electron impact processes. HO_2 is dominantly consumed by,

$$OH + HO_2 \rightarrow H_2O + O_2, \quad (3.8a)$$

$$HO_2 + O_2(^1\Delta_g) \rightarrow OH + O_2 + O. \quad (3.8b)$$

Nitrogen atoms produced by electron impact dissociation of N_2 are not a highly reactive species on their own at ambient temperatures, and so a large fraction of N atoms simply recombine to form N_2. However, their presence contributes significantly to formation of N_xO_y (especially NO) and HNO_x through reactions with ROS. NO primarily forms by $O_2 + N \rightarrow NO + O$ during early pulses. However, during later pulses N_2O begins to accumulate, and the reaction $N_2(A^3\Sigma_u) + N_2O \rightarrow N_2 + N + NO$ dominates the formation of NO. As a result, during later pulses, NO forms dominantly during the discharge pulse when the density of $N_2(A^3\Sigma_u)$ is large,

instead of during the afterglow. NO_2 and NO_3 are intermediate species to the formation of acids, and can also form higher order RNS (N_2O_3, N_2O_4, N_2O_5) which further facilitate acid formation.

The densities of the reactive species O, NO, $O_2(^1\Delta_g)$ and OH at the end of each interpulse period have a counter intuitive evolution over long time scales. These are species that undergo transients during each pulse – generation followed by consumption, but are not completely depleted before the next pulse. The consumption following each pulse increases with pulse number, resulting in their decaying to lower densities between pulses at the 5,000th pulse compared, for example, to the 100th pulse. Although their production during each pulse changes very little, the consumption of these species is more rapid as the gas phase RONS accumulate. These consuming reactions include

$$O + O_3 \rightarrow O_2 + O_2, \quad (3.9a)$$

$$O + NO_2 + M \rightarrow NO_3 + M, \quad (3.9b)$$

$$NO + O_3 \rightarrow NO_2 + O_2, \quad (3.9c)$$

$$O_2(^1\Delta_g) + O_3 \rightarrow O_2 + O_2 + O, \quad (3.9d)$$

$$OH + O_3 \rightarrow HO_2 + O_2. \quad (3.9e)$$

The presence of O_3 produces some additional O by dissociative attachment forming O_2^-, however in later pulses accumulating O_3 reacts with any remaining O.

The third group of species, with reactive timescales much longer than the interpulse period (here, 2 ms), includes several relatively stable species: H_2O_2 (from $OH + OH + M \rightarrow H_2O_2 + M$), O_3 (from $O + O_2 + M \rightarrow O_3 + M$), N_2O (from $O_2 + N_2(A^3\Sigma_u) \rightarrow N_2O + O$), and HNO_3. These species are generally unreactive in the absence of organic molecules and at ambient temperatures. Most of these stable species react with other reactive species (e.g. N_2^+, O), but not with other accumulated neutrals. Other species in this category are reactive, but have

longer reactive timescales. The cluster species HO_2NO_2 forms by $HO_2 + NO_2 + M \rightarrow HO_2NO_2 + M$, is stable in air and accumulates to 2×10^{14} cm^{-3}. NO_2 has long timescale dynamics, but is slowly converted to HNO_3 by $NO_2 + OH + M \rightarrow HNO_3 + M$. This reaction limits its maximum density to 1×10^{14} cm^{-3}. HNO_2 is a weak acid which accumulates to a density of 1×10^{14} cm^{-3} over many pulses, and eventually forms HNO_3.

During the long timescales (seconds to 10 s) diffusion losses by solvation to the liquid, based on the dynamic sticking coefficient defined in Eq. 2.12, can be significant for this group of species. The maximum fraction of the gas phase density that can be transferred from the gas to the liquid is a function of the Henry's law constant. Species whose densities continue to increase through the 5,000th pulse include H_2, O_3, N_2O, HNO_2, HO_2NO_2, and NO_2, all of which have lower Henry's law constants and, therefore, lower rates of loss by solvation into the liquid. Species with the highest Henry's law constants, H_2O_2 and HNO_3 reach a steady state because they are lost to the liquid through solvation at the same rate as their production.

3.3.2 Base Case: Plasma activated liquid chemistry

During each discharge pulse, fluxes of ions and electrons reach the surface of the liquid as a consequence of ambipolar diffusion. Upon entering the liquid, most of the positive ions (N_2^+, N_4^+, O_2^+, O_4^+, NO^+, H_2^+, NO_2^+ and their corresponding water cluster species) quickly charge exchange with H_2O_{aq}, forming $H_2O^+_{aq}$. The H_2O^+ quickly forms hydronium, $H_3O^+_{aq}$ by reacting with water, $H_2O_{aq} + H_2O^+_{aq} \rightarrow H_3O^+_{aq} + OH_{aq}$. The increasing density of $H_3O^+_{aq}$ then decreases the pH of the water. Electrons quickly solvate, which in our mechanism is represented by $H_2O^-_{aq}$, which then forms $O_2^-_{aq}$ by $H_2O^-_{aq} + O_{2aq} \rightarrow H_2O_{aq} + O_2^-_{aq}$. (Depending on the pH, some fraction of the $O_2^-_{aq}$ recombines with $H_3O^+_{aq}$, to form HO_{2aq} decreasing the pH). Excited state species from the gas phase which enter the water and which have enough energy to

dissociate water are assumed to quickly undergo dissociative excitation transfer, $M^*_{aq} + H_2O_{aq} \rightarrow M_{aq} + H_{aq} + OH_{aq}$. The excited state and ion chemistry occurs primarily during the first 100 ns after each pulse. In a spatially resolved model, the majority of these reactions would occur in the near-surface layer. Almost all of the rest of the neutral chemistry in the liquid happens over timescales longer than the interpulse period of 2 ms, accumulating over several pulses, as shown in Fig. 3.5. In a spatially resolved model, these reactions would occur deeper in the liquid.

Several acids formed in the gas or liquid dissociate in the liquid, generating $H_3O^+_{aq}$, and lowering the pH of the water. Nitric acid (HNO_{3aq}) is a strong acid which dissociates to form $NO_3^-_{aq}$, and it is the largest contributor to the plasma-induced acidification of the liquid. This acidification results in an $H_3O^+_{aq}$ density of 5×10^{16} cm^{-3} (8×10^{-5} M), and a final pH of 4.1 at the end of 5 minutes. For weak acids, which only partially dissociate, this process is described by pK_a, where $pK_a = -\log(K_a)$. K_a is the acid dissociation constant which is the equilibrium value of the products of the conjugate ions to the acid. In our reaction mechanism, these processes are represented by two reactions for each acid

$$HA_{aq} + H_2O_{aq} \rightarrow H_3O^+_{aq} + A^-_{aq}, \quad (3.10a)$$

$$H_3O^+_{aq} + A^-_{aq} \rightarrow HA_{aq} + H_2O_{aq}, \quad (3.10b)$$

The ratio of the reactions rates is 10^{-pKa}. (The liquid in this study does not contain a pH buffer.) Weak acids produced by the plasma include HNO_{2aq} ($pK_a = 3.4$), HO_{2aq} ($pK_a = 4.8$) and $ONOOH_{aq}$ ($pK_a = 6.8$). If the pH of the liquid is above the pK_a value for a given weak acid, that weak acid will be mostly in dissociated form (A^-_{aq}). So HNO_{2aq} will be mostly in the form $NO_2^-_{aq}$ even as the liquid pH drops to 4.1. However, $ONOO^-_{aq}$ will revert back to $ONOOH_{aq}$ once the pH falls below 6.8.

O_{3aq} is a dominant ROS in the liquid accumulating to 5×10^{16} cm^{-3} (8×10^{-5} M), primarily from the solvation of gas phase O_3. The negative ion $O_3^-{}_{aq}$ then forms by $O_2^-{}_{aq} + O_{3aq} \rightarrow O_{2aq} + O_3^-{}_{aq}$. $O_2(^1\Delta_g)$ solvates from the gas resulting in 1×10^{10} cm^{-3} (2×10^{-11} M) of $O_2(^1\Delta_g)_{aq}$, which decays by excitation transfer to H_2O_{aq}.

OH_{aq} has several significant sources including the solvation of gas phase OH and $O_{aq} + H_2O_{aq} \rightarrow OH_{aq} + OH_{aq}$. OH_{aq} rapidly forms H_2O_{2aq}. HO_{2aq} comes from solvation of HO_2 as well as from $O_{2aq} + H_{aq} \rightarrow HO_{2aq}$.

In general, in spite of there being a small equilibrium density of N_{2aq} in the liquid, the source of aqueous RNS is dominantly from N_xO_y species generated in the gas phase solvating into the liquid. The dominant reactions of N_xO_{yaq} are formation of acids, HNO_{xaq}. For example,

$$NO_{2aq} + NO_{2aq} + H_2O_{aq} \rightarrow HNO_{3aq} + HNO_{2aq}, \quad (3.11a)$$

$$NO_{aq} + NO_{2aq} + H_2O_{aq} \rightarrow HNO_{2aq} + HNO_{2aq}, \quad (3.11b)$$

$$NO_{2aq} + H_{aq} \rightarrow HNO_{2aq}, \quad (3.11c)$$

$$NO_{2aq} + OH_{aq} \rightarrow HNO_{3aq}, \quad (3.11d)$$

$$N_2O_{4aq} + H_2O_{aq} \rightarrow HNO_{3aq} + HNO_{2aq}, \quad (3.11e)$$

$$N_2O_{5aq} + H_2O_{aq} \rightarrow ONOOH_{aq} + ONOOH_{aq}. \quad (3.11f)$$

These acids can then dissociate by hydrolysis,

$$HNO_{3aq} + H_2O_{aq} \rightarrow NO_3^-{}_{aq} + H_3O^+{}_{aq} \quad (3.12a)$$

$$HNO_{2aq} + H_2O_{aq} \rightarrow NO_2^-{}_{aq} + H_3O^+{}_{aq} \quad (3.12b)$$

$$ONOOH_{aq} + H_2O_{aq} \rightarrow ONOO^-{}_{aq} + H_3O^+{}_{aq} \quad (3.12c)$$

As a result of these reactions, $NO_3^-{}_{aq}$ continues to accumulate in the liquid through the 5,000th pulse with a density of 5×10^{16} cm^{-3} (8×10^{-5} M). Peroxynitrous acid ($ONOOH_{aq}$) primarily forms by the reaction Eq. 3.4f. Because peroxynitrous acid ($ONOOH_{aq}$) and its conjugate base,

peroxynitrite ($ONOO^-_{aq}$), undergo different reactions, its lifetime and chemistry depends on pH. $ONOOH_{aq}$ isomerizes to form HNO_{3aq} or dissociates into OH_{aq} and NO_{2aq} in hundreds of ms. It is more stable in its dissociated form, peroxynitrite ($ONOO^-_{aq}$).

The cluster species HO_2NO_{4aq}, solvated from the gas phase, thermally decays to HO_{2aq} and NO_{2aq} with a time constant of several seconds, providing a mechanism to deliver radicals over much longer timescales than the application of plasma to the liquid. This reaction becomes important during the afterglow in the liquid. N_2O is a stable species in both the gas and liquid, originates with gas phase reactions and solvates to densities of 4×10^{15} cm^{-3} (7×10^{-6} M) in the liquid.

In plasma-liquid systems that have quiescent liquids, the top layer of the liquid can become saturated at their Henry's law equilibration value by in-diffusing gas phase species.[21] At that point, the in-coming diffusion terminates until the aqueous species either diffuse from the surface to reduce the density at the surface below their equilibrium value, or their densities decrease by reactions. In a system with a convectively dominated liquid, the in-coming solvated species are well-mixed in the entire liquid, which then reduces their densities near the surface and allows in-coming diffusion to continue. On very long time scales in *a non-reactive system*, the final densities for both systems will eventually reach the equilibrium value in the entire liquid volume. However, on intermediate times scales (short compared to in-liquid diffusion times but long compared to convective times) the well-stirred liquid is able to accept a larger fluence of reactants from the gas phase than a system that is not well-stirred. The well-stirred assumption used here should be considered an upper limit of the ability of the liquid to accept reactivity from the gas phase. The lack of a saturated liquid layer makes the solvation kinetics less sensitive to limitations on accepting reactants from the gas phase determined by Henry's law constants.

3.3.3 Base Case: Afterglow chemistry

After 5,000 discharge pulses lasting 10 s, power is removed from the DBD, and the system continues to evolve during the afterglow. Ions in the gas recombine in hundreds of microseconds after the plasma pulse, so they do not continue to deliver reactivity to the liquid during the afterglow. In the absence of gas flow, the reactive neutrals remain in the gas above the liquid until they are consumed by reactions or solvate into the liquid. First, we will discuss the behavior of the gas phase reactive neutrals.

The densities of gas phase species up to 5 minutes into the afterglow are shown in Fig. 3.6. Two distinct phases of decay occur for H_2O_2, HO_2NO_2, N_2O_5, HNO_3, HNO_2 and NO_2. For approximately 1 s after the discharge pulses terminate, the loss of these species is dominated by diffusion and solvation into the liquid while there are also small rates of production. After 1 s, the densities drop low enough that the rates of diffusion loss are on the order of their production rates. It is also possible that the diffusion into the liquid would slow when the density in the liquid approaches its equilibrium value given by Henry's law. However, that is not the case here. O_3 and N_2O do not follow this pattern because the ratio of their densities in the gas and the liquid are already close to their Henry's law equilibrium values due to their low Henry's law constant. The most reactive species, [OH, O, $O_2(^1\Delta_g)$, HO_2, N, NO] have gas-phase reaction rates with timescales much shorter than diffusion and so their losses are dominated by gas phase kinetics.

The densities of aqueous species are shown in Fig. 3.7 during the afterglow. In the liquid, the change in densities of most species results from reactions as opposed to transport. Diffusion out of the liquid into the gas can occur if a species is over-saturated, but it is not significant in this system. The most prevalent plasma produced species in the liquid are O_{3aq} and $NO_3^-{}_{aq}$. The cluster species HO_2NO_{2aq} thermally decays to HO_{2aq} and NO_{2aq} with a time constant of several

seconds. The resulting NO_{2aq} reacts with H_2O_{aq} to form HNO_{2aq} or HNO_{3aq}, which accounts for the increase in $NO_3^-{}_{aq}$ on timescales of tens of seconds. The HO_{2aq} hydrolyzes to form $H_3O^+{}_{aq}$ and $O_2^-{}_{aq}$. HO_{2aq} also reacts with OH_{aq} to form O_{2aq} and H_2O. Although H_2O_{2aq} is stable in pure water at room temperature, in this system the reaction $OH_{aq} + H_2O_{2aq} \rightarrow H_2O_{aq} + O_2^-{}_{aq}$ results in its consumption.

$ONOOH_{aq}$ isomerizes to form HNO_{3aq} or breaks down into OH_{aq} and NO_{2aq} in hundreds of ms, so it is more stable in its hydrolyzed form, $ONOO^-{}_{aq}$. This provides a source of OH_{aq} on long timescales.

3.3.4 Applied Voltage

Parametric studies were performed for otherwise identical conditions to the base case while varying the applied voltage, from 8 kV to 14 kV. It is expected that most species should increase in density with increasing voltage, due to the higher energy deposition. In this case, the total energy deposition over 5,000 pulses varies from 0.8 J-cm^{-3} (8 kV) to 1.6 J-cm^{-3} (14 kV). The maximum electron density increases from 9×10^{11} cm^{-3} (8 kV) to 1.2×10^{13} cm^{-3} (14 kV), and T_e varies from 3.7 eV to 5.5 eV. The peak gas temperature in all cases does not exceed 303 K. The temperature is kept low primarily as a result of thermal conduction, the last term in Eq. 2.9, due to the small diffusion length of the gap. This is a result of the assumption that the surfaces in contact with the plasma are held at 300 K, and a 3 K temperature difference in a 2 mm gap is enough to drive an energy fluence to the walls of 1.6 J-cm^{-3} in 10 s. In reality, the gas heating may be higher, depending on the thermal properties of materials in contact with the plasma. In a global model, the energy deposition is averaged over the volume of the reactor, whereas a multi-dimensional model enables energy to be deposited in the smaller volume of the streamer. This latter process can produce locally higher gas temperatures.

The normalized densities of gas phase species as a function of voltage are shown in Fig. 3.8 and of aqueous phase species in Fig. 3.10. Normalized values are the densities after 5,000 pulses (10 seconds) divided by the maximum value over the parameterized range. The intent here is to show the sensitivity of each species to the independent variable. The normalized densities of gas and liquid RONS after 2 minutes are shown in Fig. 3.9 and Fig 3.11.

The normalized densities of most species increase approximately linearly with voltage over the range of 8 kV to 14 kV. This corresponds to a nearly linear increase of the energy deposition with voltage, which means that the storage capacitor does not fully discharge. The gas phase species following this trend include CO, H_2O_2, O, N, HNO_3, NO_2, N_2O_5, HNO_2, NO_2, N_2O, and HO_2NO_2.

The electron impact dissociation of H_2 ($e + H_2 \rightarrow e + H + H$) has a threshold energy of 8.8 eV, so the rate of this process increases significantly with T_e, and therefore with voltage. This increase in the production of H enables the reaction $H + O_2 + M \rightarrow HO_2 + M$ to produce more HO_2, so a higher voltage favors HO_2 production.

After 5,000 pulses (10 s), the densities of O_3 and H_2 both peak at 10 kV, as shown in Fig. 3.8a. From 8 to 10 kV the inventory of O atoms produced during each pulse increases, leading to production of more O_3 by $O + O_2 + M \rightarrow O_3 + M$. As the voltage continues to rise, the production of O remains relatively constant, however less O ends up in the form of O_3. The density of NO_2 also increases with voltage and consumes much of the O during production of NO_3 (Eq. 3.9b). The HO_2 densities at the end of the last pulse are nearly independent of voltage. More HO_2 is produced with higher energy deposition, but more NO_2 is also produced, forming more of the cluster species HO_2NO_2.

Late into the afterglow, (2 minutes after the start of treatment corresponding to 10 s of plasma treatment followed by 110 s afterglow), species such as H, CO, and N in the gas phase have reacted, and their densities are negligible. The densities of the remaining RONS are shown in Fig. 3.9. The density of O is very low at this point, on the order of 10^6 cm^{-3}, but the fact that O_3 can continue to generate O in small amounts at long timescales may be significant in some applications. H_2O_2, O_3, and most of the RNS have the same dependence on voltage as at the end of the last discharge pulse. The density of H_2 has changed from increasing with voltage after the last discharge pulse (Fig. 3.8a) to decreasing approximately linearly with voltage after 2 minutes (Fig. 3.9a). This change is due to reactions with the liquid, and occurs on long timescales because only a small fraction of the H_2 is solvated at any given time. Although the lifetime of HO_2 in this system is short (in the afterglow, it is consumed by reactions $HO_2 + NO_2 + M \rightarrow HNO_2 + O_2 + M$), it is produced on long timescales by the thermal decay of the cluster HO_2NO_2. At higher voltages, the density of HO_2 remains higher long into the afterglow, as more HO_2 has been stored in HO_2NO_2. This storage of HO_2 causes the density to be nearly independent of voltage at 10 s, but increasing with voltage after 2 minutes. For the RNS, the dependence of the density of NO_3 on voltage changes slightly over 2 minutes. At higher voltages, there is more NO_2, which can slowly convert to NO_3 long into the afterglow.

The liquid phase species whose densities scale with the energy deposition after 5,000 pulses (10 s) are OH_{aq}, H_2O_{2aq}, CO_{aq}, $H_3O^+_{aq}$, $NO_3^-{}_{aq}$, $ONOOH_{aq}$, N_2O_{aq}, HO_2NO_{2aq} and NO_{2aq}. These densities are shown in Fig. 3.10. The voltage dependence of the densities of O_{3aq} and H_{2aq} at the end of the last pulse matches the voltage dependence of their gas phase counterparts (Fig. 3.8a). This indicates that the production of these species originates predominantly in the gas followed by solvation into the liquid. The density of $O_3^-{}_{aq}$ decreases with applied voltage

because it is consumed by $OH_{aq} + O_3^-{}_{aq} \rightarrow HO_{2aq} + O_2^-{}_{aq}$, and at higher voltages, the density of OH_{aq} is larger. The conjugate base of $HO_{2\,aq}$ is $O_2^-{}_{aq}$. At lower voltages, the density of $O_2^-{}_{aq}$ is significant, as the pH is close to the pK_a of HO_{2aq}. At higher voltages, the pH is less than the pK_a value, and HO_{2aq} does not dissociate. For the RNS, the conjugate base of HO_2NO_{2aq} is $O_2NO_2^-{}_{aq}$ whose density does not significantly increase for voltages above 10 kV as the liquid becomes too acidic for net dissociation.

After 2 minutes, the voltage dependence of the densities of OH_{aq}, H_{2aq}, $O_3^-{}_{aq}$, and $O_2NO_2^-{}_{aq}$ have significantly changed while the voltage dependence of densities of $O_2^-{}_{aq}$, NO_{2aq}, $ONOOH_{aq}$ and HO_2NO_{2aq} have changed to a lesser extent, as shown in Fig. 3.11. OH_{aq} has a short lifetime, so by 2 minutes, the majority of OH_{aq} that was produced during the plasma-on period has reacted to form H_2O_{2aq}. The OH_{aq} after 2 minutes arises from a few slow processes, primarily the reaction

$$H_{2aq} + H_2O_{2aq} \rightarrow H_{aq} + OH_{aq} + H_2O_{aq}. \qquad (3.13)$$

The density of $O_3^-{}_{aq}$ increases with voltage due to its production by charge exchange between $O_2^-{}_{aq}$ and O_{3aq}, both of whose densities increase with voltage. At 10 s, the trend in the density of $O_3^-{}_{aq}$ with voltage is dominated by the reaction $OH_{aq} + O_3^-{}_{aq} \rightarrow HO_{2aq} + O_2^-{}_{aq}$. However, after 2 minutes, the density of OH_{aq} is too low to significantly affect the density of $O_3^-{}_{aq}$.

In the afterglow, H_{2aq} is consumed by reaction with H_2O_{2aq} (Eq. 3.13). H_2 has a low Henry's law constant, so most of the H_2 resides in the gas. However, H_2O_2 has a large Henry's law constant, so most of the H_2O_2 resides in the liquid. This means that the reaction between these two species is limited by the transport of H_2 from the gas to the liquid. Since the density of H_2O_{2aq} increases with energy deposition, after a long enough afterglow, H_2 and H_{2aq} both decreases with increasing voltage.

$O_2^-{}_{aq}$ and $O_2NO_2^-{}_{aq}$ are both the dissociated forms of weak acids with a $pK_a = 4.8$. During the afterglow, the pH continues to decrease due to transport of RNS from the gas phase and acid formation. At low voltage, these changes in pH are more significant and have a larger influence on the fractional dissociation of these weak acids. As a result, from 10 s to 2 minutes, both species have a relative decrease in density at low voltage.

The densities of NO_{2aq}, HO_{2aq}, $ONOOH_{aq}$, and HO_2NO_{2aq} are more sensitive to voltage at 2 minutes than at 10 s. The densities of these species fall more rapidly at low voltages. There is less stored HO_2NO_{2aq} at low voltage, so it is depleted more rapidly in the liquid. NO_{2aq} and HO_{2aq} production at long timescales is a result of the slow decay of HO_2NO_{2aq}, so they follow the same dependence as HO_2NO_{2aq}. $ONOOH_{aq}$ production at long timescales is an indirect result of this slow decay by the reaction $NO_{aq} + HO_{2aq} \rightarrow ONOOH_{aq}$.

3.3.5 Gas Flow Rate

In most experiments using DBDs to treat liquids and tissue, there is no deliberate effort to control the flow of gas through the volume in which the plasma is sustained. Some mixing of the gas in the plasma region with the ambient gas is expected from natural convection. On the other hand, forced convection could be used as a control mechanism for regulating RONS in both the gas and liquid phases. To investigate these possibilities, forced convective flow was included in the model. The resulting normalized densities of gas phase species are shown in Fig. 3.12 and of aqueous phase species in Fig. 3.13 after 5,000 pulses. Important scaling parameters in varying the flow rate are the residence time of the gas in the discharge region (τ_r) and the interpulse period (τ_p). Their ratio, τ_r/τ_p is the average number of discharge pulses each gas molecule is exposed to before it flows out of the system.

There are at least three ways in which flow can affect the reactive species densities in the gas at the end of the 5,000 pulses. First, the evaporating water vapor into the gas phase is flushed out, so increasing flow decreases the relative humidity in the gas. Second, some of the reactive species flow out before they have time to undergo higher order reactions. Third, O_3 does not accumulate since it flows out the system which then prevents the previously discussed changes in the negative ion processes during later pulses.

Over the range of flow rates of 1 to 2000 sccm (τ_r/τ_p = 6,000 to 3), the gas phase H_2O density varies from 8.6×10^{17} cm^{-3} to 1.3×10^{17} cm^{-3}. The air is less saturated with water vapor for shorter residence times. The peak electron density during the last pulse varies from 2.2×10^{12} cm^{-3} (flow rate of 1 sccm) to 2.4×10^{12} cm^{-3} (2000 sccm). This small increase in electron density is due to a combined effect of smaller densities of H_2O and O_3. The maximum value of T_e increases slightly as the humidity decreases with increasing flow rate, from 4.2 eV for 1 sccm to 4.3 eV for 2000 sccm, due to the decrease in H_2O. In short, as flow rates increase, O_3 and H_2O densities decrease, so n_e and T_e increase slightly. These small changes do not result in major changes in the initial production of reactants during the discharge pulse. The exceptions are those species whose production or consumption are dependent on the density of H_2O which decreases with increasing flow rate.

The gas phase RONS can be divided into three types of dependencies on flow rate. The densities of some species decrease with increasing flow rate simply because of a shorter residence time, which causes the species or its precursors to flow out of the system. There are also species whose densities decrease more gradually with flow rate because the RONS they react with also decrease with flow. Lastly, some species have a maximum density at an intermediate flow rate.

In the gas phase, O_3, H_2, N_2O, HO_2NO_4, N_2O_5 behave simply with flow rate – their densities decrease with increasing flow rate because their residence times decrease. This means there is less accumulation and, in the case of RNS, less opportunity for the multiple reactions required for their formation.

The second category of species, HNO_2, CO, HNO_3, HO_2 and H_2O_2, also decrease with increasing flow rate, however not as rapidly as the first group. For these species, there is some increase in their production as flow increases, but that increase in production is less significant than losses due to the increase in flow rate. The reactions which produce this slower decrease with flow include:

$$NO + OH + M \rightarrow HNO_2 + M, \quad (3.14a)$$

$$CO_2 + N \rightarrow CO + NO, \quad (3.14b)$$

$$OH + NO_2 + M \rightarrow HNO_3 + M. \quad (3.14c)$$

Each of these reactions have one or more reactants whose density increases with flow at some point in the range of 1 to 2,000 sccm. For example, the density of HNO_2 decreases with flow but has a plateau between 20 sccm and 200 sccm. This range corresponds to a rapid increase in the density of NO (discussed below). For CO, the recombination with O_3 decreases as flow rate increases with there being less O_3, resulting in the density of CO decreasing more slowly with flow rate. The density of HO_2 also decreases more slowly with flow rate because its losses by the reaction $HO_2 + NO_2 + M \rightarrow HO_2NO_2 + M$ are also reduced.

As the flow rate increases, the density of H_2O_2 generally decreases. However at intermediate flow rates, 20 sccm to 100 sccm, there is no decrease. The OH produced with each discharge pulse decreases with increasing flow rate, as the relative humidity decreases. However there are several reactions that can deplete OH after its production, including

$$OH + OH + M \rightarrow H_2O_2 + M, \quad (3.15a)$$

$$OH + NO_2 + M \rightarrow HNO_3 + M. \quad (3.15b)$$

As the flow rate increases, the density of NO_2 decreases, and so more of the OH generated during each pulse is available to produce H_2O_2. These opposing effects as flow rate increases cause the H_2O_2 density to stay approximately constant between 20 and 100 sccm.

The third category of gaseous species, which peak at an intermediate flow, includes $O_2(^1\Delta_g)$, OH, O, NO, and NO_2. The dependence of the densities of these species on flow rate should be evaluated not only in terms of their rates of production, but also in terms of how quickly they are consumed by reactions. The maximum rates of production of these species change very little with flow rate, but they are consumed by reactions more quickly at low flow rates due to there being larger densities of O_3 and NO_x. The dominant consuming reactions for each of these species are:

$$O_2(^1\Delta_g) + O_3 \rightarrow O_2 + O_2 + O, \quad (3.16a)$$

$$O + O_3 \rightarrow O_2(^1\Delta_g) + O_2, \quad (3.16b)$$

$$OH + O_3 \rightarrow HO_2 + O_2, \quad (3.16c)$$

$$NO + O_3 \rightarrow NO_2 + O_2, \quad (3.16d)$$

$$NO_2 + NO_3 + M \rightarrow N_2O_5 + M. \quad (3.16e)$$

These reactions occur on timescales on the order of the interpulse period and so their rates are not affected by flow out of the system until high flow rates. In general, the most stable gaseous RONS (O_3, H_2, N_2O, HO_2NO_4, N_2O_5, HNO_2, HO_2, CO, HNO_3, H_2O_2) decrease with increasing flow rate, while the species with a lifetime on the order of the interpulse period ($O_2(^1\Delta_g)$, OH, O, NO, and NO_2) peak at intermediate flow rates.

In this model, the liquid is well-stirred, but stagnant. That is, there is no convective flow as there is in the gas phase. Nevertheless, the composition of the liquid is a function of gas flow rate due to the rates of solvation of gas phase species. The dependence of the density of aqueous species on the gas phase flow rate is shown in Fig. 3.13. These dependencies can be separated into the same three groups: densities decreasing with flow due to residence time of gas phase species, decreasing with flow more slowly, and peaking at an intermediate flow rate.

The first category (aqueous densities decreasing with flowrates) includes all of the gas phase RNS, shown in Fig. 3.13c, with the exception of NO_{2aq}. The RNS tend to take several reactions to form in the gas, and as a result, the gas phase RNS or their precursors leave the system at high flow rates before they can solvate into the liquid. O_{3aq}, H_{2aq}, $H_3O^+_{aq}$, and CO_{aq} also simply decrease with flow rate due to a shorter residence time of their gas phase precursors.

The second category of species, densities which generally decrease with flow rate, include NO_{2aq}, H_2O_{2aq}, OH_{aq}, and CO_{aq}. The dependence of NO_{2aq} on flow rate differs from that of its gas phase precursor NO_2. At low flow rates when the densities of HO_2 and NO_2 are both high, the NO_2 can be stored in the cluster molecule HO_2NO_2, which then solvates in the liquid and produces NO_{2aq} at later times. At higher flow rates, the cluster molecule does not form in abundance, and the NO_{2aq} is mostly a result of direct solvation of NO_2. H_2O_{2aq} and CO_{aq} follow the dependence on gas phase flow rate of their gas phase precursors. The density of OH_{aq} decreases with flow rate until 50 sccm. Above 50 sccm, the density of OH_{aq} continues to decrease, but more slowly. This dependence differs from that of the density of gas phase OH because there are significant sources of OH_{aq} in the liquid, such as

$$O_3^-{}_{aq} + H_3O^+_{aq} \rightarrow O_{2aq} + OH_{aq} + H_2O_{aq}, \quad (3.17a)$$

$$OH^-_{aq} + H_3O^+_{aq} \rightarrow H_{aq} + OH_{aq} + H_2O_{aq}, \quad (3.17b)$$

$$O_{aq} + H_2O_{aq} \rightarrow OH_{aq} + OH_{aq}, \quad (3.17c)$$

$$ONOOH_{aq} + H_2O_{aq} \rightarrow OH_{aq} + NO_{2aq} + H_2O_{aq}. \quad (3.17d)$$

These sources of OH_{aq} are more significant at low flow rates as there are higher densities of $ONOOH_{aq}$ and $O_3^-{}_{aq}$. Above 50 sccm, the solvation of OH from the gas is the more significant source of OH_{aq}.

Liquid species whose densities are maximum at intermediate flow rates include $O_2(^1\Delta_g)_{aq}$, HO_{2aq}, and $O_2^-{}_{aq}$. The variation of the density of $O_2(^1\Delta_g)_{aq}$ with flow rates simply matches the density of its gas phase precursor having a maximum at 500 sccm. HO_{2aq} hydrolyzes to form $H_3O^+{}_{aq}$ and $O_2^-{}_{aq}$ if the liquid is not too acidic. At higher flow rates the liquid is less acidic due to there being less solvated RNS. At flow rates above 100 sccm, the dissociated form of HO_{2aq} ($O_2^-{}_{aq}$) dominates. The sum of the densities of HO_{2aq} and $O_2^-{}_{aq}$ monotonically increases with flow rate, which differs from the behavior of HO_2 in the gas. This sum increases with flow rate because OH_{aq} decreases with flow rate, and OH_{aq} consumes HO_{2aq} by the reaction $OH_{aq} + HO_{2aq} \rightarrow O_{2aq} + H_2O_{aq}$.

3.3.6 Pulse Repetition Frequency

When varying the pulse repetition frequency (PRF), comparing the reactive species densities at the end of the same number of pulses is misleading because species have had less time to react and solvate at high PRF. For this reason, we compared the reactive species as a function of PRF after 110 s, corresponding to 12 s after completing 5,000 pulses at the lowest PRF. These results are shown in Fig. 3.14 for PRFs from 51 Hz to 5.1 kHz. The gas temperature is essentially 300 K at the lowest frequencies and reaches 307 K at 5.1 kHz. T_e is unaffected by PRF and the peak n_e decreases with PRF (from 2.9×10^{12} cm^{-3} to 2.4×10^{12} cm^{-3}).

The densities of most of the RONS, including OH_{aq}, H_2O_{2aq}, $O_3^-{}_{aq}$, HO_{2aq}, $O_2^-{}_{aq}$, $O_2NO_2^-{}_{aq}$, $HO_2NO_2^-{}_{aq}$, $ONOOH_{aq}$, and NO_{2aq} are strongly influenced by the time since the last voltage pulse. For the lowest frequency, 51 Hz, only 12 s have elapsed since the last discharge pulse and so most of the RONS have not yet decayed. For the highest frequency, 5.1 kHz, the time since the last pulse has been 109 s, and so more decay of the RONS has occurred. This trend is expected since, as shown in Fig. 3.7, most of the reactive densities decay in the afterglow.

The exceptions to this pattern are the most stable species – H_{2aq}, O_{3aq}, $H_3O^+{}_{aq}$, $NO_3^-{}_{aq}$, N_2O_{aq} – whose densities do not monotonically decrease with increasing PRF. At higher PRF there is a greater tendency to form O_3, H_2, and N_2O, instead of HNO_3. A higher PRF means that the interpulse period is shorter than the diffusion time of gas phase species into the liquid and so gas phase reactions tend to dominate.

HNO_3 production is by $OH + NO_2 + M \rightarrow HNO_3 + M$, while the HNO_3 solvates with a large Henry's law constant. At high PRF, more NO_2 ends up in N_2O, rather than HNO_3, because the density of N is, on the average, higher for higher PRF

$$N + NO_2 \rightarrow N_2O + O. \qquad (3.18)$$

In the end, this trend results in less production of HNO_3, and suggests that in an air plasma, PRF may be used to control the acidification of the liquid.

3.3.7 Biomolecules

In order to examine the consequences of biological molecules on the in liquid reactivity, peptidoglycan (PG) was added to the water. Peptidoglycan is the structural component of bacterial cell walls. Recent molecular dynamics (MD) simulations by Yusupov, *et al*. [26] have provided reaction probabilities for ROS with PG. The MD simulations did not include the mitigating effects of surrounding water molecules, so the reaction probabilities are likely an

upper limit. The reaction rates used for the breaking of carbon-oxygen bonds (C-O), carbon-carbon bonds (C-C), and carbon-nitrogen bonds (C-N) are listed in Table 3.3.

The ROS in the liquid react with PG molecules that have not already reacted with RONS. The PG that does react is converted to a radical like form. Since PG is a large molecule, it is highly likely that the RONS will continue to react with the PG-radical. The initial concentration of PG in the liquid was chosen to be 100 ppm so that the PG was not depleted at the end of the simulation. The conditions are otherwise the same as the base case. Actual bio-relevant solutions may have a large range of densities of different biomolecules, and the biomolecules themselves will likely undergo very different reactions with in-liquid ROS. The goal of this parameterization is to emphasize the importance of the participation of biomolecules in the reaction mechanism. Reactions were only included for O_3, O, OH, and H_2O_2 with PG as those reaction probabilities were available, but reactions with RNS and HO_2 may also be significant.

Most of the densities of RONS, in both the gas and the liquid, as shown in Fig. 3.15, are lower with PG since PG consumes several radical species in these liquids. These processes correspond to a transfer of reactivity from the plasma produced species to the biological molecules. The end result is PG with broken bonds or radical sites, that could initiate a cascade of other reactions.

The PG influences the densities of reactive species in the gas by consuming their analogues in the liquid, whose replenishment may be limited by Henry's law saturation. Since the density of the species in the liquid is lowered by reaction with PG, the fluid can accept a larger fluence of this species from the gas during a given treatment time. This increase in the acceptance of gas phase species into the liquid is particularly true for O_3, which is at or near its Henry's law equilibrium value in the liquid for most of the plasma-on period. The maximum

density of O_3 in the gas phase with PG (4.7×10^{15} cm^{-3}) is only 3% of the O_3 density in the base case (1.7×10^{17} cm^{-3}) without PG. O_{3aq} is largely depleted by reactions with PG, which then enables more O_3 from the gas phase to enter the liquid. In the base case, the buildup of O_3 decreases n_e by attachment towards the end of each plasma pulse. The final pulses with PG in the liquid have a slightly (4.7%) higher n_e in the gas phase than the base case because the density of O_3 is lower. This higher electron density during the later pulses results in an increased gas phase density of N, O, OH, and $O_2(^1\Delta_g)$. The density of H_2 in the gas is also higher with PG as a result of the reduced density of O_3. The production of H is higher with the higher n_e, and the H is more likely to combine into H_2 than undergo the reaction $H + O_3 \rightarrow OH + O_2$.

In the liquid, the species which react with PG (H_2O_{2aq}, OH_{aq}, O_{aq}, O_{3aq}) have lower densities than in the base case. Most of the RONS densities in the liquid decrease with the addition of PG because the PG consumes several ROS important to their formation. Even though the RNS in the liquid do not directly react with the PG, they generally require ROS in their formation pathways and the ROS do react with PG. There are a few exceptions, however. The densities of HO_{2aq} and $O_2^-{}_{aq}$ are significantly larger with PG in the liquid. The density of HO_{2aq} is larger because it is not consumed by OH ($OH + HO_2 \rightarrow H_2O + O_2$), whose density decreases with the addition of PG. NO_{aq} is also higher, but recall that this is a short lived species, so its density is due to the last voltage pulse.

Although the production of HNO_3 in the gas is higher with PG, the density of its conjugate base $NO_3^-{}_{aq}$ is lower with PG. This is a result of the decrease in production of $NO_3^-{}_{aq}$ in the liquid from other radicals such as NO_{2aq} and NO_{3aq}. As a result, the liquid is less acidic with PG. The decrease in NO_2, NO_3, NO_{2aq}, NO_{3aq} and N_2O_{5aq} with PG also results in less $ONOOH_{aq}$ and HO_2NO_{2aq}.

In summary, the presence of organic molecules consumes much of the initial ROS reactivity, such as O_{aq}, OH_{aq}, and O_{3aq}, reducing the production of species which require many steps to form, such as HO_2NO_{2aq} and $ONOOH_{aq}$. The PG in the liquid also increases the fluence of ROS, especially O_3, that can be transferred from gas to the liquid over the treatment period.

3.4 Concluding Remarks

Global modeling is a valuable method to address plasma-liquid interactions for long timescales with complete reaction mechanisms and without an unreasonable computational burden. This method is not suitable for addressing systems with unique geometrical dependencies, but is valuable to providing insights to systematic trends.

In an air DBD over liquid covered tissue, the positive ion dynamics are fairly consistent over several thousand discharge pulses. However, the negative ion dynamics evolve over thousands of pulses because of the accumulation of O_3 and NO_x which undergo attachment processes. Excited states and ions have lifetimes shorter than the interpulse period of 2 ms of the base case, but many more stable species accumulate with each pulse. In a well-stirred liquid, the rate of solvation of plasma produced species is a less sensitive function of their Henry's law constants than a system that is not well stirred due to the lack of a surface layer that may quickly saturate. However, at long enough time scales when equilibrium is fully established, these differences are less important. The dynamics of RONS in the liquid are pH dependent, as the dissociated and undissociated forms of weak acids undergo different reactions. O_{3aq} and $NO_3^-{}_{aq}$ are the most prevalent plasma produced liquid species and the nitric acid so formed lowers the final pH to 4.1 for the base case.

Increasing applied voltage generally increases the reactivity produced in the liquid, as the energy deposition is higher. Most of the species increase approximately linearly with applied

voltage in both the gas and the liquid. The O_3 and the H_2 however, peak at an intermediate voltage. H_2 dissociates if T_e gets too high, and O begins to react with larger densities of NO_2 instead of O_2 at higher voltages.

As the gas flow rate increases in an air DBD, the relative humidity decreases, and reactive but long lived species, including O_3, flow out of the system. Since O_3 and H_2O decrease with increasing flow rate, n_e and T_e increase. The densities of the most stable RNS decrease with flow rate, as they take several steps to form. Species with a lifetime on the order of the interpulse period peak at higher values of flow because there is not as much NO_x and O_3 in the gas for them to react with.

The presence of a biomolecule in the liquid reduces some of the accumulating effects in the liquid of previous pulses by consuming ozone. This is especially true for cases where the treatment time is longer than the time it takes for O_3 to solvate and react with a biomolecule. The reduction of density in the liquid of species that may otherwise be near their Henry's law equilibrium enables more of the species to solvate from the gas phase. Although reactions of RNS with the PG were not considered, the RNS in the liquid also decrease, as the ROS are precursors to RNS. This lower level of RONS (including H_2O_{2aq}, O_{3aq}, OH_{aq}, HO_2NO_{2aq}, and $ONOOH_{aq}$) is a transfer of reactivity from the gas and liquid phase radical species to the biological system rather than a destruction of the reactivity.

3.5 Tables

Table 3.1. Henry's Law Constants (Ref. [27])

Species	h (unitless)	Note
H_2O_2	1.92×10^{6}	
HO_2	1.32×10^{5}	
OH	6.20×10^{2}	
H	6.48×10^{3}	
H_2	1.80×10^{-2}	
O, $O(^1D)$	1	a,b
O_2, $O_2(v)$, $O_2(^1\Delta_g)$, $O_2(^1\Sigma_u)$	3.24×10^{-2}	a
O_3	3.00×10^{-1}	
N_2, $N_2(A^3\Sigma_u)$, $N_2(v)$, N, $N(^2D)$, $N_2(a`^1\Sigma)$	1.60×10^{-2}	a
N_2O_3	6.00×10^{2}	
N_2O_4	3.69×10^{1}	
N_2O_5	4.85×10^{1}	
N_2O	5.99×10^{-1}	
HO_2NO_2	2.99×10^{5}	
NO	4.40×10^{-2}	
NO_2	2.80×10^{-1}	
NO_3	4.15×10^{1}	
HNO_2, HNO	1.15×10^{3}	a
HNO_3, ONOOH	4.80×10^{6}	
CO, CO(v)	2.42×10^{-2}	a
CO_2, $CO_2(v)$	8.23×10^{-1}	a
NH	1.47×10^{3}	c

[a)] Value corresponds to the first species in the list. Other species were assumed to have the same Henry's law constant.

[b)] Approximated. Species reacts quickly in water and will not reach Henry's law saturation.

[c)] Approximated by analogy to NH_3.

Table 3.2. Aqueous Reaction Mechanism

Reaction	Rate Coefficient[a]	Ref.
Ions		
$e_{aq} + H_2O_{aq} \rightarrow H_2O^-_{aq}$	5×10^{-15}	b
$M^+_{aq} + H_2O_{aq} \rightarrow H_2O^+_{aq} + M_{aq}$, $M^+_{aq} = N_2^+_{aq}, N^+_{aq}, O_2^+_{aq}, NO^+_{aq}, H_2^+_{aq}, NO_2^+_{aq}, CO_2^+_{aq}, CO^+_{aq}$	5×10^{-15}	b
$N_4^+_{aq} + H_2O_{aq} \rightarrow H_2O^+_{aq} + N_{2aq} + N_{2aq}$	5×10^{-15}	b
$O_4^+_{aq} + H_2O_{aq} \rightarrow H_2O^+_{aq} + O_{2aq} + O_{2aq}$	5×10^{-15}	b
$H^+_{aq} + H_2O_{aq} \rightarrow H_3O^+_{aq}$	5×10^{-15}	b
$N_3^+_{aq} + H_2O_{aq} \rightarrow H_2O^+_{aq} + N_{2aq} + N_{aq}$	5×10^{-15}	b
$H_2O^+_{aq} + H_2O_{aq} \rightarrow H_3O^+_{aq} + OH_{aq}$	1×10^{-17}	[28]
$H^-_{aq} + H_2O_{aq} \rightarrow H_2O^-_{aq} + H_{aq}$	5×10^{-15}	b
$H_2O^-_{aq} + H_2O_{aq} \rightarrow H_{aq} + OH^-_{aq} + H_2O_{aq}$	3×10^{-20}	[28]
$O^-_{aq} + H_2O_{aq} \rightarrow OH^-_{aq} + OH_{aq}$	3×10^{-15}	[29]
Cluster ions		
$M^+(H_2O)_{naq} \rightarrow M^+_{aq} + nH_2O_{aq}$, $M^+_{aq} = H_3O^+_{aq}, H_2O^+_{aq}, NO^+_{aq}, O_2^+_{aq}, N^+_{aq}$	1.68×10^8 s^{-1}	b
$M^-(H_2O)_{aq} \rightarrow M_{aq} + H_2O^-_{aq} + (n-1)\ H_2O_{aq}$, $M^-_{aq} = O_2^-_{aq}, O^-_{aq}, OH^-_{aq}$	1.68×10^8 s^{-1}	b
$NO^+O_2 \rightarrow NO^+_{aq} + O_{2aq}$	1.68×10^8 s^{-1}	b
Electronic and Vibrational Excited States		
$N_2(v)_{aq} + H_2O_{aq} \rightarrow N_{2aq} + H_2O_{aq}$	5×10^{-15}	b
$N(^2D)_{aq} + H_2O_{aq} \rightarrow NH_{aq} + OH_{aq}$	6.9×10^{-39}	[30][c]
$N(^2D)_{aq} + H_2O_{aq} \rightarrow N_{aq} + H_2O_{aq}$	2.4×10^{-14}	[31][c]
$N_2(a`^1\Sigma)_{aq} + H_2O_{aq} \rightarrow OH_{aq} + H_{aq} + N_{2aq}$	5×10^{-15}	b
$O_2(v)_{aq} + H_2O_{aq} \rightarrow O_{2aq} + H_2O_{aq}$	5×10^{-15}	b
$O_2(^1\Sigma_u)_{aq} + H_2O_{aq} \rightarrow O_{2aq} + H_2O_{aq}$	5×10^{-15}	b
$O(^1D)_{aq} + H_2O_{aq} \rightarrow O_{aq} + H_2O_{aq}$	1.2×10^{-11}	[31][c]
$O_2(^1\Delta_g)_{aq} + H_2O_{aq} \rightarrow O_{2aq} + H_2O_{aq}$	7.7×10^{-18}	[32][c]
$N_2(A^3\Sigma_u)_{aq} + H_2O_{aq} \rightarrow N_{2aq} + H_2O_{aq}$	1×10^{-10}	b
$N_2(A^3\Sigma_u)_{aq} + H_2O_{aq} \rightarrow N_{2aq} + OH_{aq} + H_{aq}$	6×10^{-14}	[30][c]
Acid Dissociation		
$ONOOH_{aq} + H_2O_{aq} \rightarrow H_3O^+_{aq} + ONOO^-_{aq}$	5×10^{-15}	b
$ONOO^-_{aq} + H_3O^+_{aq} \rightarrow H_2O_{aq} + ONOOH_{aq}$	1.75×10^{-6}	d
$HO_{2aq} + H_2O_{aq} \rightarrow H_3O^+_{aq} + O_2^-_{aq}$	1.43×10^{-17}	d
$H_3O^+_{aq} + O_2^-_{aq} \rightarrow HO_{2aq} + H_2O_{aq}$	5×10^{-11}	b

$HNO_{2aq} + H_2O_{aq} \rightarrow H_3O^+_{aq} + NO_2^-_{aq}$	5×10^{-15}	[b]
$H_3O^+_{aq} + NO_2^-_{aq} \rightarrow H_{aq} + HO_{2aq} + H_2O_{aq}$	6.81×10^{-10}	[d]
$HNO_{3aq} + H_2O_{aq} \rightarrow H_3O^+_{aq} + NO_3^-_{aq}$	3×10^{-18}	[33][d]
$H_3O^+_{aq} + NO_3^-_{aq} \rightarrow HNO_{3aq} + H_2O_{aq}$	7×10^{-16}	[d]
$HO_2NO_{2aq} + H_2O_{aq} \rightarrow O_2NO_2^-_{aq} + H_3O^+_{aq}$	5×10^{-15}	[b]
$O_2NO_2^-_{aq} + H_3O^+_{aq} \rightarrow HO_2NO_{2aq} + H_2O_{aq}$	1.05×10^{-7}	[d]

Reactive Oxygen Species (ROS)

$OH_{aq} + H_{aq} \rightarrow H_2O_{aq}$	3×10^{-11}	[29]
$H_2O^-_{aq} + H_{aq} \rightarrow H_{2aq} + OH^-_{aq}$	4×10^{-11}	[28]
$H_2O^-_{aq} + O_{aq} \rightarrow O^-_{aq} + H_2O_{aq}$	3×10^{-11}	[29]
$H_2O^-_{aq} + O_{2aq} \rightarrow O_2^-_{aq} + H_2O_{aq}$	3×10^{-11}	[28]
$H_2O^-_{aq} + OH_{aq} \rightarrow OH^-_{aq} + H_2O_{aq}$	5×10^{-11}	[28]
$H_2O^-_{aq} + H_2O_{2aq} \rightarrow OH_{aq} + OH^-_{aq} + H_2O_{aq}$	2×10^{-11}	[28]
$H_2O^-_{aq} + O^-_{aq} \rightarrow OH^-_{aq} + OH^-_{aq}$	2×10^{-11}	[28]
$H_2O^-_{aq} + HO_2^-_{aq} \rightarrow OH^-_{aq} + OH^-_{aq} + OH_{aq}$	5×10^{-12}	[28]
$H_2O^-_{aq} + H_2O^-_{aq} \rightarrow H_{2aq} + OH^-_{aq} + OH^-_{aq}$	1×10^{-11}	[28]
$H_3O^+_{aq} + OH^-_{aq} \rightarrow H_{aq} + OH_{aq} + H_2O_{aq}$	1×10^{-10}	[29]
$H_2O_{aq} \rightarrow H_2O^+_{aq} + e_{aq}$	$1 \times 10^{-20}\ s^{-1}$	[f]
$H_2O_{aq} \rightarrow OH_{aq} + H$	$1 \times 10^{-20}\ s^{-1}$	[30][c,f]
$OH_{aq} + H_{aq} \rightarrow H_2O_{aq}$	3×10^{-11}	[29]
$H_2O^-_{aq} + H_2O^+_{aq} \rightarrow H_{aq} + OH_{aq} + H_2O_{aq}$	1×10^{-9}	[28]
$OH_{aq} + OH_{aq} \rightarrow H_2O_{2aq}$	1.7×10^{-11}	[28]
$OH_{aq} + H_{2aq} \rightarrow H_{aq} + H_2O_{aq}$	6×10^{-14}	[28]
$OH_{aq} + HO_{2aq} \rightarrow O_{2aq} + H_2O_{aq}$	2×10^{-11}	[29]
$OH_{aq} + H_2O_{2aq} \rightarrow HO_{2aq} + H_2O_{aq}$	1×10^{-13}	[29]
$OH_{aq} + OH^-_{aq} \rightarrow O^-_{aq} + H_2O_{aq}$	8×10^{-12}	[29]
$OH_{aq} + O^-_{aq} \rightarrow HO_2^-_{aq}$	4×10^{-11}	[28]
$OH_{aq} + O_2^-_{aq} \rightarrow O_{2aq} + OH^-_{aq}$	1.5×10^{-11}	[28]
$OH_{aq} + HO_2^-_{aq} \rightarrow HO_{2aq} + OH^-_{aq}$	1.5×10^{-11}	[28]
$H_{aq} + H_2O_{aq} \rightarrow H_{2aq} + OH_{aq}$	1.5×10^{-21}	[29]
$H_{aq} + H_{aq} \rightarrow H_{2aq}$	1.5×10^{-11}	[29]
$H_{aq} + OH^-_{aq} \rightarrow H_2O^-_{aq}$	3×10^{-14}	[28]
$H_{aq} + HO_{2aq} \rightarrow H_2O_{2aq}$	3×10^{-11}	[28]
$H_{aq} + H_2O_{2aq} \rightarrow OH_{aq} + H_2O_{aq}$	1.5×10^{-13}	[28]
$H_{2aq} + H_2O_{2aq} \rightarrow H_{aq} + OH_{aq} + H_2O_{aq}$	1×10^{-14}	[28]
$H^-_{aq} + H_2O^+_{aq} \rightarrow H_{aq} + H_2O_{aq}$	3×10^{-6}	[34][g]
$H^-_{aq} + H_3O^+_{aq} \rightarrow H_{2aq} + H_2O_{aq}$	3×10^{-6}	[34][g]
$O_{aq} + H_2O_{aq} \rightarrow OH_{aq} + OH_{aq}$	2.2×10^{-17}	[28][h]
$O_{aq} + O_{2aq} \rightarrow O_{3aq}$	5×10^{-12}	[29]
$O_{2aq} + H_{aq} \rightarrow HO_{2aq}$	5×10^{-11}	[28]

$O^-_{aq} + H_{2aq} \rightarrow H_{aq} + OH^-_{aq}$	1.3×10^{-13}	[28]
$O^-_{aq} + O_{2aq} \rightarrow O_3{}^-_{aq}$	5×10^{-12}	[28]
$O^-_{aq} + H_2O_{2aq} \rightarrow O_2{}^-_{aq} + H_2O_{aq}$	8×10^{-13}	[28]
$O^-_{aq} + HO_2{}^-_{aq} \rightarrow O_2{}^-_{aq} + OH^-_{aq}$	8×10^{-13}	[28]
$O(^1D)_{aq} + H_2O_{aq} \rightarrow H_{2aq} + O_{2aq}$	2.3×10^{-12}	[30][c]
$O(^1D)_{aq} + H_2O_{aq} \rightarrow OH_{aq} + OH_{aq}$	2.2×10^{-10}	[30][c]
$O(^1D)_{aq} + O_{2aq} \rightarrow O_{aq} + O_{2aq}$	3.8×10^{-11}	[30][c]
$O(^1D)_{aq} + O_{3aq} \rightarrow O_{2aq} + O_{aq} + O_{aq}$	1.2×10^{-10}	[30][c]
$O(^1D)_{aq} + O_{3aq} \rightarrow O_{2aq} + O_{2aq}$	5.04×10^{-10}	[30][c]
$O(^1D)_{aq} + N_2O_{aq} \rightarrow NO_{aq} + NO_{aq}$	6.7×10^{-11}	[30][c]
$O_3{}^-_{aq} + OH_{aq} \rightarrow O_2{}^-_{aq} + HO_{2aq}$	1.41×10^{-11}	[29]
$O_3{}^-_{aq} + O^-_{aq} \rightarrow O_2{}^-_{aq} + O_2{}^-_{aq}$	1.7×10^{-13}	[29]
$O_3{}^-_{aq} + H_3O^+_{aq} \rightarrow O_{2aq} + OH_{aq} + H_2O_{aq}$	1.50×10^{-10}	[29]
$O_3{}^-_{aq} \rightarrow O_{2aq} + O^-_{aq}$	$2.6 \times 10^{3}\ s^{-1}$	[29]
$O_2{}^-_{aq} + HO_{2aq} + H_2O_{aq} \rightarrow O_{2aq} + H_2O_{2aq} + OH^-_{aq}$	$2.68 \times 10^{-34}\ cm^6s^{-1}$	[29]
$O_2{}^-_{aq} + H_2O_{2aq} \rightarrow O_{2aq} + OH_{aq} + OH^-_{aq}$	2.16×10^{-22}	[29]
$O_2{}^-_{aq} + O^-_{aq} + H_2O_{aq} \rightarrow O_{2aq} + OH^-_{aq} + OH^-_{aq}$	$2.98 \times 10^{-35}\ cm^6s^{-1}$	[29]
$O_{3aq} \rightarrow O_{2aq} + O_{aq}$	$3 \times 10^{-6}\ s^{-1}$	[29]
$O^+_{aq} + H_2O_{aq} \rightarrow H_2O^+_{aq} + O_{aq}$	1.2×10^{-12}	[31][c]
$O^+_{aq} + O_{2aq} \rightarrow O_2{}^+_{aq} + O_{aq}$	1.9×10^{-11}	[35][c]
$O_{3aq} + OH^-_{aq} \rightarrow O_2{}^-_{aq} + HO_{2aq}$	1.16×10^{-19}	[29]
$O_{3aq} + O_2{}^-_{aq} \rightarrow O_3{}^-_{aq} + O_{2aq}$	2.66×10^{-12}	[29]

Reactive Nitrogen Species (RNS)

$N_{aq} + N_{aq} \rightarrow N_{2aq}$	5×10^{-14}	[30][c]
$N_{aq} + H_2O_{aq} \rightarrow NH_{aq} + OH_{aq}$	6.93×10^{-39}	[30][c]
$H_{aq} + HNO_{aq} \rightarrow OH_{aq} + NH_{aq}$	2.18×10^{-22}	[30][c]
$NH_{aq} + NO_{aq} \rightarrow N_2O_{aq} + H_{aq}$	1.3×10^{-12}	[30][c]
$NH_{aq} + O_{2aq} \rightarrow HNO_{aq} + O_{aq}$	2.3×10^{-13}	[31][c]
$O^+_{aq} + N_{2aq} \rightarrow NO^+_{aq} + N_{aq}$	1.2×10^{-12}	[31][c]
$OH_{aq} + NO_2{}^-_{aq} \rightarrow OH^-_{aq} + NO_{2aq}$	1.7×10^{-11}	[29]
$H_{aq} + NO_2{}^-_{aq} \rightarrow NO_{aq} + OH^-_{aq}$	2×10^{-12}	[29]
$O^-_{aq} + NO_2{}^-_{aq} + H_2O_{aq} \rightarrow NO_{2aq} + OH^-_{aq} + OH^-_{aq}$	$1.82 \times 10^{-35}\ cm^6s^{-1}$	[29]
$O_2{}^-_{aq} + NO_{aq} \rightarrow NO_3{}^-_{aq}$	6×10^{-12}	[29]
$NO_{2aq} + NO_{2aq} + H_2O_{aq} + H_2O_{aq} \rightarrow H_3O^+_{aq} + NO_3{}^-_{aq} + HNO_{2aq}$	$1.26 \times 10^{-56}\ cm^9s^{-1}$	[29]
$NO_{2aq} + NO_{2aq} + H_2O_{aq} + H_2O_{aq} + H_2O_{aq} \rightarrow H_3O^+_{aq} + NO_3{}^-_{aq} + H_3O^+_{aq} + NO_2{}^-_{aq}$	$1.30 \times 10^{-79}\ cm^{12}s^{-1}$	[29]
$NO_{aq} + NO_{aq} + O_{2aq} \rightarrow NO_{2aq} + NO_{2aq}$	$6.28 \times 10^{-36}\ cm^6s^{-1}$	[29]
$NO_{aq} + NO_{2aq} + H_2O_{aq} \rightarrow HNO_{2aq} + HNO_{2aq}$	$5.55 \times 10^{-34}\ cm^6s^{-1}$	[29]
$NO_{3aq} + H_2O_{aq} \rightarrow HNO_{3aq} + OH_{aq}$	4.8×10^{-14}	[29]
$NO_{aq} + HO_{2aq} \rightarrow HNO_{3aq}$	5.33×10^{-12}	[29]

$NO_{2aq} + H_{aq} \rightarrow HNO_{2aq}$	1.67×10^{-11}	[29]
$OH_{aq} + NO_{aq} \rightarrow HNO_{2aq}$	3.3×10^{-11}	[33]
$OH_{aq} + NO_{2aq} \rightarrow HNO_{3aq}$	2×10^{-11}	[33]
$OH_{aq} + HNO_{3aq} \rightarrow NO_{3aq} + H_2O_{aq}$	2.17×10^{-13}	[29]
$H_{aq} + HNO_{2aq} \rightarrow NO_{aq} + H_2O_{aq}$	7.5×10^{-13}	[29]
$O_{2aq} + NO_{aq} + NO_{aq} \rightarrow NO_{2aq} + NO_{2aq}$	7.7×10^{-36} cm^6s^{-1}	[29]
$N_2O_{3aq} + H_2O_{aq} \rightarrow HNO_{2aq} + HNO_{2aq}$	1.93×10^{-17}	[30][c]
$N_2O_{4aq} + H_2O_{aq} \rightarrow HNO_{2aq} + HNO_{3aq}$	1.33×10^{-18}	[30][c]
$N_2O_{5aq} + H_2O_{aq} \rightarrow NO_{2aq} + NO_{3aq} + H_2O_{aq}$	1.4×10^{-19}	[30][c]
$N_2O_{5aq} + H_2O_{aq} \rightarrow HNO_{3aq} + HNO_{3aq}$	2×10^{-21}	[30][c]
$NO_2^-{}_{aq} + O_{3aq} \rightarrow NO_3^-{}_{aq} + O_{2aq}$	6.15×10^{-16}	[29]
$N_2O_{5aq} + H_2O_{aq} \rightarrow ONOOH_{aq} + ONOOH_{aq}$	2×10^{-21}	[30][c]
$NO_{aq} + HO_{2aq} \rightarrow ONOOH_{aq}$	5.33×10^{-12}	[29]
$NO_{2aq} + OH_{aq} \rightarrow ONOOH_{aq}$	1.99×10^{-11}	[8]
$H_2O_{2aq} + NO_2^-{}_{aq} + H_3O^+{}_{aq} \rightarrow ONOOH_{aq} + H_2O_{aq} + H_2O_{aq}$	3.04×10^{-39} cm^6s^{-1}	[8]
$ONOOH_{aq} + H_2O_{aq} \rightarrow H_3O_{aq} + NO_3^-{}_{aq}$	2.9×10^{-23}	[8]
$ONOOH_{aq} + H_2O_{aq} \rightarrow OH_{aq} + NO_{2aq} + H_2O_{aq}$	1.24×10^{-23}	[8]
$NO_{aq} + O_2^-{}_{aq} \rightarrow ONOO^-{}_{aq}$	7.14×10^{-12}	[8]
$HNO_{aq} + O_{2aq} \rightarrow HO_{2aq} + NO_{aq}$	8.01×10^{-21}	[30][c]
$HNO_{aq} + O_{3aq} \rightarrow O_{2aq} + HNO_{2aq}$	9.61×10^{-15}	[30][c]
$HNO_{aq} + OH_{aq} \rightarrow H_2O_{aq} + NO_{aq}$	8.00×10^{-11}	[30][c]
$OH_{aq} + N_2O_{aq} \rightarrow HNO_{aq} + NO_{aq}$	3.8×10^{-17}	[31][c]
$NO_2^-{}_{aq} + N_2O_{aq} \rightarrow NO_3^-{}_{aq} + N_{2aq}$	5×10^{-13}	[31][c]
$O_2NO_2^-{}_{aq} \rightarrow NO_2^-{}_{aq} + O_{2aq}$	$1\ s^{-1}$	[29]
$HO_2NO_{2aq} + HNO_{2aq} \rightarrow HNO_{3aq} + HNO_{3aq}$	1.99×10^{-20} s^{-1}	[29]
$HO_2NO_{2aq} \rightarrow HNO_{2aq} + O_{2aq}$	7×10^{-4} s^{-1}	[29]
$HO_2NO_{2aq} \rightarrow HO_{2aq} + NO_{2aq}$	4.6×10^{-3} s^{-1}	[29]
CO_x		
$CO_{2aq} + H_{aq} \rightarrow CO_{aq} + OH_{aq}$	1.4×10^{-29}	[30][c]
$CO_{2aq} + O_{aq} \rightarrow CO_{aq} + O_{2aq}$	1.2×10^{-49}	[30][c]
$CO_{2aq} + M_{aq} \rightarrow CO_{aq} + O_{aq} + M$	3.2×10^{-90}	[30][c]
$CO_{2aq} + O(^1D)_{aq} \rightarrow O_{2aq} + CO_{aq}$	2×10^{-10}	[30][c]
$CO_{2aq} + O(^1D)_{aq} \rightarrow O_{aq} + CO_{2aq}$	2.5×10^{-10}	[30][c]
$CO_{2aq} + O_2(^1\Delta_g)_{aq} \rightarrow O_{2aq} + CO_{2aq}$	3×10^{-18}	[30][c]
$CO_2(v)_{aq} + M_{aq} \rightarrow CO_{aq} + M_{aq}$	1×10^{-13}	[36][c,i]
$CO_{aq} + H_2O_{aq} \rightarrow CO_{2aq} + H_{2aq}$	1.72×10^{-13}	[37][c]
$OH_{aq} + CO_{aq} \rightarrow CO_{2aq} + H_{aq}$	1.2×10^{-13}	[30][c]
$CO_{aq} + O_{2aq} \rightarrow CO_{2aq} + O_{aq}$	7.6×10^{-47}	[30][c]
$CO_{aq} + HO_{2aq} \rightarrow OH_{aq} + CO_{2aq}$	1.5×10^{-27}	[30][c]
$CO_{aq} + NO_{2aq} \rightarrow CO_{2aq} + NO_{aq}$	4.44×10^{-35}	[30][c]

$CO_{aq} + O_{3aq} \rightarrow O_{2aq} + CO_{2aq}$	4×10^{-25}	[30][c]
$CO(v)_{aq} + M_{aq} \rightarrow CO_{aq} + M_{aq}$	1×10^{-14}	[36][c,i]
$O(^1D)_{aq} + CO_{2aq} \rightarrow O_{2aq} + CO_{aq}$	2×10^{-10}	[30][c]
$O(^1D)_{aq} + CO_{2aq} \rightarrow O_{aq} + CO_{2aq}$	2.5×10^{-10}	[30][c]
$O^+_{aq} + CO_{2aq} \rightarrow CO_2{}^+_{aq} + O_{aq}$	1×10^{-9}	[31][c]

a) Aqueous species have an "aq". Rate coefficients are for 300 K and have units of cm^3s^{-1} unless noted otherwise. $1\ cm^3s^{-1} = 6.02 \times 10^{20}\ M^{-1}s^{-1}$.

b) The solvation rate coefficient was estimated to be faster than other liquid reactions in order to not be rate limiting.

c) Approximated by analogy to gas phase reactions.

d) Estimated based on the rate of the reverse reaction and the pK_a.

e) The rate coefficient is estimated according to thermodynamic hydrolysis in liquid water.

f) Actual rate is lower, rate is negligible in both cases.

g) Based on a general ion-ion recombination rate.

h) Approximated by analogy.

i) Approximated based on measured V-T relaxation time.

Table 3.3. Rate Coefficients for Reactions with Peptidoglycan (cm^3/s) [26]

Radical	C-O breaking	C-C breaking	C-N breaking
O_{aq}	6.35×10^{-10}	3.43×10^{-10}	3.96×10^{-10}
OH_{aq}	5.42×10^{-10}	2.92×10^{-10}	8.20×10^{-10}
O_{3aq}	4.80×10^{-10}	2.63×10^{-10}	4.74×10^{-10}
H_2O_{2aq}	2.32×10^{-10}	1.55×10^{-10}	-

3.6 Figures

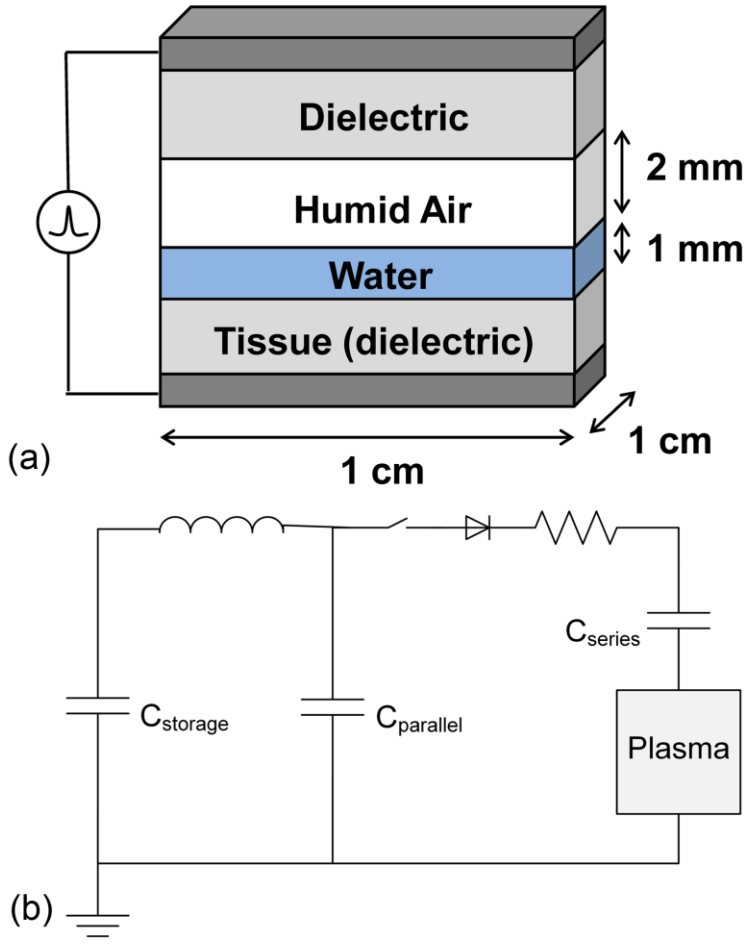

Fig. 3.1 (a) The geometry used in the model. The area being treated is 1 cm^2. (b) The circuit applied to the DBD in the model. The values of each circuit element are $C_{storage}$ = 200 nF, R = 1 Ω, L = 100 nH, and C_{series} = $C_{parallel}$ = 1 pF. C_{series} in the circuit includes the capacitance of the dielectric, the water layer, and the tissue. The storage capacitor is charged to the line voltage at the beginning of each pulse, and the circuit module turns off after the current switches polarities.

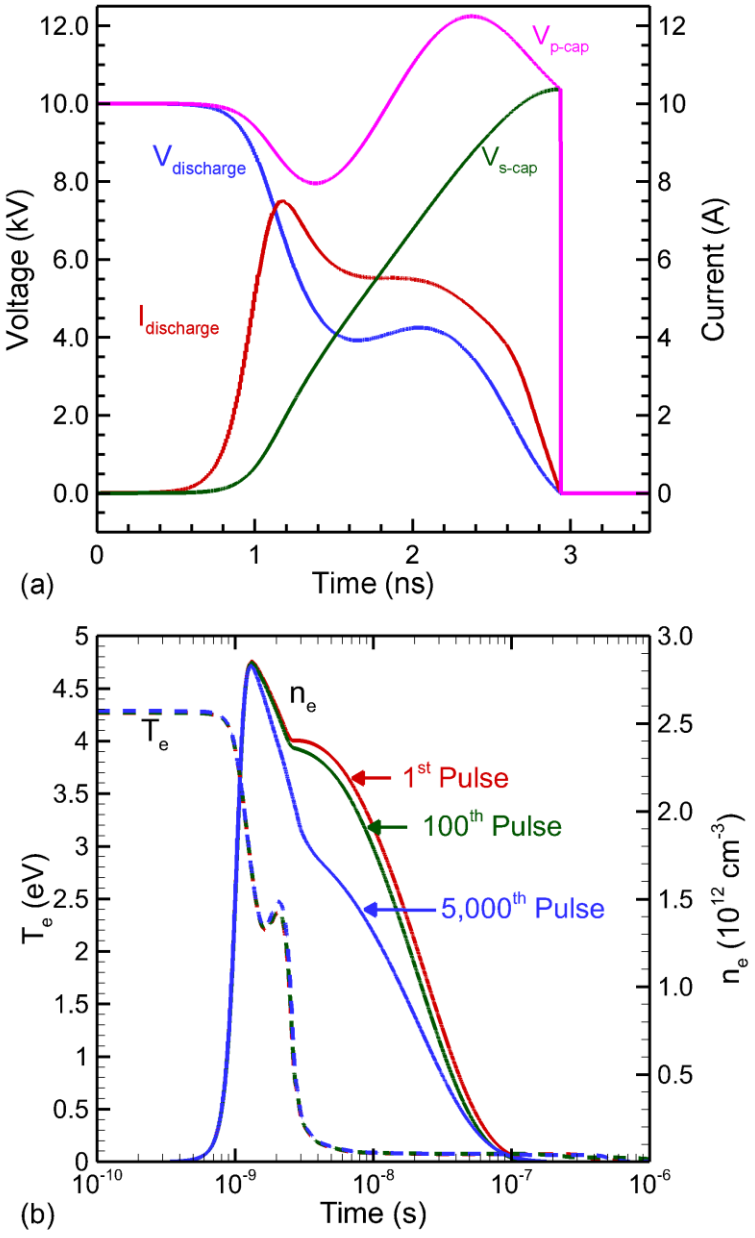

Fig. 3.2 Circuit and plasma parameters during the discharge pulse for the base case. (a) Current and voltage. The combination of the parallel capacitance and inductance produces a local peak in discharge voltage at 2 ns. (b) Electron temperature (T_e) and density (n_e) during the 1st pulse, 100th pulse, and 5,000th pulse. T_e and the maximum value of n_e are unchanged after thousands of pulses, but the electron attachment rates increase at later pulses which decreases n_e.

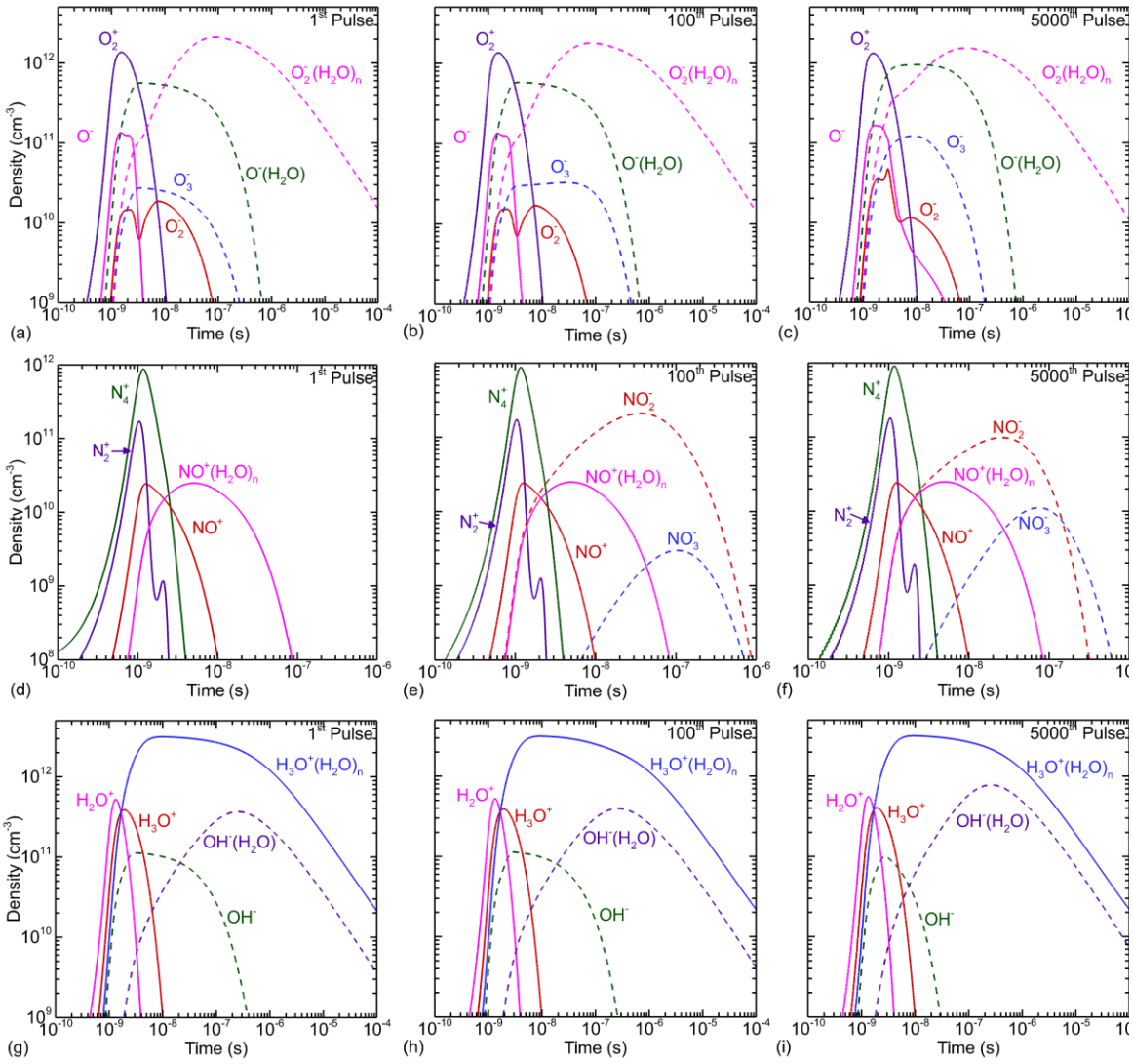

Fig. 3.3 Densities of gas phase charged species during the discharge pulse and afterglow in the base case after the 1st, 100th and 5000th pulses. These species are roughly grouped into those originating from (a-c) O_2, (d-f) N_2 and (g-i) H_2O. The negative ion dynamics evolve over the 5,000 pulses due to the accumulation of neutral species, however the positive ion dynamics are less affected. The high humidity in this case results in the formation of water cluster ions.

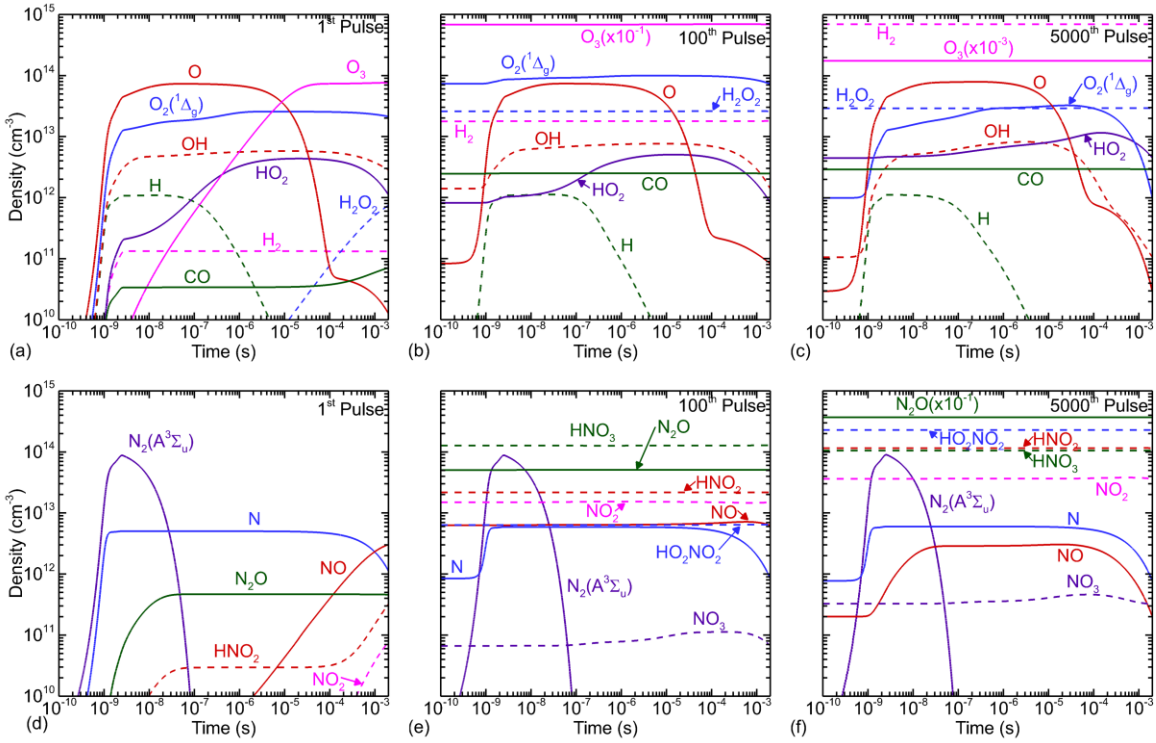

Fig. 3.4 Densities of gas phase neutral species during the discharge and afterglow in the base case after the 1st, 100th and 5000th pulses. These species are grouped into those (a-c) without nitrogen and (d-f) those containing nitrogen. Several neutral species accumulate over many pulses, but the more reactive species form and are consumed with each pulse.

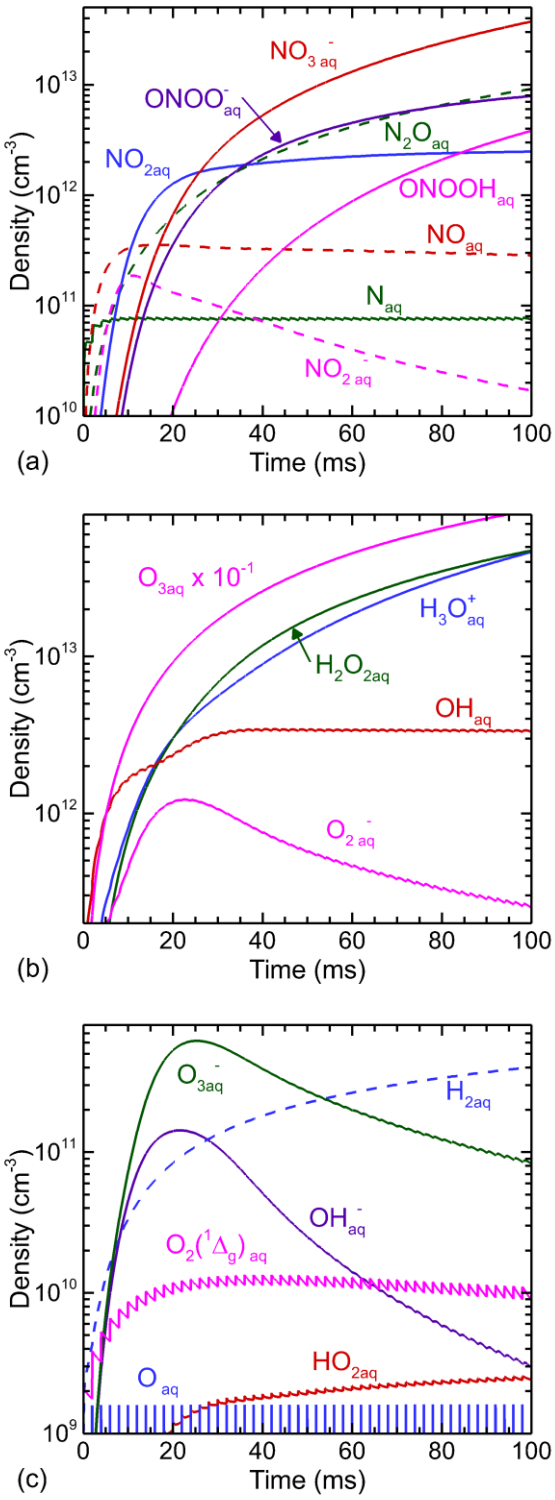

Fig. 3.5 The densities of aqueous (a) RNS and (b-c) ROS for the first 50 pulses of the base case. The most reactive species, including many ions and excited states were omitted as they appear as delta functions on these timescales. Several species establish a pulsed equilibrium, while the others evolve over timescales much longer than the interpulse period. A concentration of 1 M is equivalent to a number density 6×10^{20} cm^{-3}.

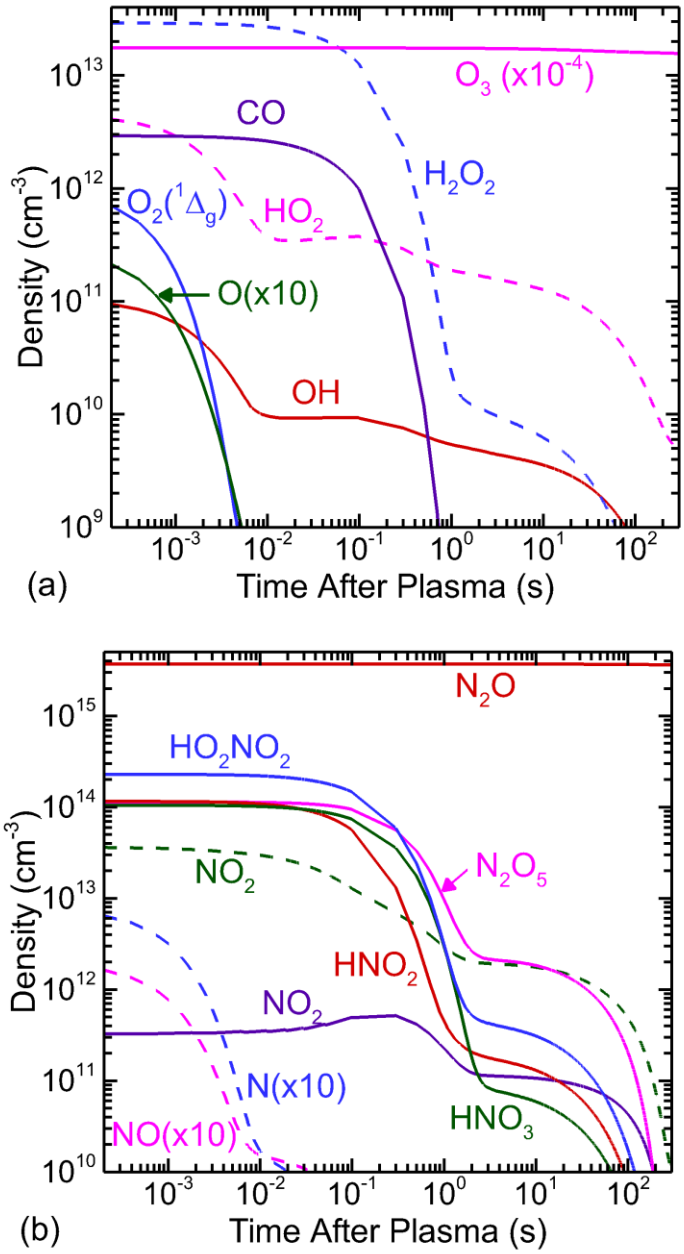

Fig. 3.6 Afterglow evolution of densities of gas phase (a) ROS and (b) RNS. The time is relative to the end of the last discharge pulse. The species densities decrease due to solvation into the liquid during seconds of afterglow.

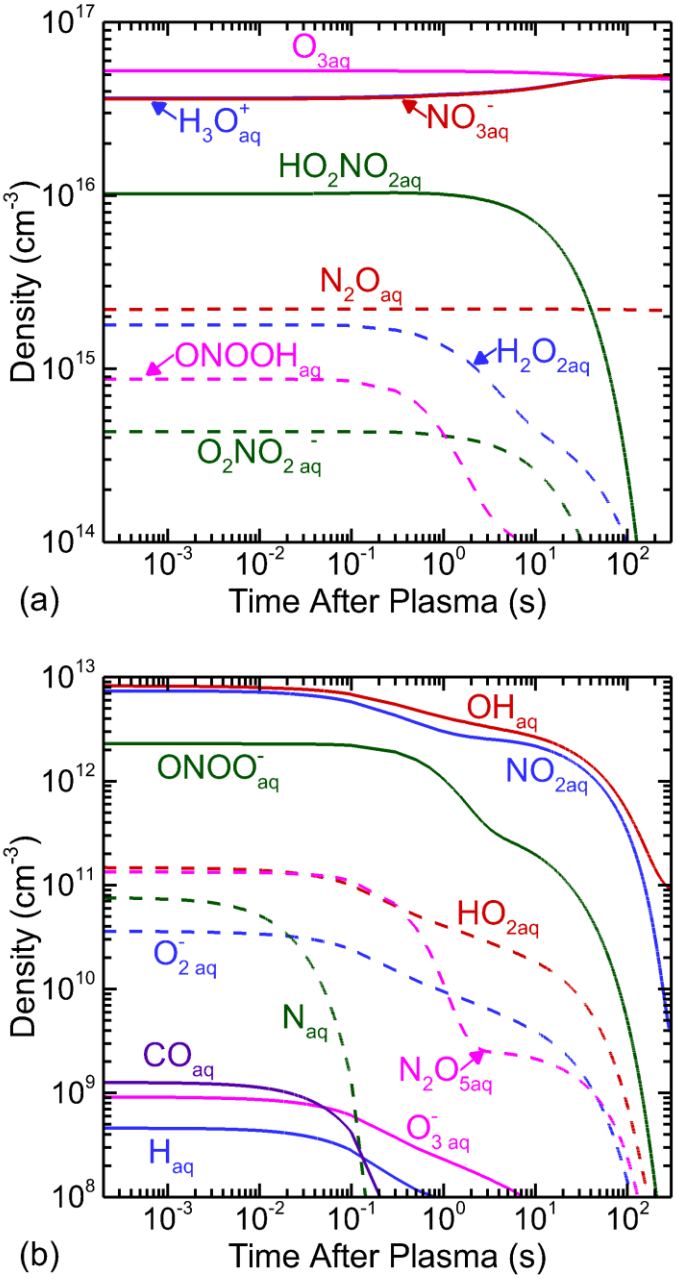

Fig. 3.7 The decay of reactivity in liquid after the treatment has been completed for species with densities (a) above 10^{14} cm^{-3} and (b) below 10^{13} cm^{-3}. Time is relative to the end of the last pulse. Gas phase RONS continue to solvate during the afterglow, which provides a source of these liquid resident RONS. Reactions deplete most of the RONS at long timescales.

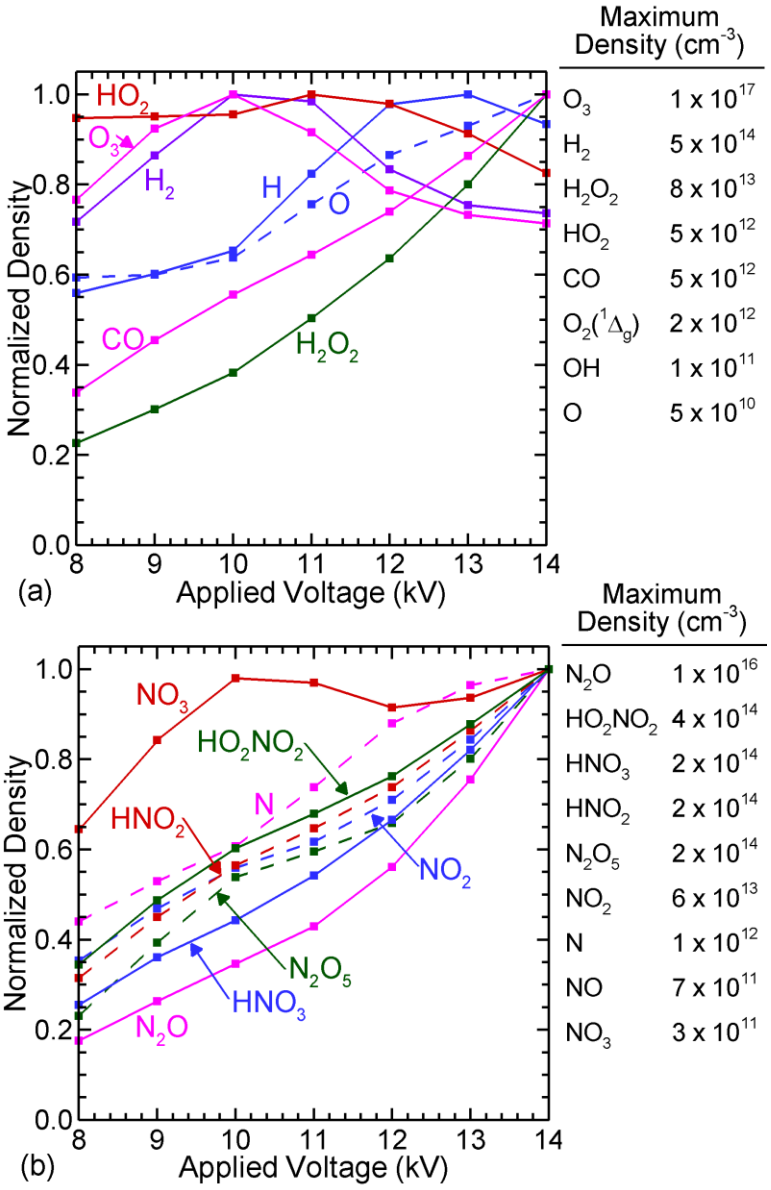

Fig. 3.8 The densities of gas phase (a) ROS and (b) RNS at the end of the last pulse (10 s) for different applied voltages. Values are shown normalized by their maximum density as a function of voltage, shown to the right of each figure. Energy deposition increases with applied voltage, so the density of RONS generally increases.

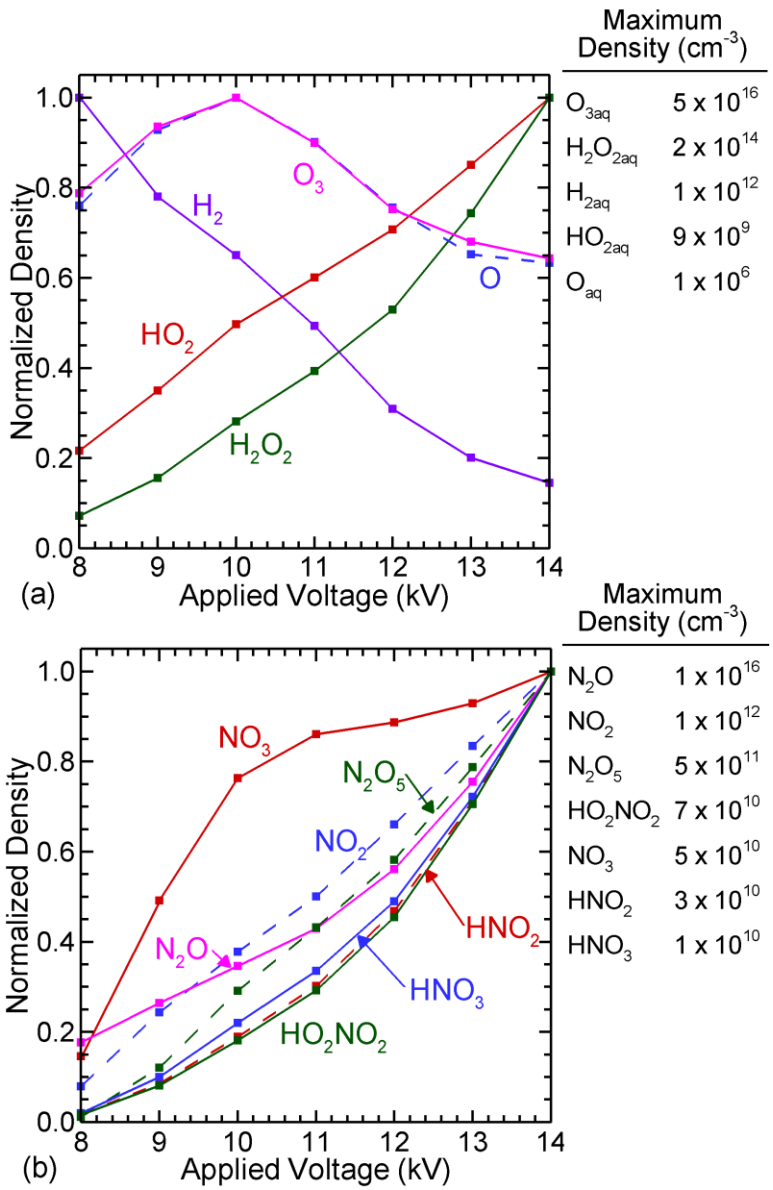

Fig. 3.9 The densities of gas phase plasma produced reactive species at 2 minutes (10 s treatment and 110 s afterglow) for different applied voltages. (a) ROS and (b) RNS. Values are shown normalized by their maximum density as a function of voltage, shown to the right of each figure. By this time, several of the species (H, O, CO, and N) have decayed to negligible densities.

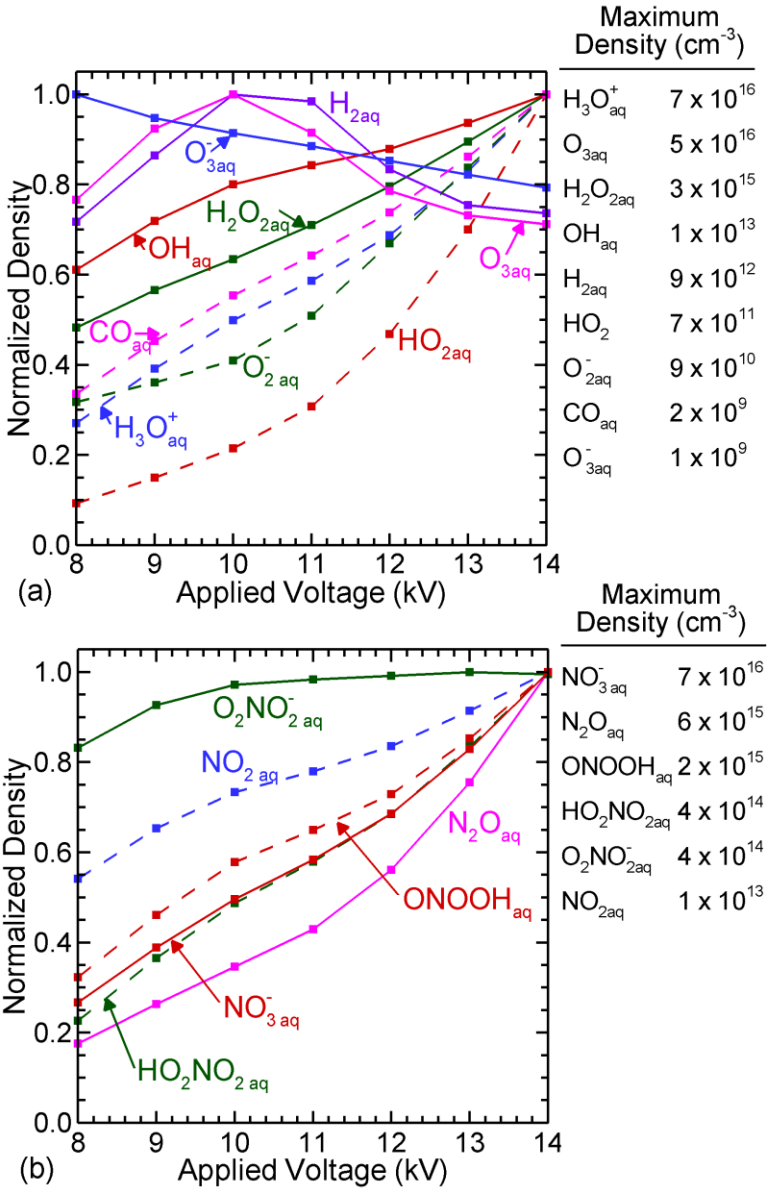

Fig. 3.10 The densities of aqueous plasma produced reactive species at the end of the last pulse (10 s) for different applied voltages. Values are shown normalized by their maximum density as a function of voltage, shown to the right of each figure. (a) ROS and (b) RNS generally increase with voltage, but ROS have a more complex dependence on voltage, making selectivity possible.

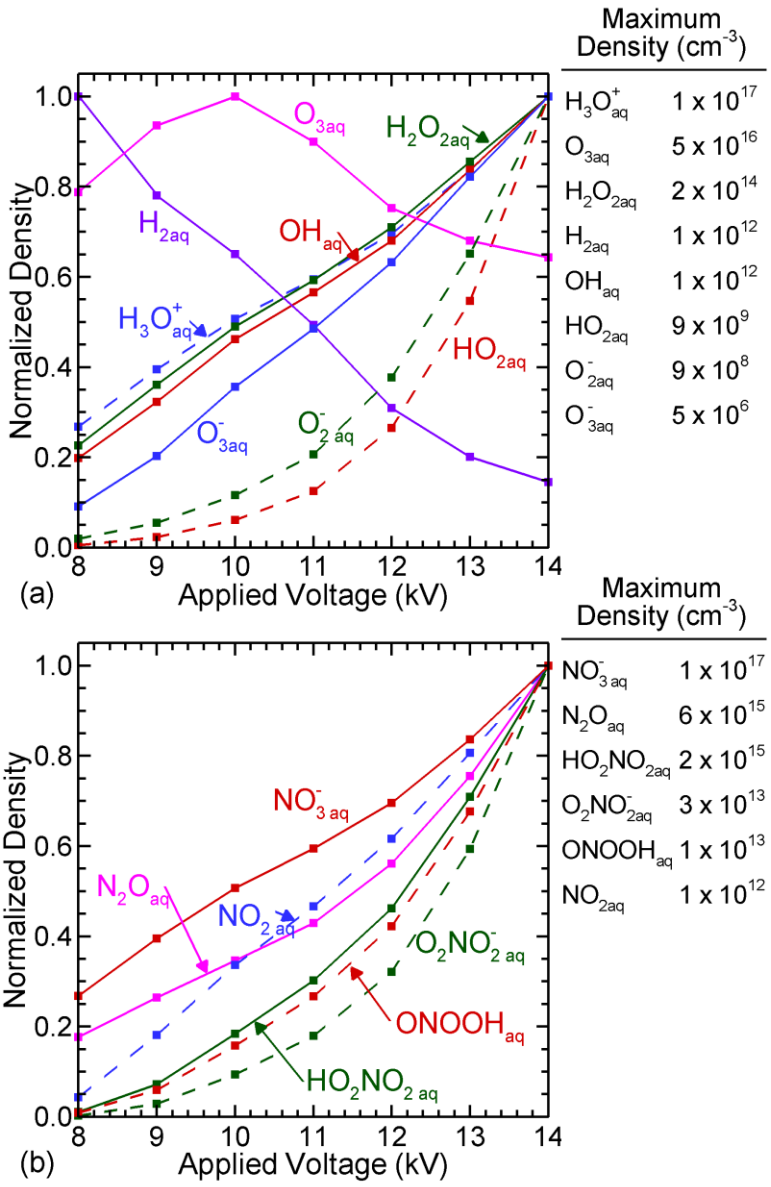

Fig. 3.11 The densities of aqueous plasma produced (a) ROS and (b) RNS for different applied voltages at 2 minutes (10 s treatment and 110 s afterglow). Values are shown normalized by their maximum density as a function of voltage, shown to the right of each figure.

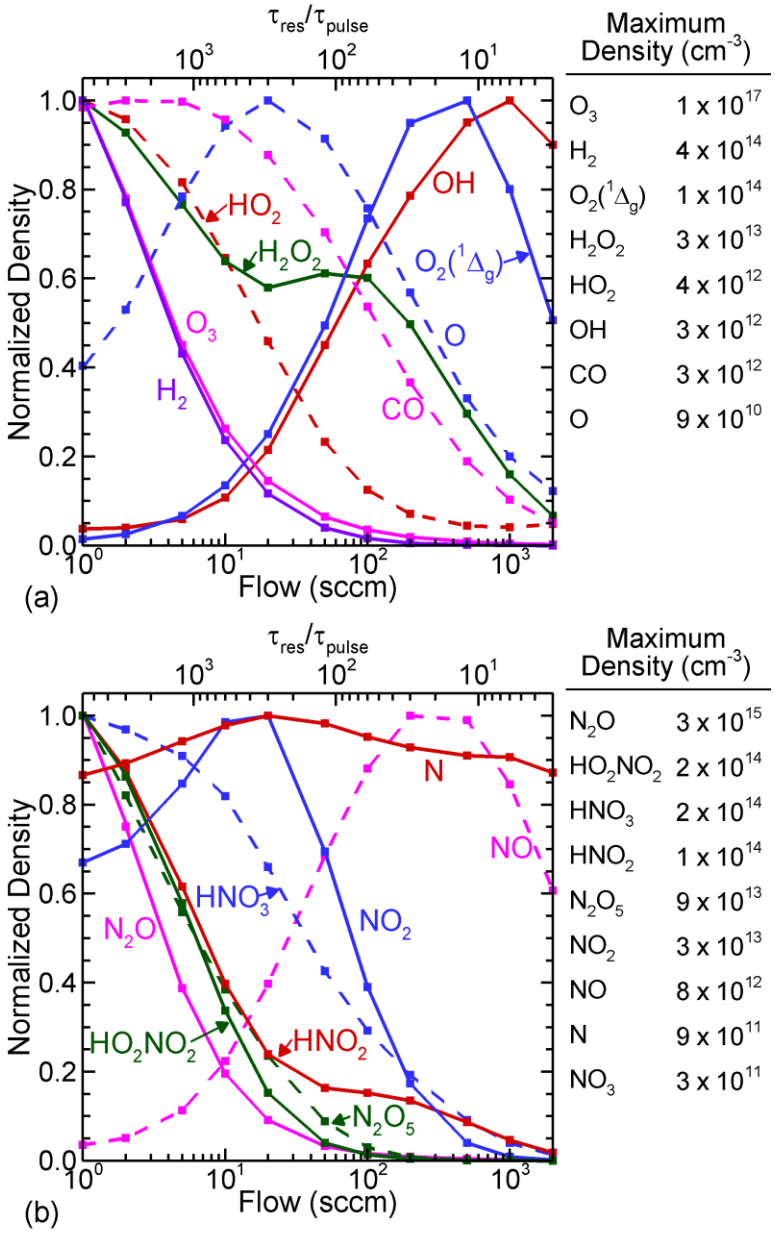

Fig. 3.12 The densities of gas phase plasma produced RONS at the end of the last pulse (10 s) for different air flow rates. (a) ROS and (b) RNS. τ_r/τ_p is the average number of discharge pulses the average input gas molecule is exposed to before flowing out of the system. Values are shown normalized by their maximum density as a function of flow rate, shown to the right of each figure.

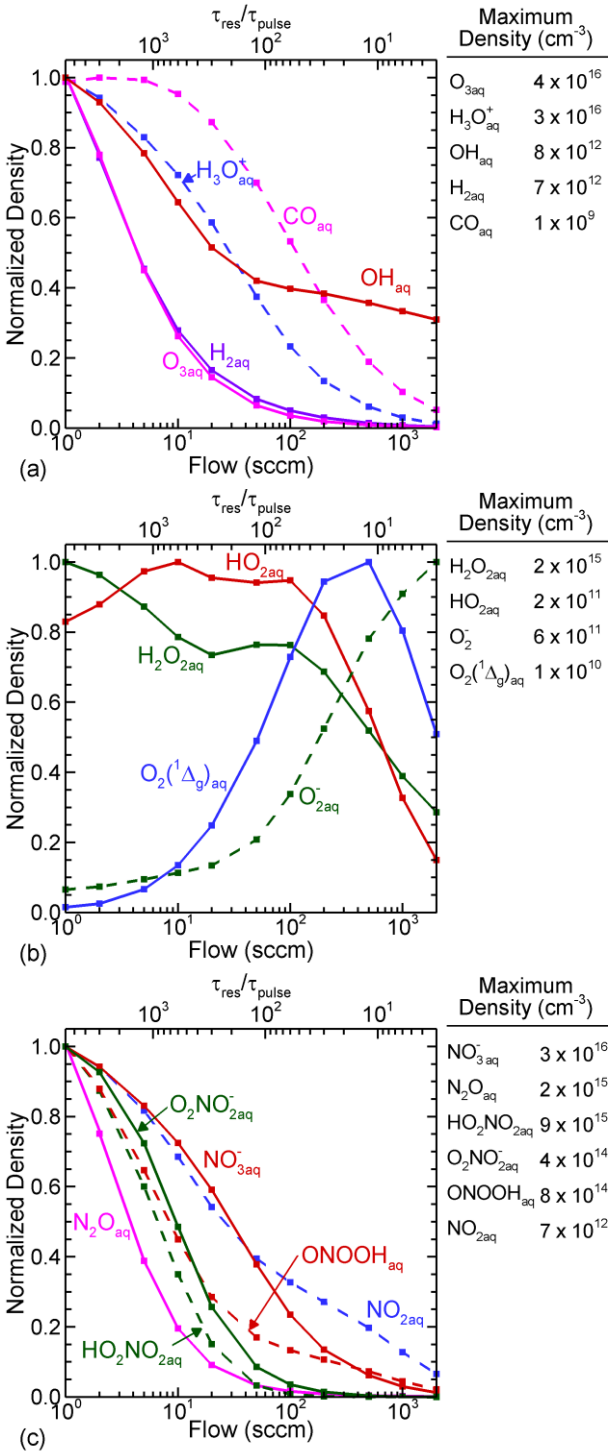

Fig. 3.13 The densities of aqueous plasma produced reactive species at the end of the last pulse (10 s) for different air flow rates. (a-b) ROS and (c) RNS. τ_r/τ_p is the average number of discharge pulses the average input gas molecule is exposed to before flowing out of the system. Higher flow rates deliver more ROS than RNS to the liquid. Values are shown normalized by their maximum density as a function of flow rate, shown to the right of each figure.

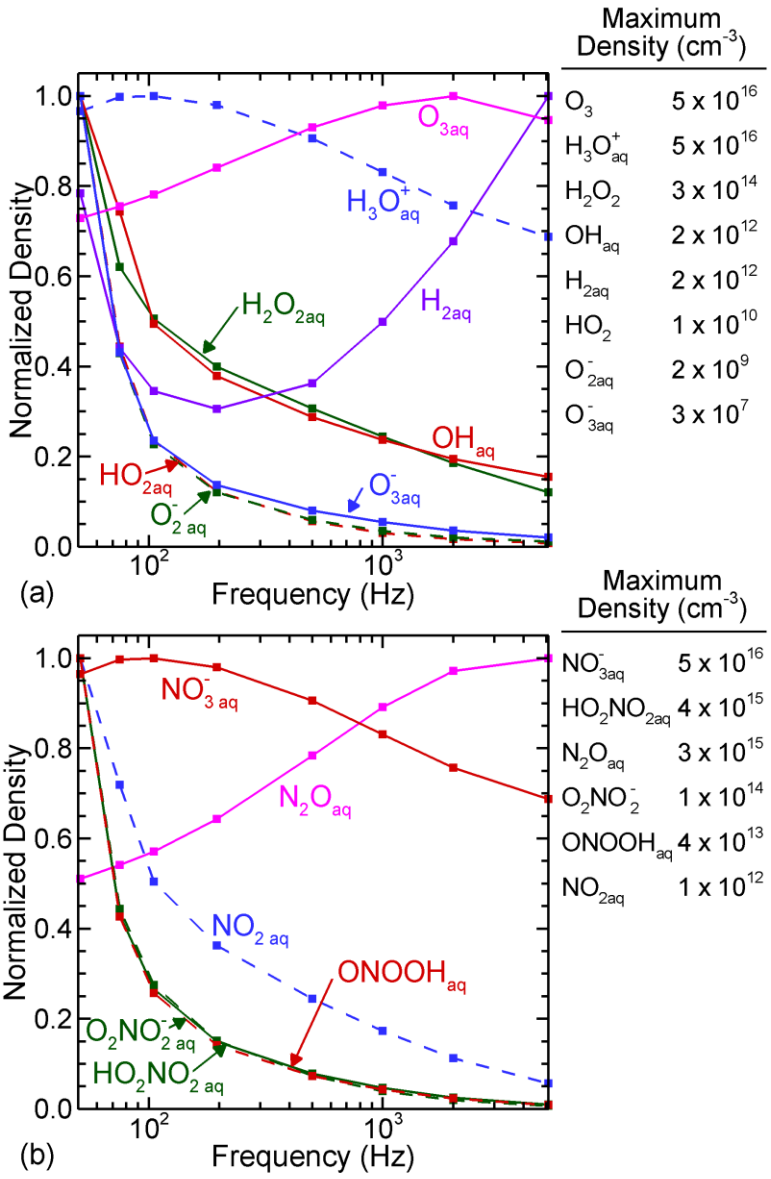

Fig. 3.14 The densities of aqueous plasma produced reactive species at 110 s (relative to the beginning of the first pulse) for different pulse repetition frequencies. (a) ROS and (b) RNS. The reactive species decrease with PRF because for higher PRF it has been a longer time since the last voltage pulse. Values are shown normalized by their maximum density as a function of PRF, shown to the right of each figure.

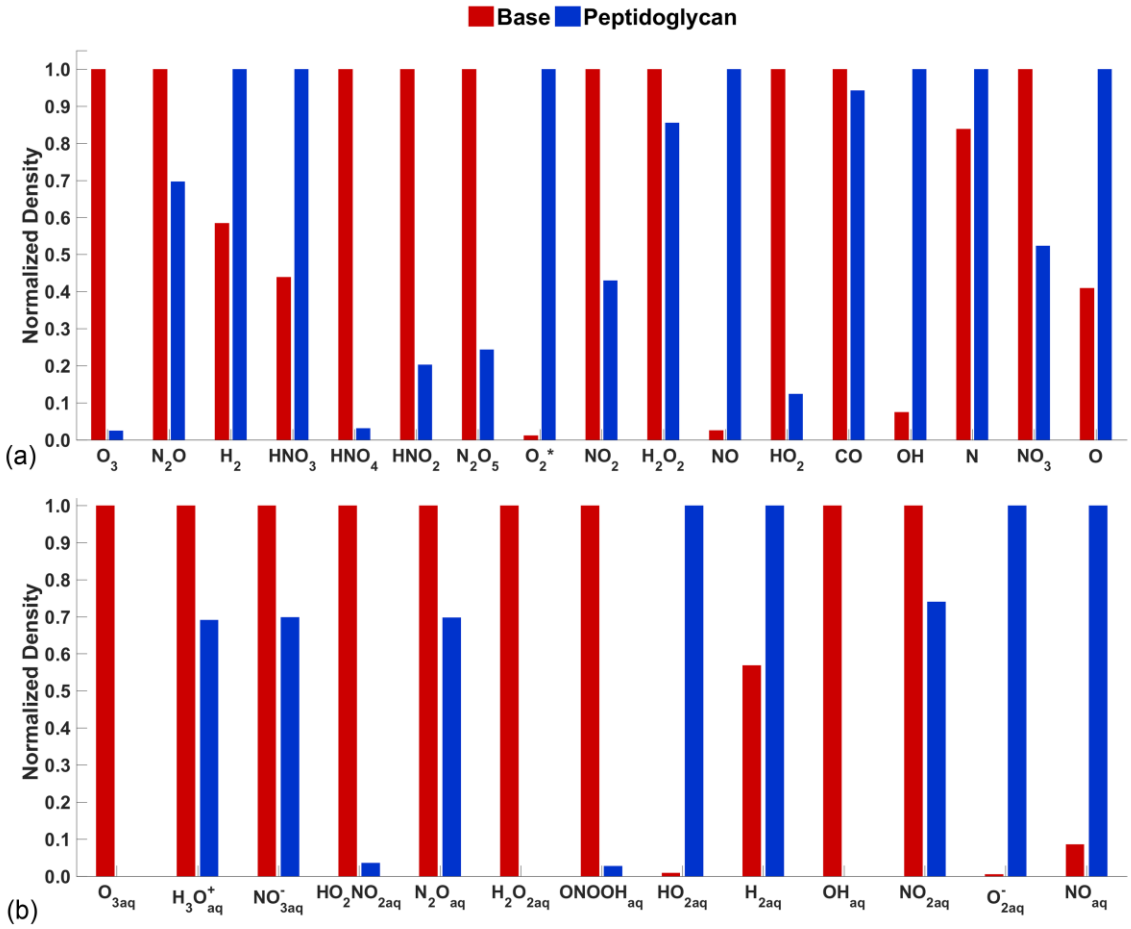

Fig. 3.15 Densities of species in the (a) gas and (b) liquid after the 5,000th discharge pulse (10 s) with and without peptidoglycan in the liquid. Species which directly react with PG in this mechanism include O, OH, O_3, and H_2O_2.

3.7 References

[1] S. Arndt, P. Unger, E. Wacker, T. Shimizu, J. Heinlin, Y. F. Li, H. M. Thomas, G. E. Morfill, J. L. Zimmermann, A. K. Bosserhoff and S. Karrer, PLoS One **8,** 1 (2013).

[2] N. Kaushik, N. Uddin, G. B. Sim, Y. J. Hong, K. Y. Baik, C. H. Kim, S. J. Lee, N. K. Kaushik and E. H. Choi, Sci. Rep. **5,** 8587 (2015).

[3] G. Daeschlein, M. Napp, S. von Podewils, S. Lutze, S. Emmert, A. Lange, I. Klare, H. Haase, D. Gümbel, T. von Woedtke and M. Jünger, Plasma Process. Polym. **11,** 175 (2014).

[4] D. B. Graves, Clin. Plasma Med. **2,** 38 (2014).

[5] B. Wegiel, D. W. Hanto and L. E. Otterbein, Trends Mol. Med. **19,** 3 (2013).

[6] P. D. Ray, B. W. Huang and Y. Tsuji, Cell. Signal. **24,** 981 (2012).

[7] P. Pagsberg, H. Christensen, J. Rabani, G. Nilsson, J. Fenger and S. O. Nielsen, J. Phys. Chem. **73,** 1029 (1969).

[8] P. Lukes, E. Dolezalova, I. Sisrova and M. Clupek, Plasma Sources Sci. Technol. **23,** 015019 (2014).

[9] M. J. Traylor, M. J. Pavlovich, S. Karim, P. Hait, Y. Sakiyama, D. S. Clark and D. B. Graves, J. Phys. D. Appl. Phys. **44,** 472001 (2011).

[10] H. Tresp, M. U. Hammer, K. Weltmann and S. Reuter, Plasma Med. **3,** 45 (2013).

[11] J. E. Foster, G. Adamovsky, S. N. Gucker and I. M. Blankson, IEEE Trans. Plasma Sci. **41,** 503 (2013).

[12] P. Rumbach, D. M. Bartels, R. M. Sankaran and D. B. Go, Nat. Commun. **6,** 7248 (2015).

[13] H. Tresp, M. U. Hammer, J. Winter, K.-D. Weltmann and S. Reuter, J. Phys. D. Appl. Phys. **46,** 435401 (2013).

[14] S. Ognier, D. Iya-Sou, C. Fourmond and S. Cavadias, Plasma Chem. Plasma Process. **29,** 261 (2009).

[15] Y. Matsui, N. Takeuchi, K. Sasaki, R. Hayashi and K. Yasuoka, Plasma Sources Sci. Technol. **20,** 034015 (2011).

[16] N. Takeuchi, Y. Ishii and K. Yasuoka, Plasma Sources Sci. Technol. **21,** 015006 (2012).

[17] S. Kelly and M. M. Turner, Plasma Sources Sci. Technol. **23,** 065012 (2014).

[18] Z. C. Liu, D. X. Liu, C. Chen, D. Li, A. J. Yang, M. Z. Rong, H. L. Chen and M. G. Kong, J. Phys. D. Appl. Phys. **48,** 495201 (2015).

[19] S. J. Beebe, P. F. Blackmore, J. White, R. P. Joshi and K. H. Schoenbach, Physiol. Meas. **25,** 1077 (2004).

[20] W. Van Gaens and A. Bogaerts, Plasma Sources Sci. Technol. **23,** 035015 (2014).

[21] W. Tian and M. J. Kushner, J. Phys. D. Appl. Phys. **47,** 165201 (2014).

[22] S. Große-Kreul, S. Hübner, S. Schneider, D. Ellerweg, A. von Keudell, S. Matejčík and J. Benedikt, Plasma Sources Sci. Technol. **24,** 044008 (2015).

[23] C. A. J. van Gils, S. Hofmann, B. K. H. L. Boekema, R. Brandenburg and P. J. Bruggeman, J. Phys. D. Appl. Phys. **46,** 175203 (2013).

[24] K. Ding and M. A. Lieberman, J. Phys. D. Appl. Phys. **48,** 035401 (2015).

[25] V. Guerra, P. A. Sá and J. Loureiro, J. Phys. D. Appl. Phys. **34,** 1745 (2001).

[26] M. Yusupov, A. Bogaerts, S. Huygh, R. Snoeckx, A. C. T. van Duin and E. C. Neyts, J. Phys. Chem. C **117,** 5993 (2013).

[27] R. Sander, "Compilation of Henry's law constants (version 4.0) for water as solvent", Atmos. Chem. Phys. **15,** 4399 (2015).

[28] K. P. Madden and S. P. Mezyk, J. Phys. Chem. Ref. Data **40,** (2011).

[29] NDRL/NIST Solution Kinetics Database, available at http://kinetics.nist.gov/solution/

[30] NIST Chemical Kinetics Database, available at http://kinetics.nist.gov/kinetics/

[31] J. C. Person and D. O. Ham, Radiat. Phys. Chem. **31,** (1988).

[32] R. Atkinson, D. L. Baulch, R. A. Cox, J. N. Crowley, R. F. Hampson, R. G. Hynes, M. E. Jenkin, M. J. Rossi and J. Troe, Atmos. Chem. Phys. **3,** 6179 (2003).

[33] S. N. Pandis and J. H. Seinfeld, J. Geophys. Res. **94,** 1105 (1989).

[34] I. A. Kossyi, A. Y. Kostinsky, A. A. Matveyev and V. P. Silakov, Plasma Sources Sci. Technol. **1,** 207 (1992).

[35] M. A. Lieberman and A. J. Lichtenberg, "Principles of Plasma Discharges and Materials Processing", 273 (2005).

[36] F. Lepoutre, G. Louis and I. I. Manceau, Chem. Phys. Lett. **48,** 3 (1977).

[37] W. M. Graven and F. J. Long, J. Am. Chem. Soc. **76,** 2602 (1954).

Chapter 4 Atmospheric Pressure Plasma Activation of Water Droplets[1]

Many configurations for chemical activation of liquids by low temperature, atmospheric pressure plasmas have been investigated for its use in biomedical, agricultural, and sterilization applications. Exposing droplets or mists to an air plasma may be an efficient way to transfer reactivity into the liquid due to the high surface area to volume ratio of the liquid. In this chapter, 0-dimensional modeling and analytical analysis is used to discuss the scaling of plasma activated liquid chemistry with system parameters including droplet size and droplet density. Exposure to 500 pulses in an air plasma and an afterglow period of 5 s is simulated. The aqueous densities of species with high Henry's law constants, scale differently than that of species with low Henry's law constants, with a much greater sensitivity to the total liquid volume and longer equilibration timescales.

4.1 Introduction

Plasma-activated liquids and plasma-activated media have been investigated as an alternative method to deliver plasma-produced reactivity to tissue.[1,2] This entails treating a liquid with a non-equilibrium plasma, then introducing the liquid to tissue or a wound. Because much of the effects of plasma on biological systems are a result of the chemistry, many of the same beneficial results have been observed with this type of indirect treatment.[2,3] Plasma activated liquids have been shown to induce apoptosis in cancer cells and to kill bacteria and fungi in a number of experimental investigations.[4–8]

[1] The results discussed and portion of the text in this chapter have been previously published in J. Kruszelnicki, A. M. Lietz, and M. J. Kushner, "Atmospheric pressure plasma activation of water droplets", J. Phys. D.: Appl. Phys. **52**, 355207 (2019).

One practical advantage of using plasma-activated liquid is the plasma can be operated in a more controlled environment than would be possible with direct treatment of tissue. When directly treating a patient, it may be challenging to control, for example, the air currents and relative humidity around the device. The surrounding environment can also interact with the plasma source electrically, by introducing stray capacitance and unintentional nearby electrodes. Indirect plasma treatment provides the opportunity to operate the plasma in a controlled environment, and provide a more consistent dose of reactive oxygen and nitrogen species (RONS).

In many cases when liquids are treated by a plasma, a saturation layer develops at the surface of the liquid, where the densities of RONS is large at the surface, but does not rapidly penetrate the bulk liquid.[9,10] This saturation layer limits the total reactivity which can be transferred to the liquid. One configuration for plasma activation of liquids that has been investigated recently is the plasma treatment of droplets and mists.[11] Through the high surface area to volume ratio of small droplets, the solvation of reactive species in this configuration is less limited by the saturation of the surface of the liquid.

Plasma treatments involving droplets and mists have been the subject of a number of recent investigations. Electrospray of water in conjunction with plasma treatment has been studied for sterilization. Adding electrospray to corona discharges substantially increased the inactivation of biofilms.[12] Plasma-treated mist has been shown to sterilize *E. coli*, and the presence of mist influences the quantities of RONS in the liquid.[13] The plasma activation and dispersal of droplets may also be an efficient way to apply plasma to agriculture or sterilize irregular surfaces.[8,14] Plasma interactions with droplets have also been investigated for efficient production of the H_2O_2.[15,16]

In this chapter, results are discussed from a computational investigation of plasma treatment of water droplets. The scaling of the plasma-activated liquid chemistry was investigated using a global model and an analytical analysis. O_{3aq}, H_2O_{2aq}, $NO_{x\,aq}^-$, and $H_3O_{aq}^+$ are all produced in significant densities and accumulate in the droplet, and survive into the afterglow. The reactive species scale differently with the system parameters (droplet diameter, number of droplets) depending on their Henry's law constant, *h*. Species with a high *h* are almost completely transferred into the liquid phase, so their final densities are sensitive to the liquid volume, and therefore to the droplet diameter and number of droplets. The aqueous densities of species with a low *h* are relatively insensitive to the liquid volume. Most of the acids formed in an air plasma, including HNO_3, have a high *h*, and therefore the pH of the droplet is also sensitive to the droplet diameter. The difference in scaling between these categories of species provides an opportunity to tailor the liquid chemistry for the desired application.

The reaction mechanisms and initial conditions are discussed in Sec. 4.2. Results from global modeling including the dynamics of the base case, the effect of droplet diameter, the role of depletion of species from the gas phase, and the number of droplets are discussed in Sec. 4.3. Concluding remarks are in Sec. 4.4.

4.2 Description of the Model

GlobalKin is a 0-dimensional plasma chemistry model which has been extended to address plasma-liquid interactions. Detailed descriptions of the model and the manner of treating liquids are described in Chapter 2.

The approach to evaporation (Eq. 2.15) in this model is a simplifying assumption, while more detailed studies of aerosol evaporation have been performed with and without the presence of plasma.[17,18] Losses by evaporation from the liquid are assumed to be negligible and so the

liquid volume does not change. The gas phase conditions in this study have 100% relative humidity and the gas heating is small; and it is unlikely that this simplifying has a major effect on the results. This approach also does not consider additional factors impacting adsorption and solvation, such as changes in surface tension or desorption energy barriers.[19] While these factors are important under select conditions, the fundamental data to include these effects is not available for all species. The Henry's law constants used in simulations are listed in Table I. These values were taken primarily from work by Sander in Ref. [20] with extensions described in Ref. [21].

Numerous studies have been performed in the area of atmospheric aerosols and their ability to scavenge compounds. For example, Djikaev and Tabazadeh modeled a droplet's ability to adsorb and solvate organic species as a function of the droplet diameter.[22] Their theory predicted large increases in the effective Henry's law constant for small droplets. The model requires an affinity parameter, *b*, that is related to the probabilities of adsorption and desorption which can be calculated from molecular dynamics simulations.[23] Based on these results, $b = 1.01$ for O_3 and $b = 11.1$ for H_2O_2. Using the theoretical formulation of Djikaev and Tabazadeh for the conditions in this chapter, the effective *h* increases by no more than 50% for O_3 and 5% for H_2O_2 for the smallest droplet diameter included in this study (0.1 μm). These enhancements in *h* are small compared to the variation in Henry's law constants between species, which span 7 orders of magnitude.

4.2.1 Reaction Mechanism

This investigation addresses humid air plasma activation of liquid water droplets. The mechanism includes 88 gas phase species, 93 liquid species, 1855 gas phase reactions, and 176

liquid reactions. *Pumpkin*, a reaction pathway analysis tool, was used to determine the dominant reactions producing a species of interest.[24]

In the gas phase during the discharge pulse, the generation of electrons is driven by electron impact ionization of N_2, O_2, and H_2O including the reactions

$$e + N_2 \rightarrow N_2^+ + e + e, \quad (4.1)$$

$$e + N_2 \rightarrow N^+ + N + e + e, \quad (4.2)$$

$$e + O_2 \rightarrow O_2^+ + e + e, \quad (4.3)$$

$$e + O_2 \rightarrow O^+ + O + e + e, \quad (4.4)$$

$$e + H_2O \rightarrow H_2O^+ + e + e. \quad (4.5)$$

The dominant mode of electron energy loss is inelastic collisions producing electronic, vibrational, or rotational excitation. In this reaction mechanism, the rotational and vibrational states of O_2 and N_2 are each approximated as a single state [$O_2(r)$, $O_2(v)$, $N_2(r)$, and $N_2(v)$], and only a single vibrational excited state of H_2O [$H_2O(v)$] is included.

The dissociation of O_2, N_2, and H_2O is critical for generating the RONS that activate water. Electron impact dissociation generates reactive products while the electron temperature is elevated during the voltage pulse, including

$$e + N_2 \rightarrow N + N + e, \quad (4.6)$$

$$e + O_2 \rightarrow O + O + e, \quad (4.7)$$

$$e + H_2O \rightarrow OH + H + e, \quad (4.8)$$

$$e + H_2O \rightarrow O + H + H + e, \quad (4.9)$$

$$e + H_2O \rightarrow O + H_2 + e, \quad (4.10)$$

Attachment to O_2 and H_2O result in electron losses during and immediately after the plasma pulse, with the dissociative processes producing additional radicals,

$$e + O_2 \rightarrow O^- + O, \quad (4.11)$$

$$e + O_2 + M \rightarrow O_2^- + M, \quad (4.12)$$

$$e + H_2O \rightarrow O^- + H_2, \quad (4.13)$$

$$e + H_2O \rightarrow OH + H^-, \quad (4.14)$$

$$e + H_2O \rightarrow OH^- + H, \quad (4.15)$$

where M is a third body. After initial dissociation produces reactive neutrals, reactions among these species generate more complex species such as O_3, H_2O_2, NO_x, and HNO_x, through pathways that will be discussed in Sec. 4.3.

The gas-phase reaction set is a modified version of the mechanism developed by Van Gaens *et al.*[25] A schematic of the liquid water reaction mechanism is in Fig. 4.1. The mechanism has been previously discussed in detail and so will only be summarized here.[21] The plasma produced species that come in contact with the liquid include electrons, positive and negative ions, excited neutrals, and ground state neutrals. The electrons that enter the liquid are rapidly solvated, and then undergo dissociative attachment with water, forming H_{aq} and OH^-_{aq}. Most of the positive ions (with the exception of H_3O^+) which solvate charge exchange with H_2O_{aq}, forming $H_2O^+_{aq}$, followed by

$$H_2O^+_{aq} + H_2O_{aq} \rightarrow H_3O^+_{aq} + OH_{aq}, \quad (4.16)$$

producing hydronium and a hydroxyl radical. Electronically excited gas phase species entering the liquid that have enough energy to dissociate a water molecule are assumed to undergo dissociative excitation transfer reaction with H_2O_{aq} producing H_{aq} and OH_{aq}. Excited states with less energy than this threshold energy, such as vibrationally excited molecules, simply collisionally de-excite.

The mechanism includes forward and reverse reactions for acids in the liquid, HA_{aq}, which enable them to dissociate and recombine according to their equilibrium pKa ($HA_{aq} + H_2O_{aq} \leftrightarrow A^-_{aq} + H_3O^+_{aq}$). These acids include HNO_{3aq}, HNO_{2aq}, $ONOOH_{aq}$, HO_2NO_{2aq}, H_2O_{2aq}, and HO_{2aq}. HNO_{3aq} is the only strong acid which completely dissociates into $NO_3^-{}_{aq}$ and $H_3O^+_{aq}$. During the afterglow following repetitive discharge pulses, the other weak acids stay predominately in the form of HA_{aq} rather than as their conjugate bases, A^-_{aq}.

The reactive neutrals in the liquid are primarily produced by solvation of their gas phase counterparts. Important reactions occurring in the liquid which convert solvated species from the plasma into more stable compounds include the reactive oxygen species (ROS) reactions,

$$OH_{aq} + OH_{aq} \rightarrow H_2O_{2aq}, \quad (4.17)$$

$$H_{aq} + H_{aq} \rightarrow H_{2aq}, \quad (4.18)$$

$$O_{aq} + H_2O_{aq} \rightarrow OH_{aq} + OH_{aq}, \quad (4.19)$$

$$O_{aq} + O_{2aq} \rightarrow O_{3aq}, \quad (4.20)$$

and the reactive nitrogen species (RNS) reactions,

$$N_{aq} + N_{aq} \rightarrow N_{2aq}, \quad (4.21)$$

$$N_2O_{5aq} \rightarrow NO_{2aq} + NO_{3aq}, \quad (4.22)$$

$$N_2O_{5aq} + H_2O_{aq} \rightarrow HNO_{3aq} + HNO_{3aq}, \quad (4.23)$$

$$N_2O_{5aq} + H_2O_{aq} \rightarrow ONOOH_{aq} + ONOOH_{aq}, \quad (4.24)$$

$$NO_{2aq} + OH_{aq} \rightarrow HNO_{3aq}, \quad (4.25)$$

$$NO_{3aq} + H_2O_{aq} \rightarrow HNO_{3aq} + OH_{aq}. \quad (4.26)$$

The mechanism includes slow-decay processes. Several species, including O_3, H_2O_2, ONOOH, and HO_2NO_2 are relatively stable and often survive for several minutes after the plasma treatment. However as slow reactions or thermal decay occur at long timescales, these

relatively stable species can produce more reactive products, such as OH_{aq}, NO_{aq}, HO_{2aq}, O_{aq}, and NO_{2aq}. These chain reactions enable plasma activated liquids to deliver reactivity long after the plasma treatment has ended. Several important slow-decay reactions include

$$H_2O_{2aq} + OH_{aq} \rightarrow HO_{2aq}, \tag{4.27}$$

$$O_3^-{}_{aq} + H_3O^+{}_{aq} \rightarrow OH_{aq} + O_{2aq} + H_2O_{aq}, \tag{4.28}$$

$$O_{3aq} \rightarrow O_{aq} + O_{2aq}, \tag{4.29}$$

$$H_2O_{2aq} + H_{2aq} \rightarrow H_{aq} + OH_{aq} + H_2O_{aq}, \tag{4.30}$$

$$ONOOH_{aq} + H_2O_{aq} \rightarrow OH_{aq} + NO_{2aq} + H_2O_{aq}, \tag{4.31}$$

$$HO_2NO_{2aq} \rightarrow HO_{2aq} + NO_{2aq}. \tag{4.32}$$

In the discussion that follows, particular attention will be paid to ozone and hydrogen peroxide due to the large difference in their Henry's law constants (≈ 0.274 and $\approx 1.92 \times 10^6$, respectively), their stability in aqueous form, and their use in biological processes and abatement of pollutants. Note will also be made of the pH of the droplets. The pH of the droplets was calculated based on the molarity of hydronium, $H_3O^+{}_{aq}$,

$$pH = -\log_{10}\left([H_3O^+_{aq}]\right), \tag{4.33}$$

where the density of $H_3O^+{}_{aq}$ is in moles/liter.

4.2.2 Model Parameters

The base case geometry is a cylinder with a radius of 2.5 mm and a height of 2 mm containing one 10 μm droplet of water at its center. This geometry corresponds to a plasma volume of 39.3 mm^3, a plasma surface area of 39.3 mm^2 (when reactions are ignored on the outer walls), a liquid volume of 523 μm^3, and a liquid surface area of 314 μm^2, or a surface-to-volume ratio of 600/cm. In cases with a single droplet, the diffusion length was defined as the d/π, where d is the distance between the droplet surface and the top or bottom surfaces of the cylinder.

The diffusion length was 317 μm for the base case. The radial surface was not considered a wall for loss processes, which then represents a periodic boundary condition, or an infinite planar DBD. No convective gas flow was considered. The gas phase initially consisted of $N_2/O_2/H_2O/CO_2$ = 76.6/20.3/3.52/0.03 at 1 atm and 300 K. The water initially contained dissolved gases at their Henry's law equilibrium concentrations of N_{2aq} (8.9 ppm), O_{2aq} (4.8 ppm), and CO_{2aq} (0.14 ppm). The pulse repetition rate of the discharge was 10 kHz. The discharge was simulated for 500 pulses followed by an afterglow bringing the total simulation time to 10 s. During the afterglow, the discharge is not pulsed but otherwise the full reaction mechanism is employed. This may represent a reactor where, for example, a mist with a very low density of droplets flows through a small plasma reactor with a residence time of 0.05 s, and the droplet remains entrained in the gas flow for several seconds after treatment. It should be noted that by approximating the liquid as well-stirred in the 0-dimensional model, the saturation layer on the liquid surface will not be addressed. This is especially relevant for larger droplets when no liquid convection occurs.

4.3 Global Modeling of Plasma Activated Droplets

4.3.1 Base Case

Each discharge pulse is simulated in full detail, with conditions prior to the pulse being initialized with an electron density of $n_e = 10^8$ cm^{-3} and an electron temperature of T_e = 0.025 eV. The first discharge pulse and plasma properties are shown in Fig. 4.3a. As the power begins to increase, T_e increases to a maximum of 6.4 eV. As the gas begins to avalanche, increasing the plasma density and increasing conductivity, the power is dissipated by a larger number of electrons, resulting in a lower T_e. The volume averaged electron density reaches 1.8×10^{11} cm^{-3} near the peak power of 1 kW or 25.4 kW/cm^3 The energy deposition is 5 μJ/pulse (127 μJ/cm^3)

or an average power of 50 mW (1.27 W/cm^3) at 10 kHz. The energy deposition corresponds to 0.016 eV per gas molecule over 500 pulses.

Attachment dominates in the afterglow, producing an ion-ion plasma prior to the next discharge pulse (Figs. 4.2b and 4.2c). The dominant ions in this afterglow are $H_3O^+(H_2O)_n$, and $O_2^-(H_2O)_n$, $O^-(H_2O)$, and OH^-. The dominance of water cluster ions begins during the discharge pulse, becoming the most abundant positive ion by 6 ns. The most abundant cluster ion is $H_3O^+(H_2O)_6$, which is the largest water cluster ion included in the reaction mechanism. The density of $H_3O^+(H_2O)_6$ reaches a maximum of 4×10^{11} cm^{-3} 20 ns after the start of the pulse and decays by ion-ion recombination to 2×10^{10} cm^{-3} before the start of the next discharge pulse.

Electron impact dissociation of water during the discharge pulse produces OH, H, and H_2, dissociation of O_2 produces O, and dissociation of N_2 produces N. These species also continue to be produced for approximately 10 μs after each pulse by the cascade of reactions that results from charge exchange, recombination, and excitation transfer. For example, the reactions

$$N_2^* + O_2 \rightarrow N_2 + O + O, \tag{4.34}$$

$$O^-(H_2O) + H_2O \rightarrow OH^-(H_2O) + OH, \tag{4.35}$$

$$OH^-(H_2O)_n + H_3O^+(H_2O)_n \rightarrow H + OH + (H_2O)_n, \tag{4.36}$$

$$H_2NO^+ + M^-(H_2O)_n \rightarrow N + M + (H_2O)_n, \tag{4.37}$$

$$O^+ + N_2 + M \rightarrow NO^+ + N + M, \tag{4.38}$$

continue to produce reactive species as long as 10 μs into the afterglow. The electrons undergo rapid attachment in the afterglow, with densities that decrease an order of magnitude within 20 ns. As a result, dissociative recombination of electrons (e.g., $e + O_2^+ \rightarrow O + O$) does not significantly contribute to the production of OH, O, and N. (In contrast, in prior studies of He atmospheric pressure plasma jets with air impurities, dissociative recombination of impurity ions

[O_2^+, N_2^+, H_2O^+] were found to be major sources of O, N and OH radicals in the afterglow. [26]) The dissociation products then react with other RONS and the surrounding air, for example,

$$O + O_2 + M \rightarrow O_3 + M, \quad (4.39)$$

$$H + O_2 + M \rightarrow HO_2 + M, \quad (4.40)$$

$$OH + OH + M \rightarrow H_2O_2 + M, \quad (4.41)$$

$$OH + N \rightarrow NO + H, \quad (4.42)$$

$$N + O_2 \rightarrow NO + O, \quad (4.43)$$

$$NO + O_3 \rightarrow NO_2 + O_2, \quad (4.44)$$

$$N_2^* + O_2 \rightarrow N_2O + O, \quad (4.45)$$

where M is a third body.

The evolution of gas phase RONS during the first 10 discharge pulses is shown in Figs. 4.3a-4.3b. These species can be grouped based on their lifetimes. Several of the most reactive species [e.g., $O_2(^1\Sigma)$, $O(^1D)$, N_2^*, and $OH(A^2\Sigma)$] are depleted by chemical reactions or collisional relaxation before the beginning of the next pulse, and are not shown in the figure. (These species would appear to be delta-functions in the figure.) Even though the lifetimes of these species may be short, they nevertheless can make important contributions to radical production. For example, dissociative excitation transfer of N_2^* to O_2 produces 56% of the O atoms by 20 ns after the discharge pulse, with the rest being produced by electron impact dissociation of O_2. The next group of species reaches a pulsed periodic steady-state, where they are produced during the discharge pulse and partly consumed between pulses. Species in this group include O, OH, and HO_2. The density of O atoms reaches 3×10^{13} cm^{-3} 100 ns after the start of the pulse, and is reduced by a factor of nearly 100 by the formation of O_3 (Eq. 4.39) before the next pulse. The densities of OH (with a maximum of 1.5×10^{13} cm^{-3}) and HO_2 (3.5×10^{13} cm^{-3}) are not as

significantly depleted between the pulses, with the densities decreasing only 10-50% before the next pulse.

Lastly, there are species which accumulate from pulse to pulse or whose densities come into a steady state over many pulses, summarized in Fig. 4.3c. ROS which accumulate over the 500 pulses (and their maximum densities) include O_3 (1×10^{16} cm^{-3}), H_2O_2 (1×10^{14} cm^{-3}), and H_2 (2×10^{13} cm^{-3}).

The RNS further react to form higher order nitrogen oxides and acids. For example,

$$OH + NO + M \rightarrow HNO_2 + M, \quad (4.46)$$

$$OH + NO_2 + M \rightarrow HNO_3 + M, \quad (4.47)$$

$$HO_2 + NO_2 + M \rightarrow HO_2NO_2 + M. \quad (4.48)$$

These products generally take many steps to form, and therefore have a slower, smoother evolution in time, despite the pulsed nature of the plasma. RNS which accumulate over the 500 pulses (and their maximum densities) include N_2O (2×10^{14} cm^{-3}), HNO_3 (1×10^{14} cm^{-3}), HNO_2 (4×10^{13} cm^{-3}), NO_2 (2×10^{13} cm^{-3}) and HO_2NO_2 (2×10^{12} cm^{-3}). The density of NO initially increases over many pulses, and reaches a pulsed periodic steady state after tens of pulses with a density of 1×10^{13} cm^{-3}.

Densities of aqueous species during the first ten pulses of the base case (a single 10 μm diameter water droplet) are shown in Figs. 4.4a and 4.4b. The evolution of aqueous species during the 500 discharge pulses and the afterglow is shown in Fig. 4.4c. Ions and electrons from the plasma directly solvate into the water droplet while neutrals solvate if the liquid densities are below their Henry's law saturation values. In the droplet, several charged species are stable and accumulate (e.g., $H_3O^+_{aq}$, $O_2^-_{aq}$, and $NO_3^-_{aq}$). $H_3O^+_{aq}$ and $NO_3^-_{aq}$ are the most abundant ions, with densities of 7×10^{16} cm^{-3} (1×10^{-4} M, where M is moles/liter) at the end of the plasma period.

$O_2^-{}_{aq}$ reaches a density of 9×10^{13} cm^{-3} (1×10^{-7} M). $O_2NO_2^-{}_{aq}$, the conjugate base of HO_2NO_{2aq}, reaches a density of 2×10^{13} cm^{-3} (3×10^{-8} M). These negative liquid ions and hydronium are to some extent due to solvation of gaseous ions, but are predominately a result of the solvation of neutral acids, followed by hydrolysis in water. With the exception of H_3O^+ (and its cluster ions), positive gas phase ions (e.g. N_2^+, O_2^+) rapidly charge exchange with water, followed by the hydrogen abstract reaction $H_2O^+{}_{aq} + H_2O_{aq} \rightarrow H_3O^+{}_{aq} + OH_{aq}$. (The ionization energy of O_2 is less than that of H_2O in the gas phase, but in the presence of water, formation of H_3O^+ and OH is energetically favorable. [27]) Though electronically excited states are allowed to solvate, their lifetimes are short as they undergo a collisional de-excitation in the liquid. The more stable species solvating into the water tend to build up from pulse to pulse.

OH_{aq} and H_{aq} are a result of electron impact reactions in the gas phase that produce OH and H, followed by their solvation, as well as excited states that enter the liquid with enough energy to dissociate water. H_2O_{2aq} is a product of reactions of OH in the gas phase, followed by solvation, and by reactions of OH_{aq} in liquid. $O_3^-{}_{aq}$ results primarily from charge exchange between other aqueous negative ions and O_{3aq}. From pulse to pulse, the pH of the droplet decreases, becoming more acidic, with a pH of 3.9 by the end of the pulsing period. The decreasing pH is due to the production of HNO_{3aq}, which is a strong acid which dissociates into $H_3O^+{}_{aq}$ and $NO_3^-{}_{aq}$. HNO_{3aq} continues to form and solvate for seconds after the discharge pulses terminate, and the pH is 1.25 after 10 s. There are also several weak acids produced, including HNO_{2aq}, HO_{2aq}, HO_2NO_{2aq}, $ONOOH_{aq}$, and H_2O_{2aq}.

Several of the more complex RNS were a result of reactions in the liquid. For example, N_2O_5 is formed in the gas phase from reactions between NO_2 and NO_3. Upon solvating into the water droplet, N_2O_5 is converted to $ONOOH_{aq}$ or HNO_{3aq} (Eq. 4.23-4.24). As a result $ONOOH_{aq}$

accumulates to a density of 4×10^{15} cm^{-3} (6×10^{-6} M) by the end of 500 pulses. $ONOOH_{aq}$ and HO_2NO_{2aq} are important species for long timescale liquid activation, as they can generate more reactive species several seconds after the plasma treatment. HO_2NO_{2aq} decays into HO_{2aq} and NO_{2aq} (Eq. 4.31), and $ONOOH_{aq}$ decays into OH_{aq} and NO_{2aq} (Eq. 4.32). HO_2NO_{2aq} reaches a density of 1×10^{15} cm^{-3} (2×10^{-6} M) by the end of 500 pulses, and due to solvation of HO_2NO_2 continues to increase in the afterglow to a density of 4×10^{17} cm^{-3} (7×10^{-4} M).

4.3.2 Droplet Diameter: Finite Plasma Volume

The range of Henry's law constants for RONS produced in air plasmas is nearly 10^7. This large range results in significantly different activation of the liquid, leading to droplet dependent densities of aqueous species. These trends are illustrated by the densities of O_{3aq} and H_2O_{2aq} in 1 μm and 1 mm droplets shown in Fig. 4.5. Densities are shown during 500 discharge pulses in humid air at 10 kHz (elapsed time of 0.05 s) followed by a 10 s afterglow. O_3 accumulates in the gas phase, reaching a density of 1.5×10^{16} cm^{-3} after 500 pulses. O_3 also has a low Henry's law constant of 0.274, which has two important implications. Given the small volume of the droplet compared to the plasma (gas to liquid volume ratios are 7.50×10^7 for a 1 μm droplet and 73.9 for a 1 mm droplet), most of the O_3 produced in the plasma remains in the gas phase instead of solvating into the droplet. As a result, the gaseous O_3 is not depleted by solvation into the droplet. Second, with such large densities of O_3 and large fluxes incident onto the surface of the droplet, the equilibration time for saturating the droplet with O_{3aq} is shorter than the inter-pulse period. As a result, $n_l \approx h n_g$ (that is, O_3 and O_{3aq} are at equilibrium) during the majority of the plasma treatment. The end result is that O_3 and O_{3aq} densities were nearly independent of the diameter of the droplet.

H_2O_2, on the other hand, has a high Henry's law constant of 1.92×10^6. This value of h is smaller than the ratio of volumes of the smaller droplet but larger than the ratio of the volumes of the larger droplet. These combinations of volume ratios and Henry's law constant implies that the smaller droplet can be saturated with H_2O_{2aq} and most of the H_2O_2 produced in the gas phase remains in the gas phase. For the larger droplet, most of the H_2O_2 produced in the gas phase (which reaches a density of 1.0×10^{14} cm^{-3}) is solvated, resulting in a depletion of gas phase H_2O_2. In terms of aqueous densities, small droplets saturate (that is, H_2O_2 and H_2O_{2aq} are at equilibrium). For the larger droplet, the same gas phase production of H_2O_2 is diluted in a larger liquid volume, resulting in the density of H_2O_{2aq} being 4 orders of magnitude lower for the 1 mm droplet compared to the 1 μm droplet. The maximum density of H_2O_{2aq} is 1.2×10^{20} cm^{-3} (0.2 M) in the 1 μm droplet and 9.7×10^{15} cm^{-3} (2×10^{-5} M) for the 1 mm droplet. The equilibration time for the 1 mm droplet is longer than the time the discharge is on, as indicated by $n_l < hn_g$ for most of the simulation time.

Varying the droplet diameter for a single droplet can have a significant impact on the activation of the liquid by species having different Henry's law constants. Consider a non-reacting species which initially entirely resides in the gas phase with an initial density, n_{g0}. Equilibrium of the gas phase species with its aqueous counterpart in the droplet occurs when $n_{l\infty} = hn_{g\infty}$, where $n_{l\infty}$ and $n_{g\infty}$ are the final densities in the liquid and the gas. Ignoring other reactions, the total number of molecules in the gas phase and liquid must be conserved,

$$V_g n_{g0} = V_l n_{l\infty} + V_g n_{g\infty}, \tag{4.49}$$

where V_l is the droplet volume and V_g is the gas volume. The final equilibrium liquid density would then be

$$n_{l\infty} = \frac{h}{1 + h\frac{V_l}{V_g}} n_{g0}. \tag{4.50}$$

This relationship has two limiting values:

$$n_{l\infty} = hn_{g0} \text{ for } h\frac{V_l}{V_g} << 1, \tag{4.51}$$

$$n_{l\infty} = \frac{V_g}{V_l} n_{g0} \text{ for } h\frac{V_l}{V_g} >> 1. \tag{4.52}$$

In the first case (Eq. 4.51), the density of the solvent in the water saturates, and so $n_{l\infty}$ is independent of V_l/V_g, and so is also independent of droplet diameter. This limit applies to species with low Henry's law constants, including O_3, N_2O, and H_2. The end result is that the density of their aqueous partners are independent of droplet diameter. In the second case (Eq. 4.52), the majority of the molecules that started in the gas phase are solvated, and the concentration of the aqueous partner in the liquid is limited by depletion of the gas phase. This limit results in $n_{l\infty}$ being a function of V_g/V_l and so is also a function of droplet diameter. This limit applies to species with a high Henry's law constant, including H_2O_2, HO_2NO_2, and HNO_3.

The limits presented in Eq. 4.51 and 4.52 describe the steady state conditions but not the timescales to reach this equilibrium. Using the assumptions of solvation dynamics which are applied in the global model, it is possible to estimate these timescales. Based on Eq. 2.12 and 2.14, the equilibration time (neglecting reactions) for activating a droplet, τ, is

$$\tau = \frac{\Lambda^2}{Df_l\left(\frac{V_g}{hV_l} + 1\right)}, \tag{4.53}$$

where Λ is the diffusion length, D is the diffusion coefficient, and f_l is the fractional area of the liquid.

The derivation of τ is in Appendix A. This equilibration time is plotted for D = 0.19 cm^2/s in Fig. 4.6. The equilibration time, τ, initially increases with droplet diameter, as the SVR decreases, and increases with Henry's law constant. The species with the largest h, such as H_2O_{2aq}, are the slowest to equilibrate, which is consistent with the results shown in Fig. 4.5. Above a critical diameter, the equilibration time begins to decrease as hV_l/V_g exceeds 1 and the gas phase begins to become depleted. The depletion of gas phase partners results in an equilibration time which is limited by the area of the droplet (f_l).

Aqueous species densities as a function of droplet diameter for a single droplet after 500 discharge pulses and an afterglow bringing the total time to 5 s are shown in Fig. 4.7. The densities of species with high Henry's law constants, H_2O_{2aq}, HO_2NO_{2aq}, $NO_3^-{}_{aq}$, and $ONOOH_{aq}$, shown in Fig. 4.7a, rapidly decrease as the droplet diameter increases. For example, the density of H_2O_{2aq} decreases more than 4 orders of magnitude from 2×10^{20} cm^{-3} (0.3 M) for a 0.1 μm droplet to 4×10^{15} cm^{-3} (6×10^{-6} M) for a 1 mm droplet. There are three perspectives on this decrease in density. The first is that the same gas production of the precursors of the aqueous species is diluted in a larger volume (i.e., the limit in Eq. 4.52). The second is that for high h and large droplets, the gas phase is depleted of the precursor, thereby decreasing the flux into the surface of the droplet. The third is that the smaller droplets have larger surface-to-volume ratios (SVR). The influx of reactive species to the droplet scales with surface area, while density scales with the inverse of volume. Therefore if the incoming fluxes of reactants are constant, in the absence of saturation, smaller droplets will have a larger aqueous density of the solvation partner.

The density of species with the lowest Henry's law constants, O_{3aq}, N_2O_{aq}, and H_{2aq}, shown in Fig. 4.7b, have aqueous densities that are nearly independent of diameter (i.e., the limit in Eq. 4.51). In this case, the aqueous densities are saturated, and do not consume enough of

their gas phase precursors to deplete densities in the gas phase. With low Henry's law constants, the liquid densities of these species also tend to remain relatively low, with densities at 5 s being: O_{3aq}, 4×10^{15} cm^{-3} (7×10^{-6} M); N_2O_{aq}, 1×10^{14} cm^{-3} (2×10^{-7} M); and H_{2aq}. 4×10^{11} cm^{-3} (6×10^{-10} M).

Several species deviate from these general trends dictated by low or high Henry's law constants. These deviations are generally due to the consequences of long timescale reactions. NO_2 has a Henry's law constant of 0.28. Based on the proposed scaling, NO_{2aq} should fully saturate the droplet and its density should not be directly affected by depletion of gas phase NO_2 in this range of diameters. The density of NO_{2aq} does however decrease with increasing droplet diameter. The NO_{2aq} density at the end of the plasma on period is, indeed, nearly independent of diameter. However, there is generation of NO_{2aq} in the afterglow as a result of the decay of HO_2NO_{2aq}. HO_2NO_2 has a high Henry's law constant and so the density of HO_2NO_{2aq} is sensitive to the depletion of the gas phase densities that occurs at large droplet diameter. This reduction in the density of HO_2NO_{2aq} at large droplet diameters decreases the post-plasma production of NO_{2aq}, which decreases its density with increasing droplet diameter. The generation of NO_{2aq} by HO_2NO_{2aq} results in densities as high as 4×10^{13} cm^{-3} (7×10^{-8} M) at 5 s which exceeds the Henry's law equilibrium density. As a result, the net flux of NO_2 is out of the liquid during the late afterglow.

The density of HNO_2 (total of the gas and liquid phase) was larger at smaller droplet diameters. For droplets having diameters 1 μm or less, HNO_2 was at Henry's law equilibrium between the gas phase and droplet – $n_l = hn_g$. For larger droplets, the liquid is not saturated and $n_l << hn_g$. The equilibration time for large droplets is longer because of the lower SVR. At the same time, there are losses of HNO_{2aq} in the droplet by reactions with O_3 and N_2O at all

diameters. These losses scale with the volume of the droplet. For small droplets (large SVR), the rate of solvation of gas phase HNO_2 is large enough to replenish the HNO_{2aq} that is lost by volumetric reactions. This enables HNO_{2aq} to remain at equilibrium. For large droplets (small SVR) the rate of replenishment of HNO_{2aq} by solvating HNO_2 cannot keep up with the volumetric losses, resulting in a lower HNO_{2aq} density. As a result, the density of HNO_{2aq} decreases from 4×10^{16} cm^{-3} (6×10^{-6} M) for a 0.1 μm droplet to 1×10^{10} cm^{-3} (2×10^{-11} M) for a 1 mm droplet.

H_{aq} has a relatively short lifetime in the liquid, as it self-reacts to make H_{2aq} and reacts with O_{2aq} to form HO_{2aq}. The conversion of H_{aq} to HO_{2aq} occurs on timescales of ns if O_{2aq} is not depleted. Therefore the significant density of H_{aq} in the afterglow (5×10^{11} cm^{-3}, 8×10^{-10} M), must be produced by reactions among or decay of more stable RONS. H_{aq} is generated late in the afterglow by the slow decay of $NO_2^-{}_{aq}$ (which is at equilibrium with the corresponding acid HNO_{2aq}) reacting with $H_3O^+{}_{aq}$. The dependence of the density of H_{aq} on droplet diameter therefore approximately follows the behavior of HNO_{2aq}.

N_2O_{5aq} has a Henry's law constant of 48.5 and is under-saturated in the droplet throughout the discharge and afterglow for droplet diameters greater than 1 μm. N_2O_{5aq} reacts with water on timescales of hundreds of μs to decay into NO_{2aq} and NO_{3aq} or to produce $ONOOH_{aq}$ or HNO_{3aq}. Reactions of NO_2 and NO_3 in the gas phase produce N_2O_5 at long timescales and solvation of this continuous generation of N_2O_5 helps sustain N_2O_{5aq} into the afterglow period. For small enough droplets, this replenishment can compensate for in-droplet losses due to reactions and maintain a near equilibrium. For large droplets, the replenishment is not able to compensate for losses.

HO_2 has a Henry's law constant of 1.32×10^5. At a droplet diameter of 170 μm, hV_l/V_g = 1. This diameter marks the transition between droplets in which HO_{2aq} is saturated and so independent of diameter (smaller droplets); and droplets in which the density of HO_{2aq} decreases due to depletion of HO_2 in the gas phase (larger droplets). For droplets below 10 μm, the HO_{2aq} density is saturated at 5×10^{14} cm^{-3} (8×10^{-7} M). Depletion of gaseous HO_2 by solvation explains the dependence of the HO_{2aq} on droplet diameters greater than 100 μm. For 1 mm droplets, the liquid was under-saturated because the equilibration time was on the order of tens of seconds. The increase in the density of HO_{2aq} with diameters between 10 and 100 μm is due to a decrease in the de-solvation rate. When the diameter is below 170 μm, the main losses of HO_{2aq} are by de-solvation followed by gas phase reactions with NO_2. With the de-solvation rate in Eq. 2.13, this occurs more slowly as the droplet size increases, resulting in an increase in density as the droplet diameter increases from 10 to 100 μm.

The primary acid and its conjugate base in this system are HNO_{3aq} and $NO_{3\ aq}^-$. The $H_3O^+_{aq}$ density is essentially equal to the NO_{3aq}^- density for all conditions. With pH being a function of the density $H_3O^+_{aq}$, it is also for these conditions a function of the production of $NO_{3\ aq}^-$. HNO_3 has a high Henry's law constant of 4.8×10^6, and its aqueous density is highly sensitive to droplet diameter. The density of NO_{3aq}^- and $H_3O^+_{aq}$ decrease from 1.7×10^{21} cm^{-3} (2.8 M) in a 0.1 μm droplet to 1.6×10^{16} cm^{-3} (2.7×10^{-5} M) in a 1 mm droplet. This results in a corresponding increase in pH from -0.47 in a 0.1 μm droplet to 4.56 in a 1 mm droplet.

4.3.3 Droplet Diameter: Infinite Plasma Volume

To artificially eliminate the impact of gas phase depletion on activation of the droplet, the base case simulations were repeated with a gas volume of $V_g = 6.3 \times 10^5$ cm^3 such that $V_g >> hV_l$ for all species at all diameters. The diffusion length was kept the same as in the prior studies

discussed in Sec. B. The resulting aqueous densities, shown in Fig. 4.8, do not have a steep decrease for droplets larger than 100 μm as with the finite gas volume. The depletion of gas phase RONS, rather than SVR, reaction chemistry or equilibration time, was responsible for this steep drop in aqueous densities with a finite gas volume. For example, with a large gas volume, the H_2O_{2aq} density in 1 mm droplet is 1×10^{18} cm^{-3} (2×10^{-3} M), compared to 4×10^{15} cm^{-3} (6×10^{-6} M) when the gas volume is finite.

However, for droplet diameters less than 100 μm, the aqueous densities of species with high *h* still depend on diameter. This decrease is a result of the characteristic equilibration time for Henry's law solvation, and the increasing SVR. As the droplet diameter increases, the equilibration time increases as the SVR of the droplet is smaller. With the large volume, the maximum equilibration time occurs with a droplet diameter ≈650 μm for $h = 10^0$ - 10^6. With a finite gas volume, the maximum equilibration time occurs for a 30 μm droplet (Fig. 4.6, $h = 10^6$). As a result, each of the species which are sensitive to equilibration time (H_2O_{2aq}, $NO_3^-{}_{aq}$, $H_3O^+{}_{aq}$, HO_2NO_{2aq}, $ONOOH_{aq}$, HNO_{2aq}, and N_2O_{5aq}) has an aqueous density that is minimum with a 600 μm droplet.

The pH is lower (more acidic) for droplets activated in the large gas volume because the densities of $H_3O^+{}_{aq}$ and $NO_3^-{}_{aq}$ are no longer limited by depletion of the gas phase. The maximum pH of 2.89 occurs for a 600 μm droplet with the large volume, compared to a maximum of 4.56 when the gas volume was finite. The values of pH of the smaller droplets are unaffected by gas volume. For example, the pH of the 0.1 μm droplet is -0.47 independent of the gas volume, because the densities of $H_3O^+{}_{aq}$ and $NO_3^-{}_{aq}$ are not limited by depletion.

Although these results demonstrate the importance of gas phase depletion, they do so on a volume averaged basis. In reality, the depletion of gas phase precursors is most severe closest to the droplet.

The scaling of most of the densities of low Henry's law species, O_{3aq}, N_2O_{aq}, H_{2aq}, and H_{aq} are unchanged by having the large gas volume. The low-*h* species whose densities significantly changed by increasing the gas volume are NO_{2aq}, N_2O_{5aq}, and HNO_{2aq}. The source of NO_{2aq} at long times is primarily the decay of HO_2NO_{2aq}, which has a high Henry's law constant and is sensitive to gas phase depletion. Eliminating the gas phase depletion of HO_2NO_2 results in an increase in the density of NO_{2aq} in a 1 mm droplet from 3×10^{11} cm^{-3} (6×10^{-10} M) to 3×10^{13} cm^{-3} (6×10^{-8} M). Even though HO_{2aq} has a large *h* (1.32×10^5), its density remains nearly constant with droplet diameter, because it no longer depletes the gas phase for diameters above 170 μm.

N_2O_{5aq} has a Henry's law constant of 48.5 and is produced primarily from solvation of gaseous N_2O_5. The lifetime of N_2O_{5aq} is hundreds of μs. With this short lifetime, N_2O_{5aq} must be replenished by solvation from the gas phase to maintain its density. As a result, the long-time density of N_2O_{5aq} depends on the SVR of the droplet, which decreases with increasing droplet diameter. Smaller SVR is unable to replenish N_2O_{5aq} rapidly enough to offset losses due to volumetric reactions. The dependence of N_2O_{5aq} on droplet diameter and gas phase depletion also results from cyclic synergistic processes between the droplet and gas phase reactants. These processes involve HO_2NO_{2aq}, a precursor for N_2O_{5aq} production at long times. The decay of HO_2NO_{2aq} produces NO_{2aq} which becomes oversaturated and de-solvates into gaseous NO_2. The NO_2 then reacts with O_3 to produce NO_3, which reacts with an additional NO_2 to form N_2O_5. This N_2O_5 then solvates, forming N_2O_{5aq} long into the afterglow.

HNO_2 has a Henry's law constant of 1.15×10^3. The density of HNO_{2aq} for a 1 mm droplet in a large gas volume is 1×10^{14} cm^{-3} (2×10^{-7} M) compared to 1×10^{10} cm^{-3} (2×10^{-11} M) for the small volume. HNO_{2aq} reacts with O_{3aq} and N_2O_{aq} which have densities nearly independent of droplet diameter. The replenishment of HNO_{2aq} is by solvation of HNO_2. However this replenishment decreases with increasing droplet diameter due to the decreasing SVR. HNO_{2aq} is sensitive to gas phase depletion because the steady state density of HNO_{2aq} in the afterglow is a result of a reaction involving NO_{2aq},

$$NO_{2aq} + NO_{2aq} + H_2O_{aq} + H_2O_{aq} \rightarrow HNO_{2aq} + NO_3^-{}_{aq} + H_3O^+{}_{aq}. \quad (4.54)$$

As a result, the HNO_{2aq} density at large droplet diameter increases when gas phase depletion is not a factor due to the now larger NO_{2aq} densities.

4.3.4 Number of Droplets

To extend this study to a technologically more relevant parameter space, the number of droplets in the system was increased to simulate an aerosol. To increase the droplet density, the liquid volume and surface area were increased, the gas volume was decreased, and the diffusion length was defined as the average distance between the droplets divided by π. The droplet diameter was fixed at 10 μm, the same as in the base case. The droplet density, or the number of droplets per reactor volume, had a significant impact on the liquid activation, as shown in Figs. 4.9 and 4.10. The maximum activation for this system occurred with 300 droplets, or 7.6×10^3 droplets/cm^3.

The densities of the stable low-*h* species, O_{3aq}, N_2O_{aq}, and H_{2aq}, were independent of the number of droplets, limited by the Henry's law saturation of the liquid. These species also equilibrate quickly because of their low Henry's law constant, and were therefore relatively

independent of diffusion length which would increase (or decrease) fluxes to the surface of the droplet.

The species with higher *h*, on the other hand, were sensitive to the number of droplets. If the number of droplets was too low, the solvation was transport limited by the large diffusion length. The equilibration times were on the order of tens of seconds for 3 droplets in the gas volume. The diffusion length was large, and on average the plasma produced species had further to diffuse before reaching the droplet surface. However, if there are too many droplets, the activation becomes limited by depletion of the gas phase RONS, effectively diluting the RONS in a larger liquid volume.

For example, HO_2NO_{2aq} has a density of 2×10^{16} cm^{-3} (4×10^{-5} M) for 3 droplets in the gas which increases to 8×10^{17} cm^{-3} (1×10^{-3} M) for 200 droplets. When the number of droplets is further increased and the HO_2NO_{2aq} is diluted into a larger total volume of liquid, the density decreases to 2×10^{16} cm^{-3} (3×10^{-5} M) for 30,000 droplets. Since $NO_3^-{}_{aq}$ is sensitive to both equilibration time and depletion of gaseous HNO_3, its density also has a maximum at 300 droplets. As a result, pH (a function of $H_3O^+{}_{aq}$ and $NO_3^-{}_{aq}$ in this system) has a minimum of 1.3 for 300 droplets. In contrast for 30,000 droplets, $H_3O^+{}_{aq}$ and $NO_3^-{}_{aq}$ are diluted and the pH is 3.3.

The inventory of aqueous species is the average density in individual droplets multiplied by the total liquid volume. The total inventory of reactive species is the metric of interest when, for example, using an activated aerosol spray to treat a surface. These inventories of RONS are shown in Fig. 4.10 as a function of number of droplets. Stable species with low *h* (O_{3aq}, N_2O_{aq}, and H_{2aq}) have inventories that are nearly linear functions of the number of droplets because their densities in individual droplets do not vary. For example, the inventory of O_{3aq}, increases from 2×10^7 to 2×10^{11} when increasing the number of droplets from 3 to 30,000. H_2O_{2aq}, $NO_3^-{}_{aq}$,

$H_3O^+_{aq}$, and HO_2NO_{2aq}, have inventories that are nearly constant above 10^3 droplets in the volume. The maximum inventories of $NO_3^-_{aq}$ and $H_3O^+_{aq}$ are both 2×10^{13} molecules, while inventories of H_2O_{2aq} are maximum at 1×10^{13} and of HO_2NO_{2aq} at 1×10^{12}. The nearly constant inventories above 10^3 droplets indicates that the decrease in the density of these species with increasing number of droplets (Fig. 4.9) was due to diluting the same number of molecules into a larger volume of liquid.

$ONOOH_{aq}$, HNO_{2aq}, HO_{2aq}, and N_2O_{5aq} experience significant decreases in inventory above 10^3 droplets. For example, the inventory of $ONOOH_{aq}$ is maximum at 1×10^{11} molecules for 600 droplets, and decreases to 2×10^{10} molecules for 30,000 droplets. These species are slightly less stable as they undergo long timescale reactions after solvating. The decrease in their inventories can be attributed to shorter equilibration times and smaller diffusion lengths resulting in more rapid solvation. These species all decay in the liquid, so increasing the solvation rate (smaller Λ) results in the aqueous densities rising more rapidly in the afterglow (shorter equilibration time). They then become depleted in the gas phase more quickly, resulting in a lower flux of these species into the droplet later in the afterglow. The lower incoming fluxes are then unable to replenish losses by reactions as they convert to $NO_3^-_{aq}$. For example, for 600 droplets, the HNO_{2aq} inventory slowly decreases from 2×10^{10} at the end of the pulsing period to 9×10^8 by 5 s as it is replenished by solvation from the gas phase. For 3×10^4 droplets, the inventory of HNO_{2aq} rapidly decreases from 3×10^{11} at the end of the pulsing period to 6×10^6 by 5 s. So for the densities shown in Fig. 4.9, the decrease above 10^3 droplets was in part due to the dilution, but also due to the more rapid solvation and conversion of species to their final products.

4.3.5 Dispersing a Finite Volume of Water into Droplets

In optimizing, for example, a plasma activated water spray of droplets having a given flow rate (or volume) of liquid, a decision must be made about the number and diameter of the droplets. This optimization was investigated using the volume of liquid for a 1 mm droplet and dispersing that constant volume into a different number of droplets having the appropriate diameters to maintain constant volume. In the global model, this was accomplished by adjusting the diffusion length and area of plasma contacting the liquid. The results of this study are shown in Fig. 4.11.

In this parameterization, V_g/V_l remains constant while the diffusion length varies. Species with higher Henry's law constants are more sensitive to diffusion length because they have longer equilibration times. O_{3aq}, N_2O_{aq}, and H_{2aq} were less affected by the method of dispersal of the droplets because they rapidly saturate the liquid, even for a single 1 mm droplet, due to their low Henry's law constants.

The high-*h* species were more sensitive to the method of dispersal. Most of the densities of RNS decreased with increasing number of droplets while the density of H_2O_{2aq} increased. The H_2O_{2aq} density was minimum at 3×10^{15} cm^{-3} (8×10^{-5} M) for 10 droplets and increased to 5×10^{16} cm^{-3} (6×10^{-5} M) for 10^6 droplets. The densities of $NO_3^-{}_{aq}$ and $H_3O^+{}_{aq}$ showed the opposite trend, with maxima of 2×10^{16} cm^{-3} (3×10^{-5} M) for 10 droplets and 5×10^{15} cm^{-3} (8×10^{-6} M) for 10^6 droplets.

A larger number of smaller droplets resulted in a larger SVR and a shorter diffusion length. These factors both increased the fluence of reactive species that have short gas phase lifetimes that reached the droplets, such as ions, electronically excited states, and O. When striking the water surface, these species were much more likely to dissociate H_2O_{aq}, rather than

react with N_2 or O_2 in the gas phase. For example, the pathway for electronically excited states is

$$M^* + H_2O_{aq} \rightarrow M_{aq} + H_{aq} + OH_{aq}, \quad (5.55)$$

$$OH_{aq} + OH_{aq} \rightarrow H_2O_{2aq}. \quad (4.56)$$

OH that was formed in the gas phase was more likely to solvate when the diffusion length was smaller, rather than reacting with N_xO_y to form HNO_x. As a result, the pulsed periodic equilibrium density of OH_{aq} increases by more than a factor of 4 across the range of droplets investigated. Therefore dividing a liquid volume into many smaller droplets resulted in more H_2O_{2aq} than $NO_3^-{}_{aq}$.

4.4 Concluding Remarks

Activation of droplets by exposure to a low temperature air plasma has been investigated using a 0-dimensional model accompanied by an analytical analysis. The densities of reactive species in the droplet after the plasma treatment depend on the droplet diameter, the droplet density, and the Henry's law constant (h) of the individual RONS. The characteristic timescales of equilibration between the gas and liquid densities varies over many orders of magnitude, with low-h species equilibrating in the interpulse period (~10^{-4} s), and high-h species equilibrating in 10s of seconds.

Though a 0-dimensional model is useful in describing the limits of this system, in which a plasma is uniform, there are significant limitations to this approach. In reality, dielectric barrier discharges would most likely produce streamers, and surface ionization waves which selectively produce reactive species near the droplet. This may produce an increased reactive species concentration at short timescales with each pulse, before diffusion occurs. This approximation becomes more reasonable if any convection occurs in the gas or liquid, which

makes the distributions of RONS more uniform. Additionally the change in size or shape of the droplet due to evaporation and applied electric fields is expected to cause some deviations from these first-order trends.

For high-*h* species, most of the molecules generated are eventually transferred to the liquid. For larger droplets, a similar amount of reactivity is diluted in a larger liquid volume compared to smaller droplets. The density of species such as NO_x^- decreases as the droplet diameter increases. For low-*h* species, the density in the droplet saturates after only a small fraction of the reactivity generated in the gas phase has solvated. As a result the aqueous densities of these species are often independent of the droplet diameter.

The densities of high-*h* species in the liquid were maximized at a droplet density of 7.6×10^3 droplets/cm^3 for 10 μm droplets in this system. Below this density of droplets, the larger spacing between the droplets slows the transfer of the reactive species into the liquid and limits the activation. This analysis provides the opportunity to tailor the ratio of RONS in plasma activated droplets using the operational parameters, and could provide insights into which reactive species are effective in a given application.

4.5 Tables

Table 4.1 Henry's Law Constants (Ref. [21])

Species	h (unitless)	Note
H_2O_2	1.92×10^6	
HO_2	1.32×10^5	
OH, OH($A^2\Sigma$)	620	a
H, H*	6.00×10^3	a
H_2, H_2(r), H_2(v), H_2*	1.9×10^{-2}	a
H_2O(v)	1	b
O, O(^{1}D)	1	a,b
O_2, O_2(r), O_2(v), $O_2(^1\Delta_g)$, $O_2(^1\Sigma_u)$	3.24×10^{-2}	a
O_3, O_3*	0.274	
N_2, N_2(r), N_2(v), N_2*, N_2**, N, N(^{2}D),	1.6×10^{-2}	a
N_2O_3	600	
N_2O_4	37.0	
N_2O_5	48.5	
N_2O, N_2O(v)	0.599	a
HO_2NO_2	9.73×10^4	
NO	4.4×10^{-2}	
NO_2	0.28	
NO_3	41.5	
HNO_2, HNO	1.15×10^3	a
HNO_3, ONOOH	4.80×10^6	
CO, CO(v)	2.42×10^{-2}	a
CO_2, CO_2(v)	0.823	a
NH	1.47×10^3	c

a) Value corresponds to the first species in the list. Other species were assumed to have the same Henry's law constant.

b) Approximated. Species reacts quickly in water and will not reach Henry's law saturation.

c) Approximated by analogy to NH_3.

4.6 Figures

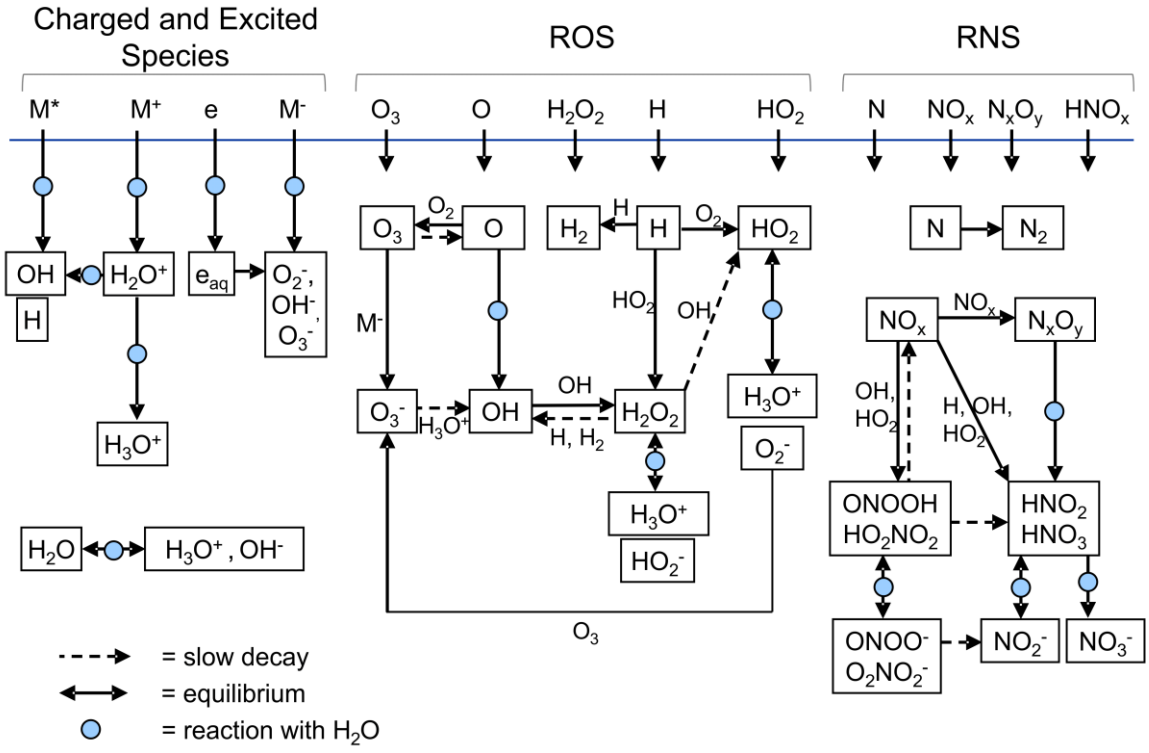

Fig. 4.1 Schematic of the liquid reaction mechanism used in this investigation highlighting the most important reactions.

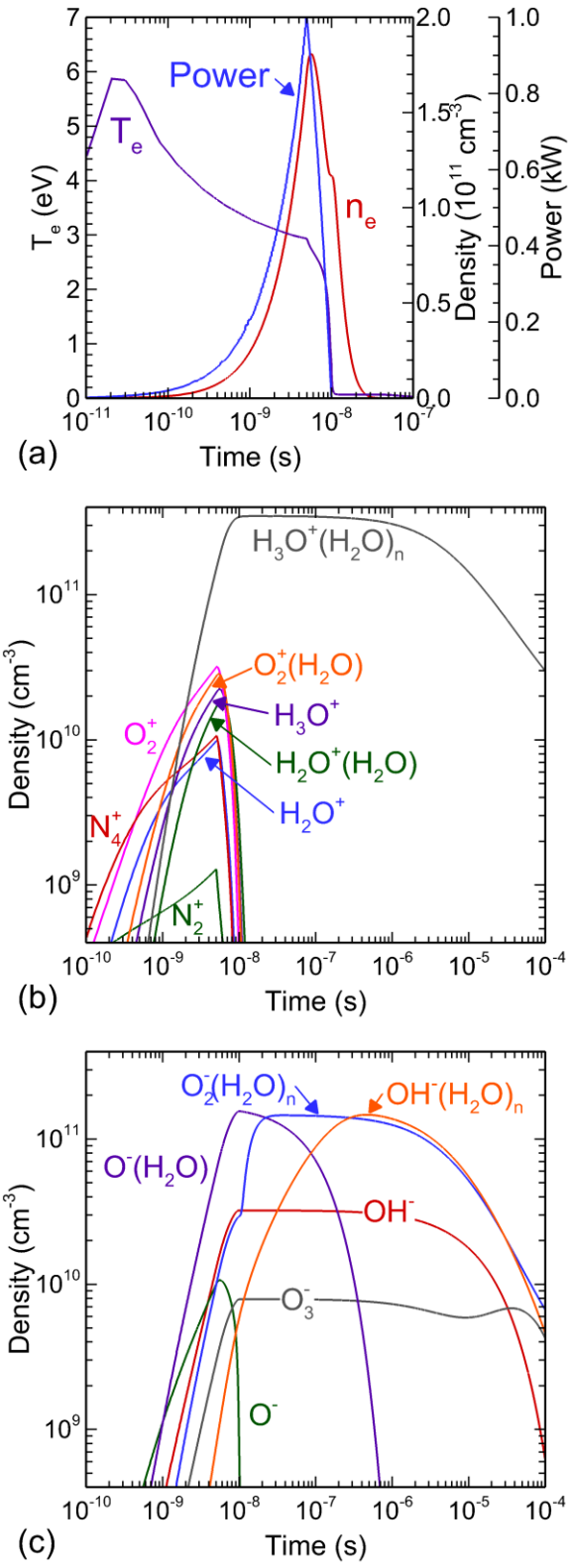

Fig. 4.2 Plasma properties of the first discharge pulse. (a) The applied power deposition at each pulse as a function of time, and the resulting electron temperature (T_e) and electron density (n_e). The power deposition is a triangular pulse with a total duration of 10 ns. (b) Positive and (c) negative ions during the first discharge pulse and afterglow.

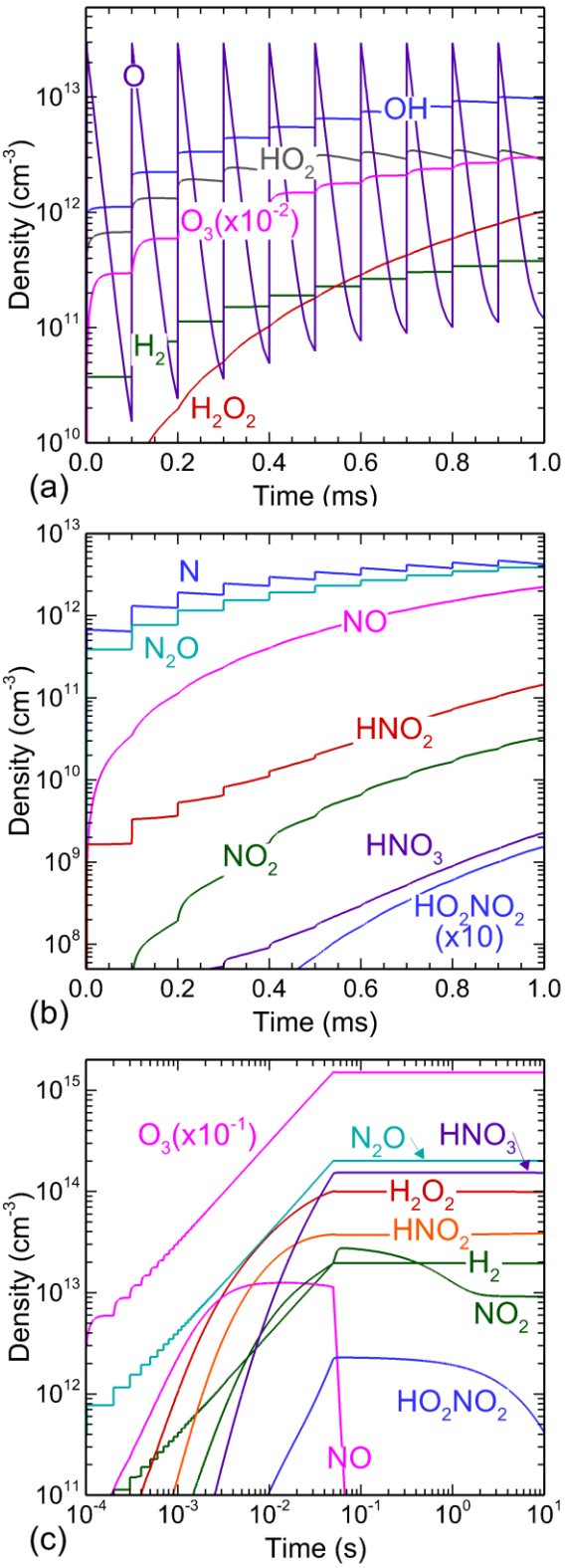

Fig. 4.3 Gas phase reactive neutral species generated in a humid air discharge containing a single 10 µm droplet. (a) Reactive oxygen species (ROS) and (b) reactive nitrogen species (RNS) during the first 10 discharge pulses. (c) Accumulation of selected species during 500 pulses and an afterglow period.

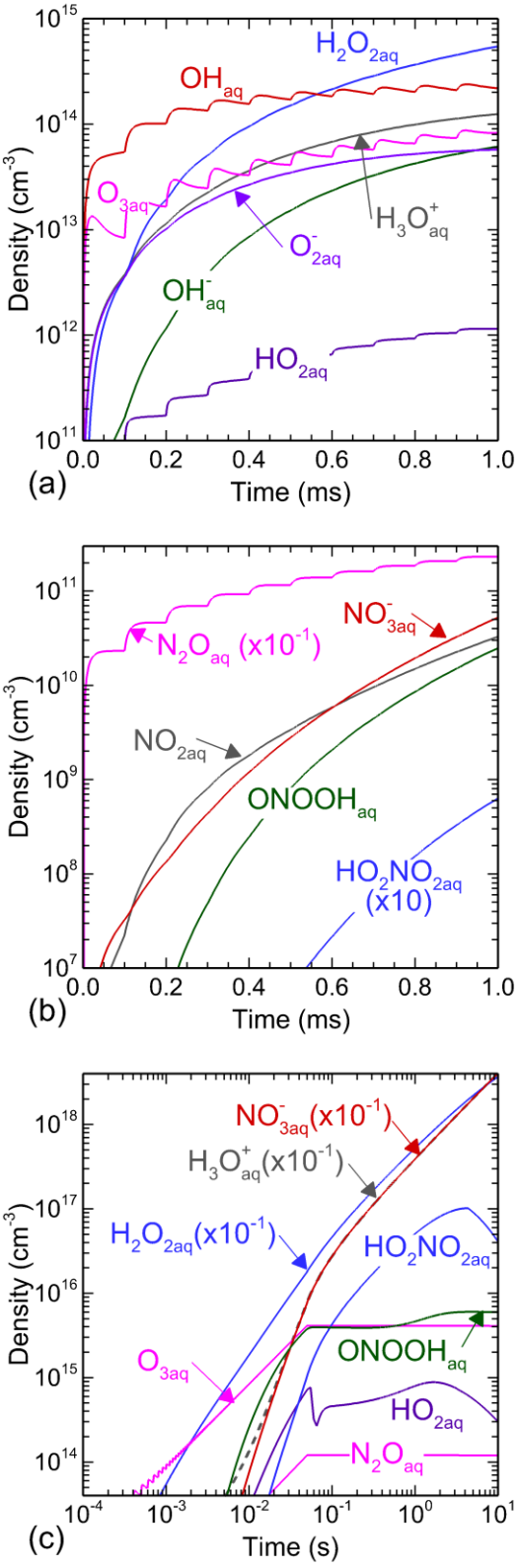

Fig. 4.4 Liquid phase reactive species produced in a single 10 μm droplet in a humid air discharge. (a) ROS and (b) RNS during the first 10 discharge pulses. (c) Accumulation of selected aqueous species during 500 pulses and an afterglow period.

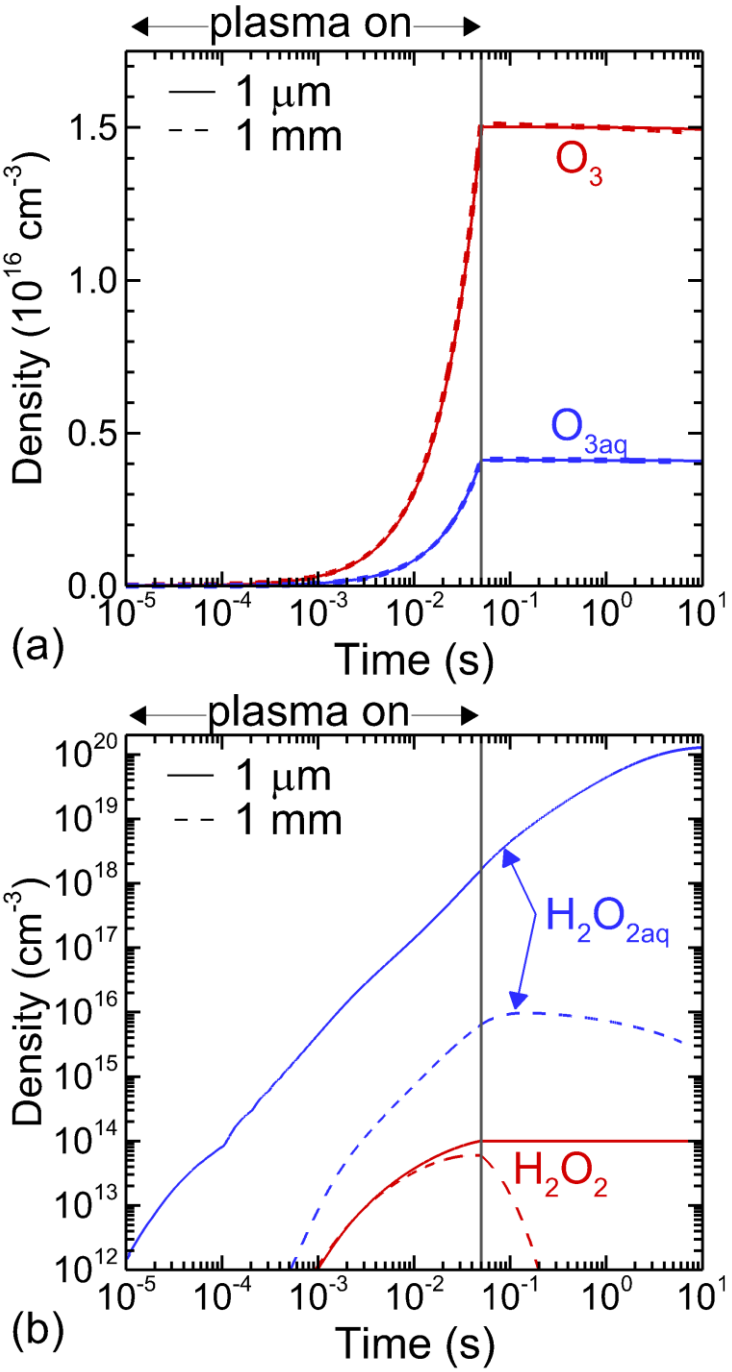

Fig. 4.5 Comparison of densities for species with a low Henry's law constant *h,* O_3 (*h* = 0.274 and high *h*, H_2O_2 (*h* = 1.92×10^6) for single droplets of 1 μm and 1 mm diameter as a function of time. (a) Densities of O_3 and O_{3aq}. Note that densities for both diameters are plotted, but are nearly indistinguishable. (b) Densities of H_2O_2 and H_2O_{2aq}. The liquid density differs significantly based on droplet diameter. The plasma on period, which includes 500 pulses at 10 kHz, is indicated. Note that in (a) the densities are plotted on a linear scale and in (b) the densities are plotted on a log scale.

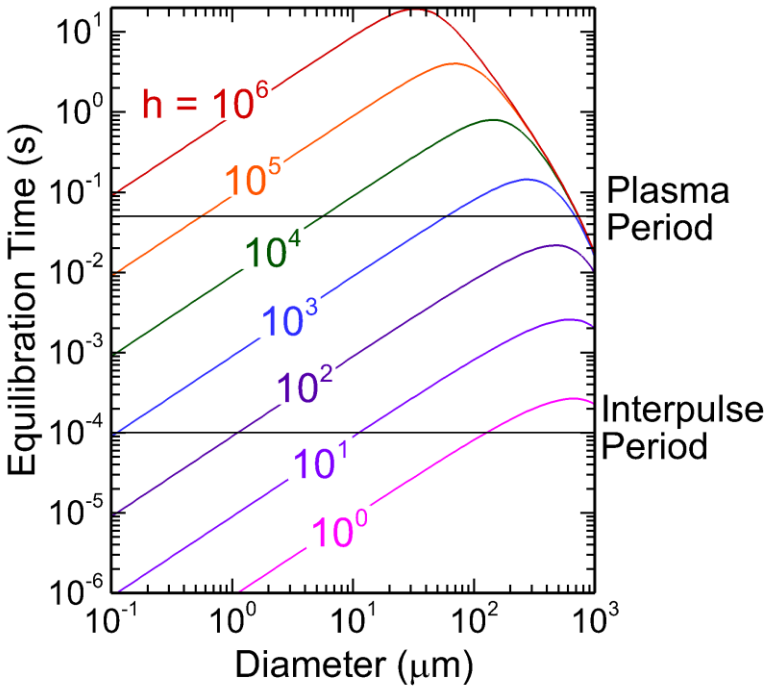

Fig. 4.6 Equilibration time for solvation as a function of droplet diameter and Henry's law constant (Eq. 2.53). The horizontal lines show the inter-pulse period and the duration of the total plasma-on period (500 pulses).

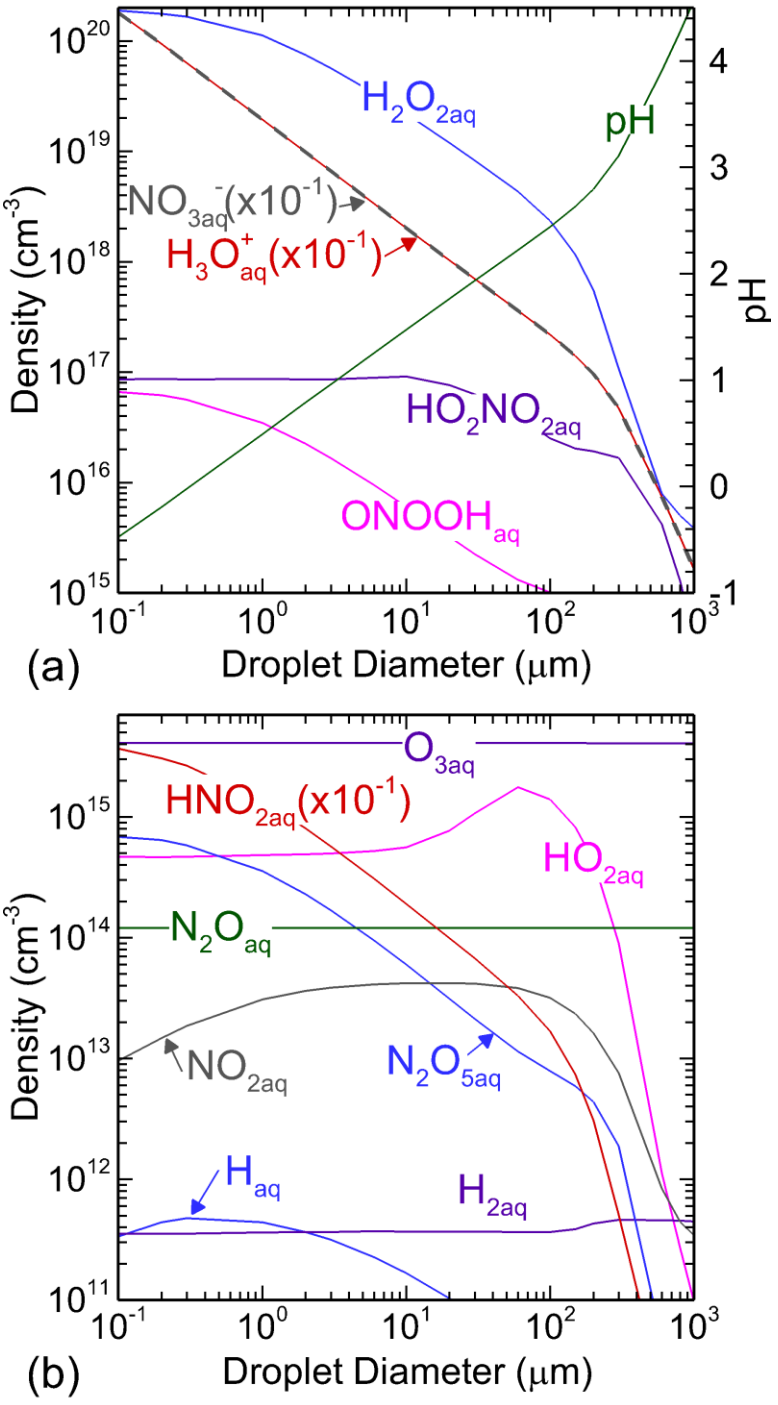

Fig. 4.7 Density of liquid RONS as a function of droplet diameter for species with (a) $h \gtrsim 10^5$ and (b) $h \lesssim 10^5$. The data are compared after 500 pulses and an afterglow period for a total time of 5 s. The simulation was for a single droplet.

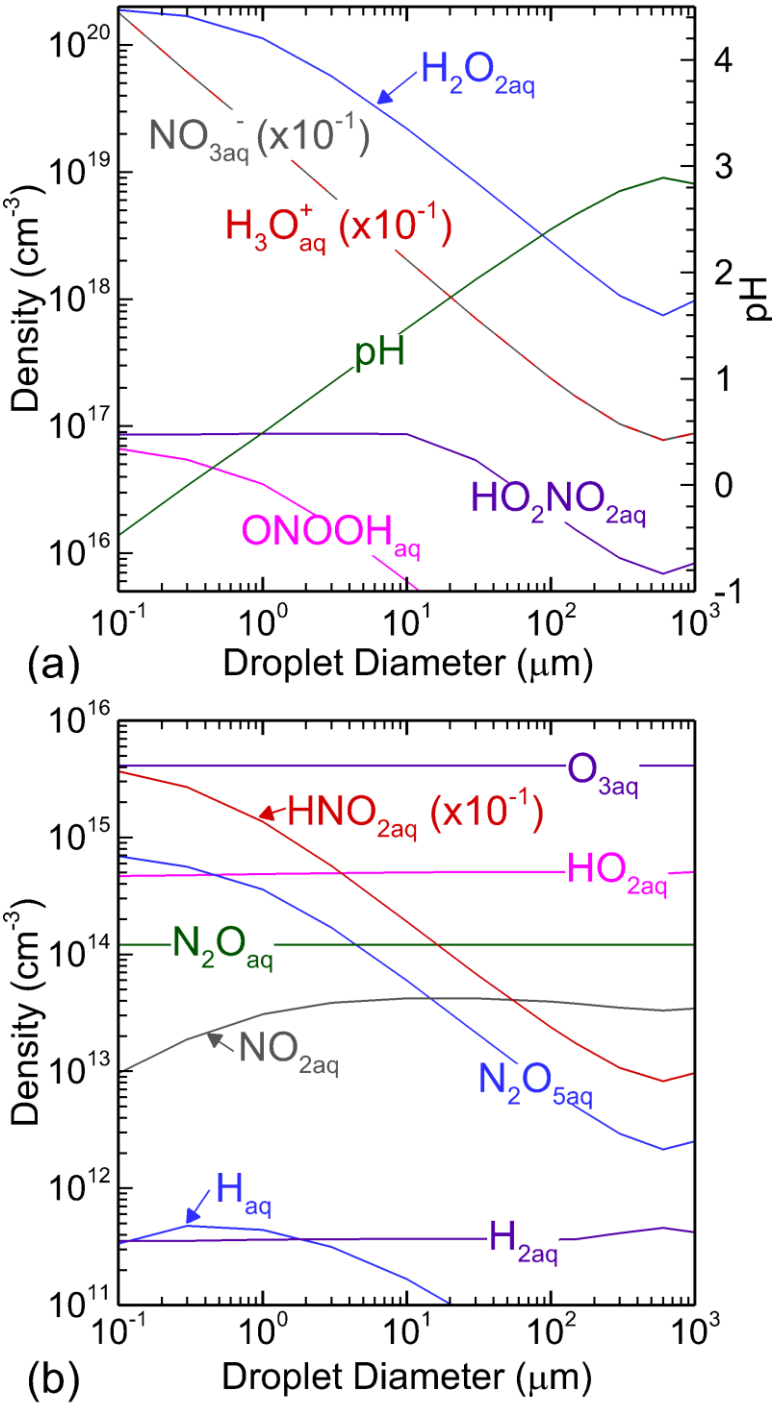

Fig. 4.8 Density of liquid RONS as a function of droplet diameter in an "infinite" gas volume ($V_g = 6.3 \times 10^5$) for species with (a) $h \gtrsim 10^5$ and (b) $h \lesssim 10^5$. The data are compared after 500 pulses and an afterglow period for a total time to 5 s. The large gas volume essentially eliminates the effect of depletion of the gas phase RONS.

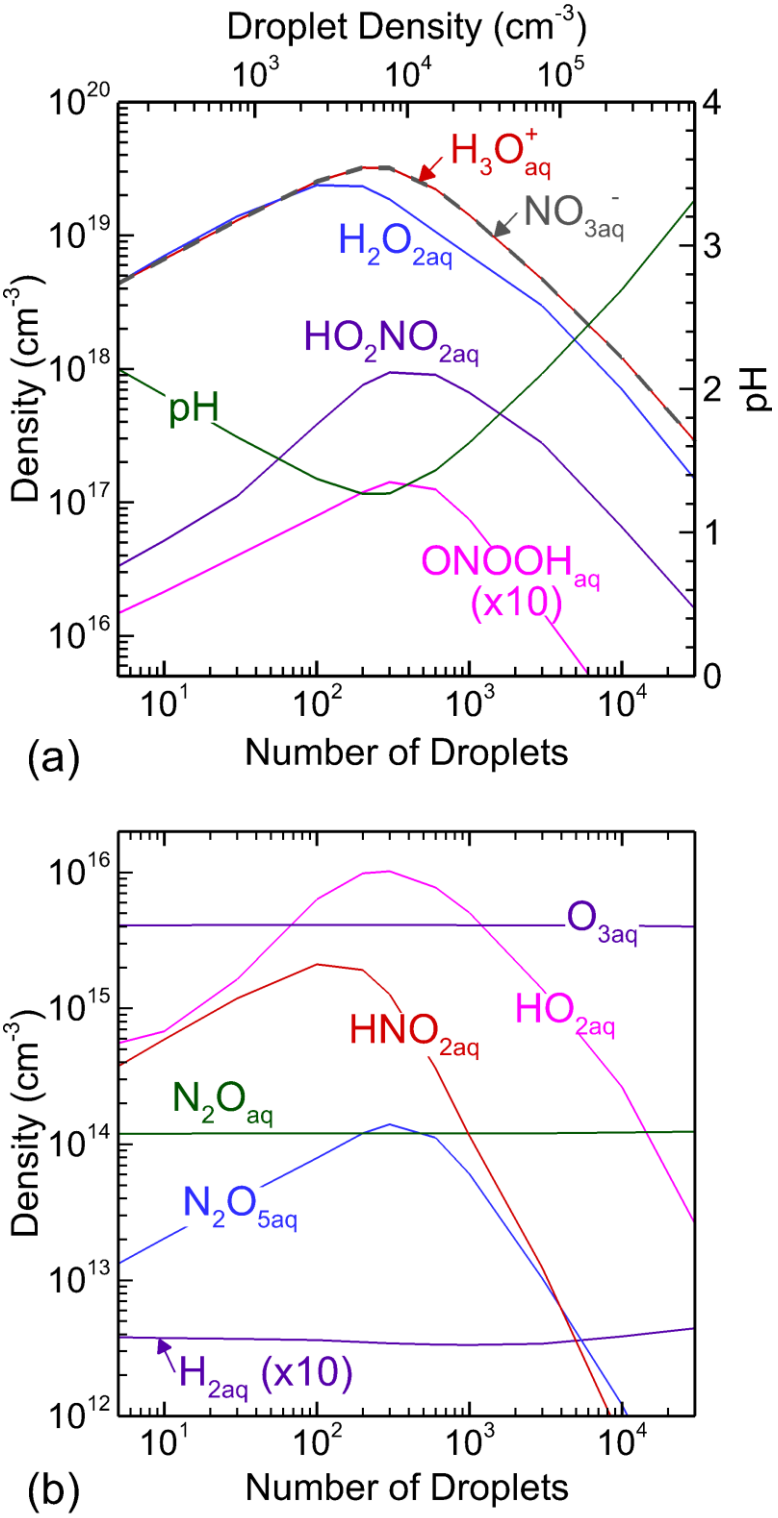

Fig. 4.9 Density of liquid RONS as a function of the number of 10 μm droplets for species with (a) $h \gtrsim 10^5$ and (b) $h \lesssim 10^5$. The densities were compared after 5 s total time.

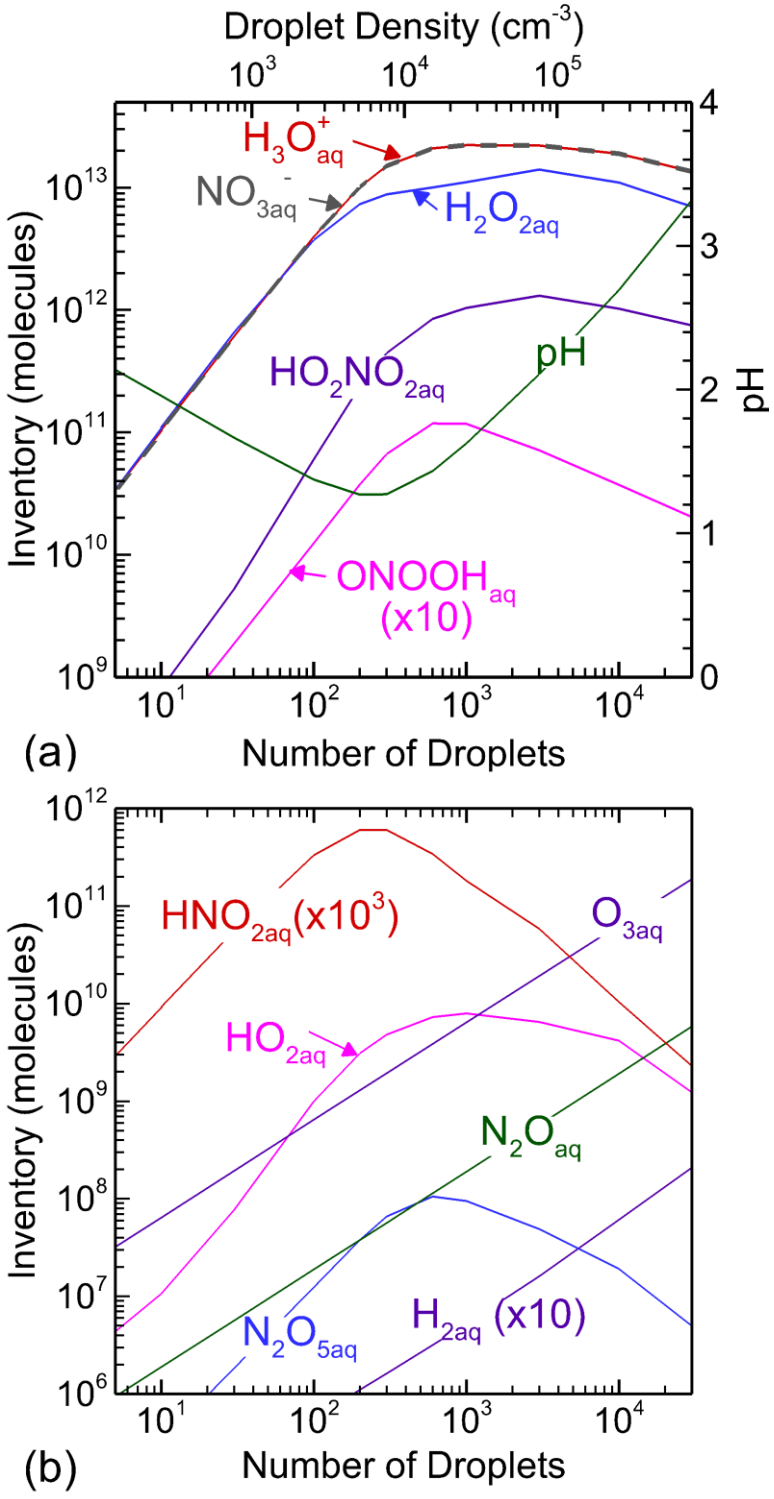

Fig. 4.10 Inventory of liquid RONS with (a) $h \gtrsim 10^5$ and (b) $h \lesssim 10^5$ as a function of the number of droplets having a 10 μm diameter. The inventory is the aqueous number density multiplied by the total liquid volume. The inventories are compared after 5 s total time.

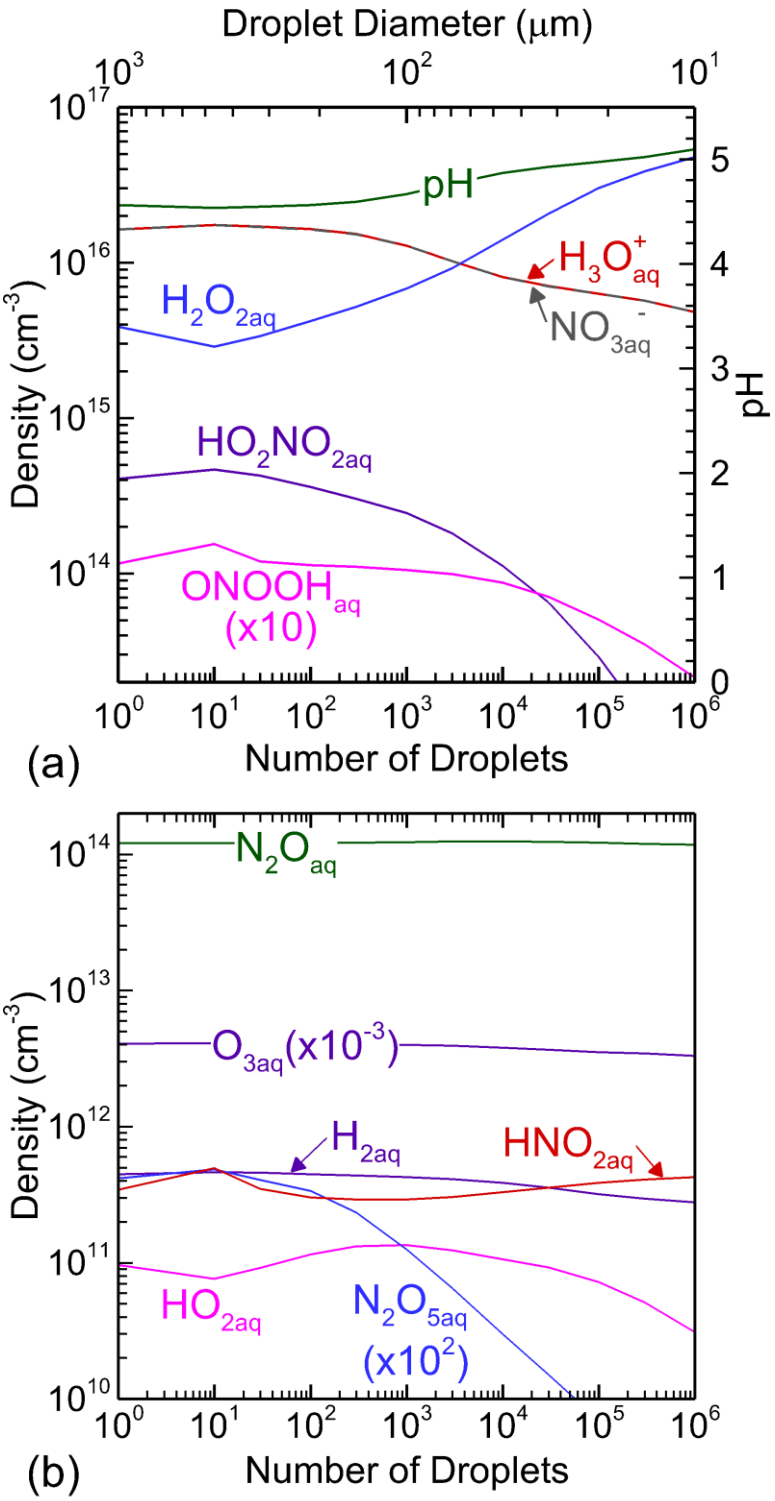

Fig. 4.11 Liquid species densities as a function of the number of droplets. The total liquid volume was held constant and the diameter was decreased as the number of droplets was increased. The densities were compared at 5 s total time for species with (a) $h \gtrsim 10^5$ and (b) $h \lesssim 10^5$.

4.7 References

[1] K. Wende et al., Biointerphases **10,** 029518 (2015).

[2] N. K. Kaushik et al., Biol. Chem. **400,** 39 (2018).

[3] S. Mohades, M. Laroussi, J. Sears, N. Barekzi and H. Razavi, Phys. Plasmas **22,** 12201 (2015).

[4] S. Mohades, N. Barekzi, H. Razavi, V. Maruthamuthu and M. Laroussi, Plasma Process. Polym. **13,** 1206 (2016).

[5] M. J. Traylor, M. J. Pavlovich, S. Karim, P. Hait, Y. Sakiyama, D. S. Clark and D. B. Graves, J. Phys. D: Appl. Phys. **44,** 472001 (2011).

[6] R. Laurita, D. Barbieri, M. Gherardi, V. Colombo and P. Lukes, Clin. Plasma Med. **3,** 53 (2015).

[7] W. Van Boxem, J. Van der Paal, Y. Gorbanev, S. Vanuytsel, E. Smits, S. Dewilde and A. Bogaerts, Sci. Rep. **7,** 16478 (2017).

[8] G. G. Bălan et al., Infect. Drug Resist. **11,** 727 (2018).

[9] J. E. Foster and J. Lai, IEEE Trans. Plasma Sci. **44,** 1127 (2016).

[10] W. Tian and M. J. Kushner, J. Phys. D: Appl. Phys. **48,** 494002 (2015).

[11] G. Fridman et al., IEEE Trans. Plasma Sci. **47,** 395 (2019).

[12] Z. Machala, L. Chládeková and M. Pelach, J. Phys. D: Appl. Phys. **43,** 222001 (2010).

[13] K. Patel, A. Mannsberger, A. Suarez, H. Patel, M. Kovalenko, A. Fridman, V. Miller and G. Fridman, Plasma Med. **6,** 447 (2016).

[14] R. Thirumdas, A. Kothakota, U. Annapure, K. Siliveru, R. Blundell, R. Gatt and V. P. Valdramidis, Trends Food Sci. Technol. **77,** 21 (2018).

[15] B. R. Locke and K. Shih, Plasma Sources Sci. Technol. **20,** 034006 (2011).

[16] R. J. Wandell and B. R. Locke, Ind. Eng. Chem. Res. **53,** 609 (2014).

[17] C. Heinisch, J. B. Wills, J. P. Reid, T. Tschudi and C. Tropea, Phys. Chem. Chem. Phys. **11,** 9720 (2009).

[18] M. M. Iqbal, C. P. Stallard, D. P. Dowling and M. M. Turner, Plasma Process. Polym. **12,** 1256 (2015).

[19] P. Davidovits, C. E. Kolb, L. R. Williams, J. T. Jayne and D. R. Worsnop, Chem. Rev. **106,** 1323 (2006).

[20] R. Sander, Atmos. Chem. Phys. **15,** 4399 (2015).

[21] A. M. Lietz and M. J. Kushner, J. Phys. D: Appl. Phys. **49,** 425204 (2016).

[22] Y. S. Djikaev and A. Tabazadeh, J. Geophys. Res. **108,** 4689 (2003).

[23] R. Vácha, P. Slavíček, M. Mucha, B. J. Finlayson-Pitts and P. Jungwirth, J. Phys. Chem. A **108,** 11573 (2004).

[24] A. H. Markosyan, A. Luque, F. J. Gordillo-Vázquez and U. Ebert, Comput. Phys. Commun. **185,** 2697 (2014).

[25] W. Van Gaens and A. Bogaerts, Plasma Sources Sci. Technol. **23,** 035015 (2014).

[26] A. M. Lietz and M. J. Kushner, J. Appl. Phys. **124,** 153303 (2018).

[27] F. C. Fehsenfeld, M. Mosesman and E. E. Ferguson, J. Chem. Phys. **55,** 2115 (1971).

Chapter 5 Electrode Configurations in Atmospheric Pressure Plasma Jets: Production of Reactive Species[1]

Atmospheric pressure plasma jets (APPJs) are a preferred plasma source for many biomedical applications. These jets typically consist of a rare gas flowing through a dielectric tube, possibly with an O_2 or H_2O admixture, and flowing into the ambient and are powered by pulsed or sinusoidal voltage waveforms. However, in most other aspects APPJ designs differ greatly. In this chapter, APPJ design parameters and their consequences on ionization wave propagation and reactive oxygen and nitrogen species (RONS) production are discussed using results from a 2-dimensional plasma hydrodynamics model. The base case is an APPJ with a single powered ring electrode wrapped around a dielectric tube. This configuration was varied by changing the powered and grounded electrode positions, adding a grounded ring electrode, and moving the powered electrode to the inside of the tube. Placing the powered electrode closer to the outlet of the tube increased the RONS production by increasing the energy deposition outside the tube. Adding a grounded ring increased the ionization wave intensity inside the tube while slightly increasing the power deposition outside of the tube. An inner powered electrode increased the ionization wave intensity and propagation velocity, and the resulting RONS production. Co-axial ground planes within 5 cm of the APPJ significantly affected the ionization wave behavior, increasing its intensity and increasing RONS production. The consequences of

[1] The results discussed and portion of the text in this chapter have been previously published in A. M. Lietz and M. J. Kushner, "Electrode configurations in atmospheric pressure plasma jets: production of reactive species", Plasma Sources Sci. Technol. **27,** 105020 (2018).

voltage rise time and dielectric constant of the tube are also discussed. The systematic trends from this investigation may facilitate more informed APPJ design choices that may be tailored to the goals of a specific application.

5.1 Introduction

The reactive species produced by atmospheric pressure plasmas have been the focus of a recent body of work investigating their use for biomedical applications including wound healing, cancer treatment, and stimulating anti-tumor immune responses.[1–6] The effects of atmospheric pressure plasma jets (APPJs) on biological systems are often attributed to the reactive oxygen and nitrogen species (RONS) generated by the plasma, although electric fields and UV photons may also have significant influences.[7,8] Although the ideal balance of RONS has not yet been determined and likely varies by biological system, there is evidence that OH, H_2O_2, $O_2(^1\Delta_g)$, and ONOOH all have important roles in cancer treatment.[9–11] APPJs have been preferred in many of these studies because their operation with rare gases keeps the gas temperatures low and enables greater control of the species that are generated compared to discharges in ambient air.

There is a large variety of APPJ designs, including electrode configurations that have pin and ring electrodes either inside or outside of the dielectric tube forming the jet, or some combination of electrodes located inside and outside.[12] In each design variation, an ionization wave (IW) propagates through and out of the tube and into the ambient air. A rare gas is usually flowed through the tube, either pure or with a small (< 2%) admixture of a molecular gas such as oxygen or water vapor.[4,13–15] As the ionization wave propagates out of the jet, the IW interacts with the ambient air, producing RONS. The gas flow carries the RONS to the surface or tissue being treated by the plasma. (Note, that even the purest rare gases available from gas

suppliers have sufficient impurities, ~10 ppm, to produce RONS inside the tube before the IW encounters the ambient.)

The large variety of designs and configurations makes optimizing APPJs for a particular application difficult, as is assessing the differences between observed biological effects achieved with different jet designs. Several experimental studies have examined the influence of APPJ design parameters on performance. Time resolved optical emission and electrical properties of APPJs were shown to be sensitive to electrode configuration by Maletic *et al*.[16] Increasing the contact area of ring electrodes around the dielectric tube of an APPJ increases the power coupled into the plasma at a given voltage. Jogi *et al*. investigated the effect of tube diameter on a sub-mm jet with a single ring electrode. Increasing tube diameter did not require as high of a voltage to sustain the discharge, increased the excitation temperature as measured by optical emission, and decreased the electron density.[17] Maletic *et al*. also showed that for an APPJ with two outer ring electrodes, the distance the electrodes were placed from the end of the tube greatly affected the propagation distance of the IW into the ambient.[18] Yue *et al*. have shown through laser induced fluorescence (LIF) measurements of an APPJ sustained in He that adding additional ring electrodes can increase the OH production by as much as a factor of 5, which in turn increases the bactericidal effects of the jet.[19] In two APPJs examined by Xu *et al.*, the electrode configuration had a significant effect on the RONS produced in a liquid downstream of the jet.[13]

Modeling studies of APPJs often focus on operational parameters, rather than design parameters. Norberg, *et al*. studied the effect of pulse repetition frequency, gas flow rate, and gas composition of an APPJ having a fixed geometry.[20] Van Gaens *et al*. examined the consequences of gas flow rate, power, and ambient humidity using a 1-D plug flow model.[21]

Kelly *et al*. investigated the outcome of changing the concentration of the O_2 in a He APPJ and the influence of the distance between the jet and the surface being treated for a fixed geometry of the APPJ.[22]

The focus of this chapter is on the consequences of physical and electrical design parameters, and of electrode configurations in particular, on the behavior of APPJs, including IW propagation and RONS production. Electrical ground surfaces that are integral components of the jet as well as distant (often unintentional) ground planes were investigated. Placing a coaxial ground within 5-6 cm of the jet increases the IW propagation speed and the production of all RONS for a constant voltage. Moving the powered ring electrode closer to the end of the tube also produces more RONS, as most of the RONS are produced outside of the tube. Adding a grounded ring electrode on the tube increases the initial IW speed and intensity, however both are significantly attenuated upon passing the grounded ring. Placing the powered electrode inside of the tube increases the IW speed. Generally, changes in electrode configuration which increase the total energy deposition (such as adding a grounded ring) also decrease the energy efficiency of the RONS production.

The model is described in Sec. 5.2, while the results of our investigation are discussed in Sec. 5.3. The base case is an APPJ with a single powered ring electrode outside of the tube powered by a negative voltage pulse. The other designs are variations of the base case. The discussion includes consequences of the radius of a coaxial ground, the position of the powered electrode along the tube, the addition of a grounded ring electrode (and distance between ring electrodes) and using a powered electrode inside the tube. The discussion concludes with examining the effects of electrical parameters including voltage rise time and the dielectric constant of the tube. Concluding remarks are in Sec. 5.4.

5.2 Description of the Model

The model used in this study, *nonPDPSIM*, is a 2-dimensional plasma hydrodynamics model which is described in detail in Chapter 2. The model uses time slicing algorithms to address the multiple timescales of the discharge and flow dynamics. The model includes a solution of Boltzmann's equation for the electron energy distribution to provide transport coefficients as a function of average electron energy, a solution of the compressible Navier-Stokes equations for fluid flow, and a radiation transport module. Poisson's equation is solved for the electrical potential, including applied voltages, charged species in the gas phase, surface charging, and different electrical solid material properties as expressed through dielectric constant and conductivity. The electron energy transport and conservation equation that provides the average electron energy is also implicitly solved following the update of densities and potential. The neutral flow is allowed to reach a steady state before the plasma calculations begin, which takes 12 ms in these cases.

Boltzmann's equation is solved for the electron energy distribution (EED) to provide electron impact rate and transport coefficients. The computational domain is divided into zones having different gas composition. In this case, one zone has the majority gas being helium, while the second zone has the majority gas being air. Boltzmann's equation for the EED is solved using a two-term spherical harmonic expansion in the electron density weighted gas composition of each zone. The two-term approximation is expected to provide accurate ionization rate coefficients within 10% at the highest E/N for our conditions.[23] Although the gas composition of each zone is nearly constant in time (the dissociation fraction is low), as the ionization wave propagates out of the tube, the electron density weighted composition changes. This evolution necessitates an update to the lookup table, which was recalculated every 0.05 ns

during the plasma calculation. In parametric studies of the required frequency for updating the lookup table, nearly identical results were obtained with 1 ns between updates.

The radiation transport module addresses a maximum range of the photon of 750 μm in order to reduce the computational cost. The photoionization processes included in these simulations are emission from the He excimer (He_2*) ionizing N_2, O_2 and H_2O. The He_2* is a lumped state of several excimers, and the photoionization cross sections for excimer radiation at 18 eV are used for N_2 (2.5×10^{-17} cm^2), O_2 (1.5×10^{-17} cm^2), and H_2O (2.3×10^{-17} cm^2).[24] The integral of the Green's function is calculated once at the beginning of the calculation and not updated to reduce the computational burden. This is a reasonable approximation because the gas flow is stationary on the timescales of the plasma discharge. The photons emitted by excited states of the He monomer are highly trapped at these pressures due to reabsorption by abundant ground state He. The excimer emission does not have a resonant reabsorption, and can therefore produces non-local ionization. The contribution of photoionization of O_2 by emission from N_2**, (the lumped state including $N_2(C^3\Pi_u)$ and $N_2(E^3\Sigma_g^+)$) was included in isolated cases and determined to be inconsequential for the conditions of this study.

5.3 Consequences of APPJ Design Parameters on RONS Production.

5.3.1 Base Case

The base case geometry, shown in Fig. 5.1a, is a quartz tube with an external powered ring electrode wrapped around the exterior 8 mm from the end of the tube and covered by a thin layer of dielectric. The geometry is cylindrically symmetric containing 12,572 nodes with 9,268 nodes in the plasma region. The tube and material covering the electrode have a relative dielectric constant of $\varepsilon_r = 4$ (where dielectric constant $\varepsilon = \varepsilon_r\varepsilon_0$, and ε_0 is the permittivity of free space). The top surface of the computational domain, 1.55 cm from the end of the tube, is

electrically grounded and acts as a pump. This surface should be thought of as a fine metal mesh with spacing not resolved in the model. The radial boundary of the domain is also an electrical ground which is 1.44 cm in radius in the base case, and is referred to as the coaxial ground. In studies discussed below, the diameter of the coaxial ground was varied. In order to minimize the possibility that small changes in the numerical mesh could affect the computed results as the diameter of the coaxial ground was changed, the following procedure used. A numerical mesh was created for the largest diameter of the coaxial ground, as shown in Fig. 5.1b. Annular zones were also defined in the mesh having diameters corresponding to the coaxial grounds to be studied. These zones could be defined as being either metal or dielectric (i.e., air) while not changing the underlying numerical mesh. A second grounded ring electrode was also used in the study, shown in Fig. 5.1b. Its electrical properties were controlled by specifying its material properties to be metal for an active electrode or dielectric with $\varepsilon_r = 1$ without changing the mesh or modifying the gas flow. Several refinement zones were included in the mesh to better resolve the regions where the plasma would be propagating, resulting in a mesh spacing of approximately 50 μm inside the tube, as shown in Fig. 5.1c.

He with impurities of $O_2/H_2O/N_2 = 2.4/2.9/4.7$ ppm was flowed through the tube from an inlet on the bottom boundary of the computational domain. These impurities were chosen based on the specifications provided by a gas supplier for He having 99.999% purity. Humid air with $N_2/O_2/H_2O = 79.5/20/0.5$ (14% relative humidity) flowed from the annular face on the bottom boundary of the computational domain coaxial to the tube. The He flowed at 2 slm and the air at 4 slm. The pressure was maintained at 1 atm at the face of the pump. The steady state gas flow was established by running only the fluid module of the model for 12 ms before pulsing the negative voltage on the powered electrode to initiate the plasma. The He density of this steady

state flow is shown in Fig. 5.2a. The flow velocity on-axis at the end of the tube is 1.1×10^4 cm/s, and the Reynolds number is ≈350, which is well within the laminar flow regime. As the He flows out of the jet, humid air diffuses into the helium plume, also shown in Fig. 5.2a.

The reaction mechanism is documented in Ref. [25], and contains 51 species addressing helium and humid air, and 753 reactions. In the following discussion, N_2* is a lumped state including $N_2(A^3\Sigma)$, $N_2(B^3\Pi)$, $N_2(W^3\Delta)$, $N_2(B^3\Sigma)$, $N_2(A`^1\Sigma)$, $N_2(A`^1\Pi)$, $N_2(w^1\Delta)$. N* represents $N(2^2D)$ and $N(2^2P)$, O_2* represents $O_2(^1\Delta)$ and O_2** represents $O_2(^1\Sigma)$. Excitation into the first 8 vibrational levels is lumped into the state $N_2(v)$.

As shown in global modeling by Schröter, *et al*., surface reaction probabilities are generally not well characterized and can influence the long-term chemistry.[26] In this work, all ions are assumed to recombine at surfaces. Excited states were assumed to be quenched at surfaces with unity probability, except $N_2(v)$, O_2*, and O_2** which have quenching probabilities of 0.5, 10^{-5}, and 0.1. Neutral recombination probabilities on surfaces are assumed to be 0.01 for $N \rightarrow ½N_2$, 0.02 for $O \rightarrow ½O_2$, 0.2 for $H \rightarrow ½H_2$, and 0.2 for $OH \rightarrow ½H_2O_2$. All other ground state neutral species do not undergo surface reactions.

The full plasma dynamics including solution of Poisson's equation were simulated for 200 ns, which includes a negative pulsed voltage applied to the powered electrode and a short afterglow. After this period, the plasma is assumed to be neutral at all spatial points, while continuing to react and recombine. Poisson's equation is then no longer solved and the charged species diffuse with an effective ambipolar diffusion coefficient. During this period, the electron temperature is fixed at 0.025 eV. This procedure significantly decreases the computational expense while allowing the charged species to persist and continue to influence the chemistry. The computation is continued in this mode for 4 ms at which time all reactive species have

flowed out of the computational domain. A single discharge pulse and afterglow was computed. As species pass through the plane of the pump, their fluxes are integrated over the area of the face of the pump and in time. This integration provides a total fluence of reactive species produced by a single discharge pulse that would conceptually be available for treating a surface located at approximately the height of the pump plane.

With the flow rates and residence times investigated in these simulations, the details of the results strictly apply to an APPJ having a pulse repetition frequency (PRF) no higher than 250 Hz. At these PRF, all plasma produced species will have flowed out of the computational domain prior to the next pulse. As discussed by Norberg, *et al*.[20], operating at higher PRFs introduces the possibility that RONS produced during a current discharge pulse react with the species produced during previous pulses that have not yet flowed out of the domain. These conditions favor production of more complex (H)NO_x over simpler species such as NO. At the same time, the properties of the ionization wave that are sensitive to geometry (as discussed here) and material properties are weak functions of PRF. The results of this investigation therefore broadly apply to higher PRF.

The pulsed voltage applied to the powered electrode, shown in Fig. 5.2b, has a total duration of 170 ns and a maximum amplitude of -10 kV. The voltage has a 20 ns rise time, followed by 130 ns at the maximum amplitude and terminates with a 20 ns fall time. The full plasma calculation continues 30 ns after the voltage returns to zero, for a total of 200 ns. At the beginning of the plasma calculation, a small cloud of plasma with a peak electron density of 1×10^{11} cm^{-3} is placed inside the tube near the powered electrode. This initial density of the electron cloud has an exponential spatial distribution with a characteristic length of 100 μm in the radial

direction, and 300 μm in the axial direction. The plasma is neutralized by a density of He^+ and O_2^+ equal to that of the electrons.

The preionization electron density of 10^{11} cm^{-3} applies to only a small region near the powered electrode to initialize the discharge, and contains approximately 10^7 electrons. This number of electrons is large enough to initiate the discharge but small enough that it does not affect the end result. Changing the density for the initial seed did not affect the behavior of the IW or the resulting chemistry. At worst there are minor differences during the first few ns of the discharge, which dissipate once the ionization wave develops. The precise choice of ions to balance the electrons, in this case He^+ and O_2^+, also has no significant impact on the results. After the discharge develops, the positive ion density in the preionization region is as high as 10^{14} cm^{-3}, compared to the 10^{11} cm^{-3} that was used to initiate the discharge.

This study was not intended to replicate the results of any single experiment. Rather the study was intended to systematically investigate the consequences of varying experimentally accessible parameters, such as electrode placement, materials and voltage waveforms, in a manner that has not yet been experimentally performed. As such, data are not available to make side-by-side comparisons to experiments – such studies have not been comprehensively performed using similar enough devices to enable such comparisons. That said, throughout the following discussion, comparisons are made to experimental data for similar devices, acknowledging that in this diversity of data from different devices, geometries and operating conditions, there are no precise replicates to the systematic study performed here.

The plasma is produced by an ionization wave (IW) which propagates through the tube and into the He dominated plume, as discussed in previous studies.[27] The IW is primarily driven by electron impact ionization, and the electron impact source term (S_e) is shown in Fig.

5.3a. During propagation of the IW in the tube, the S_e at the leading edge of the IW has values of 2×10^{19} - 3×10^{20} $cm^{-3}s^{-1}$, sustained by an *E/N* (electric field over neutral number density) of 30 – 50 Td. In the plasma column created by and trailing the IW, $S_e \approx 1 \times 10^{19}$ $cm^{-3}s^{-1}$ and $E/N \approx 20$ Td. The IW propagates inside the tube with an annular shape, and the maximum electron impact ionization occurs near the surface of the dielectric tube. As the IW exits the tube, the maximum S_e follows the interface between the helium and the ambient air, converging on the axis 1.5 mm from the end of the tube. The lower threshold energies for inelastic collisions, including vibrational and electronic excitation of N_2, O_2, and H_2O, cause S_e in the IW front to decrease after exiting the tube. After 150 ns, the voltage begins to fall. This leads to a discharge which neutralizes the charge accumulated on the dielectric tube. At this point, there is a second burst in S_e as high as 9×10^{20} $cm^{-3}s^{-1}$ in the conductive channel formed by the plasma, as current flows in the opposite direction – a restrike.[28]

As shown in Fig. 5.3b, the IW propagates with a steadily decreasing electron temperature (T_e), due to the charging of the dielectric tube at the powered electrode, which shields out some of the applied voltage. This is conceptually the behavior of a dielectric barrier discharge (DBD). T_e decreases more rapidly as the IW contacts the in-diffusing air due to electron energy losses to exciting low threshold energy vibrational and electronic states. There is an elevated T_e inside the tube, where a conductive channel enables current to flow through the plasma to neutralize the charged surface. T_e is substantially higher near the powered electrode (11.1 vs. 5.8 eV) due to a positive ionization wave driven by photoionization in this region. The electron density (n_e) increases during the period of the applied voltage, as well as immediately after the voltage drops when the plasma current is flowing in the opposite direction to neutralize the surface charge (the restrike), as shown in Fig. 5.4a. The electron density continues to increase until 200 ns due to

ionization processes which occur in the afterglow, such as Penning ionization. The electron density decreases by an order of magnitude by 10 μs after the voltage pulse due to both recombination and attachment.

The space charge density, appearing in Fig. 5.4b, shows the initialization of the IW by charge separation. The IW contains a negative space charge due to the negative applied voltage, while positive charge accumulates in the vicinity of and on the surface of the tube at the powered electrode, progressively screening out the applied voltage. In the rest of the tube, the surface charges negatively producing an electropositive plasma, and a sheath containing positive space charge forms in the plasma near the surface. Upon exiting the tube, the positive charge remains in the area of the highest plasma density, while the more mobile electrons diffuse out into the humid air.

As a result of the annular distribution of S_e inside the tube, the peak electron density is also annular, with the exception of the region in the vicinity of the powered electrode. Outside the tube during the voltage pulse, the electron density is more diffuse than the positive ions, a result of their higher temperature and mobility. This produces a net space charge where the electrons diffuse out of the ion containing region, with a charge density up to -2×10^{11} cm^{-3} and an electron density of approximately 3×10^{11} cm^{-3} (label B in Fig. 5.4b). This large space charge can be maintained because of the negative polarity of the applied electric field. When the magnitude of the applied voltage begins to decrease, the electrons in contact with humid air quickly attach to oxygen forming O_2^-, shown by the lack of electrons at label A in Fig. 5.4a. In the regions of higher helium density, the electron density continues to increase even after the voltage is terminated (200 ns).

The structure in the plasma near the powered electrode is partly due to the photoionization model. He_2* is initially produced near the powered electrode, and the resulting VUV radiation propagates isotropically, both upwards towards the end of the tube and downwards towards the gas inlet. Due to the impurities in the helium, photoionization occurs both above and below the powered electrode. This seed ionization then produces a cathode-directed IW, which propagates more slowly (downwards in the figures) than the primary anode directed IW (traveling upwards in the figures). The cathode directed IW occurs with an E/N of approximately 500 Td (5×10^{-15} V/cm^2). The IW begins on axis, where the initial ionization seed was placed, propagates directly toward the powered electrode and upon reaching the surface of the dielectric tube, propagates along the surface as a surface ionization wave (SIW). This sequence generates a cathode-fall like structure at the inner surface of the tube at the powered electrode.

The ions and excited states produced by the plasma are shown in Fig. 5.5. The most abundant positive ions during the voltage pulse are He_2^+ inside the tube, and N_4^+ and O_2^+ outside the tube. He_2^+ is a result of electron impact ionization of He followed by dimerization, $He + He^+ + M \rightarrow He_2^+ + M$, where M refers to a third body which is dominantly He inside the tube. N_4^+ is a result of Penning ionization of N_2 by He*, electron impact ionization, or to a lesser extent charge exchange from He^+ to N_2, followed by dimerization $N_2 + N_2^+ + M \rightarrow N_4^+ + M$. O_2^+ is primarily a result of Penning ionization by electronically excited helium. During the afterglow, the He_2^+ inside the tube charge exchanges to form O_2^+ in approximately 20 μs. After the voltage is turned off, the O_2^+ begins to dominate the N_4^+ outside of the tube and O_2^+ is the dominant positive ion for the remainder of the simulation. Although water cluster ions would be expected to form, they were not included in this reaction mechanism due to the computational cost of

including a large number of ions.[29,30] Given the small amount of water impurity inside the tube, water cluster ions would form in several microseconds, and therefore would not affect the IW or energy deposition dynamics. Outside the tube, where the water concentration is higher, cluster ions could form in tens of ns. The simplified reaction mechanism may lead to an underestimation of the recombination rates, but the neutral RONS produced in electron-ion recombination or ion-ion neutralization are generally independent of the additional water molecules present in higher order clusters.[29]

Outside of the tube, O^- dominates in regions where the mole fraction of helium exceeds 87%, while O_2^- dominates in the regions containing more air. This change in dominant negative ion is due to the lower electron temperature in regions with higher mole fractions of air. Electron attachment forming O_2^- occurs with thermal electrons, while dissociative attachment to form O^- has a threshold energy of 4.3 eV. Within 100 ns of the end of the plasma period, most of the O^- has neutralized with positive ions. Any electron attachment that occurs by the thermal electrons during the afterglow forms O_2^-, which is therefore the dominant negative ion everywhere at this time. The plasma becomes an ion-ion plasma approximately 150 μs after the voltage pulse. The total ion densities are less than 10^8 cm^{-3} as the quasi-neutral cloud of ions exits the computational domain through the pump.

Although the ion-ion plume exiting the computational domain in this model is charge neutral, that assumption requires sufficient charge in the plume to produce the required ambipolar electric fields to maintain the charge neutrality. These ambipolar electric fields are typically associated with electron-ion plasmas and result from the differences in mobilities and temperatures of the negative (electrons) and positive (ions) charge carriers. When the total electron or ion density falls below a critical value, the maximum net charge in the plasma is

insufficient to produce the ambipolar electric fields required to maintain charge neutrality (actually, quasi-neutrality). At that point, diffusion transitions to being free, and charge separation can occur. Ambipolar electric fields will also be produced in an ion-ion plasma if the mobilities or temperatures of the negative and positive ions are different, as will be the case in APPJs. As the total ion density decreases in the plume below the critical value to maintain charge-neutral fluxes, the negative and positive ions will separately freely diffuse. For simplicity, the model enforces charge neutrality in the afterglow, while in reality the dynamics would transition to free diffusion as neutralizing collisions deplete the ion density.

The densities of the more abundant excited states are shown in Fig. 5.5. The He excited states are most populous in areas containing less than 1% humid air. The helium excited states of $He(2^3S)$, $He(2^1S)$, $He(2^3P)$ and $He(2^1P)$ are explicitly in the model, and all states above $He(3^3S)$ and $He(3^3P)$ are lumped into those two states. These states are dominantly formed by electron impact excitation of ground state He. In Fig. 5.5, He* refers to the sum of all of these explicit and lumped states. $He(2^3S)$ is the most abundant of these states both inside and outside of the tube, as it has the lowest energy and does not radiate. Each of the He excited states can combine with ground state He to form a dimer by the reaction $He^* + He + M \rightarrow He_2^* + M$. The state He_2^* is itself a lumped state including several excimers. The photons emitted by He_2^* are the most important with respect to photoionization. These VUV photons are not reabsorbed by ground state He, have a long mean free path and so can produce non-local photoionization. For this reason, radiation transport was included only for the excimer emission. Radiation trapping factors accounted for the emission of resonant radiation. The photoionization source, shown in Fig. 5.5, is defined by the extent of transport of the VUV photons and the influx of humid air that absorbs the radiation. Even at its peak (2×10^{19} $cm^{-3}s^{-1}$), the photoionization source is small

compared to that due to electron impact ionization though photoionization may occur in regions where electron impact ionization is small. The photoionization source in the tube due to ionization of impurities is small in comparison (8×10^{14} $cm^{-3}s^{-1}$).

The densities of key reactive oxygen species (ROS) and reactive nitrogen species (RNS), shown in Fig. 5.6, reach their maxima at different times. The density of O is maximum at 2×10^{13} cm^{-3} at about 61 μs after the beginning of the plasma pulse. Most O is produced at the He/air interface outside the tube. During propagation of the IW, O is formed by electron impact dissociation, and dissociative attachment to O_2. Later in time, when the IW propagates through the He/air interface and produces excited states of nitrogen, $N_2^* + O_2 \rightarrow N_2 + O + O$ produces O, as does the ion-ion neutralization $O_2^- + O_2^+ \rightarrow O_2 + O + O$. O atoms are produced to a lesser extent in the tube by electron impact dissociation of impurity O_2. O_3 production results from three body reactions of O and O_2. There is a longer delay in the formation of O_3 for two reasons. First O_3 formation is a two-step process, and so it simply takes more time to undergo both processes. Second, the process requires some transport of the O atoms to reach large densities of O_2. By 50 μs, the gas that was originally in the middle of the tube has reached the tube exit. At this time, O atoms formed by dissociation of oxygen inside the tube come into contact with the humid air which greatly increases the rate of O_3 formation. Using molecular beam mass spectrometry, van Ham *et al*. reported that O_3 did not have a significant density until 1 cm downstream of the APPJ.[30] The O_3 densities of 3×10^{13} cm^{-3} measured in this experiment are consistent with the densities predicted by the model in spite of the larger energy deposition.

The density of OH peaks at 2×10^{13} cm^{-3} at the interface of the He and the air immediately outside the tube at 21 μs. This localized OH production corresponds to the region of high rates of photoionization. In this region VUV photons ionize N_2, forming N_2^+ which then

charge exchanges with H_2O. OH is then produced by the formation of hydronium, $H_2O^+ + H_2O \rightarrow OH + H_3O^+$. More OH is produced inside the tube than O, due to the H_2O impurities having a higher concentration than O_2 and a larger cross section for electron impact dissociation of H_2O compared to O_2. OH later combines to form H_2O_2 in the gas phase, but the reaction occurs more rapidly on surfaces. Measurements of OH densities 1 mm outside of a radio frequency powered APPJ showed densities of 8×10^{13} cm^{-3}, which is larger than that predicted here (6×10^{12} cm^{-3}) due to a higher average specific energy deposition.[31] Laser induced fluorescence (LIF) measurements of OH densities outside of a pure He 8 kHz pulsed APPJ were approximately 5×10^{13} cm^{-3} for 9 kV at 1 μs after the plasma pulse, which is larger than the value calculated here. The larger densities in the experiment are due to a larger energy deposition outside of the tube that likely occurs with a longer pulse duration as well as some accumulation of OH from one pulse to the next.[19]

HO_2 is generated from H atoms, produced from dissociation of water, reacting with O_2 in the air, reaching a peak density of 2×10^{13} cm^{-3}. After 150 μs, HO_2 densities decrease due to reactions with itself ($HO_2 + HO_2 \rightarrow H_2O_2 + O_2$), and its consumption in forming RNS, primarily by the reactions $HO_2 + NO \rightarrow HNO_3$ and $HO_2 + NO \rightarrow ONOOH$.

The densities of RNS in Fig. 5.6b are shown at the time when their individual densities are maximum. N is initially produced inside the tube by dissociative recombination of electrons and N_2^+, the latter produced by electron impact ionization, charge exchange from He^+, and Penning ionization of the impurity N_2. NO forms outside the tube dominantly by $N^* + O_2 \rightarrow NO + O^*$, reaching a peak density of 5×10^{12} cm^{-3} after 61 μs. When operating at high frequency, RONS can accumulate on a pulse-to-pulse basis. This is demonstrated by the results of molecular beam mass spectrometry measurements of the average NO density for an Ar APPJ

operating at 13.56 MHz which are factor of 20 larger than the single pulse, low frequency density predicted here due to the accumulation from successive pulses that occurs at high frequency.[30] Once NO forms, it can react with ROS (OH, HO_2, O, H) to form more complex NO_x and HNO_x. The more complex RNS tend to form later in time due to the several reaction steps required for their formation. The density of NO_2 peaks at 4×10^{10} cm^{-3} after 180 μs, and it is primarily produced by $NO + HO_2 + M \rightarrow NO_2 + OH$ and $NO + O + M \rightarrow NO_2 + M$. Since NO_2 is produced by reactions between multiple RONS, which are at lower densities, 10^{12} - 10^{13} cm^{-3}, than the background air it is produced later than either N or NO. HNO_x represents the sum of HNO_2, HNO_3, and ONOOH. It is the final state of RNS with the longest lifetime in this mechanism in the absence of organic species with which the species could react. The total density of HNO_x, peaks at 3×10^{11} cm^{-3} at 220 μs. This density is comprised of 5×10^9 cm^{-3} HNO_2, 1×10^{11} cm^{-3} HNO_3, and 2×10^{11} cm^{-3} ONOOH. The total inventory of HNO_x continues to rise until the plume of RONS reaches the pump, however convective and diffusive transport disperses HNO_x, lowering its peak density.

5.3.2 Coaxial Ground

The location of the electrical ground outside the APPJ is important to the production of RONS due to the sensitivity of the IW to electrostatic coupling to ground. Computationally, this occurs through solution of Poisson's equation where the metal ground is a boundary condition having zero potential. From a circuit perspective, a ground plane is the return path for current produced in the plasma. This current is dominantly displacement current for the coaxial ground and may contain conduction current for the ground represented by the pump port. The location of electrical ground is often not mentioned in reports of experimental studies, which may imply that the location of ground is not being controlled. As a result, replicating the experimental

result could be difficult. In this study, the radius of the coaxial ground was varied to examine the sensitivity of the plasma properties and RONS production. The propagation of the IW, shown by the electron density in Fig. 5.7, changes significantly as the radius of the coaxial ground is increased from 0.4 cm to 5.4 cm. With a closer coaxial ground, the radial electric fields at the surface of the electrode are larger and so the IW is more intense (higher S_e). The resulting plasma is also more annular, resulting in larger energy deposition in areas where the He is in direct contact with the air. The total capacitance seen by the plasma, C_{tot} can be approximated by two annular capacitors:

$$\frac{1}{C_{tot}} = \frac{1}{C_t} + \frac{1}{C_a} \tag{5.1}$$

where C_t, the capacitance of the dielectric tube, and C_a, the capacitance of the ambient air in the gap between the tube and the coaxial ground, are added as capacitors in series. In terms of capacitance per unit length:

$$\frac{C_t}{L} = \frac{2\pi\varepsilon_r\varepsilon_0}{\ln\left(\frac{r_o}{r_i}\right)} \tag{5.2}$$

Where r_i and r_o are the inner and outer radii of the dielectric tube, and ε_r is the relative dielectric constant of the tube. The capacitance of the ambient space between the tube and the coaxial ground is similarly

$$\frac{C_a}{L} = \frac{2\pi\varepsilon_0}{\ln\left(\frac{r_g}{r_o}\right)} \tag{5.3}$$

where r_g is the radius of the coaxial ground. As r_g increases, the capacitance decreases. C_{tot}/L is dominated by the smaller capacitance, which under usual circumstances would be C_a.

With this approximation, C_t/L varies from 2.5×10^{-13} to 1.2×10^{-13} F/cm as r_g increases from 0.4 to 5.4 cm. The charging of the inner wall of the tube by the plasma reflects this change in capacitance. The charge density at the surface of the tube at a height of 1 cm at 150 ns decreases in magnitude from -9.4×10^{-7} to -5.6×10^{-7} C-cm^{-3} as r_g increases from 0.4 cm to 5.4 cm. For a given voltage, this capacitance is a measure of the maximum charge transfer by the plasma inside the tube. As a result, the total energy coupled to the plasma decreases from 40 μJ to 6.7 μJ with increasing radius of the coaxial ground for the same voltage pulse. A nearby coaxial ground plane increases the maximum charge transfer as well as the electric field. Therefore the total energy deposition (time integrated $\vec{j} \cdot \vec{E}$) increases by a factor of 6 when the capacitance increases by only a factor of 2.

To compare RONS production for different geometries and conditions, the fluxes of reactive species crossing the face of the pump were time integrated for 4 ms after the voltage pulse to produce a fluence as the gas flows out of the computational domain. This is enough time for all of the plasma produced species to be flushed out of the system for a single discharge pulse. Integrating the fluence over the area of the pump produces the total number of each species exiting the computational domain – or the total fluence of a species. This total fluence is not necessarily the same as the total production of individual RONS as some species are consumed between their site of production and reaching the pump. However, this total fluence is an indication of the reactive species that might, for example, reach a surface being treated.

The resulting total fluences of RONS as a function of radius of the coaxial ground are shown in Fig. 5.8. (Recall that the voltage pulse waveform is constant.) The total fluences of RONS have approximately a dependence of r^{-n} on the radius of the coaxial ground, where n varies from 0.3 to 1.1. This scaling corresponds to decreases in the total fluences by 57%-97%

as the radius of the coaxial ground increases. In the case of O_3, the most abundant ROS, the total fluence from a single pulse decreases from 1.9×10^{11} molecules to 1.3×10^{10} molecules as the radius increases from 0.4 to 5.4 cm. The total fluences of excited states [O_2* O_2**, $N_2(v)$] which are dominantly formed by direct electron impact are the most sensitive to propagation of the IW outside the tube, and therefore the most sensitive to the location of the coaxial ground. The total fluences of these species drop by more than 95% as the radius of the ground increases. The species that are produced from reactions among several RONS are next most sensitive to the radius of the coaxial ground. These species include HNO_2, HNO_3, ONOOH, NO_2, and H_2O_2, whose total fluences decrease by 81-87% as the radius increases.

As the radius of the coaxial ground plane increases with a constant voltage waveform, the energy deposition and the dissociation fraction decrease. This means that after an initial dissociation, with increasing radius a given molecule is more likely to react with background air compared to reacting with other RONS. The species that are formed following an initial dissociation and potentially followed by reaction with the background air are least sensitive to the radius of the ground, and include O_3, O, N, NO, OH, and HO_2. The total fluences for these species decrease by 57-77% as the radius of the coaxial ground increases. These species still decrease with increasing radius of the ground as the energy deposition decreases, however, not as severely as the prior two groups of species. This reduced sensitivity is due to these species not being exclusively produced outside of the tube or being generated by successive reactions among RONS. For example, in the case of a close coaxial ground, the energy deposition is high and an OH radical formed by dissociation of H_2O is likely to react with another OH to form H_2O_2. However, if the ground plane is distant with less energy deposition, the density of OH is lower, and the OH is more likely to reach the pump before reacting with another OH. This results in the

total fluence of H_2O_2 being sensitive to ground plane placement because its formation scales with the square of the OH density.

The exception to this group of less sensitive species is H_2, with a total fluence which decreases by only 70% in spite requiring a reaction between radicals ($H + H + M \rightarrow H_2 + M$). As the coaxial ground plane is moved closer to the tube, there is greater dissociation of molecules in the tube and more interaction between plasma produced species. The reaction $O + H + M \rightarrow OH + M$, depletes the H available for H_2 formation, which occurs approximately a factor of 4 slower. This translates to H_2 formation being less sensitive to the location of the coaxial ground because of the competition for H from other reactions.

APPJs can be operated in a constant voltage (as in the previous examples) or a constant power (or energy/pulse) mode. Since the total energy deposition changes with the radius of the coaxial ground, part of the change in the total fluence of RONS is a consequence of the change in energy deposition and not necessarily due to a change in the structure of the discharge. To minimize variations due to energy deposition, total fluences were normalized by the energy deposition per pulse. The resulting total fluences, expressed as molecules/eV (called the specific total fluence), are shown in Fig. 5.9. The dependence of the specific total fluence on radius of the coaxial ground has less variation than the raw total fluences. The specific total fluences as a function of radius can be parsed into the same groups. The specific total fluences for O_2*, O_2** and $N_2(v)$, decrease monotonically as the ground radius is increased. These species are particularly sensitive to IW propagation outside of the tube. As the radius of the coaxial ground increases, the IW is slower and less energy is deposited outside of the tube. The species that require interaction between multiple RONS generally have specific total fluences that decrease with increasing ground radius. At small radius, there is a higher dissociation fraction, enabling

the RONS to interact with each other to a greater degree. The species which require an initial dissociation or excitation followed by a reaction with the ambient air have specific total fluences which increase with increasing ground radius (or decreasing energy) – meaning more efficient production. Generally, at lower total energy, the production of reactive species is more efficient.

In this study the ground plane is cylindrically symmetric about the jet axis, which would likely not be the case for coincidental grounds in the vicinity of the jet. It is reasonable to expect that these asymmetric grounds could lead to asymmetries in the plasma.

5.3.3 Electrode Position

Even with a well-controlled coaxial ground, the placement of the single powered electrode along the axis of the tube will affect RONS production. To investigate this sensitivity, the powered electrode was moved from 3 mm from the end of the tube to 10 mm, with the coaxial ground fixed at a radius of 1.4 cm. (Again, the voltage waveform is first held constant.) The total fluences of species exiting the computational domain as a function of position of the electrode are shown in Fig. 5.10. Placing the powered electrode further from the end of the tube results in the IW exiting the tube later during the voltage pulse, thereby depositing less energy outside of the tube in the ambient air environment. The end result is decreasing RONS production. The total energy deposition also decreases as the electrode is moved further from the end of the tube. The time for the IW to reach the end of the tube increases from 19 ns to 106 ns as the electrode is moved from 3 to 10 mm from the end of the tube. With this shift in the electrode, the total energy deposition decreases from 28.1 to 13.6 μJ, and the fraction of energy deposited outside the tube decreases from 18.3% to 2.3%. The distance that the IW propagates past the end of the tube decreases as the electrode is moved further from the end of the tube. This trend is consistent with experimental observations by Maletic *et al*., although these studies

were performed in a different electrode configuration with a grounded ring.[18] Recall that a less intense IW also propagates backwards from the ring electrode towards the He nozzle, and this IW also contributes to radical production which is also eventually blown out of the tube.

The species with total fluences that are most sensitive to the electrode placement are O_2*, O_2**, and N_2(v), decreasing by 90-93% as the powered electrode is moved away from the outlet. These species are initially produced by electron impact excitation, and eventually they collisionally de-excite. Their production occurs primarily outside of the tube where the air concentration is highest. Electron impact rate coefficients for production of these species are less sensitive to the decrease in T_e outside the tube (≤ 2 eV), as excitation of these species have relatively low threshold energies (0.3, 1.0, and 1.6 eV for N_2(v), O_2*, and O_2**). As a result, their production is sensitive to the propagation of the IW outside of the tube. When the electrode is further from the end of the tube, the IW does not propagate as far outside of the tube into regions of higher air concentration, and less O_2*, O_2** and N_2(v) are produced, facilitated by energy deposition outside of the tube decreasing from 5.1 to 0.3 μJ.

O_3, O, H_2O_2, NO_2, HNO_2, HNO_3, and ONOOH are moderately sensitive to the position of the electrode, with total fluences that decrease by 30-51% as the electrode is moved from 3 mm to 10 mm from the outlet. O_3 is sensitive because the amount of O generated is nearly a linear function of the total energy deposition in the plasma, which increases as the electrode is moved closer to the outlet. This O is converted to O_3 by reaction with humid air on timescales of ~100 μs. The initial OH production is moderately sensitive to the electrode placement, and the OH is eventually converted to H_2O_2, making the H_2O_2 moderately sensitive. The total fluence of OH itself is less sensitive to electrode placement, because producing more OH increases H_2O_2 production, which depletes the OH total fluence by the time the RONS reach the pump.

NO_2 production is primarily by the reaction of NO with O or HO_2, requiring reactions between multiple plasma produced RONS. Since all RONS decrease as the electrode is moved further from the outlet and NO_2 is at least second order in overall RONS production, the decrease in the total fluence of NO_2 is more sensitive to the electrode moving further from the end of the tube. The more significant decreases in total fluences of HNO_2, HNO_3 and ONOOH as the electrode moves away from the outlet are also due to their requiring reactions between multiple RONS. For example, HNO_3 is primarily produced by $NO + HO_2 \rightarrow HNO_3$, so this is at least second order with respect to RONS production.

NO, OH, N, H_2, and HO_2 are least sensitive to electrode placement, with total fluences decreasing by 18-28% as the electrode is moved from 3 mm to 10 mm from the outlet. The production of N predominantly originates inside the tube near the powered electrode, being produced in the afterglow by dissociative recombination, $e + N_2^+ \rightarrow N + N^*$. Since N is primarily produced inside the tube, its total fluence is not sensitive to propagation of the IW outside of the tube, and therefore not very sensitive to electrode position. The total fluence of N does decrease by 24% with electrode position because the energy deposition inside the tube increases. NO largely originates from the N* produced inside or outside of the tube reacting with O_2. The N* produced in the tube is the more significant source, and as a result the NO only varies by 28% as the electrode is moved from 3 mm to 10 mm from the end of the tube. Initial OH production decreases by 30% as the electrode is moved away from the end of the tube, however, the total OH fluence collected at the pump decreases by only 25%. This decrease in sensitivity is a consequence of larger production of OH being more rapidly converted to H_2O_2. H is primarily produced inside of the tube, and H is consumed in making HO_2, H_2 and OH. The

total fluences of these stable species are least sensitive to the electrode position, varying by only 18% over the electrode positions studied.

The specific total fluences as the distance between the electrode and the end of the tube is increased are shown in Fig. 5.11. The specific total fluences decrease by 81-84% for $N_2(v)$, O_2*, and O_2** as the electrode is moved further from the end of the tube. These species are dominantly produced outside of the tube in regions of high air concentration, and so their densities decrease as the fraction of energy deposited outside of the tube decreases. This occurs when the electrode is moved further from the end of the tube.

All of the other species have specific total fluences that increase as the electrode is moved away from the end of the tube. This trend results in configurations producing higher energy deposition in the plasma (e.g., electrode closer to the end of the tube) being less efficient at producing RONS while the total fluence of RONS is larger. Species that are primarily produced from energy deposition inside the tube, including HO_2, H_2, N, OH and NO, have specific total fluences which increase by 48-69% as the electrode moves further from the end of the tube. Recall that the fraction of energy deposited outside of the tube decreases from 18.3% to 2.3% when moving the electrode further from the end. The energy deposited outside of the tube is significantly less efficient at producing HO_2, H_2, N, OH, and NO. The electron temperature T_e is lower outside of the tube, and with a larger mole fraction of molecular species a larger fraction of the energy deposition occurs by vibrational and rotational excitation which have low threshold energies. These processes primarily result in gas heating and produce little reactive chemistry.

O, H_2O_2, NO_2, and HNO_x have specific total fluences which increase by 15-46% as the electrode is moved away from the end of the tube. H_2O_2, NO_2, and HNO_x require reactions

between multiple RONS, and therefore their production is favored at higher energy deposition (when the electrode is closer to the outlet). Although the efficiency of their production is lower when as the electrode is near the outlet, this effect is mitigated by the increase in rates of reaction among the larger densities of RONS that are produced. The specific total fluence of O_3 is unexpectedly almost independent of electrode placement, varying by only 1.5%. This result suggests that regardless of where the energy is deposited, the efficiency of producing O is nearly the same, and that the lifetime of O is long enough to form O_3 by collisions with O_2 before reacting with other species.

5.3.4 Grounded Ring Electrode

Adding a grounded ring electrode around the tube produces a higher electric field between the powered electrode and the grounded ring. For example, the IW in a jet with a grounded ring separated from the powered electrode by 4 mm is shown in Fig. 5.12a. The IW traveling between the powered and grounded ring has an average speed of 2.7×10^7 cm-s^{-1} which is 43% faster than in the base case. The IW is also volumetric (as opposed to surface-hugging). Upon reaching the grounded ring, the IW slows down to 6.9×10^6 cm-s^{-1}, as the IW charges the higher capacitance at the location of the grounded ring electrode. During this time, the electron density in the volume between the electrodes increases from 2×10^{12} cm^{-3} to 6×10^{12} cm^{-3}. After passing the grounded electrode, the ionization wave becomes more annular, shifting from a volume IW to a SIW. The end result is an increase in energy deposition in the tube by a factor of 9 compared to the base case, and a decrease in energy deposited outside of the tube, which is reflected in the electron density shown in Fig. 5.12a. Experimental observations by Yue *et al*. of a factor of 5 increase in energy deposition with the addition of a grounded ring are consistent with the modeling results.[19] With the grounded ring electrode, the IW in the model reaches

the end of the tube 8 ns earlier than in the base case in spite of E/N and T_e being lower – T_e = 3.6 eV for the base case compared to 3.2 eV with the grounded ring. With the proximity of ground provided by the ring electrode, the capacitance of the tube is larger which results in more charging of the tube. The larger charge shields out the applied voltage resulting in the IW not extending as far into the ambient. With more energy deposition in the tube, the electron density between the electrodes increases from 9×10^{12} cm^{-3} in the base case to 1×10^{14} cm^{-3} with the grounded ring. This increase in electron density inside the tube comes at the cost of a reduction in electron density outside the tube, from 4×10^{12} cm^{-3} for the base case to 2×10^{12} cm^{-3} with the ring electrode.

In the next configuration, shown in Fig. 5.12b, the powered and grounded ring electrodes are switched. Placing the powered electrode closer to the outlet also produces a reverse IW (propagating opposite the direction of He flow) that is more intense than the IW exiting the tube. This configuration also produces an electric field that is larger inside the tube between the electrodes, and weaker in the direction of the tube exit. The two counter-propagating IWs are initially comparable in magnitude of the ionization source S_e and speed. However, as the reverse IW approaches the grounded ring, the peak value of S_e and speed increase. At 18 ns, S_e for the forward IW is 3×10^{20} cm^{-3}s^{-1}, while it is 2×10^{21} cm^{-3}s^{-1} for the reverse IW approaching the grounded electrode. The electron density at the end of the pulse is highest between the electrodes, as shown in Fig. 5.12b, reaching 6×10^{14} cm^{-3}. The IW outside of the tube is more intense compared to having the grounded electrode close to the exit (Fig. 12a), producing an electron density of 4×10^{13} cm^{-3}, a factor of 10 higher than the base case, and a factor of 5 higher than having the grounded ring close to the exit. The effects of these configurations on RONS production are compared to the base case in Part G.

5.3.5 Electrode Gap

In the configuration having a powered ring electrode on the bottom and grounded ring electrode on the top (as in Fig. 5.12a), the position of the powered electrode was varied from 1.5 mm to 6 mm from the ground electrode. The resulting total fluences of plasma produced species are shown in Fig. 5.13. The total fluences of reactive species vary by approximately a factor of 3. The total energy deposition decreased from 144 μJ to 92 μJ as the gap between the electrodes increased. The increasing gap reduced the electric field between the electrodes, resulting in a slower and less intense IW, reducing T_e in the IW from 6.5 eV to 6.1 eV, and delaying the time the IW exits the tube by 64 ns. The later exit is in large part due to the powered electrode moving further from the tube outlet.

With the electrode gap increasing, the energy deposition decreases and the propagation of the IW outside of the tube decreases while the volume of plasma between the electrodes increases. The end result is that the total fluences of electronically and vibrationally excited states disproportionately decrease – lower total energy deposition with a smaller fraction outside the tube, producing a lower n_e outside where the majority of the $N_2(v)$, O_2* and O_2** are produced. Other RONS have total fluences which increase with the gap between the electrodes and are all less sensitive to gap separation. The more complex species, which require reactions between several RONS, are moderately sensitive to gap separation. These species include ONOOH, HNO_3, HNO_2, H_2O_2, NO_2, and H_2. Though the plasma density and energy deposition are lower with a larger gap, the plasma volume is also larger. As a result, the total inventory (volume integrated number density) of electrons and nearly all of the reactive species increase with increasing gap. With the higher power density for the shorter gap, the impurities of N_2, O_2,

and H_2O are depleted by up to 30%, thereby decreasing the production rate of RONS in the region of highest energy deposition.

The specific total fluences are shown in Fig. 5.14 as a function of the gap between the ring electrodes. Smaller gaps produce higher energy deposition and lower production of most species, making these configurations significantly less efficient for generating most species compared to larger gaps. The exceptions to this trend are O_2*, O_2**, and N_2(v), due to their sensitivity to IW propagation into volumes of high air concentration. As the gap is increased, the distance from the powered electrode to the end of the tube increases, and there is less propagation of the IW outside of the tube. Overall, although placing the electrodes further apart decreases the energy coupled to the plasma, for the range of gap investigated RONS production increased.

5.3.6 Powered Electrode Inside the Tube

Placing an annular powered electrode inside the tube eliminates the charging of the inner surface of the tube at the powered electrode – that is, there is no longer a capacitor between the plasma and the high voltage electrode which would both limit current and shield voltage. Two ground ring placements were compared using an internal, powered annular electrode – 8 mm (Fig. 15a), and 3 mm (Fig. 15b) from the powered electrode. Both cases display similar qualitative behavior, however the placement of the grounded electrode affects the timescales of the dynamics. With an 8 mm gap between the electrodes, the IW begins at the powered electrode, and propagates toward the grounded ring with a high speed (1×10^7 cm-s^{-1}), and an intensity on the order of the base case (1×10^{19} cm^{-3}s^{-1}). Upon reaching the grounded electrode, the IW slows to 5×10^6 cm-s^{-1}. After passing the grounded electrode, the IW becomes more annular resembling a SIW, and its speed increases back to 1×10^7 cm-s^{-1}. The energy deposition

is 346 μJ, significantly higher than in other cases previously discussed. This higher energy deposition is enabled by current to the powered electrode not being limited by charging of an intervening dielectric.

With the grounded ring 3 mm from the powered electrode, the IW propagates faster between the electrodes by a factor of 3 (3×10^7 cm-s^{-1}). Upon reaching the grounded electrode, the IW slows to 1×10^7 cm-s^{-1}. After passing the grounded ring the speed returns to 3×10^7 cm-s^{-1}. As a result, the IW reaches the exit of the tube at 54 ns, compared to 102 ns for the more distant ground. The total energy deposition of 405 μJ is also higher. Placing a grounded electrode close to the powered electrode enables more energy to be deposited outside of the tube (9 μJ compared to 5 μJ), though this is not a large fraction of the total energy deposition. Moving the grounded ring further from the powered electrode (and closer to the tube outlet) allows a larger fraction of the energy to be deposited inside of the tube. These trends may be useful for tailoring the reactive species production by controlling the location of energy deposition.

APPJs with similar electrode configurations have been investigated in several experiments. Electron densities and temperatures were measured by Klarenaar, *et al*, in an APPJ having a 5 mm gap between the electrodes.[32] As the ionization wave passed 2 mm from the outlet of the tube, measurements showed T_e = 3 eV and $n_e = 3 \times 10^{12}$ cm^{-3}. In the simulation, as shown in Fig. 5.15a, T_e at this point is marginally higher, 3.5 eV, possibly due to a higher applied voltage, and n_e is in agreement with the experiment. The electric field in this jet was measured to be 5-15 kV/cm, which is commensurate to but lower than the electric field calculated outside the tube in this work (12-17 kV/cm) due the lower applied voltage.[33]

5.3.7 Reactive Species Generation

RONS production with the electrode configurations already discussed are compared with the base case in this section. Changing the electrode configuration can significantly change the energy deposition for a given applied voltage. In a given configuration, increasing the energy deposition usually increases RONS production and so efficiency should also be compared. Energy deposition is the largest for the jets with the powered electrode directly exposed to the plasma, 346 - 405 μJ, as is shown in Fig. 5.16a. This is due to there being no dielectric barrier between the powered electrode and the plasma which can charge, screen out the applied voltage and limit current. The 2-external ring configurations have a moderate energy deposition, about half that of the exposed electrode. The single ring electrode configurations have the lowest energy depositions of 15 - 28 μJ.

The ROS having the largest total fluences are shown in Fig. 5.16b and the RNS in Fig. 5.16c. These total fluences are again the time and area integrated fluxes over the surface of the pump to represent the total number of molecules flowing out of the computational domain. To highlight trends in selectivity, the resulting total fluences for each species were normalized by values for the base case. Generally, the production of RONS tends to increase with the increasing energy deposition, though not linearly in each case. For example, with the center powered electrode, the total fluence of O_3 increases by only a factor of 4.2 from the base case while the energy deposition increases by a factor of 28. Moving the single powered electrode closer to the end of the tube increases all RONS for the reasons discussed in Sec. C.

First the consequences of adding a grounded ring to the base case will be discussed. This change in electrode configuration increases energy deposition but does not equally affect the production of all species. The increase in energy deposition is dominantly inside the tube

between the electrodes (as opposed to outside the tube). The RONS that take one or two steps to form (O_3, HO_2, OH, O, NO, N), are least sensitive to this increase in energy, increasing in total fluence by less than 80% in spite of energy deposition increasing by more than a factor of 4. Production of these species does not require reactions between multiple plasma-produced species or radicals. Each requires an initial dissociation or excitation, possibly followed by a reaction with the background gas. For example,

$$O + O_2 + M \rightarrow O_3 + M, \tag{5.4}$$

$$H + O_2 + M \rightarrow HO_2 + M, \tag{5.5}$$

$$N^* + O_2 \rightarrow NO + O^*. \tag{5.6}$$

Each of these reactions occurs rapidly in volumes having higher air concentration.

The OH total fluence increases by 35% when a grounded ring is added, which is consistent with measurements by Yue, *et al*. which show an 14-80% increase in OH densities when a grounded ring is added.[19] Yonemori and Ono also measured the OH and O densities in a pulsed He APPJ with a powered and grounded ring electrode. [34] The O density measured by TALIF on axis at the outlet is approximately 10^{14} cm^{-3}, which is larger than the maximum density at this position calculated in this work of 2×10^{13} cm^{-3} because the gas residence time is much longer than the interpulse period in the experiment, so there is some accumulation of species. Despite this, the OH density of 6×10^{12} cm^{-3} on axis at the outlet is consistent with the modeling results of the maximum OH density of 8×10^{12} cm^{-3} at this position. The better agreement with experiment for OH is due to its shorter lifetime which is less sensitive to pulse-to-pulse accumulation. The spatial distributions observed in the experiment – with the maximum OH density on axis and the maximum O density in the mixing zone of the He with the surrounding air – are also consistent with the model.

Species that require reactions among plasma produced species, such as H_2, H_2O_2, HNO_3, ONOOH, NO_2, and HNO_2 are more sensitive to the addition of the grounded ring which produces most of the RONS between the electrodes inside the tube. The result is the RONS tend to more rapidly react with each other to produce higher order species.

A few species are overly sensitive to energy deposition outside of the tube, including O_2*, O_2**, and N_2(v). Adding a grounded ring increases the total energy deposition, but the energy deposition outside of the tube decreases, resulting in a 3-44% decrease in the production of these species. As a result, the total fluences of these species are significantly higher when the powered electrode is close to the outlet and there is no grounded ring.

When adding a grounded ring electrode to configurations with a powered ring electrode, most of the resulting trends are generally independent of the location of the powered electrode. Generally, the inventories of species that take only one or two steps to form increase slightly with the addition of a grounded ring, and the inventories of the more complex RONS have a more significant increase, and the inventories of excited states decrease. The inventories of the excited states are larger when the powered ring is closer to the exit than in the base case, and are more sensitive to the addition of grounded electrode, decreasing by as much as 77%. The inventory of O_3 also decreases with the addition of a grounded electrode. The production of O_3 requires a significant background density of O_2. With the upper powered electrode, most of the O atoms are produced at the interface between the He and the humid air, and so are rapidly converted to O_3. When a grounded ring is added, a significant amount of O is produced between the rings, which results in a long flow time to reach the ambient O_2, enabling O to recombine or react with other RONS (e.g., NO or H) that are generated by the He impurities inside the tube.

Moving the powered electrode inside the tube increases the energy deposition and the production of all RONS compared to both the single and two ring configurations. Again, some species increase more than others. The species most sensitive to moving the powered electrode inside the tube are O_2*, O_2**, and N_2(v). In spite of the fraction of energy deposited outside the tube decreasing, the total amount of energy deposited outside the tube increases, which enables production of these species from interaction with humid air. Species which are more sensitive to moving the electrode inside include H_2O_2, HNO_3, ONOOH, NO_2, and HNO_2, which require reaction between multiple RONS. H_2 is less sensitive, which is inconsistent with the previous discussion as it should require reactions among plasma generated species to form. This counter-intuitive trend occurs because inside the tube other reactions which consume H also increase, including $O + H + M \rightarrow OH + M$.

Moving the grounded ring closer to the powered electrode inside the tube increases energy deposition by 17%, but actually decreases the production of most species. The exceptions to this trend are O_2*, O_2**, N_2(v), and O_3 (to a lesser extent) as these species are more exclusively produced outside of the tube at the He/air interface. With the ground electrode closer to the powered electrode, the IW is a factor of 3 faster and the energy deposited outside of the tube nearly doubles. The plasma density is the highest between the electrodes, and much of the increase in RONS production is a result of dissociation of the impurities in this region. Moving the grounded electrode closer to the powered electrode decreases the volume of this region, and the production of complex RONS becomes limited by depletion of the impurities. In the region of high plasma density between the electrodes, more than half of the impurities of H_2O, N_2, and O_2 are consumed by dissociation, meaning the production of RONS is beginning to be limited by depletion.

The specific total fluences (molecules/eV) are shown in Fig. 5.17 for the various electrode configurations. The most energy efficient RONS production occurs in jets with the lowest energy deposition, a single ring electrode, with the least energy efficient being the center powered electrode having the largest energy deposition. When a grounded ring is added to either the base or upper powered ring configurations, the specific total fluence of all RONS decreases. O_2*, O_2**, and N_2(v) have specific total fluences which decrease the most (more than 89%). The species which take one or two steps to form decrease by 65-85% when a grounded ring is added. The more complex species, H_2, H_2O_2, HNO_3, ONOOH, NO_2, and HNO_2 have specific total fluences which only decrease by 54-78%. When adding the grounded ring electrode, the additional energy deposition increases the dissociation fraction, and results in the RONS being more likely to react with each other.

5.3.8 Voltage Rise Time

The consequences of voltage rise time on total fluences of RONS for the single ring electrode (base case) geometry are shown in Fig. 5.18. Most of the total fluences scale similarly with voltage rise time – increasing the rise time from 1 ns to 50 ns generally produced about an order of magnitude reduction in total fluence. This effect is magnified by the relatively short duration of the voltage pulse, 170 ns. A longer rise time means that the applied voltage is at its maximum value for a smaller fraction of the pulse. As a result, increasing the voltage rise time from 1 ns to 50 ns decreases the total energy deposition from 22.0 to 2.0 μJ. In the case of a 1 ns rise time, the IW exits the tube at 34 ns, while for a 50 ns rise time the IW exits at 124 ns. Increasing the voltage rise time also produces a less intense ionization wave. These two affects work together to reduce RONS production as the rise time increases.

The decrease in energy deposition with increasing voltage rise time significantly decreases energy deposition outside the tube, which affects production of excited states [O_2*, O_2**, and N_2(v)] to the greatest degree. Species which require reactions between multiple RONS are slightly more sensitive to voltage rise time than the average, with total fluences that decrease by 94-97% as the rise time increases from 1 ns to 50 ns. The total fluences of the species that are least sensitive to rise time (O_3, O, N, H_2, NO, OH, and HO_2) still decrease by 80-90% as the rise time increases. H_2 is the exception, as its production requires reaction between two H atoms, but it is one of the least sensitive species. As the energy deposition decreases, there is less O produced inside the tube, and less H is depleted in OH formation. This reduced competition for H at low energy deposition makes H_2 less sensitive to the rise time than the other species which require reactions among RONS.

The specific total fluences for RONS are shown in Fig. 5.19 as function of voltage rise time. As the rise time increases and energy deposition decreases, the energy efficiency for species which require reactions among RONS (ONOOH, HNO_3, HNO_2, H_2O_2, and NO_2) generally decreases. At lower energy deposition (longer rise time), the dissociation fractions of impurities inside the tube are lower, and the RONS are less likely to interact with one another to form higher order species such as HNO_x, and instead survive until they reach the humid air and produce O_3 and HO_2. The specific total fluence of O_2*, O_2**, and N_2(v) decrease most significantly with increasing rise time because these species are most sensitive to IW propagation outside of the tube.

5.3.9 Dielectric constant

The dielectric constant of the tube determines the local capacitance/unit-area (F/cm^2) which bounds the maximum surface charge on the inside of the tube for a given voltage. (The

conductivity of the tube is negligible and so there no charge migration through the tube.) With a larger capacitance, a larger charge density is required to shield out the same applied voltage. The dielectric constant also affects the initial electric field profile. Higher dielectric constant materials expel the electric field in both the radial and axial directions. For the base case, increasing the dielectric constant reduces the electric field in the tube while increasing the electric field at the end of the tube. For example, for $\varepsilon_r = 20$, the IW is significantly weaker in the tube.

In the base case, $\varepsilon_r = 4$ and the energy deposition is 14.7 μJ. Above $\varepsilon_r = 4$, the energy deposition decreases with increasing ε_r (1.7 μJ for $\varepsilon_r = 20$) because the electric field inside the tube is weaker, and as a result the IW is less intense. This systematic reduction in energy deposition reduces the total fluence of all RONS exiting the computational domain with increasing ε_r, as shown in Fig. 5.20. For this electrode configuration energy deposition is maximum for $\varepsilon_r \approx 4$. At smaller ε_r, energy deposition is limited by the small capacitance of the tube at the powered electrode. For example, for $\varepsilon_r = 2$, energy deposition decreases to 12.1 μJ.

The specific total fluences as a function of ε_r are shown in Fig. 5.21. The energy efficiency of the production of species which do not require interaction among RONS, including O_3, O, N, NO, OH, and HO_2, generally increase with lower energy deposition and larger ε_r. H_2 also follows this trend because at higher energy deposition, H is more likely to react with O. The more complex RONS which require reaction among multiple RONS tend to have efficiencies that peak at higher energy deposition and lower ε_r. The excited states are produced preferentially in the cases of higher energy deposition (peaking at $\varepsilon_r = 4$) because these are also the conditions where the IW exits the tube the earliest. Again, higher energy deposition (ε_r closer to 4) favors the production of more complex RONS which requires reaction between several RONS. The

excited states are also produced most efficiently near $\varepsilon_r \approx 4$, conditions for which the IW propagates the furthest outside of the tube.

The dielectric constant of the tube has a completely different effect on RONS production if the powered electrode is inside the tube, as shown by total fluences and specific total fluences in Figs. 5.22 and 5.23. For these results, the powered electrode inside the tube is separated from a ground ring electrode by 8 mm. As the dielectric constant increases, the IW propagates more slowly, because the capacitance of the tube is higher, and it takes more time to fully charge this capacitance. The IW exits the tube after 90 ns for $\varepsilon_r = 2$ compared to 170 ns for $\varepsilon_r = 12$. The total energy deposition increases from 185 μJ at $\varepsilon_r = 2$ to 493 μJ at $\varepsilon_r = 8$, and then decreases to 436 μJ at $\varepsilon_r = 12$. The energy deposited outside of the tube decreases from 6.0 μJ to 3 nJ as ε_r increases from 2 to 12, and n_e between the electrodes increases from 1×10^{14} to 7×10^{14} cm^{-3}.

Compared to the other parameters, the total fluences are relatively insensitive to the dielectric constant when the powered electrode is inside the tube, in spite of the energy deposition changing by nearly a factor of 3. Although energy deposition is highest at $\varepsilon_r = 8$, the production of most species is largest at $\varepsilon_r = 4$ or $\varepsilon_r = 6$. These configurations have a larger energy deposition than $\varepsilon_r = 2$ with an IW that propagates further outside of the tube than $\varepsilon_r = 8$. The total fluences of excited states [$N_2(v)$, O_2*, and O_2**] are greatest at $\varepsilon_r = 3$ because they are more sensitive to propagation outside of the tube (which occurs at low ε_r) than the other species.

The specific total fluences of all species decrease as ε_r increases, with $N_2(v)$, O_2*, and O_2** decreasing the most, by more than 97%. The specific total fluences of most other species decrease by 60-75% as the dielectric constant increases. The specific total fluences which are the least sensitive to ε_r are those for HO_2, H_2, and H_2O_2, which decrease by 55-60%. Species which are formed by dissociation of H_2O are less sensitive to propagation of the IW outside of

the tube. These species are more likely to be produced inside the tube, where they represent a larger fraction of the impurities.

5.4 Concluding Remarks

Results from a computational investigation of helium atmospheric pressure plasma jets flowing into humid air have demonstrated the importance of electrode configurations in the production of reactive oxygen and nitrogen species. For an APPJ with a single powered ring electrode (and external electrical ground) the IW begins at the powered electrode, and upon exiting the tube follows the interface between the He and the surrounding humid air. Much of the RONS are produced at the interface between the He and humid air, but non-negligible RONS are also produced in the tube due to impurities in the He flow. The ground planes in the vicinity of the plasma jet can increase the total energy deposition in the plasma for a constant voltage, substantially influencing which RONS are produced and flow to surfaces, here referred as the total fluence. Total fluences of electronically excited states such as O_2* are the most sensitive to these nearby ground planes, followed by species which require reactions among several RONS (e.g. HNO_2, HNO_3). Though the production of most RONS decrease as the ground plane is moved further from the jet, the specific total fluence (i.e., energy efficiency of production) of most species increases.

For configurations with a single powered ring electrode, moving the electrode closer to the outlet of the tube produces larger total fluences of all RONS as the total energy deposition increases. Depending on their origin, there is some selectivity of the total fluences of reactive species based on the placement of the ring electrode. For most species, the specific total fluence decreases as the electrode moves closer to the outlet.

Adding a grounded ring electrode to the APPJ results in more overall energy deposition for a constant voltage, most of which is deposited inside the tube between the electrodes. The IW propagates faster due to the higher electric field, but significantly slows when passing the grounded ring to charge the large capacitance of the dielectric tube at the ground electrode. Total fluences of species that require reactions among RONS, such as H_2, H_2O_2, HNO_3, ONOOH, NO_2, and HNO_2 are more sensitive to the addition of the grounded ring, and the total fluences of excited states such as O_2* are most sensitive.

Moving the powered electrode inside the dielectric tube results in more rapid IW propagation, as the applied voltage is no longer shielded by the charging of the dielectric tube. The speed of the IW in this configuration is sensitive to the placement of the ground electrode, as are the total fluences of species that require reactions among several RONS. Changing the position of the grounded electrode can significantly increase the energy deposition but decrease the total fluences of RONS as the volume of plasma between the electrodes is smaller. The RONS production then becomes limited by depletion of the molecular impurities in the He inside the tube. The energy efficiency of production of all RONS, with the exception of excited states such as O_2*, decreases as energy deposition increases with the addition of a grounded ring.

For the two ring configuration (powered and grounded), increasing the gap between the electrodes tends to increase the total fluence of RONS. Though the electric fields are lower and the IW is less intense, the increased volume of the higher density plasma that forms between the electrodes increases the total fluences of RONS produced by the jet.

A shorter voltage rise time can significantly increase the total energy deposition in the plasma by producing a more intense IW. As a result, the total fluences of most species increase by about a factor of 10 as the rise time decreases from 50 ns to 1 ns. Short rise times increase the

specific total fluences (energy efficiency) of RONS that require interaction between multiple plasma produced species, such as HNO_x. Longer rise times increase the specific total fluence of species that do not require reaction between RONS, such as NO and OH.

A dielectric constant of the tube material of $\varepsilon_r \approx 4$ produces maximum energy deposition into the plasma when the powered electrode is outside of the tube. Energy deposition for dielectric constants below this value is limited by the charging of the tube at the powered electrode. Dielectric constants in excess of $\varepsilon_r \approx 4$ expel the electric field from the tube, producing electric field enhancement only at the end of the tube, which produces a less intense IW in the tube. The efficiency of production of complex RONS is at a maximum when $\varepsilon_r \approx 4$ (higher energy deposition), while the efficiency is minimized for other RONS. If the electrode is inside the tube, increasing the dielectric constant results in slower ionization wave propagation, and therefore an increase in energy deposition inside the tube, and a decrease in energy deposition outside of the tube.

Overall, the details of the configuration of the electrodes are important to both IW propagation dynamics and total fluences of RONS in He APPJs. Generally configurations which increase the energy deposited in the plasma increase the RONS production, but the efficiency of this production decreases. Small differences in design parameters between APPJs may produce significant disparities in RONS production. For example, it is important for the electrical grounds in the vicinity of APPJs to be controlled (and reported), as the proximity of these ground planes can have a substantial impact on IW propagation and the total fluences of RONS of a given APPJ. When comparing electrode configurations and reactive species production, it is important to consider not only the amount of energy coupled into the plasma, but also the location and volume over which this energy deposition occurs.

5.5 Figures

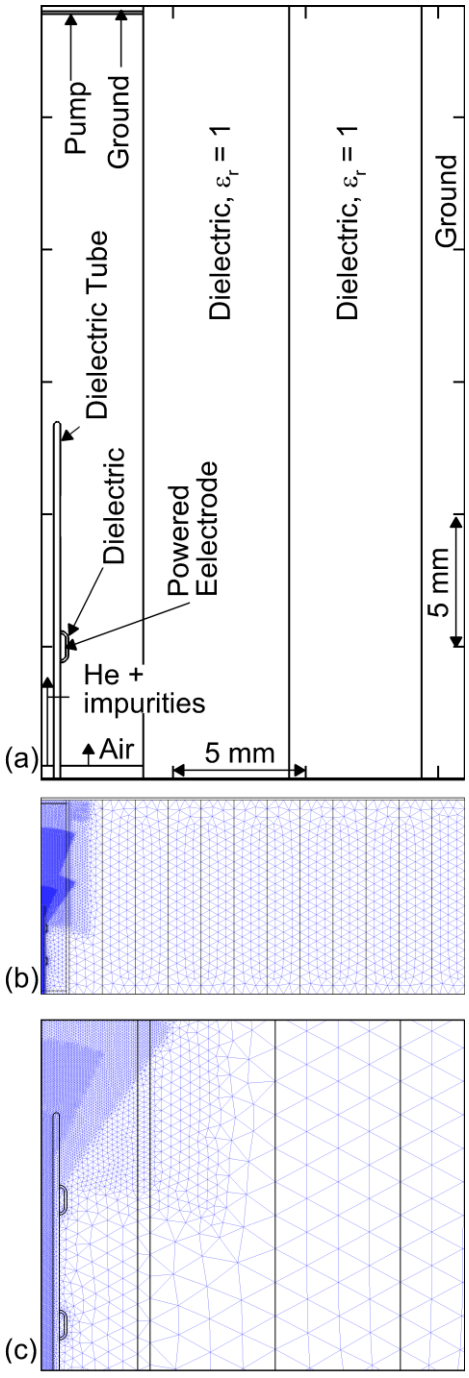

Fig. 5.1 Schematic of the setup for the base case. (a) The geometry, with a dielectric tube inner diameter of 1 mm. The powered electrode is an external ring. (b) The geometry extends beyond the figure in the radial direction, and the thickness of the radial dielectric can be varied so that the distance to the radial ground plane is also varied. The powered electrode is covered with a thin dielectric with $\varepsilon_r = 4$. (c) The computational mesh with refinement zones inside the tube and in regions of higher helium concentration.

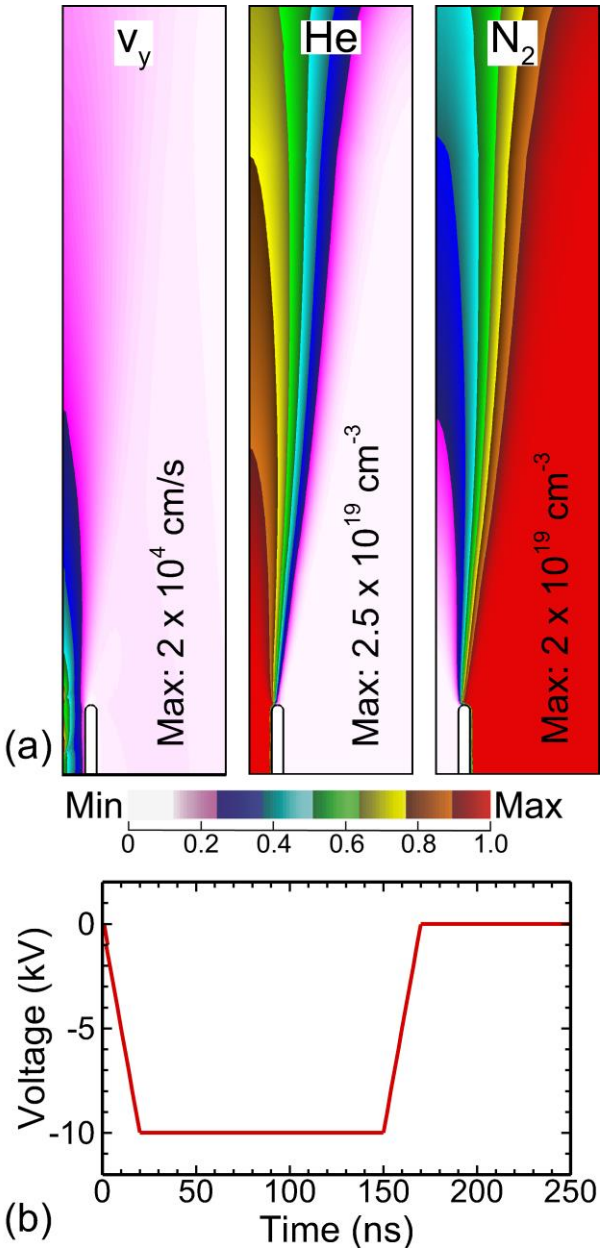

Fig. 5.2 Fluid and electrical properties for the simulation. (a) The steady state gas flow profile after 12 ms: (left) axial velocity, (center) He density, and (right) N_2 density. The scales are linear, and the maximum value is listed in each frame. As the He flows into the ambient, humid air begins diffusing in to the helium, the velocity profile broadens due to the viscosity of the fluid causing entrainment. (b) The negative voltage pulse waveform applied to the powered electrode.

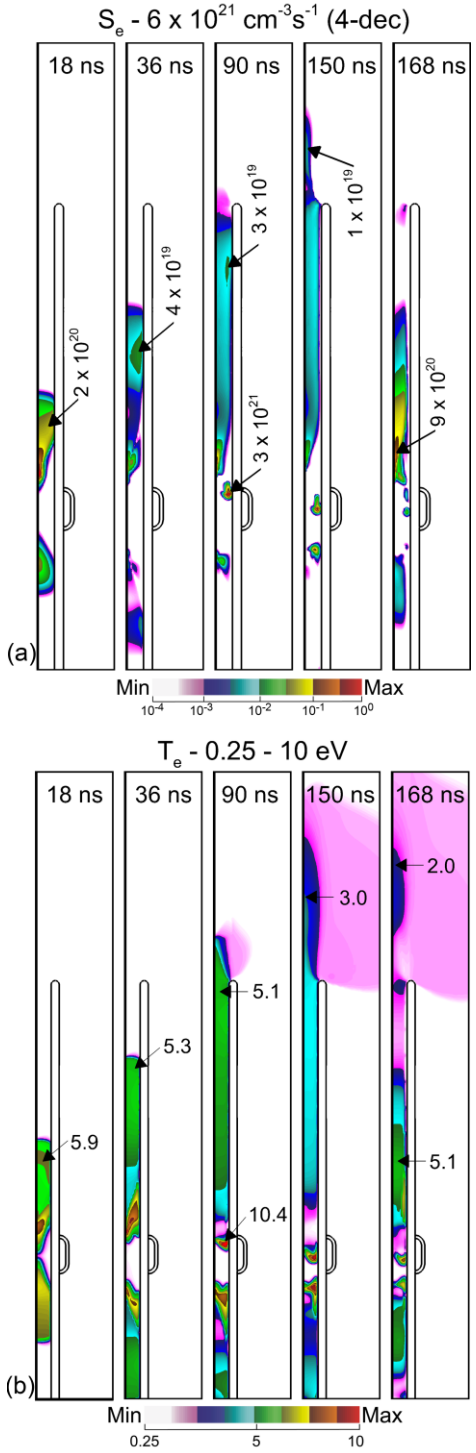

Fig. 5.3 Ionization wave (IW) propagation in the base case. (a) The electron impact ionization source term (S_e) shows the IW propagating in both directions, though primarily towards the outlet of the tube. At 150 ns as the applied voltage begins to fall, a restrike occurs producing a second IW inside the tube. (b) Electron temperature and as the ionization wave propagates. After 90 ns, the plasma begins interacting with the ambient air, T_e decreases and the IW propagation slows. At 168 ns, as the voltage decreases, T_e increases. S_e is shown on a 4-decade log scale. T_e is shown on a linear scale.

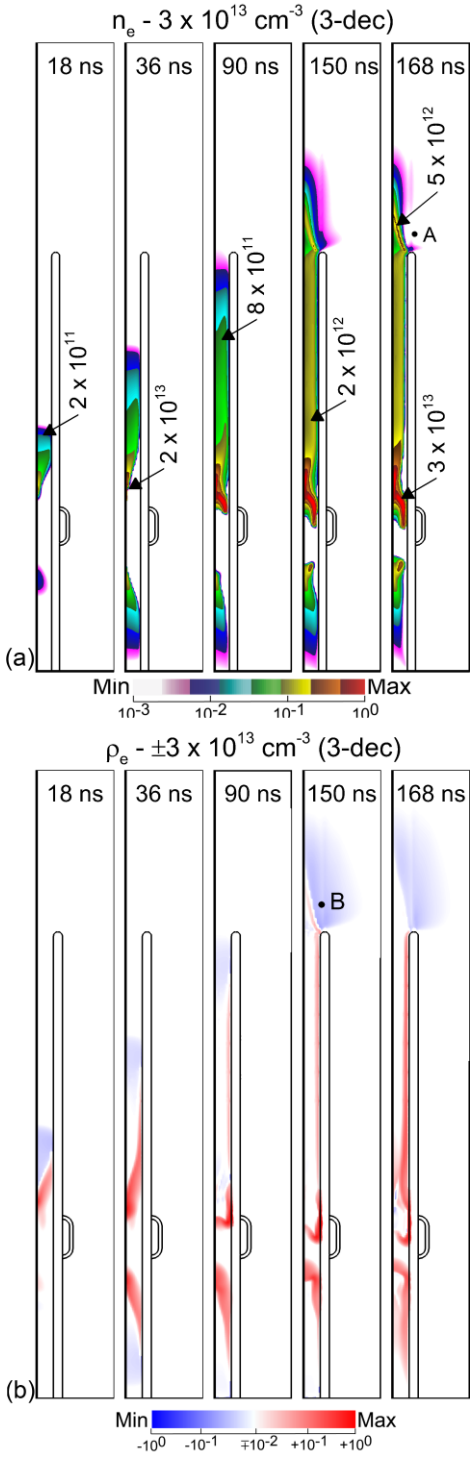

Fig. 5.4 Charged species dynamics during IW propagation for the base case. (a) Electron density (n_e). Upon exiting the tube, the electron density transitions from annular to axial due to interactions with in-diffusing air. A high electron density develops close to the powered electrode. (b) Total space charge. The negatively charged streamer head negatively charges the inner wall of the tube as the IW propagates. A sheath forms inside the tube with the walls charged negatively and a layer of positive space charge in the gas. Quantities are shown on a 3-decade log scale with maximum values indicated.

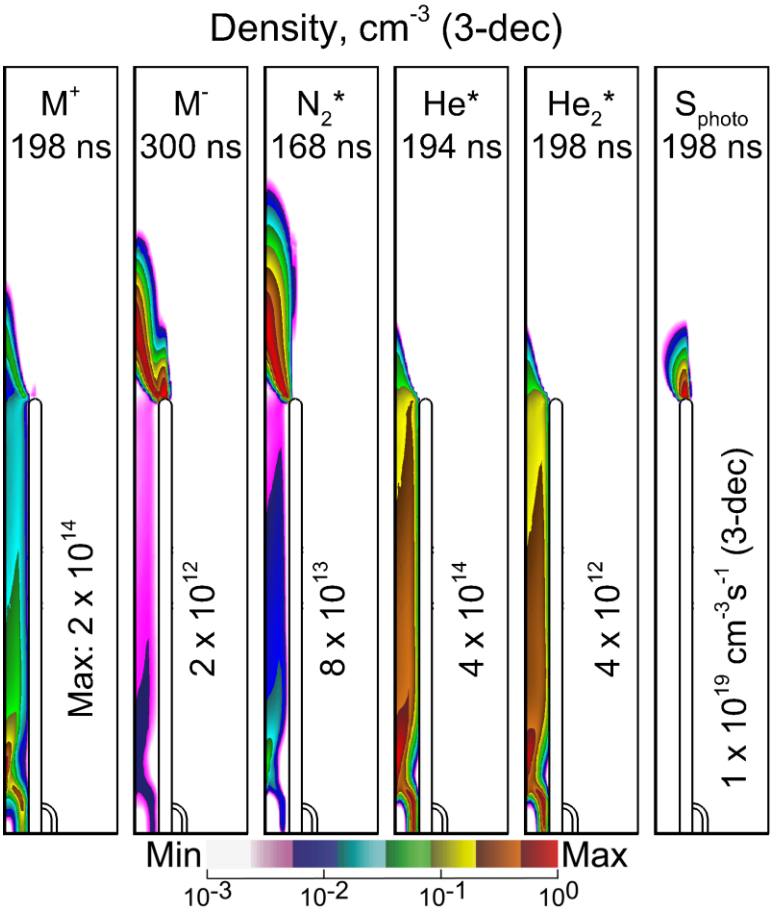

Fig. 5.5 Total positive and negative ion density, shown at the time where they reach their maximum density. Several excited state species and the photoionization term are also shown. N_2* is a lumped state including $N_2(A^3\Sigma)$, $N_2(B^3\Pi)$, $N_2(W^3\Delta)$, $N_2(B^3\Sigma)$, $N_2(A`^1\Sigma)$, $N_2(A`^1\Pi)$, $N_2(w^1\Delta)$. He* is the sum of the electronically excited states $He(2^3S)$, $He(2^1S)$, $He(2^3P)$, $He(2^1P)$, and the lumped states He(3P) and He(3S). Photoionization is due to He_2* ionizing humid air. Quantities are shown on a 3-decade log scale with maximum values indicated.

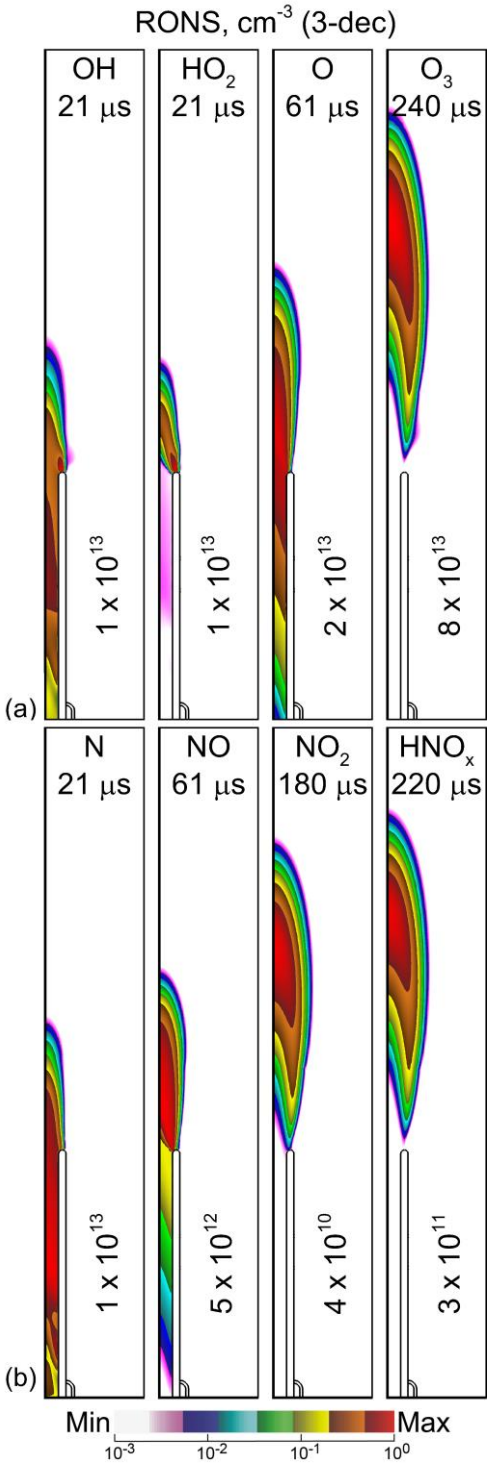

Fig. 5.6 The most abundant species formed in the afterglow at the time of their maximum density. (a) Species which do not contain nitrogen (OH, HO_2, O, O_3) and (b) nitrogen containing species (N, NO, NO_2, HNO_x). This sequence of maxima in densities illustrates the conversion of initial reactive species to intermediate and terminal reactive species in time as the gas flow convects the species downstream. Species are shown on a 3-decade log scale, with the maximum density and time at which that density occurs indicated on each frame.

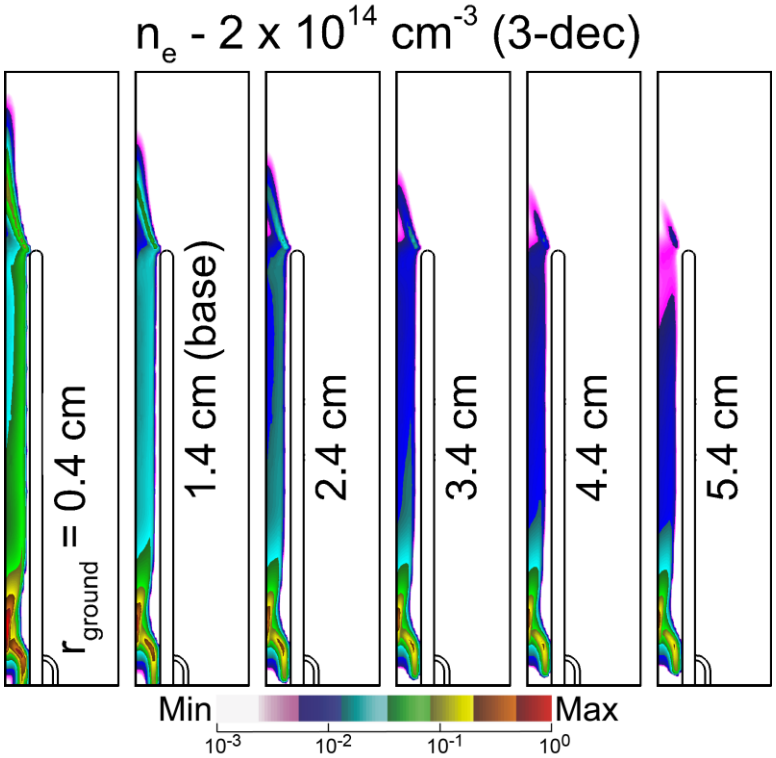

Fig. 5.7 Electron density at 168 ns for jets with increasing radius of the coaxial ground plane. Having a nearby ground plane increases the IW velocity and results in more ionization outside of the tube, where many of the RONS are produced. n_e is shown on a 3-decade log scale, and the radius of the coaxial ground is indicated on each frame.

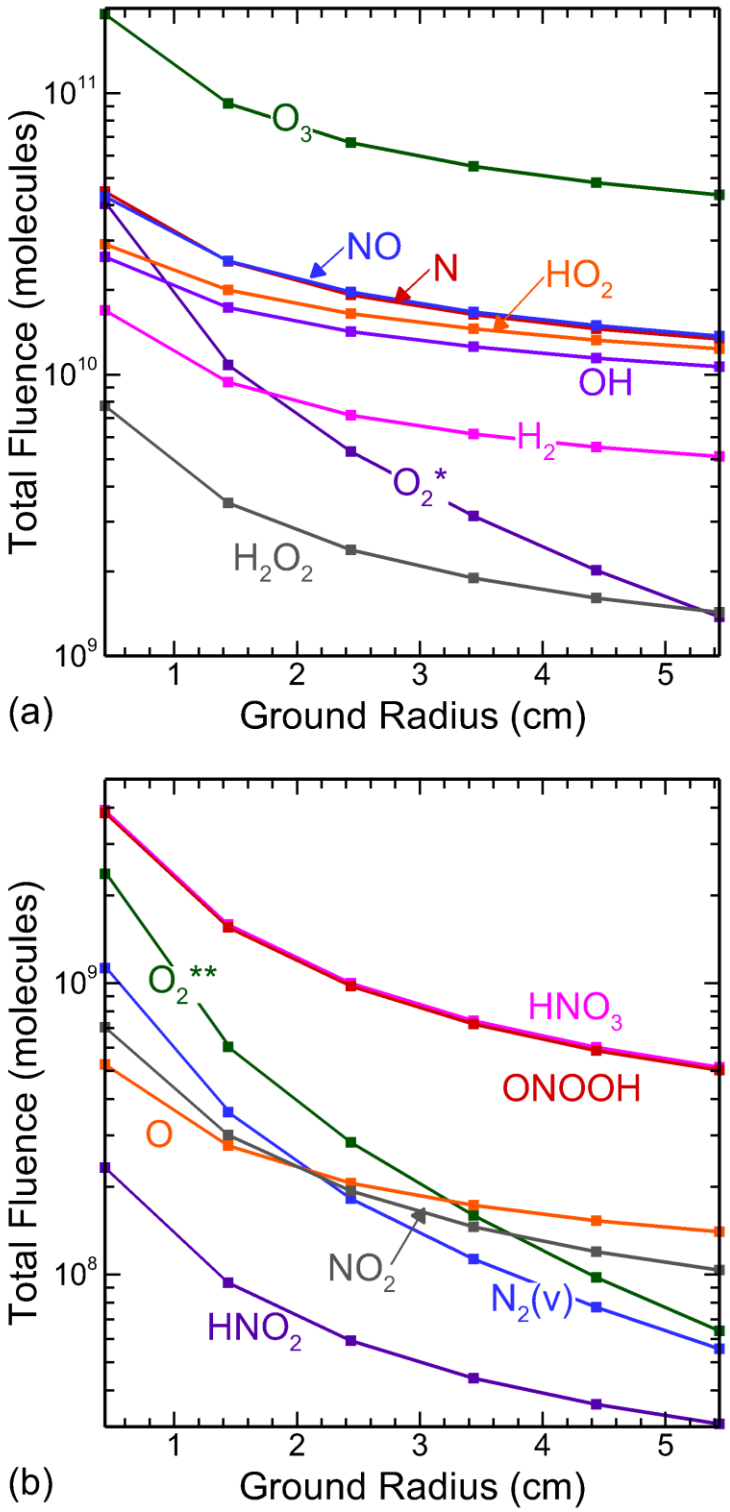

Fig. 5.8 Plasma produced species as a function of the radius of the coaxial ground plane. The total fluence refers to the time and spatially integrated flux crossing the pump surface, or the total number of molecules which have exited the computational domain. (a) O_2*, O_3, OH, H_2O_2, HO_2, H_2, N, and NO. (b) O_2**, N_2(v), O, NO_2, HNO_2, HNO_3, and ONOOH.

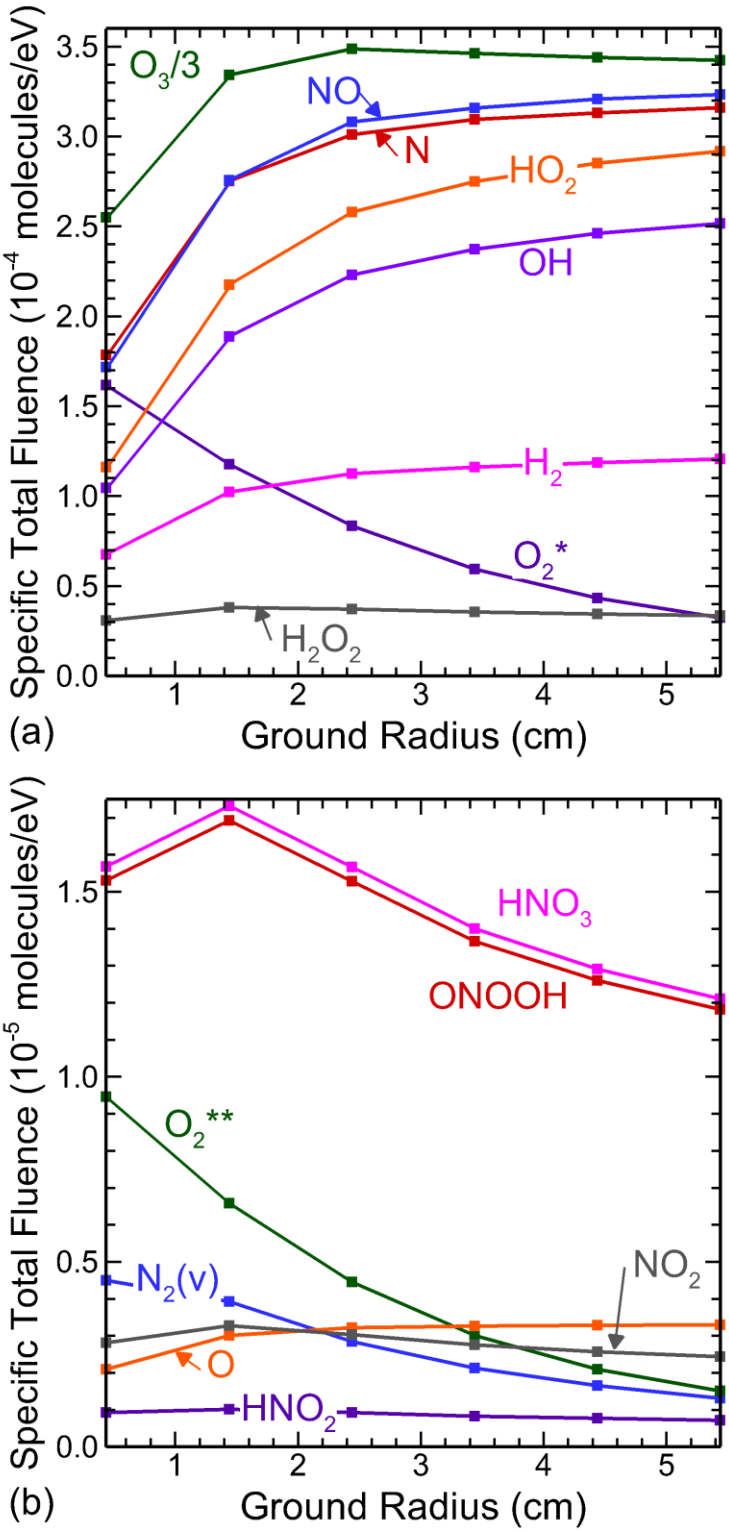

Fig. 5.9 Total fluence of species per eV of energy deposition (specific total fluence) as a function of radius of the coaxial ground. The total fluence is the time and spatially integrated flux crossing the pump surface. (a) O_2*, O_3, OH, H_2O_2, HO_2, H_2, N, and NO. (b) O_2**, N_2(v), O, NO_2, HNO_2, HNO_3, and ONOOH.

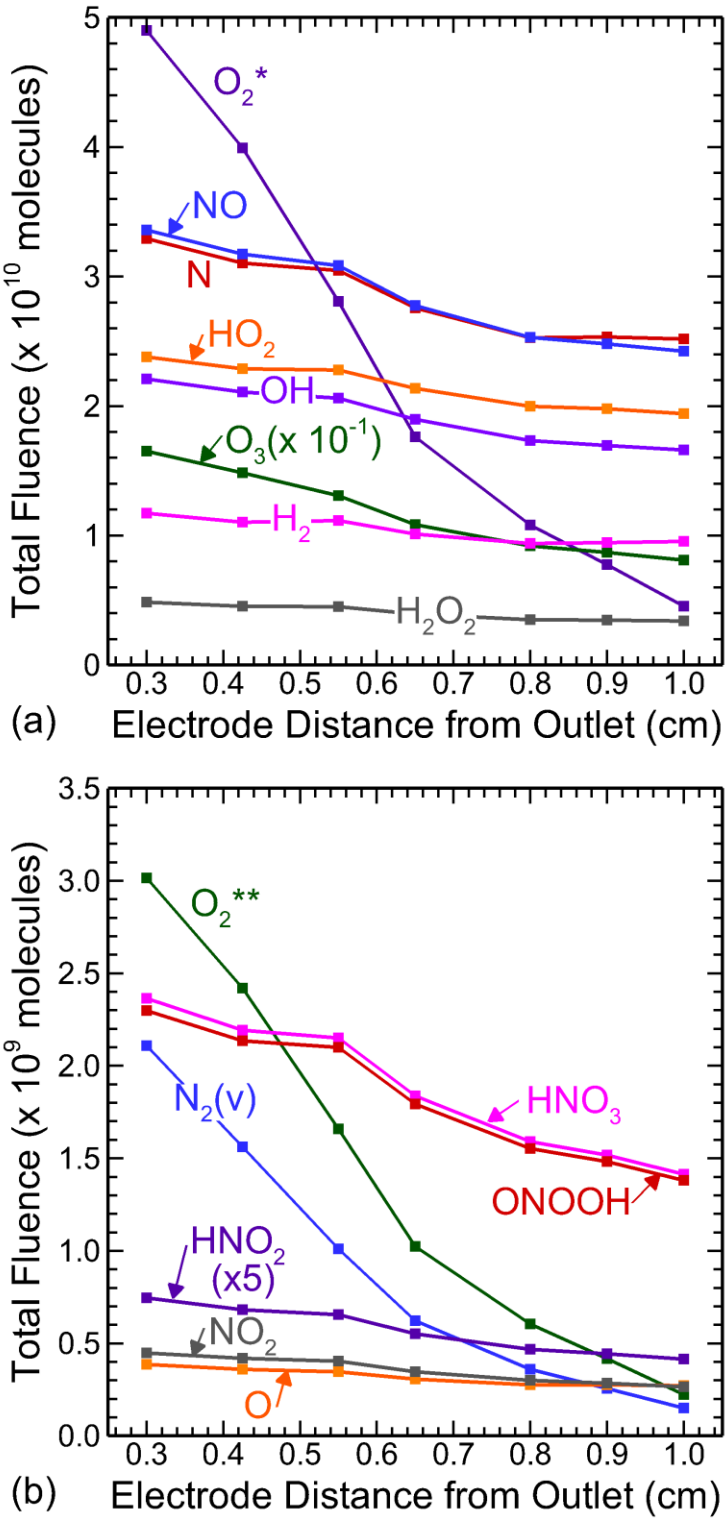

Fig. 5.10 The total fluence of plasma produced species as a function of distance of the powered electrode from tube outlet for a jet with a single powered ring electrode. The total fluence is the fluence integrated across the pump outlet surface, resulting in units of molecules. (a) O_2*, O_3, OH, H_2O_2, HO_2, H_2, N, and NO. (b) O_2**, N_2(v), O, NO_2, HNO_2, HNO_3, and ONOOH.

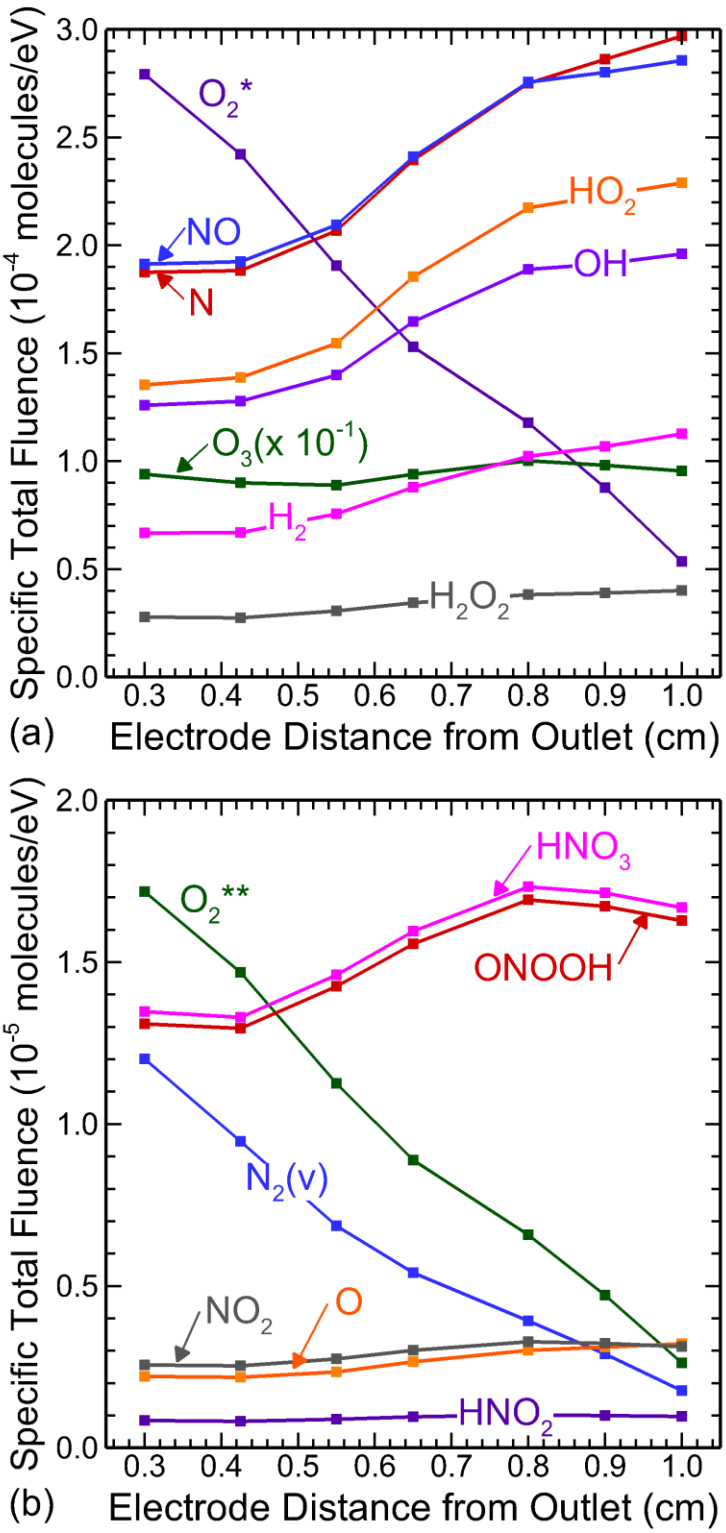

Fig. 5.11 The total fluence of species per eV of energy deposition (specific total fluence) as a function of distance of the powered electrode from tube outlet for a jet with a single powered ring electrode. Electrodes close to the outlet lead to a higher energy deposition and less energy efficient production. (a) O_2*, O_3, OH, H_2O_2, HO_2, H_2, N, and NO. (b) O_2**, N_2(v), O, NO_2, HNO_2, HNO_3, and ONOOH.

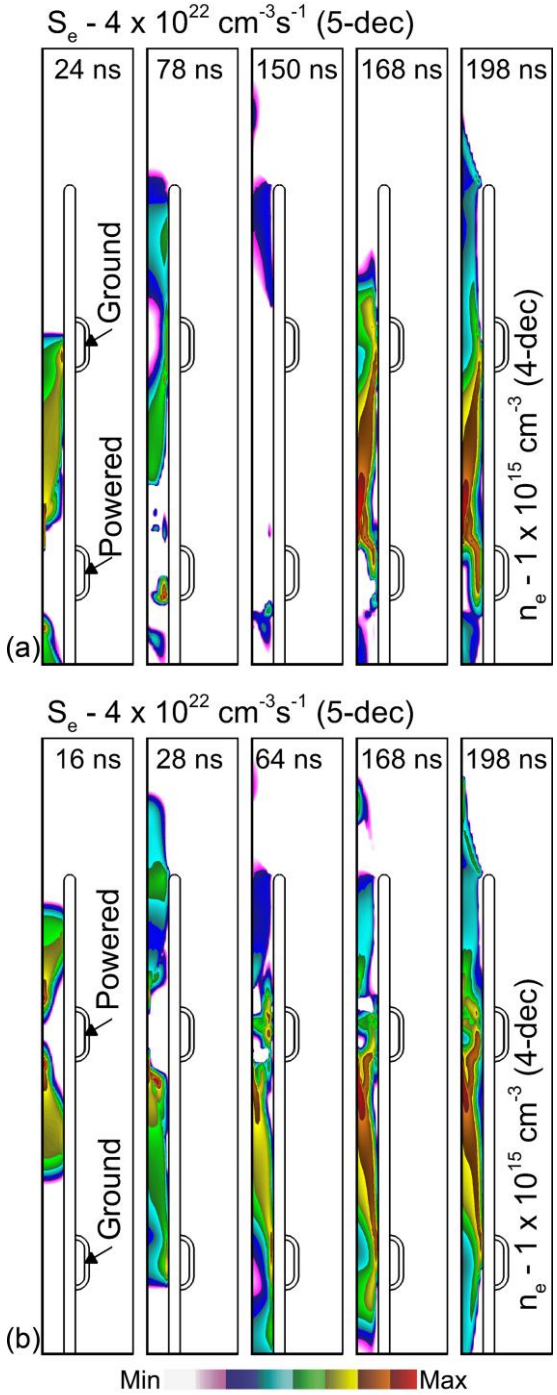

Fig. 5.12 Ionization wave propagation for a 2-ring electrode jet. The left four frames show the electron impact ionization source term (S_e) on a 5-decade log scale. The rightmost frame shows the electron density (n_e) on a 4-decade log scale. (a) The ground electrode is closer to the outlet. The plasma is more concentrated between the two electrodes where the electric field is initially highest. (b) The powered electrode is closer to the outlet. The plasma is most intense between the two electrodes, but the ionization wave does rapidly exit the tube producing significant ionization where the He meets the air.

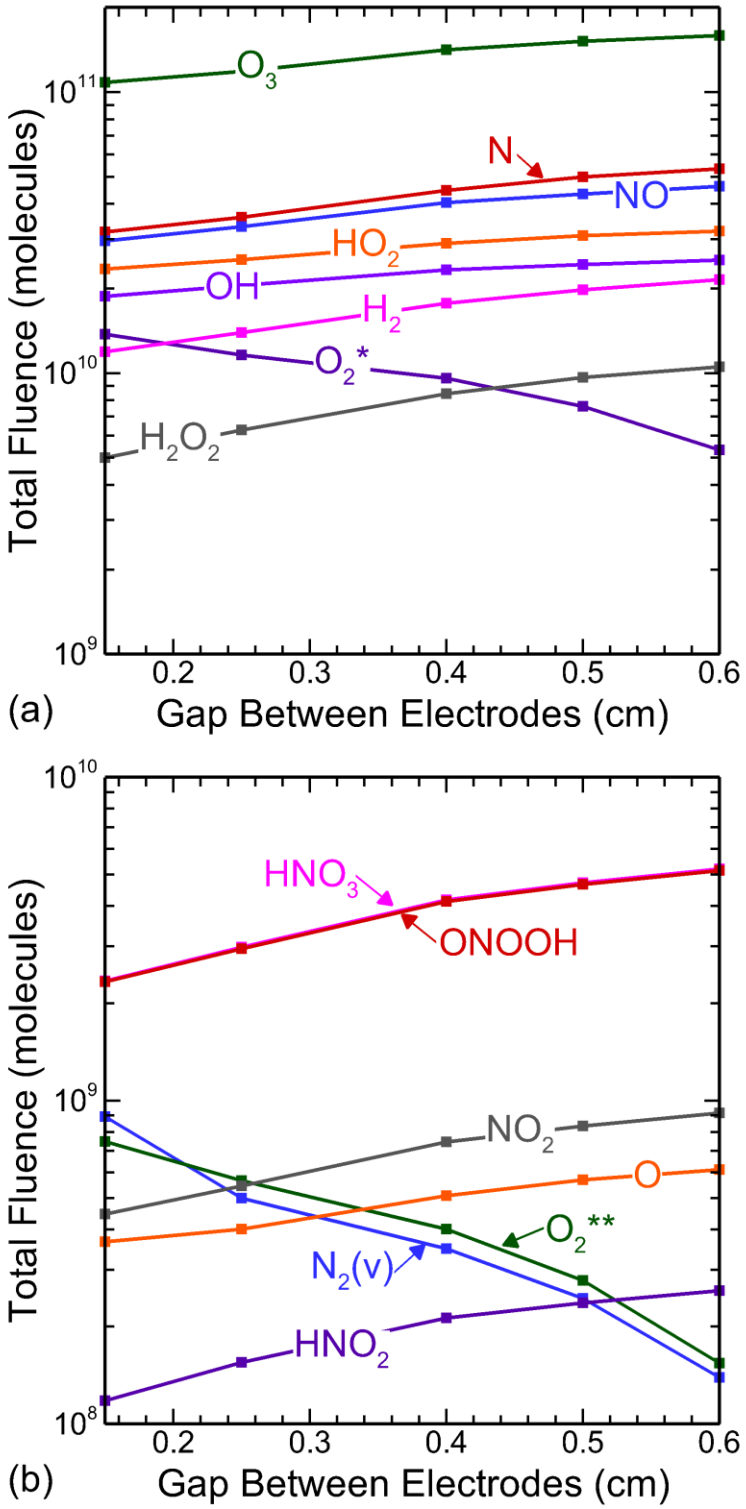

Fig. 5.13 The total fluence of species exiting the computational domain for jets with two ring electrodes as a function of the gap between the electrodes. The grounded ring electrode is fixed on the top (as in Fig. 5.12a), the position of the powered electrode was varied from 1.5 mm to 6 mm from the ground electrode. (a) O_2*, O_3, OH, H_2O_2, HO_2, H_2, N, and NO. (b) O_2**, N_2(v), O, NO_2, HNO_2, HNO_3, and ONOOH.

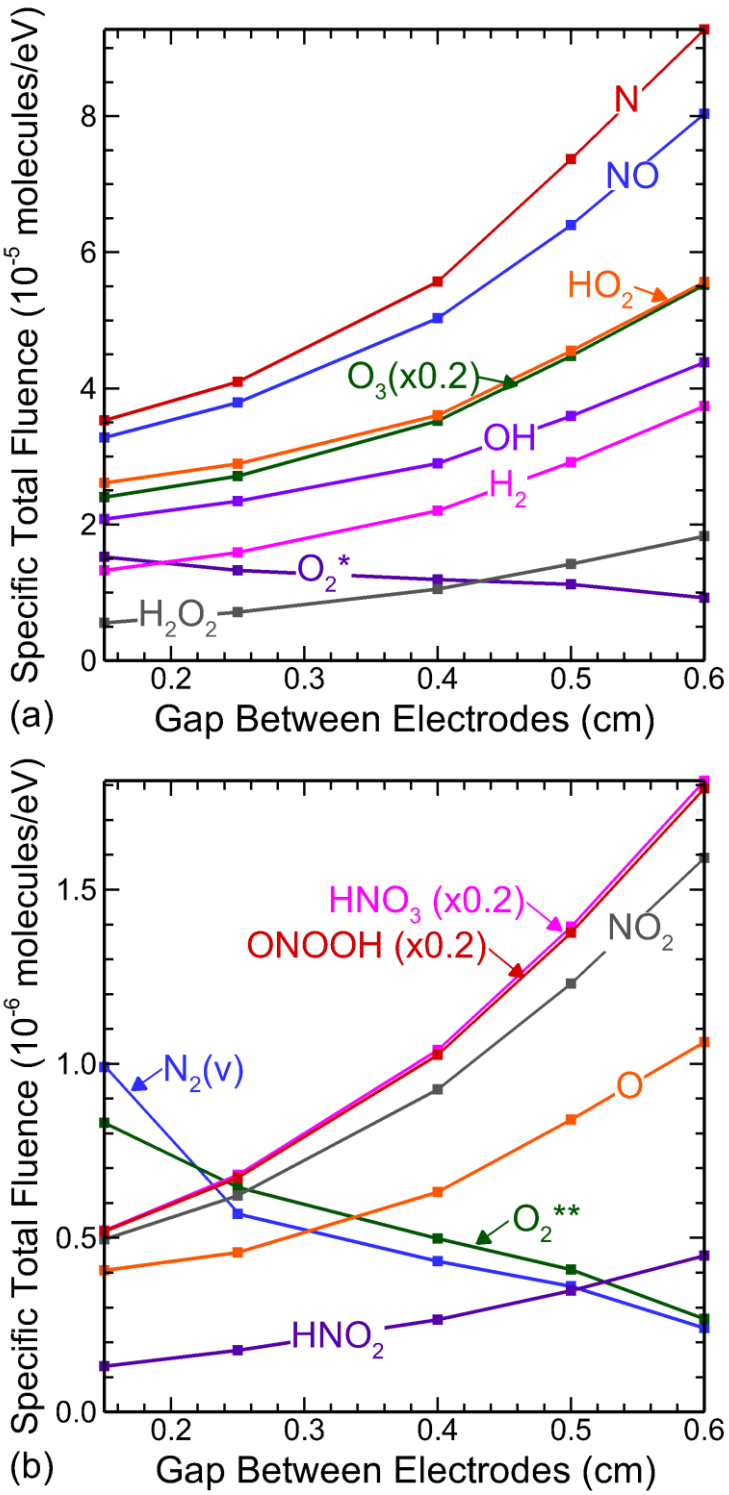

Fig. 5.14 The total fluence of species per eV of energy deposition (specific total fluence) for jets with two ring electrodes as a function of the gap between the electrodes. The grounded ring electrode is fixed on the top (as in Fig. 5.12a), the position of the powered electrode was varied. As this gap is increased, the energy deposition decreases and the energy efficiency increases. (a) O_2*, O_3, OH, H_2O_2, HO_2, H_2, N, and NO. (b) O_2**, N_2(v), O, NO_2, HNO_2, HNO_3, and ONOOH.

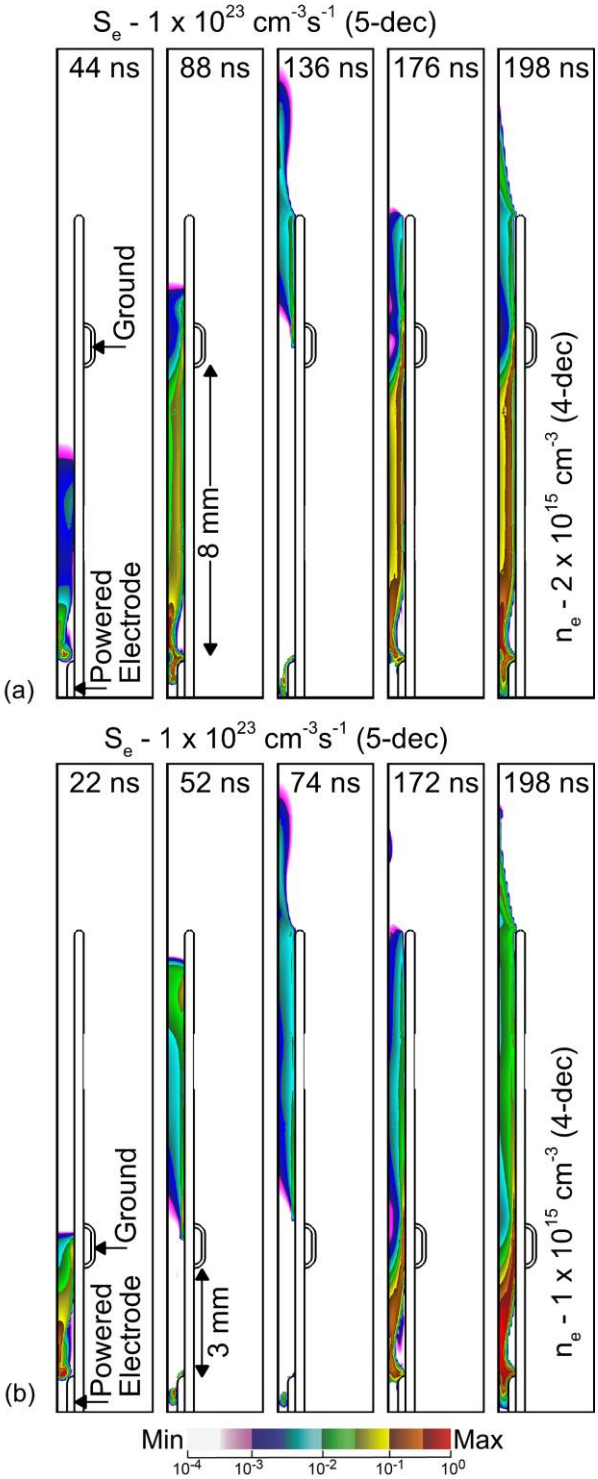

Fig. 5.15 Ionization wave behavior with the powered ring electrode inside the tube and the grounded ring outside of the tube. The left four frames are the electron impact ionization source term, S_e, on a 5-decade log scale, and the rightmost frame is the electron density, n_e, on a 4-decade log scale. (a) Ground electrode is 8 mm and (b) 3 mm from the powered electrode.

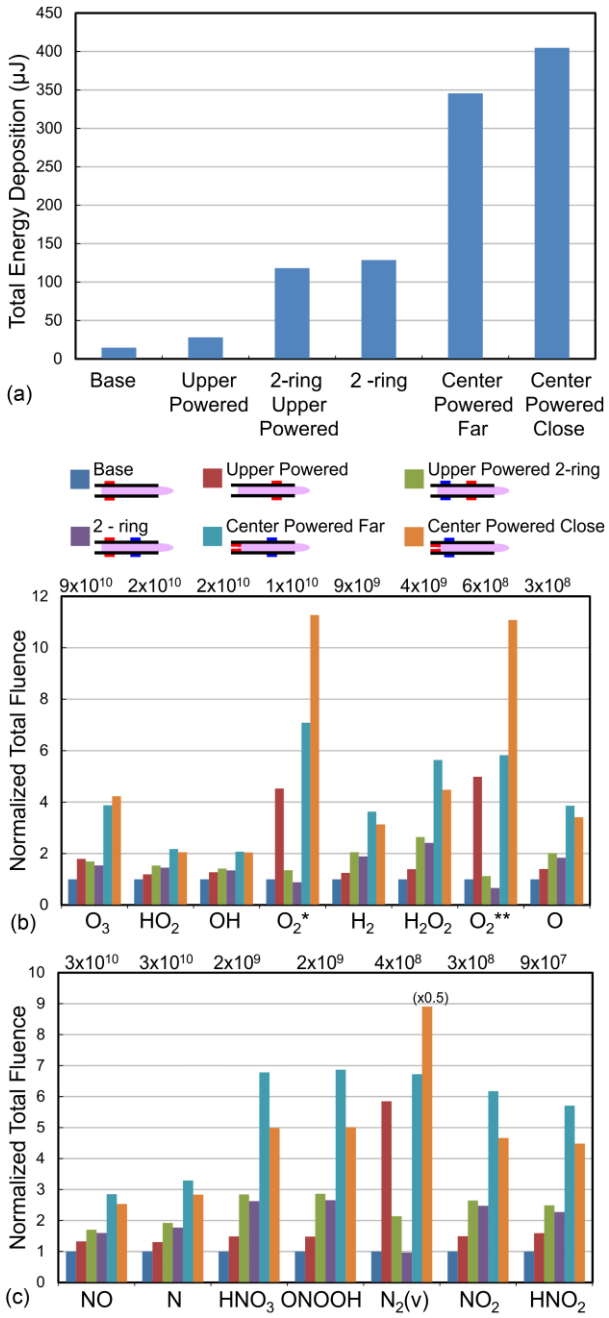

Fig. 5.16 Comparisons of energy and total fluences between different electrode configurations. In each schematic, red indicates a powered electrode, and blue indicates a grounded electrode. The configurations are "Base" (single ring electrode 8 mm from outlet, Fig. 5.3), "upper powered" (single ring electrode 3 mm from the outlet), "2-ring upper" (2 ring electrodes with powered on top, Fig. 5.12b), "2-ring" (2 ring electrodes with powered on bottom, Fig. 5.12a), "Center powered far" (internal electrode with large gap to ground, Fig. 5.15a), and "center powered close" (internal electrode with small gap to ground, Fig. 5.15b). (a) Volume integrated energy deposition (j·E). The normalized total fluence of (b) species which do not contain nitrogen and (c) the nitrogen containing species. These values are normalized to the base case total fluence whose value in molecules is listed.

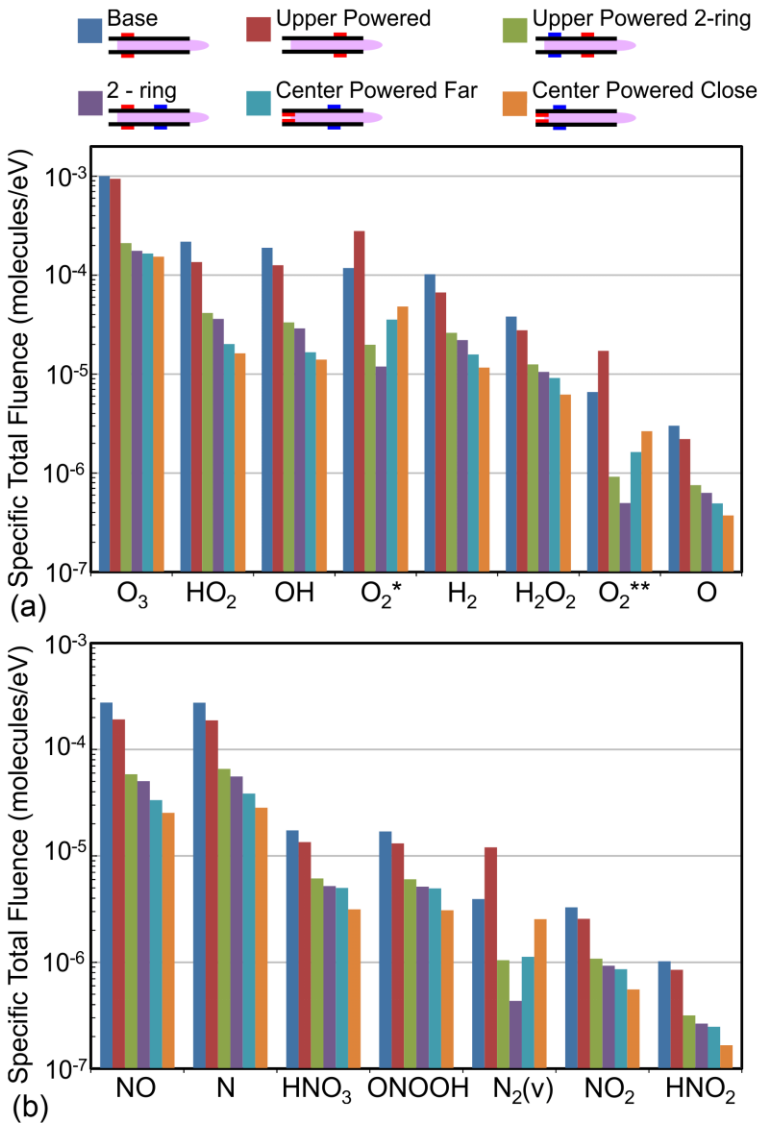

Fig. 5.17 The total fluence of each species per eV of energy deposition (specific total fluence) for different electrode configurations. (a) Species which do not contain nitrogen and (b) nitrogen containing species. The descriptions of electrode placement are the same as in Fig. 5.16.

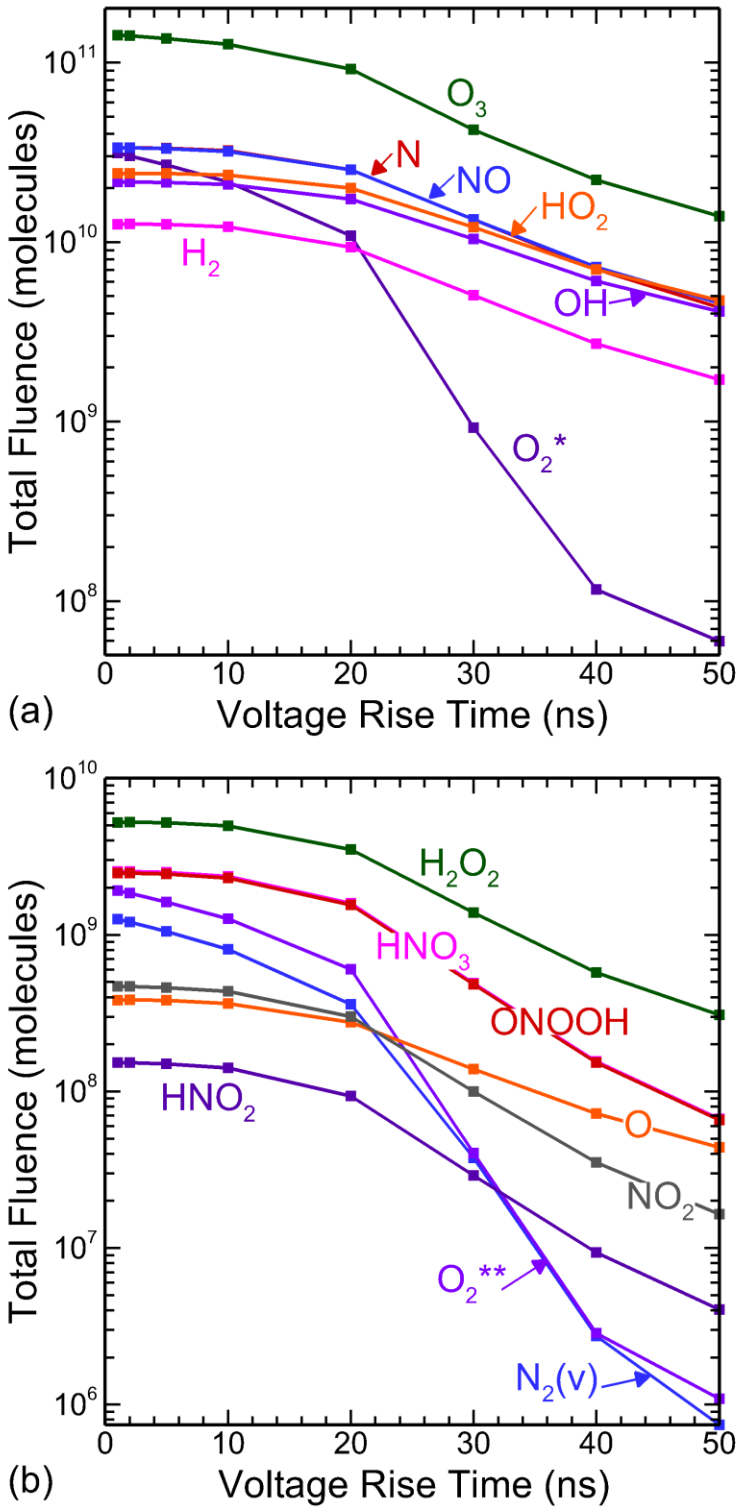

Fig. 5.18 The total fluence of species exiting the computational domain as a function of the voltage rise time. Increasing the rise time leads to a slower ramp and slower ionization wave propagation. (a) O_2*, O_3, OH, HO_2, H_2, N, and NO. (b) O_2**, N_2(v), O, H_2O_2, NO_2, HNO_2, HNO_3, and ONOOH.

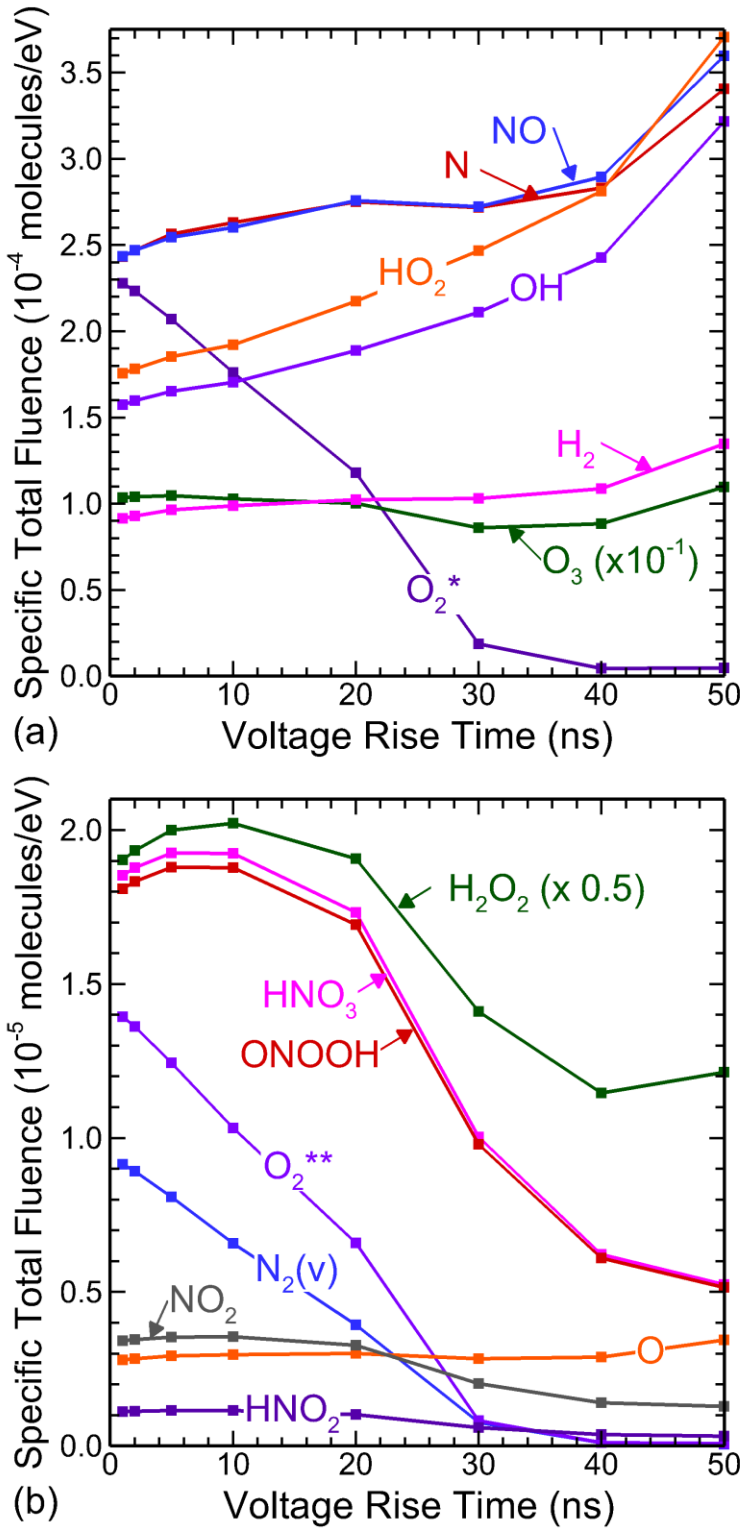

Fig. 5.19 The total fluence of species collected at the pump per eV of energy deposition (specific total fluence) as a function of the voltage rise time. (a) O_2*, O_3, OH, HO_2, H_2, N, and NO. (b) O_2**, N_2(v), O, H_2O_2, NO_2, HNO_2, HNO_3, and ONOOH.

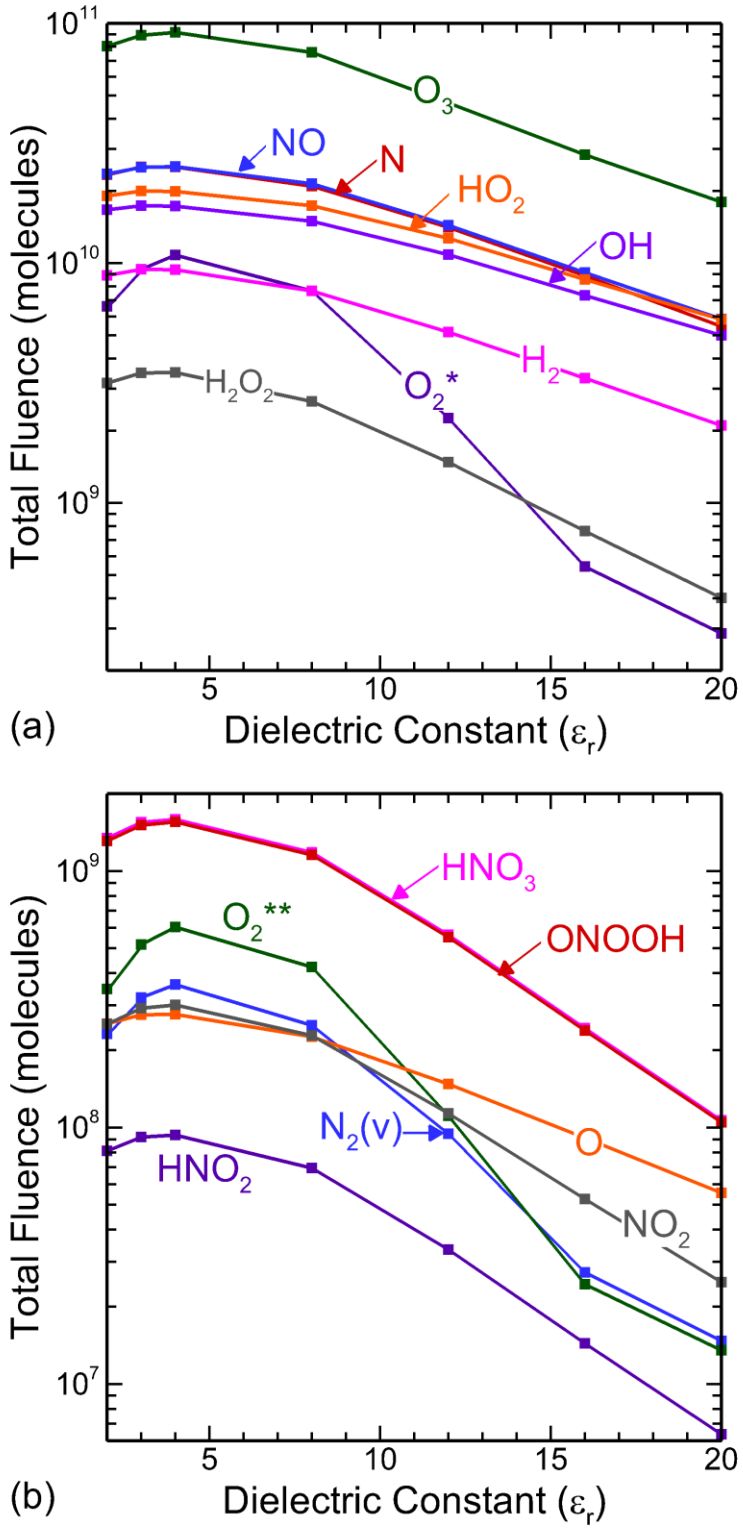

Fig. 5.20 The total fluence of species exiting the computational domain as a function of dielectric constant for the configuration with the single powered electrode outside of the tube. The maximum production for all species occurs at $\varepsilon_r = 4$. (a) O_2*, O_3, OH, H_2O_2, HO_2, H_2, N, and NO. (b) O_2**, N_2(v), O, NO_2, HNO_2, HNO_3, and ONOOH.

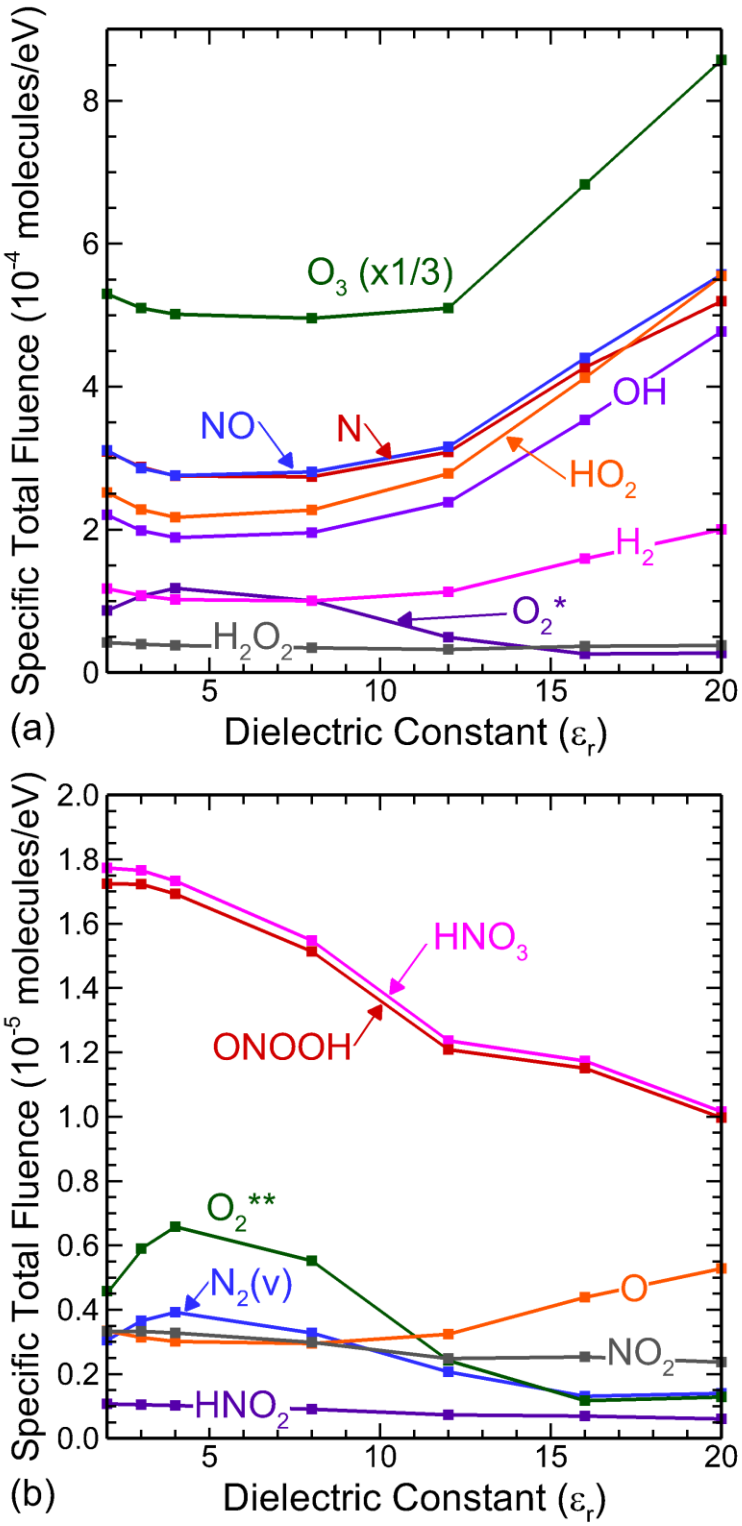

Fig. 5.21 The total fluence of species collected at the pump per eV of energy deposition (specific total fluence) as a function of the dielectric constant of the tube for the configuration with a single powered electrode outside of the tube. (a) O_2*, O_3, OH, H_2O_2, HO_2, H_2, N, and NO. (b) O_2**, N_2(v), O, NO_2, HNO_2, HNO_3, and ONOOH.

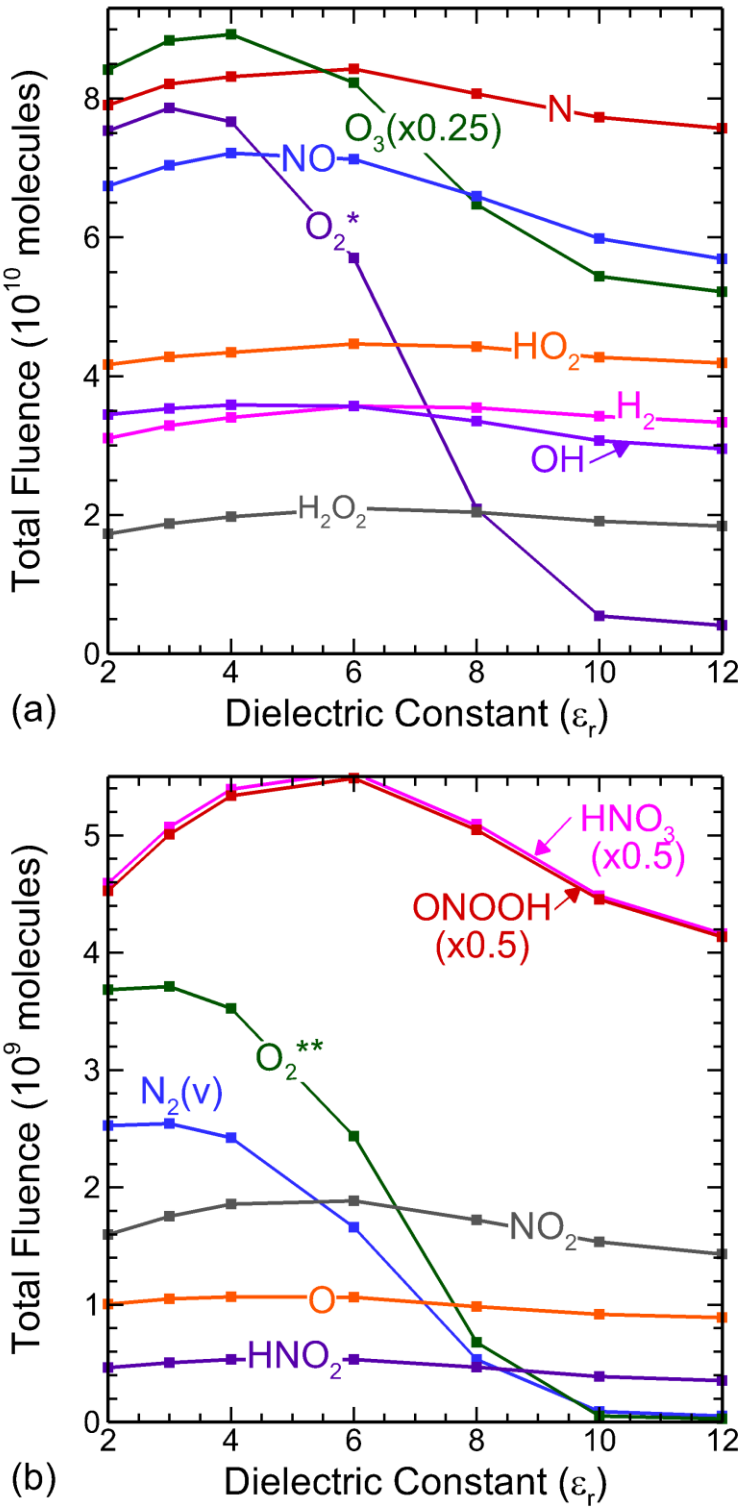

Fig. 5.22 The total fluence of species exiting the computational domain as a function of the dielectric constant of the tube. The electrode configuration, shown in Fig. 5.15a, has the powered electrode inside the tube and 8 mm between the electrodes. (a) O_2*, O_3, OH, H_2O_2, HO_2, H_2, N, and NO. (b) O_2**, N_2(v), O, NO_2, HNO_2, HNO_3, and ONOOH.

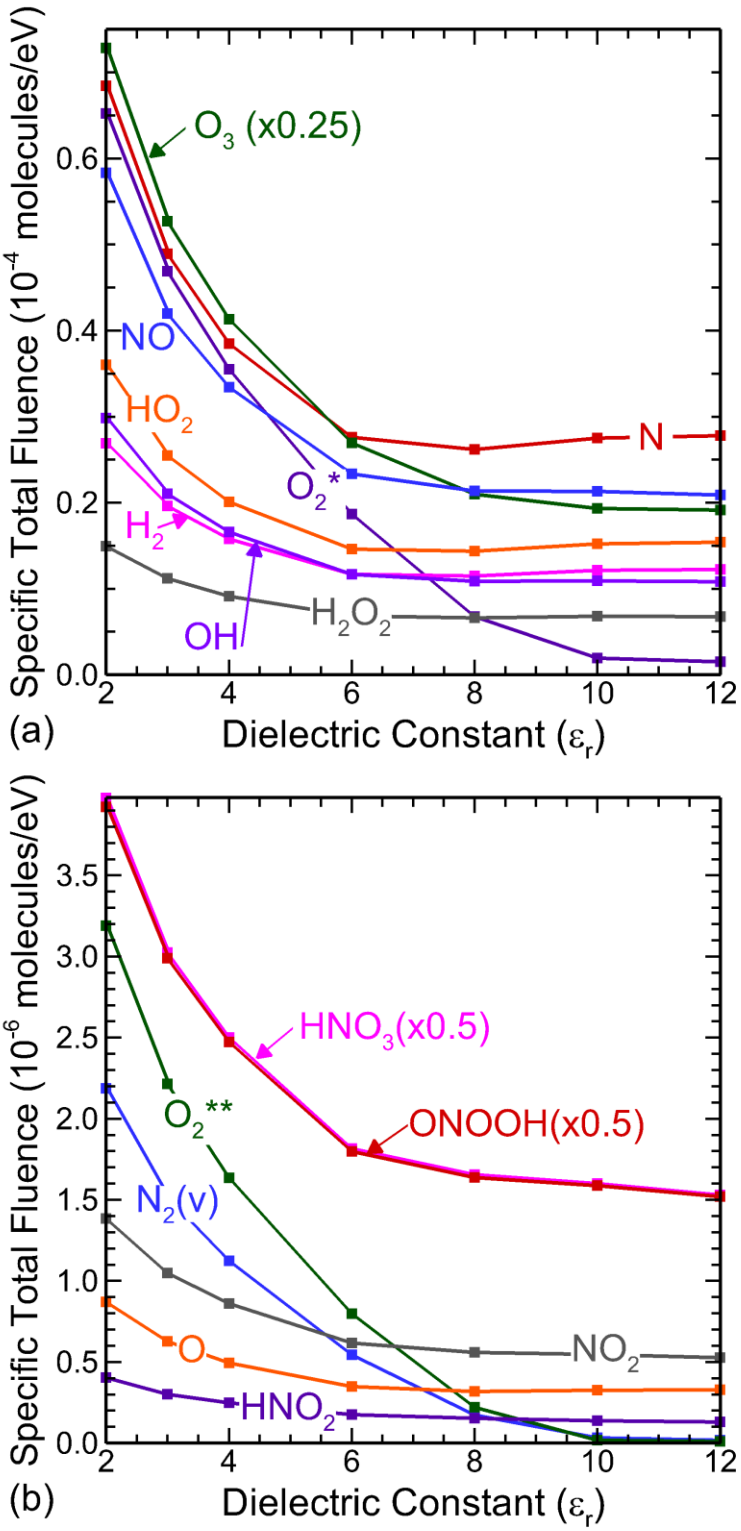

Fig. 5.23 The total fluence of species collected at the pump per eV of energy deposition (specific total fluence) as a function of the dielectric constant of the tube. The electrode configuration, shown in Fig. 5.15a, has the powered electrode inside the jet and 8 mm between the electrodes. (a) O_2*, O_3, OH, H_2O_2, HO_2, H_2, N, and NO. (b) O_2**, N_2(v), O, NO_2, HNO_2, HNO_3, and ONOOH.

5.6 References

[1] D. Dobrynin et al., Plasma Med. **1,** 93 (2011).

[2] S. Arndt et al., PLoS One **8,** 1 (2013).

[3] F. Brehmer et al., J. Eur. Acad. Dermatology Venereol. **29,** 148 (2014).

[4] H. M. Joh, S. J. Kim, T. H. Chung and S. H. Leem, Appl. Phys. Lett. **101,** 053703 (2012).

[5] M. Vandamme, E. Robert, S. Dozias, J. Sobilo, S. Lerondel, A. Le Pape and J.-M. Pouvesle, Plasma Med. **1,** 27 (2011).

[6] K. Mizuno, K. Yonetamari, Y. Shirakawa, T. Akiyama and R. Ono, J. Phys. D: Appl. Phys. **50,** 12LT01 (2017).

[7] D. B. Graves, J. Phys. D: Appl. Phys. **45,** 263001 (2012).

[8] D. B. Graves, Clin. Plasma Med. **2,** 38 (2014).

[9] N. Kaushik, N. Uddin, G. B. Sim, Y. J. Hong, K. Y. Baik, C. H. Kim, S. J. Lee, N. K. Kaushik and E. H. Choi, Nat. Sci. Reports **5,** 8587 (2015).

[10] G. Bauer and D. B. Graves, Plasma Process. Polym. **13,** 1157 (2016).

[11] Z. Ke, P. Thopan, G. Fridman, V. Miller, L. Yu, A. Fridman and Q. Huang, Clin. Plasma Med. **7–8,** 1 (2017).

[12] J. Winter, R. Brandenburg and K.-D. Weltmann, Plasma Sources Sci. Technol. **24,** 064001 (2015).

[13] H. Xu, C. Chen, D. Liu, D. Xu and Z. Liu, J. Phys. D: Appl. Phys. **50,** 245201 (2017).

[14] J. Winter et al., J. Phys. D: Appl. Phys. **47,** 285401 (2014).

[15] E. A. J. Bartis, P. Luan, A. J. Knoll, C. Hart, J. Seog and G. S. Oehrlein, Biointerphases **10,** 029512 (2015).

[16] D. Maletić, N. Puač, G. Malović, A. Đorđević and Z. L. Petrović, J. Phys. D: Appl. Phys. **50,** 145202 (2017).

[17] I. Jõgi, R. Talviste, J. Raud, K. Piip and P. Paris, J. Phys. D: Appl. Phys. **47,** 415202 (2014).

[18] D. Maletić, N. Puač, N. Selaković, S. Lazović, G. Malović, A. Đorđević and Z. L. Petrović, Plasma Sources Sci. Technol. **24,** 025006 (2015).

[19] Y. Yue, X. Pei and X. Lu, J. Appl. Phys. **119,** 033301 (2016).

[20] S. A. Norberg, E. Johnsen and M. J. Kushner, Plasma Sources Sci. Technol. **24,** 035026 (2015).

[21] W. Van Gaens and A. Bogaerts, J. Phys. D: Appl. Phys. **47,** 079502 (2014).

[22] S. Kelly and M. M. Turner, Plasma Sources Sci. Technol. **23,** 065013 (2014).

[23] L. C. Pitchford and A. V Phelps, Phys. Rev. A **25,** 540 (1982).

[24] J. W. Gallagher, C. E. Brion, J. A. R. Samson and P. W. Langhoff, J. Phys. Chem. Ref. Data **17,** 9 (1988).

[25] S. Norberg, PhD Thesis, "Modeling atmospheric pressure plasma jets: plasma dynamics, interaction with dielectric surfaces, liquid layers and cells", (University of Michigan, 2015).

[26] S. Schröter, A. R. Gibson, M. J. Kushner, T. Gans and D. O'Connell, Plasma Phys. Control. Fusion **60,** 014035 (2018).

[27] X. Lu, M. Laroussi and V. Puech, Plasma Sources Sci. Technol. **21,** 034005 (2012).

[28] T. Darny, J.-M. Pouvesle, V. Puech, C. Douat, S. Dozias and E. Robert, Plasma Sources Sci. Technol. **26,** 045008 (2017).

[29] D. X. Liu, P. Bruggeman, F. Iza, M. Z. Rong and M. G. Kong, Plasma Sources Sci. Technol. **19,** 025018 (2010).

[30] B. T. J. van Ham, S. Hofmann, R. Brandenburg and P. J. Bruggeman, J. Phys. D: Appl. Phys. **47,** 224013 (2014).

[31] T. Verreycken, R. Mensink, R. van der Horst, N. Sadeghi and P. J. Bruggeman, Plasma Sources Sci. Technol. **22,** 055014 (2013).

[32] B. L. M. Klarenaar, O. Guaitella, R. Engeln and A. Sobota, Plasma Sources Sci. Technol. **27,** 085004 (2018).

[33] V. V Kovačević, G. B. Sretenović, E. Slikboer, O. Guaitella, A. Sobota and M. M. Kuraica, J. Phys. D: Appl. Phys. **51,** 065202 (2018).

[34] S. Yonemori and R. Ono, J. Phys. D: Appl. Phys. **47,** 125401 (2014).

Chapter 6 Molecular Admixtures and Impurities in Atmospheric Pressure Plasma Jets[1]

Adding molecular gases to the noble working gas which flows through atmospheric pressure plasma jets (APPJs) is a common method to tailor the production of reactive oxygen and nitrogen species (RONS). In this chapter, results are discussed from a computational investigation of the consequences of H_2O and O_2 admixtures on the reactive chemistry of He APPJs flowing into humid air. This investigation, performed with a 2-dimensional plasma hydrodynamics model, addresses the RONS that are initially produced and the evolution of that chemistry on longer timescales. Without an admixture, the impurities in 99.999% pure helium are a major source of RONS. The addition of H_2O decreases the production of reactive nitrogen species (RNS) and increases the production of reactive oxygen species (ROS). The addition of O_2 significantly decreases the production of RNS, as well as hydrogen-containing ROS, but increases the production of ROS without hydrogen. This selectivity comes from the lower ionization energy of O_2 compared to N_2 and H_2O, which then allows for charge exchange reactions. These charge exchange reactions change the RONS which are produced in the afterglow by dissociative recombination. The consequences of impurities were also examined. Humid air impurities as low as 10 ppm in the helium can account for 79-98% of the production of most RONS in the absence of an intentional admixture. The degree to which the impurities affect the RONS production depends on the electrode configuration and can be reduced by molecular admixtures.

[1] The results discussed and portion of the text in this chapter have been previously published in A. M. Lietz and M. J. Kushner, "Molecular admixtures and impurities in atmospheric pressure plasma jets", J. Appl. Phys. **124,** 15330 (2018).

6.1 Introduction

As discussed in Sec. 1.3 and Sec. 5.1, most of the desirable biological effects of APPJs are attributed to the production of RONS which result from dissociation of admixtures or impurities in the initial gas flow or by reaction with the ambient.[1,2] APPJs allow more flexibility and control of the plasma chemistry by controlling the gas composition, compared to devices such as dielectric barrier discharges which typically operate in ambient air.

Even a small mole fraction of a molecular gas in a rare gas plasma can significantly affect the electron energy distribution (EED) by introducing inelastic processes with lower threshold energies. For example, the excitation of vibrational and rotational molecular states generally have thresholds on the order of 0.01 - 0.1 eV. This means that molecular admixtures or impurities, even in small amounts, can change the discharge dynamics, including the electron density and the amount of energy that is coupled into the discharge during a voltage pulse. H_2O and O_2 are typical admixtures added to APPJ feed-gases with the goal of increasing the generation of particular reactive oxygen species (ROS). Due to the non-linear coupling between the impurities, EEDs, flow dynamics and mixing with the ambient, the reactive chemistry resulting from the admixtures is not always a straightforward function of concentration.

Several experiments have provided insights into the consequences of admixtures on aspects of the plasma-produced chemistry. In a helium atmospheric pressure glow discharge, Bruggeman *et al*. observed that impurities at concentrations as low as hundreds of ppm dominate the ion chemistry.[3] Increasing the H_2O concentration in the He decreases the positive ion density and increases the negative ion density, particularly $OH^-(H_2O)_n$. In laser induce fluorescence (LIF) measurements in an Ar jet, OH densities 1 mm from the jet outlet were found to be maximum at 0.5% H_2O.[4] In an radio frequency (RF) helium APPJ, two photon

absorption laser-induced-fluorescence (TALIF) measurements by Knake *et al*. indicated that the O atom density at the jet outlet is a maximum for 0.6% O_2 at constant RF power.[5]

Gas composition in APPJs has been the subject of several modeling studies. Naidis investigated the effects of an air admixture and the humidity of the air in a He APPJ.[6] Increasing the air admixture from 1% to 3% (while increasing the voltage to keep the IW velocity constant) significantly increased production of O_3 and NO. Increasing the humidity of the air admixture increased the production of OH, decreased the production of O and O_3, and did not significantly affect NO. Park *et al*. used a global model to study admixtures of O_2 in He and Ar atmospheric pressure glow discharges.[7] At 1% O_2, most of the electron energy losses were by collisions with O_2. At constant power, adding O_2 decreased the electron density (n_e), and increased the production of O and O_3, with the effects being most dramatic in the first 1% of O_2 added. Schröter *et al*. used a global model to study a humid He radio-frequency APPJ, showing a decrease in the electron density and an increase in nearly all reactive oxygen species with an increase in the H_2O admixture.[8]

Admixtures have also been shown to change the biological outcomes in applications of APPJs. In experiments by Joh *et al*., an O_2 admixture in a helium APPJ increased plasma-induced apoptosis in cancer cells.[9] Humidified He and humidified He/O_2 have been less effective than dry He/O_2 at inducing apoptosis.[10] Lin *et al*. have shown that an O_2 admixture of 0.02% in an Ar plasma jet is most effective for deactivating bacterial endospores.[11]

In this chapter, we report on a 2-dimensional computational investigation of the effects of O_2 and H_2O admixtures in He APPJs having *as delivered impurities* on IW propagation and the initial production of RONS. The amounts of RONS that flow out of the computational domain are compared as a measure of the maximum reactivity available for surface processing. These

products are generated after allowing several ms for initially produced radicals to react with each other and the admixture, mix with the surrounding air, and flow downstream. The energy normalized RONS production was also compared to distinguish the role of the changes in energy coupled to the plasma as the admixture is varied from changes in the gas composition. The model is described in Sec. 6.2. The discussion of results in Sec. 6.3 includes a brief overview of the base case in Sec. 6.3.1, the consequences of H_2O admixtures in Sec. 6.3.2 and O_2 admixtures in Sec. 6.3.3, and the role of impurities in Sec. 6.3.4. Concluding remarks are in Sec. 6.4.

6.2 Description of the Model

The model used in this investigation, *nonPDPSIM,* is a 2-dimensional plasma hydrodynamics simulation that is described in detail in Chapter 2. The reaction mechanism contains 51 species addressing helium and humid air – 16 charged species, 35 neutral species. The mechanism contains 753 reactions, including 175 electron impact reactions. The reaction mechanism is discussed by Norberg *et al*., and therefore will only be summarized here.[12,13] (Note that in Ref. 13, species having the same rate coefficient for a reaction are grouped into a single entry. For example, a Penning ionization reaction having the same rate coefficient for all excited states of He is represented by the species He*.)

The mechanism treats the lower energy levels of electronically excited helium explicitly [He(2^3S), He(2^1S), He(2^3P), He(2^1P)], while the more highly excited states are lumped into He(3P) and He(3S). The He excimers are lumped into a single excimer state (He_2*), which is not radiatively trapped. The primary ions, which are generated by electron impact on the flowing gases, are He^+, N_2^+, O_2^+, O_2^-, and H_2O^+. For these conditions He^+ is dominantly produced by direct electron impact ionization of ground state He, and to a lesser extent by stepwise ionization and Penning ionization (He* + He* $\rightarrow$ He + He^+ + e, where He* includes all

electronically excited states of He). Although the rate coefficient for electron impact ionization of excited states greatly exceeds that for He, the mole fraction of the excited states is also small, resulting in the stepwise process not dominating ionization. N_2^+, O_2^+, and H_2O^+ are produced by electron impact ionization, Penning ionization, and charge exchange. O_2^- is a result of 3-body electron attachment to O_2. Dissociative electron impact ionization or dissociative attachment produces N^+, O^+, O^-, H^+ and OH^-. The reaction mechanism contains a limited number of higher order and cluster ions including N_4^+, H_3O^+ and $H_3O^+(H_2O)$. In the presence of water vapor, more and larger water cluster ions would actually form, however these have not been included due to the additional computational cost. These water-cluster ions may have some effect on the recombination rate, but the neutral RONS produced as a result of recombination and ion-ion neutralization reactions are typically unaffected by the surrounding water molecules.[14]

The electronically excited states associated with humid air are N_2* [a lumped state including $N_2(A^3\Sigma)$, $N_2(B^3\Pi)$, $N_2(W^3\Delta)$, $N_2(B^3\Sigma)$, $N_2(A`^1\Sigma)$, $N_2(A`^1\Pi)$, $N_2(w^1\Delta)$], and N_2** [$N_2(B^3\Pi)$ and $N_2(E^3\Sigma)$]. Excited states of oxygen include O_2* referring to $O_2(^1\Delta)$ and O_2** referring to $O_2(b^1\Sigma_g)$. O* [$O(2^1D)$ and $O(2^1S)$] and N* [$N(2^2D)$ and $N(2^2P)$] are included as a result of dissociation of O_2 and N_2. $N_2(v)$ is the only vibrationally excited state that is explicitly tracked in the mechanism. All other vibrational and rotational collisions are accounted for in the electron energy losses and the gas heating, but the density of the vibrationally and rotationally excited products are not calculated.

The main species of interest in the biological applications are RONS, which can have longer lifetimes allowing them to reach a biological sample. Reactive oxygen species include O, which forms by dissociation of O_2, then reacts with O_2 to form O_3. The dissociation of H_2O leads to the production of H and OH. H then either reacts with itself to form H_2 or reacts with O_2,

generating HO_2. OH reacts with itself to form H_2O_2. The reactive nitrogen species generally begin with the conversion of N* reacting with O_2 to form NO. Once NO forms, it can remain in that form or react with other ROS and RNS producing various N_xO_y (including NO_2, NO_3, N_2O_3, N_2O_4, and N_2O_5). Many of these N_xO_y species react with H_2O or OH producing HNO_x (including HNO_2, HNO_3, and ONOOH).

The geometry and flow conditions of the APPJ of this study are shown in Fig. 6.1a. The base case is the same as that described in Chapter 5. The APPJ is a dielectric tube (relative permittivity, $\varepsilon_r = 4$) with an inner diameter of 1 mm and an outer diameter of 1.5 mm. A powered ring electrode 1 mm wide is located 8 mm from the end of the tube and is covered with a thin shielding dielectric. The entire computational domain, using cylindrical symmetry, is 2.95 cm by 6.44 cm. The electrical ground is at the pump face, located 1.55 cm from the end of the tube and at a radius of 1.4 cm.

The fluid module for neutral gas flow was initially run for 12 ms, which was sufficient for the fluid dynamics to reach a steady state, before the voltage pulse was applied. He containing impurities of $O_2/N_2/H_2O$ = 2.4/2.9/4.7 ppm flowed through the tube at 2 slm. This choice of impurities was based on specifications from Matheson and Linde Gas for 99.999% pure He. In the cases of an admixture, the total mass flow rate remained at 2 slm, and only the composition of the gas changed. Humid air flowed into the domain through the annular area around the tube at 4 slm. This humid air flow represents the air entrainment by the helium which would occur in an open air environment and which is not captured in this limited computational domain. A pressure boundary condition of 1 atm was applied at the pump surface. The steady state axial fluid speed is shown in Fig. 6.1b.

The simplified radiation transport model included photoionization of N_2, O_2, and H_2O by He_2*, which is a lumped state of all He excimers. The plasma was initialized with a small cloud of electrons 1.4 mm in diameter at the height of the powered electrode having a peak density of 10^{11} cm^{-3}. A -10 kV pulse with a 20 ns rise time was applied to the powered electrode. The applied voltage remained at -10 kV for 130 ns, followed by a 20 ns voltage fall time, bringing the total voltage-on period to 170 ns. Poisson's equation was solved for 30 ns after the voltage returned to 0 kV (200 ns total). After this time, the plasma was assumed to be charge neutral, Poisson's equation was no longer solved, and the electron temperature (T_e) was fixed at 0.025 eV. Transport and chemistry of charged and neutral species were addressed while enforcing charge neutrality for the remainder of the simulation (16 ms total) as the RONS flowed out of the computational domain at the pump. The times that are that required for each fluid element to reach the pump surface are shown in Fig. 6.1b, which indicate that all of the RONS have exited the domain by the end of the simulation. Results will be discussed for a single voltage pulse for each condition, which limits the applicability of these results to repetition rates of hundreds of Hz to perhaps a few kHz. Higher repetition rates would result in there being significant mixing between reactants produced on previous pulses with those produced during the current pulse.

Computational diagnostics were used to characterize RONS production. The first is the *inventory* of species in the computational domain, which is the volume integral of densities. The second, more appropriate to gauge treatment of surfaces, is the number of atoms or molecules of a species flowing out of the computational domain at the pump face. This *total fluence* is the time integral of the fluxes at each point of the pump-face, which is then integrated over the area of the pump face. Diagnostics intended to measure the efficiency of production were also used.

The *specific inventory* is the inventory divided by the energy deposition during the pulse. The *specific total fluence* is the total fluence divided by the energy deposition during the pulse.

6.3 RONS Production for He APPJs with Admixtures and Impurities

6.3.1 Base Case

An overview of the ionization wave dynamics of the jet appears in Fig. 6.2. When the voltage is applied, the plasma propagates as an ionization wave (IW) beginning at the powered electrode. While propagating inside the tube, the IW intensity has a maximum at the surface of the tube, making the IW annular in shape. Upon exiting the tube, the IW follows the interface between the helium and humid air, where many of the RONS are generated. The behavior of the IW and RONS production in this APPJ with a single ring electrode was discussed in Chapter 5, and the analysis will not be repeated here.[15]

The inventories in the entire computational domain are shown as a function of time after the discharge pulse in Fig. 6.3, and demonstrate the conversion of the initially generated reactivity to more complex and stable species. At approximately 400 μs, the cloud of RONS first generated by the plasma comes into contact with the pump, and the species inventories decrease as these species exit the computational domain. Some RONS present before 1 μs are a direct result of electron impact processes by the IW. For example, N_2* and N_2(v) are a result of electron impact excitation of N_2. O_2^- forms through three body electron attachment on O_2, and O_2* is generated by electron impact excitation of O_2.

One feature of the inventories in Fig. 6.3 is that many of the dissociation products such as O, N, N*, OH, and H, trace much of their production to the afterglow. The plasma-on period is 200 ns, after which the electron temperature was fixed to 0.025 eV, resulting in most inelastic electron impact processes having a negligible rate. However, the dissociation producing these

species occurred between 1 and 10 μs. The production of these species is result of a cascade of charge exchange and electron-ion recombination reactions that occur after the plasma pulse terminates, including

$$e + H_2O^+ \rightarrow OH + H, \quad (6.1)$$

$$e + H_2O^+ \rightarrow O + H + H, \quad (6.2)$$

$$H_2O^+ + H_2O \rightarrow OH + H_3O^+, \quad (6.3)$$

$$e + O_2^+ \rightarrow O + O, \quad (6.4)$$

$$e + N_2^+ \rightarrow N + N^*. \quad (6.5)$$

These reactions are the primary source of OH, H, O, N and N* in the base case. The H_2O^+, O_2^+, and N_2^+ form by electron impact ionization, charge exchange reactions, and Penning ionization. O produced inside the tube dominantly results from dissociative recombination of O_2^+ (Eq. 6.4). O is also produced outside of the tube by dissociative excitation transfer, $N_2^* + O_2 \rightarrow N_2 + O + O$, where N_2^* is dominated by $N_2(A^3\Sigma)$.

On timescales of 100 μs, these initially produced species react with other RONS and with the surrounding humid air. O atoms, with an inventory as high as 9×10^{10} atoms, are nearly completely converted to O_3, which reaches inventories as high as 1×10^{11} molecules. H reacts with O_2 to form HO_2 as it flows out of the tube and contacts the air. To a lesser degree, some of the H recombines to form H_2. OH reacts to form 5×10^9 molecules of H_2O_2, but this occurs slowly enough that much of the OH (3×10^{10} molecules) flows out of the domain. NO primarily forms by $N^* + O_2 \rightarrow NO + O^*$, a reaction which occurs when the N*, formed inside of the tube, flows out of the tube and contacts air. NO_2 production primarily comes from $NO + HO_2 \rightarrow NO_2 + OH$ and $NO + O + M \rightarrow NO_2 + M$. Some of these RONS react through several pathways to

convert NO or NO_2 into HNO_2, HNO_3, and ONOOH. Only a fraction of the NO (with an inventory of 3×10^{10} molecules), is converted to HNO_x, which remains below 4×10^9 molecules.

The times required for RONS to transit to the pump from each point in the computational domain are shown in Fig. 6.1b. These values were calculated by integrating v^{-1}, where v is the fluid velocity, along a streamline to the pump surface. Reactants produced on-axis near the powered electrode take 0.75 ms to reach the pump, while species produced at r = 250 μm near the powered electrode require 1.1 ms to reach the pump. Species produced in the shear layer just outside of the tube take 1.7 ms to reach the pump. Viscosity results in the peak velocity to be on-axis, resulting in a longer transit time to the pump at larger radii. By 2 ms after the plasma pulse, most of the RONS have reached the pump surface.

The spatially integrated fluxes of plasma produced species integrated over the area of the pump surface as a function of time, normalized to each individual maximum flux, are shown in Fig. 6.4. Had the initial reactive species been produced as a delta-function in space and time, and the gas flow had a uniform speed, the reactants would arrive as a delta-function at the pump face. The dashed line in Fig. 6.4 represents the theoretical flux of an inert species generated uniformly inside the tube. This theoretical flux was calculated by instantaneously adding a uniform density of an inert species inside the tube in the steady state flow field, and simulating the advection and diffusion of this species as the plume flows toward the pump. The flux of this species rises sharply at 0.45 ms, when it first reaches the surface and decreases over the next 2 ms as the species which have diffused away from the axis continue to arrive at the surface. The time dependencies of the total fluxes result from several effects. Due to the spatial dynamics of the IW, reactivity is produced with a distribution of axial and radial locations. Even with a constant gas speed, reactants from these different locations would arrive at the pump face with a

distribution of time delays. Due to viscous forces, the axial flow speed is also a function of position. Species produced at the edge of the plume will be entrained in the slower shroud flow of air and arrive at the pump face considerably later. O_2*, O_2**, and N_2(v) were primarily produced outside of the tube closer to the pump, and therefore reach the pump earlier and have an earlier increase in their fluxes. The fluxes of most species increase more rapidly earlier in time than the ideal case, because there is some production of these species outside of the tube closer to the pump. These rise times indicate that O_3 and HO_2 production is largely close to the axis and at greater heights, while species such as H_2 and H_2O_2 trace their origins to larger radii deeper inside the tube.

6.3.2 Water Admixture

Water vapor is typically added to the feedstock gas with the goal of increasing the production of hydrogen containing species such as OH and H_2O_2. The admixture of H_2O to the He flow discussed in this section is in addition to the impurities that are in the base case ($O_2/N_2/H_2O$ = 2.4/2.9/4.7 ppm). The helium mole fraction was reduced when having an admixture so that the total flow rate through the tube remained constant at 2 slm. The admixture values are referred to in percent number density (i.e., mole fraction). As the H_2O admixture increased from 2.9 ppm to 0.7% (7,000 ppm), the IW speed increased, exiting the tube 46 ns earlier compared to the base case. The electron impact ionization rate in the IW increased with increasing admixture from 3×10^{19} to 7×10^{20} $cm^{-3}s^{-1}$. The maximum electron density outside of the tube at t = 200 ns increased from 8×10^{12} to 4×10^{13} cm^{-3}. The total energy deposited in the plasma as a function of the H_2O mole fraction is shown in Fig. 6.5a, and increased from 14.7 μJ to 135 μJ as the H_2O admixture increased from 2.4 ppm to 0.7%. With higher admixtures, T_e was slightly lower in the IW front (5.7 vs. 5.2 eV), and T_e thermalized more quickly after the IW

passed. The more rapid electron thermalization is due to the more rapid electron energy losses provided by low threshold inelastic collisions with H_2O, such as vibrational excitation. Penning ionization increases with H_2O admixture, resulting in higher electron density, higher conductivity, and higher energy deposition for a given voltage. Direct electron impact ionization of H_2O also occurs, but this process is not the primary source of electrons. In the base case, the rate coefficient for electron impact ionization rate of helium is about 3 orders of magnitude smaller than that of H_2O. However, the density of He is 5 orders of magnitude larger, resulting in direct electron impact ionization of He dominating over that of H_2O. Penning ionization of H_2O by He excited states becomes the primary source of electrons for admixtures above 0.02%. At 0.5% H_2O, the number of electrons generated by Penning ionization of H_2O is approximately 10 times greater than those generated by electron impact ionization reactions. The plasma more rapidly recombined when containing higher mole fractions of H_2O by recombination of electrons with $H_3O^+(H_2O)$. In the base case, the electron density decreased by an order of magnitude after about 12 μs. In the 0.7% H_2O case, this decrease in electron density occurred in 1 μs.

The volume integrated number densities, the inventories, of various RONS are shown in Fig. 6.5. These are the inventories 1 μs after the start of the voltage pulse, which largely reflect the initial RONS production. At this time, most of the initial ions have reacted or recombined, however the fluid motion has not convected species produced in the tube into the ambient. Most of the initially produced RONS increased with H_2O density, in part because the energy deposition, electron density, and IW propagation outside the tube increased with increasing H_2O admixture. The exceptions to this behavior are N and N*, which decreased with H_2O admixture, and N_2*, H_2, and O, whose inventories were maximum at 0.05% H_2O. In the base case and at low admixtures, most of the N and N* was generated in the afterglow, between 200 ns and 3 μs

by dissociative recombination, $e + N_2^+ \rightarrow N + N^*$. This process resulted in N and N* inventories as high as 1×10^{10} atoms at 1 μs. As the H_2O admixture increased, N_2^+ charge exchanged with H_2O to produce H_2O^+, resulting in little production of N or N* in the afterglow. In this case most of the N was produced by electron impact dissociation of N_2 during the voltage pulse. As the electron density and IW intensity increased with H_2O admixture, N_2^* production by electron impact reactions initially increased its inventory up to 1.5×10^{10} molecules. As the H_2O admixture increased above 0.1%, the depletion of high energy electrons by inelastic collisions with H_2O decreased the rate of electron impact excitation of N_2. Much of the O in the base case was formed between 200 ns and 3 μs after the voltage pulse by $e + O_2^+ \rightarrow O + O$ and $N_2^* + O_2 \rightarrow N_2 + O + O$. As the H_2O admixture increases, the dissociative recombination reaction $e + H_2O^+ \rightarrow H + H + O$ dominates the production of O inside the tube. As the admixture continues to increase above 0.1%, the H_2O^+ ions begin to react with H_2O ($H_2O^+ + H_2O \rightarrow H_3O^+ + OH$) instead of recombining with electrons, and less O is formed. Therefore at higher admixtures, O is predominantly produced outside the tube by reactions of N_2^* with O_2.

H_2 is largely produced by recombination of H atoms. However for a density of H of 10^{14} cm^{-3}, this conversion occurs in hundreds of ms, and so would not significantly affect the inventory at 1 μs. Wall recombination of H was the dominant source of H_2 at 1 μs, though several electron impact and recombination processes also generate H_2. The importance of wall recombination reaction in humid He plasma chemistry was investigated by Schröter *et al.*[8] As the H_2O admixture increased beyond 0.1%, the H was selectively generated outside of the tube by the more deeply penetrating IW, where it rapidly reacted with O_2 to form HO_2.

The largest change in densities of species occurred in the first 0.1% of addition of H_2O. OH, H, and H_2O_2 inventories were the most sensitive, all increasing by nearly 2 orders of

magnitude from the initial mixture to 0.1%. These species require water in their formation, and particularly benefit from dissociative recombination of H_2O^+ producing either the species themselves or their precursors. The inventories of these species were increased not only by the increased mole fraction of H_2O, but also by the increased energy deposition and plasma densities.

The inventories of species 1 μs after the start of the voltage pulse divided by the energy deposition in the plasma, referred to as the *specific inventories*, are shown in Fig. 6.6. The specific inventory of H reaches 4×10^{-3} atoms/eV, while the specific inventory of NO does not exceed 3×10^{-6} molecules/eV. As the first 0.05% of H_2O was added, the energy efficiency of the production of all RONS, except N and N*, increased. Therefore, for the first 0.05% of H_2O, the increase in most species was not solely due to the increase in energy deposition. As H_2O is added, discharge power is preferentially channeled into H_2O, thereby initially producing larger densities of H and OH leading to a greater specific inventory of H_2, H_2O_2, and HO_2. The IW also propagates more quickly as the admixture is increased to 0.05%, with a speed of 1.2×10^7 cm/s compared to 8×10^6 cm/s in the base case. As the IW exits the tube earlier in the pulse, the fraction of energy deposited outside the tube increases from 5.7% to 9.3%. The species which require the excitation of O_2 [O_2* and O_2**] and some species which are a result of dissociation or excitation of N_2 [N_2*, NO, $N_2(v)$] also have specific inventories which increased as H_2O admixture was increased up to 0.05%. These species are dominantly produced outside of the tube at these timescales, especially at low admixture concentration.

As the H_2O admixture increases from the base case to 0.05%, the dominant mechanism of O generation is $e + H_2O^+ \rightarrow H + H + O$ inside the tube, and therefore the specific inventory of O shows the same trends as that of H. At larger admixtures, hydronium production occurs more

rapidly than electron ion recombination, and the trend of O specific inventory is more consistent with that of N_2* producing O by dissociative excitation transfer to O_2.

Increasing the H_2O mole fraction above 0.1% increased the total energy deposition from 34 to 135 μJ, while resulting in diminishing incremental RONS production and decreasing specific inventory for nearly all species. The HO_2, however, has a specific inventory which continues to increase slightly with the H_2O admixture. This additional production of HO_2 results from the increase in IW speed, further penetration of the IW into the ambient and increase in the H produced outside of the tube, where it is more quickly converted to HO_2 due to the higher local O_2 density.

The total number of atoms or molecules of each species that exit the computational domain are shown in Fig. 6.7. These values, referred to as the *total fluence*, are the flux across the pump surface integrated in space and time. These fluences result from the initial reactive species shown in Fig. 6.5 after they were processed by mixing and reacting with the surrounding humid air and other RONS. The fluences of H_2O_2, HO_2, and O_3 directly follow the trends of their precursors at 1 μs – OH being the precursor for H_2O_2, H for HO_2, and O for O_3. The H_2O_2 and HO_2 total fluences are nearly unchanging above 0.05% H_2O, as were the OH and H inventories at 1 μs. The O_3 total fluence is maximum at 0.02% H_2O, and slowly decreasing with additional admixture, as is the case for O inventories. OH, H_2, N, O_2*, O_2**, and N_2(v) follow the same trends with admixture as their inventories at 1 μs, though their absolute densities change significantly between 1 μs and when they exit at the pump. Most of these species inventories decrease by a factor of 2-4 from their values at 1 μs to the pump as they undergo reactions or collisional quenching. The inventory of N_2(v) decreases more significantly, by a

factor of 10^4, due to collisional quenching. The inventory of H_2 increases by 25% as H atoms recombine on longer timescales.

The fluences of reactive nitrogen species (RNS) all significantly decreased with increasing H_2O admixture. The inventory of N* decreases with H_2O admixture (shown in Fig. 6.5) while N* is the primary precursor to rapidly forming NO at room temperature. The total fluence of NO decreases from 2×10^{10} to 1×10^9 molecules as the H_2O admixture increases. NO formation is the first step required to form most of the other RNS – NO_2, HNO_2, HNO_3, and ONOOH – and so their fluences also decrease.

The total fluences integrated at the pump divided by the total energy deposited in the plasma, referred to as *the specific total fluences*, as a function of H_2O admixture are shown in Fig. 6.8. The trends for specific total fluence as a function of H_2O admixture generally reflect the specific inventories of their precursors (shown in Fig. 6.6). The specific total fluences of H_2O_2, HO_2, and O_3, were within a factor of 5 of the specific inventories of their precursors at 1 μs and follow the same trends. OH, N, O_2*, O_2**, and $N_2(v)$ followed the same trends as at 1 μs, though the magnitudes are reduced due to reactions or collisional quenching. The H_2 specific total fluence follows the same trends as its specific inventory at 1 μs, but is larger as H continues to recombine.

The species whose production requires the dissociation of N_2 (N, NO, NO_2, and HNO_x) all had specific total fluences which decreased monotonically by 2 orders of magnitude with increasing H_2O admixture. The specific total fluences of N and NO decreased from 3×10^{-4} to 2×10^{-6} molecules/eV, while that of HNO_3 decreased from 2×10^{-5} to 3×10^{-7}. The specific RNS production decreased monotonically as the H_2O fraction increased, in spite of the fraction of energy deposited outside of the tube having a maximum at 0.05% H_2O. Even when the IW

propagation (and energy deposition) outside of the tube increases, production of N* inside the tube is still the main source of RNS production.

As the H_2O admixture is increased from 0.1% to 0.7%, the energy deposition in the plasma increases from 34 to 135 μJ, however the production of most RONS changes little. Although the energy deposited outside the nearly doubles, the fraction of energy deposited outside the tube decreases from 8.7% to 4.1%. With larger admixtures of H_2O, a larger fraction of the energy deposition is through vibrational and rotational excitation of H_2O, resulting in less efficient dissociation of H_2O.

6.3.3 Oxygen Admixture

Addition of O_2 to the He feed gas is typically performed with the goal of increasing the production of O, O_2*, and O_3. The breakdown and IW dynamics with O_2 admixtures are similar to those for an H_2O admixture. As the O_2 concentration was increased from 2.4 ppm (the *as delivered impurities*) to 0.7%, the speed of the IW increased resulting in the plasma reaching the outlet of the tube 30 ns earlier. (The IW wave arrives at the end of the tube at 74 ns for 2.4 ppm.) Electron impact ionization in the IW front increased from 1.6×10^{20} $cm^{-3}s^{-1}$ to 7.5×10^{20} $cm^{-3}s^{-1}$ and the electron density increased by a factor of 11 with increasing O_2 admixture, indicating a more intense IW.

With adding O_2 to the He flow, the electron lifetime decreased even more rapidly than for H_2O admixtures due to the more energetically favorable attachment to O_2. The thermal rate coefficient for 3-body electron attachment to O_2 is 2×10^{-31} cm^6s^{-1}. Dissociative electron attachment to H_2O has a threshold energy of 4.3 eV. For the 0.7% O_2 case, n_e in the tube decayed to 9×10^8 cm^{-3} within 600 ns, whereas at this time for the base case, $n_e = 5 \times 10^{12}$ cm^{-3}. The total energy deposition increased monotonically with O_2 admixture, starting at 14.7 μJ for

the base case and increasing to 127 μJ for 0.7% O_2. As the mole fraction of O_2 increased, the electron density increased from 3×10^{12} to 9×10^{12} cm^{-3} while T_e remained similar in the IW front ($T_e \approx 5.8$ eV), but was elevated for a shorter time (lower T_e in the bulk plasma). The rate of energy loss by electrons after the initial IW propagation was more rapid for larger O_2 mole fractions due to the higher rate of energy loss collisions with the molecular additive.

The energy deposition and volume integrated number densities (or inventories) of RONS as a function of O_2 admixture at 1 μs after the voltage pulse are shown in Fig. 6.9. The energy deposition initially increases with the O_2 admixture as Penning ionization increases and the ionization rate, electron density, and conductivity increase. At larger admixtures electron attachment to O_2 begins to reduce this conductivity and limit further increases in energy deposition. The species with initial inventories which increased with O_2 admixture include O_2*, O_2**, O, O_3, and N_2(v). The production of O_2* and O_2** was a direct result of the increase in electron impact collisions with O_2. The production of O increased as a result of increasing electron densities, with O_2^+ being the dominant ion leading to O formation by $e + O_2^+ \rightarrow O + O$. The inventory of O_3 initially increased with O_2 admixture because its production is a direct consequence of O formation. The N_2(v) increased due to increased energy deposition and further propagation of the faster IW outside of the tube. A few species have inventories which decreased monotonically with O_2 admixture, including H, H_2, N, and N*. As more O_2 was added, H_2O^+ and N_2^+ charge exchanged with O_2, which prevented these ions from undergoing the dissociative recombination reactions which are a dominant source of N, N*, and H: $e + N_2^+ \rightarrow N + N^*$ and $e + H_2O^+ \rightarrow OH + H$.

The other species with significant densities at this time, OH, NO, HO_2, and N_2* have a maximum inventory at an intermediate O_2 admixture. At low O_2 admixture, OH was dominantly

produced during the first μs inside the tube by dissociative recombination, $e + H_2O^+ \rightarrow OH + H$. Following this initial sourcing of OH, most of the OH production occurred later by formation of hydronium, $H_2O^+ + H_2O \rightarrow H_3O^+ + OH$. As the O_2 density increased, the production of OH inside the tube fell as H_2O^+ charge exchanged with O_2 instead of undergoing dissociative recombination. The production of OH outside of the tube increased as the IW propagated more rapidly with a larger O_2 admixture. These effects roughly balanced at 1 μs and the result was a weak dependence of OH on O_2 admixture, with an inventory around 6×10^9 molecules.

In the base case, NO was primarily formed outside of the tube by $N^* + O_2 \rightarrow NO + O^*$, as the N* produced in the tube flowed out into the ambient. As the O_2 admixture increased, this reaction could also occur inside the tube, producing NO more rapidly. However, as the admixture increased further (> 0.1%) N_2^+ rapidly charge exchanged with O_2, instead of undergoing dissociative recombination. As a result, the maximum inventory of NO was 2×10^9 atoms at 0.1% O_2. HO_2 is produced by $H + O_2 + M \rightarrow HO_2 + M$. Initially the increasing O_2 increased the rate of this reaction and so increased the amount of HO_2 produced at short times. However, further increasing O_2 decreased the production of H, eventually limiting the early production of HO_2. Initially the N_2^* density increased with O_2 admixture as the electron density and IW propagation outside of the tube increased. As the O_2 admixture further increased, the inventory of N_2^* decreased because it is rapidly quenched by reactions with O_2.

The inventories of species 1 μs after the voltage pulse divided by energy deposition, the specific inventories, are shown in Fig. 6.10 for O_2 admixtures. OH, N, H, H_2, N*, and HO_2 have specific inventories that monotonically decreased as the O_2 admixture increased. The specific inventories decreased as H_2O^+ and N_2^+ increasingly charge exchanged with O_2, which prevented their dissociative recombination reactions, the source of these species. The specific inventory of

HO_2 decreased because its formation requires H. The specific inventory of HO_2 is less sensitive to admixture as the increase in O_2 allows for faster conversion of H to HO_2.

O, O_2*, O_2**, O_3, N_2*, N_2(v), and NO have specific inventories with a more complex dependence on O_2 admixture. The maximum fraction of energy deposited outside of the tube, 10.2%, occurs for 0.02% O_2, while the total energy deposited outside the tube increases from 0.8 to 6.5 μJ with admixture. Several species have specific inventories with a local maximum at 0.02%, including N_2(v), NO, O, and O_3. N_2(v) is dominantly produced outside the tube, and so its specific inventory correlates with the fraction of energy deposition outside of the tube. As a result of this energy deposition outside of the tube, N* is formed close to the interface between the He and air, enabling production of NO by $N^* + O_2 \rightarrow NO + O^*$ to occur on these short timescales. The O inventory increases monotonically with O_2 admixture, but as the admixture is increased beyond 0.02%, much of the additional energy does not contribute to dissociation of O_2. The rapid attachment of electrons limits the production of O by $e + O_2^+ \rightarrow O + O$, and instead O_2^+ is consumed by ion-ion neutralization – $O_2^+ + O_2^- \rightarrow O_2 + O_2$. As the O_2 admixture increases above 0.2%, the O specific inventory increases, as the admixture results in more electron impact dissociation of O_2* (i.e. two-step dissociation). O_3 has a similar behavior as its precursor, O, but with a less significant peak at 0.02% O_2. The conversion from O to O_3 occurs more slowly at lower admixtures (such as 0.02%), and so the specific inventory is low in spite of a larger inventory of O.

O_2* and O_2** have specific inventories which monotonically increase with O_2 admixture, except for a slight decrease between 0.05% and 0.1% (less efficient). This minimum occurs as the production of these species transitions from being dominantly produced outside of the tube in the base case to dominantly inside the tube at higher admixtures.

N_2* is primarily produced outside of the tube and has a specific inventory that peaks at 8 $\times$ 10^{-5} molecules/eV with 0.01% O_2. As the O_2 fraction increases, the energy deposited outside of the tube increases, but the quenching rate of N_2* also increases and the combination of these effects leads to the local maximum in N_2*.

The integrated fluences of species that exit the computational domain as a function of O_2 admixture are shown in Fig. 6.11. Only a few of these fluences increase monotonically with O_2 admixture, including O_2*, O_2**, and N_2(v). The fluences of O_2* and O_2** increase because both n_e and the O_2 density increased and these species are a direct result of electron impact reactions. N_2(v) is primarily produced outside of the tube, and its fluence increased as the propagation of the IW outside of the tube increased.

Most RONS fluences monotonically decreased with O_2 admixture, including OH, HO_2, H_2, H_2O_2, NO, N, NO_2, HNO_3, ONOOH, and HNO_2. These species are produced by reactions involving OH, H, N, and N*, which are dominantly produced by dissociative recombination of H_2O^+ and N_2^+. Adding O_2 results in charge exchange reactions which rapidly deplete these ion densities prior to dissociative recombination.

The fluences of O_3 and O have a more complex behavior as a function of O_2 admixture. By the time the reactive plume reaches the pump, most of the O has converted into O_3. The primary mechanism of O production at low admixtures is $e + O_2^+ \rightarrow O + O$. At higher O_2 densities, electron impact processes dominate in producing O, in particular $e + O_2^* \rightarrow O^* + O + e$. As a result, the O_3 fluence initially increased (due to increasing O_2^+ production), reaching 5 $\times$ 10^{11} molecules, then decreases as the electron attachment to O_2 occurs faster than recombination with O_2^+. At O_2 mole fractions greater than 0.1%, the O_3 fluence increases with admixture because of the increase in two step dissociation of O_2*. The O fluence decreases to 7 $\times$ 10^7

atoms as the admixture increases up to 0.05% O_2 as a result of faster conversion to O_3. For admixtures greater than 0.05%, there is some long timescale production of O by the quenching of O_3 ($O_2^* + O_3 \rightarrow O_2 + O_2 + O$ and $O_2^{**} + O_3 \rightarrow O_2 + O_2 + O$).

The total fluences divided by the energy deposition as a function of O_2 admixture are shown in Fig. 6.12. The specific fluences of O_2^*, O_2^{**}, OH, N, and $N_2(v)$ follow the same trends as their specific inventories at 1 μs, though quenching and reactions deplete the initial inventories. $N_2(v)$ still has a local maximum at 0.02% O_2, while O_2^* and O_2^{**} still generally increase with admixture, except for a slight decrease between 0.05% and 0.1% O_2. The trends of the specific total fluence of O_3, H_2O_2, H_2, and HO_2 follow the same trends as the specific inventory of their precursors – O for O_3, OH for H_2O_2, and H for HO_2 and H_2. O_3 has a local maximum at 0.02% O_2, which is consistent with the trends for O atoms at 1 μs. The specific total fluence for H_2O_2 decreases by approximately 2 orders of magnitude as the first 0.1% O_2 is added, while the specific inventory of OH decreases by approximately an order of magnitude in this range. The H specific inventory decreased by more than 2 orders of magnitude as the admixture increased to 0.7%, as did the specific total fluences of HO_2 and H_2. NO_2 and HNO_x, have specific fluences which monotonically decrease with O_2 admixture because they are formed from NO, and therefore their efficiency of generation generally follow the trends for NO. The significant decrease in the specific inventory of NO is a result of rapid charge exchange from N_2^+ with O_2, limiting dissociative recombination which forms N* and leads to NO production. The specific total fluence of NO decreases from 3×10^{-4} to 2×10^{-6} molecules/eV as the O_2 admixture is increased to 0.7%. The specific fluence of O has a minimum at 0.2% O_2, for the reasons described above (rate of conversion to O_3 verses production of O by reaction of O_3 with O_2^* or O_2^{**}).

6.3.4 Comparing Admixtures

The consequences of H_2O and O_2 admixtures on RONS production are compared in Fig. 6.13. The total energy deposition, shown in Fig. 6.13a, increases more rapidly when adding O_2 before leveling off around 0.5% O_2. Electron attachment to O_2 begins to limit the electron density during the voltage pulse and therefore the energy deposition at higher admixtures. The more rapid initial rise in energy deposition with O_2 admixture is due to the lower power deposition in non-ionizing collisions in O_2 enabling a higher electron density compared to H_2O. The energy deposition increases nearly linearly with H_2O admixture as attachment has a relatively minor effect on the electron density on timescales of the voltage pulse. Adhakari *et al*. observed a sharper current rise when O_2 or H_2O was added to a He APPJ with a 1 ms voltage pulse. This observation is consistent with the increased energy deposition for the shorter voltage pulse predicted in this study.

The reactive species produced with each admixture can be grouped into RNS (N, NO, NO_2, and HNO_x), hydrogen containing ROS (H-ROS: OH, H_2O_2, and HO_2), and ROS not containing hydrogen (O-ROS: O, O_2*, O_2**, and O_3). H_2 and N_2(v) have not been included in this analysis as they are less reactive and are not typically considered RONS. The sum of the total fluences of each group of species is shown in Fig. 6.13b. The most abundant RNS are N and NO. The most abundant H-ROS are OH and H_2O_2, and the most abundant O-ROS is O_3. Adding the first 0.15% of either H_2O or O_2 decreases the RNS fluence by an order of magnitude. Any N_2^+ formed from the impurities charge exchanges with the admixture before undergoing dissociative recombination to form N*. Above 0.15%, the RNS production is relatively insensitive to admixture. This portion of the RNS generation is primarily a result of electron impact reactions with N_2 inside the tube as well as production outside of the tube, rather than the

dissociative recombination of N_2^+. This behavior was observed with NO measurements by van Gessel *et al*. upon adding O_2 to an Ar APPJ.[16]

The selectivity of producing RONS with H_2O compared to O_2 admixtures is also shown in Fig. 6.13b. Adding O_2 increases O-ROS, but decreases H-ROS. O_2 has a lower ionization potential than H_2O. H_2O^+ which is formed from impurities charge and which exchanges with O_2 before undergoing dissociative recombination disrupts the production of OH and H. Adding H_2O increases both H-ROS and O-ROS. This lack of specificity is due to the production of O from H_2O dissociation, and charge exchange from H_2O^+ to O_2 impurities, followed by dissociative recombination of O_2^+.

6.3.5 Impurities

The base case used a gas mixture based on expected impurities in ultra-high purity helium as provided by gas suppliers. In this section, the IW and RONS generated by the base case (with impurities in the He of $O_2/N_2/H_2O$ = 2.4/2.9/4.7 ppm) are compared to a case that uses absolutely pure helium flowing into the tube. This comparison contrasts the ideal plasma jet to a more common plasma jet where the He is not additionally purified from its *as delivered* composition to reduce the role of these impurities. Impurities from the ambient can also certainly contaminate even absolutely pure He, but since those sources are usually system specific due to leak rates and bake-out procedures, they will not be discussed here. S_e, n_e, and T_e during the 200 ns plasma-on period were nearly indistinguishable for the pure-He case due to the impurities being at such a low concentration. The total energy deposition in the base case with *as delivered impurities* was 14.7 μJ, and 14.2 μJ without impurities. During the afterglow, the electron density had a slightly faster decay rate in the base case because of the possibility of attachment reactions inside the tube.

The cascade of charge exchange and dissociative recombination that occurred inside the tube in the base case, producing much of the RONS, does not occur in the absence of impurities. Without impurities, the dominant positive ion was He_2^+ and the dominant negative species was electrons well into the afterglow. In contrast, by 5 μs into the afterglow in the base case, the dominant positive ion was O_2^+. The fluences of RONS which were collected at the pump were significantly influenced by the impurities. The differences in the fluences of RONS generated by the base case compared to the ideal case can be attributed to the impurities. These differences are shown as a percent of the total generation of the base case in Fig. 6.14. These values were calculated by running one simulation with impurities (the base case) and one with absolutely pure helium, and calculating the percent difference in the total integrated fluences collected at the pump. For nearly all species, the impurities were responsible for more than 70% of the generation of the RONS. The exceptions are O_2*, O_2** and N_2(v). O_2** actually showed an increase in its fluence in the case of absolutely pure He. In the base case, these species were mainly produced outside of the tube during the plasma-on period, so they were relatively insensitive to impurities.

These results are highly sensitive to the time and length of propagation of the IW in the ambient compared to the time of propagation in the tube. For example, moving the powered electrode closer to the end of the tube (from 8 mm to 3 mm) results in the IW propagating further into the ambient. The IW extends 4 mm from the end of the tube when the powered electrode is moved closer to the end of the tube, compared to 3 mm in the base case. The energy deposited outside of the tube increases from 0.8 to 5.1 μJ.[15] This change in the IW propagation leads to greater RONS production, and more of the reactivity being generated outside of the tube. The sensitivity of RONS production to the impurities in the He flow is up to 26% lower than for the

base case, as shown in Fig. 6.14. This is in part because more RONS are produced in the 3 mm case than the base case and so the contributions of the impurities are smaller fractions of the total RONS.

Including an intentional molecular admixture also reduces the consequences of the impurities on RONS production, as shown in Fig. 6.15. The production due to impurities was calculated by repeating the simulations without the 10 ppm impurities in the He flow in the case of 0.5% H_2O and 0.5% O_2. The concentration of admixture, however, was kept constant even when removing impurities. For example, when the 0.5% H_2O case was repeated without impurities, only the N_2 and O_2 flowing into the tube were removed, and the H_2O mole fraction was unchanged. The total fluence at the pump was then subtracted from the case containing impurities to yield the production due to impurities, which is shaded on Fig. 6.15. Both admixtures significantly reduce the fraction of RONS production that is a result of impurities.

With an H_2O admixture, the production of species which originate from H_2O dissociation (OH, HO_2, H_2, and H_2O_2) are independent of having impurities because the H_2O density is the same with and without impurities. O_3 production is also nearly independent of impurities with an H_2O admixture (impurities contribute <0.1%) because the production of O, its precursor, occurs inside the tube primarily by $e + H_2O^+ \rightarrow O + H + H$. The production of excited states [O_2*, O_2**, $N_2(v)$] tend to be much less dependent on impurities because they are primarily generated outside of the tube. 10-45% of the production of nitrogen containing species is still a result of the N_2 impurities in the He even with H_2O admixtures. Though the fraction of production due to impurities, remains above 10% for RNS, the total of amount of RNS produced is also reduced by the addition of an admixture. Therefore the production of, for example, NO by impurities decreases from 2×10^{10} molecules for the base case to 3×10^{8} molecules when an

H_2O admixture is present. The decrease in the contribution of impurities to RNS production with admixtures results from charge exchange depleting the N_2^+ before dissociative recombination can produce the N and N* precursors. The energy deposition outside of the tube is also larger, so more RNS are produced outside the tube, where the gas composition is independent of impurities.

For an O_2 admixture, O_3 and O production are not dependent on impurities, because they are a result of dissociation of O_2 in the tube, which does not change based on the H_2O or N_2 impurities. The species which require the dissociation of H_2O (OH, HO_2, H_2, and H_2O_2) attribute 20-80% of their production to impurities, with a significant portion of the H_2O dissociation occurring inside the tube. The RNS generation is less dependent on the impurities with an O_2 admixture (3-32%) than a H_2O admixture. In addition to the charge exchange that depletes N_2^+ densities, rapid electron attachment occurs in the presence of O_2. N_2^+ is more likely to undergo ion-ion recombination ($O_2^- + N_2^+ \rightarrow O_2 + N_2$) rather than the dissociative recombination which facilitates NO formation ($e + N_2^+ \rightarrow e + N + N^*$). As a result, an O_2 admixture makes the RNS production even less sensitive to impurities than an H_2O admixture.

These results indicate that an admixture can be used to improve the control and consistency of the chemistry generated by an APPJ, rather than having reactive species production depend on the impurities in the gas supply which may not be well controlled or well known.

6.4 Concluding Remarks

This computational investigation has shown that the addition of a molecular admixture to a He atmospheric pressure plasma jet can have a significant impact on the ionization wave propagation speed, electron density, electron temperature, initial RONS production, and the final chemistry which is delivered in the effluent. In the base case, which contained *as delivered*

impurities in the helium, most of the dissociation occurred in the cascade of charge exchange and dissociative recombination in the afterglow, rather than during the discharge pulse. At constant voltage, adding an H_2O or O_2 admixture as high as 0.7% increased the energy deposition and the IW speed due to increased Penning ionization. The majority of the effects on the chemistry were achieved within the first 0.1% of admixture, above which changes in composition began to saturate.

For H_2O admixtures, rapid charge exchange depleted the density of N_2^+ resulting from the base *as delivered impurities*, decreasing the production of N*, and therefore the production of NO and all other RNS. H_2O_2, OH, H_2, and HO_2 fluences increased as these species are all a result of chemistry originating from H_2O dissociation. The production of O_3 and O generally increased, but had a more complex dependence as the mechanism of production shifted from dissociative recombination of O_2^+ to that of H_2O^+. The production efficiency of H_2O_2, OH, H_2, and HO_2 reach their maxima between 0.01% and 0.05% H_2O. Adding H_2O beyond this value significantly increased the energy deposition, while only slightly increasing the production of these species.

O_2 admixtures decreased the fluences of all RNS and the species which require the dissociation of H_2O. Significant O_2 in the He flow resulted in rapid charge exchange to consume N_2^+ and H_2O^+, which would otherwise undergo dissociative recombination. O fluences had a local minimum at 0.05% O_2. Below this value, O reached the pump face prior to reacting with O_2 to form O_3. Above this value, the slow quenching of O_3 by O_2* and O_2** generated significant amounts of O downstream. The O_3 fluence had a non-monotonic dependence on admixture because the primary production pathway for O atoms changed from dissociative recombination of O_2^+ at low admixture to electron impact dissociation of O_2* at large admixture.

The production efficiency of species that require the dissociation of H_2O or N_2 decreased monotonically as the O_2 admixture increased. The O_3 production efficiency was maximum at 0.01% O_2, while the energy efficiency of O_2* and O_2** generally increased with admixture.

Without intentional admixtures, manufacturer stated impurities accounted for 79-98% of the O_3, NO, N, HO_2, OH, H_2, H_2O_2, HNO_3, ONOOH, NO_2, O and HNO_2 fluences which reach the pump. APPJs having a larger energy deposition outside of the tube or using O_2 or H_2O admixtures reduces the sensitivity of RONS generation to impurities at the ppm level and may provide better control of that generation.

The addition of O_2, because it has a lower ionization energy than N_2 or H_2O, provides more selectivity as it only increases the production of O, O_3, O_2*, and O_2**, and decreases the production of RNS and hydrogen-containing ROS (OH, H_2O_2, HO_2). The tradeoff is that the production of hydrogen-containing ROS, while lower, is still sensitive to impurities at the ppm level (which are often uncontrolled). H_2O admixtures demonstrate less selectivity in RONS production as increasing the H_2O mole fraction tends to increase the production of all ROS. This decreased selectivity has the advantage of making the production of all of the ROS nearly independent of impurities in the helium.

6.5 Figures

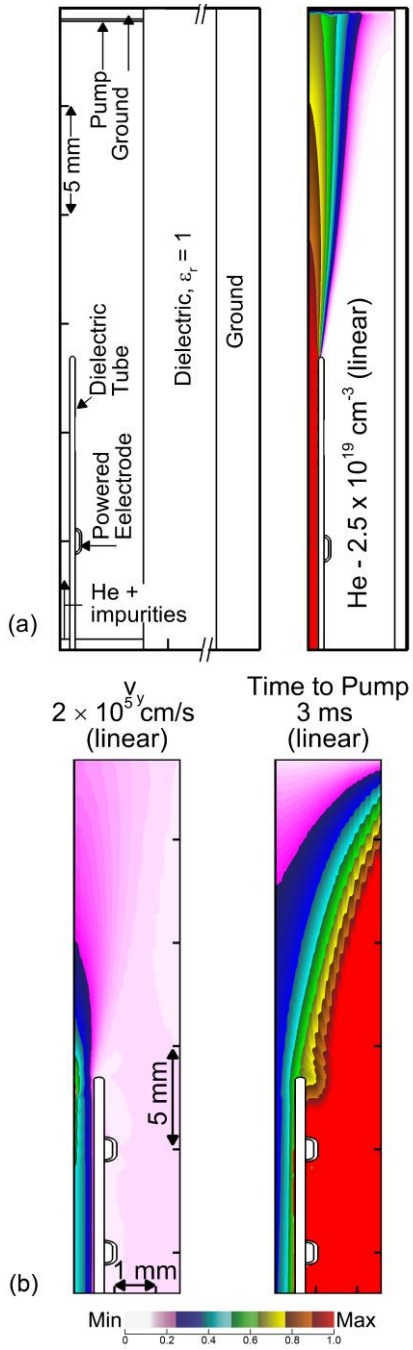

Fig. 6.1 Computational geometry and flow dynamics for the base case simulations. (a) (left) Geometry and (right) steady state He density. The dielectric tube has a 1 mm inner diameter. (b) (left) Axial component of the fluid velocity and (right) time to reach the pump from each point in the computational domain.

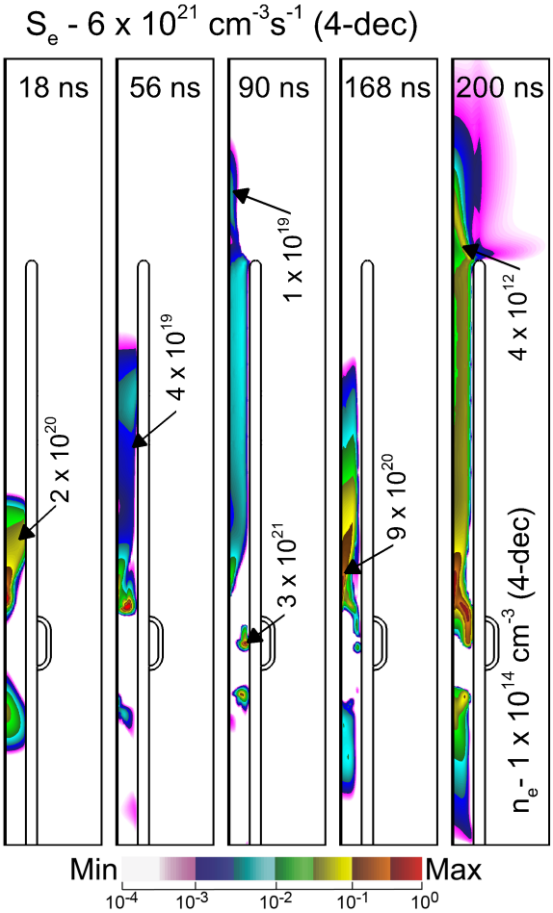

Fig. 6.2 Ionization wave propagation in the base case atmospheric pressure plasma jet. S_e is the electron impact ionization source term, shown in the left four frames. The electron density, n_e at the end of the voltage pulse is in the rightmost frame. The values are plotted on a 4-decade log scale with the maxima indicated on the figure.

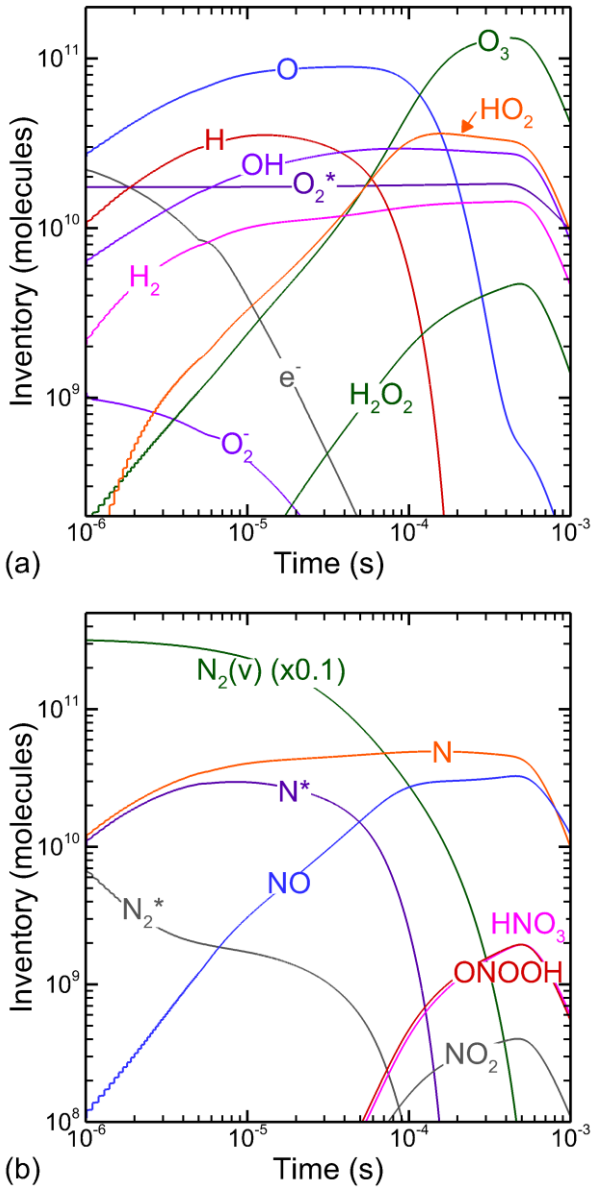

Fig. 6.3 The inventory (volume integrated number density) of reactive species as a function of time after the start of the voltage pulse. At 400 μs reactive species reach the pump and begin exiting the computational domain. The plots have been smoothed. (a) Species which do not contain nitrogen. (b) Species which contain nitrogen.

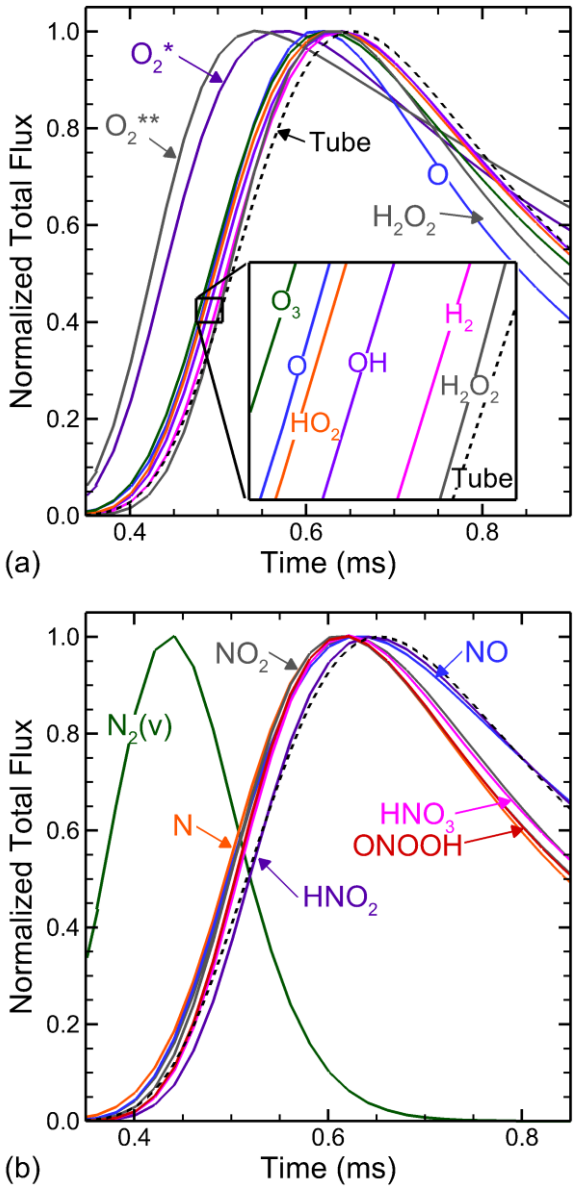

Fig. 6.4 The flux of plasma produced species at the pump as a function of time in the base case. The values are normalized to the maximum flux for each species. There is a delay following the voltage pulse before a significant flux arrives at the pump, which indicates the location of production based on Fig. 1b. The dashed line is the resultant flux from the simple case of an unreactive species generated uniformly within the tube. (a) ROS and (b) RNS.

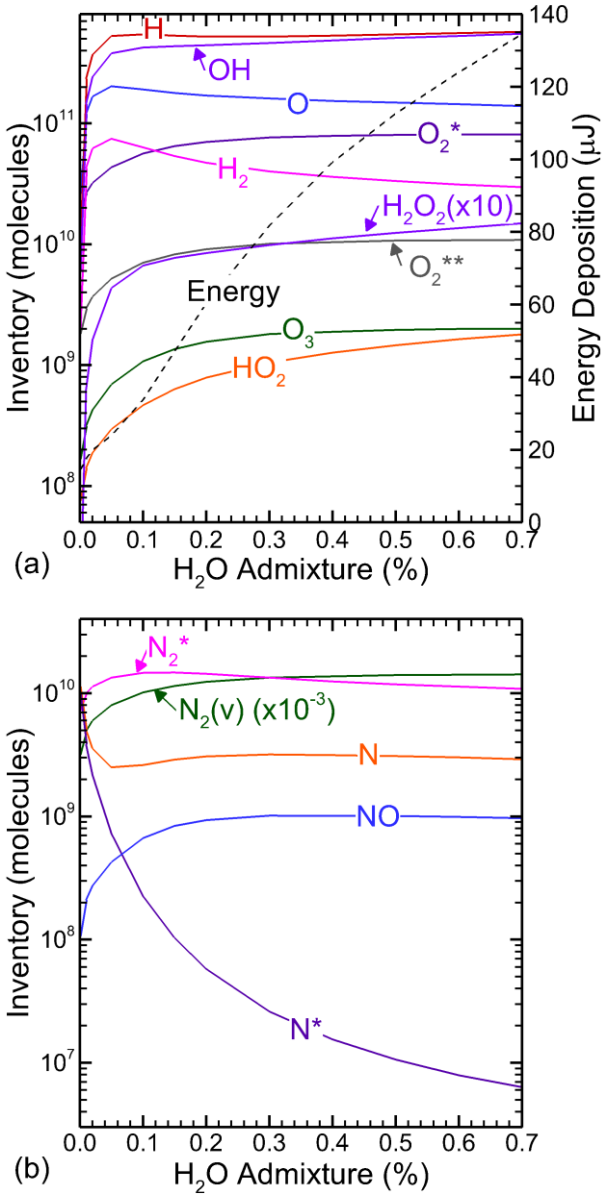

Fig. 6.5 The inventory of RONS at 1 μs after the start of the voltage pulse as a function of H_2O admixture in the He flow. (a) ROS and (b) RNS.

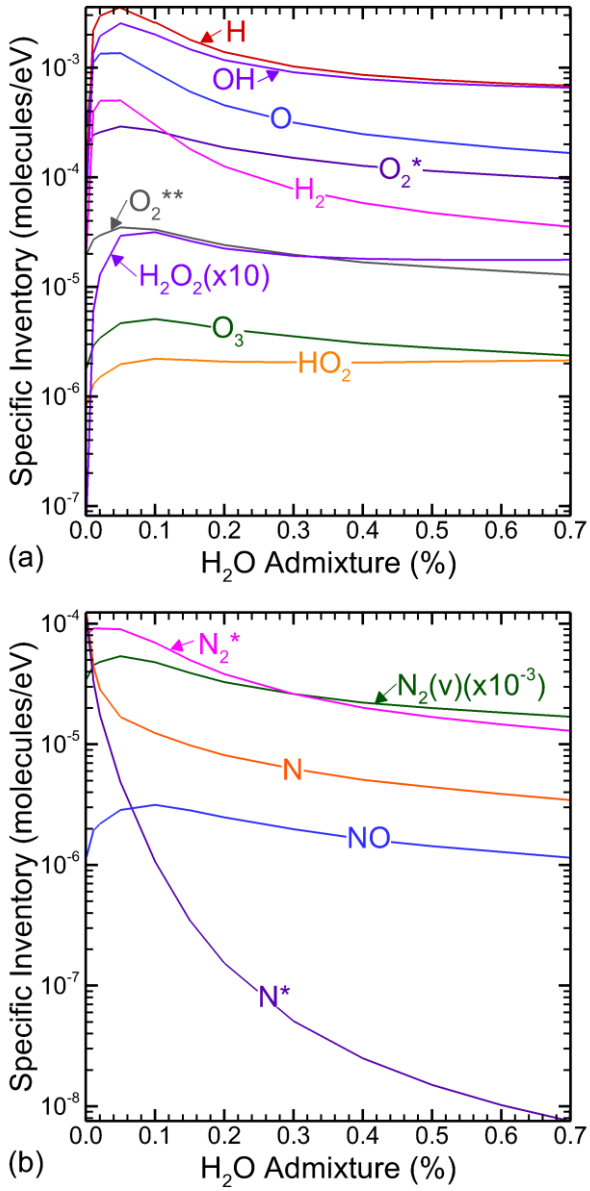

Fig. 6.6 The inventory of RONS at 1 μs after the start of the voltage pulse per eV of energy deposition in the plasma (the specific inventory) as a function of H_2O admixture in the He flow. (a) ROS and (b) RNS.

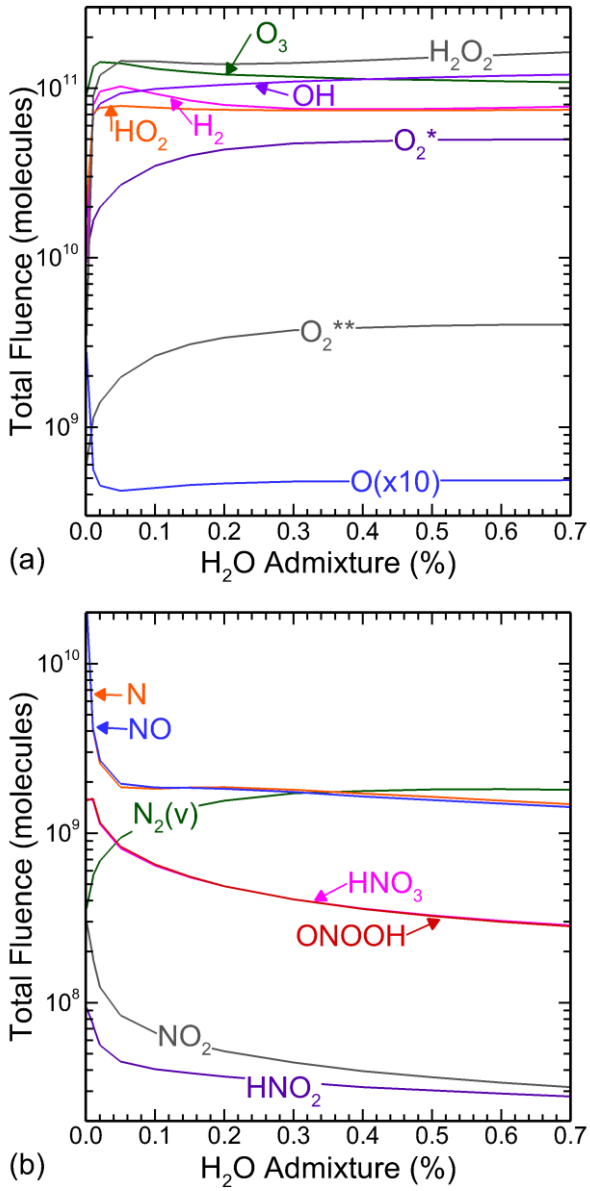

Fig. 6.7 The total fluence of RONS crossing the pump as a function of H_2O admixture in the He flow. The fluence was integrated across the area of the pump surface which yields the total number of molecules exiting the computational domain. (a) ROS and (b) RNS.

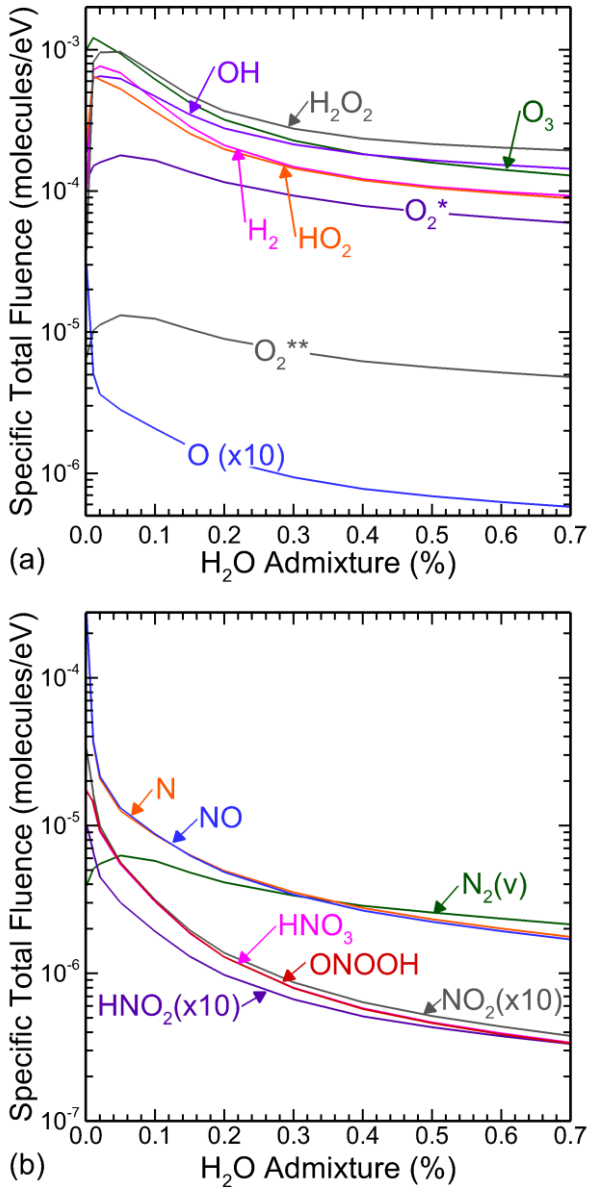

Fig. 6.8 The total fluence of RONS across the pump surface per eV of energy deposition in the plasma (the specific total fluence) as a function of H_2O admixture to the He flow. (a) ROS and (b) RNS.

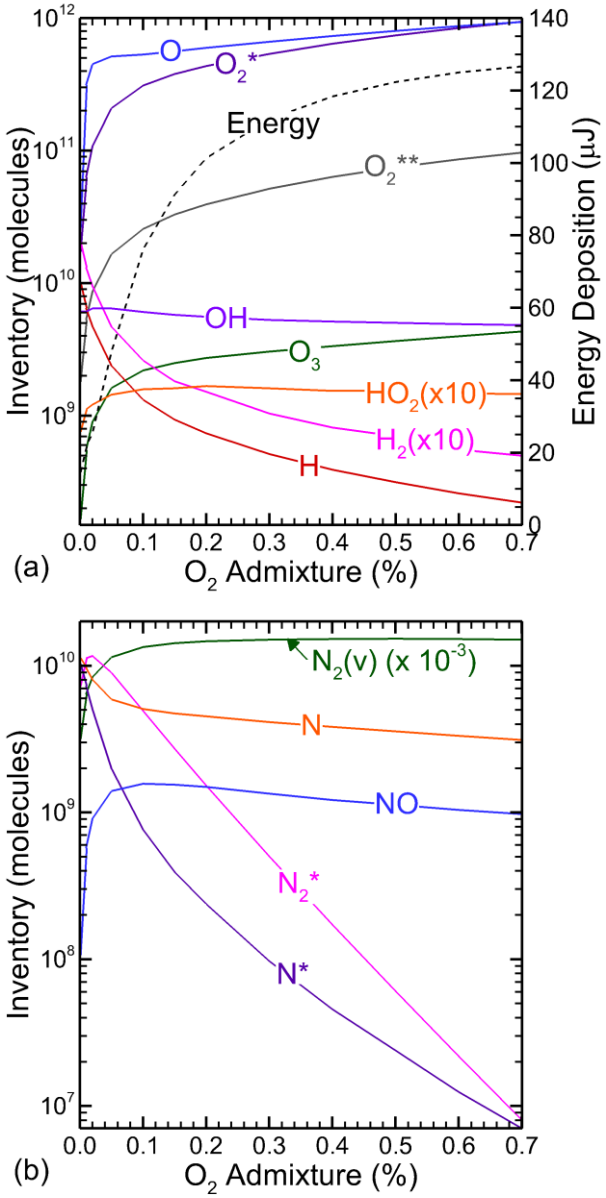

Fig. 6.9 The inventory of RONS 1 μs after the start of the voltage pulse as a function of O_2 admixture to the He flow. (a) ROS and (b) RNS. The energy deposited in the plasma is also plotted in (a).

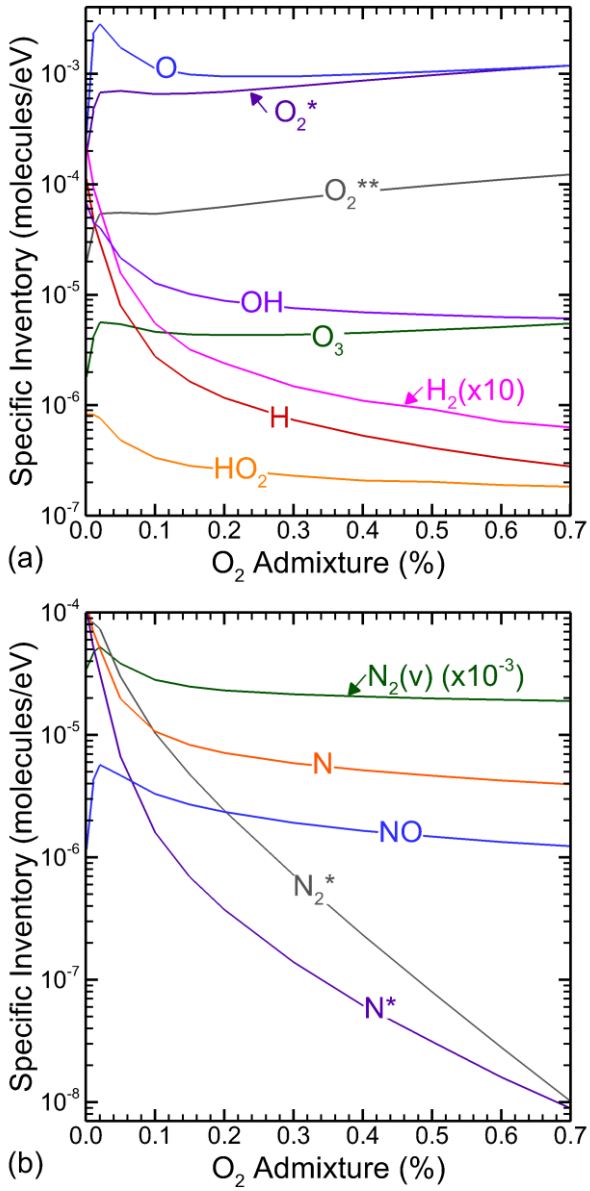

Fig. 6.10 The inventory of RONS at 1 μs after the start of the voltage pulse per eV of energy deposition in the plasma (the specific inventory) as a function of O_2 admixture. (a) ROS and (b) RNS.

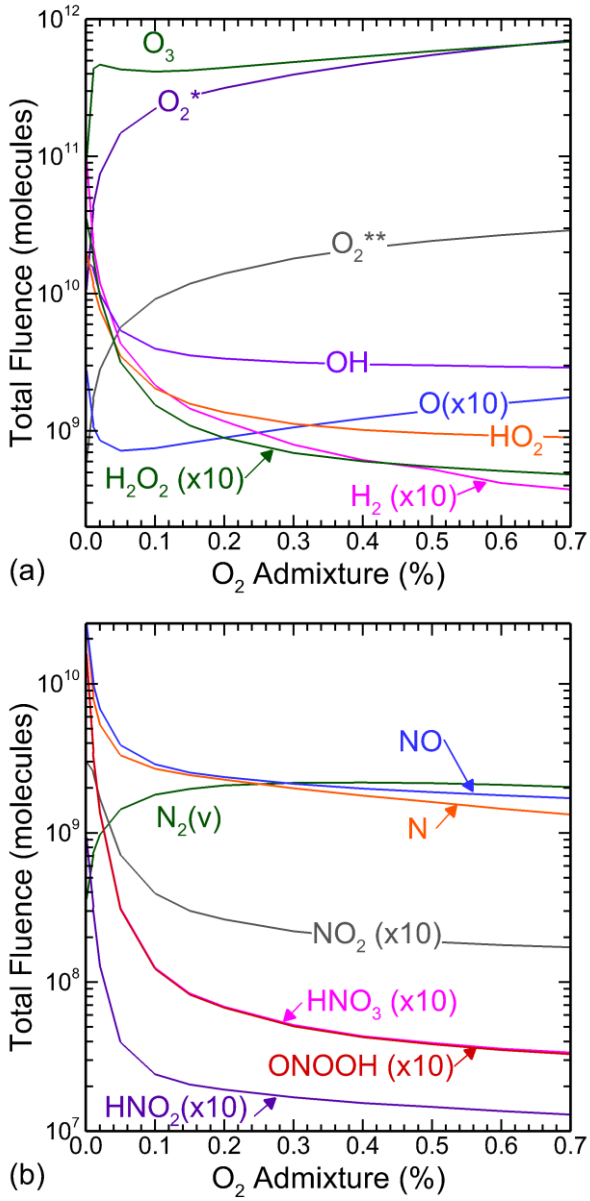

Fig. 6.11 The integrated fluence of RONS across the pump as a function of O_2 admixture to the He flow. Despite increasing energy deposition, the fluences of many RONS decrease with increasing O_2. (a) ROS and (b) RNS.

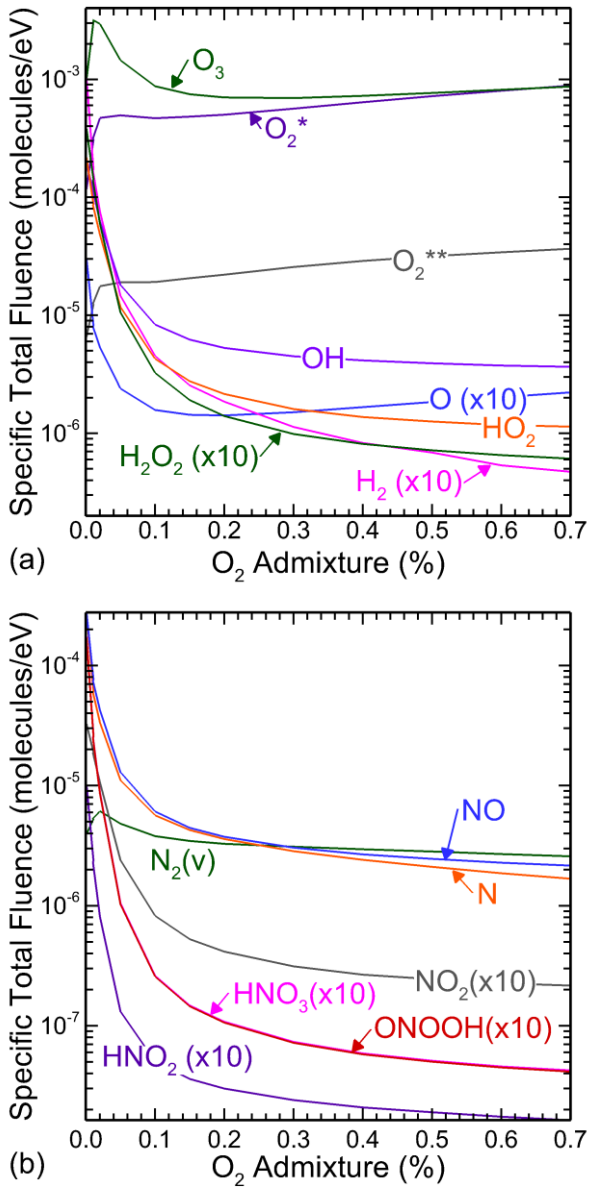

Fig. 6.12 The total fluence of RONS exiting through the pump per eV of energy deposition in the plasma (the specific fluence) as a function of O_2 admixture to the He flow. (a) ROS and (b) RNS.

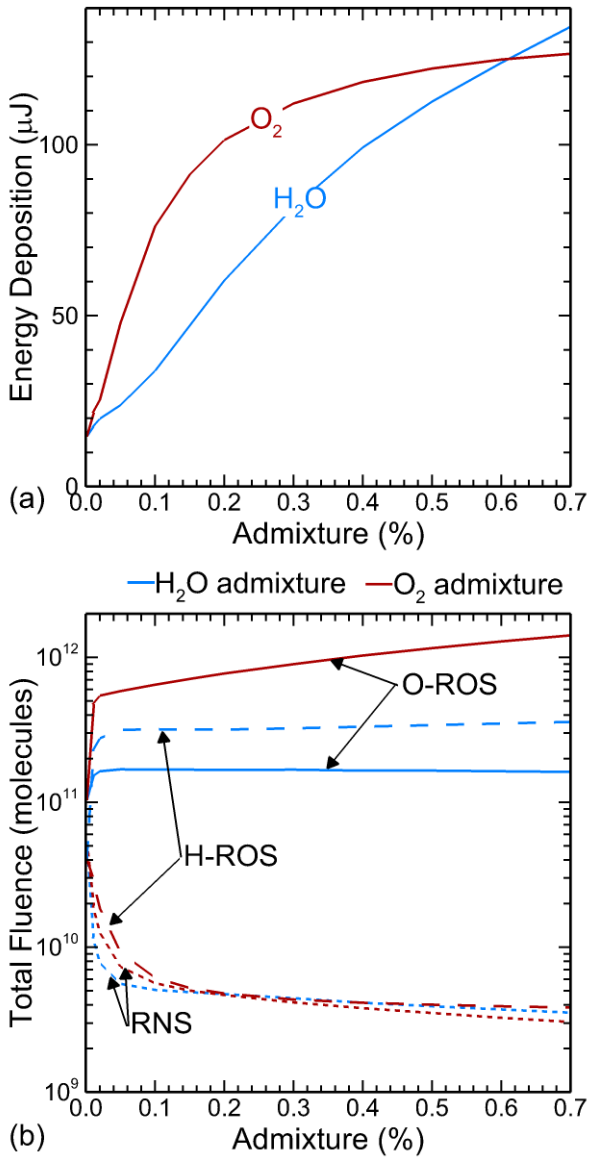

Fig. 6.13 Comparison of trends for H_2O and O_2 admixtures. (a) Energy deposition. (b) Fluences of hydrogen containing ROS (H-ROS) including the sum of OH, H_2O_2, and HO_2, ROS which do not contain hydrogen (O-ROS) including O, O_2*, O_2**, and O_3, and RNS including N, NO, NO_2, HNO_2, HNO_3, and ONOOH.

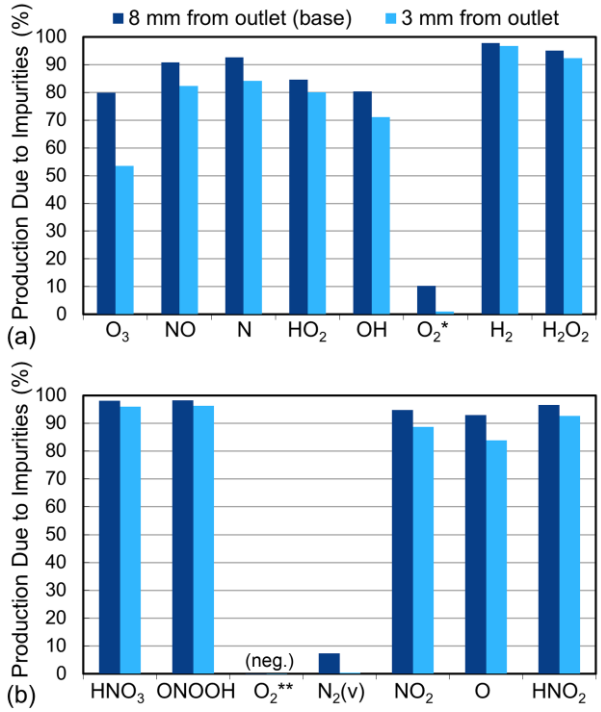

Fig. 6.14 Percent of the production in the base case of RONS that can be attributed to humid air impurities in the He totaling 10 ppm. These values were obtained by repeating the simulation without impurities and comparing the total fluences of RONS crossing the pump surface. Species are listed from left to right in order of decreasing total fluence. This value depends on the position of the powered electrode, with results shown here for the powered electrode being 8 mm from the outlet (the base case) and 3 mm. (a) O_3, NO, N, HO_2, OH, O_2*, H_2, and H_2O_2. (b) HNO_3, ONOOH, O_2**, N_2(v), NO_2, O, and HNO_2.

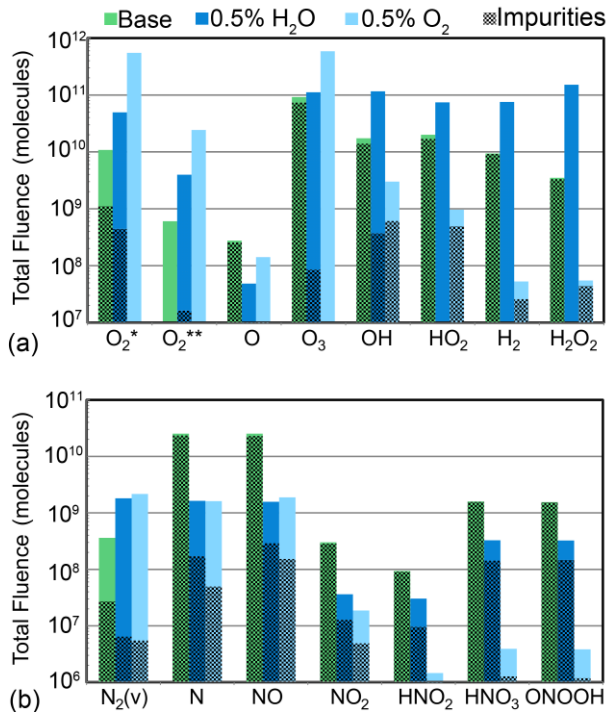

Fig. 6.15 Total fluence of RONS for the base case, a 0.5% H_2O admixture, and a 0.5% O_2 admixture. The amount of each species fluence can be attributed to humid air impurities in the He totaling 10 ppm is shaded. (a) ROS and (b) RNS.

6.6 References

[1] G. Bauer and D. B. Graves, Plasma Process. Polym. **13,** 1157 (2016).

[2] D. B. Graves, Clin. Plasma Med. **2,** 38 (2014).

[3] P. Bruggeman, F. Iza, D. Lauwers and Y. A. Gonzalvo, J. Phys. D: Appl. Phys. **43,** 12003 (2010).

[4] T. Verreycken, R. Mensink, R. van der Horst, N. Sadeghi and P. J. Bruggeman, Plasma Sources Sci. Technol. **22,** 055014 (2013).

[5] N. Knake, S. Reuter, K. Niemi, V. Schulz-von der Gathen and J. Winter, J. Phys. D: Appl. Phys. **41,** 194006 (2008).

[6] G. V. Naidis, Plasma Sources Sci. Technol. **23,** 065014 (2014).

[7] G. Park, H. Lee, G. Kim and J. K. Lee, Plasma Process. Polym. **5,** 569 (2008).

[8] S. Schröter, A. R. Gibson, M. J. Kushner, T. Gans and D. O'Connell, Plasma Phys. Control. Fusion **60,** 014035 (2018).

[9] H. M. Joh, J. Y. Choi, S. J. Kim, T. H. Chung and T.-H. Kang, Sci. Rep. **4,** 6638 (2014).

[10] S. Bekeschus, K. Wende, M. M. Hefny, K. Rödder, H. Jablonowski, A. Schmidt, T. von Woedtke, K.-D. Weltmann and J. Benedikt, Sci. Rep. **7,** 2791 (2017).

[11] Z.-H. Lin, C.-Y. Tobias Tschang, K.-C. Liao, C.-F. Su, J.-S. Wu and M.-T. Ho, IEEE Trans. Plasma Sci. **44,** 3140 (2016).

[12] S. A. Norberg, E. Johnsen and M. J. Kushner, Plasma Sources Sci. Technol. **24,** 035026 (2015).

[13] S. Norberg, PhD Thesis, "Modeling atmospheric pressure plasma jets: plasma dynamics, interaction with dielectric surfaces, liquid layers and cells", (University of Michigan, 2015).

[14] D. X. Liu, P. Bruggeman, F. Iza, M. Z. Rong and M. G. Kong, Plasma Sources Sci. Technol. **19,** 025018 (2010).

[15] A. M. Lietz and M. J. Kushner, Plasma Sources Sci. Technol. **27,** (2018).

[16] A. F. H. van Gessel, K. M. J. Alards and P. J. Bruggeman, J. Phys. D: Appl. Phys. **46,** 265202 (2013).

Chapter 7 Plasma-Induced Flow Instabilities in Atmospheric Pressure Plasma Jets[1]

Pulsed plasma excitation of rare gases flowing into air has been shown to impact the stability of the flow in non-equilibrium atmospheric pressure plasma jets (APPJs). In this chapter, results from a numerical modeling investigation of the stability of a round He APPJ with a powered electrode exposed to the gas flow are discussed. Localized gas heating at the powered electrode occurs on the time scale of the voltage pulse, tens to 100 ns, which is short compared to the fluid timescales. An acoustic wave propagates from this heated, expanding gas and exits the jet. The wave disturbs the shear layer between the He and surrounding humid air, exciting a shear instability which grows downstream with the flow and increases the mixing of the humid air into the He. The effects of eddy-dominated flow on ionization wave (IW) propagation in an APPJ were investigated. The IW followed the regions of highest helium concentration, resulting in an increased production of NO, HO_2, and NO_2.

7.1 Introduction

Atmospheric pressure plasma jets (APPJs) produce repetitively pulsed ionization waves (IWs) which propagate through the rare gas in the tube and into the mixed gas of the plume. Much of the reactive oxygen and nitrogen species (RONS) which induce desirable biological responses are produced at the interface of the rare gas and humid air. Understanding the mixing of the air into the rare gas in the presence of the IW is critical to controlling RONS production and biological outcomes. For reproducibility and clarity, most APPJs are intended to operate as

[1] The results discussed and portion of the text in this chapter have been previously published in A. M. Lietz, E. Johnsen, and M. J. Kushner, "Plasma-induced flow instabilities in atmospheric pressure plasma jets", Appl. Phys. Lett. **111,** 114101 (2017).

laminar jets. However, propagation of the IW can induce eddies and turbulence in the otherwise laminar flow of the plume [4,5], increasing mixing between the rare gas and air, and so affecting RONS production. Boselli, *et al*. reported that an induced turbulent front moved through the plume at approximately the speed of the gas. Schlieren imaging has shown that an instability appears with each voltage pulse and moves at a speed commensurate with the gas flow.[6] In other cases, a naturally turbulent jet can be stabilized by the plasma, particularly when the helium buoyancy opposes the flow.[7]

The onset of turbulence by IWs in plasma jets has been attributed to one or a combination of electrical or thermal forces. The electrical forces result from the charge separation combined with the large electric field that occurs in the IW passing through the plume. These forces result in a localized momentum transfer from charged species to the bulk fluid flow. Results from a computational investigation discussed in this chapter suggest that gas heating by the plasma can be an important stimulus to induce instabilities in the gas flow of typical APPJs.

A round gas jet propagating from a tube into a quiescent fluid is susceptible to instabilities even in the absence of a plasma.[8,9] For jets that are laminar when exiting the tube, these instabilities are first manifested as large unsteady structures at greater than ten L/d (distance from the outlet divided by diameter of the jet) from the jet outlet. These structures then develop into turbulence at larger L/d.[10] The Reynolds number for which jet flow transitions from laminar to turbulent at 10 L/d is approximately 1500.[9] At atmospheric pressure and a tube diameter of 1 mm, this corresponds to a speed of 1.8×10^4 cm/s or flow rate of 8.6 slm. However, this transition strongly depends on perturbations of the incoming jet flow, and unsteady flow can develop at lower Reynolds numbers.[10] The critical Reynolds number above which a slot jet is unstable is as small as 4 according to linear stability theory.[11] A more

detailed jet stability analysis, which accounts for viscosity, cylindrical symmetry, and an experimental initial velocity profile was performed by Petersen and Samet.[12]

7.2 Model Description

In this investigation, *nonPDPSIM*, a 2-dimensional plasma hydrodynamics simulation was used to model the plasma, gas dynamics and stability of an atmospheric pressure He plasma jet propagating into humid air. The model is described in detail in Chapter 2. The reaction mechanism includes plasma and neutral chemistry for $He/N_2/O_2/H_2O$.[13] The cylindrically symmetric geometry used in the study is shown in Fig. 7.1. Helium was flowed into the tube at 8 slm with impurities of $N_2/O_2/H_2O$ = 4.7/2.4/2.9 ppm. Humid air with a composition $N_2/O_2/H_2O$ = 79.5/20/0.5 flowed coaxially around the jet, with a total flow rate of 2 slm over a larger area. The unstructured mesh used in the calculation includes 7,089 total nodes and 6,011 plasma nodes.

nonPDPSIM includes a fluid dynamics module which solves modified Navier-Stokes equations. A description of the coupling of the calculations of plasma and chemistry to that of the fluid dynamics is in the Chapter 2, Sec. 2.2.6. Although large-scale vortical structures are produced by the algorithms *nonPDPSIM,* fine scale turbulent dissipation is not represented if occurring on spatial scales smaller than the mesh resolution (67 - 100 μm in the shear layer). Even if the mesh were fine enough, the 3-dimensional character of turbulence would not be captured in this 2-dimensional code. This means that *nonPDPSIM* should be considered accurate in determining the source of the flow disturbance, but it should not be considered an exact solution to the long timescale fluid evolution.

7.3 Plasma-Induced Flow Instabilities

The steady state gas flow field, shown in Fig. 7.1, was established in 5 ms of computational time before launching the ionization wave. The Reynolds number based on the

tube inner diameter is Re = 1250, which produces a stable flow before the voltage pulse is applied. For this essentially laminar flow, as the helium convects out of the tube (average speed of 1.7×10^4 cm/s at the outlet), the ambient air diffuses into the flow, producing the steady state N_2 density shown in Fig. 7.1. A -14 kV pulse with a 30 ns rise time, a 10 ns fall time and a 50 ns total duration was applied to the annular electrode inside the tube. Poisson's equation and the full plasma dynamics were solved for 70 ns, including 20 ns after the applied voltage returns to zero. After this point, the plasma is assumed to be charge neutral and Poisson's equation is no longer solved. (By this time, the IW has dissipated.) Enforcing charge neutrality, the plasma chemistry and fluid dynamics are then integrated until the end of the simulation, with the electron temperature fixed at T_e = 0.025 eV and the electric field set to zero.

The propagation of the IW in this jet begins at the powered electrode and propagates out of the tube, as shown in Fig. 7.2a by the electron impact ionization source. The peak electron temperature in the wavefront of the IW is T_e = 7.4 eV. The IW is annular in the tube adjacent to the wall due to the electric field enhancement that occurs at the inner surface. Outside of the tube, the IW follows the interface between the helium and the ambient air, returning to the axis within 1.3 mm of the tube outlet. These trends are commonly observed in experiments.[14–16] The majority of the RONS production by the IW occurs at the interface between the helium and the air, though some ROS are formed in the tube due to the impurities in the flow (for example O and OH), as shown in Fig. 7.2b. The major production of RONS at the interface places increased importance on the gas flow dynamics in the mixing layer between the helium and the air.

There is a region of high electron impact ionization and high electron density surrounding the powered electrode in a cathode-fall like structure. The high electron density and temperature near the surface of the powered electrode produces highly localized energy

deposition, resulting in gas heating of ΔT_g = 523 K, as shown in Fig. 7.3a, nearly tripling of T_g. The plasma-induced gas heating includes Ohmic heating, Frank-Condon heating, and the heating due to exothermic neutral and ion reactions. This heating occurs within the 70 ns pulse, which is nearly instantaneous compared to the fluid timescales (d/u = 6 μs, where d is the diameter and u is the flow speed). The end result is a doubling of the pressure in this boundary layer. As this gas expands, a strong acoustic wave propagates along the tube, out into the plume, and into the region of shear flow between the helium and the air. This acoustic wave causes an oscillation in the total number density, which is represented by ΔN_{tot} in Fig. 7.3a. The gas cools as it expands, and after 3 μs the gas temperature is 350 K over a much larger volume than the initial region of heating.

To visualize the motion of the interface between the He and the air, ΔN_2 is shown in Fig. 7.3a, where ΔN_2 is the current density of N_2 minus the density of N_2 before the voltage pulse. The acoustic wave perturbs this interface and induces a shear instability, as shown in Fig. 7.3b. This alternating pattern of increasing and decreasing ΔN_2 is a wave in the interface between the He and air. This wave propagates at the gas flow velocity, which is characteristic of a shear instability, and consistent with experimental observations.[5,6] When gas heating was turned off in the model by excluding all forms of heating due to plasma processes, the acoustic wave and instability did not develop (i.e., $\Delta N_{tot} \approx \Delta N_2 \approx 0$). Including or excluding momentum transfer due to charged species did not have a significant effect on the gas flow, and so for these conditions the induced flow instability can be attributed to gas heating.

The flow disturbance produced by the plasma becomes more severe with increasing voltage, commensurate with the increase in energy deposition with voltage. The disturbance can be quantified by integrating the absolute value of ΔN_2 over the computational domain, the results

of which are shown in Fig. 7.4. Experimental observations that the onset of turbulence occurs closer to the jet outlet as voltage is increased are consistent with these results.[4,6]

The shear instability produces a disturbance of the gas flow in an important region for RONS production – the mixing zone. Since much of the RONS of interest for biological applications are produced where the He and humid air merge, entrainment of air by flow instabilities into the path of the IW can affect RONS production and the propagation of the subsequent IWs. To demonstrate the effect of this mixing on the behavior of an APPJ, the propagation of an IW into an eddy-dominated flow was simulated, as shown in Fig. 7.5. The geometry is a slot jet 1 mm wide in Cartesian coordinates, a configuration which produces a less stable flow by allowing the development of asymmetric modes.[8] To approach turbulent conditions, a helium flow of 15 slm/mm and a shroud air flow of 5 slm/mm were used. These conditions correspond to an average He speed at the outlet of 2.5×10^4 cm/s, an average air speed of 430 cm/s, and a Reynolds number of 2,380. The simulation produced a pattern of vortex shedding, alternating from each side of the channel. The powered electrode was driven by a -15 kV DC pulse with a 30 ns rise time, a 10 ns fall, and a total duration of 110 ns. The IW follows the region of highest He density, curving around the eddies where the mole fraction of air is large due to entrainment. The electric field for which the IW can be sustained is lower in He than in air, due to inelastic electron energy loss to low lying vibrational and electronic states, and attachment to O_2 and H_2O. Even in laminar jets, the IW typically terminates at the axial location where the air mole fraction exceeds about 10%.[17] These patterns of the IW following the rare gas flow have been experimentally seen in jets with eddy-dominated flow.[5,6,17] This manifests itself in the plasma jet appearing “brush-like” as described by Robert, *et al*.[18]

To quantify the effects of eddy-dominated flow on RONS production, the simulation shown in Fig. 7.5, was repeated with a He flow of 1 slm/mm which produced a laminar plume. The total inventory of RONS was calculated 2 μs after the beginning of the IW, which dominantly captures the RONS production resulting from the immediate propagation of the IW before advective motion becomes significant. The case with eddy-dominated flow generally results in more RONS, particularly of more complex species such as HO_2, NO, and NO_2. In the eddy dominated case, the inventories of these species increases by factors of 1.5 to 2.1. The other species examined, O, O_2*, OH, N, and O_3, increase by 10% - 27%. The eddy-dominated flow provides a larger surface area for the plasma to interact with the humid air, and therefore produces more RONS.

7.4 Concluding Remarks

The gas flow in an atmospheric pressure plasma jet is fundamentally unstable to a shear instability. In APPJs localized heating at the powered electrode produces an acoustic wave which disturbs the shear layer between the helium and the ambient air. This results in a shear instability, which causes unsteady flow, and generates a disturbance that propagates with the local gas speed. This could develop into plasma-induced turbulence downstream. Ionization waves propagating into an unsteady plume are influenced by the gas composition profile, and follow the region of highest helium concentration. The result is differences in the type and amount of reactive species which are produced, depending on whether or not the plume is laminar.

7.5 Figures

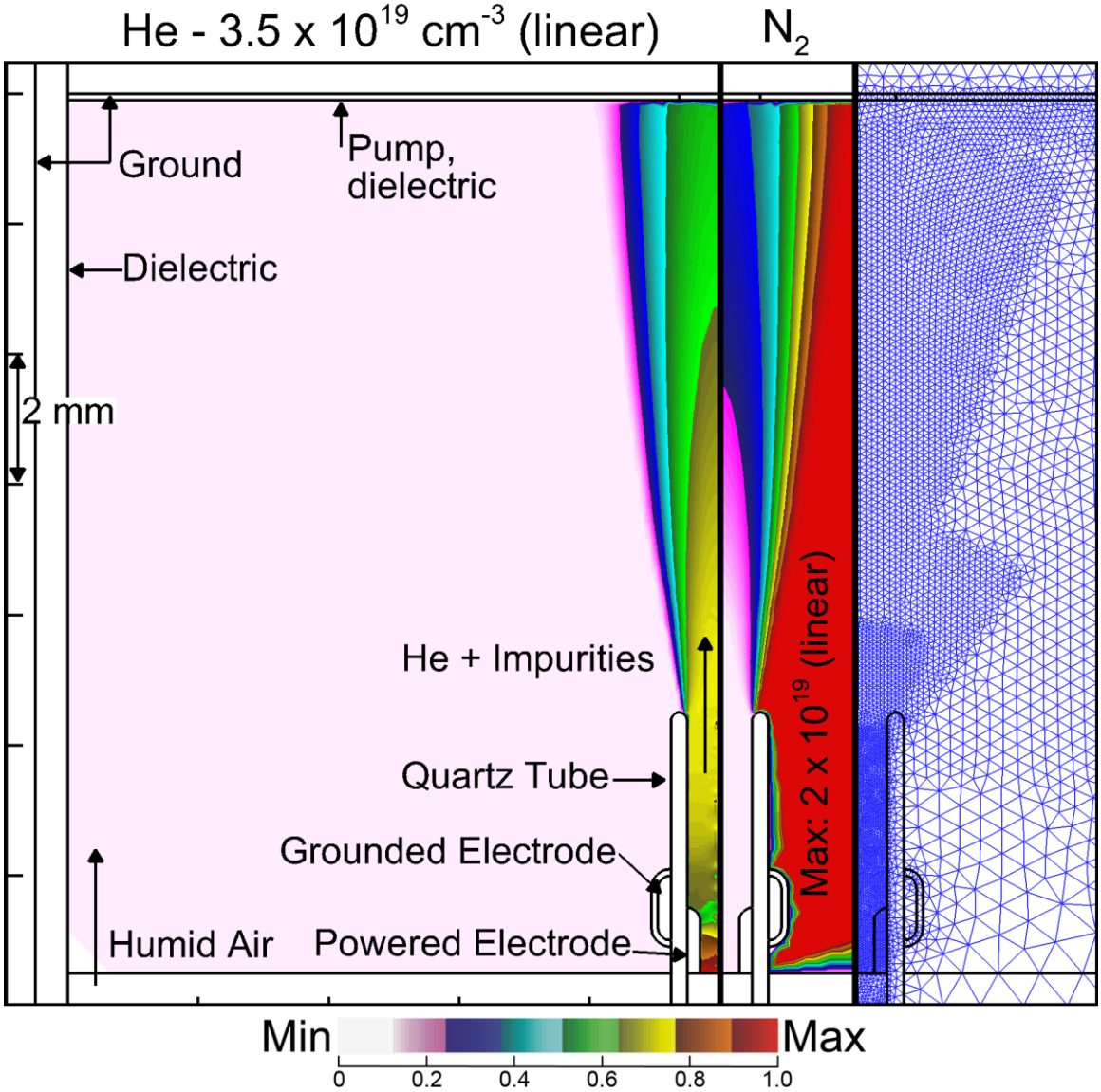

Fig. 7.1 Cylindrically symmetric geometry used in the model of a plasma jet. The internal electrode is powered and ring electrode is grounded. He and N_2 densities are shown after 5 ms. The mesh contains refinement zones in the tube and spreading radially outward. The mesh spacing is 35 μm in the tube and 90 μm at the pump.

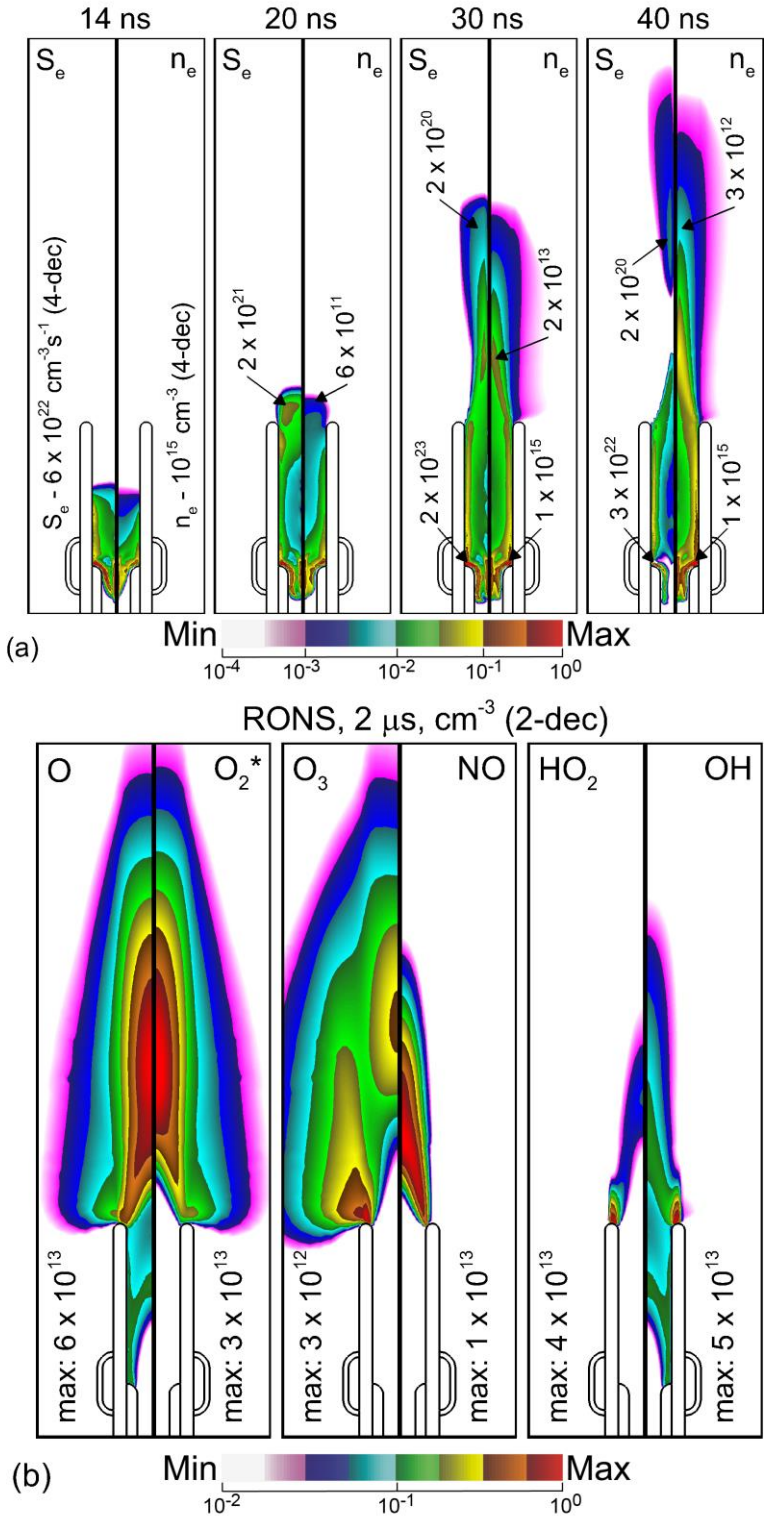

Fig. 7.2 Plasma properties during and after the IW. (a) Electron impact ionization source (S_e) [left] and electron density (n_e) [right] during the IW, with the maxima indicated (4-decade log scale). (b) The density of RONS 2 μs after the voltage pulse (2-decade log scale).

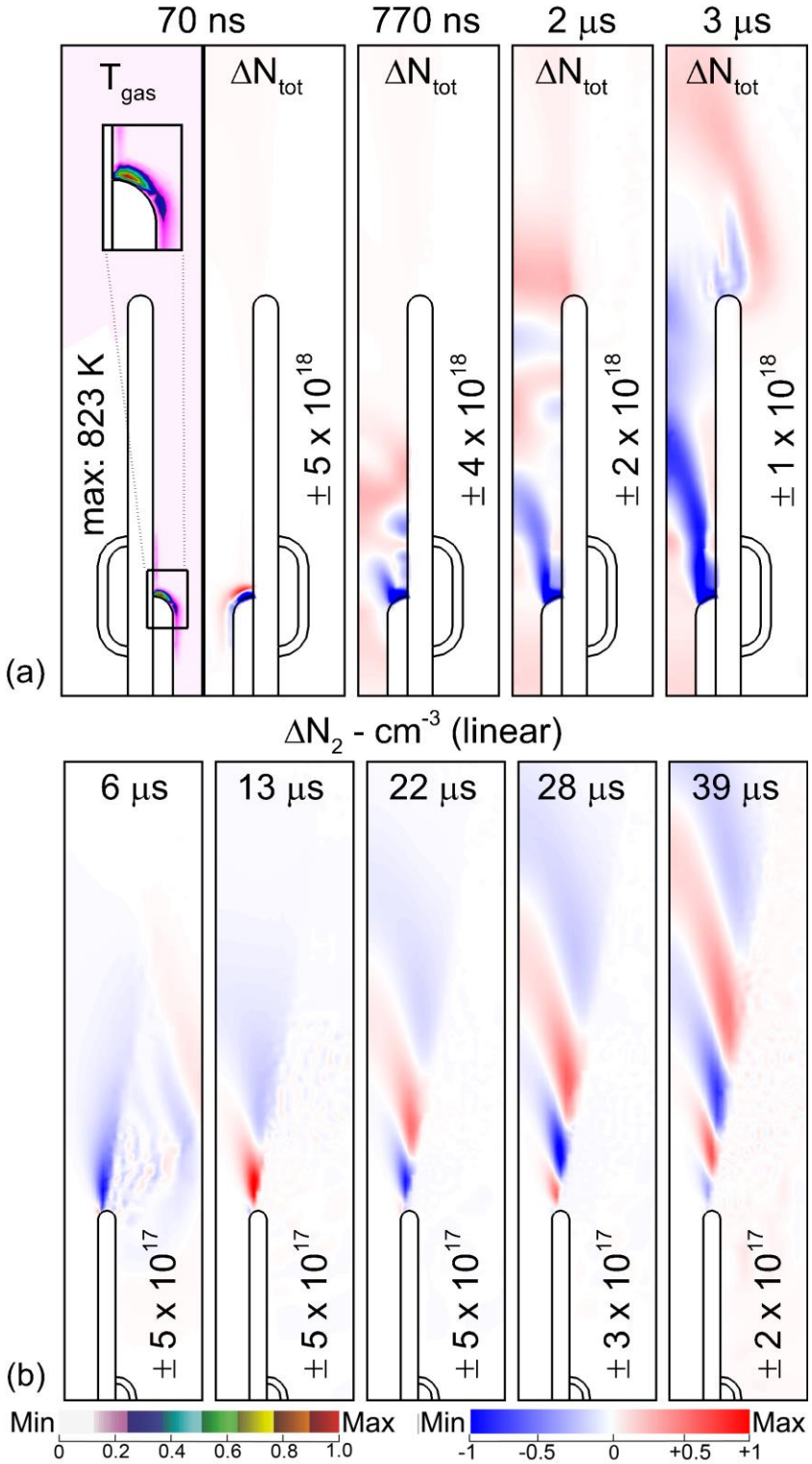

Fig. 7.3 Plasma produced instabilities. (a) Gas temperature (T_{gas}) at the end of the plasma calculation is shown in the leftmost frame with ΔN_{tot} (total number density minus the total number density at the start of the voltage pulse). (b) $\Delta N_2 = N_2(t) - N_2(t=0)$ which visualizes the oscillations in the characteristic of a shear instability.

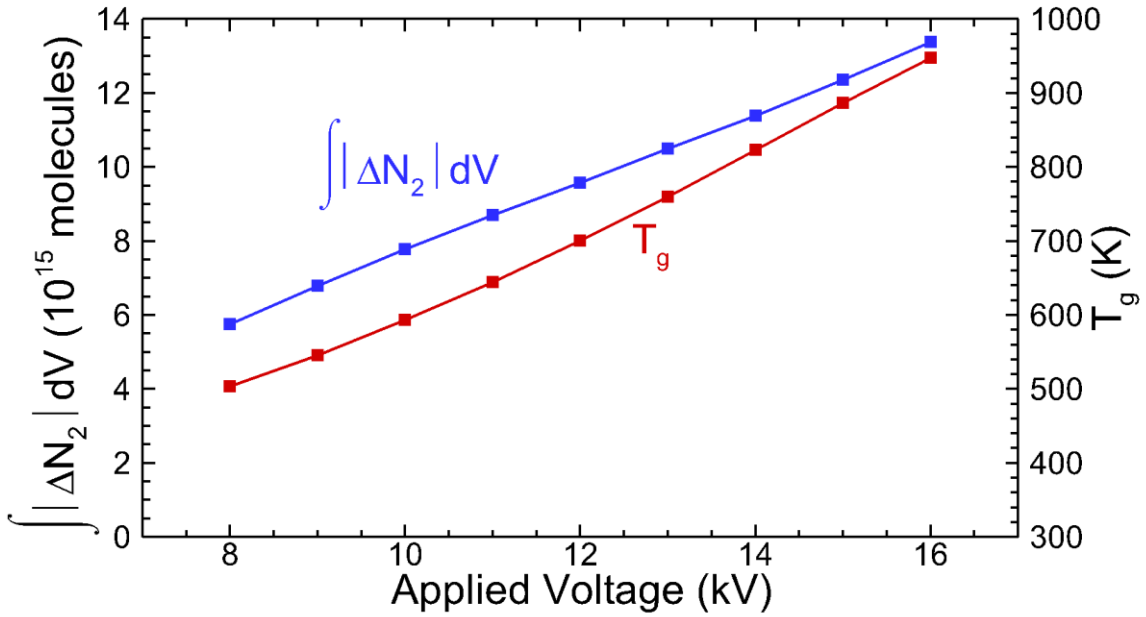

Fig. 7.4 The plasma-induced fluid disturbance is represented as the absolute value of ΔN_2 integrated over the computational domain where $\Delta N_2 = N_2(t) - N_2(t=0)$. Energy deposition and gas temperature increase with voltage, which produces a stronger flow disturbance.

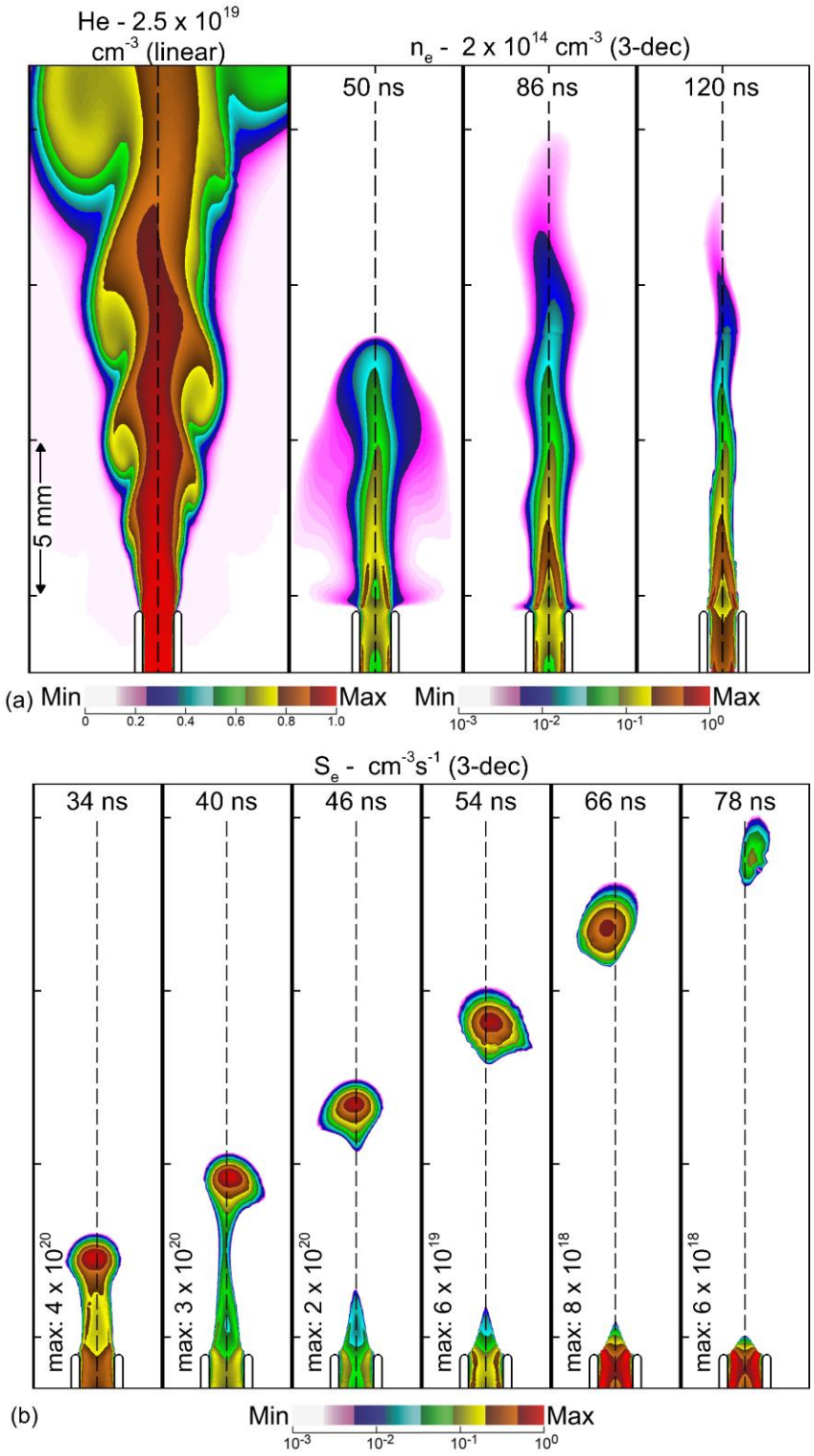

Fig. 7.5 Characteristics of a slot jet. (a) Initial eddy-dominated helium density for flow rate of 15 slm/mm, with electron densities as the plasma propagates into the unstable flow. (b) Time evolution of the electron impact ionization source term as the IW propagates into the eddy-dominated He plume.

7.6 References

[1] M. G. Kong, G. Kroesen, G. Morfill, T. Nosenko, T. Shimizu, J. Van Dijk and J. L. Zimmermann, New J. Phys. **11,** 115012 (2009).

[2] N. Kaushik, N. Uddin, G. B. Sim, Y. J. Hong, K. Y. Baik, C. H. Kim, S. J. Lee, N. K. Kaushik and E. H. Choi, Nat. Sci. Reports **5,** 8587 (2015).

[3] S. Sasaki, M. Kanzaki and T. Kaneko, Appl. Phys. Express **7,** 026202 (2014).

[4] R. D. Whalley and J. L. Walsh, Nat. Sci. Reports **6,** 31756 (2016).

[5] M. Boselli, V. Colombo, E. Ghedini, M. Gherardi, R. Laurita, A. Liguori, P. Sanibondi and A. Stancampiano, Plasma Chem. Plasma Process. **34,** 853 (2014).

[6] M. H. Qaisrani, Y. Xian, C. Li, X. Pei, M. Ghasemi and X. Lu, Phys. Plasmas **23,** 063523 (2016).

[7] E. Robert, T. Darny, S. Dozias, S. Iseni and J. M. Pouvesle, Phys. Plasmas **22,** 122007 (2015).

[8] S. C. Crow and F. H. Champagne, J. Fluid Mech. **48,** 547 (1971).

[9] T. B. Gohil, A. K. Saha and K. Muralidhar, Comput. Fluids **64,** 1 (2012).

[10] P. O'Neill, J. Soria and D. Honnery, Exp. Fluids **36,** 473 (2004).

[11] P. G. Drazin and W. H. Reid, "*Hydrodynamic Stability*", (Cambridge University Press, 2004).

[12] R. A. Petersen and M. M. Samet, J. Fluid Mech. **194,** 153 (1988).

[13] S. A. Norberg, E. Johnsen and M. J. Kushner, Plasma Sources Sci. Technol. **24,** 035026 (2015).

[14] D. Maletić, N. Puač, G. Malović, A. Đorđević and Z. L. Petrović, J. Phys. D: Appl. Phys. **50,** 145202 (2017).

[15] I. Jõgi, R. Talviste, J. Raud, K. Piip and P. Paris, J. Phys. D: Appl. Phys. **47,** 415202 (2014).

[16] N. Mericam-Bourdet, M. Laroussi, A. Begum and E. Karakas, J. Phys. D: Appl. Phys. **42,** 055207 (2009).

[17] S. Iseni, A. Schmidt-Bleker, J. Winter, K.-D. Weltmann and S. Reuter, J. Phys. D: Appl. Phys. **47,** 152001 (2014).

[18] E. Robert, V. Sarron, T. Darny, D. Riès, S. Dozias, J. Fontane, L. Joly and J.-M. Pouvesle, Plasma Sources Sci. Technol. **23,** 12003 (2014).

Chapter 8 Ionization Wave Propagation in an Atmospheric Pressure Plasma Multi-jet[1]

The atmospheric pressure multi-plasma jet produces an array of individual plasma jets, which originate from the branching of a single ionization wave. The use of arrays of such plasma jets could enable treatment of larger surface areas than is possible with a single plasma jet. In this chapter, the results from a combined experimental and 2-dimensional modeling investigation of the behavior of ionization waves in an atmospheric pressure plasma multi-jet device are discussed. In this multi-jet, a rare gas is flowed through a tube having a line of holes, producing gas jets into the ambient from each of the holes. A primary ionization wave (PIW) propagates through the tube which launches a series of secondary ionization waves (SIWs) propagating out each hole through the plumes of the individual gas jets. The propagation of the SIWs is more intense using a positive polarity voltage pulse due to the higher electric field at the ionization front. The diameter of the holes determines the delay of the SIW after passage of the PIW past the hole, with smaller holes resulting in larger delays. The larger delay results from a smaller view angle for photoionization outside the tube from photons originating in the PIW. Higher helium flow rates result in a greater tendency for SIW propagation because the air concentrations in the individual gas jets outside the tube are lower and so the electron temperature is higher. The interaction between SIWs is primarily electrostatic, and is a sensitive function of geometric parameters including ground planes and the spacing between the holes through which these SIWs emerge.

[1] The experiments discussed in this chapter were performed by X. Damany, E. Robert, and J.-M. Pouvesle at GREMI, CNRS Université d'Orléans, Orléans, France.

8.1 Introduction

Atmospheric pressure plasma jets (APPJs) may be advantageous for biomedical applications compared to dielectric barrier discharges (DBDs), due to the ability to tailor the reactive species produced in APPJs by controlling the gas composition.[1,2] However, APPJs typically treat only a small area at a time (on the order of mm^2) compared to DBDs that can treat many cm^2 (or larger) surfaces. Rapidly treating large surfaces with APPJs can be accomplished using arrays of APPJs, however this mode of operation can be complicated by interactions between individual plasma jets as observed in experimental studies.[3–8] The plasma in repetitively pulsed APPJs is produced by the propagation of a guided ionization wave (IW) which occurs with each voltage pulse.[9,10] These IWs contain space charge which disturb the electrical potential of nearby IWs if spaced too closely.

Since APPJs are accompanied by a gas flow, the gas composition outside of the APPJ is influenced by nearby APPJs. Z. Fang *et al*. reported on the effect of gas flow rate on the modes of a honeycomb array of 7 APPJs operating in Ar flowing into air.[11] For low flow rate, only the center APPJ generated a plasma which extended to the surface being treated. When the flow rate was increased, the IW from each individual APPJ reached the surface. Stancampiano *et al*. observed this same mode transition in a honeycomb cluster of plasma jets and measured an increase in negative ion fluxes from the conjoined single IW using molecular beam mass spectrometry.[5] Zhang *et al*. observed a less intense IW propagating through the center jet of an array of three jets, a non-uniformity (i.e., interactions between jets) that was greater with positive polarity than negative polarity.[4] This non-uniformity could be mitigated by a 0.1% O_2 admixture which provided an increase in ionization due to Penning processes.

Kim *et al*. observed electrostatic interactions in a linear array of APPJs, where jets on the end of the array diverged from other jets while producing increased optical emission.[8] Babaeva and Kushner computationally investigated the effects of electrostatic, hydrodynamic, and some photolytic coupling of arrays of up to 3 APPJs.[12] When jets were placed close together, their electrostatic interaction became particularly significant, resulting in the propagation through the central jet to dominate.

There has also been progress in generating arrays of APPJs, including jets operating in a glow discharge mode.[13] In this case, Cao *et al*. showed that with proper electrical ballasting of each jet, the array can treat the surface of 3-dimensional objects with better uniformity than could be achieved by scanning a single jet along the surface. Lee *et al*. used a 3×3 array of microplasma jets to deactivate bacteria and treat wounds. In this particular device, interaction between the individual jets was not observed.[14] Although some arrays of APPJs have been reasonably successful at achieving uniformity of treating surfaces [13–15], a more systemic understanding of interactions between the APPJs would aid in designing such sources.

Other designs have also been investigated to increase the area of plasma treated surface. Nayak *et al.* studied a microhollow dielectric barrier discharge array in dry air as a means to increase the area of plasma treated surfaces.[16] O'Connor *et al*. used a larger tube downstream of several APPJs which enabled the individual IWs to merge to have a larger cross sectional area and a more diffuse plasma.[17] Li *et al*. investigated a device in which an IW expands to fill a larger tube (15 mm diameter) which is capped at the end.[7] Individual IWs propagated out from holes in the bottom of the downstream chamber.

Another potential design for generating an array of IWs is the multi-jet APPJ in which a single primary ionization wave launches several secondary ionization waves (SIWs). This

device, introduced by Robert *et al*. [18], consists of a dielectric tube with a series of holes along one side. A primary ionization wave is launched from one side of the tube from a pair of coaxial electrodes in a DBD configuration. The primary IW propagates through the dielectric tube and, when passing over the holes, launches SIWs which propagate through the holes. An advantage of this multi-APPJ is its ability to simultaneously treat large areas of surface by increasing the number of secondary ionization waves (i.e., more holes in a longer tube) all of which are produced by the same primary IW generated by a single voltage source.[18] In this chapter, we discuss a pulsed-DC version of this device. The sensitivity of IW dynamics in a multi-jet device to geometric and operational parameters was investigated through experiments and modeling. We found that the interaction between adjacent secondary ionization waves during their propagation is primarily electrostatic, although perturbations in the electrical potential as the earlier launched secondary IWs contact the grounded target also impact propagation of subsequent secondary IWs. Propagation of positive polarity IWs through holes on the order of hundreds of μm is highly dependent on the aspect ratio of the hole due to the view angle for photoionization through the hole of photons originating from the primary IW in the tube. Larger helium flow rates produced plumes emanating from the holes which have lower mole fractions of air, resulting in a greater tendency for IW propagation. Closer ground planes producing more intense vacuum electric fields outside the tube result in the formation of a more conductive channel when the IWs contact the target, which can disturb propagation of later secondary IWs, but reduces the effect of electrostatic interaction between adjacent secondary IWs.

The experimental setup is described in Sec. 8.2, and the setup of the 2-dimensional computational model is described in Sec. 8.3. The results of both experimental and modeling are discussed in Sec. 8.4. The base case of a positive polarity, multi-jet with five secondary

ionization waves is discussed in detail. Then a simplified geometry containing only one secondary ionization wave is discussed to facilitate analysis of electric field and IW behavior. The other parameters investigated include the voltage polarity, gas flow rate, hole diameter, the distance between the holes, and the distance to a grounded surface.

8.2 Description of the Experiment

A schematic of the experimental setup is in Fig. 8.1a. The multi-jet device used in this investigation is similar to that reported in Ref. [18]. The multi-jet consists of a dielectric tube with an inner diameter of 4 mm and an outer diameter of 6 mm having two segments which have a total length of 19 cm. The first segment is a straight quartz tube 12 cm long and houses the high voltage and grounded electrodes, and through which gas in introduced. This length of tube is required to ensure a laminar gas flow is established before the first hole. The second segment is the multi-jet tube made of Delrin® having the same inner and outer diameters as the quartz assembly. The Delrin® tube has a row of five holes along one side and is capped at the end with 20 mm thick Delrin®. For the base case the holes are 800 μm in diameter with a 5 mm gap between the holes. A grounded target is placed below the row of holes, 1.5 cm away except where otherwise indicated. He (99.999% purity) is flowed through the device at 1 slm, exiting out the five holes and mixing with the surrounding ambient air.

The electrodes consist of an annular powered metal tube inside the quartz tube, and a ground electrode ring wrapped around the outside of the tube. This configuration was selected due to its ability to generate IWs which propagate over large distances. The annular powered electrode was 2 cm long, with an outer diameter of 4 mm, and an inner diameter of 2.4 mm. The ground electrode is a 5 mm wide ring electrode which overlaps the powered electrode by 3.75 mm. The applied voltage waveform, shown in Fig. 8.1b, had a maximum of 14 kV, and a rise

time of about 2 μs, operated at 1 kHz. A positive polarity pulse was used, unless otherwise indicated, which produces an IW which propagates from the high voltage electrode, along the tube, and out each of the holes.

The experimental diagnostics used to asses this system include ICCD (intensified charge-coupled device) imaging, probe measurements of electric field, and Schlieren imaging of the gas flow field. An ICCD Pinmax3 gated camera was used to image the plasma propagation. An EOS Kapteos probe leveraging the Pockels effect to measure the components of the electric field in the vicinity of the plasma.[19] This fiber-like probe contains an isotropic crystal which is 5 mm in diameter and 1 mm long, and is probed with a 0.5 mm laser beam. Schlieren imaging (using the setup described in Ref. [24]) was used to identify the mixing of helium with the humid air. These measurements were used to ensure that the flow field computed by the model flow is consistent with that of the experiment, which may be disturbed by gas heating or the ion wind that can occur at long timescales and over many pulses.[18]

8.3 Model Geometry, Initial Conditions, and Reaction Mechanism

nonPDPSIM, the 2-dimensional plasma hydrodynamics model described in Chapter 2, was used in this investigation. After the initial fluid simulation has reached its steady state, computational nodes are binned in zones by the mole fraction of a specified species. In the case of a molecular gas (air) mixing with an atomic gas (He), the electron energy distribution (EED) is highly sensitive to small mole fractions of the molecular gas due to the low threshold energy of electron impact excitation to rotational and vibrational modes. In this investigation, the mole fraction of N_2 was used to assign zones for solving Boltzmann's equation and making rate-coefficient lookup tables. The computational domain was divided into 50 Boltzmann zones distributed on a log scale in mole fraction. The first Boltzmann zone includes nodes with an N_2

mole fraction from 0 to 10^{-6}, and the last zone includes nodes with an N_2 mole fraction from 0.754 to 0.795. The number of zones was selected to produce a lookup table that has a smooth transition in rate coefficients as a function of N_2 mole fraction.

The base case geometry used in this study uses 2-dimensional Cartesian geometry as shown in Fig. 8.2a. (The depth of the mesh is 1 mm, which is only relevant for specifying gas flow rates). The computational mesh, shown in Fig. 8.2b-8.2c, contains 13,286 nodes, 9,540 of which are in the plasma region. The powered electrode is inside the dielectric tube with the grounded electrode on the outside. The relative dielectric constant of the tube is $\varepsilon/\varepsilon_0 = 4$, appropriate for both quartz and Delrin®. Electrical ground planes were placed 15 cm above the tube assembly and 10 cm to the right of the end of the tube. He with impurities ($H_2O/N_2/O_2$ = 1002.9/4.7/2.4 ppm) was flowed at 1 slm through the tube. Since the experimental setup was not operated in a vacuum system or heated to eliminate water vapor impurities, it was assumed that the He contained water impurities of 0.1% in addition to impurities that are expected from the gas bottle based on gas supplier specifications. A pressure boundary condition is applied at the grounded pump faces, thereby enabling the gas to exit the computational domain. This is necessary to exhaust the gas in the 2-dimensional simulation, whereas in the experiment the gas exhausts perpendicular to the jets in all directions. Outside the tube, regions above the tube and beyond the holes in were modeled as a dielectric with $\varepsilon/\varepsilon_r = 1$ to represent air, with fore-knowledge that plasma does not occur in these volumes.

In the computational geometry, the distance from the powered electrode to the first hole is 3.625 cm, which is less than in the experiment. Experiments were performed varying the distance between the electrodes and the first hole. No critical differences were observed in the IW propagation, and so this length was reduced in the model to reduce the computational burden.

The actual 3-dimensional device has circular holes which produce gas jets that entrain air from all sides that comes from a nearly inexhaustible source – the surrounding ambient. In our 2-dimensional simulation the gas jets and ionization waves are slots (as opposed to circular jets) which can only entrain air between the jets which is not replenished from the ambient. To enable replenishment of the ambient air in the computational geometry, nozzles were included on the surface of the tube between the holes to account for air entrainment which occurs in 3-dimensional space. The flow rate of humid air from these nozzles ($N_2/O_2/H_2O$ = 79.5/20/0.5) was adjusted to 3 slm to achieve qualitative agreement with Schlieren imaging of the He jets leaving the holes, shown in Fig. 8.3a. Since disturbances in the flow have been observed after igniting the plasma, the Schlieren imaging was performed while the plasma discharge was on. The simulated Schlieren imaging, calculated by taking the spatial derivative of the mass density of the gas, is shown in Fig. 8.3b for comparison. The Boltzmann zones generated based on this steady state flow profile are shown in Fig. 8.3c.

A +28 kV pulse with a 5 ns rise time was applied to the powered electrode. This voltage amplitude is double that used in the experiments, based on the differences in IW propagation in an infinite channel (modeled in 2-dimensions here) compared to cylindrically symmetric tubes (which occurs in the experiments).[20] This discrepancy originates from the increased electric field enhancement that occurs in 3-dimensions. The rise time is shorter in the model to account for the fact that the IW in the experiment reaches the first hole at a later time because it has a greater distance to travel compared to the model. By this time, the voltage is already near its maximum value. The discharge is initialized with two small electron clouds near the top and bottom edges of the powered electrode each having a diameter of 80 μm and a peak density of 10^{12} cm^{-3}. This choice of initial conditions is based on past experiences in modeling similar

devices. In general, the time to launch the IW scales with the magnitude of the plasma density in the initial spot, but otherwise the IW dynamics are not significantly affected. The IW wave dynamics are different if the entire volume is initialized with a uniform plasma density. In particular, the IW dynamics in the holes will be different. For example, since the gas flow speed through the holes is high, it is not expected that there would be any plasma density remaining in the holes by the time of the next pulse in a repetitive device. In this approach, only a single pulse is simulated, which does not take into account some charge which may remain on the surface of the dielectric tube from previous pulses.

The reaction mechanism used in this study is a reduced version of that discussed by Norberg, *et al.*, to limit the scale of the simulation.[21] The mechanism has 36 species, including 12 charged species. The total number of reactions, including 4 photoionization reactions, is 483. The electronically excited states of He, He(2^3S), He(2^1S), He(2^3P), and He(2^1P) are treated explicitly, and more energetic excited states are lumped as He(3P) and He(3S). All of the He excimers are lumped into a single state, He_2*. Two electronically excited states of N_2 are included: N_2* includes $N_2(A^3\Sigma)$, $N_2(B^3\Pi)$, $N_2(W^3\Delta)$, $N_2(B`^3\Sigma)$, $N_2(a`^1\Sigma)$, $N_2(a^1\Pi)$, and $N_2(w^1\Delta)$, and N_2** includes $N_2(C^3\Pi)$ and $N_2(E^3\Sigma)$. The other electronically excited states include O_2* [$O_2(^1\Delta)$] and O* [$O(^1D)$]. The dissociation products of N_2, O_2, and H_2O are included, but the species that typically form many microseconds after the discharge pulse, or only after many pulses are not included in the mechanism. For example, NO_2, NO_3, and HNO_x are not in the reaction mechanism since their densities are negligibly small during the time of the simulation and chemistry in the afterglow is not a focus of this study. A table of the complete reaction mechanism is in Appendix B.

Photoionization in the reaction mechanism includes ionization of N_2, O_2 and H_2O by emission from He_2*. The ionization cross sections are 2.5×10^{-17}, 1.5×10^{-17}, and 2.0×10^{-17} cm^2. In order for propagation of the SIW outside of the tube to occur, it was also necessary to include ionization processes in the ambient air, which consisted of N_2** emission ionizing O_2 with a cross section of 5×10^{-18} cm^{-2}. Air diffusing into the He plume is also excited by the SIW passing through the plume, which produces critical seed ionization that helps to sustain the SIW. The photoelectron emission coefficient of the tube was 1% for all photon species. The maximum photon path was 3 cm. That is, radiation transport was following for a maximum of 3 cm from the site of photon emission.

8.4 Ionization Waves in Multi-jets

8.4.1 Base Case

The initialization of the IW propagation in the base case is shown by the electron impact ionization source term (S_e) in Fig. 8.4a and the electron density (n_e) in Fig. 8.4b. This IW propagating from left to right through the tube will be referred to as the primary ionization wave (PIW). The electron impact ionization source term (S_e) indicates the IW. The discharge begins near the powered electrode, as the initial seed electrons accelerate toward the positive polarity electrode. An intense surface ionization wave ($S_e \sim 10^{24}$ $cm^{-3}s^{-1}$) develops along the inner surface of the tube adjacent to the ground electrode, producing an electron density as high as 1.6×10^{15} cm^{-3} in this region. Here the tube serves as a capacitor which rapidly charges due to the high conductivity of the adjacent plasma. Upon charging this surface, the IW begins to propagate along the walls of the tube, transitioning from a surface ionization wave to a volume filling IW at the center of the tube. When the IW propagates beyond the edge of the grounded electrode, the effective capacitance of the wall decreases, leading to more rapid charging of the

wall. The fully charged wall capacitance is less able to support a surface IW. With the small mole fraction of impurities, the primary ionization mechanism in the IW is electron impact ionization of He, contributing more than 97% of the generation of electrons. After the initial ionization wave passes, the electric field behind the PIW decreases and S_e becomes negative, meaning attachment and electron-ion recombination exceed electron impact ionization. The electron density continues to increase during this time, however, as the generation of electrons ($\sim 10^{19}$ $cm^{-3}s^{-1}$) by Penning ionization ($He^* + H_2O \rightarrow He + H_2O^+ + e$) is greater than the losses of electrons. The electron density in the bulk of the PIW is much less than that in the vicinity of the powered electrode, reaching approximately 5×10^{12} cm^{-3}.

The dominant ion in the tube is He^+ for about 10 ns after the PIW passes, after which H_2O^+ becomes the dominant ion due to charge exchange with He^+ and Penning ionization by excited states. Approximately 30 ns after the PIW has passed, the most abundant ion in the tube transitions to H_3O^+ due to the reaction $H_2O^+ + H_2O \rightarrow H_3O^+ + OH$.

The PIW continues to propagate into the region of the tube containing the holes, as shown in the experimental imaging in Fig. 8.5 and the modeling results in Figs. 8.6 and 8.7. In the ICCD imaging, when the PIW reaches the first hole, a secondary ionization wave (SIW) propagates through the hole and downward towards the grounded target. After the SIW contacts the grounded surface, the light emission from just above and below the hole in the conductive channel significantly increases. Based on the results in Fig. 8.5 at 370 ns and 410 ns, there appears to be a short delay between the time the PIW reaches a hole, and the SIW appears below the hole. The SIW speed through the hole is slower than that of the main PIW due to the increased charged particle losses due to the larger surface-to-volume ratio of the holes compared to the tube and the beginning of encroachment of the ambient air. The SIWs continue to

propagate out each subsequent hole and contact the grounded surface, but the intensity of the light emission decreases with each subsequent SIW.

In the modeling results (Fig. 8.6), the PIW reaches the end of the tube after 260 ns, and continues to produce electron impact ionization until the surface of the end cap is electrically charged. As the PIW propagates past each hole, SIWs propagate through the holes and downward towards the grounded pump surface. These SIWs experience a brief delay of approximately 10 ns from the time that the PIW reaches the top of a hole, to the time that the SIW emerges from the bottom of the hole. During this delay, S_e inside the hole reaches 1×10^{20} $cm^{-3}s^{-1}$, but is non-uniform. S_e in the first SIW as it propagates towards the target is initially large in the region of high helium concentration (9×10^{20} $cm^{-3}s^{-1}$), but decreases by more than an order of magnitude (2×10^{19} $cm^{-3}s^{-1}$) as the SIW propagates into regions having a higher air concentration. As electron energy is more rapidly lost in collisions with N_2 and O_2 due to rotational and vibrational excitation, and low lying electronic states, there is less ionization at a given *E/N*. As the SIW forms a conductive channel, the *E/N* decreases behind the ionization front which, increases the electric field in front of the SIW which helps to sustain the IW. When the SIW is within 5 mm of the grounded surface, this increase in electric field results in a progressive increase in S_e as the SIW approaches the ground (Fig. 8.6, t = 260 ns). As the SIW begins to contact the surface the enhancement in electric field is at a maximum, and there is brief increase in S_e to 1×10^{21} $cm^{-3}s^{-1}$ which is aided by secondary electron emission from the surface. Once the conductive channel bridges the entire gap, *E/N* decreases at the surface while increasing throughout the remainder of the channel and there is then a second instance of electron-impact ionization, shown in Fig. 8.6, for the first hole at 285 ns and the third hole at 500 ns. This behavior will be referred to as a potential rebound, because the lines of electric potential

are redistributed in the conductive channel after the SIW contacts the ground, as shown in Fig. 8.6 (285 ns and 500 ns). The mechanism is analogous to that of a restrike, but because of the nonuniform gas composition and complex geometry, it is not significant enough to produce net ionization at every point in the conductive channel. In much of the conductive channel S_e simply becomes less negative, but in certain regions ionization rates exceed recombination rates and there is a net production of electrons.

As the first SIW propagates and produces a conductive channel, the *E/N* is reduced in the channel which reduces the voltage drop between the hole and the head of the SIW. This *shorting* of the potential in the path of the adjacent SIW limits the field enhancement that can occur ahead of the second SIW. This is essentially an electrostatic interaction between the SIWs. This electrostatic interaction affects all subsequent SIWs, resulting in more intense propagation for the first, third, and fifth SIWs compared to the second and fourth SIWs. This SIW-to-SIW interaction is over-emphasized in the simulations compared to the experiments. In the 2-d simulation, the plasma columns are computationally sheets of conductivity which affect the electric potential to greater distances than the cylinders of conductivity that occur in the experiment.

The electron density in the multi-jet is shown in Fig. 8.7. Inside the tube, the electron density remains elevated with values of 4×10^{12} cm^{-3} after the PIW has passed. The electron density continues to increase after S_e has become negative due to Penning ionization. Outside of the tube, after the SIW passes and the electron temperature decreases, rapid attachment of the electrons to O_2 and H_2O from the surrounding air results in the electron density decreasing from 1×10^{12} to 4×10^{10} cm^{-3} over 120 ns. In the regions of highest helium concentration, just outside the holes, the mole fraction of air is small, attachment does not occur as rapidly and the electron

density remains elevated, remaining above 4×10^{12} cm^{-3} for 120 ns. Outside the tube, O_2^+ is the most abundant positive ion. Initially O_2^+ balances the charge of the electrons. After the SIW passes, OH^- begins to accumulate as the system transitions to an ion-ion plasma. In order to summarize the behavior of the SIWs, it is useful to refer to the maximum value of the electron density at each position, also shown in Fig. 8.7 ("max(n_e)"). This shows the largest electron density that occurs at each computational node over the timescales of the simulation, and is a useful metric for comparisons with time-integrated ICCD imaging.

The propagation of the PIW is sustained by photoionization which produces an electron density of 5×10^8 cm^{-3} approximately 5 mm in front of the PIW. These electrons are accelerated in the electric field back towards the PIW, which facilitates the propagation. The sources of electrons due to photoionization, S_{photo}, at t = 155 ns are shown in Fig. 8.8 for each of the photoionization reactions included in the model. The main impurity in the He is H_2O, and so the primary source of photoionization generated electrons ahead of the SIW in the tube is photoionization of H_2O by excimer radiation from He_2*, shown in Fig. 8.8c. Outside of the tube, where the helium mixes with humid air, other photoionization reactions are also significant. The dominant photoionization reaction outside the tube is due to photons emitted by N_2** ionizing O_2. This photoionization reaction is essential for propagation of the SIW, which occurs in regions of higher air concentration where He_2* is not generated or is rapidly quenched by reactions with N_2 and O_2. In these regions, a lower T_e results in less He* production, the precursor to He_2*, and the He density is lower, which reduces the rate of the 3 body process the forms He_2*, both of which result in a lower density of He_2*,

At t = 155 ns, when the photoionization rates are shown in Fig. 8.8, the SIW at the first hole has already developed and propagated 2.5 mm outside of the tube. At this time, the rate of

photoionization by N_2** outside the tube (2×10^{19} $cm^{-3}s^{-1}$) is much greater than that of the He_2* (3×10^{17} $cm^{-3}s^{-1}$). However, the role of photoionization outside the tube by excimer radiation from He_2* is essential before 140 ns, when the SIW is first emerging from the hole. Since the excimer emission is not radiation trapped, the photons are lost only through absorption by impurities. The long absorption mean free path for excimer emission from He_2* (2 cm in He with 0.1% H_2O) enables photons emitted by He_2* inside the tube to propagate through the hole and illuminate the air molecules diffusing into the He plume (something of an excimer flashlight). The excimer radiation is then abruptly absorbed by the infusing air, producing ionization outside of the tube. These seed electrons produced by photoionization (5×10^7 cm^{-3}) facilitate SIW propagation through the hole.

Photoelectron emission from the surfaces of the tube also provides a source of electrons ahead of the PIW and in the holes for the SIW. For an estimated photoemission probability of 0.01, the VUV photons striking surfaces produce an electron source as high as 3×10^{15} $cm^{-3}s^{-1}$ at nodes adjacent to the surface, which is comparable to the contribution by direct photoionization. However, because the source of electrons by photoemission is limited to one mean free path for electron collisions from the surface (in the model, the numerical node next to the surface), the total volume of the plasma benefiting from photoelectron emission is small. The integrated contributions from photoionization in the bulk gas phase are more significant for both PIW and SIW propagation.

The surface and volumetric space charge is shown in Fig. 8.8e at t = 430 ns. As the PIW propagates, the inner surface of the dielectric tube charges positively (1×10^{11} cm^{-3}) because of the positive polarity of the applied voltage. Inside the holes, the surface charge is also positive, with a larger magnitude of approximately 1×10^{12} cm^{-3}. As the SIW propagates out of the hole,

the front of the SIW contains space charge as large as 7×10^{12} cm^{-3}. This region of positive space charge results in a reduction of the electric field in the bulk plasma, and an enhancement of the electric field in the front region of the space charge. This localized field enhancement facilitates the local ionization which occurs in SIW propagation.

Although there is generally good qualitative agreement between the model and experiment, there are several quantitative differences between the propagation of the IWs in the experiment compared to the model. The speed of the PIW propagation in the experiment is approximately 0.9×10^7 cm/s compared to 2×10^7 cm/s in the model, a discrepancy of a factor of 2. This discrepancy is a result of the increased voltage used in the model used to approximate the propagation of a 3-dimensional IW (which naturally has more electric field enhancement in the head of the IW) in 2-dimensions. Other sources discrepancy include differences in the level of impurities in the helium (the experimental value is not well known) and ignoring photoionization by resonant He photons which can be significant. As discussed earlier, the electrical interaction between SIWs is overestimated in the model due to the limitations of the 2-dimensional framework. In the model, the SIWs are approximated as sheets of plasma, which produces a greater disturbance in the potential for neighboring SIWs. In the experiment, each SIW is a column of plasma, which limits its effect on the potential of adjacent SIWs.

8.4.2 Single Hole Assembly

Although having an array of SIWs is the goal of the multi-jet, having multiple SIWs exiting the holes and contacting the grounded target at different times complicates the dynamics of the electric field and complicates interpretation of both experimental and computed results. In this section, the plasma properties of a multi-jet assembly having a single hole are discussed to better isolate the transition from PIW to SIW. An 800 μm hole was used and the helium flow

rate was reduced to 0.2 slm, so that the amount of gas flowing through the hole was the same as in the base case. The air flow rate is the same as that of the base case, 3 slm. In this section, time-resolved measurements of electric field for a jet having a single hole are first compared to the modeling results at several axial locations around the device for the tube being 1.5 cm above the grounded pump. Then the effect of changing the distance between the tube and the ground plane will be discussed.

The IW behavior predicted by the model is shown by S_e and n_e in Fig. 8.9. The qualitative behavior of the PIW and SIW are the same as the propagation of the first SIW in the base case multi-jet having 5 holes. When the SIW reaches the grounded target, *E/N* in the tube to the left of the hole increases from 7×10^{-18} V-cm^2 to 4×10^{-17} V-cm^2 (0.7 to 4 Td). There is a second pulse of ionization up to 2×10^{19} cm^{3}s^{-1} in some regions of the conductive channel (compared to 1×10^{20} cm^{3}s^{-1} the SIW) which travels faster than the SIW (8×10^7 cm/s compared to 1×10^7 cm/s). This potential rebound propagating in the reverse direction is analogous to that which occurs in a restrike.[22] After the SIW reaches the target, there is spreading of plasma along the surface of the target. Since the target is metal, this spreading of the plasma is not a classical surface ionization wave which requires differential charging of the surface and bending of electric field lines. (Electric field lines are perpendicular to a metal surface.) The appearance of a surface ionization wave results from bending of electric field lines in the bulk plasma by the adjacent conductive column of the SIW.

Experimental measurements of the electric field in this configuration were made at locations labeled in Fig. 8.9. For comparison to the experimental measurements, the electric field calculated in the model was averaged over the volume of the probe to emulate the signal produced by the probe. Perturbations to the electric field that might occur by the presence of the

probe were not accounted for in the model. The x-component of electric field (parallel to the tube), E_x, measured in the experiment and predicted by the model at several vertical positions are shown in Fig. 8.10 as a function of time. The y-component of the electric field (perpendicular to the tube), E_y are shown in Fig. 8.11.

The vacuum values of E_x would be positive for all of the probe positions. As the PIW passes above the probe in the tube E_x increases (positive) due to the shorting of the positive potential in the plasma column, which extends the anode potential closer to the probe, and due to the positive space charge in the head of the PIW. This electric field has the largest magnitude at the probe placed closest to the tube, 2.5 kV/cm. When the SIW propagates through the hole and outside the tube, positive potential and positive space charge are produced to the right of the probe, which reduces E_x and eventually reversing the direction of E_x to point to the left (negative). As the SIW passes to the right of the probe points, the value of E_x is maximum, -1.5 kV/cm at the top probe point.

The positive space charge contained in the head of the SIW appears to be a point-like positive potential translating from top to bottom. As this point-like positive potential passes by the probe, an electric component pointing to the left (negative) is produced. The most negative value of E_x tends to increase at probe positions closer to the grounded target reaching -3 kV/cm when the probe is at 6.5 mm. The negative increase in E_x is due to progressively more positive potential (and positive space charge) being produced to the right of the probes as the conductive column extends further from the tube. There is a delay in the negative maximum due to the finite propagation time of the SIW. For example, between probe positions 12.5 mm and 6.5 mm there is a delay of 31 ns, corresponding to a propagation speed of 2×10^7 cm/s. The most negative value of E_x occurs at approximately the same time for prove positions 3.5 mm and 6.5

mm. The time averaging from the probe response results in the 3.5 mm signal appearing earlier in time. After the SIW contacts the target, there is a rapid decrease in the magnitude of E_x as the potential of the conductive channel drops. As the potential of the plasma increases after the SIW contacts the ground, much of the potential drop becomes confined to the cathode fall layer at the grounded surface, and magnitude of E_x increases again.

Results from the model reproduce all of these systematic trends, with the exception of the magnitude of the electric field. The magnitude of the electric field in the model is larger than that measured in the experiment. First, the voltage applied in the model is larger than in the experiment to compensate for the slot (model)-vs-cylinder (experiment) nature of the SIWs. However, much of the overestimate results from the 2-dimensional nature of the model compared to the 3-dimensional experiment. In the experiment, the space charge at the SIW front is, to first order, a small sphere of charge. In the model, the space charge at the head of the SIW is, to first order, a cylinder of charge of infinite length. These two space charge configurations produce quite different behavior in the electric field as the probe is moved away from the SIW. For a sphere of charge, the electric field is proportional to $1/r^2$ (r is distance from the charge) whereas for a cylinder of charge, the electric field is proportional to 1/r. Said otherwise, there is more geometric electric field enhancement around a sphere compared to the cylinder but only within a radii or two of the space charge. For probe positions that are outside the field enhancement for the passing space charge (beyond a few radii of the space charge), electric fields will be smaller for the sphere (experiment) compared to the cylinder (model). The probe is measuring the electric field as much as 3.5 mm from the SIW which is much larger than the diameter of the space charge region (~650 μm). These geometric effects can explain the higher predicted electric fields in the model while being able to reproduce the systematic trends. Since

the voltage pulse in the experiment has a longer rise time than in the model, the applied voltage may not be at its maximum value as the SIWs exit the tube which could also contribute to the overestimation of the electric field in the model.

E_y in the model and the experiment is shown in Fig. 8.11. As the PIW passes above the probe, $E_y < 0$ with a magnitude which is increasing, as is the case with the vacuum electric field. With the positive potential produced by the PIW above the probe, there is an increasing downward pointing component of the electric field. In the modeling results, E_y is approximately the same for all probe positions, before the SIW exits the tube. In the experimental measurements, the magnitude of E_y is significantly higher when the probe is closer to the tube. This discrepancy is again a result of the 3-dimensional nature of this device. In the experiment, the anode potential that is extended by the PIW through the tube is, to first order, a cylinder of charge, which would have a potential which decreases like 1/r. In the model, the anode potential extended by the PIW is a sheet of charge, which would produce a uniform axial electric field. As the SIW approaches each probe position, the electric field enhancement in front of the SIW results in an increasingly negative E_y if the head of the SIW is above the probe. As the SIW passes the probe position, the contribution to E_y from the positive space charge in the head of the SIW flips to being positive, resulting in a decrease in the magnitude of E_y. The consequences of the space charge produced are more pronounced in model due to the previously discussed discrepancies between 2-d and 3-d.

The gap between the tube and the grounded target was varied in both the experiment and the model using the single hole configuration. The center of the probe was placed 7.5 mm below the tube, indicated in Fig. 8.9a. The time evolution of the x-component of the electric field for different gap sizes of 10 mm to 24 mm is shown in Fig. 8.12. E_x generally increases as the gap

increases because when the gap is small, the electric field is more strictly vertical. As the gap increases, the speed of the PIW and SIW decrease due to an overall lower electric field. The maximum electric field therefore occurs later in time for a larger gap, and has a smaller maximum magnitude. As the SIW exits the tube and passes the probe, the minimum (most negative) value of E_x is relatively consistent because the potential of the SIW is not sensitive to the gap size. In the model, for gaps larger than 18 mm, the SIW does not reach the target. In both the experiment and the model, the electric field remains at its minimum (most negative) value for a longer time when the gap is larger. There are two components for this delay. For a larger gap, the SIW takes longer to travel the greater distance between the probe and the target. Then the disturbance in the potential that occurs after the contact is delayed in propagating from the target back up to the probe location. This potential rebound, propagating in the reverse direction is analogous to that which occurs in a restrike.[22]

8.4.3 Voltage Polarity

The voltage polarity is the parameter that most significantly affects the character of the SIW propagation in the multi-jet. Time-resolved ICCD images, averaged over 100 pulses, for positive and negative polarity pulses are shown in Fig. 8.13. For negative applied voltage, the SIWs do not reach the grounded target. The SIWs extinguish where the humid air diffusing into the He channel becomes significant (a mole fraction of about 20%), as the SIWs cannot be sustained at high molecular gas concentration. The SIWs for negative polarity stop emitting light before the PIW reaches the end of the tube. Under the same conditions, but for positive polarity, the SIWs do reach the grounded target and remain illuminated as the PIW reaches the end of the tube. The speed of the PIW is also approximately a factor of 2 slower for negative polarity, 9×10^6 cm/s compared to 2×10^7 cm/s.

This sensitivity to polarity also occurs in the modeling results shown in Fig. 8.14. The PIW for positive polarity (base case) was concentrated at the center of the tube, as electrons that are generated from photoemission or photoionization are accelerated toward the IW. With negative polarity, electrons generated by electron impact ionization in the bulk plasma are directed ahead of the IW by the applied electric field. As a result, the electron impact ionization rate, S_e, was maximum at the lower surface of the tube the opposite direction of the applied vacuum electric field. This asymmetry inside the tube occurs before the PIW reaches the holes, and is a result of a lower electrical ground being closer to the tube (1.5 cm) than the upper electrical ground (15 cm). This closer proximity produces a larger acceleration for electrons in the vacuum electric field downwards than upwards. This asymmetry is also consistent with the ICCD imaging, where the light emission on the lower surface of the tube is greater for negative polarity.

With positive polarity, SIWs reach the surface whereas with negative polarity SIWs extinguish upon contacting regions exceeding 20% mole fraction of air. This difference is a result of the amount of field enhancement which occurs ahead of the IW for each polarity. With a positive polarity, electrons accelerating toward the IW produces a sharper gradient in potential. The space charge in the head of the IW is comparable for the positive polarity (3.4×10^{11} |q|cm^{-3}) and negative polarity (-4.0×10^{11} |q|cm^{-3}). However because the shape of the PIW is different for the positive polarity, being confined to a smaller diameter, *E/N* in the PIW is 125 Td for positive polarity and 54 Td for negative polarity. The lower *E/N* with the negative polarity is not sufficient to produce avalanche with significant fractions of air in He.

The speed of the PIW in the model is overestimated compared to the experiments. For both polarities, the same voltage was applied in the model, which was higher than in the

experiment to approximate 3-dimensional effects. However, in the experiment this 3-dimensional electric field enhancement is expected to be greater for positive polarity, because of the smaller diameter of the avalanche front of the PIW. In the modeling results, the PIW is faster for negative polarity, which is the opposite of the experimental trend, because the positive polarity PIW has more electric field enhancement due to 3-dimensional effects.

In several experiments, disturbances of the bulk gas flow in APPJs by the plasma have been observed. These disturbances have been well documented in single APPJs but also occur in multi-jets, and typically depend on the polarity of the applied voltage.[18,23] In the modeling results, the initial flow conditions were the same for both polarities, and qualitatively match the experiment. Therefore the observed differences in the SIW behavior are not simply a result of the change in gas composition, but a more fundamental feature of the IWs.

8.4.4 Gas Flow Rate

Varying the He flow rate changes the mole fraction of air in the path of the SIW. Higher flow rates extend the length of the gas plume that is dominated by He. With lower flow rates the in-diffusion of air results in larger mole fractions of air nearer the hole. To investigate these effects, the He flow rate was varied from 0.5 to 2 slm for positive polarity discharges while keeping the air flow constant a 3 slm. As the flow rate is increased, the experimental ICCD imaging in Fig. 8.15 indicates more intense SIWs, but greater decrease in the SIW intensity with each subsequent hole. For 2 slm, the light emitted from the fifth SIW is small compared to that from the first SIW. With increasing flow rate, the brightest region of the SIWs, which occurs at the outlet of the hole, is elongated as the region of high helium mole fraction is extended.

These features can be explained based on results from the model shown in Figs. 8.16 and 8.17. The maximum electron density which is reached at each computational node is shown in

Fig. 8.16 for He flow rates of 0.5, 1.0 and 2.0 slm. The N_2 density, electron temperature and ionization source in the vicinity of the first holes are show in Fig. 8.17 for the same He flow rates. The gas is essentially stationary on the timescales of the IW propagation (500 ns), and the pressure variation among flow rates is negligible. As a result, He flow rate likely affects the SIW through variation in the gas composition outside of the tube, as shown for the first hole in Fig. 8.17, as opposed to a flow induced instability.

The spatial extent of S_e in the SIWs increases with He gas flow rate because there is a lower concentration of air in the He plume further from the hole. Air, being composed of molecular gas, results in greater rates of electron energy loss due to vibrational and rotational excitation, and lower lying electronic states compared to He. At higher He flow rates, air concentrations are lower in the plume, resulting in a higher T_e for a given E/N. T_e in the SIW increased from 3.1 to 4.7 eV as the flow rate was increased from 0.5 to 2 slm. As a result S_e increased from 1×10^{19} to 5×10^{20} $cm^{-3}s^{-1}$. The extended region of the plumes having small air mole fractions with higher flow rates produced the elongated brighter regions in the ICCD images.

The PIW attenuates as it passes each hole and sequentially launches SIWs. This attenuation is indicated by the decreasing electron density in the tube shown in Fig. 8.16 for a He flow rate of 2 slm. The lower concentration of air in the plume at higher He flow rates enables a more intense SIW which produces a more conductive channel. For example, the electron density in the conductive channel increases from 4×10^{11} cm^{-3} for 1 slm to 1×10^{12} cm^{-3} for 2 slm. The higher conductivity in the channel produced by the SIW results in a more intense potential rebound when the SIW contacts ground, and so a larger potential drop occurs in the tube. As a result, E/N in the PIW inside the tube decreases as each successive SIW contacts the grounded

target. The ICCD brightness of the PIW near the end of the tube decreases with increasing flow rate because of this decrease in *E/N* in the PIW. In time-resolved ICCD imaging, at larger flow rates, the PIW speed slows with the propagation of each successive SIW (data not shown). In both the experiment and the model, increasing the flow rate in a negative polarity multi-jet also elongated the SIWs as the He flow rate increased (data not shown). In the model, the SIWs reach the target when the He flow rate is increased above 2 slm.

At low He flow rate, the diffusion of air into the He plumes occurs within a few mm of the holes, as shown in Fig. 8.17. The SIWs fail to propagate beyond an air mole fraction of about 25% and a conduction channel to ground is not formed, shown in Fig. 8.16. As a result, there is no conduction current that connects the powered electrode to ground, and no potential rebound. Current continuity from the powered electrode is maintained by displacement current, either directly to ground through the air as the SIWs successively penetrate through the holes, or by displacement current through the dielectric tube. With there being no power dissipation by the successive waves through formation of a conductive channel, the electron density inside the tube remains nearly constant as each SIW is launched.

Modification of the flow as a result of the plasma pulse have been observed in the multi-jets, just like those of single atmospheric pressure plasma jets. In this range of operation parameters in the experiment, however, flow disturbances were not observed. Plasma-induced flow disturbance would be expected to disrupt these trends by leading to an increased rate of mixing of the He with the surrounding air.

The interaction between the SIWs is more significant in the model than in the experiment, which is expected based on the 2-dimensional approximation of the device. It is likely for this reason that in the experiment, the SIW for 0.5 slm propagates (though very weakly) to the

ground plane whereas the SIW does not propagate in the modeling results. At the same time, this interaction may be underestimated in the ICCD imaging as these images are the average of 100 pulses. So if stochastic behavior resulted in a different SIW failing to propagate with each pulse, this isolated behavior would not be visible in the pulsed averaged images.

8.4.5 Hole Diameter

The diameters of the holes on the multi-jet greatly affect the propagation of SIWs out of the holes. A comparison of experimental ICCD imaging for SIWs propagating through 200 and 800 μm holes is shown in Fig. 8.18. Results from the model for electron density for hole sizes of 200, 500 and 800 μm are shown in Fig. 8.19. The computed N_2 density, photoionization source and electron impact ionization source for these holes are shown in Fig. 8.20. The delay between the PIW passing above a hole and the SIW appearing outside of the tube increases as the holes decrease in size. Experimentally, with 200 μm holes, the first SIW does not exit the tube until approximately 250 ns after the PIW reaches the end of the tube. With 800 μm holes, the SIW propagates out the first hole 20 ns after the PIW passes above the hole (180 ns before the PIW reaches the end of the tube). This increase in delay is also observed in the model. The first SIW emerges from the hole 105 ns after the PIW passes for d = 200 μm and 15 ns for d = 800 μm.

The SIW propagates more quickly through larger holes due to the combined effects of gas composition and photoionization. The maximum photoionization source outside of the tube is 10^3-10^4 smaller in magnitude than the electron impact ionization source. However, the photoionization is critical to providing the initial electrons which enable the SIW to develop. The number of photons emitted by He_2* in the PIW which pass through the hole to reach the outside of the tube depends on the aspect ratio of the hole. For a smaller diameter hole, the aspect ratio is large, the view angle is small, and fewer photons reach the outside of the tube to

produce photoionization. As a result, the rate of photoionization outside the tube before the SIW emerges increases from 6×10^{15} to 3×10^{16} with increasing hole diameter (200 to 800 μm), as shown in Fig. 8.20.

The ability of the SIW to fully develop and bridge the tube-to-ground gap in part depends on the diffusion of air into the plume of He exiting the holes. Air diffuses into the He plume more rapidly with smaller holes which have larger concentration gradients. This large concentration of air in the He plume results in more inelastic, non-ionizing electron energy losses and attachment in the plume with smaller holes. The result is that SIWs have lower electron densities and do not reach the target with 200 μm holes, while only the last SIW reaches the target with 500 μm holes.

In the experiment, the SIWs propagate out the fifth hole at the end of the tube first with 200 μm holes. In the model, the SIWs first propagated out of the first hole. The precise timing and sequencing of the SIW are sensitive to the location of ground planes around the tube. For example, there is an effective ground plane in the experiment on the right hand side of the jet, which in the model was assumed to be 10 cm away. This ground plane location produces a small increase in *E/N* when the PIW reaches the end of the hole, but the capacitance is too small to produce significant ionization. If the effective ground is closer, a stronger potential rebound may occur as the end of the tube charges, producing a more dense plasma near the fifth hole, and more photoionization as a result.

8.4.6 Spacing Between Holes

It is expected that electrostatic interactions between SIWs should decrease as the spacing between the holes increases. The maximum electron densities are shown in Fig. 8.21 for hole spacings of 3 mm to 10 mm with 800 μm holes. For the smallest spacing, none of the SIWs

reach the target. If the spacing is increased to 5 mm (the base case) the SIWs do not reach the target for the second, fourth, and fifth hole, but do so for the first and third. When the spacing is increased to 10 mm, the SIWs reach the grounded target in all cases. With the 10 mm spacing, the pulse duration was increased to 700 ns, to allow time for the PIW to propagate through the longer tube before the end of the voltage pulse.

When the holes are closer together, the interaction between SIWs is not only closer in space, but also closer in time. The delay between the SIW exiting the first hole to exiting the second hole is approximately 15 ns for a 3 mm spacing, 25 ns for a 5 mm spacing, and 45 ns for a 10 mm spacing. For a 10 mm spacing, the first SIW has almost reached the grounded surface when the second SIW begins to emerge from its hole. As a result, the second SIW cannot electrostatically interfere with the propagation of the first SIW (though there can be residual interference of the first SIW with the second). When there is only 3 mm between the holes, the first SIW is still developing and has propagated less than 1.5 mm from the hole when the second SIW begins to emerge from its hole. As a result, the propagation of the first SIW is affected electrostatically by the second SIW, and similarly for the 2^{nd} to 3^{rd} SIW.

In a previous study of a multi-jet by Darny *et al.*, a metal multi-jet assembly (rather than the dielectric tube) was used to generate SIWs which were synchronized in time.[18] Those results suggest that the interactions between SIWs are more pronounced when SIWs are simultaneously generated, compared to a dielectric multi-jet where the SIWs are staggered in time.

The 3 mm spacing represents a qualitative lower limit of hole separation which must be exceeded to uniformly treat a surface by the plasma produced in the multi-jet. This limit of hole spacing is smaller in the experimental device, because the disturbance in potential surrounding

the SIW is less in 3-dimensions than in 2-dimensions. For example, SIWs contacted the surface with a 3 mm spacing in the experimental results discussed in Ref. [18]. The design goal of this device is to produce more spatially uniform treatment. To achieve this goal, a larger separation between the holes is needed, so that a SIW does not emerge until the previous SIW is close to the surface.

8.4.7 Distance To Grounded Target

The distance from the tube to the lower ground plane significantly affects the propagation of both the PIW and SIWs. For example, the maximum electron density is shown in Fig. 8.22 for tube-to-lower ground plane gaps of 5 to 20 mm. Before the PIW reaches the first hole, its propagation is affected by the lower ground plane. A closer ground plane results in a higher electric field, larger capacitance and charging of the tube, and higher PIW speeds before the first hole. When the grounded target is 5 mm from the tube, the PIW reaches the first hole after 65 ns, compared to 140 ns for a 20 mm gap (the average speed decreasing from 5.7×10^7 to 2.6×10^7 cm/s). The electron impact ionization rate decreases from 2.5×10^{21} $cm^{-3}s^{-1}$ for a 5 mm gap to 1.8×10^{20} $cm^{-3}s^{-1}$ for a 20 mm gap, producing electron densities in the tube of 5×10^{14} cm^{-3} to 4×10^{12} cm^{-3}.

The SIWs are affected by the tube-to-ground gap through both the electric field and the gas composition. As the SIW exits the tube, there is an initially higher electric field if the gap is smaller. As the SIW approaches the grounded target, electric field enhancement in the ionization front increases due to the shorting of the electric field in the trailing conductive channel. This effect is larger with a smaller gap as the initial vacuum electric field is larger. The SIW therefore propagates toward the ground faster with a smaller gap. The SIW crosses from hole to ground plane in less than 10 ns for a 5 mm gap while requiring and 150 ns for 15 mm gap. The amount

of air in the path of the SIW through the He plume increases with distance from the hole to the ground plane, which additionally contributes to the SIW slowing and eventually stalling.

The consequences of an SIW contacting the grounded target are more severe when the grounded target is closer. If the multi-jet is close to the grounded target, the SIWs contact the grounded surface while still propagating through a He plume with a low fraction of air. The electron density and conductivity of the plasma channel are higher, and as a result the disturbances in potential due to the potential rebound are more significant. For small gaps, the potential rebound can occur before the PIW reaches the next hole. The potential rebound decreases *E/N* in the PIW front after each SIW reaches the ground. The PIW therefore slows as it propagates through the tube for closer ground planes. For example, with the 5 mm gap, the PIW has an initial speed (before the first hole) of 6×10^7 cm/s and a final speed (at the last hole) of 1×10^7 cm/s. As a result the PIWs reach the end of the tube within about 45 ns of each other for all gaps, in spite of the PIW with the 5 mm gap having a higher initial speed. With the electric field in the PIW decreasing as each SIW contacts ground and with the PIW slowing down, the intensity of the PIW decreases with each subsequent SIW. For the 5 mm gap, the maximum electron density in the tube decreases from 1×10^{14} cm^{-3} above the first hole to 3×10^{10} cm^{-3} above the last hole. This decrease in electron density inside the tube is less significant for the 15 mm gap where the density decreases from 5×10^{12} at the first hole to 4×10^{12} cm^{-3} at the last hole. The decrease in intensity of the PIW translates to decrease in maximum electron density with each successive SIW. For the 5 mm gap, the maximum electron density in the SIW decreases from 2×10^{14} cm^{-3} at the first hole to 4×10^{13} cm^{-3} at the last hole.

The electrostatic interaction between SIWs decreases when the ground plane is closer because the vertical electric field is larger. However, the decrease in intensity of successive

SIWs also intensifies with smaller gaps, implying that there is a maximum number of holes that will support SIWs for a given gap and voltage.

With a tube-to-target gap of 10 mm, the maximum electron density in the first SIW (1×10^{13} cm^{-3}) is higher that than in the following SIWs, all of which have approximately the same maximum electron density (2×10^{12} cm^{-3}). The first SIW reaches the target as the second SIW emerges from the hole, which reduces the electrostatic interaction between the SIWs and may improve the uniformity of the multi-jet treating surfaces. For the computational conditions, between gaps of 10 to 15 mm, electrostatic interactions between the SIWs intensify to the point of preventing propagation of SIWs from adjacent holes.

When the gap increases to 20 mm, none of the SIWs reach the target – the vertical electric field is smaller and the electrostatic interaction between SIWs is greater. The electrostatic interaction increases due to the relative timing of the SIWs. With the vertical electric field being smaller, the first SIW propagates only ~1 mm outside the hole by the time the second SIW begins to form. The electrostatic interaction between the SIWs can be reduced by increasing the spacing between the holes. Computational experiments confirmed that for a 20 mm gap, increasing the spacing of holes to 10 mm reduced the electrostatic interactions. However, increasing the likelihood for all SIWs reaching the ground plane is best accomplished by decreasing the tube-to-groundgap. Having said that, the computed multi-jet performance as a function of tube-to-target gap suggests that there is an optimum gap for a given voltage, gas flow rate, hole diameter, and spacing. Increasing the gap decreases perturbations in potential that occur when SIWs contact the ground plane that affect subsequent SIWs; however the magnitude of perturbations are in turn functions of these operational parameters. These interactions are

expected to be less severe when treating a dielectric surface, where the impact of the SIW contacting the surface is limited by the charging of the surface.

8.5 Concluding Remarks

A multi-jet, a device that produces an array of atmospheric pressure plasma jets from a single initial ionization wave, was investigated through experiments and modeling. The design objectives of this device include providing large-area, relatively uniform plasma treatment of materials and tissues. Critical design parameters were investigated with these objectives in mind. There are likely two limits to the total number of SIWs that can be produced. First, the power supply has a finite capacitance which limits the total charge that can be transferred per pulse. If the total charge transfer through the conductive channels of the SIWs exceeds the capacitive limit of the power supply, the applied voltage will decrease. The result is that propagation of the PIW and SIWs may stall, and new SIWs may not be launched. Second, between the powered electrode and the fronts of the PIW and SIW, there is a finite electric field, and so there is a decrease in the electric potential at the fronts of these waves. As the length of the tube and the number of SIWs increase, the electric field at the front of the PIW may be insufficient for further propagation or launching of new SIWs.

The most important parameter in device performance is the polarity of the voltage pulse, which determines the nature of the breakdown and IW dynamics. A positive polarity pulse provides more electric field enhancement at the front of the IW, but is more sensitive to radiation transport including ionization of impurities. Propagation of the positive SIWs rely on photoionization by photons emitted by both He_2* and N_2**. The excimer radiation from He_2* produced in the PIW and propagating through the holes is most influential in initiating the SIWs. Photoionization resulting from emission by N_2** is most influential in sustaining the SIWs. As a

result, the SIWs reach the grounded target with a positive polarity while not reaching the target for the same conditions with a negative polarity. The positive polarity discharges may therefore be preferable for direct surface treatment.

A single hole device was used to qualitatively validate the modeling results and provide a geometry in which to interpret experimental electric field measurements. The trends for the time and spatial dynamics of the electric field and IWs generally agree between the experiment and the model, with the computed magnitude of the field being larger than the experiment due to the 2-dimensional geometry used in the model.

Increasing the He flow rate promotes propagation of SIWs by increasing the helium mole fraction outside of the tube and thereby reducing electron energy losses to air diffusing into the He plume. Increasing He gas flow rate enables SIW propagation with lower electric fields (e.g., larger tube-to-ground gap). Decreasing the hole diameter results in a longer delay between the passage of the PIW and the SIW emerging from each hole. This delay is primarily due to a reduced view angle for photoionization outside the tube, which is required to initialize the propagation of positive SIWs.

The relative timing of SIW propagation is also critical to the interactions between the SIWs. If the spacing between holes is small, the likelihood for SIWs reaching the target is smaller. For these conditions, subsequent SIWs emerge from the hole while the previous SIW is still at a similar height. The resulting perturbation of the electric field by the conductivity and space charge of the adjacent SIWs disturbs the propagation of both SIWs. The proximity of the multi-jet to the grounded target is an important control mechanism. Decreasing the tube-to-target gap increases the effects of the potential rebound when SIWs contact the ground, but decreases the likelihood of electrostatic interaction that might interfere with propagation of

subsequent SIWs. A moderate distance, in this case a 10 mm gap, provides a tradeoff in which the PIW minimally fades with each subsequent SIW, while electrostatic interactions do not prevent subsequent SIWs from reaching the surface.

8.6 Figures

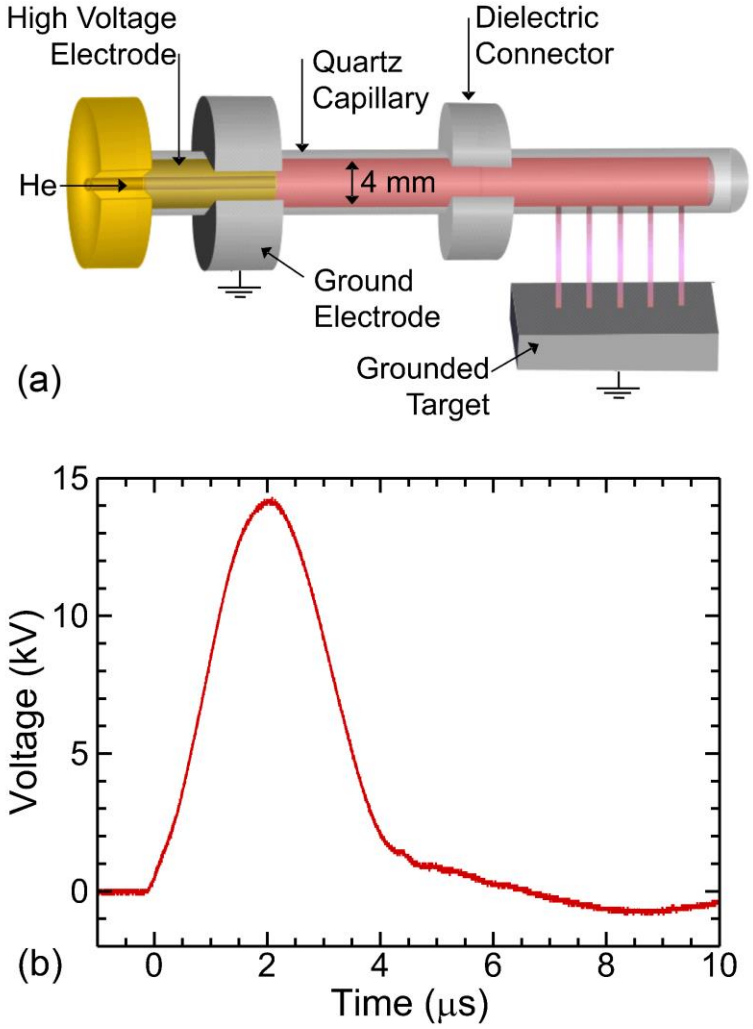

Fig. 8.1 The experimental multi-jet device. (a) Schematic of the multi-jet device with the plasma indicated as the pink shading. (b) The voltage pulse used in the experiment.

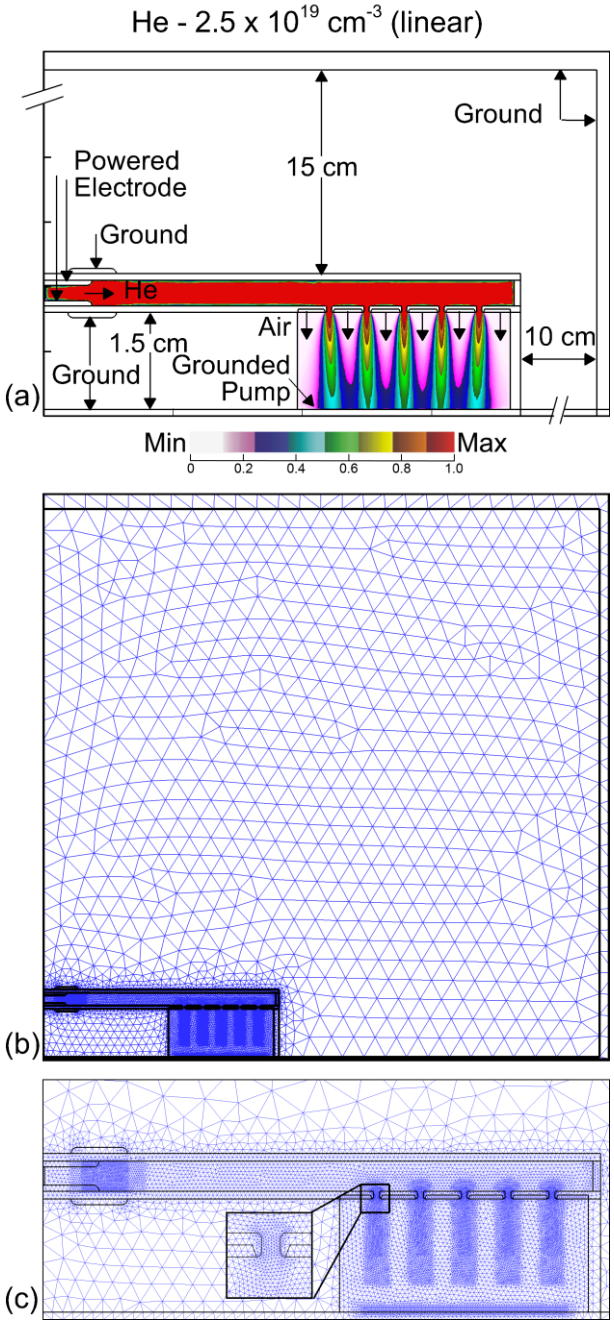

Fig. 8.2 The geometry used to model the multi-jet device. (a) Schematic of the Cartesian geometry. Note the axes are broken to show the distant ground planes. The contour plot shows the density of helium flowing out of the holes and mixing with the humid air. (b) The computational mesh for the entire domain. (c) The refinement regions of the mesh for the regions where the plasma propagates, and more refined regions as the plasma propagates inside of the holes and interacts with electrodes. The vertical lines below the tube on either side of the holes separate the region in which the full plasma simulation was performed and the material having $\varepsilon/\varepsilon_r = 1$. Where only Poisson's equation is solved.

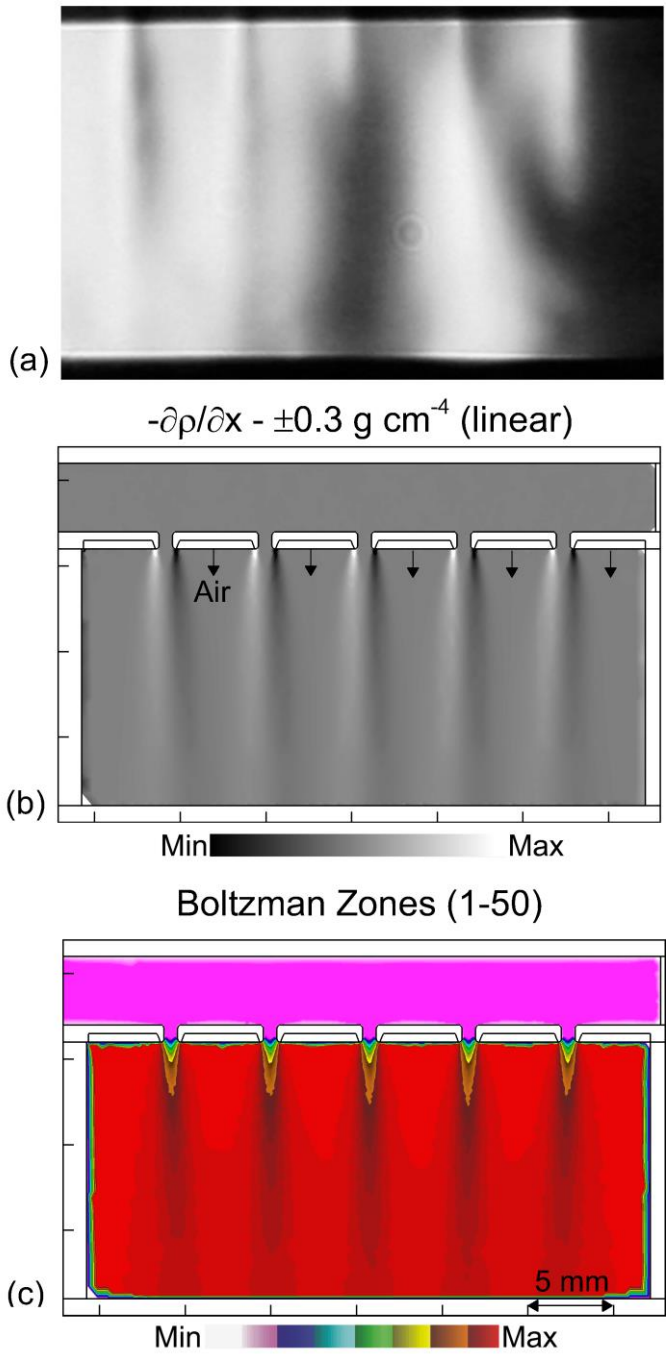

Fig. 8.3 The gas flow and resulting Boltzmann zones. (a) Experimentally measured Schlieren imaging of the mixing of He with the surrounding air in the base case. (b) Simulated Schlieren imaging based on steady state flow predicted by the model with a total of 3 slm of air flowing between the holes. (c) The 50 zones for which Boltzmann's equation is solved for the average gas composition. The zones are determined by the mole fraction of N_2 on a log scale.

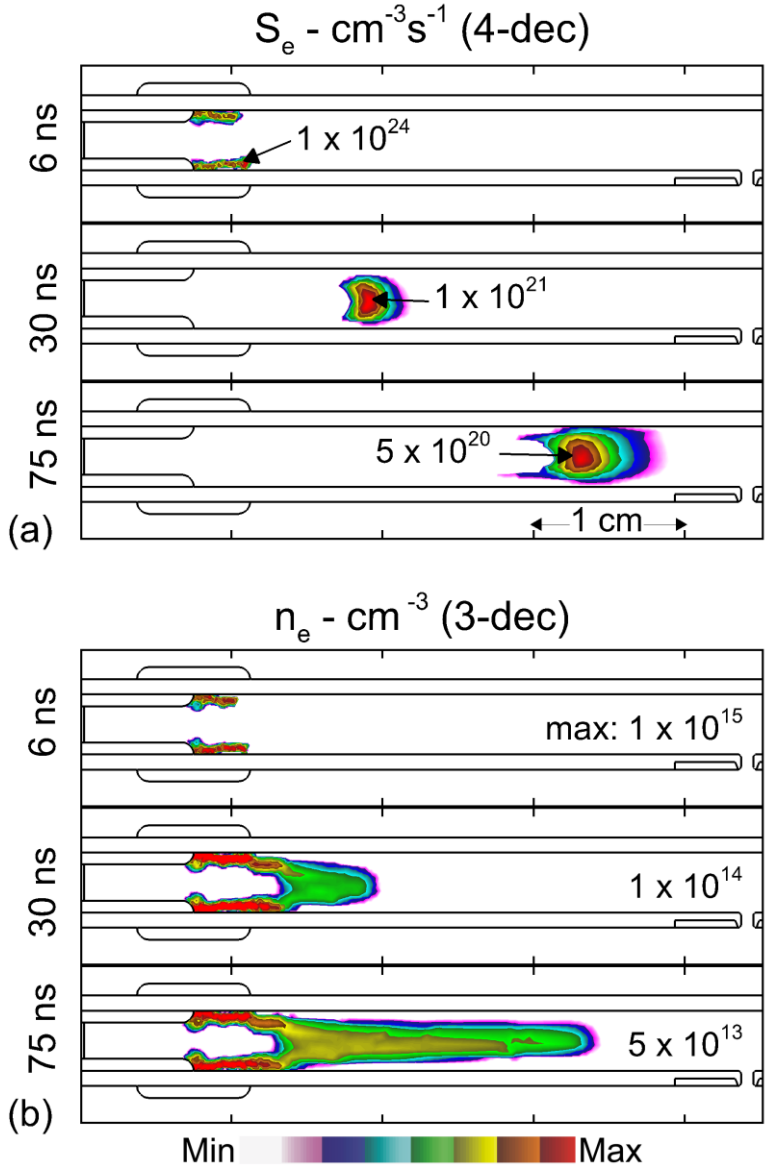

Fig. 8.4 The initial breakdown at the powered electrode and development of an ionization wave inside the tube. (a) Electron impact ionization source term (S_e) plotted on a 4-decade log scale, with the maximum value in each frame indicated on the figure. (b) Electron density (n_e) plotted on a 3-decade log scale, with the maximum value indicated on each frame. Note the asymmetry due to the closer proximity of the lower ground plane.

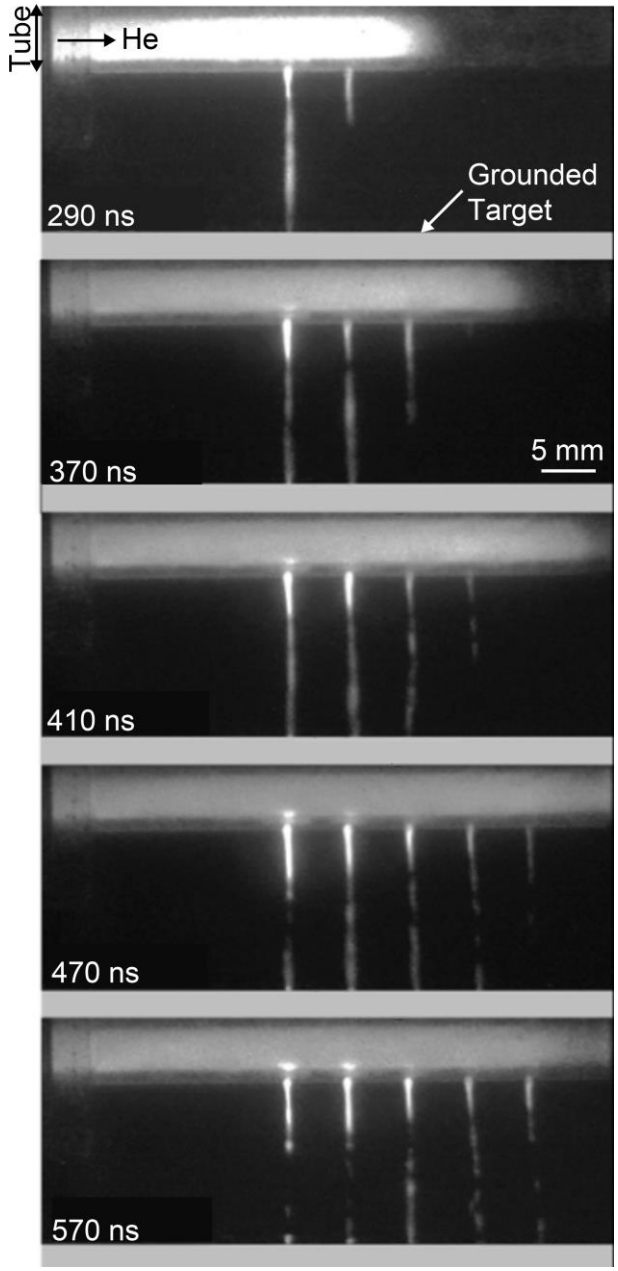

Fig. 8.5 ICCD imaging of IW propagation in the base case. The camera gate was 10 ns, and the images are accumulated over 100 pulses. The times indicated in the figure are measured from the moment the PIW is visible in the camera frame, which is 2.3 μs after the start of the voltage pulse.

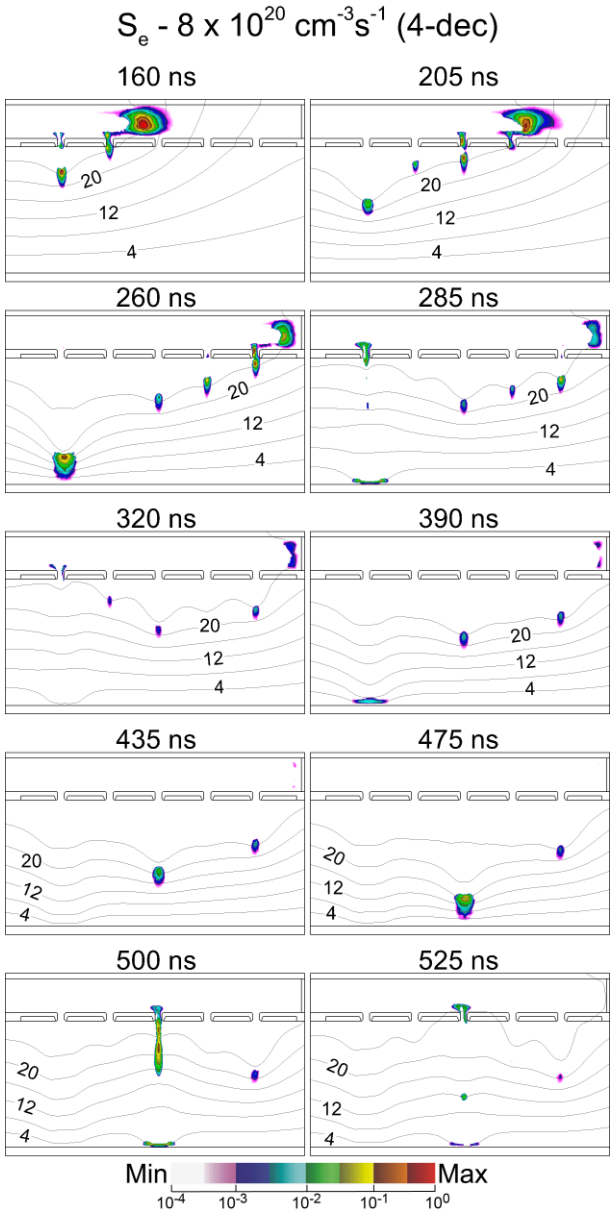

Fig. 8.6 Ionization wave propagation out of the holes in the base case. The electron impact ionization source term (S_e) is plotted on a 4-decade log scale. Electric potential contours are labeled with potential in kV. The propagation of secondary ionization waves disturbs the potential profile of neighboring holes.

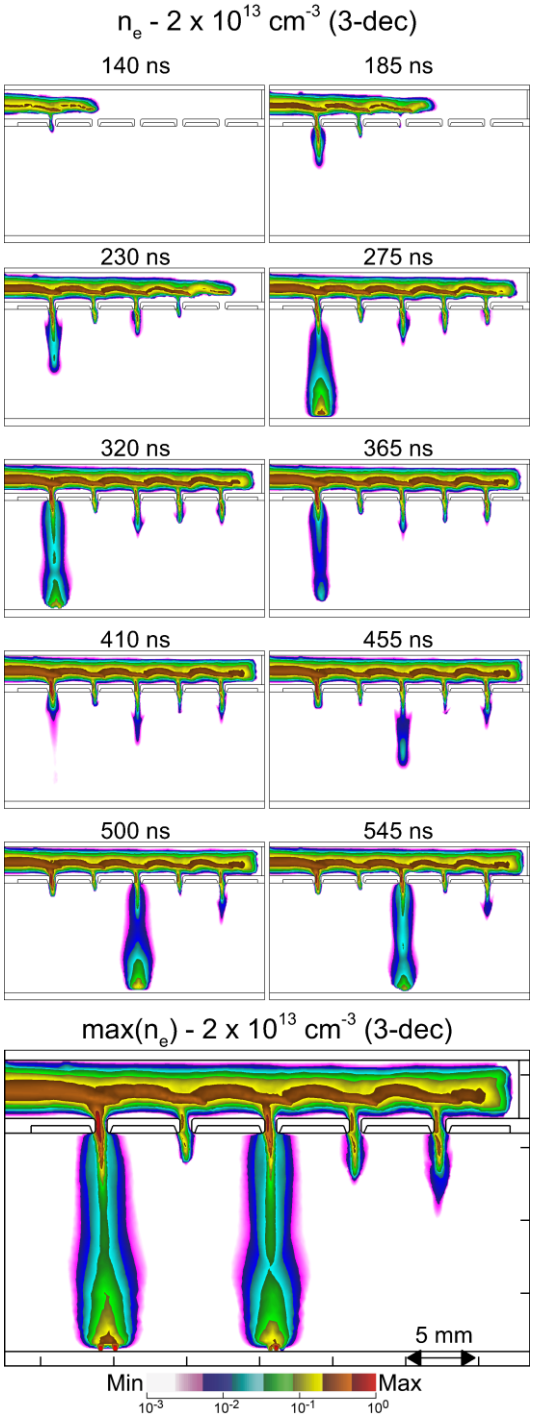

Fig. 8.7 Electron density (n_e) as a function of time for the base case. The electron density in the tube remains elevated after the primary ionization wave (PIW) passes. Secondary ionization waves (SIWs) propagate through each of the holes, but only reach the surface through the first and third holes. Outside of the tube, thermal electron attachment to O_2 results in the electron density dropping more rapidly after the SIW passes. The bottom frame shows the maximum electron density that occurs during the simulation at each computational node. This mode of display records the time history of the propagation of the SIWs.

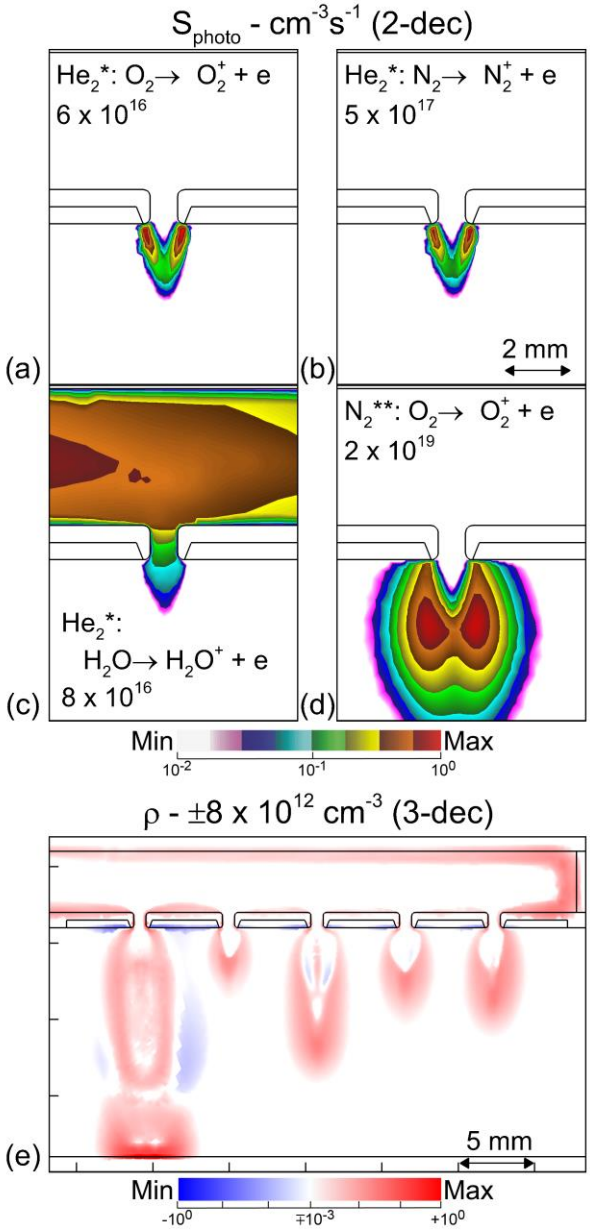

Fig. 8.8 Photoionization rate and space charge as the ionization waves propagate through the holes. (a)-(d) The photoionization source term (S_{photo}) at 155 ns at the first hole, plotted on a 2-decade log scale with the maximum value indicated on each frame. Values of S_{photo} are shown resulting from each emitter-absorber pair included in the model: (a) photoionization of O_2 by photons emitted by He_2*, (b) photoionization of N_2 by photons emitted by He_2*, (c) photoionization of H_2O by photons emitted by He_2*, (d) photoionization of O_2 by photons emitted by N_2**. (e) The total space charge density at 430 ns. The positive and negative spacecharge are each plotted on 3-decade log scales.

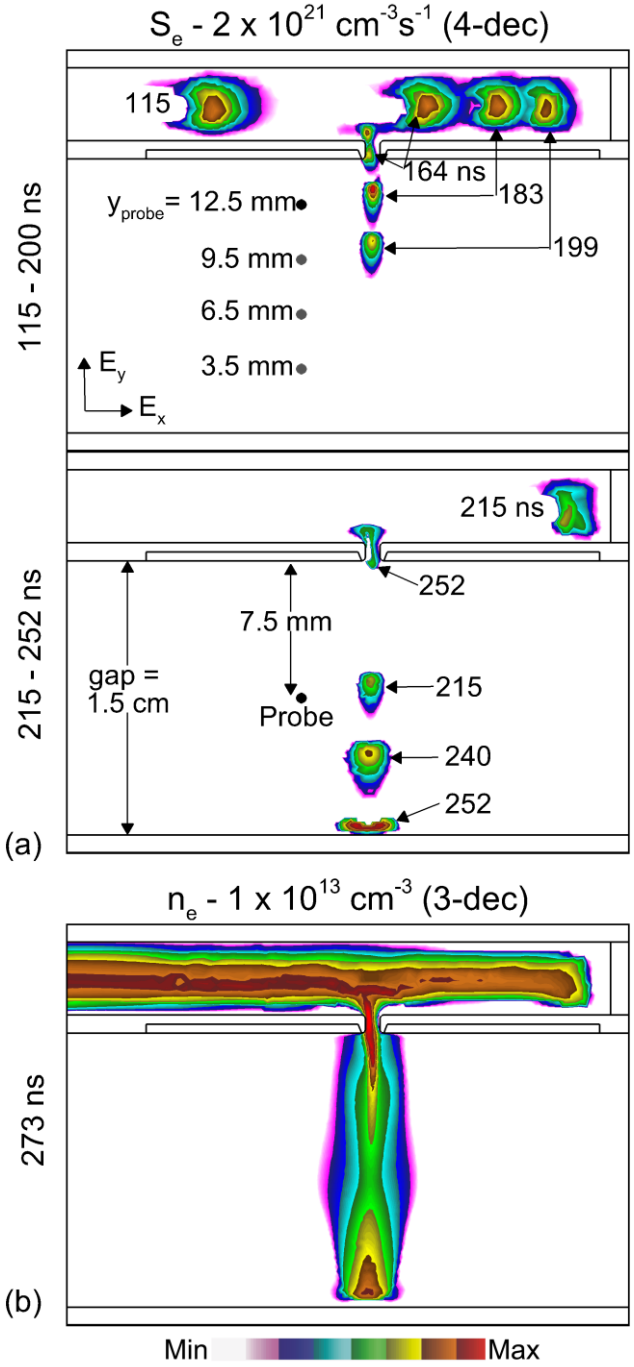

Fig. 8.9 A summary of IW propagation in a multi-jet assembly with a single hole and single secondary ionization wave. (a) The electron impact ionization source term (S_e) is shown for four subsequent moments in time, on a 4-decade log scale. The time corresponding to each position of the IW is indicated on the frame. The position at which the electric field measurements were made with the electrooptic probe shown in Fig. 8.10 are in the upper frame. The probe positions for the measurements plotted in Fig. 8.11 are indicated in the lower frame. (b) The electron density at 273 ns, 172 ns after the secondary ionization wave has contacted the grounded pump surface.

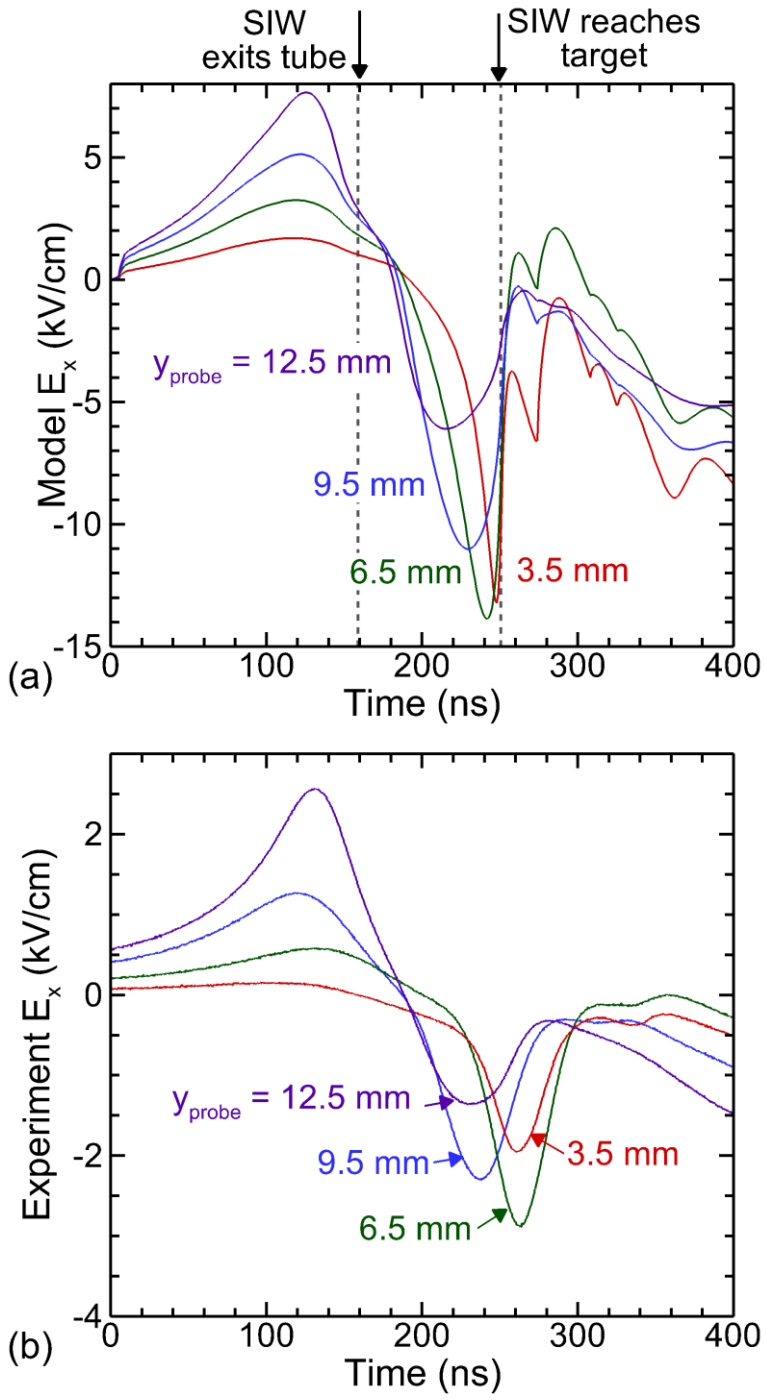

Fig. 8.10 The horizontal component of the electric field (E_x) for 4 vertical positions 1 mm to the left of the hole, as indicated on Fig. 8.9. The position above the grounded target surface is indicated for each line. Values of E_x are sown (a) calculated in the model and (b) measured in the experiment. The modeling results are averaged over the volume of the probe. In the experiment the distance from the electrode to the first hole is larger, and so the experimental timing has been shifted to align with the modeling results.

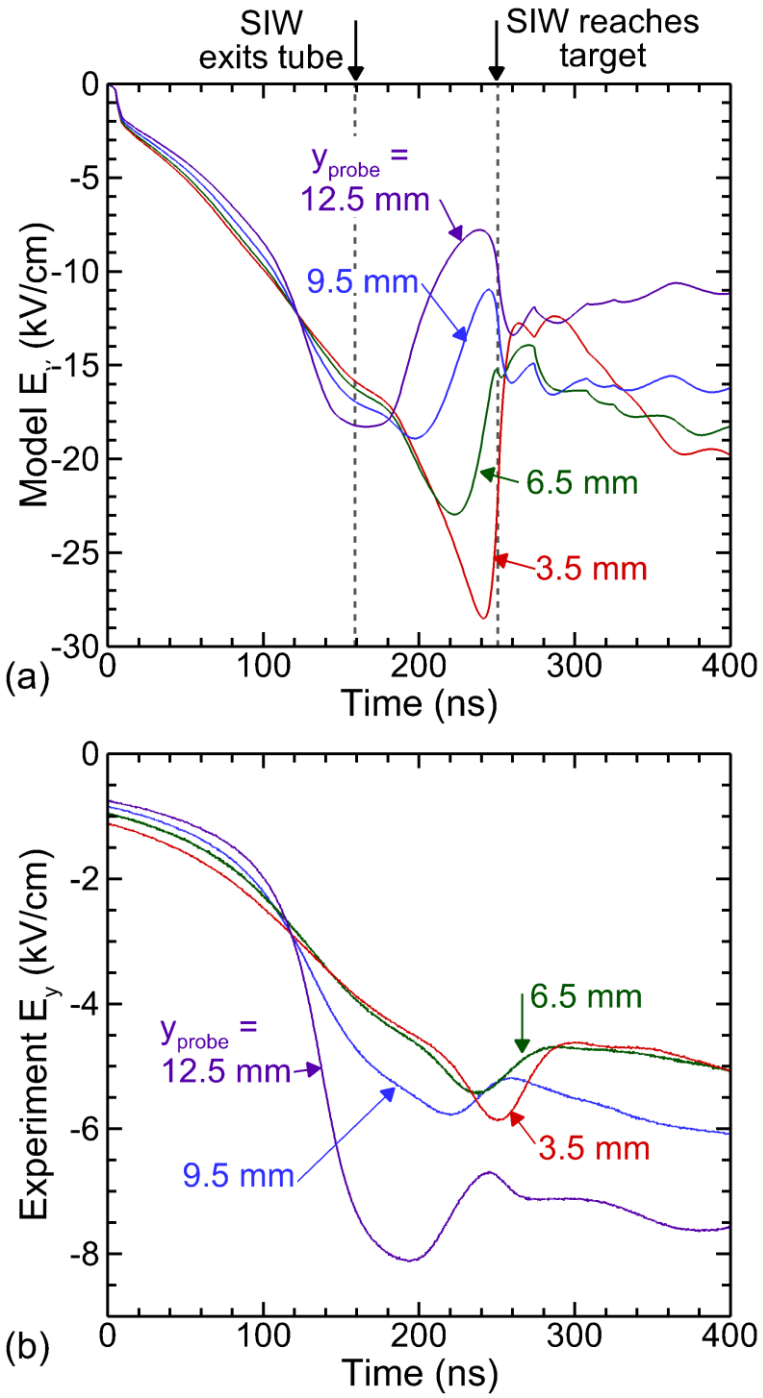

Fig. 8.11 The vertical component of the electric field (E_y) for 4 vertical positions 1 mm to the left of the hole, as indicated on Fig. 8.9. The position above the grounded target surface indicated for each line. Values of E_y are shown (a) calculated in the model and (b) measured in the experiment. The modeling results are averaged over the volume of the probe. In the experiment the distance from the electrode to the first hole is larger and so the experimental timing has been shifted to align with the modeling results.

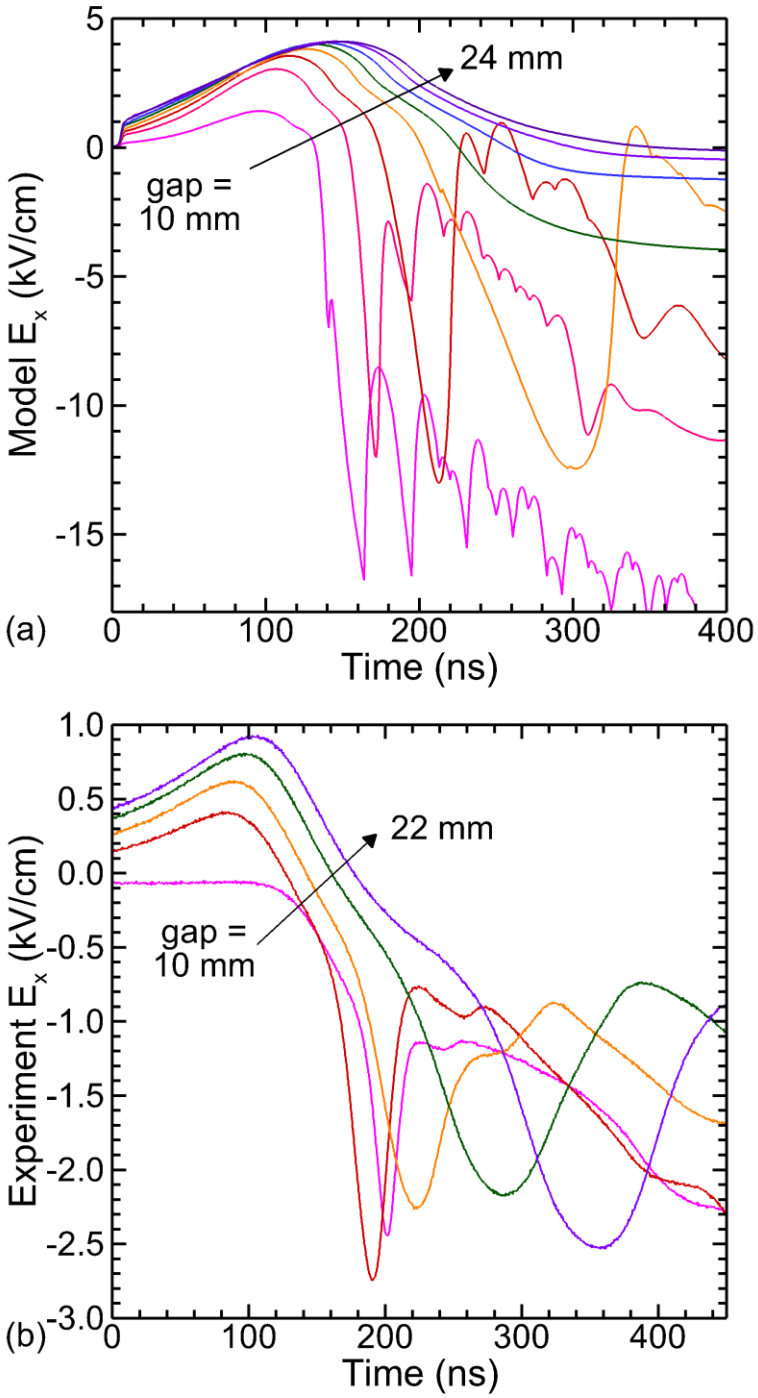

Fig. 8.12 The electric field measurements probed at 3.5 mm to the left of the hole and 7.5 mm below the tube for different gap distances between the tube and the ground. (a) E_x in the model (gap distances of 10, 12, 14, 16, 18, 20, 22, and 24 mm) and (b) E_x in the experiment (gap distances of 10, 13, 16, 19, and 22 mm)..

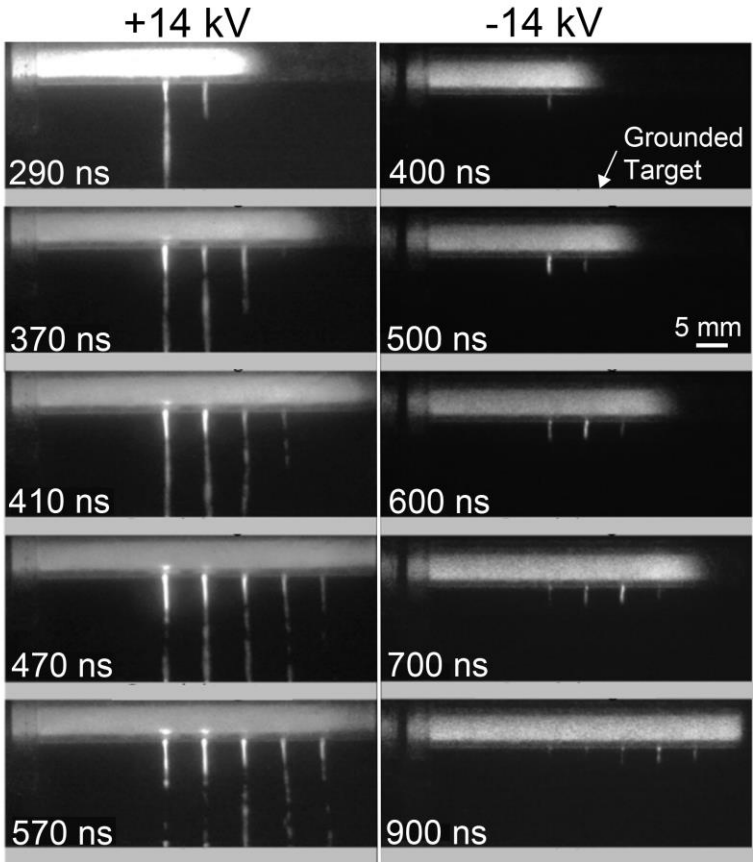

Fig. 8.13 ICCD imaging of ionization wave propagation in a multi-jet with (left) +14 kV positive polarity and (right) -14 kV negative polarity. The imaging gate was 10 ns and the images are averaged over 100 pulses.

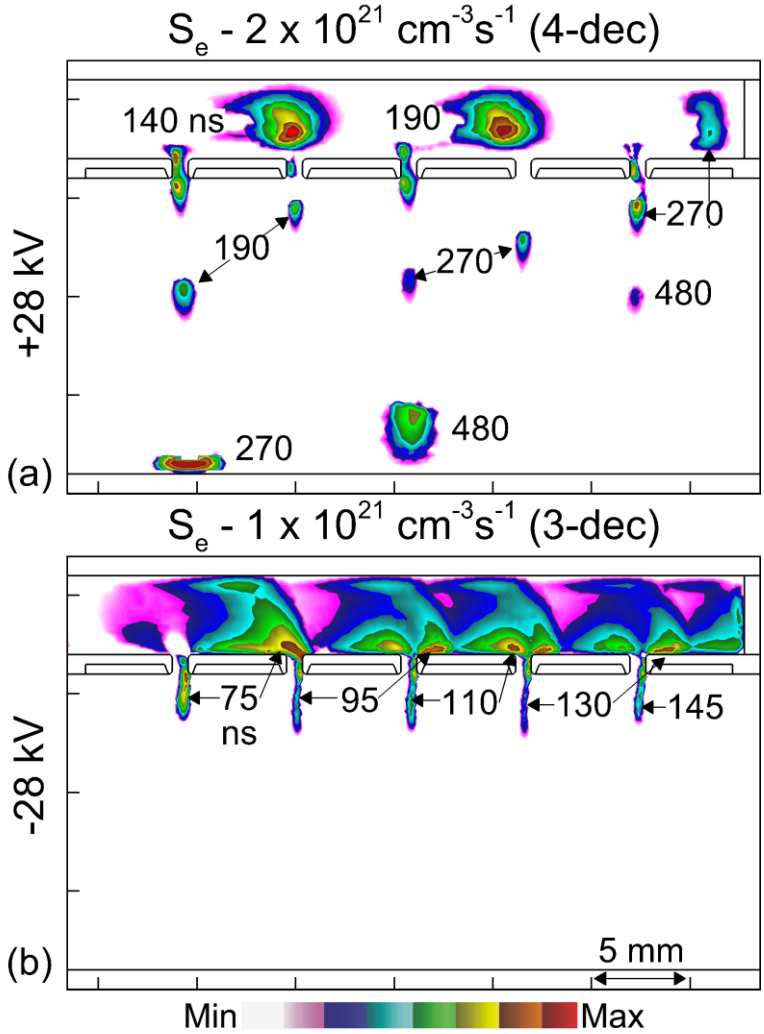

Fig. 8.14 The effect of polarity on ionization wave propagation, shown by the electron impact ionization source term, S_e computed with the model. S_e is plotted at several moments in time, with the time in ns indicated near each source term. (a) S_e for a +28 kV applied voltage, plotted on a 4-decade log scale. (b) S_e for a -28 kV applied voltage, plotted on a 3-decade log scale.

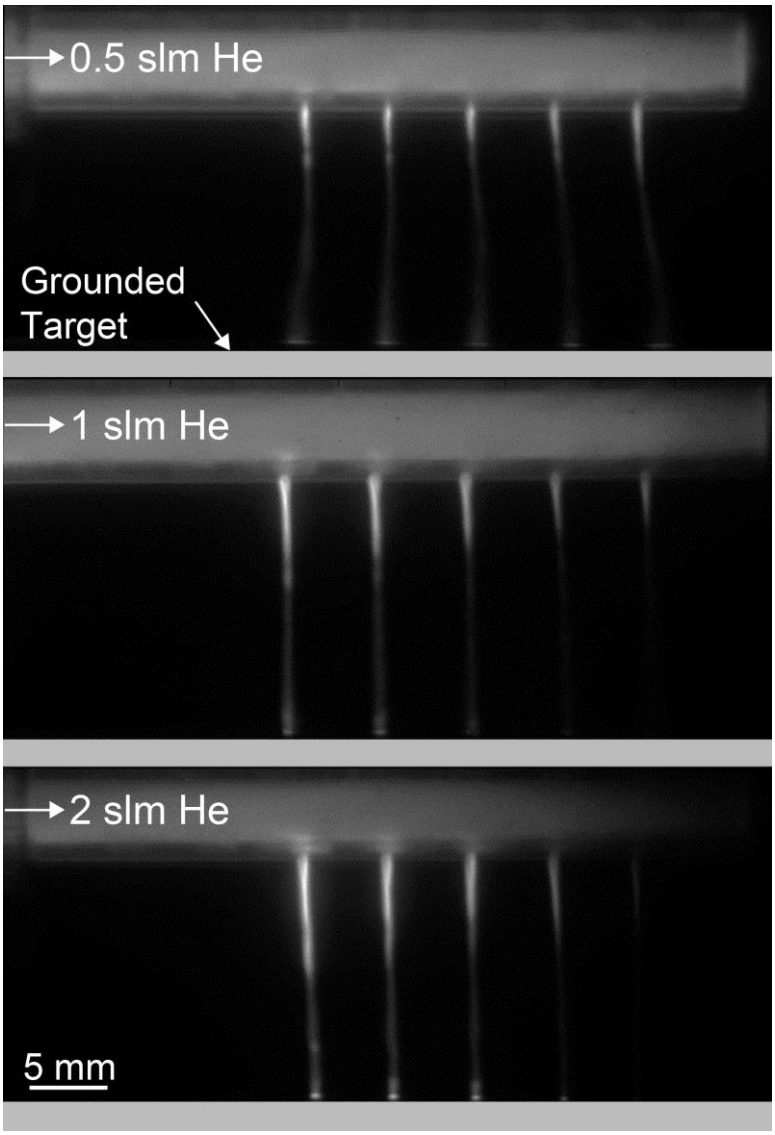

Fig. 8.15 ICCD imaging of total emission as a function of helium flow rate. The gate was 10 ns and the images are averaged over 100 pulses.

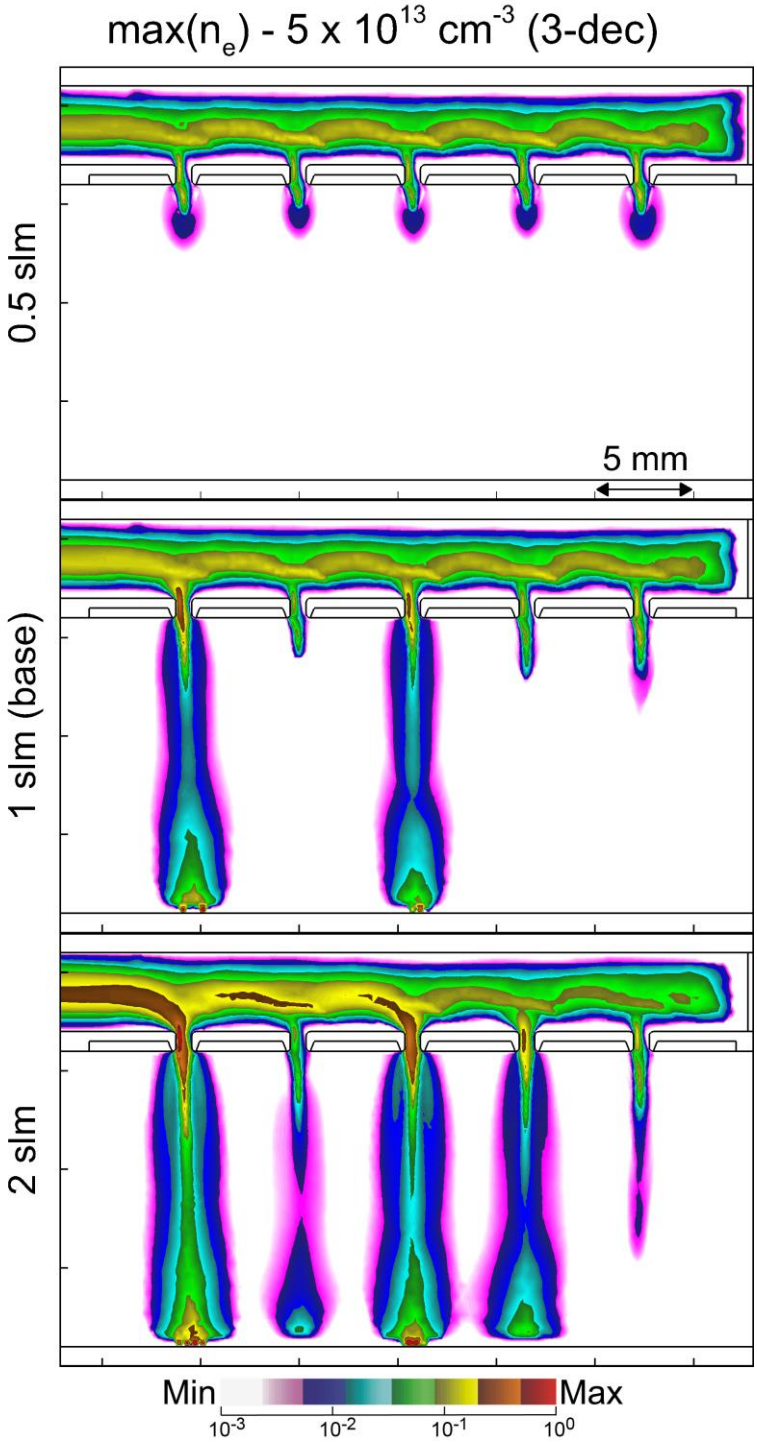

Fig. 8.16 The maximum electron density [max(n_e)] at each numerical mesh point computed with the model as a function of He flow rates, 0.5 to 2.0 slm. Densities are plotted on a 3-decade log scale.

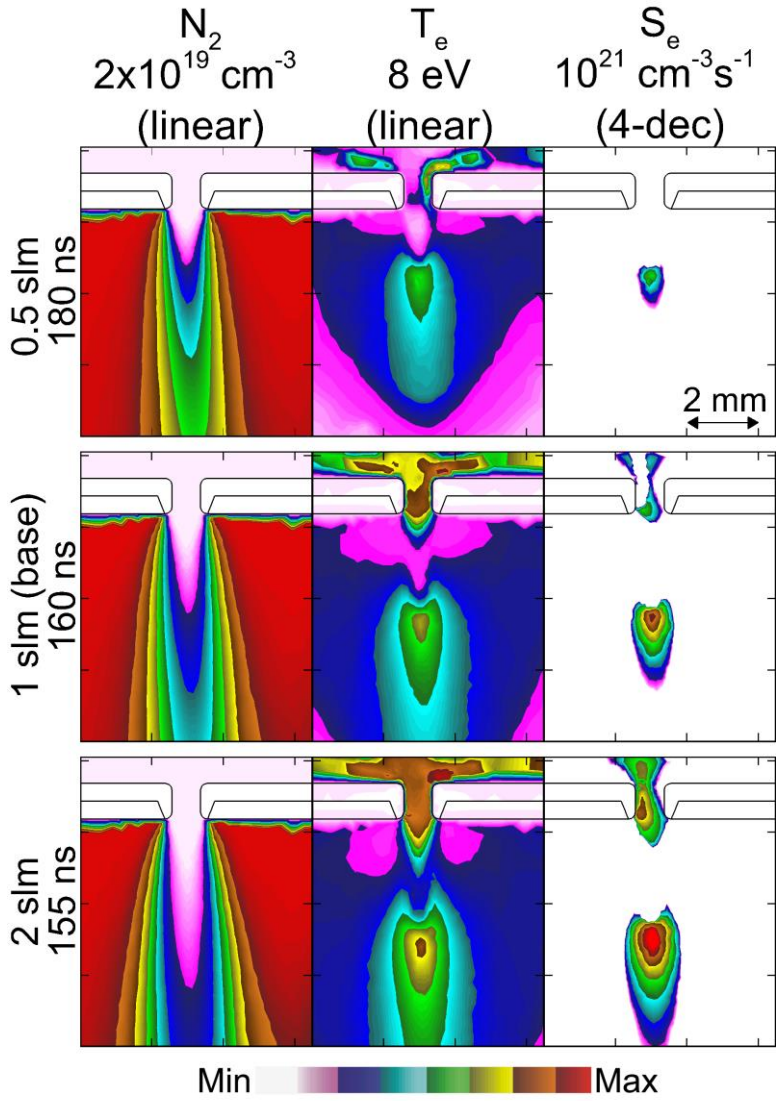

Fig. 8.17 IW propagation through the first hole as a function of helium flow rate. (left) N_2 density with a steady state flow, plotted on a 4-decade log scale. (center) Electron temperature as the IW exits the hole and begins to interact with in-diffusing air, plotted on a linear scale. (right) Electron impact ionization source of the SIW at the same position, plotted on a 4-decade log scale. The speed at which the SIW develops outside of the tube was sensitive to He flow rate, and so results are when the SIW is at approximately the same position. The time at which T_e and S_e are plotted is indicated at the left.

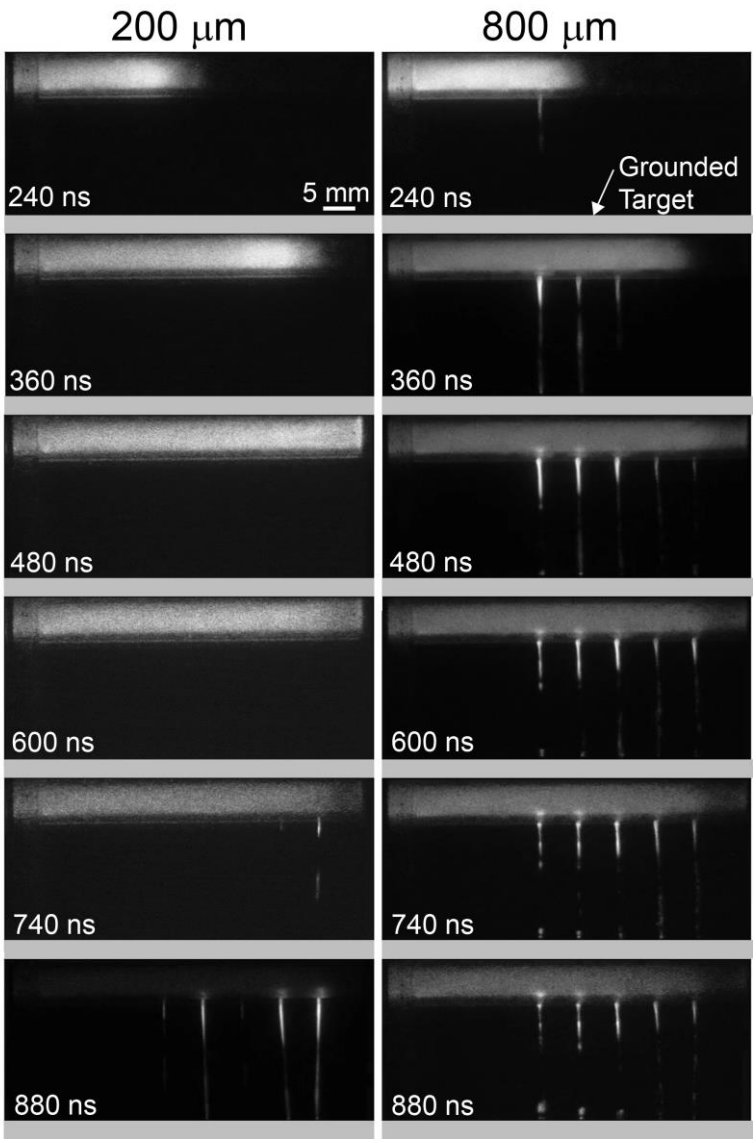

Fig. 8.18 ICCD imaging of IW propagation for a multi-jet with 200 μm and 800 μm diameter holes. The camera gate was 10 ns, and images are averaged over 100 pulses. The time indicated on the figure is measured from the moment the PIW is visible in the camera frame.

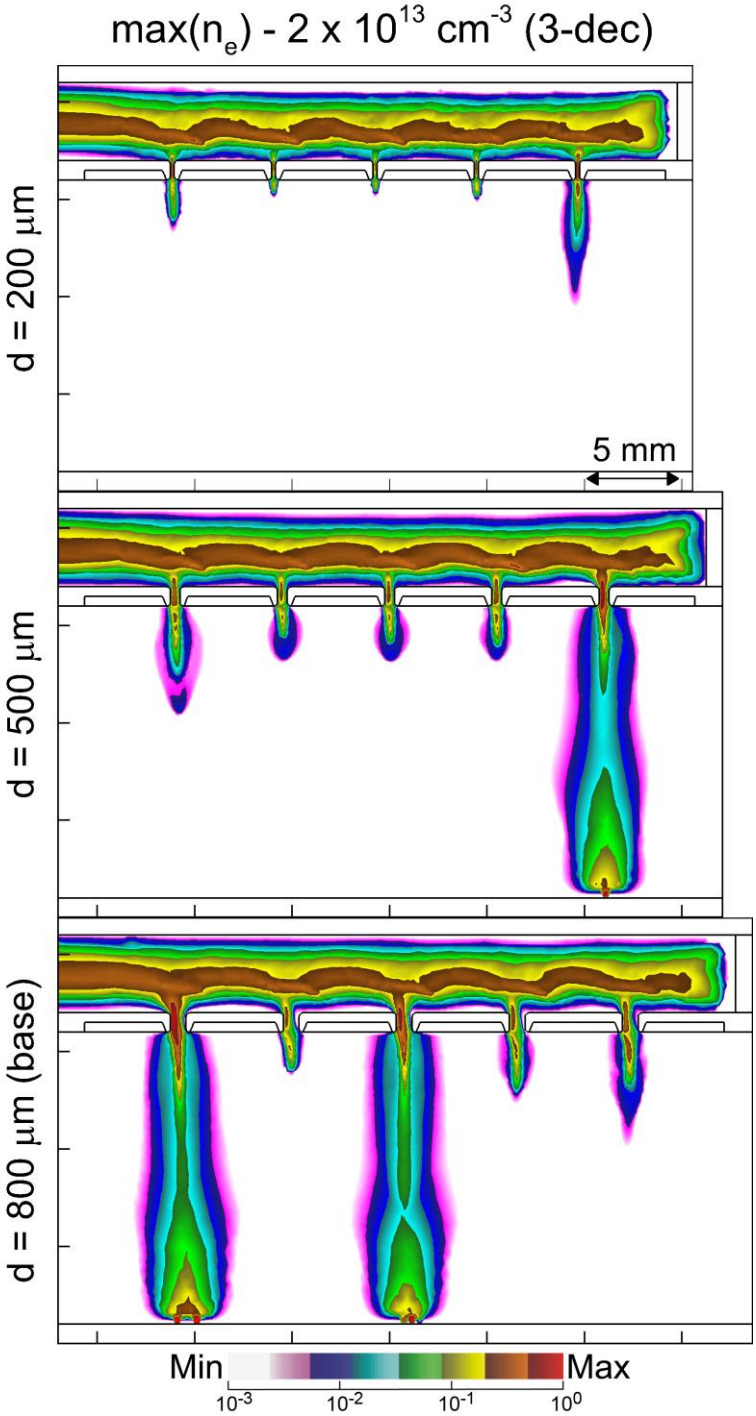

Fig. 8.19 The maximum electron density [max(n_e)] for hole diameters of 200, 500, and 800 µm, plotted on a 3-decade log scale.

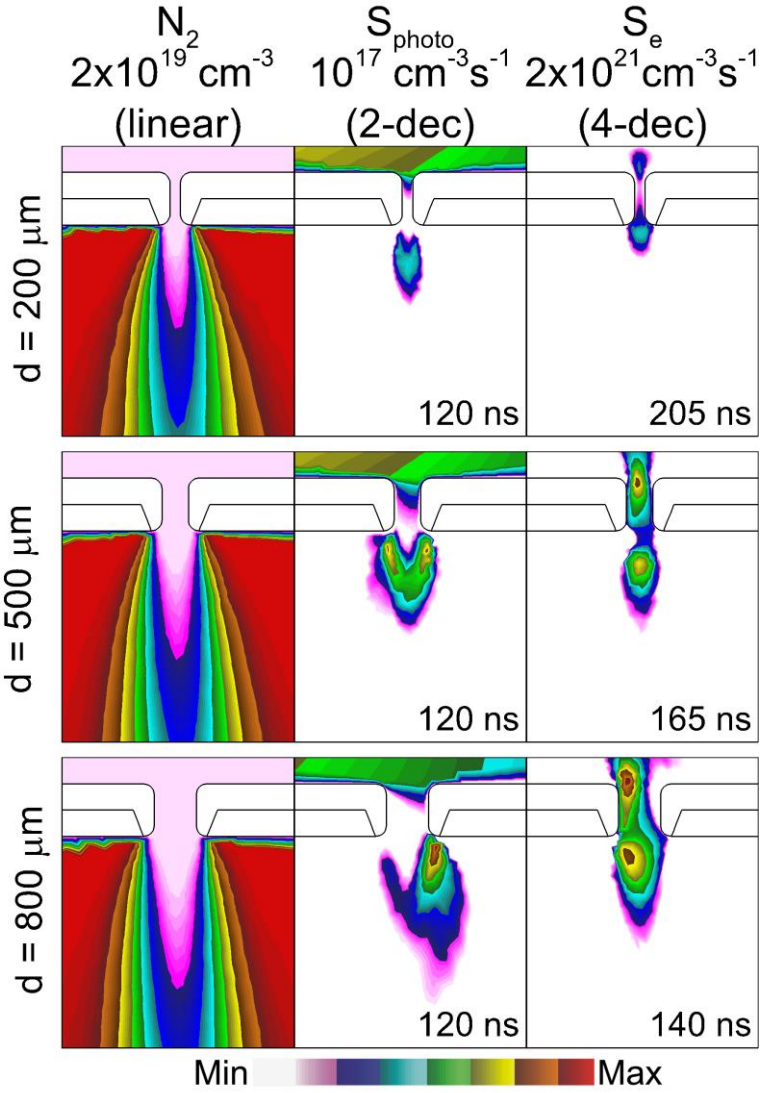

Fig. 8.20 Mechanisms of IW propagation through the first hole of a multi-jet for different hole diameters. (left) N_2 density for a steady state flow, plotted on a 4-decade log scale. (center) Total photoionization rate, S_{photo}, at t = 120 ns, before the IW has exited the tube on a 2-decade log-scale. (right) Electron impact ionization rate, S_e, on a 4-decade log-scale after the IW has propagated through the hole for the IW being at approximately the same location. The SIW initiates later for smaller holes and the time for each image is shown.

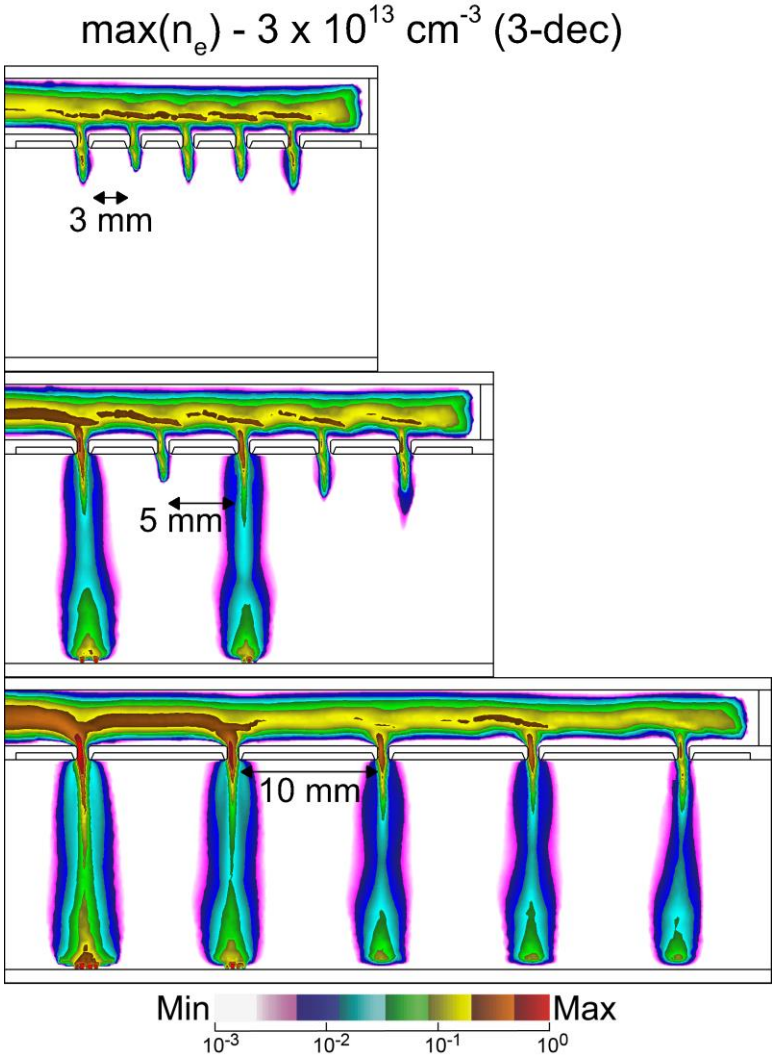

Fig. 8.21 The maximum electron density [max(n_e)] for 3 mm, 5 mm, and 10 mm spacing between the holes in a multi-jet for hole diameters of 800 μm. The densities are plotted on a 3-decade log scale.

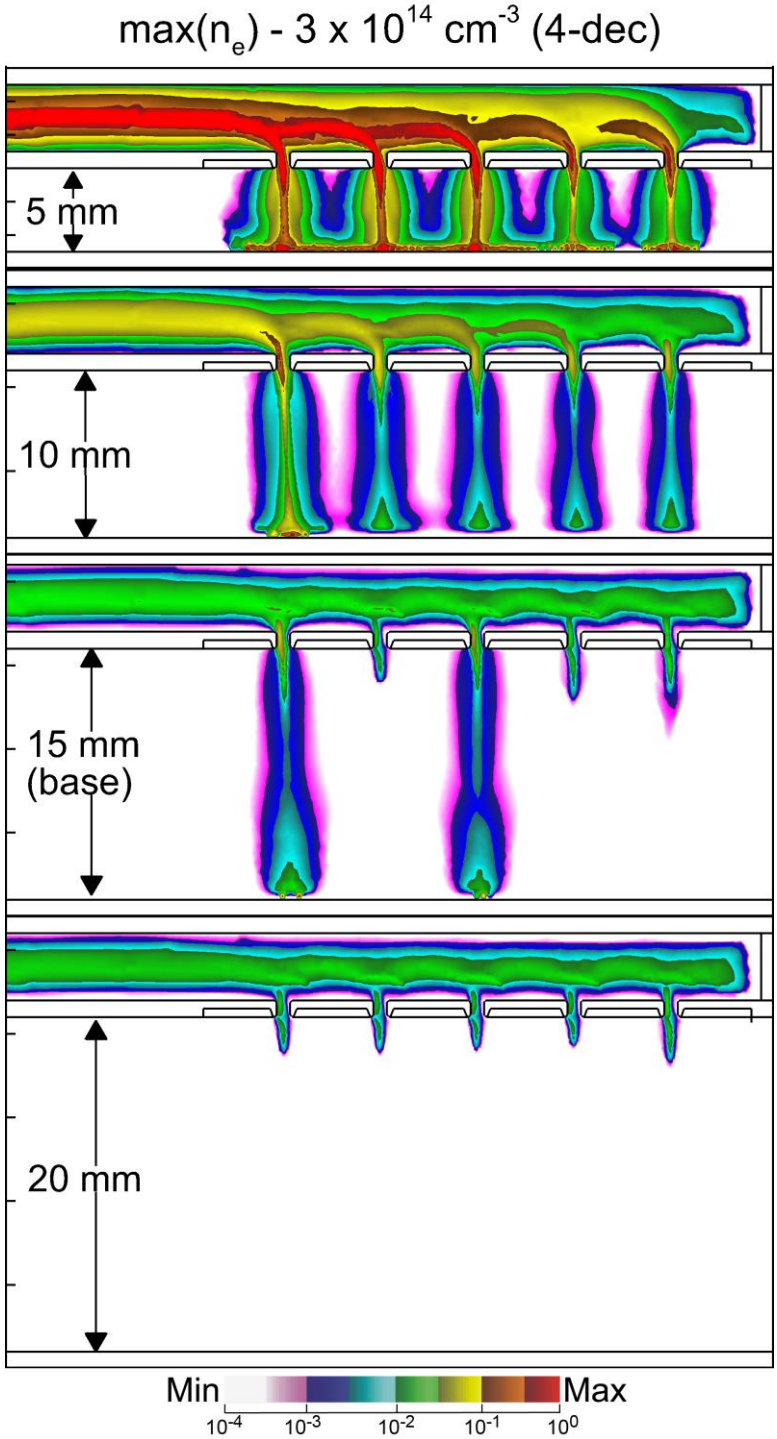

Fig. 8.22 The maximum electron density [max(n_e)] for tube-to-grounded target gaps of 5 mm to 20 mm. The electron density is plotted on a 4-decade log scale.

8.7 References

[1] N. Knake, S. Reuter, K. Niemi, V. Schulz-von der Gathen and J. Winter, J. Phys. D: Appl. Phys. **41,** 194006 (2008).

[2] Z.-H. Lin, C.-Y. Tobias Tschang, K.-C. Liao, C.-F. Su, J.-S. Wu and M.-T. Ho, IEEE Trans. Plasma Sci. **44,** 3140 (2016).

[3] Z. Fang, Z. Ding, T. Shao and C. Zhang, IEEE Trans. Dielectr. Electr. Insul. **23,** 2288 (2016).

[4] C. Zhang, T. Shao, Y. Zhou, Z. Fang, P. Yan and W. Yang, Appl. Phys. Lett. **105,** 044102 (2014).

[5] A. Stancampiano, N. Selaković, M. Gherardi, N. Puač, Z. L. Petrović and V. Colombo, J. Phys. D: Appl. Phys. **51,** 484004 (2018).

[6] R. Wang, H. Sun, W. Zhu, C. Zhang, S. Zhang and T. Shao, Phys. Plasmas **24,** 093507 (2017).

[7] D. Li, D. Liu, Z. Chen, M. Rong and M. G. Kong, IEEE Trans. Plasma Sci. **44,** 2648 (2016).

[8] S. J. Kim, T. H. Chung, H. M. Joh, J.-H. Cha, I. S. Eom and H.-J. Lee, IEEE Trans. Plasma Sci. **43,** 753 (2015).

[9] X. Lu, G. V. Naidis, M. Laroussi and K. Ostrikov, Phys. Rep. **540,** 123 (2014).

[10] Y. Xian, P. Zhang, X. Lu, X. Pei, S. Wu, Q. Xiong and K. Ostrikov, Sci. Rep. **3,** 1599 (2013).

[11] Z. Fang, C. Ruan, T. Shao and C. Zhang, Plasma Sources Sci. Technol. **25,** 01LT01 (2016).

[12] N. Y. Babaeva and M. J. Kushner, Plasma Sources Sci. Technol. **23,** 015007 (2014).

[13] Z. Cao, J. L. Walsh and M. G. Kong, Appl. Phys. Lett. **94,** 021501 (2009).

[14] O. J. Lee, H. W. Ju, G. Khang, P. P. Sun, J. Rivera, J. H. Cho, S.-J. Park, J. G. Eden and C. H. Park, J. Tissue Eng. Regen. Med. **10,** 348 (2016).

[15] V. Zablotskii, O. Churpita, Z. Hubička, L. Jastrabík and A. Dejneka, Plasma Med. **1,** 135 (2011).

[16] G. Nayak, Y. Du, R. Brandenburg and P. J. Bruggeman, Plasma Sources Sci. Technol. **26,** 035001 (2017).

[17] N. O'Connor, H. Humphreys and S. Daniels, IEEE Trans. Plasma Sci. **42,** 756 (2014).

[18] E. Robert, T. Darny, S. Dozias, S. Iseni and J. M. Pouvesle, Phys. Plasmas **22,** 122007 (2015).

[19] M. Bernier, G. Gaborit, L. Duvillaret, A. Paupert and J.-L. Lasserre, Appl. Opt. **47,** 2470 (2008).

[20] Z. Xiong, E. Robert, V. Sarron, J.-M. Pouvesle and M. J. Kushner, J. Phys. D: Appl. Phys. **45,** 275201 (2012).

[21] S. Norberg, PhD Thesis, "Modeling atmospheric pressure plasma jets: plasma dynamics, interaction with dielectric surfaces, liquid layers and cells", (University of Michigan, 2015).

[22] T. Darny, J. M. Pouvesle, V. Puech, C. Douat, S. Dozias and E. Robert, Plasma Sources Sci. Technol. **26,** 045008 (2017).

[23] M. H. Qaisrani, Y. Xian, C. Li, X. Pei, M. Ghasemi and X. Lu, Phys. Plasmas **23,** 063523 (2016).

Chapter 9 Ionization Wave Propagation and Surface Interactions in a He Plasma Jet in a Controlled Environment

Accurate modeling of ionization wave propagation in atmospheric pressure plasma jets is critical to predictions of plasma chemistry and plasma-surface interactions for biomedical applications. In this chapter, detailed measurements of a He plasma jet in a simplified environment are used for comparison with numerical modeling. The plasma jet is operated in a vacuum chamber to provide a controlled gas flow and composition. The ionization wave is observed using ICCD imaging and time and spatially resolved electron density measurements by laser-collision-induced fluorescence. The plasma jet is initially investigated in pure He at 200 Torr, and the effects of pressure, voltage, and a humid He shroud are also discussed. Increasing the operating pressure reduces speed and isotropic expansion of the ionization wave. The presence of a humid shroud results in the electron density increasing and having an annular profile due to the lower ionization energy of H_2O compared to He and localized photoionization in the mixing region. Numerical modeling highlighted the importance of resonance radiation emitted by the plasma and photoelectron emission from the quartz tube.

9.1 Introduction

Atmospheric pressure plasma jets usually consist of a low temperature plasma sustained in a rare gas coming in contact with humid air. The resulting plasma chemistry can be complex, including excited states and dissociation products of N_2, O_2, and H_2O, and the more stable species which occur by reactions of the dissociation products, including N_xO_y and HNO_x. The short lifetime and spatial nonuniformity of many of these species make measurements of their

densities challenging. Some advanced diagnostics have been used to make measurements of species densities such as H, O, OH, NO and O_3 in atmospheric pressure plasma jets.[1–7] Even given these measurements of atomic and radical species, reaction pathways in these devices are in a large part derived from numerical modeling. Uncertainty quantification of atmospheric pressure plasma chemistry models has shown that the uncertainties in rate coefficients and cross sections used as input data can lead to significant uncertainties in the final predicted densities of reactive species.[8] By analyzing available published data for several critical rates, these uncertainties can be reduced in specific systems.[9]

Validation of plasma chemistry models can be challenging for the reasons described above. Luo *et al*. used a 0-dimensional model to analyze the dominant pathways in a high electron density (~10^{16} cm^{-3}) plasma filament sustained in humid Ar.[10] The resulting OH and H densities were in agreement with time resolved measurements by laser induced fluorescence (LIF) and two-photon laser induced fluorescence (TALIF). Vasko *et al*. compared experimental measurements of H_2O_2 in an atmospheric pressure radiofrequency discharge with results from a 0-dimensional global model and a 1-dimensional fluid model.[11] The 1-dimensional model better predicted H_2O_2 densities while both models indicated the same dominant pathways for production and loss of H_2O_2. Zhang *et al*. used a 0-dimensional model to calculate O_3 densities in an Ar plasma jet and compared these to measurements by UV absorption.[6] The trends and magnitude of the O_3 density and the gas temperature are in agreement with experiment.

Several other studies have focused on validating the plasma behavior (e.g. ionization wave propagation, electric fields) in models, which is an essential first step in order to accurately predict the chemistry. Tholin *et al*. validated a 2-dimensional fluid model by comparing simulated emission from the modeling results with ICCD imaging for a pin-to-pin discharge in

atmospheric pressure air.[12] Viegas *et al*. presented a combined experimental and modeling study of electric fields inside dielectric materials being treated by an atmospheric pressure plasma jet.[13] An electro-optic target enabled the measurement of the spatially resolved electric field within the target, and the axial and radial electric fields calculated in the model agreed with the measured fields. Dubinova *et al*. compared cylindrically symmetric fluid modeling with ICCD imaging of a streamer propagating toward and around a dielectric rod in air.[14] The model captured the behavior of the cylindrically symmetric inception cloud which occurred before the transition to streamer propagation.

In this chapter, we compare time and spatially resolved measurements of the electron density in a plasma jet sustained in He to 2-dimensional modeling results. In order to make the high quality electron density measurements required for a detailed comparison, the system is primarily operated at reduced pressure (200 Torr) and in a simplified chemistry (pure helium and humid helium). The plasma jet consists of two coaxial quartz tubes. The plasma propagates inside the central tube, where pure He flows. Gas can also be flowed through the outer tube to produce a shroud of a different gas composition. Comparison of predictions from the model to experimental results emphasized the importance of resonant radiation from He to photoionization and photoelectron emission from the inner surface of the tube. The experimental results indicate that the molecular gases surrounding the rare gas plume enable ionization through Penning reactions and photoionization.

A humid He shroud was used to investigate the consequences of molecular gases surrounding a He jet. The composition of shroud gases has been previously investigated by others. Razavizadeh *et al*. found that the speed of IWs increased when the gas surrounding a He plasma jet contained O_2 due to the photoionization of O_2 and electron detachment from

anions.[15] Xian *et al.* observed that atmospheric pressure plasma jets (APPJs) surrounded by molecular gas are more confined than those surrounded by a rare gas. Even more confinement of the plasma occurs with attaching gases (air and O_2) than with N_2. Schmidt-Bleker *et al*. used combined experiments and modeling to compare the consequences of N_2 and air shield gases around a He APPJ.[16] The formation of anions reduced the radial spread of electrons into the shielding gas. Akman *et al*. also reported a transition from a diffuse plasma in a pure He environment to a columnated jet when the He plume was surrounded by air.[17]

In this chapter, laser-collision-induced fluorescence was used to make time and spatially resolved electron density measurements in a plasma jet in contact with an alumina target. The system was also modeled using a 2-dimensional plasma hydrodynamics model, and the results are compared. The experiment, including design of the plasma jet and the laser-collision-induced fluorescence analysis are described in Sec. 9.2. The geometry and initial conditions for the model are described in Sec. 9.3. Sec. 9.4 contains the experimental and modeling results, including the consequences of pressure, applied voltage, humid shroud and flow rate. Concluding remarks are in Sec. 9.5.

9.2 Description of the Experiment

9.2.1 Plasma Jet

The plasma jet used in this investigation, shown in Figs. 1a-1c, is a co-axial flow system designed to be vacuum compatible to enable operation in pure He environments. The electrode configuration was based on the work of Robert *et al*.[18], and it is able to generate IWs which propagate in long tubes (10s of cm). The jet consists of two coaxial quartz tubes. He flows through the central tube as in a conventional plasma jet. The central tube has a 2 mm inner diameter (ID) and 4 mm outer diameter (OD). The outer tube has a 10.5 mm ID and a 12.7 mm

OD, which produces an annulus of width 3.25 mm through which the shroud gases flow. An annular powered electrode on the inside of the central quartz tube has an ID of 1.55 mm and an OD of 2 mm, to fit just within the center tube. The inner edge of the powered electrode, where the breakdown is expected to begin is rounded.

The grounded electrode was UHV compatible copper tape wrapped around the central tube. The tubes were mounted in a support structure made of PEEK which was 5.08 cm in diameter and 3.81 cm long. The two quartz tubes were mounted into a channel (shroud tube) and a hole (center tube) in the PEEK and sealed using vacuum epoxy. The PEEK support structure included connections for gas lines which provide separate gas flow through the central and shroud tubes.

A spacer between the inner and outer tubes at the end of the grounded electrode was PEEK with 8 equally spaced holes 1 mm in diameter which served to evenly distribute the shroud gases azimuthally while also keeping the two tubes properly centered and spaced. The applied voltage pulse was generated by a DEI PVX-4110 pulse generator whose input voltage was provided by a Spellman SL600 power supply. The applied voltage pulse, shown in Fig. 9.2, has approximately a 100 ns rise time, a 140 ns fall, 430 ns duration and a +6 kV amplitude for the base case.

9.2.2 Vacuum System

The jet was operated in a cylindrical vacuum chamber with two 6” flanges on the top and bottom, and eight 2¾” flanges around the circumference. The jet was mounted at the top of the chamber on a ½” Ultra-Torr feedthrough attached to a 6” to 2¾” reducer flange. The system base pressure was approximately 20 mTorr, which indicates that at an operating pressure of 200 Torr, the minimum level of impurities was approximately 100 ppm.

While operating the jet, gases were pumped through a cylindrical manifold consisting of eight holes (1.25 mm in diameter) distributed around the jet at a radius of 3.84 cm. The manifold was connected to the vacuum system by a tube 1/4" in diameter. The conductance through this manifold is sufficient to operate as high as 1 slpm, while maintaining a gas flow which is essentially axially symmetric.

The target toward which the jet is directed is a 650 μm thick, 1" diameter disc of alumina backed with a metal film. This target was placed on a metal washer serving as ground which in turn was placed on a PEEK pedestal having a 3.1 cm diameter. The current through the ground electrode was measured using a Pearson Current Monitor (Model 2877).

9.2.3 Bubbler System

Two bubblers connected in series, shown in Fig. 9.1d, was used to humidify the He feedgas to 100% relative humidity. Both bubblers were made of borosilicate glass with a 40 mL capacity (Ace Glass Inc.) and sealed using an Ace-Thread seal with the gas lines attached with Ultra-Torr fittings. The bubblers were operated with a gas dispersion tube having a fritted glass end with holes in the range 145-174 μm (Ace Glass Inc.). The first bubbler was heated with 7.2 W silicone heating tape. The second bubbler was kept at room temperature. Any water vapor above the vapor pressure condenses in this second bubbler, helping to ensure the gas leaving the second bubbler is at 100% relative humidity.

Three mass flow controllers were used, all supplied with pure He (99.999%). The first mass flow controller supplied the central tube with He. The second controlled the He which was mixed with the output of the bubbler system to tune the relative humidity of the shroud. The third supplied the He which flowed through the bubbler. By adjusting the relative flow rates of

the second and third mass flow controllers, the humidity could be controlled while keeping the total flow rate constant.

9.2.4 Laser-Collision-Induced Fluorescence

Laser-collision-induced fluorescence (LCIF) is a technique able to measure electron density and temperature in rare gas mixtures. LCIF has been developed for He at atmospheric pressure using the scheme shown in Fig. 9.3a.[19] In LCIF, a 389 nm laser excites the metastable He(2^3S) produced by the plasma to the He(3^3P) state. The He(3^3P) state will radiatively relax by emission of a 389 nm photon back to the He(2^3S) level, and this emission is referred to as laser induced fluorescence (LIF). In the presence of electrons, some of the He(3^3P) can be collisionally excited to the He(3^3D) state by

$$e + He(3^3P) \rightarrow He(3^3D) + e. \qquad (9.1)$$

This reaction has a threshold energy of only 0.06 eV and a rate coefficient which is relatively insensitive to the electron temperature. The He(3^3D) state then radiatively relaxes by emitting a 588 nm photon, which is referred to as laser-collision-induced fluorescence (LCIF). The ratio of the 588 nm LCIF to the 389 nm LIF can be used to determine the electron density. This technique is described in detail by Barnat, *et al*.[19]

A schematic of the setup used for LCIF measurements is shown in Fig. 9.1b. A mode locked Ti:Sapphire laser produced 780 nm pulses with duration < 80 fs. At 1 kHz, one of these pulses is amplified by a Spectra-Physics Spitfire regenerative amplifier to approximately 2 mJ. The beam passes through a β-Barium borate (BBO) frequency doubling crystal reducing the wavelength to 390 nm. This BBO crystal was also used to fine-tune the wavelength to the transition at 388.9 nm. A wave plate attenuated the laser energy to 15 - 20 μJ. A set of lenses was used to increase the beam size which was then reduced by a series of apertures to ~7.5 mm.

The circular beam passes through a cylindrical lens to generate a sheet of laser light which then passes through the plasma between the end of the central tube of the jet and the alumina surface.

To reduce laser light scattering which can overwhelm the LIF signal, the sides of the central tube of the jet were blackened, and the inside of the polished vacuum chamber was covered in anodized aluminum foil. The windows through which the laser passed were at an angle adjusted to reduce scattering signal, and covered by antireflective coatings for 389 nm. Apertures inside the chamber were also used to block the scattered light.

The light from plasma emission, LIF, and LCIF was imaged using an Andor iStar camera using bandpass filters (10 nm FWHM): 390 nm, 589 nm, 450 nm, 656 nm. The camera gate was 5 ns for all measurements.

9.2.5 Analysis of Laser-Collision-Induced Fluorescence Measurements

The LCIF data for the base case at 310 ns is shown in Fig. 9.3b. To obtain an electron density, it is necessary to take the ratio of the intensity of LIF signal emitted from He(3^3P) at 389 nm to the LCIF signal emitted from He(3^3D) at 588 nm. In the LIF and LCIF plotted in Fig. 9.3b, the emission from the plasma, the contribution of the laser scattering and the background have been subtracted. The ratio of these two signals is called the LCIF ratio, which is expected to be linearly proportional to the electron density for these conditions. Some portion of this LCIF ratio can be a result of collisions with the background gas,

$$\mathrm{He}(3^3\mathrm{P}) + \mathrm{He} \rightarrow \mathrm{He}(3^3\mathrm{D}) + \mathrm{He}. \qquad (9.2)$$

By collecting LCIF in the late afterglow when the electrons have thermalized, (4.5 μs after the pulse) this value could be determined experimentally. The contribution of this reaction to the LCIF ratio is proportional to the total background gas density, and has a value of (7×10^{-4} Torr^{-1})P, where P is the pressure in Torr. This value has been subtracted from all LCIF ratios.

The constant of proportionality required to convert the LCIF ratio to electron density must be derived as its value depends on the time delay from the laser pulse as well as the camera gate. Ohm's law was used to estimate the electron density. Since the current is constant, at any given height,

$$I = \frac{e^2}{m_e}\frac{N}{\upsilon_m}\frac{E}{N} n_e(z) A(z) \tag{9.3}$$

where I is the current measured at the electrode under the alumina, e is the elementary charge, m_e is the mass of electrons, N is the total number density of the background gas, υ_m is the momentum transfer collision frequency of electrons, and E is the electric field. $n_e(z)$ is the electron density and $A(z)$ is the cross-sectional area of the plasma at height z.

E/N can be estimated from the ratio of the optical emission from the He(4^3D) state at 447 nm to that of the He(3^3D) state at 588 nm. The reaction e + He(3^3P) $\rightarrow$ e + He(4^3D), also shown in Fig. 9.3a, has a 0.74 eV threshold energy and a rate constant which is sensitive to T_e.[19] Assuming the local electric field approximation applies (T_e is at equilibrium with E/N) enables an estimate of E/N from this ratio. E/N was estimated as approximately 2 Td. The momentum transfer collision frequency at 2 Td is approximately $\upsilon_m/N = 5 \times 10^{-8}$ cm^{3}s^{-1}.

In this plasma jet, the cross sectional area of the plasma and the electron density (which is proportional to the LCIF Ratio) are functions of height. The diameter of the plasma at each height was estimated as the diameter containing 95% of the electrons based on the LCIF ratio. Based on these estimated values, an average electron density as a function of height, $n_e(z)$, was calculated. This value is compared to the average LCIF ratio in Fig. 9.3c. The plasma immediately above the surface was omitted from this analysis because E/N near surfaces can

differ from that of the bulk plasma. The conversion factor plotted in Fig. 9.3c is the electron density estimated from Ohm's law divided by the LCIF ratio.

As indicated in Fig. 9.3c, an LCIF ratio of 1 is equivalent to an electron density of approximately 4×10^{12} cm^{-3}. Previously, the value of this conversion factor was estimated to be a factor of 3 higher (1.5×10^{13} cm^{-3}) for conditions where *E/N* was more controlled and better known. The conditions were a He pressure of 600 Torr, having a shorter camera gate and a shorter delay after the laser pulse.[20] Although the experimental results in this chapter are plotted in terms of electron density and there is significant uncertainty in the calibration factor that produces these values, that uncertainty applies only to the absolute value of n_e. The relative values of n_e are not influenced by this uncertainty.

The LCIF measurements rely on laser absorption by the He(2^3S) state. When the density of He(2^3S) is too low, a reliable electron density cannot be obtained from the LCIF data. He(2^3S) density is usually proportional to electron density in pure He, so it is expected that the electron density would be low in regions where the density of He(2^3S) is also low. From a procedure perspective, when the LIF intensity is not sufficiently above the background to produce a reliable density, the electron density was set to zero. We acknowledge that there is likely a low electron density in these regions which simply not detectable due to the low density of He(2^3S).

For each LCIF measurement, the number of pulses over which the data were collected was optimized for those particular conditions. The data were collected over a sufficient number of pulses to produce a reasonable signal to noise ratio in both the LIF and LCIF signals. Typically for data collected before the IW contacted the surface, the 588 nm and 389 nm fluorescence were each averaged over approximately 10^6 pulses.

9.3 Description of the Model

The 2-dimensional plasma hydrodynamics model described in Chapter 2, *nonPDPSIM*, was used to model this plasma jet. The options for radiation transport, solving Navier-Stokes equations, and the electron monte carlo (eMCS) were used for the model in this chapter.

9.3.1 Geometry and Initial Conditions

The cylindrically symmetric geometry used in the model is shown in Fig. 9.4. The dimensions match that of the experiment as closely as possible. The central quartz tube has ID = 2 mm and OD = 4 mm. The shroud tube has ID = 10.5 mm and OD = 12.7 mm. Both quartz tubes have a dielectric constant of $\varepsilon_r = 4$. All metals are perfect conductors, and all dielectrics are perfect insulators. The ground electrode around the centeral tube in the computational geometry is thicker than the copper tape used in the experiment to avoid an excessively dense mesh. The target is a 650 μm thick piece of alumina ($\varepsilon_r = 10$) which rests upon a 500 μm thick ground electrode. This ground electrode is also thicker than that of the experiment to avoid a prohibitively fine mesh. The target rests on a PEEK pedestal ($\varepsilon_r = 4$) which is 4 cm in diameter.

The geometry of the vacuum chamber which surrounds the gas was also included in the computational mesh. The grounded surface surrounding the jet in the experiment was composed of the ultratorr feedthrough, the reducer flange, and the chamber (refer to Fig. 9.1b). These features have been included in the computational geometry as a single ground electrode. The pump is a ring at the bottom of the chamber, which is consistent with the pumping manifold in the experiment. This surface uses a constant pressure boundary condition which is 200 Torr for the base case.

The computational geometry does differ from the experimental setup in the following way. The length of the powered and ground electrode around the inner tube were increased by 3

cm (i.e. the electrodes extend further into the tube). While using the same electrode configuration, this elongation decreases computational time by reducing the distance the IW needs to propagate through the tube from 8.5 to 5.5 cm. Computational tests have shown that the qualitative behavior of the IW is generally the same in this geometry as in the case when the IW must propagate the full distance (the electron density is within 20%).

The numerical mesh is shown in Fig. 9.5, and includes 36,427 nodes, 20,907 of which are in the plasma. The mesh size is approximately 52 μm above the alumina surface and 65 μm in the tube. Several refinement zones expand the mesh size to as large as 1.2 mm far from where the plasma occurs.

In the base case, 500 sccm of He/H_2O = 99.95/0.05 flows through the central nozzle with there being no flow through the shroud nozzle. The steady state flow dynamics are established by calculating the fluid dynamics and neutral transport only for at least 30 ms before initializing the plasma pulse. The applied voltage is a +6 kV pulse with a 100 ns rise time which is consistent with the pulse applied in the experiment.

9.3.2 Reaction Mechanism

The electronic states of helium that are explicitly included in this reaction mechanism are $He(2^3S)$, $He(2^1S)$, $He(2^3P)$ and $He(2^1P)$. The higher states are grouped into He(3P) and He(3S). All of the excimers are grouped into a single species, He_2*. The resulting reaction mechanism contains the species listed in Table 9.1. The reaction mechanism for H_2O is that of Van Gaens *et al*.,[21] with the He reactions added from Norberg *et al*.[22] A humid gas mixture was used in all cases even when no intentional water admixture was included to represent outgassing and impurities in the vacuum system that result in some residual H_2O vapor. In humid plasmas, even with unintentional water impurities, water cluster ions can make up a significant portion of the

ions in the plasma.[23] To limit the computational burden, only a limited water cluster ion chemistry was included, with a maximum of one added water molecule for each ion. In practice, more complex clusters may form in these conditions.

9.3.3 Photoionization Model

With the applied voltage having positive polarity, the IW is highly sensitive to photoionization. In helium discharges, photons having high enough energy to ionize water include emission from electronically excited states (He*) relaxing to the ground state, and radiation from the excimers (He_2*). The emission from these states can ionize all impurities, and the dominant impurity was assumed to be H_2O, having a photoionization cross section of approximately 2.3×10^{-17} cm^2 at a wavelength of 58.4 nm.

In these simulations, the radiation transport was included for two or three photons. Emission at 58.4 nm and 53.7 nm from He(2^1P) and the lumped state He(3P) was included in all simulations, and emission at 81 nm from He_2* was included in limited simulations for testing. The photons emitted from He(2^1P) and He(3P) [which includes He(3^1P)] have the highest intensity. These two photons can be reabsorbed by ground state He atoms, and therefore are trapped in the plasma with a short absorption mean free path approximately 200 nm. Pressure broadening results in photons on the wings of the lineshape function escaping the plasma. A radiation trapping factor is the average number of times a photon is emitted and reabsorbed before escaping the plasma volume. Using the method of Holstein [24] and the analytical solutions by van Trigt [25] for an infinite cylindrical plasma, the trapping factor is estimated as 900 for the 58.4 nm photon emitted from the He(2^1P) state. The Einstein emission coefficient for He(2^1P) in the reaction mechanism was divided by this trapping factor, and only the photons emitted in the wings of the lineshape function that escape from the plasmas are tracked using the

radiation transport module. He(3P) is also a significant source of photoionization. Since this is a lumped state, it is assumed that the most abundant excited state is the lowest energy state, He(3^1P). The radiation trapping factor and Einstein emission coefficient are based on He(3^1P). The result is that 53.7 nm radiation from the He(3^1P) state has a trapping factor of 620, which was used to modify the effective emission coefficient of He(3P) in the reaction mechanism. The details of the calculation of the radiation trapping factors can be found in Appendix C.

Due to the computational expense of the radiation transport calculations, only emission from the He(2^1P) and He(3P) states were included in the results presented here. Photoionization resulting from emission from He_2* was also included for a limited number of cases, was found to be insignificant (lower than that of He(2^1P) by a factor of 10^3) and therefore was not included. However, at higher pressure, photoionization from He_2* may become more significant as the rate of conversion of He* to He_2* increases with pressure (He* + He + M $\rightarrow$ He_2* + M).

The concentration of impurities in the system determines the rate of photoionization ahead of the IW and therefore has important consequences on the IW dynamics. The concentration of impurities is expected to be at least 0.01% (100 ppm) for the base pressure. The actual partial pressure of impurities is expected to be larger during operation because outgassing H_2O has a longer residence time at the operating pressure than when the vacuum system is pumped down to the base pressure. The concentration of H_2O impurity in the model was selected to provide sufficient preionization ahead of the IW to sustain the IW. An impurity concentration of 0.05% H_2O was used for the pure He flowing through the central tube, a value that provided qualitative agreement with speed and shape of IWs measured in the experiment. At this concentration of impurity, the mean free path for photoionization is approximately 13 cm, meaning that most photons exit the plasma region without undergoing ionization.

Photoelectron emission from the surfaces of the quartz and the alumina was also included in the model. The materials were assumed to be completely opaque to the VUV photons in the radiation transport model. Experimental measurements of the photoelectron emission coefficient for quartz is approximately 3% for photons greater than 10 eV.[26] However, better qualitative agreement with the IW shape in the tube were achieved with a photoelectron yield of 2%, which was used in this work.

9.3.4 Electron Monte Carlo Model

The electron Monte Carlo simulation (eMCS) in *nonPDPSIM* treats electrons emitted from surfaces (by photoelectron emission or ion-induced secondary electron emission) using kinetic algorithms. For the base case, only the electrons emitted from the alumina surface were addressed using the eMCS. Electrons emitted from the quartz surface were treated using fluid equations in which the secondary electrons from a surface node are apportioned among the nearest neighbor mesh points in the plasma. The structured mesh on which the eMCS is executed extends from the surface of the alumina to 6.9 mm above that surface and extends to a radius of 8.5 mm. The eMCS calculation begins before the IW enters this region, at t = 300 ns, and the eMCS is performed every 1 ns. 150 electron pseudoparticles are emitted from each surface mesh point during each update to the eMCS with an initial energy of 4 eV. These parameters are sufficient for the results to be independent of the extent of the eMCS mesh, the update frequency, and the number of particles.

Electrons produced by electron impact ionization by secondary electrons in the eMCS were also treated as particles in the eMCS. This approach is important since as the IW approaches the alumina surface, the *E/N* in the region between the alumina and the IW is high (~10^{-16} V-cm^2, 10 Td). The scope of the eMCS, which is limited to secondary electrons, does

highlight some limits on the validity of the electron dynamics in the model. These results indicate that electrons emitted from the surface must be treated kinetically as they traverse a region of high electric field in front of the IW. The electrons produced by photoionization ahead of the IW in the region of high *E/N* are addressed using the fluid approximation, although they experience the same high *E/N* as those emitted from the surface. Modifications to the model to also address the electrons produced by photoionization would improve the accuracy of the model for this plasma jet.

In select cases where the photoelectron emission coefficient of the quartz tube is varied, the eMCS is also used inside the tube for photoelectrons and secondary electrons emitted from the quartz. In this case the eMCS mesh extends from the powered electrode to the end of the quartz tube with a radius of 1 mm. The eMCS calculation begins at t = 0.5 ns and is updated every 1 ns.

9.4 Experimental and Model Results

9.4.1 Experimental Base Case

Optical emission from the plasma in the base case is shown in Fig. 9.6. Note that the plasma emission is obtained from all light which reaches the ICCD, and has not been Abel inverted to account for the cylindrically symmetric plasma. The IW emerges from the tube at 190 ns, implying an average IW speed inside the tube of 4×10^7 cm/s (assuming the initial formation time is negligible). The plasma expands nearly isotopically from 190 ns to 205 ns. In this period, the IW speed slows to approximately 2×10^7 cm/s. As the front of the IW approaches the alumina surface, the field enhancement is stronger in regions near the axis, causing the portion of the IW closer to the axis to propagate faster (3×10^7 cm/s) with more

intense emission. Meanwhile, the speed of the portion of the IW that is at further from the axis (r > 1.4 mm) decreases, creating the shape observed at t = 215 ns.

As the IW reaches the surface, the intensity of emission in the plasma column from the bottom half of the gap increases. This occurs when a conductive channel forms between the powered electrode and the dielectric, which in this case has a relatively large capacitance (280 pF). The mechanism of this increased light emission which propagates in the reverse direction is analogous to a restrike and has been observed in other plasma jets.[27]

After the IW contacts the surface, a surface ionization wave (SIW) forms and propagates radially outward along the surface. This SIW produces emission in a layer approximately 350 μm thick and spreads along the surface at an average speed of 6×10^6 cm/s. The restrike also propagates back toward the powered electrode, causing the densities of electrons and electronically excited states inside the tube to increase, resulting in a brighter plasma in the tube seen at 255 ns.

As the IW contacts the alumina at 220 ns, the current measured at the grounded electrode under the alumina increases, shown in Fig. 9.2. Before this point, there is still a nonzero current due to the displacement current as the IW approaches the surface and the electric field is increasing. As the SIW spreads, the surface of the alumina charges. As the applied voltage begins to fall at 360 ns, the current at the ground electrode under the alumina target becomes negative. The positive charge that has accumulated on the alumina surface is neutralized by current in the plasma flowing in the opposite direction during this period. The magnitude of this current is smaller than that of the forward current, but the duration is longer.

The electron densities measured using LCIF in the base case are shown in Fig. 9.7. In aligning the laser, it was necessary to maintain some gap between the bottom of the quartz tube

and the top of the laser sheet to prevent scattering of laser light off the tube which would overwhelm the LIF measurement. Therefore the region approximately 500 μm beneath the tube was outside the measurement region. Pixels with an LIF signal that is not significantly above the background noise are excluded. The maximum electron density at 200 ns is 4×10^{11} cm^{-3} during the isotropic expansion period. Just before the IW contacts the surface (210 ns), the electron density in the center of the plasma has increased to 7×10^{11} cm^{-3}. The shape of the electron density profile reflects that of the plasma emission at this time. After the IW contacts the surface the electron density in the bulk plasma increases by 40% to 1×10^{12} cm^{-3} in 15 ns.

At 250 ns, after the SIW has spread to a radius of 3.1 mm, and a region of elevated electron density near the alumina surface is visible. The electron density near the surface is approximately 3×10^{12} cm^{-3} compared to 6×10^{11} cm^{-3} in the bulk plasma. The electron density in the bulk plasma continues to increase as the SIW spreads across the surface, with the electron density reaching 1×10^{12} cm^{-3} by 310 ns.

In the n_e measurements plotted at 210 and 225 ns plotted in Fig. 9.7, an artifact of the measurement technique is visible. When the laser is applied to the plasma to make the LCIF measurements, there may be a small perturbation in the IW speed. The effect is minor enough that it is generally not apparent in time resolved ICCD imaging of plasma emission (i.e. it does not affect qualitative IW behavior). However, this momentary increase in IW speed can cause an overestimate in the electron density at the front of the IW. When the LCIF measurements are taken, an equivalent plasma emission image (without the laser) is used to subtract the light emitted by the plasma. If the IW in the plasma emission image is slightly slower than that of the LIF and LCIF data, there will be an artificial increase in the measured LIF and LCIF at the front of the IW. The interpretation that the elevated electron density measurements at the front of the

IW are not physical is consistent with the expected discharge dynamics, because the recombination rate is slow enough in pure He that the electron density would not be expected to drop significantly in 15 ns.

9.4.2 Model Base Case

The behavior of the IW as it propagates out of the tube and toward the alumina surface is summarized in Fig. 9.8. As the IW propagates in the tube, the electric field over the gas number density (E/N) is as high as 7×10^{-15} V-cm^2 (700 Td). This elevated electric field results in an electron temperature (T_e) as high as 18 eV in the front of the IW, and an electron impact ionization rate (S_e) of 6×10^{21} cm^{-3}s^{-1}. The IW speed in the model is approximately a factor of 3 slower than in the experiment. As a result, the IW does not emerge from the tube until 335 ns. The duration of the voltage pulse in the model is extended to keep the voltage at its maximum value while the IW contacts the alumina (i.e. the voltage fall is not included in the model).

As the IW passes a given point in the tube, the electron density (n_e) increases to approximately 1×10^{13} cm^{-3}. As the IW exits the tube, it remains confined to $r < 2$ mm. As the IW approaches the surface, E/N, T_e, and S_e increase as the voltage drop occurs over a smaller gap and the electric field increases. After contact with the surface, a restrike occurs resulting in an increase in the electron density in the gap to 2×10^{13} cm^{-3} by t = 425 ns (30 ns after the IW has contacted the surface). Though the magnitude of the n_e is higher than the measured value, the factor of 2 increase with the restrike is similar to the 40% increase seen in the experiment. An SIW with a thickness of approximately 290 μm (compared to 350 μm in the experiment) spreads radially outward along the surface with $S_e \approx 1 \times 10^{20}$ cm^{-3}s^{-1}. The electron density in the SIW reaches 9×10^{12} cm^{-3} at t = 425 ns, approximately a factor of 3 larger than in the experiment. Though the isotropic expansion observed in the optical emission in Fig. 9.6 is not as apparent in

the model, the same qualitative behavior occurs. The shape of the plasma at t = 215 ns (Fig. 9.6) in the experiment resembles S_e at t = 393 ns in the model.

The modeling investigation has highlighted the importance of several physical mechanisms in the dynamics of this plasma jet. The ionization processes which occur ahead of the IW as it propagates arcross the gap are illustrated in Fig. 9.9. The ionization rates in this figure are taken from along the axis at 389 ns, when the IW is 2.8 mm above the alumina surface. The electrons in this simulation are divided into two groups. Most of the electrons are treated as a fluid, and are referred to as bulk electrons. The electrons emitted from the alumina surface, and their progeny (generated by electron impact ionization) are addressed kinetically using the eMCS module. When the electrons in the eMCS have an energy which drops below 3.6 eV, they are converted into bulk electrons. The majority of the electrons in the plasma are generated by electron impact ionization of the bulk fluid electrons. However, the ionization which occurs ahead of the IW is critical in sustaining and controlling its propagation. Photoionization of impurity H_2O occurs ahead of the IW at a rate of $\sim 3 \times 10^{15}$ $cm^{-3}s^{-1}$. Electrons which are emitted from the alumina surface cause electron impact ionization ($S_e(Secondary) \approx 9 \times 10^{15}$ $cm^{-3}s^{-1}$) as they are accelerated toward the IW by the electric field. This rate is on the order of the electron impact ionization rate by electrons in the bulk fluid ($S_e(Bulk) \approx 3 \times 10^{16}$ $cm^{-3}s^{-1}$). Within 1 mm of the IW, the electric field is large enough that $S_e(Bulk)$ and $S_e(Secondary)$ increase by several orders of magnitude. Though the electron density ahead of the IW is low, $n_e \approx 3 \times 10^7$ cm^{-3}, these electrons provide an initial source which undergoes exponential growth in the high electric field of the IW.

To illustrate the importance of treating the electrons emitted from the alumina kinetically, the modeling results are compared with and without the eMCS model in Fig. 9.10. When the

eMCS module is not used, electrons emitted from the surface are immediately included in the bulk fluid electrons. Before 355 ns, the S_e and n_e are similar for both simulations, but as the IW approaches the alumina surface, the behavior diverges. When the eMCS module is not used, S_e in the IW is lower and the IW speed decreases as it approaches the surface. This behavior is unexpected, as the higher electric field should lead to an acceleration of the IW. The electron density in the SIW is also an order of magnitude higher when the eMCS is used. Using the eMCS makes it more consistent with the qualitative behavior of n_e in the experiment, in which n_e in the SIW is a factor of 5 larger than that of the bulk. This comparison illustrates that treating electrons which are produced ahead of the IW as part of the bulk fluid in these conditions (200 Torr of He) is not always adequate to accurately capture the IW dynamics. Using current modeling capabilities, it is only possible to represent electrons emitted from the surface kinetically. To be more accurate, the same Monte Carlo methods should be used to address the transport of electrons produced by photoionization ahead of the IW. Extending the model to include these capabilities and is planned for future work.

The average IW speed inside the tube in the model is 1.4×10^7 cm/s (compared to 4×10^7 cm/s in the experiment). This speed is still lower than that observed in the experiment in spite of the powered electrode being closer to the target, which increases the average IW speed. This slower IW in the model may be due to the simplified electron dynamics in the model, where only the secondary electrons are treated kinetically, but not the electrons produced ahead of the IW by photoionization.

The IW propagates from the tube to the target in 54 ns (1.5×10^7 cm/s) compared to 30 ns in the experiment. The SIW speed agrees in the model and the experiment for the first 30 ns

of contact (6×10^6 cm/s), but the SIW slows during the restrike in the model. This may be a result of the finite mesh resolution used to resolve the SIW in the model.

The isotropic expansion of the IW that is observed in the experiment as the IW exits the tube is not as apparent in the current modeling results. There are two probable reasons for this discrepancy. In the model, a single pulse is simulated, but in the experiment, the jet is repetitively pulsed at 1 kHz. Though the gas flow flushes out much of the remaining species in the tube, the residence time is longer further from the axis where the gas flow is lower. It is possible that more water cluster ions or other species survive locally at larger radii, and promote radial propagation. The second possibility is that the limiting the eMCS to electrons that originate from surfaces is not accounting for the fact that the electrons produced ahead of the IW by photoionization are likely to be more isotropic, and may be accelerated rapidly enough to require them to be treated kinetically.

Photoelectron emission from the surface of the quartz tube was critical for sustaining an IW in the tube. The IW was simulated with several different values of the photoelectron emission coefficient for the quartz tube, and the results are shown in Fig. 9.11. For these cases, the photoelectrons and secondary electrons from the inner surface of the quartz tube are treated with the eMCS. The photoelectron emission coefficient in the model to determined whether the plasma in the tube formed on the axis or propagated as a surface ionization wave along the quartz surface, making it annular in shape. A higher photoelectron emission coefficient produces an annular IW. In Fig. 9.11, the density of He(3P), a lumped state which can emit visible light, is plotted to approximate the plasma emission. The electrons that are produced ahead of the IW are critical for directing the propagation of the IW. The source of these electrons is primarily photoionization or photoelectron emission from surfaces. When the photoelectron emission

coefficient is 0%, the electron density ahead of the IW is larger on axis. When the photoelectron emission coefficient is large (> 2%), the electron density ahead of the IW is larger closer to the inner surface of the quartz tube. The density of He(3P) most consistent with the qualitative observations in the experiments occurs with a photoelectron emission coefficient of 1%. The photoelectron emission coefficient also has a minor effect on the IW speed inside the tube, with the speed increasing by 40% as the photoelectron emission coefficient increases from 0% to 5%.

9.4.3 Pressure

The emission from the IW for different pressures is compared in the Fig. 9.12. The IW speed is highly sensitive to pressure, so rather than a constant pulse duration, the voltage pulse was held at the maximum voltage for 80 ns after the IW first contacted the surface for consistency with the base case. This results in pulse durations of 370, 430, 640, 840, 1090, and 1340 ns for 150, 200, 300, 400, 500, and 600 Torr. The electron density was measured 30 ns after the plasma first contacts the alumina surface for each pressure, and the results are shown in Fig. 9.12.

At low pressure the IW emission intensity is low before contact with the surface. Generally, higher pressures reduce the role of diffusion in the discharge, and allow for steeper gradients. As the pressure increases, the electron mobility decreases. The potential gradient at the leading edge of the IW and the maximum electric field increase. After the IW passes, T_e decreases more rapidly as electrons lose energy to collisions. Therefore as the pressure increases, the plasma emission is more localized at the front of the IW and the tail of emission behind the IW front is shorter, as shown in Fig. 9.12.

The restrike is more apparent and induces a greater increase in plasma emission at lower pressures (approximately a factor of 7 at 150 Torr compared to a factor of 2 at 600 Torr). At low

pressure, the plasma is more conductive and the current increases more rapidly. The current measured at the target 30 ns after the IW contacts the surface is 28 mA for 150 Torr compared to 3.4 mA for 500 Torr. Because the restrike is weaker and less total charge is transferred to the target as pressure increases, the SIW covers a smaller area.

The IW also becomes more confined to the axis as the pressure increases. At higher pressure, the relative concentration of impurities may be similar, leading to a higher absolute density of impurities at higher pressure. The radiation trapping factors are, to first order, independent of pressure when pressure broadening dominates, which is the case in He at these pressures. The effect of the line broadening (which decreases trapping) is balanced by the increase in absorber densities (which increases trapping). At higher pressure, the density of H_2O is larger and the characteristic absorption length is shorter. Therefore at higher pressure, photoionization occurs closer to the IW than it would at lower pressure. The result is a more focused IW which does not expand as rapidly when it exits the tube.

The surface ionization wave becomes confined to a smaller layer above the alumina as the pressure increases. This layer is 600 μm thick at 150 Torr, and 180 μm thick at 600 Torr. As the pressure increases, the mobility of charged species decreases, and steeper gradients can be maintained near the alumina surface. This confinement of the SIW to a thinner layer is also apparent in the electron density measurements shown in Fig. 9.13.

As the pressure increases, the evolution of the electron density 30 ns after the IW contacts the surface is non-monotonic. The electron densities in the center of the gap are 1.2×10^{12}, 7.5×10^{11}, 1.1×10^{12}, 1.4×10^{12}, 2.2×10^{12}, 6.4×10^{11} cm^{-3} for 150, 200, 300, 400, 500, and 600 Torr, with the maximum occurring at 500 Torr. The electron density in the SIW follows a similar pattern of decreasing then increasing as the pressure increases. This complex scaling is a result

of changes in both the cross sectional area of the plasma and the total current (and, similarly, the total energy deposition). As the pressure increases, the conductivity of the plasma decreases, and the power deposition increases, which is expected to increase the number of electrons produced. However, as the pressure increases, the plasma is also confined more to the axis, and this energy deposition occurs in a smaller volume, which is expected to increase the electron density.

9.4.4 Voltage

The effect of applied voltage on the IW was also investigated experimentally using ICCD imaging and LCIF measurements. The optical emission from the experiment for voltages of 4 kV and 6.5 kV is shown in Fig. 9.14. The pulse duration was again adjusted so that the voltage remains at its maximum for 80 ns after the IW contacts the surface. The IW speed increased with the applied voltage (from 1.9×10^7 at 4 kV to 5.0×10^7 cm/s at 6.5 kV in the tube) due to a higher *E/N*.

At each voltage investigated, there is a transition from more isotropic expansion to a more surface-directed IW, but the vertical position of this change depends on the applied voltage. This transition occurs 4.3 mm above the alumina surface for 4 kV and 2.7 mm for 6.5 kV. With a higher applied voltage, the electron temperature is higher, and there is more isotropic IW propagation and a later transition to a surface-directed IW.

Increasing the applied voltage increases *E/N*, resulting in an increase in the electron temperature and the plasma emission from the IW. There is also an increase in the intensity of the restrike which occurs when the plasma contacts the alumina surface. At higher voltage, the electron density in the tube is expected to be higher before the IW reaches the alumina, resulting in a larger conductivity. Therefore when the IW contacts the surface, the current increases more rapidly, and the more energy is deposited in the plasma.

The electron density measured by LCIF 30 ns after the IW contacts the surface for each voltage is shown in Fig. 9.14. Note that the electron density measured at 6 kV in Fig. 9.14 is higher than that of Fig. 9.7 by approximately a factor of 2. For all of the LCIF measurements in Fig. 9.14, the bubbler system was connected to the chamber. While vacuum chamber was separated from the bubbler system by valves, some of the additional vacuum components increased the leak rate and therefore the impurity levels in the gas.

The electron density in the central plasma column outside of the quartz tube is not particularly sensitive to the applied voltage. The diameter of this column of elevated electron density increases with the applied voltage, because the SIW spreads to larger radius (3.7 mm compared to 1.6 mm) in the 30 ns of contact for higher applied voltage. At lower voltage, n_e on the axis is elevated near the target, while at higher voltage it is relatively uniform along the axis. At higher voltage, a faster SIW has resulted in a larger plasma diameter in the 30 ns of contact with the surface generating a wider column of plasma.

9.4.5 Humid Shroud

For applications, most APPJs are used to treat surfaces in an ambient air environment. The presence of surrounding molecular gases has been shown to significantly influence the IW propagation dynamics.[15,17] To investigate this in a more controlled system with a much simpler chemistry than humid air, a shroud flow of 500 sccm was introduced, with varying He/H_2O mixtures using the bubbler system.

The plasma emission for 2.3% H_2O in the shroud at 389 nm from He(3^3P) and at 656 nm from H_α emission is shown in Fig. 9.16. The IW speed as it crosses the gap is 4×10^7 cm/s compared to 2.5×10^7 cm/s for the base case. With a humid shroud, photoionization produces electrons ahead of the IW primarily at the interface between the He and the humid He shroud.

Once the IW reaches this mixing region, direct electron impact ionization of H_2O can be more rapid than that of He because it has a lower ionization potential (12.6 eV compared to 24.6 eV). Penning ionization of H_2O by He* also contributes to an increased ionization rate in this mixing region. These effects all cause the IW to propagate much more quickly in this region. The plasma emission from He(3^3P) appears to be annular in shape, with a SIW which is faster than in the base case, taking 20 ns to reach a radius of 3 mm rather than 30 ns in the base case.

In the presence of molecular gases, it is important to reconsider the interpretation and assumptions of the LCIF measurements, which have primarily been performed in pure He. One effect of added water vapor at sufficient concentrations is a reduction in the density of the metastable He(2^3S). The generation rate of He(2^3S) can be reduced by the decrease in electron temperature that occurs with sufficient H_2O concentration. He(2^3S) is also rapidly quenched by Penning ionization,

$$He(2^3S) + H_2O \rightarrow He + H_2O^+ + e, \qquad (9.4)$$

with a reaction rate of 1.1×10^{-10} cm^3s^{-1}. This limits the lifetime of He(2^3S) to 61 ns at 2.3% H_2O at 200 Torr. Therefore in regions of higher H_2O concentration, the electron density is not observable by LCIF due to insufficient He(2^3S) densities. In Fig. 9.17, the LIF and LCIF emissions are shown, along with the LCIF ratio for a humid shroud. The LCIF ratio is not calculated for pixels in which the LIF signal is not significantly above the background. In these regions, the electron density may still be elevated, but it is not detectable because of the insufficient He(2^3S) density.

The other effect of water vapor that should be considered is the sensitivity to the H_2O density of the electron impact reaction rate which is critical for LCIF. In order for LCIF measurements to be accurate, it is important that the reaction rate of

$$e + He(3^3P) \rightarrow He(3^3D) + e \quad (9.5)$$

is independent of *E/N* or the H_2O mole fraction. The EEDF was calculated for different concentrations of water vapor using a two-term spherical harmonic expansion and the same cross section set which was used for the 2-dimensional simulations. Then the cross section for the reaction in Eq. 9.5 from Shevelko *et al*. was used to calculate the reaction rate at different values of *E/N*, shown in Fig. 9.18.[28] Because the reaction in Eq. 9.5 has a low threshold energy of 0.06 eV (electrons at 300 K are 0.026 eV), the reaction rate becomes independent of *E/N* above approximately 1.8 Td in pure He. If 1% H_2O is present, the rate is independent of *E/N* above approximately 2 Td (T_e = 0.45 eV). The electron temperature is expected to be greater than 0.45 eV for the conditions in which LCIF is used in this work, so LCIF can be used to measure the electron density.

In the LCIF measurements shown in Fig. 9.19, "Pure He" refers to when the valves to the bubbler system are closed, and "0% H_2O" is the condition where the valves to the bubbler system are open, but no gas flows through the bubbler. Though the lowest humidity in the shroud investigated was nominally pure He, the leak rate of the bubbler system was significantly higher than that of the chamber and the impurity concentration is expected to be higher than in the base case. As a result, the IW emerged from the tube 15 ns earlier than in the base case, and the electron density was approximately 80% higher.

The electron density measurements by LCIF for varying levels of shroud humidity are shown in Fig. 9.19. Increasing the mole fraction of H_2O from pure He to 0.1% results in an increase in the electron density from 1×10^{12} to 2×10^{12} cm^{-3}, but the maximum electron density remains on axis. In this range, an increase in humidity decreases the radius of the plasma, because the electron density is higher, and the cross sectional area required to conduct the same

amount of current is smaller. As the mole fraction of water in the shroud increases from 0.1% to 0.25%, the electron density on axis is no longer the highest electron density. The electron density is a maximum in a conical region which represents the mixing zone between the He and the humid He. As the humidity of the shroud continues to increase, n_e on the axis decreases. At 0.75% H_2O, n_e in the mixing zone is a factor of 2.5 larger than n_e on the axis in the center of the gap. Photoionization and Penning ionization rates are higher in this mixing layer between the He and the humid He, resulting in preferential propagation of the IW in this region.

As the humidity exceeds 0.75%, the electron density in the SIW appears lower at the center. For 1.5% H_2O in the shroud the n_e in the SIW is approximately 3×10^{12} cm^{-3} for $r < 1$ mm compared to 9×10^{12} cm^{-3} for $r > 1$ mm. This indicates that the IW is annular as it contacts the alumina surface and primarily spreads outward away from the axis. This behavior is not apparent in the optical emission in Fig. 9.16 because this emission is not Abel inverted. So the portion of the SIW propagating toward the camera makes the SIW appear as a disc rather than a ring.

9.4.6 Modeling Humid Shroud

Modeling results of the IW in the presence of a humid shroud are shown in Figs. 9.20 and 9.21. When a humid shroud is present, the IW becomes annular after exiting the tube, and propagates more quickly, which is consistent with the experimental observations. The base case and the case with 1.5% H_2O in the shroud are compared by plotting S_e and n_e when the IW is at the same position (which is not necessarily the same time) in Fig. 9.20.

When 1.5% H_2O is present in the shroud, the IW reaches the end of the tube 30 ns earlier than in the base case, which is consistent with the experiment. The IW speed inside the tube is the same in both cases until it approaches the end of the tube (2.5 mm from the end of the tube).

After this point, when a humid shroud is present, the IW speed increases from 1.4×10^7 to 1.9×10^7 cm/s and begins to move off the axis. This acceleration is a result of greater production of electrons ahead of the IW which cause electron impact ionization as they are accelerated toward the IW. The level of H_2O impurities inside the tube is the same for both cases (i.e. diffusion of H_2O into the tube is negligible). When the IW is still 2.5 mm from the end of the tube (t = 293 ns), the photoionization rate in the gap, 6 mm ahead of the IW, is more than a factor of 2 larger with a humid shroud compared to the base case. At this time, n_e in the gap is a factor of 3 larger with a humid shroud (4.2×10^6 compared to 1.4×10^7 cm^{-3}). The profile of this preionization is also annular when a humid shroud is present, compared to radially uniform for the base case. The photoionization rate is largest in the regions where the gradient from pure He to humid He is the steepest, immediately outside the tube outlet at r = 1 mm. The photoionization rate in this region reaches 2×10^{16} $cm^{-3}s^{-1}$ as the IW approaches the outlet of the tube.

The IW propagates across the gap faster in the presence of the humid shroud, taking 30 ns (2.6×10^7 cm/s) compared to 54 ns (1.5×10^7 cm/s) in the base case. This increase in speed by approximately a factor of 2 is consistent with the experimental observations, though the model underestimates the IW speed in both cases.

With 1.5% H_2O in the shroud, the IW is already annular as it emerges from the tube. This shape is consistent with the experimental observations in Fig. 9.16, where the plasma emission appears annular immediately upon exiting the tube. The IW maintains this annular shape as it propagates across the gap, though the radius decreases as the IW approaches the surface. The electric field on axis increases as the IW approaches the surface, increasing the electron impact ionization rate at smaller radii.

The gradients at the front of the IW are less steep when a humid shroud is present. Therefore *E/N* is lower, and the maximum value of S_e is lower. There are two factors which contribute to a lower *E/N* in the IW. First, the preionization is greater with a humid shroud. This means the conductivity of the air ahead of the IW is greater, and unable to sustain high fields. Second, the geometry of the IW determines the electric field enhancement. When the IW is on axis, as in the base case, the electric field enhancement is much greater than when the plasma is annular (and the effective radius is larger). As a result of these two factors, the model indicates that n_e is lower in the presence of a humid shroud. This trend is inconsistent with the experimental results in which n_e increases by a factor of 3 in the presence of a humid shroud. For 1.5% H_2O in the shroud, n_e at the midpoint of the gap is 1×10^{12} cm^{-3} in the model compared to 4×10^{12} cm^{-3} in the experiment. This discrepancy may be due to photodetachement from negative ions remaining from previous pulses, which are not included in the simulations which address only a single pulse.

The modeled electron density 30 ns after the IW contacts the surface is shown in Fig. 9.21 for comparison with the experimental results in Fig. 9.19. The electron density with the shroud at 0.05% H_2O (the same gas composition as the base case), remains maximum on the axis, consistent with the experimental results. The electron density profile is similar to that of 0% H_2O in Fig. 9.19. The plasma rapidly transitions to a more annular shape as the humidity of the shroud is increased in the model. Some initial indication of an annular shape appears at 0.1%, and the n_e profile is clearly annular when the humidity is increased to 0.25% H_2O. This behavior is generally in agreement with the LCIF measurements, though in the experiment there is no indication of the transition to an annular shape at 0.1%.

In the SIW, n_e is elevated compared to the bulk plasma. These model results indicate that when the shroud is ≥1.5% H_2O, the LCIF measurements of n_e are in fact clipped in regions that still have an elevated electron density. The transition of the SIW from a disc (with the center at an elevated electron density) to a ring appears at 0.25% H_2O, compared to the transition at 0.75% H_2O in the experiment. Inaccuracies in the control of the gas composition may explain why the transition seems to occur at a different humidity in the model compared to the experiment. If the tubing between the bubbler system and the jet is not yet equilibrated to the humidity, condensation can lower the effective humidity of the flow.

9.4.7 He Flow Rate

With 2.3% H_2O at 500 sccm in the shroud, the flow rate of the pure helium in the central tube was varied from 300 to 700 sccm to highlight the effect of the density of H_2O as it diffuses into the pure He. At a low flow rate, the H_2O diffuses rapidly to the axis, as shown by the modeling results of the steady state profiles in Fig. 9.22. Increasing the flow rate of the central He results in flushing out the H_2O and decreasing its mole fraction on the axis. The residence time of the He inside the tube is 13 ms for 300 sccm and 5 ms for 700 sccm.

The electron density for different central He flow rates in Fig. 9.23. The electron density in all cases is highest in the mixing region between the He and the humid He. The electron density is also generally larger for low flow rates, where Penning ionization and electron impact ionization of H_2O can occur more rapidly due to the higher mole fraction of H_2O. As the flow rate increases to 700 sccm, the electron density profile becomes nearly annular, rather than conical as H_2O diffuses into the He flow.

9.5 Concluding Remarks

A helium plasma jet in a controlled atmosphere in contact with an alumina target has been investigated using ICCD imaging, laser-collision-induced fluorescence measurements of electron density, and numerical modeling. In the experiments performed in pure He the IW spreads as it exits the end of the tube, expanding almost isotropically. Then upon approaching the alumina surface, the portion of the IW closest to the axis accelerates and intensifies due to enhancement of the electric field. Upon contacting the alumina target, a surface ionization wave develops and the dielectric surface charges as the plasma expands radially.

In this positive polarity plasma jet, the propagation of the IW is sensitive to photoionization of impurities and photoelectron emission from the dielectric tube, which produce electrons ahead of the IW. Photoionization by the resonant photons emitted from $He(2^1P)$ and $He(3^1P)$ are more important than those of the excimer. A higher photoelectron emission coefficient resulted in a more annular plasma inside the jet. Photoelectron emission from the alumina target helped sustain the IW as it approached the target surface. At 200 Torr in pure He, kinetic effects of the electrons become significant ahead of the IW where the electric field is large, and the fluid approximation no longer accurately represents the IW behavior. This is especially critical as the IW approaches the target surface and E/N is large.

Increasing the operating pressure of the plasma jet results in an IW which is more confined to the axis of the jet, even in a pure He atmosphere. As the pressure increases, the diffusivity and mobility of electrons decreases, and larger gradients develop. The front of the IW and the surface ionization wave are confined to thinner layers. The restrike which occurs when the IW contacts the target is less intense because the conductivity of the plasma is lower.

The presence of humidity in a shroud surrounding the He jet results in a transition of the IW outside from being on the axis to being annular. The speed of the IW also increases in the presence of this molecular gas because of the contributions of Penning ionization and the lower ionization energy of H_2O compared to He. The preionization which occurs ahead of the IW has an annular profile with a maximum in the mixing region between the pure He and the humid shroud due to photoionization. Changing the flow rate of the pure He in the central tube can tailor the position of the maximum electron density by changing the profile of the gas composition outside of the tube. The IW preferentially propagates at the interface between the He and the surrounding molecular gas. Overall, the combination of experimental and modeling results have provided insights into the physical processes are important in plasma jet devices.

9.6 Tables

Table 9.1 Species included in the model.

Ground State Neutrals	He, H_2O, H, H_2, O, O_2, OH, H_2O_2, HO_2
Positive Ions	He^+, He_2^+, H^+, H_2^+, H_3^+, O^+, O_2^+, O_4^+, H_2O^+, H_3O^+, OH^+, $H_2O^+(H_2O)$, $H_3O^+(H_2O)$, $O_2^+(H_2O)$
Negative Ions	e, H^-, O_2^-, O^-, OH^-, $O_2^-(H_2O)$, $O^-(H_2O)$, $OH^-(H_2O)$
Excited States	He(2^3S), He(2^1S), He(2^3P), He(2^1P), He(3P), He(3S), He_2*, H*, H_2(r), H_2(v), H_2*, O_2(v), O_2(r), O_2*, O_2(1Σ), O*, H_2O(v), OH*

9.7 Figures

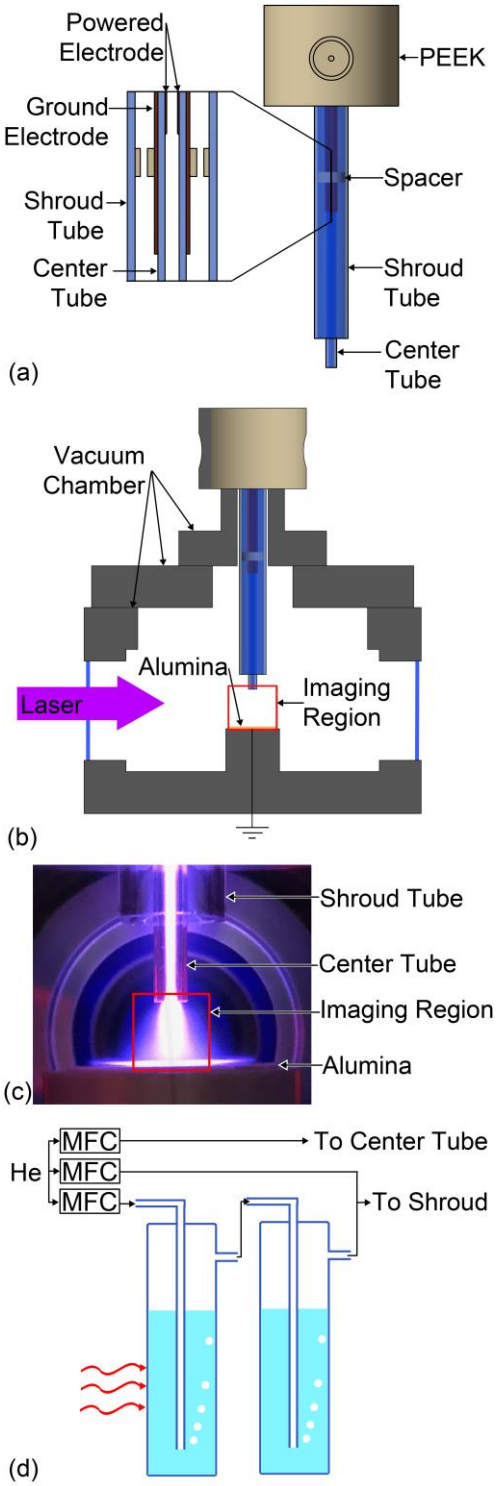

Fig. 9.1 Schematic of the experimental setup. (a) Plasma jet design. (b) Experimental setup with vacuum chamber and LCIF. (c) A photo of the plasma jet in contact with an alumina surface. (d) Schematic of the bubbler system.

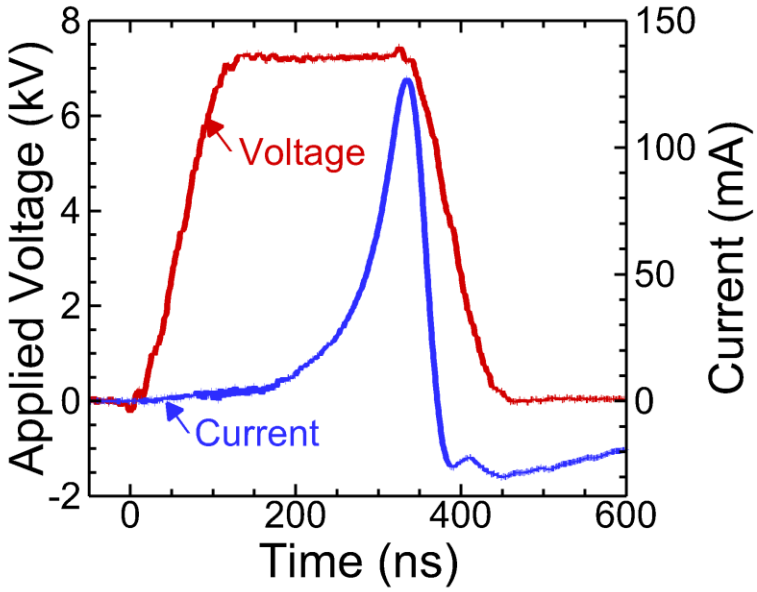

Fig. 9.2 The applied voltage pulse and the current measured at the electrode under the alumina target for the base case.

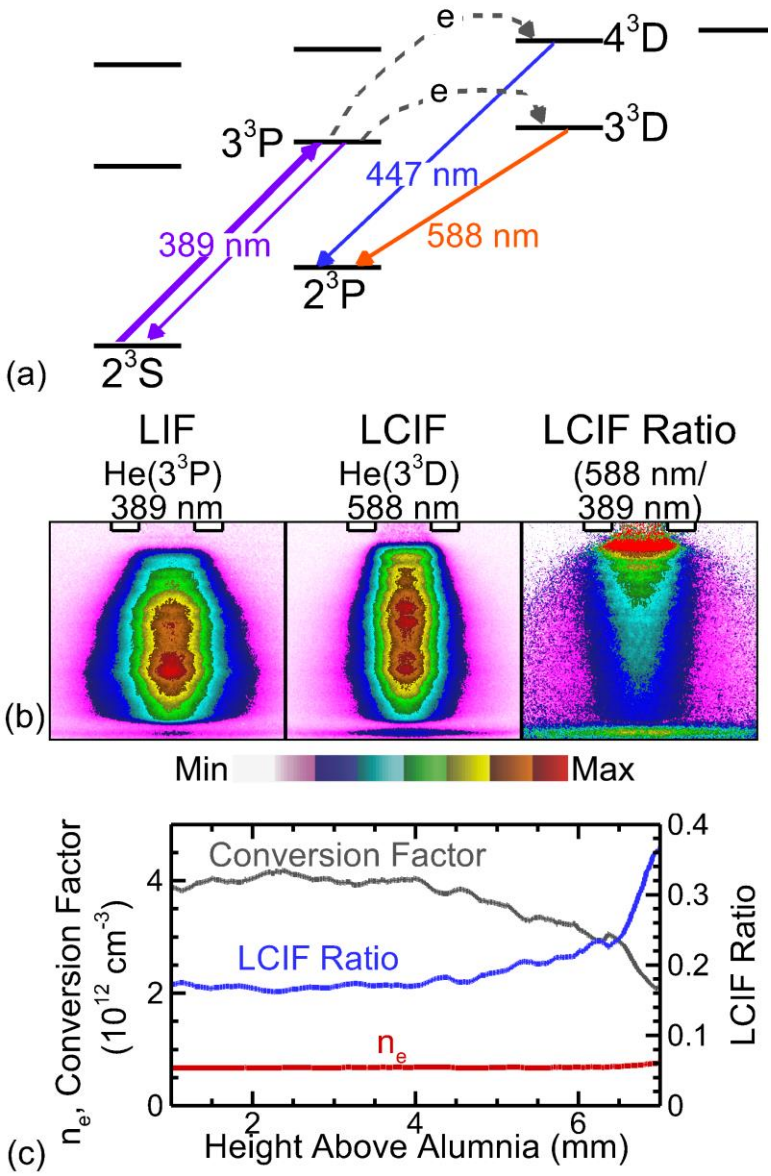

Fig. 9.3 (a) A schematic of the He triplet states which are relevant to the analysis of the LCIF diagnostic. (b) Laser-induced fluorescence (LIF), laser-collision-induced fluorescence (LCIF), and their ratio plotted from 0 to 1.25 on a linear scale for the base case at t = 310 ns. (c) The electron density estimated from Ohm's Law, the average LCIF ratio in a column containing 95% of the electrons, and the resulting calculated conversion factors a function of z-position above the alumina for the base case at t = 310 ns.

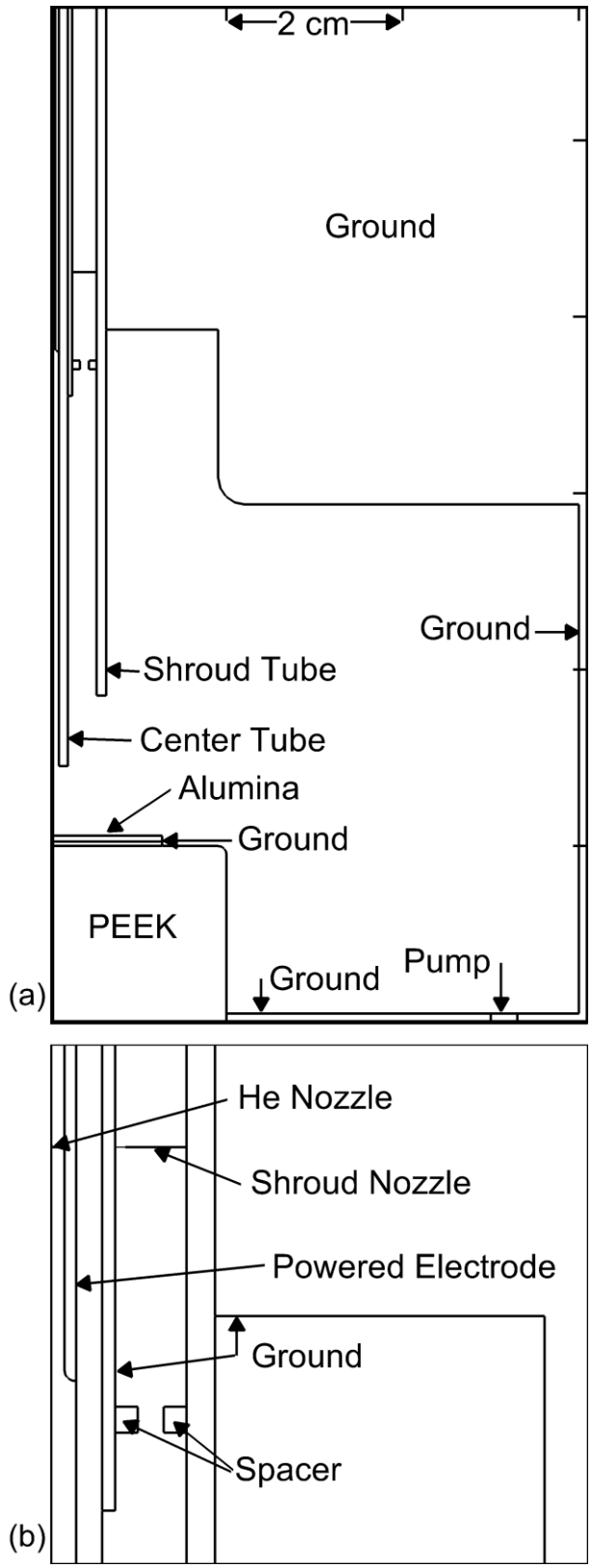

Fig. 9.4 The geometry used in the modeling investigation. The central tube has a 2 mm inner diameter and a 4 mm outer diameter. The distance from the end of the tube to the alumina surface is 7.85 mm.

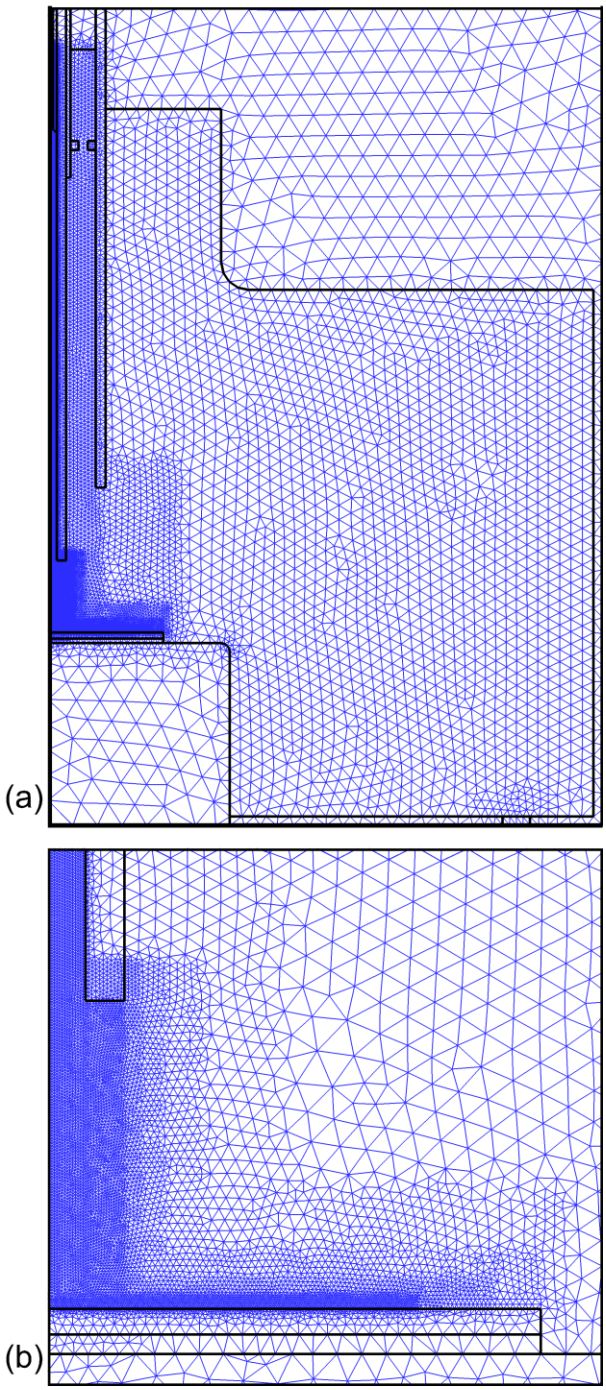

Fig. 9.5 The computational mesh used to model the plasma jet. The mesh size is approximately 52 μm at the alumina surface and 65 μm in the tube.

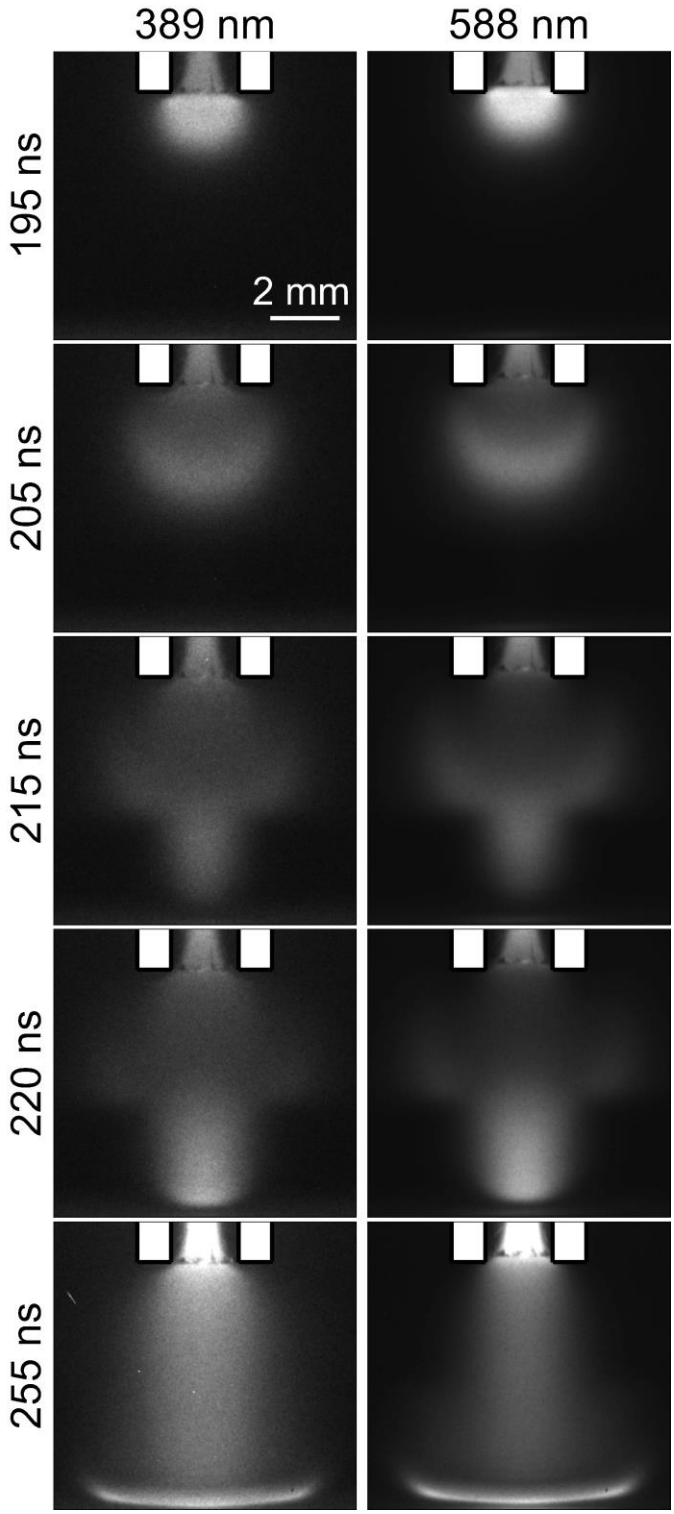

Fig. 9.6 ICCD imaging of ionization wave propagation in the base case. Time is measured from the start of the voltage pulse and the camera gate was 5 ns. Filters were applied to image emission at 389 nm (from $He(3^3P)$) and 589 nm (from $He(3^3D)$).

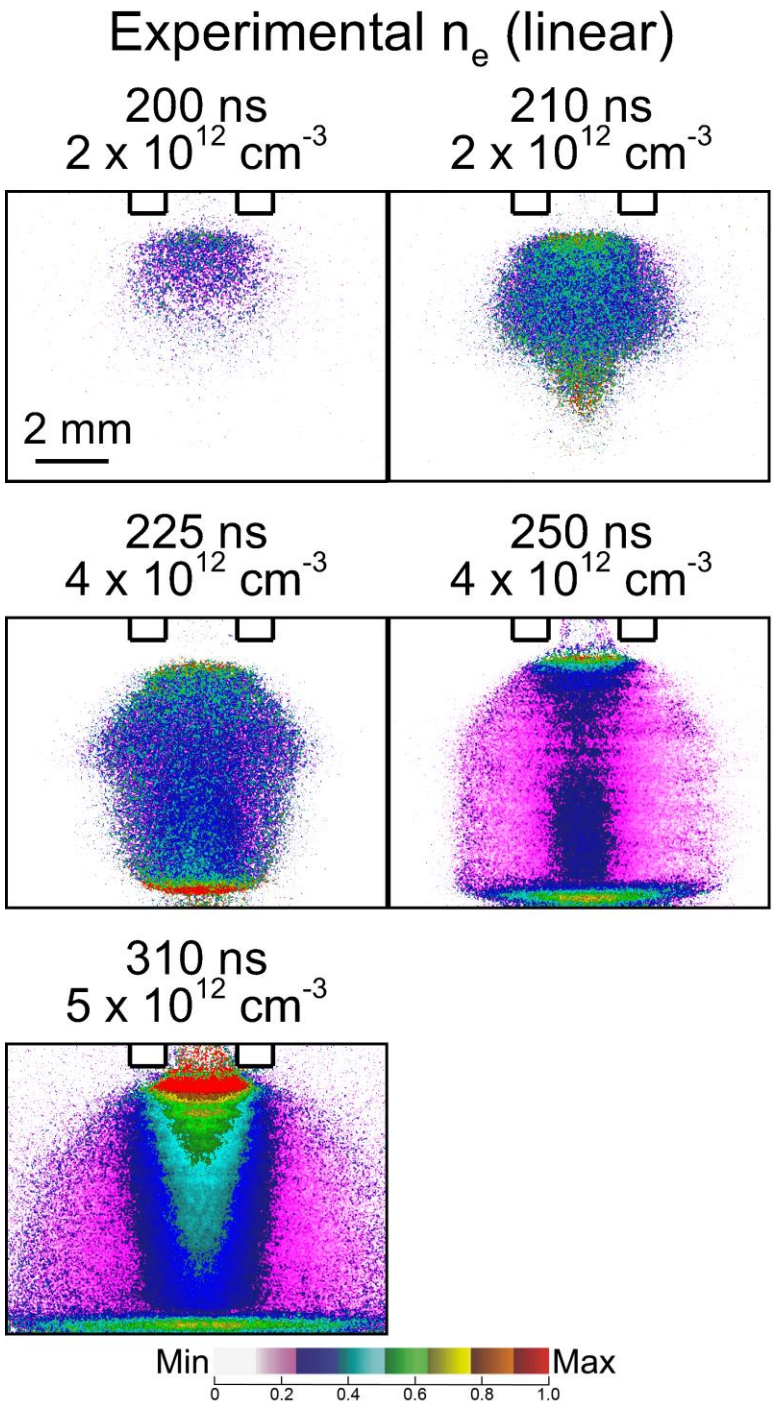

Fig. 9.7 Electron densities measured by LCIF. Time is measured from the beginning of the voltage pulse. The results are plotted in terms of electron density, there is significant uncertainty in the calibration. The relative values are expected to be accurate, but the absolute number density is uncertain.

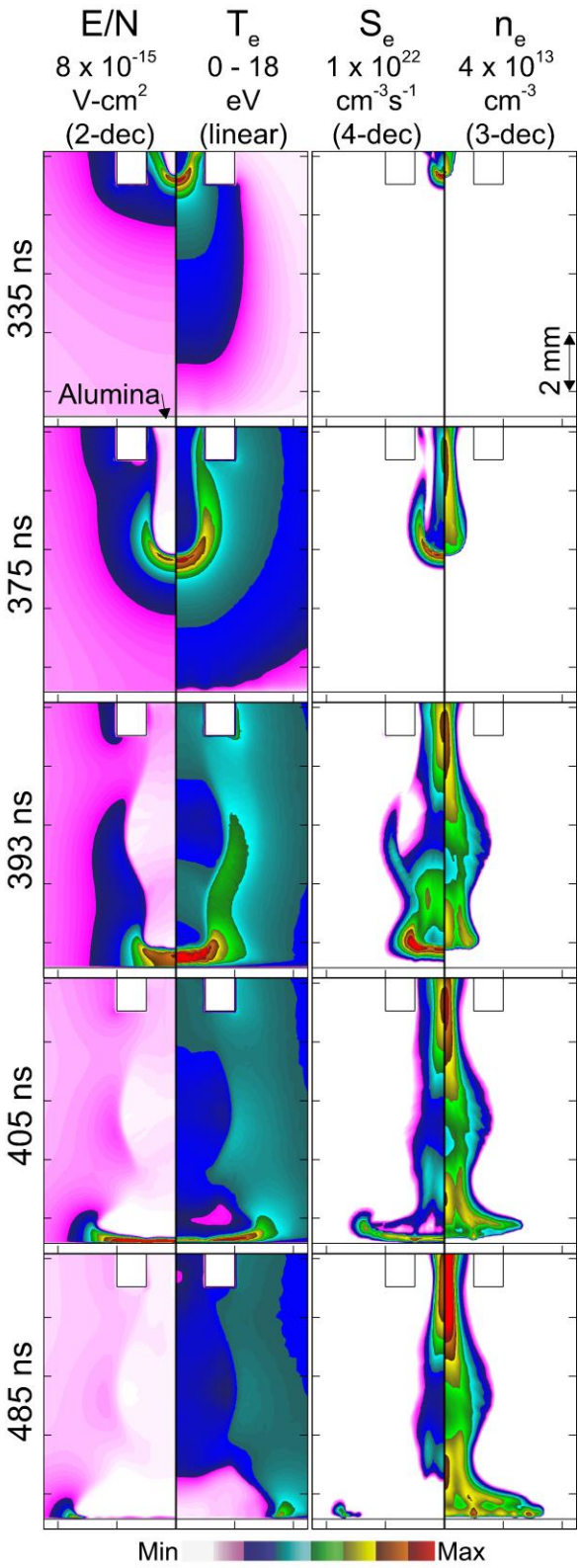

Fig. 9.8 Modeling results of ionization wave as it propagates across the gap and forms a surface ionization wave along the alumina. *E/N* is the electric field over the number density on a 2-decade log scale, T_e is the electron temperature on a linear scale, S_e is the electron impact ionization from the bulk electrons on a 4-decade log scale, and n_e is the electron density on a 3-decade log scale.

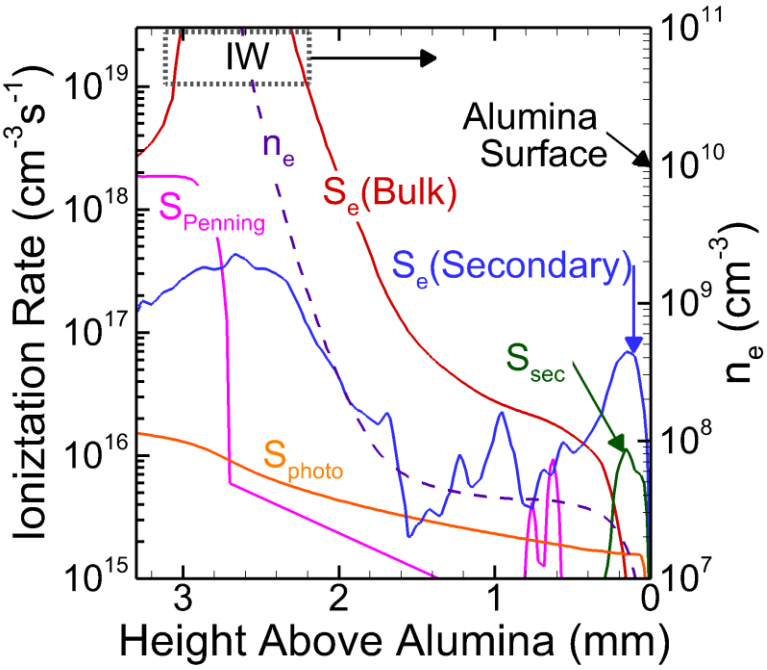

Fig. 9.9 The sources of electrons and electron density between the ionization wave and the alumina surface. This data is extracted along the z-axis at t = 389 ns. At this time, the front of the IW is on the is 2.8 mm above the alumina surface. The IW position and direction is indicated by the dashed box. $S_{Penning}$ refers to the Penning ionization rate, S_{photo} is photoionization, $S_e(Bulk)$ is electron impact ionization by the fluid electrons, $S_e(Secondary)$ is the electron impact ionization by the secondary electrons in the eMCS module. S_{sec} is the electrons emitted from the surface (secondary electrons and photoelectrons).

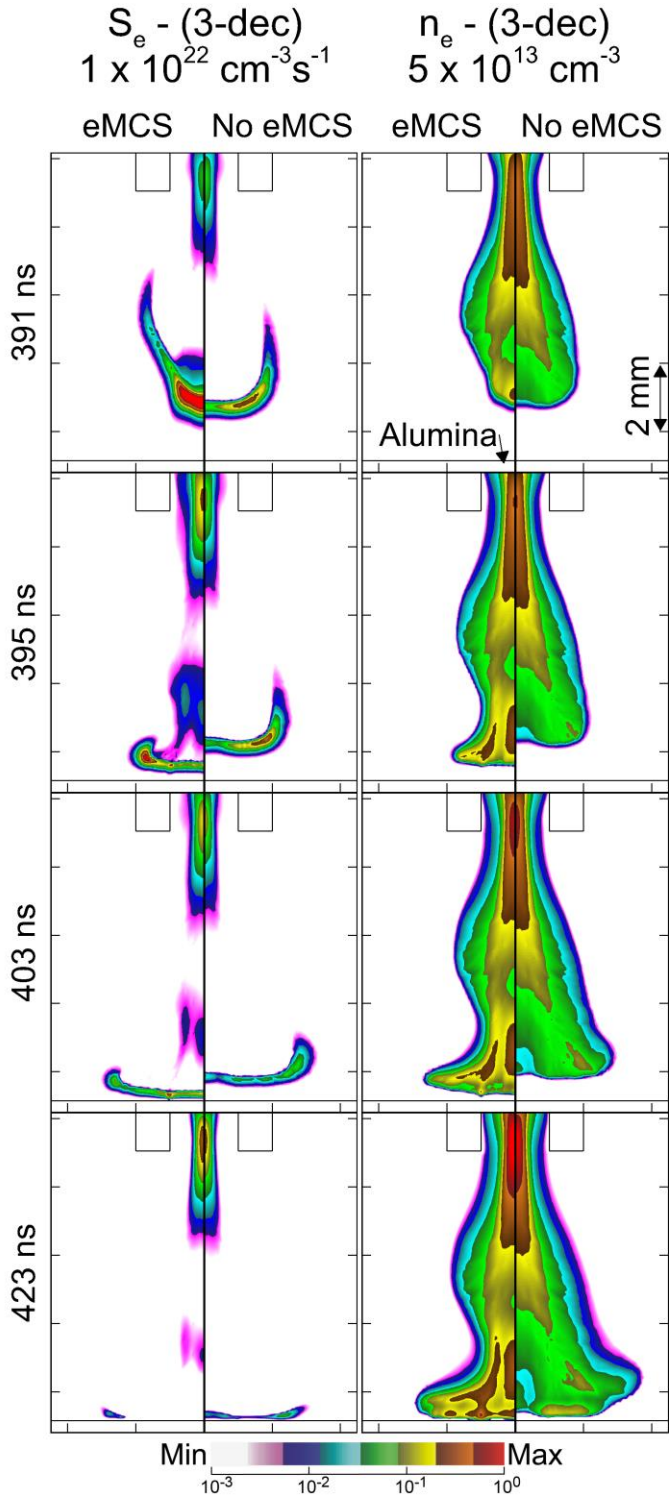

Fig. 9.10 (left) The electron impact ionization rate (S_e) and (right) the electron density (n_e) of the IW with applying the electron Monte Carlo simulation to electrons emitted from the alumina surface (eMCS) and by treating the electrons emitted from the surface as part of the bulk electron fluid (no eMCS). Densities are plotted on a 3-decade log scale.

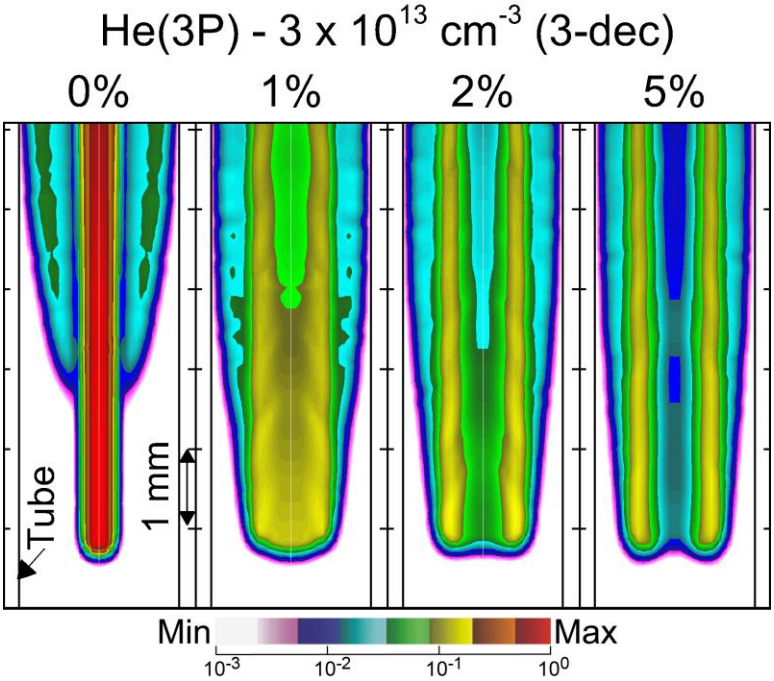

Fig. 9.11 Density of the lumped state He(3P) in the IW inside the tube calculated by the model for quartz tubes with different photoelectron emission coefficients. The density of He(3P) is expected to be proportional to total light emission. Results are plotted at 149 ns after the start of the voltage pulse, and the IW is approximately halfway between the electrodes and the outlet of the tube. The IW travels faster for larger photoelectron emission coefficients, and so the results are plotted for different y-positions for each frame (2.9 cm above the alumina for 0% and 3.5 cm above the alumina for 5%).

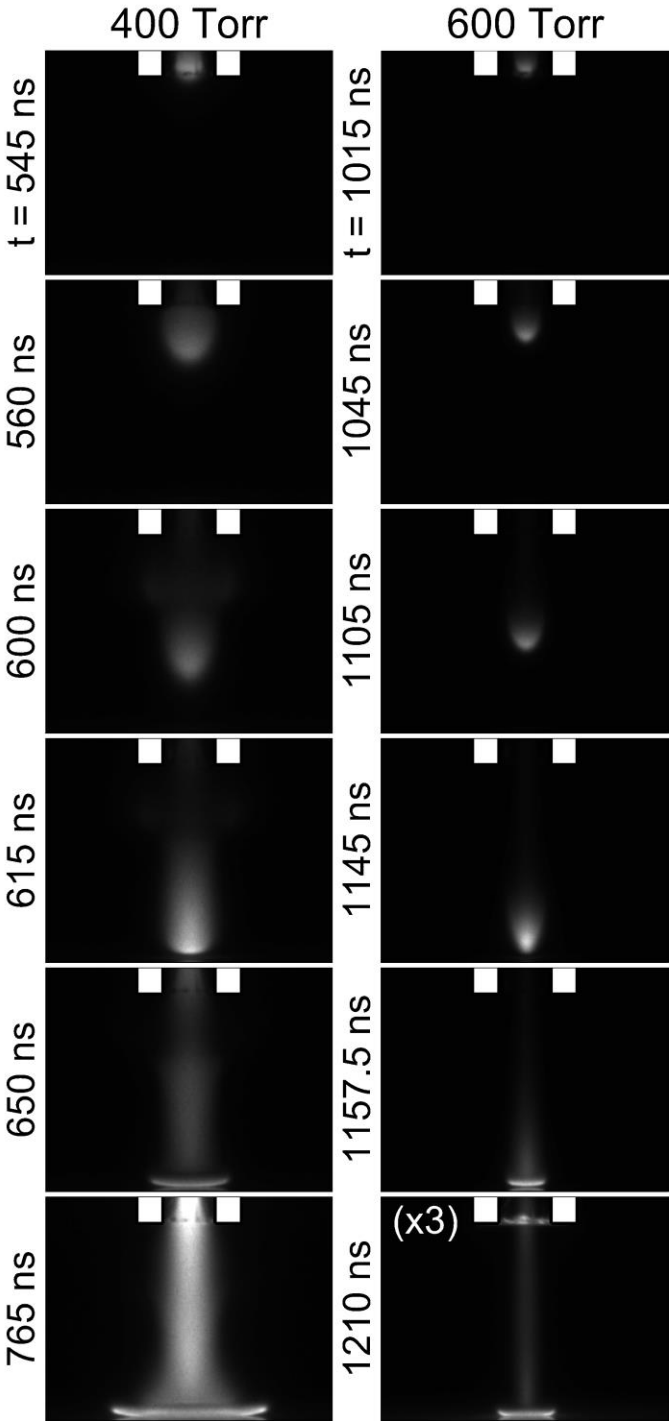

Fig. 9.12 ICCD imaging of all emission (unfiltered) from the plasma jet operated at 400 Torr (left) and 600 Torr (right). The pulse duration was increased with the pressure.

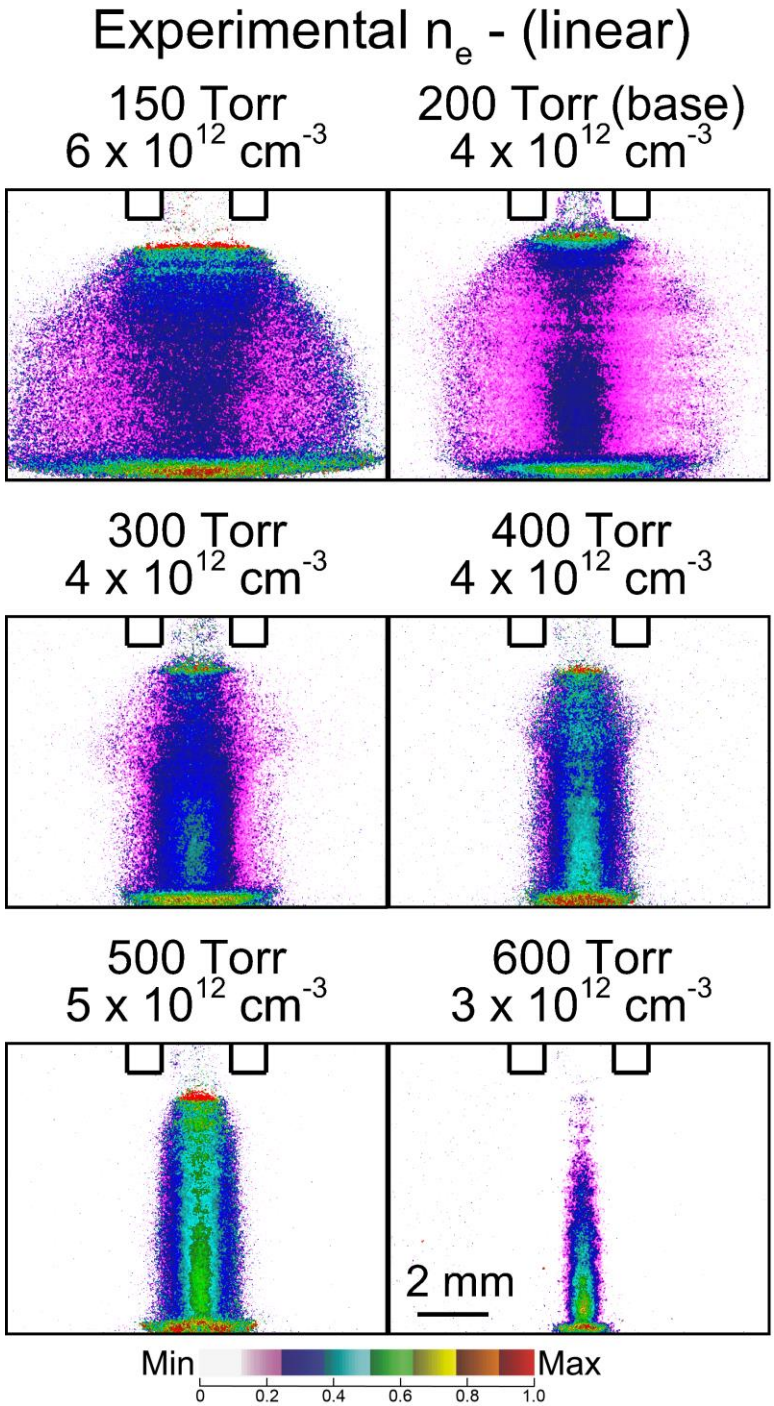

Fig. 9.13 The electron density measured by LCIF 30 ns after the IW has contacted the surface at different pressures. For each frame, the maximum value of the electron density is indicated above each frame.

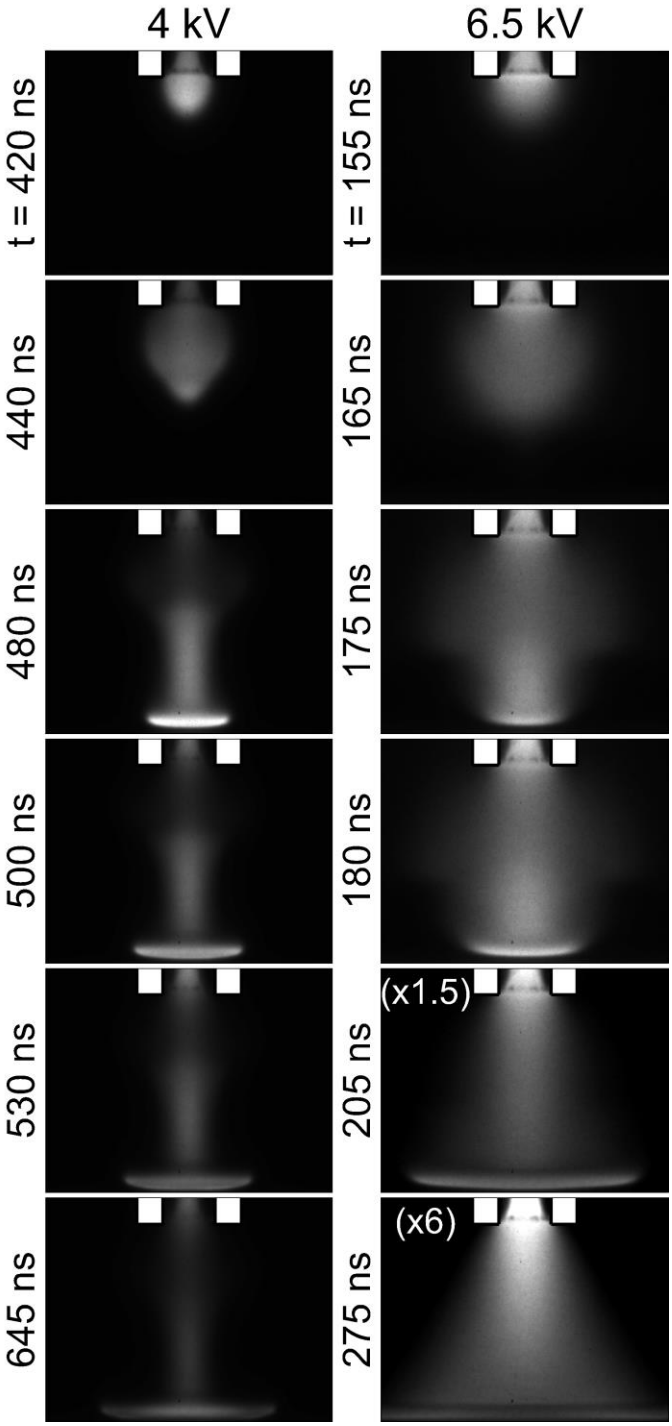

Fig. 9.14 ICCD imaging of all light (unfiltered) for 4 kV (left) and 6.5 kV (right). The camera gate was 5 ns and the images are averaged over 5,000 pulses for 4 kV and 400 pulses for 6 kV.

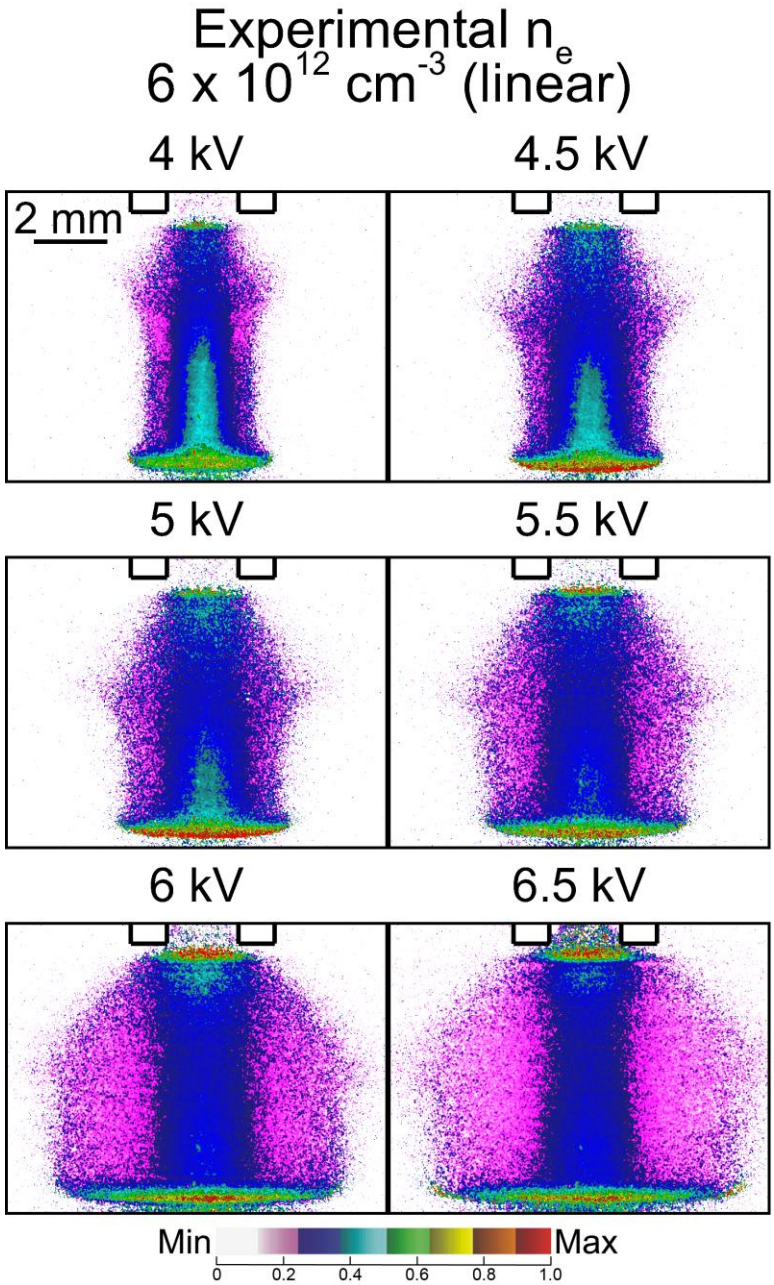

Fig. 9.15 The electron density measured by LCIF 30 ns after the IW contacts the alumina surface for different voltages.

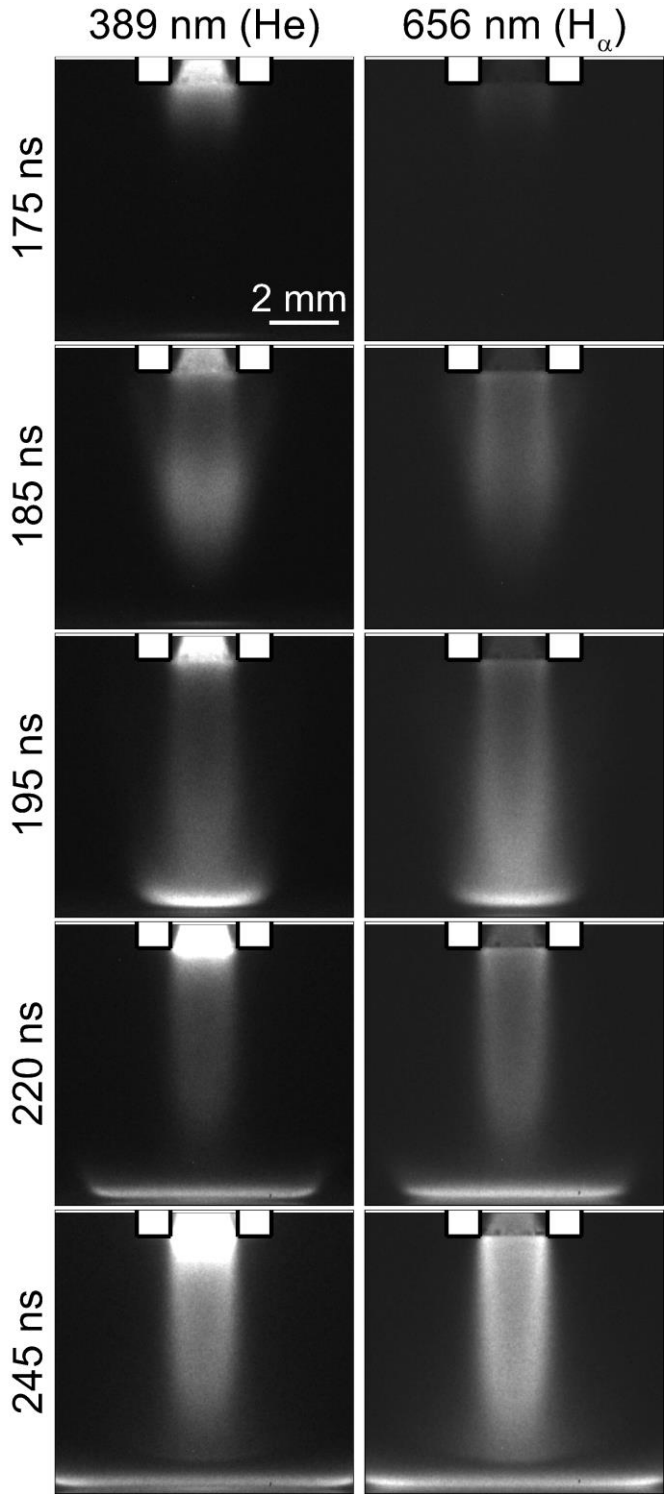

Fig. 9.16 ICCD imaging of optical emission from a plasma jet with a 2.3% H_2O in the shroud. Filters are used to image emission from the He(3^3P) (left) and H_α (right). The gate is 5 ns and the images are averaged over 14,000 pulses for 389 nm and 15,000 pulses for 656 nm.

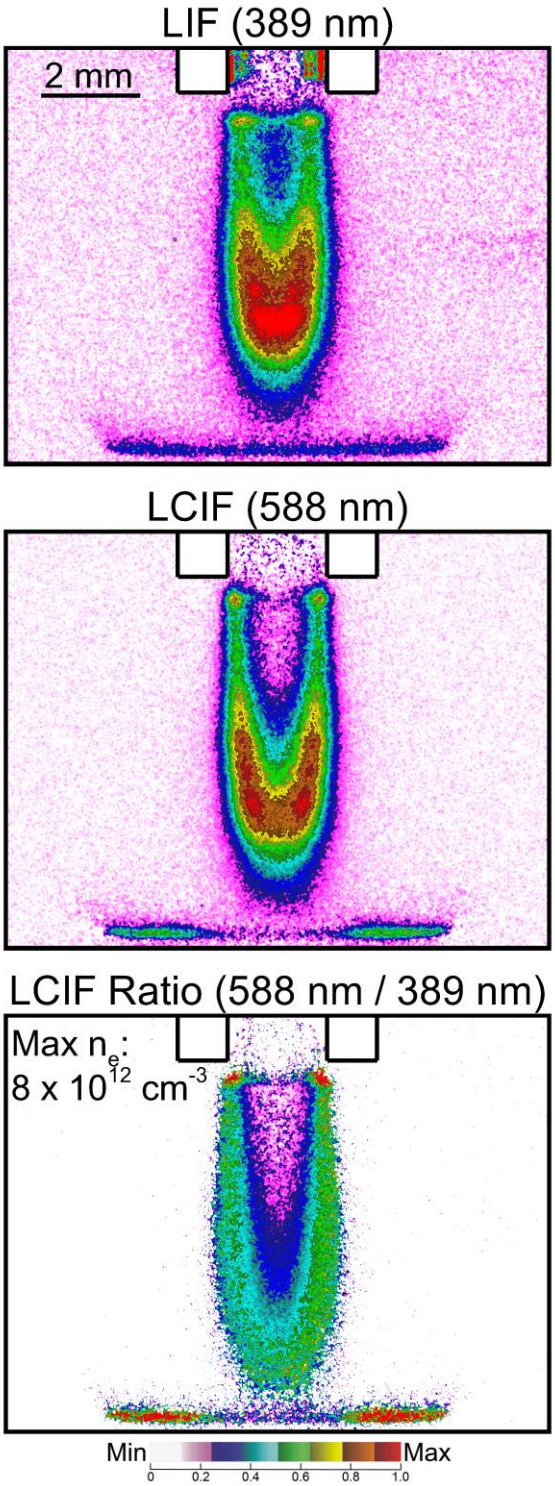

Fig. 9.17 Laser-induced emission for a plasma jet with 2.3% H_2O in the shroud. (top) The laser induced fluorescence (LIF) signal and (center) the laser-collision-induced fluorescence (LCIF) signal in arbitrary units on a linear scale. (bottom) The ratio of the LCIF to the LIF signal is only calculated on pixels where the LIF intensity exceeds that of the background noise. The LCIF ratio is plotted on a linear scale from 0 to 2, which is equivalent to an electron density from 0 to 8×10^{12} cm^{-3}.

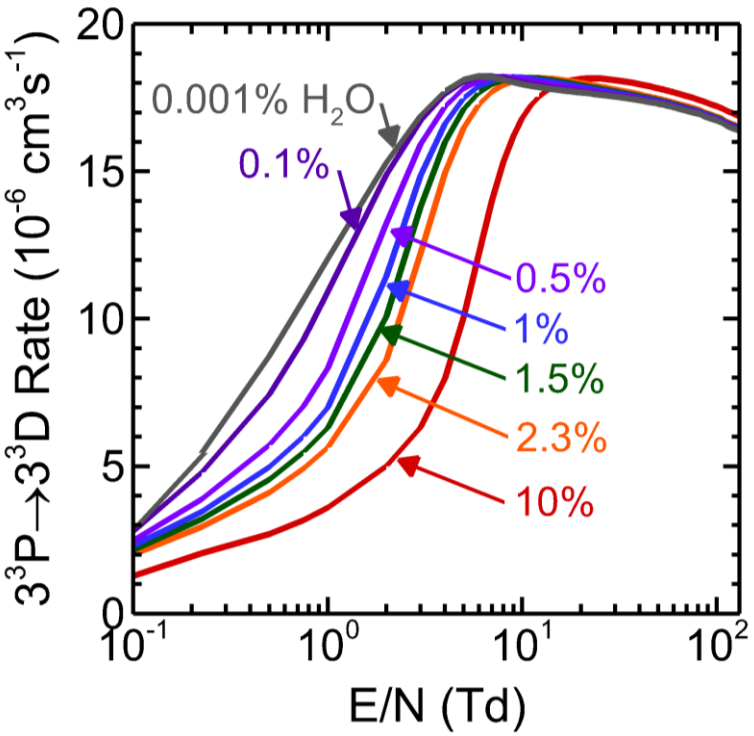

Fig. 9.18 Reaction rate of e + He(3^3P) $\rightarrow$ He(3^3D) + e as a function of E/N for He with different levels of H_2O impurities. Using LCIF emission as a measurement of electron density requires that this rate is relatively insensitive to E/N. Based on this result, the impact of H_2O on the validity of LCIF should be minimal with less than 2.3% H_2O.

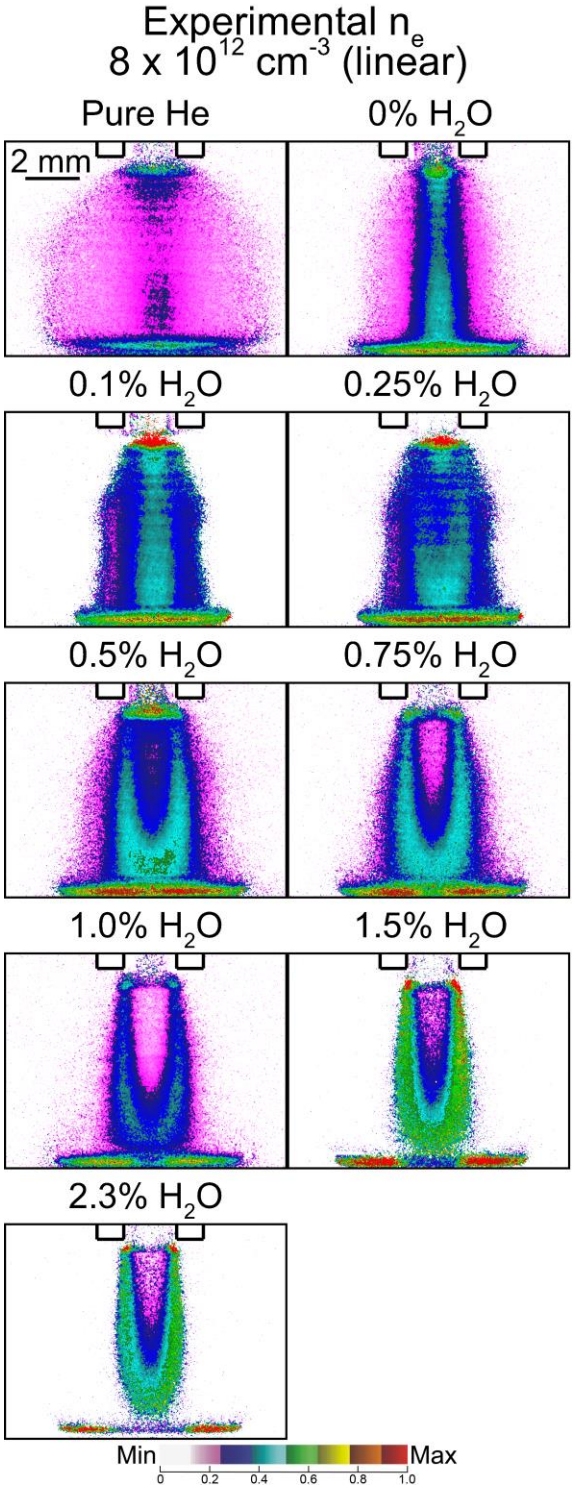

Fig. 9.19 Electron density measured by LCIF for pure He in the central tube and varying humidity in the shroud tube. "Pure He" refers to when the valves to the bubbler system are closed, and "0% H_2O" is the condition where the valves to the bubbler system are open, but no gas flows through the bubbler. The total flow in the shroud tube is held constant at 500 sccm. The densities are plotted on a linear scale. Note that there is a significant uncertainty in their absolute value based on the conversion from LCIF ratio to electron density. For cases with >1% H_2O, regions of high H_2O density have insufficient He(2^3S) densities to measure electrons by LCIF.

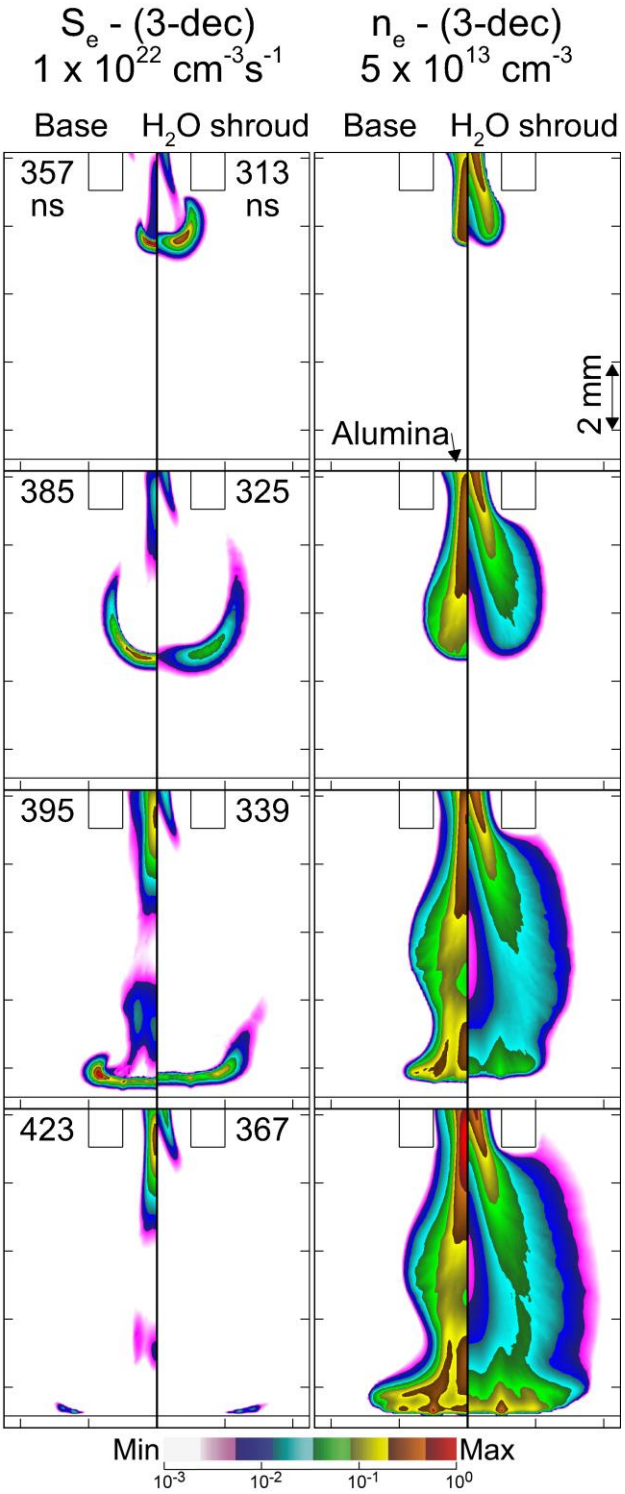

Fig. 9.20 Modeling results of the electron impact ionization rate (S_e, left) and the electron density (n_e, right) for the base case ("Base") and a shroud with 1.5% H_2O in He in a 500 sccm shroud flow ("H_2O shroud"). The IW travels faster in the presence of a humid shroud, but the results are plotted when the IW is at the same position. The time in nanoseconds is indicated on the frame for each plot of S_e. The results of n_e are plotted for the same times.

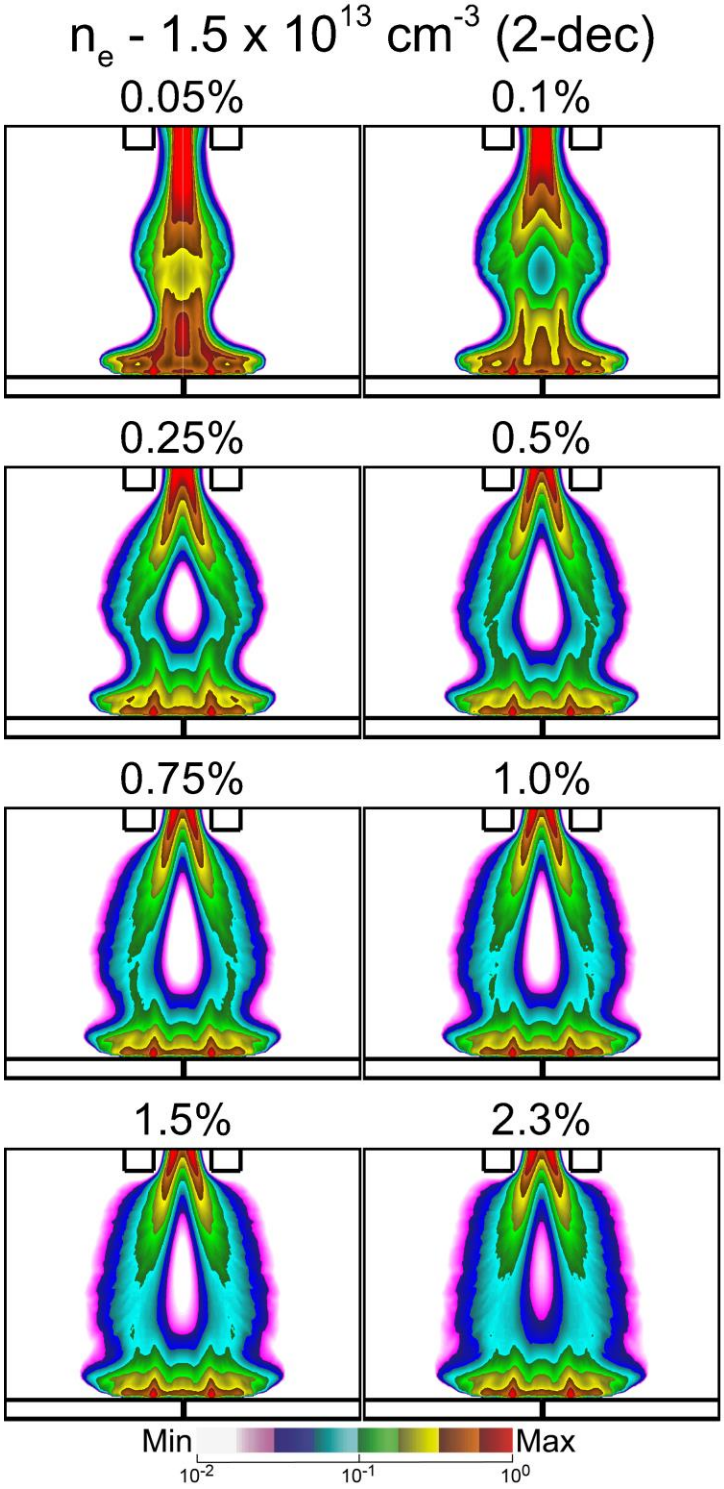

Fig. 9.21 Electron density (n_e) calculated in the in model for varying shroud humidity plotted on a 2-decade log scale. The mole fraction of H_2O in the shroud flow is indicated above each frame. The IW propagates faster for a higher mole fraction of H_2O in the shroud, and the results are compared 30 ns after the IW contacts the surface. This occurs at 425, 409, 391, 381, 375, 371, 367, and 349 ns for 0.05%, 0.1%, 0.25%, 0.5%, 0.75%, 1%, 1.5%, and 2.3%

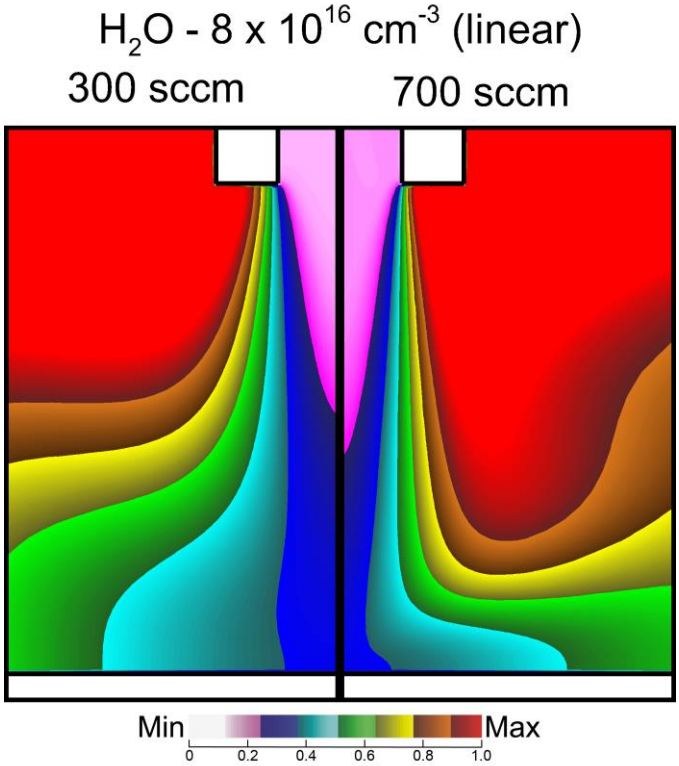

Fig. 9.22 The H_2O composition calculated in the model for 500 sccm of He/H_2O = 97.7/2.3 in the shroud and pure He in the main tube. The central flow is 300 sccm (left) and 700 sccm (right).

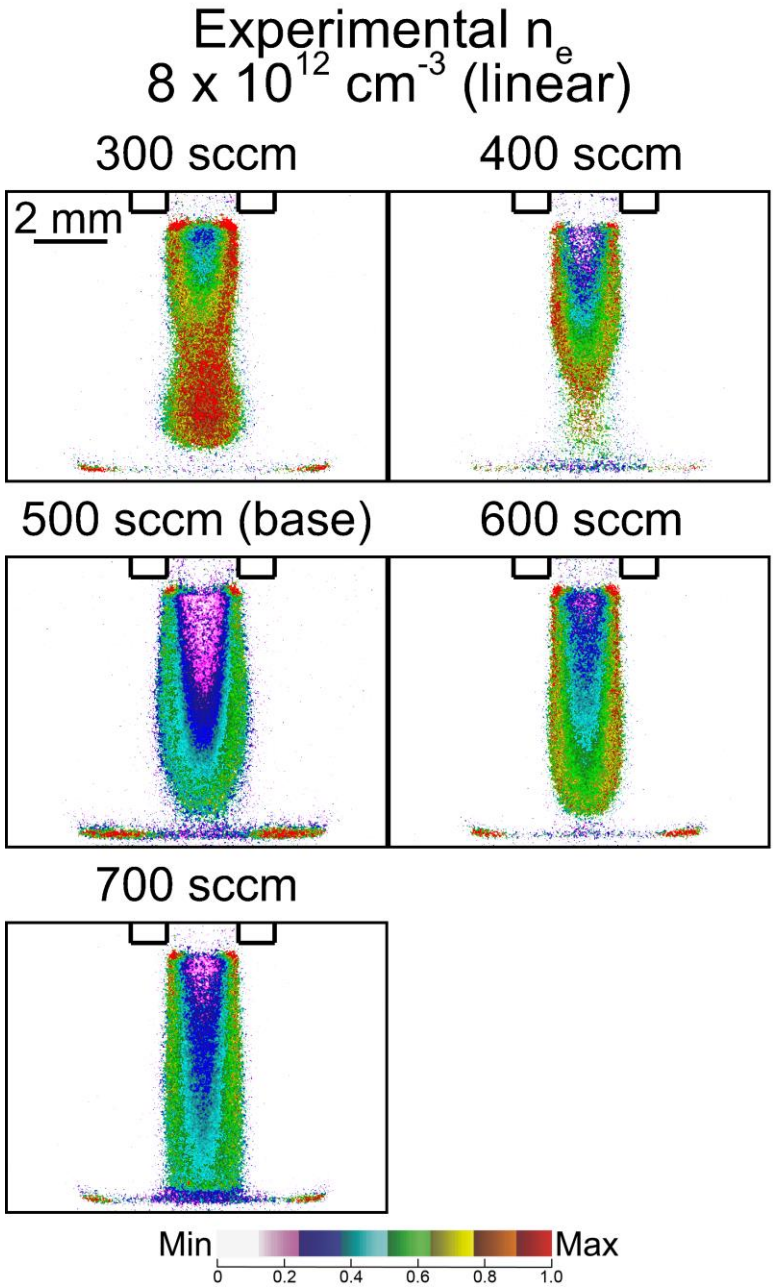

Fig. 9.23 Electron densities measured by LCIF for a jet with 500 sccm of He/H_2O = 97.7/2.3 in the shroud and varying flow rate of pure He in the central tube. Densities are plotted on a linear scale, with an absolute value that has significant uncertainty.

9.8 References

[1] S. Yatom, Y. Luo, Q. Xiong and P. J. Bruggeman, J. Phys. D: Appl. Phys. **50,** 415204 (2017).

[2] N. Knake, S. Reuter, K. Niemi, V. Schulz-von der Gathen and J. Winter, J. Phys. D: Appl. Phys. **41,** 194006 (2008).

[3] T. Verreycken, R. Mensink, R. van der Horst, N. Sadeghi and P. J. Bruggeman, Plasma Sources Sci. Technol. **22,** 055014 (2013).

[4] S. Yonemori, Y. Nakagawa, R. Ono and T. Oda, J. Phys. D: Appl. Phys. **45,** 225202 (2012).

[5] Y. Sakiyama, N. Knake, D. Schröder, J. Winter, V. Schulz-von der Gathen and D. B. Graves, Appl. Phys. Lett. **97,** 151501 (2010).

[6] S. Zhang, W. van Gaens, B. van Gessel, S. Hofmann, E. Van Veldhuizen, A. Bogaerts and P. Bruggeman, J. Phys. D: Appl. Phys. **46,** 205202 (2013).

[7] A. F. H. van Gessel, K. M. J. Alards and P. J. Bruggeman, J. Phys. D: Appl. Phys. **46,** 265202 (2013).

[8] M. M. Turner, Plasma Sources Sci. Technol. **24,** 035027 (2015).

[9] P. Bílek, A. Obrusnik, T. Hoder, M. Šimek and Z. Bonaventura, Plasma Sources Sci. Technol. **27,** 085012 (2018).

[10] Y. Luo, A. M. Lietz, S. Yatom, M. J. Kushner and P. J. Bruggeman, J. Phys. D: Appl. Phys. **52,** 044003 (2019).

[11] C. A. Vasko, D. X. Liu, E. M. van Veldhuizen, F. Iza and P. J. Bruggeman, Plasma Chem. Plasma Process. **34,** 1081 (2014).

[12] F. Tholin, D. L. Rusterholtz, D. A. Lacoste, D. Z. Pai, S. Celestin, J. Jarrige, G. D. Stancu, A. Bourdon and C. O. Laux, IEEE Trans. Plasma Sci. **39,** 2254 (2011).

[13] P. Viegas, E. Slikboer, A. Obrusník, Z. Bonaventura, A. Sobota, E. Garcia-Caurel, O. Guaitella and A. Bourdon, Plasma Sources Sci. Technol. **27,** 094002 (2018).

[14] A. Dubinova, D. Trienekens, U. Ebert, S. Nijdam and T. Christen, Plasma Sources Sci. Technol. **25,** 055021 (2016).

[15] S. Razavizadeh, H. Ghomi and A. Sobota, Plasma Sources Sci. Technol. **27,** 075016 (2018).

[16] A. Schmidt-Bleker, S. A. Norberg, J. Winter, E. Johnsen, S. Reuter, K. D. Weltmann and M. J. Kushner, Plasma Sources Sci. Technol. **24,** 035022 (2015).

[17] M. A. Akman and M. Laroussi, IEEE Trans. Plasma Sci. **41,** 839 (2013).

[18] E. Robert, V. Sarron, D. Riès, S. Dozias, M. Vandamme and J.-M. Pouvesle, Plasma Sources Sci. Technol. **21,** 034017 (2012).

[19] E. Barnat and A. Fierro, J. Phys. D: Appl. Phys. **50,** 14LT01 (2017).

[20] E. V Barnat and A. S. Fierro, in preparation (2019).

[21] W. Van Gaens and A. Bogaerts, J. Phys. D: Appl. Phys. **47,** 079502 (2014).

[22] S. Norberg, PhD Thesis, Modeling atmospheric pressure plasma jets: plasma dynamics, interaction with dielectric surfaces, liquid layers and cells, (University of Michigan, 2015).

[23] S. Große-Kreul, S. Hübner, S. Schneider, A. von Keudell and J. Benedikt, EPJ Tech. Instrum. **3,** 6 (2016).

[24] T. Holstein, Phys. Rev. **72,** 1212 (1947).

[25] C. van Trigt, Phys. Rev. A - At. Mol. Opt. Phys. **13,** 726 (1976).

[26] T. H. Distefano and D. E. Eastman, Solid State Commun. **9,** 2259 (1971).

[27] T. Darny, J. M. Pouvesle, V. Puech, C. Douat, S. Dozias and E. Robert, Plasma Sources Sci. Technol. **26,** 045008 (2017).

[28] V. P. Shevelko and H. Tawara, *Cross Sections for Electron-Impact Induced Transitions Between Excited States in He; n, n'=2, 3, and 4*, (National Institute for Fusion Science, 1995).

Chapter 10 Summary and Future Work

In this dissertation, the dynamics of atmospheric pressure plasma sources useful in the emerging field of plasma medicine have been investigated. Computational modeling along with some accompanying experiments have provided new insights to the important physical and chemical processes in atmospheric pressure plasma jets and in liquids activated by dielectric barrier discharges.

10.1 Summary

In Chapter 1, an introduction to plasmas in general and low temperature plasmas more specifically was presented. The challenges of operating low temperature plasmas at atmospheric pressure and common atmospheric pressure plasma sources including atmospheric pressure plasma jets and dielectric barrier discharges were discussed. The basic mechanisms by which energetic electrons generate reactive oxygen and nitrogen species (RONS), and the role of that reactive chemistry in biomedical applications were summarized. Current applications include cancer treatment, wound healing, dentistry, and dermatology.

In Chapter 2, two models which are used to investigate atmospheric pressure plasmas are described: *GlobalKin* and *nonPDPSIM*. *GlobalKin* is a 0-dimensional model which approximates a plasma as a well stirred reactor. Plasma activation of liquids can now be addressed in this model by also treating the liquid as a well-stirred reactor. *nonPDPSIM* is a 2-dimensional plasma hydrodynamic model which is well suited to address plasmas with gas flows and more complex geometries. The methods of solving Poisson's equation for charged species transport, for grouping nodes into zones for solving the electron energy distribution functions,

and for coupling the plasma calculation with the fluid dynamics calculation have been improved. These updates have improved the efficiency of the model, and have allowed the plasma and gas flow dynamics to be more accurately addressed.

Global modeling of plasma-liquid interactions enables the investigation of plasma-activated liquid chemistry for thousands of plasma pulses and timescales up to minutes. In Chapter 3, this approach was used to study the chemistry of liquid covered tissue treated by an air dielectric barrier discharge. The scaling of aqueous RONS in the liquid with voltage, gas flow, and pulse repetition frequency were discussed. The presence of organics in the liquid can significantly reduce the densities of many reactive species in the liquid phase, including O_{3aq}, $NO_{3\ aq}^{-}$, HO_2NO_{2aq}, and H_2O_{2aq}, while a few species densities increase including HO_{2aq} and NO_{aq}. Changes in the gas phase densities highlight the importance of closely coupling the plasma chemistry calculation with the liquid chemistry.

In Chapter 4, the 0-dimensional method is also used to investigate the first principles of plasma activation of liquid microdroplets. The densities of species have different qualitative behavior depending on their Henry's law constants (h). Species with a high Henry's law constant ($h >> V_g/V_l$, where V_g and V_l are the gas and liquid volumes) are often depleted from the gas phase and reside primarily in the liquid. Increasing the liquid volume (by increasing droplet size) results in dilution of these species and decreasing aqueous densities. Species with low h ($h << V_g/V_l$) reside primarily in the gas phase and have aqueous densities which are independent of droplet diameter. Species with lower h also equilibrate much more quickly between the gas and the liquid, rapidly saturating. These results provide some general principles which can serve as guidelines for tailoring the chemical composition of plasma-activated mists, which are being investigated for agriculture, medicine, and sterilization of surfaces.

In Chapter 5, 2-dimensional modeling was used to investigate the ionization wave (IW) propagation dynamics and the chemistry resulting from different atmospheric pressure plasma jet (APPJ) designs. Both the electrodes intentionally placed on the APPJ and electrical grounds in the vicinity of the APPJ affect the IW dynamics and resulting chemistry. Different electrode designs result in energy deposition in different regions inside or outside of the plasma jet, which in the end result in different fluxes of reactive species. Electrical grounds within 6 cm of the APPJ can increase the RONS production when there is no ground electrode on the jet. Adding a grounded electrode around the tube increases the energy deposition inside the tube. Conditions which result in higher energy deposition increase the production of RONS, but operate at a lower efficiency. Species which do not require large electron energies to form (e.g. $N_2(v)$, O_2*) are highly sensitive to propagation of the IW outside of the tube, which occurs more rapidly when the powered electrode is inside the tube or closer to the outlet.

In Chapter 6, the effect of molecular admixtures and impurities in the He flow of an APPJ is explored using 2-dimensional modeling. It was shown that the impurities on the order of parts per million can account for 79-98% of the RONS production, which is problematic because the impurities are often uncontrolled or unknown. It is possible to mitigate the effect of impurities by adding intentional admixtures of O_2 or H_2O and by selecting electrode configuration that results in more energy deposition outside of the tube of the APPJ.

In Chapter 7, the mechanisms of plasma-induced flow instabilities in APPJs are discussed. In the modeling results, localized energy deposition near the powered electrode in a He APPJ caused rapid localized gas heating. As this gas expanded, an acoustic wave perturbed the shear layer between the rapid He flow and the much slower surrounding humid air. This perturbation

caused the growth of a shear instability, which can explain many of the experimental observations of plasma-induced turbulence in APPJs.

In Chapter 8, an array of APPJs is generated from a single IW in a device called a multi-jet. The design parameters of the multi-jet device must be carefully tuned to provide a uniform surface treatment over large areas. By exploring several design and operational parameters in both modeling and experiments, design guidelines for this type of device could be developed. For example, modifying the gap between the dielectric tube and a grounded surface provides a tradeoff. If the gap is too small, the establishment of conductive channels results in a decrease in the IW intensity over the length of the device. If this gap is too large, interactions between the individual IWs results in some secondary IWs being extinguished or skipped.

In Chapter 9, an experimental study of a He APPJ in a controlled environment with some corresponding modeling results is discussed. Time resolved electron density measurements and ICCD imaging provided experimental evidence of the IW behavior. The influence of molecular gas surrounding a He APPJ was investigated through a humid He shroud flow, which increases the IW speed and electron density while making the plasma discharge more annular. Based on the modeling results, the propagation of the IW in this system is highly sensitive to the photoelectron emission from the surface of the quartz tube of the APPJ. The impact of a shroud is a result of photoionization which occurs at the interface between the pure He and the shroud. Some kinetic effects of electrons were also observed through the modeling studies.

Through the studies in this dissertation, several control mechanisms of RONS production have become apparent. In an air plasma, the RONS production is best controlled by operational parameters such as applied voltage, gas flow, and frequency, or by geometric parameters, including the gas and liquid volumes and the dispersion of the liquid into droplets. In

atmospheric pressure plasma jets, there are additional free parameters because of the nonuniform gas composition. The gas composition may be influenced by modifying flow rates, adding molecular admixtures or by plasma-induced flow instabilities that increase the mixing of the rare gas with the surrounding air.

One of the challenges in plasma medicine is to identify the species which are most important in each biological response (e.g. apoptosis in cancer cells, deactivation of bacteria, triggering an immune response). It is often only possible to measure a few species for a given plasma source in a particular laboratory, though the production of many species change with operational parameters or source design. Connecting differences in plasma source design and operational parameters to changes in production of all RONS can explain some differences in the biological outcomes that often occur with different plasma conditions. For example, an O_2 admixture in a He APPJ increased the expression of genes associated with apoptosis in cancer cells.[1] The results in this dissertation suggest that the RONS containing hydrogen or nitrogen, which decrease with O_2 admixtures, do not contribute to this cellular response.

Several potential mechanisms for a loss of control of RONS have been identified, which can now be better mitigated in the design of plasma sources. For example, surrounding electrical grounds, which are often uncontrolled, can influence the RONS production. Plasma sources for clinical use could include a surrounding ground electrode in their design, eliminating this problem. Impurities in the He often cannot be easily controlled, but contribute significantly to RONS production. Instead of attempting to reduce impurities, it is recommended that intentionally adding a known amount of H_2O or O_2 can eliminate their influence. In addressing these issues that cause a lack of control, the inconsistencies between experimental studies in plasma medicine may be reduced.

10.2 Future Work

Future work based on the studies in this dissertation can be divided into three categories. Improvements to the modeling capabilities of *GlobalKin* and *nonPDPSIM* could better capture some known phenomena. There are also several open scientific questions which further studies could help to address. Lastly, some of the conclusions in this dissertation should be confirmed by experimental validation.

In *GlobalKin*, the activation of liquids could be more accurately addressed by including an adsorbed layer on the liquid surface. Though the effects of this adsorbed layer seem to be small based our estimates, including this layer could change the solvation rates. Many pollutants are more likely to reside at this interface than in the bulk liquid, so including adsorption could make the model more versatile to address the treatment of certain compounds.

Several improvements to *nonPDPSIM* would also make the model more complete for atmospheric pressure plasmas. Based on the results discussed in Chapter 10, the kinetic behavior of electrons produced ahead of the IW may be important to the plasma propagation, especially in the case of positive polarity IWs. Currently, the model is able to address these effects for electrons which are emitted from the surface, but not for electrons produced by photoionization of the gas ahead of the IW. This could be done by treating the electrons produced by photoionization as Monte Carlo particles, instead of only the secondary electrons from surfaces. Additionally, 3-dimensional modeling capabilities would enable more accurate modeling of complex geometries such as those of the multi-jet in Chapter 8. This would also likely require improvements in the code performance and more parallelization in order to address the much larger matrices that would be produced.

Further modeling studies would also provide insights to several scientific questions in the field. It would be possible to use the gas heating predicted by *nonPDPSIM* in APPJs in Chapter 7 as an input to a large eddy simulation, in order to more accurately quantify the impact on the flow at different Reynold's number and frequencies. An additional open scientific question is on the repression or reduction of turbulence in APPJs which sometimes occurs when a plasma is turned on. The mechanism of plasma-induced flow instabilities outlined in Chapter 7 does not seem to explain the repression of turbulence seen in some experiments. This behavior is often attributed to ion wind, but gas heating could play a role as well. The role of the ion wind may be underestimated in *nonPDPSIM* due to the limited time in which Poisson's equation is solved. Extending the calculation of Poisson's equation to longer timescales, with and without the presence of a dielectric target, would provide some insights on when and if this term becomes significant. It would be necessary to reduce the chemistry and geometry to keep the computational time reasonable in order to achieve longer timescales.

In the case of plasma activated droplets discussed in Chapter 4, some additional studies on the effect of other operational parameters such as pulse repetition frequency, applied voltage, and total energy deposition per liquid volume may be beneficial. This data would provide more guidelines to the community on how to control the chemical composition of plasma-activated mists.

Experimental studies for validation would be particularly valuable for the following results. The scaling of plasma activation of droplets (Chapter 4) with droplet diameter and density for species with different Henry's law constants should be validated by experiments. Though the mechanism for plasma-induced flow instabilities discussed in Chapter 7 is consistent with experimental observations, direct measurements of an acoustic wave or the predicted

localized gas heating would further establish the validity of this mechanism. Additionally, more validation experiments are necessary for the reaction mechanisms, especially the liquid reaction mechanisms. There is still large uncertainty in many of the rates for the most highly reactive species (for example, electronically excited states). Combined experiment and modeling studies of liquid chemistry for simplified gas compositions may provide valuable insights on gaps or inaccuracies in the reaction mechanism. Currently, detailed diagnostics to measure reactive species in the liquid or on the interface *in situ* have not been developed. It should still be possible however to compare the more stable species and pH predicted by the global model with experiments.

10.3 References

[1] H. M. Joh, J. Y. Choi, S. J. Kim, T. H. Chung and T.-H. Kang, Sci. Rep. **4,** 6638 (2014).

Appendix A: Henry's Law Equilibration Time

In this appendix, the equilibration time τ for a gas phase species solvating into a liquid droplet producing a final aqueous density is derived. Beginning with Eq. 2.14 and ignoring reactions and evaporation,

$$\frac{dn_l}{dt} = \frac{Dn_g}{\Lambda^2} f_l S_l \frac{V_g}{V_l} \tag{A1}$$

where n_l is the number density of the species in the liquid, and n_g is the number density of the species in the gas phase. D is the diffusion coefficient, f_l is the fractional area of the liquid in contact with the plasma, Λ is the diffusion length of the plasma, and S_l is the reaction probability of the gas phase species with the liquid. Substituting Eq. 2.12 for S_l and assuming the liquid is not oversaturated,

$$\frac{dn_l}{dt} = \frac{Dn_g}{\Lambda^2} f_l \frac{hn_g - n_l}{hn_g} \frac{V_g}{V_l}, \tag{A2}$$

$$\frac{dn_l}{dt} = \frac{Df_l}{\Lambda^2} \frac{hn_g - n_l}{h} \frac{V_g}{V_l}. \tag{A3}$$

Neglecting reactions, the total number of molecules should be conserved. Assume at $t = 0$ the liquid density is zero and the gas density is n_{g0}.

$$V_g n_{g0} = V_g n_g + V_l n_l \tag{A4}$$

$$n_g = n_{g0} - \frac{V_l}{V_g} n_l \tag{A5}$$

Inserting Eq. A5 into Eq. A3 to eliminate n_g, we have

$$\frac{dn_l}{dt} = \frac{Df_l}{\Lambda^2} \frac{h\left(n_{g0} - \frac{V_l}{V_g} n_l\right) - n_l}{h} \frac{V_g}{V_l}, \tag{A6}$$

$$\frac{dn_l}{dt} = \frac{Df_l}{\Lambda^2} \left(n_{g0} - \frac{V_l}{V_g} n_l - \frac{n_l}{h}\right) \frac{V_g}{V_l}, \tag{A7}$$

$$\frac{dn_l}{dt} = \frac{Df_l}{\Lambda^2}\left(\frac{V_g}{V_l} n_{g0} - n_l - \frac{V_g n_l}{V_l h}\right), \tag{A8}$$

$$\frac{dn_l}{dt} = \frac{Df_l}{\Lambda^2}\frac{V_g}{V_l} n_{g0} - \frac{Df_l}{\Lambda^2}\left(\frac{V_g}{V_l h} + 1\right) n_l . \tag{A9}$$

Integrating Eq. A9 with the initial condition $n_l(t = 0) = 0$, we can solve for the integration constant,

$$n_l(t) = \frac{h n_{g0}}{1 + \frac{h V_l}{V_g}}\left(1 - e^{-t/\tau}\right), \tag{A10}$$

$$\tau = \frac{\Lambda^2}{Df_l\left(\frac{V_g}{h V_l} + 1\right)} . \tag{A11}$$

τ is the characteristic timescale to establish Henry's law equilibrium.

Appendix B: Reduced $He/N_2/O_2/H_2O$ Reaction Mechanism

Table B.1 Reduced $He/N_2/O_2/H_2O$ Reaction Mechanism.

Reaction[a]	Rate Coefficient[b]			Notes	Ref.
	A	n	E		
Electron-Neutral					
$e + He \rightarrow He + e$	$\sigma(\varepsilon)$				[1]
$e + He \rightarrow He^* + e$	$\sigma(\varepsilon)$				[1]
$e + He \rightarrow He^+ + e + e$	$\sigma(\varepsilon)$				[1]
$e + He^* \rightarrow He^* + e$	$\sigma(\varepsilon)$			c,d	[1,2]
$e + He^* \rightarrow He + e$	$\sigma(\varepsilon)$			c	[1,2]
$e + He^* \rightarrow He^+ + e + e$	$\sigma(\varepsilon)$				[3]
$e + He_2^* \rightarrow He + He + e$	1×10^{-7}			e	[4]
$e + N_2 \rightarrow N_2 + e$	$\sigma(\varepsilon)$				[5]
$e + N_2 \rightarrow N_2(v) + e$, (v=1-8)	$\sigma(\varepsilon)$				[6]
$e + N_2 \rightarrow N_2^* + e$	$\sigma(\varepsilon)$				[7,8]
$e + N_2 \rightarrow N_2^{**} + e$	$\sigma(\varepsilon)$				[8]
$e + N_2 \rightarrow N + N + e$	$\sigma(\varepsilon)$				[9]
$e + N_2 \rightarrow N_2^+ + e + e$	$\sigma(\varepsilon)$				[9]
$e + N_2(v) \rightarrow N_2(v) + e$	$\sigma(\varepsilon)$				[5]
$e + N_2(v) \rightarrow N_2 + e$	$\sigma(\varepsilon)$			c	[6]
$e + N_2(v) \rightarrow N_2^* + e$	$\sigma(\varepsilon)$				[7,8]
$e + N_2(v) \rightarrow N_2^+ + e + e$	$\sigma(\varepsilon)$				[9]
$e + N_2^* \rightarrow N_2^* + e$	$\sigma(\varepsilon)$				[5]
$e + N_2^* \rightarrow N_2 + e$	$\sigma(\varepsilon)$			c	[7,8]
$e + N_2^* \rightarrow N_2^+ + e + e$	$\sigma(\varepsilon)$				[3]
$e + N_2^* \rightarrow N_2(v) + e$	$\sigma(\varepsilon)$			c	[7,8]
$e + N_2^{**} \rightarrow N_2 + e$	$\sigma(\varepsilon)$			c	[8]
$e + N \rightarrow N + e$	$\sigma(\varepsilon)$				[10]
$e + O_2 \rightarrow O_2 + e$	$\sigma(\varepsilon)$				[6]
$e + O_2 \rightarrow O^- + O$	$\sigma(\varepsilon)$				[6]
$e + O_2 \rightarrow O_2^* + e$	$\sigma(\varepsilon)$				[6]
$e + O_2 \rightarrow O + O + e$	$\sigma(\varepsilon)$				[6]
$e + O_2 \rightarrow O^* + O + e$	$\sigma(\varepsilon)$				[6]
$e + O_2 \rightarrow O_2^+ + e + e$	$\sigma(\varepsilon)$				[6]
$e + O_2 + M \rightarrow O_2^- + M$	2×10^{-31}	-1.0		f	[11]
$e + O_2^* \rightarrow O_2^* + e$	$\sigma(\varepsilon)$			d	
$e + O_2^* \rightarrow O^- + O$	$\sigma(\varepsilon)$				[12]
$e + O_2^* \rightarrow O_2 + e$	$\sigma(\varepsilon)$			c	[6]

$e + O_2^* \rightarrow O + O + e$	$\sigma(\varepsilon)$			[6]
$e + O_2^* \rightarrow O^* + O + e$	$\sigma(\varepsilon)$			[6]
$e + O_2^* \rightarrow O_2^+ + e + e$	$\sigma(\varepsilon)$			[6]
$e + O_2^* + O_2 \rightarrow O_2^- + O_2$	1×10^{-29}		g	[11]
$e + O_2^* + N_2 \rightarrow O_2^- + N_2$	1×10^{-29}		g	[11]
$e + O \rightarrow O + e$	$\sigma(\varepsilon)$			[13]
$e + O \rightarrow O^* + e$	$\sigma(\varepsilon)$			[14]
$e + O^* \rightarrow O^* + e$	$\sigma(\varepsilon)$			[13]
$e + O^* \rightarrow O + e$	$\sigma(\varepsilon)$		c	[14]
$e + O_3 \rightarrow O^- + O_2$	$\sigma(\varepsilon)$			[15]
$e + O_3 \rightarrow O_2^- + O$	$\sigma(\varepsilon)$			[15]
$e + H_2O \rightarrow H_2O + e$	$\sigma(\varepsilon)$			[16]
$e + H_2O \rightarrow O^- + H_2$	$\sigma(\varepsilon)$			[16]
$e + H_2O \rightarrow OH^- + H$	$\sigma(\varepsilon)$			[16]
$e + H_2O \rightarrow H + OH + e$	$\sigma(\varepsilon)$			[16]
$e + H_2O \rightarrow O + H + H + e$	$\sigma(\varepsilon)$			[16]
$e + H_2O \rightarrow H_2O^+ + e + e$	$\sigma(\varepsilon)$			[16]
$e + H_2O \rightarrow H^+ + OH + e + e$	$\sigma(\varepsilon)$			[16]
$e + H_2 \rightarrow H + H + e$	$\sigma(\varepsilon)$			[17,18]
Electron-Ion				
$e + He^+ \rightarrow He(2^3S)$	6.76×10^{-13}	-0.5	f	[19]
$e + e + He^+ \rightarrow He(2^3S) + e$	2.69×10^{-26}	-4.0	f	[20,21]
$e + e + He_2^+ \rightarrow He(2^3S) + He + e$	4.5×10^{-27}	-4.0	f	[20,21]
$e + e + He_2^+ \rightarrow He_2^* + e$	1.35×10^{-26}	-4.0	f	[20,21]
$e + He_2^+ \rightarrow He(2^3S) + He$	1.6×10^{-9}	-0.5	f	[22]
$e + He^+ + M \rightarrow He(2^3S) + M$	1.2×10^{-33}	-4.0	f	[23]
$e + He_2^+ + M \rightarrow He(2^3S) + He + M$	1.3×10^{-28}	-1	f	[20]
$e + N_4^+ \rightarrow N_2 + N_2$	2×10^{-7}	-0.5	f	[24]
$e + O_2^+ \rightarrow O + O$	1.20×10^{-8}	-0.7	f	[24]
$e + O_2^+ \rightarrow O^* + O$	8.88×10^{-9}	-0.7	f	[24]
$e + H_2O^+ \rightarrow O + H_2$	2.52×10^{-6}	-0.5		[25]
$e + H_2O^+ \rightarrow OH + H$	6.60×10^{-6}	-0.5		[25]
$e + H_2O^+ \rightarrow O + H + H$	2.88×10^{-6}	-0.5		[25]
$e + H_3O^+ \rightarrow H_2O + H$	2×10^{-7}	-0.5	f	[26]
Ion-Ion				
$O_2^- + He^+ \rightarrow O_2 + He$	2×10^{-7}	-1.0	e	[27,28]
$O_2^- + He_2^+ \rightarrow O_2 + He + He$	2×10^{-6}		e	[29]
$O_2^- + N_2^+ \rightarrow N_2 + O_2$	2×10^{-6}			[29]
$O_2^- + N_4^+ \rightarrow N_2 + N_2 + O_2$	2×10^{-6}		e	[29]
$O_2^- + N_2^+ \rightarrow O_2 + N + N$	1×10^{-7}			[11,28]
$O_2^- + O_2^+ \rightarrow O_2 + O_2$	2×10^{-6}		e	[29]
$O_2^- + O_2^+ \rightarrow O_2 + O + O$	1×10^{-7}			[11,28]
$O_2^- + H_2O^+ \rightarrow H_2O + O_2$	2×10^{-6}		e	[29]
$O_2^- + H_3O^+ \rightarrow O_2 + H_2O + H$	1×10^{-7}		e	[11,28]

$O_2^- + H^+ \rightarrow H + O_2$	2×10^{-7}	-0.5	e	[11,28]
$O_2^- + H_2O^+ \rightarrow O_2 + OH + H$	1×10^{-7}		e	[11,28]
$O^- + He^+ \rightarrow O + He$	2×10^{-7}	-1.0	e	[27,28]
$O^- + He^+ + M \rightarrow O + He + M$	2×10^{-25}	-2.5	e	[27,28]
$O^- + He_2^+ \rightarrow O + He + He$	3×10^{-6}		e	[4]
$O^- + N_2^+ \rightarrow N_2 + O$	3×10^{-6}			[4]
$O^- + N_2^+ \rightarrow O + N + N$	1×10^{-7}			[11,28]
$O^- + N_4^+ \rightarrow N_2 + N_2 + O$	3×10^{-6}			[4]
$O^- + O_2^+ \rightarrow O_2 + O$	3×10^{-6}			[4]
$O^- + O_2^+ \rightarrow O + O + O$	1×10^{-7}			[11,28]
$O^- + O_2^+ + M \rightarrow O + O_2 + M$	2×10^{-25}	-2.5		[11,28]
$O^- + H_2O^+ \rightarrow H_2O + O$	3×10^{-6}			[4]
$O^- + H_2O^+ \rightarrow O + OH + H$	1×10^{-7}		e	[11,28]
$O^- + H_3O^+ \rightarrow O + H_2O + H$	1×10^{-7}		e	[11,28]
$O^- + H^+ \rightarrow H + O$	2×10^{-7}	-0.5	e	[11,28]
$OH^- + He^+ \rightarrow OH + He$	2×10^{-7}	-1.0	e	[27,28]
$OH^- + He_2^+ \rightarrow OH + He + He$	3×10^{-6}		e	[29]
$OH^- + N_2^+ \rightarrow OH + N_2$	2×10^{-7}	-0.5	e	[11,28]
$OH^- + N_2^+ \rightarrow OH + N + N$	1×10^{-7}		e	[11,28]
$OH^- + N_4^+ \rightarrow N_2 + N_2 + OH$	2×10^{-7}	-0.5	e	[11,28]
$OH^- + O_2^+ \rightarrow OH + O_2$	2×10^{-7}	-0.5	e	[11,28]
$OH^- + O_2^+ \rightarrow OH + O + O$	1×10^{-7}		e	[11,28]
$OH^- + H_2O^+ \rightarrow H_2O + OH$	2×10^{-7}	-0.5	e	[11,28]
$OH^- + H_2O^+ \rightarrow OH + OH + H$	1×10^{-7}		e	[11,28]
$OH^- + H^+ \rightarrow H + OH$	2×10^{-7}	-0.5	e	[11,28]
$OH^- + H_3O^+ \rightarrow OH + H_2O + H$	1×10^{-7}		e	[11,28]
Ion-Neutral				
$He^+ + He \rightarrow He + He^+$	1×10^{-9}	0.5		[19,30]
$He^+ + He + M \rightarrow He_2^+ + M$	1.1×10^{-31}	-0.38		[31]
$He^+ + N_2 \rightarrow N_2^+ + He$	1.3×10^{-9}			[32]
$He^+ + O_2 \rightarrow O_2^+ + He$	3.3×10^{-11}	0.5		[32]
$He^+ + H_2O \rightarrow H_2O^+ + He$	5×10^{-10}			[32]
$He^+ + H \rightarrow H^+ + He$	5×10^{-10}		e	[32]
$He^+ + O_2^* \rightarrow O_2^+ + He$	3.3×10^{-11}	0.5	e	[32]
$He_2^+ + N_2 \rightarrow N_2^+ + He + He$	1.2×10^{-9}			[33]
$He_2^+ + O_2 \rightarrow O_2^+ + He + He$	1×10^{-9}			[33]
$He_2^+ + H_2O \rightarrow H_2O^+ + He + He$	2×10^{-9}		h	[33]
$He_2^+ + H \rightarrow H^+ + He + He$	2×10^{-9}		h	[33]
$N_2^+ + N_2 + M \rightarrow N_4^+ + M$	6.8×10^{-29}	-1.64		[34]
$N_2^+ + O_2 \rightarrow O_2^+ + N_2$	5.1×10^{-11}			[29,32,35]
$N_2^+ + H_2O \rightarrow H_2O^+ + N_2$	2.3×10^{-9}			[32]
$N_4^+ + N_2 \rightarrow N_2^+ + N_2 + N_2$	2.56×10^{-15}			[36]
$N_4^+ + O_2 \rightarrow O_2^+ + N_2 + N_2$	2.4×10^{-10}			[11]
$N_4^+ + H_2O \rightarrow H_2O^+ + N_2 + N_2$	3×10^{-9}			[35]
$O_2^+ + O_2 \rightarrow O_2 + O_2^+$	1×10^{-9}	0.5		[19,30]

$O_2^- + O \rightarrow O_3 + e$	1.5×10^{-10}				[11]
$O_2^- + O \rightarrow O^- + O_2$	3.3×10^{-10}				[11]
$O_2^- + O_2^* \rightarrow e + O_2 + O_2$	2×10^{-10}				[35]
$O_2^- + N_2 \rightarrow N_2 + O_2 + e$	1.9×10^{-12}	0.5	4.99×10^3		[11]
$O_2^- + N_2^* \rightarrow N_2 + O_2 + e$	2.1×10^{-9}				[11]
$O_2^- + O_2 \rightarrow O_2 + O_2 + e$	2.7×10^{-10}	0.5	5.59×10^3		[35]
$O_2^- + O_3 \rightarrow O_3 + O_2 + e$	6×10^{-10}				[37]
$O^- + O_2 \rightarrow O_2^- + O$	1.5×10^{-20}			e	[38]
$O^- + O \rightarrow O_2 + e$	1.9×10^{-10}			h	[35]
$O^- + O_3 \rightarrow O_2^- + O_2$	1.02×10^{-11}	0.5			[19,39]
$O^- + N \rightarrow NO + e$	2.6×10^{-10}				[35]
$O^- + N_2^* \rightarrow N_2 + O + e$	1.9×10^{-9}				[35]
$O^- + O_2 \rightarrow O_3 + e$	1×10^{-12}				[40]
$O^- + O_2^* \rightarrow O_3 + e$	3×10^{-10}				[11]
$O^- + O_3 \rightarrow O_2 + O_2 + e$	3×10^{-10}				[35]
$O^- + H_2 \rightarrow H_2O + e$	7×10^{-10}				[35]
$O^- + O_2^* \rightarrow O_2^- + O$	1×10^{-10}				[11]
$O^- + H_2 \rightarrow OH^- + H$	3.3×10^{-11}				[35]
$O^- + H_2O \rightarrow OH^- + OH$	1.4×10^{-9}				[35]
$H_2O^+ + O_2 \rightarrow O_2^+ + H_2O$	4.3×10^{-10}				[35]
$H_2O^+ + H_2O \rightarrow H_3O^+ + OH$	1.7×10^{-9}				[35]
$H_2O^+ + O \rightarrow O_2^+ + H_2$	5.5×10^{-11}				[41]
$H_2O^+ + H_2 \rightarrow H_3O^+ + H$	7.6×10^{-10}				[32]
$H^+ + H_2O \rightarrow H_3O^+$	5×10^{-10}			e	[32]
$H^+ + O_2 \rightarrow O_2^+ + H$	1.17×10^{-9}				[32]
$H^+ + H_2O \rightarrow H_2O^+ + H$	8.2×10^{-9}				[32]
$OH^- + H \rightarrow H_2O + e$	1.8×10^{-9}				[35]
Penning Ionization					
$He^* + N_2 \rightarrow He + N_2^+ + e$	1.5×10^{-10}			i	[20]
$He(2^3S) + O_2 \rightarrow O_2^+ + He + e$	2.54×10^{-10}	0.5			[42]
$He(2^1S) + O_2 \rightarrow He + O_2^+ + e$	1.5×10^{-10}			i	[20]
$He(2^3P) + O_2 \rightarrow He + O_2^+ + e$	1.5×10^{-10}			i	[20]
$He(2^1P) + O_2 \rightarrow He + O_2^+ + e$	1.5×10^{-10}			i	[20]
$He(3P) + O_2 \rightarrow He + O_2^+ + e$	1.5×10^{-10}			i	[20]
$He(3S) + O_2 \rightarrow He + O_2^+ + e$	1.5×10^{-10}			i	[20]
$He^* + H_2O \rightarrow He + H_2O^+ + e$	1.5×10^{-10}			i	[20]
$He^* + H \rightarrow He + H^+ + e$	1.5×10^{-10}			i	[20]
$He^* + He^* \rightarrow He^+ + He + e$	4.5×10^{-10}	0.5			[20]
$He^* + He^* \rightarrow He_2^+ + e$	1.05×10^{-9}	0.5			[20]
$He^* + He_2^* \rightarrow He^+ + He + He + e$	2.25×10^{-11}	0.5			[20,21]
$He^* + He_2^* \rightarrow He_2^+ + He + e$	1.28×10^{-10}	0.5			[20,21]
$He(2^3S) + O_3 \rightarrow O_2^+ + O + He + e$	2.54×10^{-10}	0.5		j	[42]
$He_2^* + O_2 \rightarrow He + He + O_2^+ + e$	1.5×10^{-10}			k	[20]
$He_2^* + N_2 \rightarrow He + He + N_2^+ + e$	1.5×10^{-10}			k	[20]
$He_2^* + H_2O \rightarrow He + He + H_2O^+ + e$	1.5×10^{-10}			k	[20]

$He_2^* + H \rightarrow He + He + H^+ + e$	1.5×10^{-10}			k	[20]
$He_2^* + He_2^* \rightarrow He^+ + He + He + He + e$	2.25×10^{-11}	0.5			[20,21]
$He_2^* + He_2^* \rightarrow He_2^+ + He + He + e$	1.28×10^{-10}	0.5			[20,21]
Excited State Neutrals					
$He^* + He + M \rightarrow He_2^* + M$	2×10^{-34}				[43]
$N_2(v) + N_2 \rightarrow N_2 + N_2$	1×10^{-15}			h	[44]
$N_2(v) + O_2 \rightarrow N_2 + O_2$	1×10^{-15}			h	[44]
$N_2(v) + H_2O \rightarrow N_2 + H_2O$	1×10^{-15}			h	[44]
$N_2(v) + N \rightarrow N_2 + N$	1×10^{-16}			h	[44]
$N_2(v) + O \rightarrow N_2 + O$	1×10^{-16}			h	[44]
$N_2^* + N_2 \rightarrow N_2 + N_2$	1.9×10^{-13}			l	[45]
$N_2^* + O_2 \rightarrow O_2 + N_2$	2.8×10^{-11}			l	[45]
$N_2^* + O_2 \rightarrow O + O + N_2$	1.5×10^{-12}			h	[11,46]
$N_2^* + H_2O \rightarrow N_2 + OH + H$	6×10^{-14}				[47]
$N_2^* + H_2 \rightarrow N_2 + H_2$	2.6×10^{-11}			l	[45]
$N_2^* + O \rightarrow NO + N$	5×10^{-10}			h	[48]
$N_2^* + O_3 \rightarrow NO + NO + O$	8.4×10^{-12}				[47]
$N_2^{**} + O \rightarrow NO + N$	5×10^{-10}			h	[48]
$N_2^{**} + O_3 \rightarrow NO + NO + O$	8.4×10^{-12}			e	[47]
$O_2^* + He \rightarrow O_2 + He$	8×10^{-21}	0.5			[49]
$O_2^* + O_2 \rightarrow O_2 + O_2$	2.2×10^{-18}				[11]
$O_2^* + O_2 \rightarrow O + O_3$	2.95×10^{-21}				[49]
$O_2^* + O_3 \rightarrow O_2 + O_2 + O$	9.96×10^{-11}		3.05×10^3	h	[49]
$O_2^* + N \rightarrow O + NO$	2×10^{-14}		600		[11]
$O_2^* + NO \rightarrow O_2 + NO$	3.5×10^{-17}				[49]
$O^* + N_2 \rightarrow O + N_2$	1.8×10^{-11}		-1.07×10^2		[11]
$O^* + O_2 \rightarrow O + O_2$	3.8×10^{-11}			h	[11,49]
$O^* + H_2O \rightarrow OH + OH$	2×10^{-10}				[49]
$O^* + H_2O \rightarrow O + H_2O$	1.2×10^{-11}				[29]
$O^* + H_2O \rightarrow H_2 + O_2$	2.3×10^{-12}				[50]
$O^* + O_3 \rightarrow O_2 + O + O$	1.2×10^{-10}				[11,49]
$O^* + O_3 \rightarrow O_2 + O_2$	5.04×10^{-10}				[49]
$O^* + O_2^* \rightarrow O + O_2$	1×10^{-11}				[49]
$O^* + O \rightarrow O + O$	1×10^{-11}			h	[49]
$O^* + NO \rightarrow O_2 + N$	8.5×10^{-11}				[49]
$O^* + H_2 \rightarrow OH + H$	1.1×10^{-10}				[49]
$O^* + H_2O_2 \rightarrow H_2O + O_2$	5.2×10^{-10}				[49]
Neutrals					
$N + O_2 \rightarrow NO + O$	4.4×10^{-12}	1.0	3.27×10^3		[49]
$N + O_3 \rightarrow NO + O_2$	5×10^{-16}				[49]
$N + N + M \rightarrow N_2 + M$	3.9×10^{-33}			h	[11,49]
$N + O + M \rightarrow NO + M$	5.46×10^{-33}		-155		[49]
$N + OH \rightarrow NO + H$	4.7×10^{-11}				[49]
$N + NO \rightarrow N_2 + O$	3.14×10^{-11}				[49]
$N_2 + N_2 \rightarrow N + N + N_2$	4.289×10^{-10}		8.646×10^4	h	[49]

$N_2 + O_2 \rightarrow N + N + O_2$	4.289×10^{-10}		8.646×10^4	h	[49]
$N_2 + H_2O \rightarrow N + N + H_2O$	4.289×10^{-10}		8.646×10^4	h	[49]
$O + O_2 + M \rightarrow O_3 + M$	3.4×10^{-34}	-1.2			[49]
$O + H_2O \rightarrow OH + OH$	1.26×10^{-11}	1.3	8.605×10^3		[49]
$O + O_3 \rightarrow O_2 + O_2$	8×10^{-12}		2.06×10^3		[49]
$O + O + M \rightarrow O_2 + M$	1.18×10^{-33}			h	[49]
$O + O + M \rightarrow O_2^* + M$	9.88×10^{-35}			h	[19,27,49]
$O + H_2 \rightarrow OH + H$	1.6×10^{-11}		4.57×10^3	h	[49]
$O + H + He \rightarrow OH + He$	1.62×10^{-32}				[51]
$O + H + N_2 \rightarrow OH + N_2$	1.62×10^{-32}				[51]
$O + H + O_2 \rightarrow OH + O_2$	1.62×10^{-32}				[51]
$O + OH \rightarrow H + O_2$	3.5×10^{-11}				[49]
$O_2 + N_2 \rightarrow O + O + N_2$	5.167×10^{-10}		5.841×10^4	h	[49]
$O_2 + O_2 \rightarrow O + O + O_2$	5.167×10^{-10}		5.841×10^4	h	[49]
$O_2 + H_2O \rightarrow O + O + H_2O$	5.167×10^{-10}		5.841×10^4	h	[49]
$O_3 + M \rightarrow O_2 + O + M$	1.56×10^{-9}		1.149×10^4		[19]
$O_3 + H \rightarrow OH + O_2$	1.4×10^{-10}		480		[49]
$OH + OH \rightarrow O + H_2O$	1.03×10^{-12}	1.4	-200		[49]
$OH + H_2 \rightarrow H_2O + H$	7.7×10^{-12}		2.1×10^3	h	[49]
$OH + H \rightarrow O + H_2$	5.21×10^{-11}	0.67	518	h	[49]
$OH + OH + M \rightarrow H_2O_2 + M$	6.9×10^{-31}	-0.8			[49]
$OH + M \rightarrow O + H + M$	4×10^{-9}		5.0×10^4		[49]
$H + O_2 \rightarrow OH + O$	1.65×10^{-9}	-0.9	8.75×10^3		[49]
$H + H_2O \rightarrow H_2 + OH$	5.24×10^{-12}	1.9	9.265×10^3		[49]
$H + H + M \rightarrow H_2 + M$	4.8×10^{-33}			h	[29,49]
$H + H_2O_2 \rightarrow H_2O + OH$	4×10^{-11}		2×10^3		[49]
$H_2O_2 \rightarrow OH + OH$	1.96×10^{-9}	-4.86	2.68×10^4	h	[49,52]
Radiation					
$He(2^1P) \rightarrow He$	1.2×10^6			m	[53]
$He(2^3P) \rightarrow He(2^3S)$	1.02×10^7				[53]
$He(3P) \rightarrow He(2^3S)$	9.47×10^6			n	[53]
$He(3P) \rightarrow He(2^1S)$	1.34×10^7			o	[53]
$He(3S) \rightarrow He(2^3P)$	1.55×10^7			p	[53]
$He(3S) \rightarrow He(2^1P)$	1.83×10^7			q	[53]
$N_2^{**} \rightarrow N_2$	2×10^8			h	[54]
$N_2^{**} \rightarrow N_2^*$	2×10^8			h	[54]
$He_2^* \rightarrow He + He$	1×10^7			h	[55]
Photoionization					
$O_2 \rightarrow O_2^+ + e$	1.5×10^{-17}				[56]
$N_2 \rightarrow N_2^+ + e$	2.5×10^{-17}				[56]
$H_2O \rightarrow H_2O^+ + e$	2×10^{-17}				[56]
$O_2 \rightarrow e + O_2^+$	5×10^{-18}				[56]

Notes:

a) M represents a third body, which unless otherwise noted, has a density which is the sum of all species.
He* represents a He excited state. Reactions were included for the individual excited states $He(2^3S)$, $He(2^1S)$, $He(2^3P)$, $He(2^1P)$, He(3S), and He(3P)
$\sigma(\varepsilon)$ indicates that the rate coefficient is determined from the cross section and electron energy distribution obtained from solution of Boltzmann's equation.

b) Unless otherwise indicated, the rate coefficients are in Arrhenius form of $k = A(T_g/300\ K)^n \exp(-E/T_g)$. A has units of s^{-1} for first order, cm^3s^{-1} for second order, and cm^6s^{-1} for third order. T_g and E have units of K.

c) Superelastic cross section calculated by detailed balance.

d) For elastic collisions involving excited states, the cross section is estimated as 50 $Å^2$.

e) Rate coefficient based on analogous reaction in reference.

f) Arrhenius form depends on T_e: $k = AT_e^n \exp(-E/T_e)$. T_e and E are in eV.

g) Based on rate coefficient of $e + O_2 + M \rightarrow O_2^- + M$.

h) Estimated based on reference.

i) Based on rate coefficient of $He^* + He^* \rightarrow$ products.

j) Based on rate coefficient of $He(2^3S) + O_2 \rightarrow He + O_2^+ + e$.

k) Based on rate coefficient of $He^* + He_2^* \rightarrow$ products.

l) Based on quenching rate coefficient of $N_2(a`^1\Sigma)$.

m) Effective rate coefficient used to account for radiation trapping.

n) Rate coefficient based on $He(3^3P)$.

o) Rate coefficient based on $He(3^1P)$.

p) Rate coefficient based on $He(3^3S)$.

q) Rate coefficient based on $He(3^1S)$.

B.1 References

[1] S. F. Biagi, Biagi database v8.9 extracted from Fortran code Magboltz, (2010) http://www.lxcat.net/.

[2] J. Vlček, J. Phys. D Appl. Phys **22,** 623 (1989).

[3] L. Vriens, Phys. Lett. **8,** 260 (1964).

[4] R. Dorai, PhD Thesis, Modeling of atmospheric pressure plasma processing of gases and surfaces, (University of Illinois at Urbana-Champaign, 2002).

[5] Y. Itikawa, M. Hayashi, A. Ichimura, K. Onda, K. Sakimoto, K. Takayanagi, M. Nakamura, H. Nishimura and T. Takayanagi, J. Phys. Chem. Ref. Data **15,** 985 (1986).

[6] A. V. Phelps, Phelps database, http://www.lxcat.net/.

[7] W. L. Borst, Phys. Rev. A **5,** 648 (1972).

[8] D. C. Cartwright, S. Trajmar, A. Chutjian and W. Williams, Phys. Rev. A **16,** 1041 (1977).

[9] T. Tabata, T. Shirai, M. Sataka and H. Kubo, At. Data Nucl. Data Tables **92,** 375 (2006).

[10] S. Geltman, J. Quant. Spectrosc. Radiat. Transf. **13,** 601 (1973).

[11] I. A. Kossyi, A. Yu Kostinsky, A. A. Matveyev and V. P. Silakov, Plasma Sources Sci. Technol. **1,** 207 (1992).

[12] P. D. Borrow, J. Chem. Phys. **59,** 4922 (1973).

[13] Y. Itikawa and A. Ichimura, J. Phys. Chmical Ref. Data **19,** 637 (1990).

[14] R. R. Laher and F. R. Gilmore, J. Phys. Chem. Ref. Data **19,** 277 (1990).

[15] S. Matejcik, A. Kiendler, P. Cicman, J. Skalny, P. Stampfli, E. Illenberger, Y. Chu, A. Stamatovic and T. D. Märk, Plasma Sources Sci. Technol. **6,** 140 (1997).

[16] Y. Itikawa and N. Mason, J. Phys. Chem. Ref. Data **34,** 1 (2005).

[17] S. J. B. Corrigan, J. Chem. Phys. **43,** 4381 (1965).

[18] M. Hayashi, J. Phys. Colloq. **40,** C7/45 (1979).

[19] D. S. Stafford and M. J. Kushner, J. Appl. Phys. **96,** 2451 (2004).

[20] R. Deloche, P. Monchicourt, M. Cheret and F. Lambert, Phys. Rev. A **13,** 1140 (1976).

[21] K. Niemi, J. Waskoenig, N. Sadeghi, T. Gans and D. O'Connell, Plasma Sources Sci. Technol. **20,** 055005 (2011).

[22] A. W. Johnson and J. B. Gerardo, Phys. Rev. A **5,** 1410 (1972).

[23] M. A. Biondi, "Chapter 4", in Principles of Laser Plasmas (ed. Bekefi, G.) (Wiley, New

York, 1976).

[24] J. B. A. Mitchell, Phys. Rep. **186,** 215 (1990).

[25] B. R. Rowe, F. Vallée, J. L. Queffelec, J. C. Gomet and M. Morlais, J. Chem. Phys. **88,** 845 (1988).

[26] M. J. Jensen, R. C. Bilodeau, C. P. Safvan, K. Seiersen, L. H. Andersen, H. B. Pedersen and O. Heber, Astrophys. J. **543,** 764 (2000).

[27] B. F. Gordiets, C. M. Ferreira, V. L. Guerra, J. M. A. H. Loureiro, J. Nahorny, D. Pagnon, M. Touzeau and M. Vialle, IEEE Trans. Plasma Sci. **23,** 750 (1995).

[28] F. E. Niles, *Survey of two-body and three-body reaction-rate coefficients for the ionized stratosphere and mesosphere*, (1974).

[29] J. C. Person and D. O. Ham, Radiat. Phys. Chem. **31,** 1 (1988).

[30] H. W. Ellis, M. G. Thackston, E. W. McDaniel and E. A. Mason, At. Data Nucl. Data Tables **31,** 113 (1984).

[31] R. Johnsen, A. Chen and M. A. Biondi, J. Chem. Phys. **73,** 1717 (1980).

[32] V. G. Anicich, J. Phys. Chem. Ref. Data **22,** 1469 (1993).

[33] D. K. Bohme, N. G. Adams, M. Mosesman, D. B. Dunkin and E. E. Ferguson, J. Chem. Phys. **52,** 5094 (1970).

[34] H. Böhringer and F. Arnold, J. Chem. Phys. **77,** 5534 (1982).

[35] M. Capitelli, C. M. Ferrreira, B. F. Gordiets and A. I. Osipov, *Plasma Kinetics in Atmospheric Gases*, (Springer, Berlin, 2000).

[36] E. Tatarova, F. M. Dias, B. Gordiets and C. M. Ferreira, Plasma Sources Sci. Technol. **14,** 19 (2005).

[37] L. E. Khvorostovskaya and V. A. Yankovsky, Contrib. Plasma Phys. **31,** 71 (1991).

[38] S. Norberg, PhD Thesis, Modeling atmospheric pressure plasma jets: plasma dynamics, interaction with dielectric surfaces, liquid layers and cells, (University of Michigan, 2015).

[39] Y. Ikezoe, S. Matsuoka, M. Takebe and A. Viggiano, *Gas Phase Ion- Molecule Reaction Rate Constants Through 1986*, (Ion Reaction Research Group of the Mass Spectroscopy Society of Japan, Tokyo, Japan, 1987).

[40] A. Cenian, A. Chernukho and V. Borodin, Contrib. Plasma Phys. **35,** 273 (1995).

[41] O. Eichwald, M. Yousfi, A. Hennad and M. D. Benabdessadok, J. Appl. Phys. **82,** 4781 (1997).

[42] J. M. Pouvesle, A. Khacef, J. Stevefelt, H. Jahani, V. T. Gylys and C. B. Collins, J. Chem. Phys. **88,** 3061 (1988).

[43] F. Emmert, H. H. Angermann, R. Dux and H. Langhoff, J. Phys. D: Appl. Phys. **21,** 667 (1988).

[44] A. Kurnosov, A. Napartovich, S. Shnyrev and M. Cacciatore, J. Phys. Chem. A **111,** 7057 (2007).

[45] L. G. Piper, J. Chem. Phys. **87,** 1625 (1987).

[46] N. A. Popov, J. Phys. D: Appl. Phys. **44,** 285201 (2011).

[47] J. T. Herron, J. Phys. Chem. Ref. Data **28,** 1453 (1999).

[48] I. Shkurenkov, D. Burnette, W. R. Lempert and I. V Adamovich, Plasma Sources Sci. Technol. **23,** 065003 (2014).

[49] J. A. Manion et al., NIST Chemical Kinetics Database, (2010) https://kinetics.nist.gov (Standard Reference Database 17, Version 7.0, Release 1.6.8, Data Version 2015.09).

[50] R. Zellner, G. Wagner and B. Himme, J. Phys. Chem. **84,** 3196 (1980).

[51] R. K. Bera and R. J. Hanrahan, J. Appl. Phys. **62,** 2523 (1987).

[52] D. X. Liu, P. Bruggeman, F. Iza, M. Z. Rong and M. G. Kong, Plasma Sources Sci. Technol. **19,** 025018 (2010).

[53] Y. Ralchenko, A. Kramida, J. Reader and The NIST ASD Team, NIST Atomic Spectra Database, (2018) http://physics.nist.gov/asd (Version 5.6.1).

[54] L. W. Dotchin, E. L. Chupp and D. J. Pegg, J. Chem. Phys. **59,** 3960 (1973).

[55] S. Neeser, R. Tietz, M. Schulz and H. Langhoff, Zeitschrift für Phys. D Atoms, Mol. Clust. **31,** 61 (1994).

[56] J. W. Gallagher, C. E. Brion, J. A. R. Samson and P. W. Langhoff, J. Phys. Chem. Ref. Data **17,** 9 (1988).

Appendix C: Radiation Trapping Factors in He

A radiation trapping factor is the average number of times a photon is absorbed and reemitted before escaping a plasma. In this appendix, the radiation trapping factors for 58.4 nm photons emitted from He(2^1P) and of 53.7 nm photons emitted from He(3^1P) are calculated using the method of Holstein.[1] The assumptions intrinsic in this calculation include a uniform density of absorbers, steady state densities of emitters, and a plasma which is an infinitely long cylinder. The equations and values used therein are included in this section.

In order to calculate the trapping factors, first one must estimate the line broadening. The possible broadening processes in this system are natural broadening, resonance broadening, van der Waals broadening, Doppler broadening, and Stark broadening. Natural broadening is assumed to be negligible compared to the other possible sources and will not be discussed. Stark broadening in a plasma depends on the local electron density and will also be ignored.

The remaining broadening processes can be categorized into those which cause Lorentzian broadening (resonance, van der Waals) and Gaussian broadening (Doppler). First the broadening from each process was calculated. Then the radiation trapping factor was calculated for the total Lorentzian broadening and for the Gaussian broadening, and the lower trapping factor (typically from the process with more broadening) was used. Unfortunately, analytical solutions for the trapping factor using the Voigt profile, which would account for all processes, are not available, so the trapping factors for Lorentzian and Gaussian processes must be calculated separately.

In this appendix, the calculation is performed for emission from He(2^1P) in Sec. C.1. and repeated for emission from He(3^1P) in Sec. C.2. The results are summarized in Sec. C.3 and Table C.1.

C.1 Radiation Trapping of Emission from He(2^1P)

The radiative transition He(2^1P) $\rightarrow$ He has the following properties

$$\lambda = 58.434 \text{ nm}, \tag{C.1}$$

$$A = 1.789\times10^{9} \text{ s}^{-1}, \tag{C.2}$$

$$\Delta E = 21.218 \text{ eV}, \tag{C.3}$$

where λ is the wavelength of the emitted photon, A is the Einstein emission coefficient, and ΔE is the energy change of the transition (which is equal to the photon energy).

C.1.1 Broadening

C.1.1.1 Resonance Broadening

Resonance broadening occurs in transitions from states that are dipole-coupled to the ground state. Resonance broadening can be calculated based on Eq. 15 in Ref. [2] by Konjevic:

$$\Delta\lambda_{1/2}^{R} = (1.63\times10^{-13}\text{cm})\left(\frac{g_i}{g_k}\right)^{1/2}\lambda^2\lambda_R f_R N, \tag{C.4}$$

where g_i and g_k are the statistical weights of the lower and upper states, λ_R and f_R are the wavelength and oscillator strength of the resonant transition from the upper state to ground. In this case the transition of interest is the same as the resonant transition (He(2^1P) $\rightarrow$ He). N is the density of the ground state. Inserting the values for this transition,

$$\Delta\lambda_{1/2}^{R} = (1.63\times10^{-13}\text{cm})\left(\frac{1}{3}\right)^{1/2}\left(5.84\times10^{-6}\text{cm}\right)^3(0.276)\left(6.43\times10^{18}\text{cm}^{-3}\right), \tag{C.5}$$

$$\Delta\lambda_{1/2}^{R} = 3.33\times10^{-11}\text{cm} = 0.000333 \text{ nm}, \tag{C.6}$$

C.1.1.2 van der Waals Broadening

van der Waals broadening can be calculated based on Eqs. 12-16 in Ref. [3] by Muñoz *et al*. or Eqs. 16-20 in Ref. [2] by Konjevic:

$$\Delta\lambda_{1/2}^{W} = \left(8.18\times10^{-12}\,\frac{\mathrm{cm}^{4/5}\mathrm{amu}^{3/10}}{\mathrm{a}_0{}^{4/5}\mathrm{K}^{3/10}}\right)\lambda^2\left(\alpha<\bar{R}^2>\right)^{2/5}\left(\frac{T}{\mu}\right)^{3/10} N\,, \tag{C.7}$$

where α is the polarizability and μ is the reduced mass of the emitter and perturber. $<\bar{R}^2>$ is the difference of the square radii between the upper and lower states given by:

$$<\bar{R}^2>=<\bar{R}_U^2>-<\bar{R}_L^2>, \tag{C.8}$$

$$<\bar{R}_i^2>=\frac{1}{2}n^{*2}_i\left[5n^{*2}_i+1-3l_i(l_i+1)\right], \tag{C.9}$$

$$n^{*2}_i=\frac{E_H}{E_{IP}-E_i}, \tag{C.10}$$

where l_i is the orbital quantum number of state i, E_H is the ionization potential of H (13.6 eV), E_{IP} is the ionization potential of ground state He, and E_i is the energy of state i.

For the upper state, He(2^1P),

$$n^{*2}_U=\frac{13.6\text{ eV}}{24.6\text{ eV}-21.2\text{ eV}}=4.00, \tag{C.11}$$

$$<\bar{R}_U^2>=\frac{1}{2}(4.00)\left[5(4.00)+1-3(1)(1+1)\right]=30.0, \tag{C.12}$$

and the lower state, ground state He

$$n^{*2}_L=\frac{13.6\text{ eV}}{24.6\text{ eV}}=0.553, \tag{C.13}$$

$$<\bar{R}_L^2>=\frac{1}{2}(0.553)\left[5(0.553)+1-3(0)(1)\right]=1.04. \tag{C.14}$$

Therefore for this transition, $<\bar{R}^2>=28.96a_0^2$. The polarizability of He is $\alpha=1.38a_0^3=2.05\times10^{-25}$ cm^3.[4] Inserting the values into Eq. C.7:

$$\Delta\lambda_{1/2}^W=\left(8.18\times10^{-12}\,\frac{\text{cm}^{4/5}\text{amu}^{3/10}}{\text{a}_0{}^{4/5}\text{K}^{3/10}}\right)\lambda^2\left(\left(2.05\times10^{-25}\ \text{cm}^3\right)\left(28.96a_0^2\right)\right)^{2/5}\left(\frac{T}{\mu}\right)^{3/10}N_a\,, \quad \text{(C.15)}$$

$$\Delta\lambda_{1/2}^W=\left(4.19\times10^{-21}\,\frac{\text{cm}^2\text{amu}^{3/10}}{\text{K}^{3/10}}\right)\lambda^2\left(\frac{T}{\mu}\right)^{3/10}N_a\,, \quad \text{(C.16)}$$

$$\Delta\lambda_{1/2}^W=\left(4.19\times10^{-21}\,\frac{\text{cm}^2\text{amu}^{3/10}}{\text{K}^{3/10}}\right)\left(58.4\times10^{-7}\,\text{cm}\right)^2\left(\frac{300\ \text{K}}{2\ \text{amu}}\right)^{3/10}\left(6.43\times10^{18}\ \text{cm}^{-3}\right), \quad \text{(C.17)}$$

$$\Delta\lambda_{1/2}^W=4.13\times10^{-12}\ \text{cm}=0.0000413\ \text{nm}\,. \quad \text{(C.18)}$$

The sum of the pressure broadening processes, $\Delta\lambda_{1/2}^W+\Delta\lambda_{1/2}^R=3.74\times10^{-11}$ cm.

C.1.1.3 Doppler Broadening

Doppler broadening can be estimated by

$$\Delta\lambda_{1/2}^D=\left(7.16\times10^{-7}\,\text{amu}^{1/2}\text{K}^{-1/2}\right)\lambda\left(\frac{T}{M}\right)^{1/2}, \quad \text{(C.19)}$$

where T is the gas temperature, M is the atomic mass, and λ is the wavelength of the emitted photon.[5] For this transition in He at room temperature,

$$\Delta\lambda_{1/2}^D=\left(7.16\times10^{-7}\ \text{amu}^{1/2}\text{K}^{-1/2}\right)\left(58.4\ \text{nm}\right)\left(\frac{300\ \text{K}}{4\ \text{amu}}\right)^{1/2}, \quad \text{(C.20)}$$

$$\Delta\lambda_{1/2}^D=0.000362\ \text{nm}\,. \quad \text{(C.21)}$$

C.1.2 Pressure Trapping Factor of Emission from He(2^1P)

To convert broadening to absorption, use Holstein's argument from Eqs. 2.4 and 2.5. in Ref. [1].

$$k(\nu) = \frac{k_0}{1 + \left[4\pi(\nu_0 - \nu)/\Delta\nu_p \right]}, \tag{C.22}$$

where $k(\nu)$ is the absorption profile as a function of photon frequency. $\Delta\nu_p$ is the pressure broadening frequency. First we must combine Eqs. 2.4 and 2.5 and solve for k_0

$$\int_0^\infty \frac{k_0}{1 + \left[4\pi(\nu_0 - \nu)/\Delta\nu_p \right]} d\nu = \frac{\lambda^2}{8\pi} \frac{g_2}{g_1} NA, \tag{C.23}$$

where N is density of absorbers and A is the Einstein emission coefficient.

$$\frac{k_0 \Delta\nu_p}{4\pi} \left(1 + \frac{\pi}{2} \right) = \frac{\lambda^2}{8\pi} \frac{g_2}{g_1} NA, \tag{C.24}$$

$$k_0 = \frac{1}{2 + \pi} \frac{\lambda^2}{\Delta\nu_p} \frac{g_2}{g_1} NA, \tag{C.25}$$

$$k_0 = (0.389) \frac{\left(58.4 \times 10^{-7} \text{ cm} \right)^2}{\Delta\nu_p} (3) \left(6.43 \times 10^{18} \text{ cm}^{-3} \right) \left(1.79 \times 10^9 s^{-1} \right), \tag{C.26}$$

$$k_0 = \frac{4.58 \times 10^{17} \text{ cm}^{-1}\text{s}^{-1}}{\Delta\nu_p}. \tag{C.27}$$

For a total pressure broadening of 0.000374 nm, $\Delta\upsilon_p = 3.29 \times 10^{10}$ Hz. Inserting this into Eq. C.27,

$$k_0 = 1.4 \times 10^7 \text{cm}^{-1}. \tag{C.28}$$

The system of equations presented by Holstein [1] was solved analytically by van Trigt [6] for an infinite cylinder. The paper by van Trigt presents a solution for $\tilde{A}/A$ (the inverse of the trapping factor). We will use the infinite cylinder solution of the eigenvalues to determine the trapping factor. Beginning with Eq. 5 from Ref. [6]:

$$\frac{\tilde{A}}{A} = \frac{1 - \alpha}{1 + \alpha} \frac{\pi D^{1-\alpha}}{\sin(\frac{1}{2}\alpha\pi)} \frac{\lambda_{j,i}^{-1}(\alpha)}{(k_0 R)^\alpha}, \tag{C.29}$$

where for a Lorentz profile, $D = \pi^{-1}$ and $\alpha = ½$. R is the radius of the plasma cylinder. λ is the eigenvalue, which is in Table I in Ref. [6]. So for a Lorentz profile, the equation above becomes

$$\frac{\tilde{A}}{A} = \frac{1}{3}\frac{\pi\left(\frac{1}{\pi}\right)^{1/2}}{\sin(\pi/4)}\frac{\lambda_{j,i}^{-1}(\alpha)}{(k_0 R)^{1/2}}, \tag{C.30}$$

$$\frac{\tilde{A}}{A} = \left[\frac{\sqrt{2\pi}}{3}\lambda_{j,i}^{-1}\left(\tfrac{1}{2}\right)\right]\frac{1}{\sqrt{k_0 R}}, \tag{C.31}$$

where the factor in the brackets is available in Table I in Ref. [6]. In this case, we will consider only the zeroth order term,

$$\frac{\tilde{A}}{A} = \frac{1.123}{\sqrt{k_0 R}}. \tag{C.32}$$

For 1 mm radius and pressure broadening,

$$\frac{\tilde{A}}{A} = \frac{1.123}{\sqrt{(1.4\times10^{7}\ \text{cm}^{-1})(10^{-1}\ \text{cm})}} = 0.000949, \tag{C.33}$$

$$\text{trapping factor} = 1050. \tag{C.34}$$

C.1.3 Doppler Trapping Factor of Emission from He(2^1P)

Because Doppler broadening is typically Gaussian, the absorption coefficient takes the form

$$k(\nu) = k_0 \exp\left(-\left(\frac{\nu-\nu_0}{\nu_0}\right)^2\left(\frac{c}{\nu_0}\right)^2\right) \tag{C.35}$$

where c is the speed of light and v_0 is the gas velocity. To convert broadening to absorption coefficient (k_0), use Holstein's argument from Eqs. 2.9 and 2.10. in Ref. [1].

$$v_0 = \left(\frac{2RT}{M}\right)^{1/2}, \tag{C.36}$$

where R is the ideal gas constant, T is the gas temperature, and M is the atomic mass.

$$v_0 = \left(\frac{2(2.314 \text{ kg m}^2\text{s}^{-2}\text{K}^{-1}\text{mol}^{-1})(300 \text{ K})}{4.003\times10^{-3} \text{ kg mol}^{-1}} \right)^{1/2}, \tag{C.37}$$

$$v_0 = 588.9 \text{ m/s} = 5.89\times10^{4} \text{ cm/s}, \tag{C.38}$$

and 2.10

$$k_0 = \frac{\lambda^3 N}{8\pi} \frac{g_2}{g_1} \frac{A}{\pi^{1/2} v_0}, \tag{C.39}$$

where g_1 and g_2 are the statistical weight of the lower and upper states.

$$k_0 = \frac{\left(5.84\times10^{-6}\text{cm}\right)^3 (6.43\times10^{18}\text{cm}^{-3})}{8\pi} \frac{3}{1} \frac{(1.79\times10^{9}\text{s}^{-1})}{\pi^{1/2}(5.89\times10^{4} \text{ cm/s})}, \tag{C.40}$$

$$k_0 = 2.62\times10^{6} \text{ cm}^{-1}. \tag{C.41}$$

For a Gaussian profile, Eq. 5b from van Trigt applies.[6]

$$\frac{\tilde{A}}{A} = \frac{\pi}{4} \frac{\lambda_{j,i}^{-1}(1)}{k_0 R} \left(\ln\left(\frac{k_0 R}{\sqrt{\pi}} \right) \right)^{-1/2}. \tag{C.42}$$

where R is the radius of the plasma. In this case, we will consider only the zeroth order term.

$$\frac{\tilde{A}}{A} = \frac{1.567}{k_0 R} \left(\ln\left(\frac{k_0 R}{\sqrt{\pi}} \right) \right)^{-1/2}, \tag{C.43}$$

$$\frac{\tilde{A}}{A} = \frac{1.567}{\left(2.62\times10^{6} \text{ cm}^{-1}\right)\left(10^{-1} \text{ cm}\right)} \left(\ln\left(\frac{\left(2.62\times10^{6} \text{ cm}^{-1}\right)\left(10^{-1} \text{ cm}\right)}{\sqrt{\pi}} \right) \right)^{-1/2}, \tag{C.44}$$

$$\frac{\tilde{A}}{A} = 1.73\times10^{-6}, \tag{C.45}$$

$$\text{trapping factor} = 5.77\times10^{5}. \tag{C.46}$$

C.2 Radiation Trapping of He(3^1P)

The radiative transition He(3^1P) $\rightarrow$ He has the following properties

$$\lambda = 53.703 \text{ nm}, \tag{C.47}$$

$$A = 5.663\times10^{8} \text{ s}^{-1}, \tag{C.48}$$

$$\Delta E = 23.087 \text{ eV}. \tag{C.49}$$

C.2.1 Broadening

C.2.1.1 Resonance Broadening

Applying Eq. C.4 to this transition,

$$\Delta\lambda_{1/2}^{R} = (1.63\times10^{-13}\text{cm})\left(\frac{1}{3}\right)^{1/2}\left(5.37\times10^{-6}\text{cm}\right)^{3}\left(0.0734\right)\left(6.43\times10^{18}\text{cm}^{-3}\right), \tag{C.50}$$

$$\Delta\lambda_{1/2}^{R} = 6.88\times10^{-12}\text{cm} = 0.0000688 \text{ nm}. \tag{C.51}$$

C.2.1.2 van der Waals Broadening

Using Eqs. C.8-C.10 to solve for $<\bar{R}^2>$. First for the upper state, He(3^1P),

$$n^{*2}_{U} = \frac{13.6 \text{ eV}}{24.6 \text{ eV} - 23.09 \text{ eV}} = 8.831, \tag{C.52}$$

$$<\bar{R}^2_U> = \frac{1}{2}(8.831)\left[5(8.831)+1-3(1)(1+1)\right] = 172.9, \tag{C.53}$$

and the lower state, ground state He,

$$n^{*2}_{L} = \frac{13.6\text{eV}}{24.6\text{eV}} = 0.553, \tag{C.54}$$

$$<\bar{R}^2_L> = \frac{1}{2}(0.553)\left[5(0.553)+1-3(0)(1)\right] = 1.04, \tag{C.55}$$

Therefore for this transition, $<\bar{R}^2> = 171.9a_0^2$. The polarizability of He is $\alpha = 1.38a_0^3 = 2.05\times10^{-25}$ cm^3 .[4] Inserting the values into Eq. C.7,

$$\Delta\lambda_{1/2}^{W} = \left(8.18\times10^{-12}\,\frac{\text{cm}^{4/5}\text{amu}^{3/10}}{\text{a}_0{}^{4/5}\text{K}^{3/10}}\right)\lambda^2\left(\left(2.05\times10^{-25}\ \text{cm}^3\right)\left(171.9a_0^2\right)\right)^{2/5}\left(\frac{T}{\mu}\right)^{3/10} N\,, \quad \text{(C.56)}$$

$$\Delta\lambda_{1/2}^{W} = \left(8.54\times10^{-21}\,\frac{\text{cm}^2\text{amu}^{3/10}}{\text{K}^{3/10}}\right)\lambda^2\left(\frac{T}{\mu}\right)^{3/10} N\,, \quad \text{(C.57)}$$

$$\Delta\lambda_{1/2}^{W} = \left(8.54\times10^{-21}\,\frac{\text{cm}^2\text{amu}^{3/10}}{\text{K}^{3/10}}\right)\left(53.7\times10^{-7}\,\text{cm}\right)^2\left(\frac{300\ \text{K}}{2\ \text{amu}}\right)^{3/10}\left(6.43\times10^{18}\ \text{cm}^{-3}\right), \quad \text{(C.58)}$$

$$\Delta\lambda_{1/2}^{W} = 7.12\times10^{-12}\ \text{cm} = 0.0000712\ \text{nm}\,. \quad \text{(C.59)}$$

The sum of the pressure broadening processes, $\Delta\lambda_{1/2}^{W} + \Delta\lambda_{1/2}^{R} = 1.40\times10^{-11}\ \text{cm}$.

C.2.1.3 Doppler Broadening

From Eq. C.19 for this transition,

$$\Delta\lambda_{1/2}^{D} = \left(7.16\times10^{-7}\ \text{amu}^{1/2}\text{K}^{-1/2}\right)\left(53.7\ \text{nm}\right)\left(\frac{300\ \text{K}}{4\ \text{amu}}\right)^{1/2}, \quad \text{(C.60)}$$

$$\Delta\lambda_{1/2}^{D} = 0.000333\ \text{nm}\,. \quad \text{(C.61)}$$

C.2.2 Pressure Trapping Factor of Emission from He(3^1P)

Beginning with Eq. C.25,

$$k_0 = \frac{1}{2+\pi}\,\frac{\lambda^2}{\Delta\nu_p}\,\frac{g_2}{g_1}\,NA, \quad \text{(C.62)}$$

$$k_0 = \left(0.389\right)\frac{\left(53.7\times10^{-7}\ \text{cm}\right)^2}{\Delta\nu_p}\left(3\right)\left(6.4\times10^{18}\ \text{cm}^{-3}\right)\left(5.66\times10^{8}s^{-1}\right), \quad \text{(C.63)}$$

$$k_0 = \frac{1.22\times10^{17}\ \text{cm}^{-1}\text{s}^{-1}}{\Delta\nu_p}\,. \quad \text{(C.64)}$$

For a total pressure broadening of 0.000140 nm, $\Delta\upsilon_p = 1.46\times10^{10}$ Hz. Inserting this into Eq. C.64,

$$k_0 = 8.36\times10^{6}\,\mathrm{cm}^{-1}. \tag{C.65}$$

Eq. C.32 above can be used to calculate the trapping factor,

$$\frac{\tilde{A}}{A} = \frac{1.123}{\sqrt{k_0 R}}. \tag{C.66}$$

For 1 mm radius,

$$\frac{\tilde{A}}{A} = \frac{1.123}{\sqrt{(8.4\times10^{6}\ \mathrm{cm}^{-1})(10^{-1}\ \mathrm{cm})}} = 0.00123, \tag{C.67}$$

$$\text{trapping factor} = 820. \tag{C.68}$$

C.2.3 Doppler Trapping Factor of Emission from He(3^1P)

Beginning with Eq. C.39,

$$k_0 = \frac{\lambda_0^3 N}{8\pi}\frac{g_2}{g_1}\frac{A}{\pi^{1/2}v_0}, \tag{C.69}$$

$$k_0 = \frac{\left(5.37\times10^{-6}\mathrm{cm}\right)^3 (6.43\times10^{18}\mathrm{cm}^{-3})}{8\pi}\frac{3}{1}\frac{(5.66\times10^{8}\mathrm{s}^{-1})}{\pi^{1/2}(5.89\times10^{4}\ \mathrm{cm/s})}, \tag{C.70}$$

$$k_0 = 6.44\times10^{5}\ \mathrm{cm}^{-1}. \tag{C.71}$$

Applying the values for this transition to Eq. C.43

$$\frac{\tilde{A}}{A} = \frac{1.567}{\left(6.44\times10^{5}\ \mathrm{cm}^{-1}\right)\left(10^{-1}\ \mathrm{cm}\right)}\left(\ln\left(\frac{\left(6.44\times10^{5}\ \mathrm{cm}^{-1}\right)\left(10^{-1}\ \mathrm{cm}\right)}{\sqrt{\pi}}\right)\right)^{-1/2}, \tag{C.72}$$

$$\frac{\tilde{A}}{A} = 7.51\times10^{-6}, \tag{C.73}$$

$$\text{trapping factor} = 1.33\times10^{5}. \tag{C.74}$$

C.3 Summary

The results of the calculation in this appendix are summarized in Table C.1. The smaller trapping factors dominate because they represent broadening processes which allow the photons to escape. The radiation trapping factors calculated here are 1050 and 820 for He(2^1P) and He(3^1P) emission. These correspond to effective emission coefficients ($\tilde{A}$) of 1.7×10^6 and 6.9×10^5 s^{-1}. The trapping factors used in the model were reduced by approximately 20% in order to account for the fact that the plasma is not an infinite cylinder as the ionization wave propagates. This finite cylinder allows more photons to escape the plasma volume because of an increased surface area. The effective emission coefficients ($\tilde{A}$) used in the model were 2.0×10^6 and 9.1×10^5 s^{-1} for He(2^1P) and He(3^1P) emission.

C.4 Tables

Table C.1 Summary of Radiation Trapping.

Transition	Broadening (nm)		Trapping		Total Trapping
	$\Delta\lambda_{Doppler}$	$\Delta\lambda_{Pressure}$	Doppler	Pressure	
$He(2^1P) \rightarrow He$	3.62×10^{-4}	3.74×10^{-4}	5.77×10^{5}	1050	1050
$He(3^1P) \rightarrow He$	3.33×10^{-4}	1.40×10^{-4}	1.33×10^{5}	820	820

C.5 References

[1] T. Holstein, Phys. Rev. **72,** 1212 (1947).

[2] N. Konjevic, Phys. Rep. **316,** 339 (1999).

[3] J. Muñoz, M. S. Dimitrijević, C. Yubero and M. D. Calzada, Spectrochim. Acta Part B At. Spectrosc. **64,** 167 (2009).

[4] M. A. Thomas and J. W. Humberston, J. Phys. B At. Mol. Phys. **5,** L229 (1972).

[5] W. C. Martin and W. L. Wiese, "Atomic, Molecular, and Optical Physics Handbook (version 2.2)", (2002) https://www.nist.gov/pml/atomic-spectroscopy-compendium-basic-ideas-notation-data-and-formulas.

[6] C. van Trigt, Phys. Rev. A - At. Mol. Opt. Phys. **13,** 726 (1976).